frontiers | Research Topics

Interactions between groundwater and human communities: Perspectives on the resources, environments, threats and sustainable development

Edited by
Yong Xiao, Venkatramanan Senapathi, Lichun Wang, Chengcheng Li and Haiyan Liu

Published in
Frontiers in Environmental Science

ISSN 1664-8714
ISBN 978-2-8325-2667-5
DOI 10.3389/978-2-8325-2667-5

About Frontiers

Frontiers is more than just an open access publisher of scholarly articles: it is a pioneering approach to the world of academia, radically improving the way scholarly research is managed. The grand vision of Frontiers is a world where all people have an equal opportunity to seek, share and generate knowledge. Frontiers provides immediate and permanent online open access to all its publications, but this alone is not enough to realize our grand goals.

Frontiers journal series

The Frontiers journal series is a multi-tier and interdisciplinary set of open-access, online journals, promising a paradigm shift from the current review, selection and dissemination processes in academic publishing. All Frontiers journals are driven by researchers for researchers; therefore, they constitute a service to the scholarly community. At the same time, the *Frontiers journal series* operates on a revolutionary invention, the tiered publishing system, initially addressing specific communities of scholars, and gradually climbing up to broader public understanding, thus serving the interests of the lay society, too.

Dedication to quality

Each Frontiers article is a landmark of the highest quality, thanks to genuinely collaborative interactions between authors and review editors, who include some of the world's best academicians. Research must be certified by peers before entering a stream of knowledge that may eventually reach the public - and shape society; therefore, Frontiers only applies the most rigorous and unbiased reviews. Frontiers revolutionizes research publishing by freely delivering the most outstanding research, evaluated with no bias from both the academic and social point of view. By applying the most advanced information technologies, Frontiers is catapulting scholarly publishing into a new generation.

What are Frontiers Research Topics?

Frontiers Research Topics are very popular trademarks of the *Frontiers journals series*: they are collections of at least ten articles, all centered on a particular subject. With their unique mix of varied contributions from Original Research to Review Articles, Frontiers Research Topics unify the most influential researchers, the latest key findings and historical advances in a hot research area.

Find out more on how to host your own Frontiers Research Topic or contribute to one as an author by contacting the Frontiers editorial office: frontiersin.org/about/contact

Interactions between groundwater and human communities: Perspectives on the resources, environments, threats and sustainable development

Topic editors

Yong Xiao — Southwest Jiaotong University, China
Venkatramanan Senapathi — Alagappa University, India
Lichun Wang — Tianjin University, China
Chengcheng Li — China University of Geosciences Wuhan, China
Haiyan Liu — East China University of Technology, China

Citation

Xiao, Y., Senapathi, V., Wang, L., Li, C., Liu, H., eds. (2023). *Interactions between groundwater and human communities: Perspectives on the resources, environments, threats and sustainable development*. Lausanne: Frontiers Media SA. doi: 10.3389/978-2-8325-2667-5

Table of contents

frontiers | Frontiers in Environmental Science

TYPE Editorial
PUBLISHED 26 May 2023
DOI 10.3389/fenvs.2023.1221837

OPEN ACCESS

EDITED AND REVIEWED BY
Peiyue Li,
Chang'an University, China

*CORRESPONDENCE
Yong Xiao,
xiaoyong@swjtu.edu.cn

RECEIVED 13 May 2023
ACCEPTED 19 May 2023
PUBLISHED 26 May 2023

CITATION
Xiao Y, Liu H, Senapathi V, Wang L and Li C (2023), Editorial: Interactions between groundwater and human communities: perspectives on the resources, environments, threats and sustainable development.
Front. Environ. Sci. 11:1221837.
doi: 10.3389/fenvs.2023.1221837

Editorial: Interactions between groundwater and human communities: perspectives on the resources, environments, threats and sustainable development

Yong Xiao[1]*, Haiyan Liu[2], Venkatramanan Senapathi[3], Lichun Wang[4] and Chengcheng Li[5]

[1]Faculty of Geosciences and Environmental Engineering, Southwest Jiaotong University, Chengdu, China, [2]School of Water Resources and Environmental Engineering, East China University of Technology, Nanchang, China, [3]Department of Disaster Management, Alagappa University, Karaikudi, India, [4]Institute of Surface-Earth System Science, School of Earth System Science, Tianjin University, Tianjin, China, [5]School of Environmental Studies, China University of Geosciences, Wuhan, China

KEYWORDS

groundwater resources, hydrogeology, hydrochemistry, groundwater contamination, water supply, anthropogenic disturbance, groundwater system, water geohazards

Editorial on the Research Topic
Interactions between groundwater and human communities: perspectives on the resources, environments, threats and sustainable development

Groundwater is essential for human societal development, eco-environment protection and maintenance, surface and underground geological processes, and substance circulation among Earth's geospheres (i.e., hydrosphere, lithosphere, and biosphere) (Xiao et al., 2022b; Yang et al., 2023). With the rapid increase of human demand and the enhancement of technical procedures, human activities that affect the hydrosphere have expanded from near the surface (along rivers or surrounding lakes) to much wider regions over the past thousands of years (Luo et al., 2021; Stigter et al., 2023). This will inevitably intensify external disturbances on groundwater systems and their hydrogeological processes, which may destroy the functions and values of groundwater for nature and human communities and induce/aggravate water-related geological disasters (Xiao et al., 2022c; Qu et al., 2022). Deeply understanding interactions between groundwater systems and human societies is vital to achieve sustainable groundwater exploitation, protecting groundwater-dependent eco-environmental systems and controlling geohazard emergence.

Over recent decades, the diversity of interactions between human societies and groundwater systems has been unprecedented (Mádl-Szőnyi et al., 2023). Aquifers disturbed by intense human activities, such as the sedimentary aquifers in the North China Plain and arid north-western China, have experienced severe groundwater supply crises (e.g., depletion and deterioration), which, in turn, affects human communities and ecological environments (Qiu, 2010; Xiao et al., 2022a). Additionally, more and more groundwater-related challenges are being encountered by human communities (Li et al., 2019). Significant new knowledge, management experiences, and their disseminations can be

expected to inform understanding of relationships among groundwater, eco-environmental systems, and human societal development.

In this context, this Research Topic encouraged the academic community to contribute original outputs for sustainable groundwater development from the perspectives of water quantity, quality, and eco-environmental aspects. A total of 17 articles were collected on the interactions between groundwater and human communities. Several articles reported the water chemical status on the surface and subsurface water body in various land use areas, such as agricultural, industrial, and urban lands, and mining areas, and concluded that human activities have already widely influenced and even changed the hydrochemical features of natural water bodies distributed in and around the human community regions. Integrated approaches that include the combination of the self-organizing map and entropy-based weight determining method, *etc.*, were proposed and tried to improve the accuracy of water quality assessment. Sediment investigation and groundwater hydrochemical and isotopic tools were combined in an article to better illustrate the flow rate, renewable capability, residence time, and hydrochemical availability of groundwater in alluvial fan plains. Several articles discussed the influencing mechanisms of human activities, such as urbanization, agricultural activities, mining practices, and drainages, on groundwater circulation and hydrochemistry. Three researches explored the transport, transfer, and influencing factors of pollutants into water bodies from the micro-scale perspective. An *in situ* remediation technology, namely, the permeable reactive barrier, was improved and evaluated in terms of reaction materials for better removing heavy metal pollutants in groundwater.

In addition to the availability of groundwater quantity and quality, the secondary geological disasters related to water were reported in this Research Topic. Guo et al. combined theoretical model analysis, geotechnical tests, soil deformation, and groundwater level monitoring to get insights into the mechanism and related affecting factors of land subsidence and pointed out that the huge pumping groundwater quantity for agricultural irrigation is responsible for the land subsidence in the North China Plain. Liu et al. studied the behavior of deep clayey soil during the compression and consolidation process, and revealed the occurring mechanism of land subsidence from a micro perspective after great groundwater pumping. Gao et al. examined the role of various factors including geological conditions, earthquakes, and water for landslide occurrence in mountainous regions and indicated groundwater quantity induced into the slide body by rainfall plays an essential role in the occurrence of landslides.

In addition, some scholars explored the ways to improve the simulation and understanding of groundwater in special hydrogeological conditions. For example, Zhou et al. tried to modify the source code of SWAT to realize the simulation of sinkholes in karst groundwater modeling. Wu et al. discussed the impact of a horizontal low-k layer within a homogeneous aquifer on saltwater up-coning using the numerical approach and provided a simple tool for developing natural and artificial barriers to prevent saltwater up-coning in coastal areas and enhance the pumping efficiency. Furthermore, an article by Li et al. constructed index systems for evaluating the dynamic relationship between water resources and new urbanization, and proposed useful suggestions for coordinating the development of water resources and urbanization.

The articles collected in this Research Topic will undoubtedly improve the understanding of interactions between human communities and the hydrosphere, especially the underground hydrosphere, for the academic community from various aspects. We hope and believe this Research Topic could inspire further research in hydrology earth science and benefit the sustainable development of Earth's hydrosphere and the human community.

Author contributions

All authors listed have made a substantial, direct, and intellectual contribution to the work and approved it for publication.

Funding

This Research Topic was supported by the Natural Science Foundation of China (42007183), the Natural Science Foundation of Sichuan Province (grant number 2022NSFSC1084), the Fundamental Research Funds for the Central Universities (2682022ZTPY002, 2682022ZTPY088), and the Student Research Training Program of Southwest Jiaotong University (2022174).

Acknowledgments

The authors greatly appreciate the time and effort of the reviewers, editors, and authors who contributed valuable insights and suggestions to these papers in this Research Topic. They specially thank the Chief Editor and Associate Editors of Frontiers in Environmental Science.

Conflict of interest

The authors declare that the research was conducted in the absence of any commercial or financial relationships that could be construed as a potential conflict of interest.

Publisher's note

References

Li, C., Gao, X., Liu, Y., and Wang, Y. (2019). Impact of anthropogenic activities on the enrichment of fluoride and salinity in groundwater in the Yuncheng Basin constrained by Cl/Br ratio, $\delta^{18}O$, $\delta^{2}H$, $\delta^{13}C$ and $\delta^{7}Li$ isotopes. *J. Hydrology* 579, 124211. doi:10.1016/j.jhydrol.2019.124211

Luo, Y., Xiao, Y., Hao, Q., Zhang, Y., Zhao, Z., Wang, S., et al. (2021). Groundwater geochemical signatures and implication for sustainable development in a typical endorheic watershed on Tibetan plateau. *Environ. Sci. Pollut. Res.* 28 (35), 48312–48329. doi:10.1007/s11356-021-14018-x

Mádl-Szőnyi, J., Batelaan, O., Molson, J., Verweij, H., Jiang, X.-W., Carrillo-Rivera, J. J., et al. (2023). Regional groundwater flow and the future of hydrogeology: Evolving concepts and communication. *Hydrogeology J.* 31, 23–26. doi:10.1007/s10040-022-02577-3

Qiu, J. (2010). China faces up to groundwater crisis. *Nature* 466 (7304), 308. doi:10.1038/466308a

Qu, S., Duan, L., Shi, Z., Liang, X., Lv, S., Wang, G., et al. (2022). Hydrochemical assessments and driving forces of groundwater quality and potential health risks of sulfate in a coalfield, northern Ordos Basin, China. *Sci. Total Environ.* 835, 155519. doi:10.1016/j.scitotenv.2022.155519

Stigter, T. Y., Miller, J., and Re, V. (2023). Groundwater and climate change: Threats and opportunities. *Hydrogeology J.* 31, 7–10. doi:10.1007/s10040-022-02554-w

Xiao, Y., Hao, Q., Zhang, Y., Zhu, Y., Yin, S., Qin, L., et al. (2022a). Investigating sources, driving forces and potential health risks of nitrate and fluoride in groundwater of a typical alluvial fan plain. *Sci. Total Environ.* 802, 149909. doi:10.1016/j.scitotenv.2021.149909

Xiao, Y., Liu, K., Hao, Q., Li, Y., Xiao, D., and Zhang, Y. (2022b). Occurrence, controlling factors and health hazards of fluoride-enriched groundwater in the lower flood plain of Yellow River, Northern China. *Expo. Health* 14. doi:10.1007/s12403-021-00452-2

Xiao, Y., Liu, K., Hao, Q., Xiao, D., Zhu, Y., Yin, S., et al. (2022c). Hydrogeochemical insights into the signatures, Genesis and sustainable perspective of nitrate enriched groundwater in the piedmont of Hutuo watershed, China. *CATENA* 212, 106020. doi:10.1016/j.catena.2022.106020

Yang, H., Xiao, Y., Hao, Q., Wang, L., Zhang, Y., Liu, K., et al. (2023). Geochemical characteristics, mechanisms and suitability for sustainable municipal and agricultural water supply of confined groundwater in central North China Plain. *Urban Clim.* 49, 101459. doi:10.1016/j.uclim.2023.101459

frontiers | Frontiers in Environmental Science

ORIGINAL RESEARCH
published: 24 May 2022
doi: 10.3389/fenvs.2022.913542

Analysis of Groundwater Chemical Characteristics and Spatiotemporal Evolution Trends of Influencing Factors in Southern Beijing Plain

*Chen Li, Bao-Hui Men and Shi-Yang Yin**

College of Water Resources and Hydropower Engineering, North China Electric Power University, Beijing, China

During the rapid urbanisation of Beijing in the past two decades, the original natural underlying surface has been changed, and the groundwater recharge and discharge processes had undergone great changes. Therefore, whether these natural and human factors affect the evolution of groundwater chemical composition, and how these influences evolve, need to be studied urgently. In this study, the Daxing District was taken as a typical area to understand the evolution rules of the chemical characteristics of shallow groundwater in the plain areas of Beijing. By collecting monitoring data on shallow groundwater from 2006 to 2016, the spatiotemporal evolution trends of the chemical characteristics and influencing factors of shallow groundwater in Daxing District were studied using the hydrochemical analysis methods and principal component analysis–partial connection number method. The results show the following: 1) The cations and anions of groundwater in the study area increased with time, indicating that the groundwater quality tends to deteriorate. 2) The hydrochemical type and anion and cation components changed accordingly with the change in NO_3^-, indicating the profound impact of NO_3^- on the evolution of groundwater components. 3) The groundwater has always been affected by human factors and natural factors. Natural factors have dominated, but the influence of human factors on hydrochemical components has been increasing. From the spatial distribution of the impact of human factors and natural factors on groundwater composition, regions with higher urbanisation degrees are highly affected by human factors and vice versa. This study can provide a theoretical and methodological reference for regional groundwater management and industrial layout.

Keywords: groundwater chemical characteristics, groundwater pollution, human factors, Southern Beijing plain, spatiotemporal evolution trend

OPEN ACCESS

Edited by:
Haiyan Liu,
East China University of Technology, China

Reviewed by:
Wei Zheng,
China Institute of Water Resources and Hydropower Research, China
Zhao Yanwei,
Beijing Normal University, China
Hongyang Wang,
Chinese Research Academy of Environmental Sciences, China

****Correspondence:***
Shi-Yang Yin
yinshiyang@ncepu.edu.cn

Specialty section:
This article was submitted to Freshwater Science, a section of the journal Frontiers in Environmental Science

Received: *05 April 2022*
Accepted: *27 April 2022*
Published: *24 May 2022*

Citation:
Li C, Men B-H and Yin S-Y (2022) Analysis of Groundwater Chemical Characteristics and Spatiotemporal Evolution Trends of Influencing Factors in Southern Beijing Plain. Front. Environ. Sci. 10:913542. doi: 10.3389/fenvs.2022.913542

1 INTRODUCTION

Rapid urbanisation and rapid economic development happened in China in recent years, but these also led to a series of environmental problems. For example, the rapid growth of the urban population and the continuous expansion of urban construction leads to the sharp increase in urban water supply demands, sewage discharge, domestic waste and so on (Wang and He, 2015; Li et al., 2020a). Beijing, the political, economic and cultural centre of China, is located in the northern part of the North China Plain. Because of the lack of surface water in the region, more than 70% of the

water supply is mainly from groundwater (Ma et al., 2015). Long-term overexploitation of groundwater, coupled with the rapid development of cities, has led to the continuous decline of groundwater level (Zhou et al., 2016), deterioration of water quality (Li et al., 2020a) and surface subsidence (Zhou et al., 2015; Qin et al., 2018; Hu et al., 2019). Since the South-to-North water diversion into Beijing in December 2014, the continuous deterioration of the groundwater environment has been partially alleviated (Zhang et al., 2018a; Zhang et al., 2022), but groundwater supply still accounts for more than 40% of the city's total water supply, and the status of groundwater as the main source of the water supply has not changed.

As the uppermost layer of groundwater, shallow groundwater is closely related to the external environment and is easily affected by external natural and human factors (Baojing et al., 2013; Li et al., 2013; Martín et al., 2014; Shang et al., 2016; Zhang et al., 2016), such as atmospheric precipitation, formation lithology, surface pollutant leakage and human activities. In particular, during the rapid urbanisation of Beijing in the past two decades, the original natural underlying surface has been changed, and the groundwater recharge and discharge processes had undergone great changes (Ji et al., 2021; Qin, 2021). Therefore, studying whether these natural and human factors affect the evolution of groundwater chemical composition and changing their influence degrees are urgent. Therefore, studying the dynamic evolution of groundwater chemical characteristics and influencing factors from the perspective of hydrochemistry is necessary to provide theoretical and data support for regional groundwater resource management and protection.

Hydrochemical methods play an important role in understanding the chemical characteristics and formation processes of regional groundwater (Sarkar et al., 2017; Li et al., 2020b). Many scholars have studied the regional hydrogeochemical processes, the main sources of anions and cations, the direction of development and utilisation and the potential risks of groundwater to human health using hydrochemical methods combined with multivariate statistical methods (Li et al., 2019), geostatistics methods (Yin et al., 2019), isotope methods (Li et al., 2016), water quality assessment (Zhai et al., 2015) and other methods (Adimalla and Qian, 2019; Ji et al., 2020; Podgorski and Berg, 2020). For example, to determine the pollution sources of groundwater, hydrochemistry and multivariate statistics are combined to consider human factors in the hydrogeochemical process (Busico et al., 2020). By combining hydrochemical methods with drinking water or irrigation water standards, the applicability of regional groundwater for living and irrigation purposes can be understood, and the impact of toxicity on human health can be further evaluated (Zhang et al., 2018b; Adimalla and Li, 2019; Liu et al., 2019). Hydrochemistry and stable isotope methods can be combined to analyse the hydrochemical evolution of an area to understand the influence of wastewater irrigation on the hydrochemical processes in the surrounding area (Li et al., 2016). Therefore, the hydrochemical method is the basic method used to realise the sustainable utilisation of groundwater. However, at present, there are few studies on the evolution of groundwater chemical components over time in the process of rapid regional urbanization (Zhai et al., 2015; Xiao et al., 2017; Diamantopoulou and Voudouris, 2008; Arunprakash et al., 2014; Rao et al., 2016; He et al., 2017; Jia et al., 2018). Many studies only analysed the hydrochemistry or individual years from individual components (Martín et al., 2014; Huang et al., 2013; Yang et al., 2020). Because of the close connection of various water quality indexes in groundwater, drawing scientific conclusions from the interaction and evolution of each component in groundwater is difficult. Moreover, identifying the controlling factors causing the evolution of groundwater components based on regional hydrogeological conditions and long-term water quality monitoring data and taking corresponding measures to better protect the underground environment are necessary to further reflect the evolution direction of the groundwater environment.

From 2003 to 2019, the areas of urban land in the east and south of Beijing expanded the most, especially those in the Tongzhou District and Daxing District (Huang et al., 2015; Wu et al., 2019). As the south gate of Beijing, Daxing District is a key area to undertake the population and estrangement functions of the central urban area (Shi et al., 2014). With the construction of the Beijing Daxing International Airport, Daxing District became one of the fastest-growing areas in Beijing. In order to understand the effects of natural and human factors on the chemical composition of groundwater in the process of rapid urbanization. In this paper, the Daxing District, a typical region in the plain area of Beijing, was selected as the research area. By collecting groundwater quality monitoring data from 2006 to 2016, the evolution direction of regional groundwater chemical types was analysed and the sources of main ions were traced using hydrochemical methods such as the Piper ternary diagram, Gibbs diagram and ion combination ratio analysis. The main factors affecting the evolution of the water chemical composition were identified using the principal component–partial relation method. Moreover, the influence degree of each main factor on the groundwater composition and the change rules in time and space were analysed. This study can provide a theoretical and methodological reference for regional groundwater management and industrial layout.

2 STUDY AREA

The Daxing District is located in the southern suburbs of Beijing (**Figure 1**), with an area of 1,036 km^2. Its geographical coordinates are 116°13′–116°43′E and 39°26′–39°51′N. There are 14 towns in the jurisdiction: the northern region includes Huangcun, Xihongmen, Jiugong, Yizhuang, and Yinghai; the central region includes Beizangcun, Panggezhuang, Weishanzhuang, and Qingyundian; and the southern region includes Yufa, Lixian, Anding, Changziying, and Caiyu. The region experiences a midlatitude warm temperate continental monsoon climate, with four distinct seasons and an average annual temperature of 11.7°C. The inter-annual variation of rainfall is large, and the annual rainfall is mainly concentrated in June to September. The area belongs to the alluvial plain of the

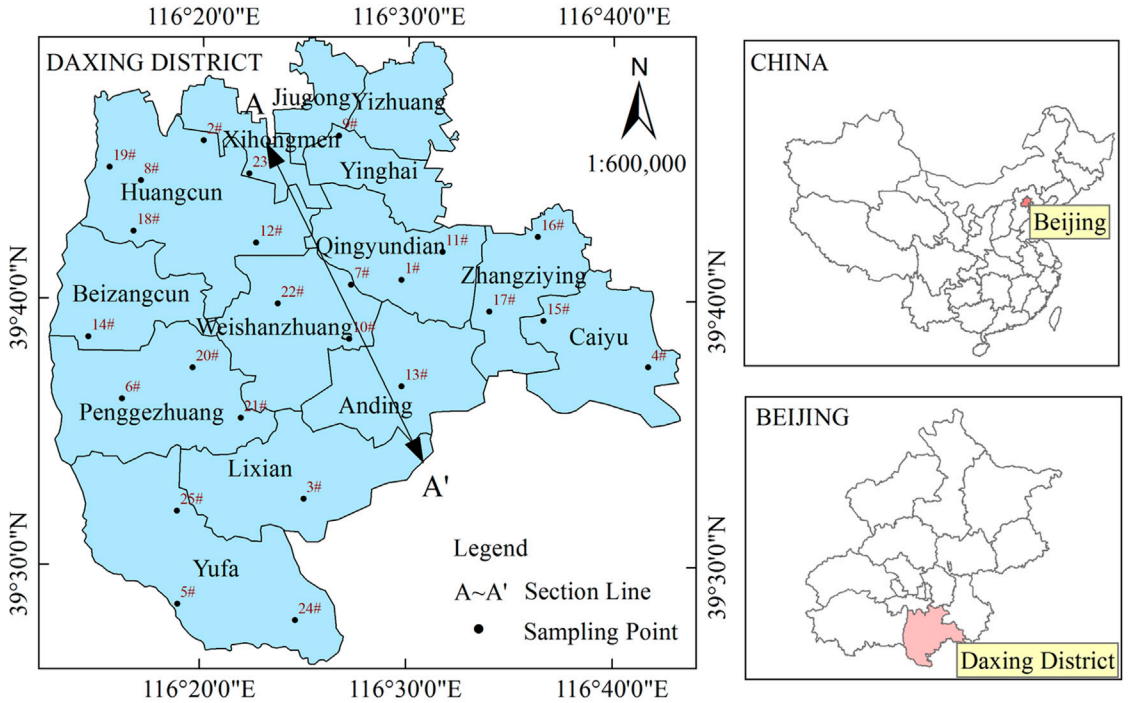

FIGURE 1 | Geographic map of the study area.

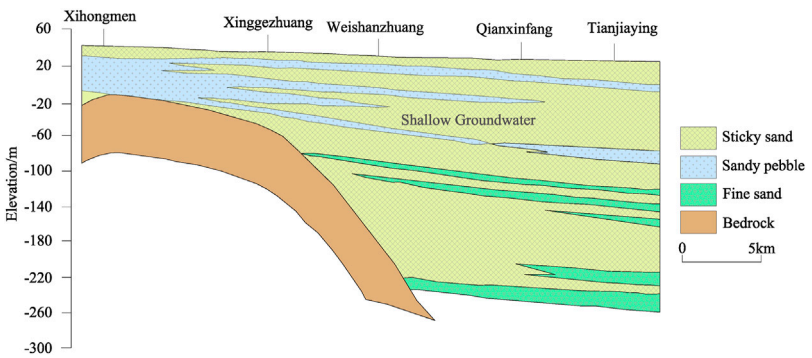

FIGURE 2 | Section A–A′ of the study area.

Yongding River, with relatively flat terrain and a slope of 0.5–2.0‰. The study area is located in the northeast tectonic belt on the southeast side of the intersection of the Yanshan and Taihang Mountains, called the "Daxing uplift". The thickness of the Quaternary unconsolidated layer is 200–300 m, and the aquifer is dominated by coarse medium sand and fine sand. Also, some areas have a certain thickness of sand and gravel layer distributions (**Figure 2**). Controlled by the uplift of the basement, the thickness of the Quaternary sediments varies greatly, from 50 m in the northwest to 300 m in the southeast. The thickness of the Quaternary deposits is 50–60 m in the northwest of study area, and 70–90 m in Huangcun, Jiugong, and Yizhuang in the east of study area. The thickness increases gradually in the south and reaches 300 m in Yufa and Kangying. Quaternary aquifer particles range from coarse to fine and water-rich from large to small.

3 MATERIALS AND METHODS

3.1 Sample Collection and Testing

A total of 275 shallow groundwater samples were collected from the study area from 2006 to 2016 from 25 sampling points, as shown in **Figure 1**. During the sampling process, water was pumped until the parameters were stable and then sampled. The sampling bottles were 2.5-L PVC plastic bottles. The water

samples were used for wetting and washing three times, and the original samples were sealed and preserved after sampling. Then, the samples were sent to the Daxing District Water Environment Monitoring Center in Beijing for testing within 48 h. The total dissolved solids (TDS) were determined using the gravimetric method (drying at 105°C). The total hardness (TH) was determined using ethylenediaminetetraacetic acid. Na^+, K^+, Ca^{2+} and Mg^{2+} were determined using inductively coupled plasma emission spectrometry. SO_4^{2-}, Cl^-, and NO_3^- were determined using ion chromatography. The CO_3^{2-} and HCO_3^- contents were determined by titration. The ion balance errors of all samples were less than 5%.

3.2 Research Methods

This study was conducted to understand the temporal–spatial evolution of groundwater chemical characteristics and influencing factors in the study area and to provide theoretical support for regional groundwater protection and industrial layout. On the basis of the hydrochemical method, the changes in the main anion and cation components and hydrochemical types in groundwater from 2006 to 2010 and 2011 to 2016 and the main factors causing these changes were analysed. The natural sources of the main ions in the groundwater in the study area were determined using the Gibbs diagram and the ion combination ratio method. The main controlling factors affecting the evolution of groundwater components were extracted using the principal component–partial relation method to further analyse the temporal and spatial evolution trend of the dominant factors affecting the evolution of the groundwater chemistry in the study area. The dynamic evolution law of the main controlling factors was analysed, which provided the basis for the protection measures of regional groundwater resources and the industrial layout scheme.

3.2.1 Hydrochemical Analysis Methods

The chemical characteristics and formation of shallow groundwater were qualitatively and quantitatively analysed using the Piper three-line diagram, Gibbs diagram and ion combination ratio method. The mineral saturation index was calculated using the Phreeqc software.

3.2.2 Principal Component Analysis–Partial Connection Number Method

Principal component analysis is a statistical method that converts multiple variables into a few principal components using dimension reduction technology to reduce the number of predicted variables (Lianne et al., 2017; Maria et al., 2012). Partial connection number is the adjoint function of set pair analysis, which is mainly used to reflect the dynamic evolution between connection numbers (Yang and Zhao, 2019; Yang et al., 2021). At present, the first-order partial connection number is commonly used (Xiang et al., 2021). Since the first-order connection number only reflects the evolution between adjacent connection numbers, the mutual transformation between identity and opposition is not considered (Li et al., 2022). The second-order connection number not only considers the mutual transformation between identity, difference and opposition but also reflects the mutual transformation between identity and opposition. Therefore, this paper adopted principal component analysis–partial connection number to extract the main control factors affecting the evolution of the shallow groundwater components and analysed the dynamic evolution rules of the main control factors.

The specific model construction steps are as follows:

3.2.2.1 Eliminating the Xij Dimension of the Raw Data

$$X_{ij}^* = \frac{X_{ij} - \overline{X_j}}{S_j} \left(i = 1, 2, \cdots, n;\ j = 1, 2, \cdots, p\right) \tag{1}$$

In the formula, X_{ij}^* is the original data X_{ij} after a standardised processing value. $\overline{X_j}$ and S_j are the mean and standard deviation of the jth index. i is the evaluation sample, and j is the j index in the i sample. n is the number of samples, and p is the number of indicators.

3.2.2.2 Calculating the Correlation Coefficient Matrix and Corresponding Eigenvector

$$R = \left[r_{ij}\right]_{p\times p} \tag{2}$$

$$r_{ij} = \frac{\mathrm{cov}\left(X_i^*, X_j^*\right)}{\sqrt{D\left(X_i^*\right)}*\sqrt{X_j^*}} \tag{3}$$

$$|\lambda I - R| = 0 \tag{4}$$

In the above formulas, R is the correlation coefficient matrix of the processed data, r_{ij} is the correlation coefficient, and $\mathrm{cov}(X_i^*, X_j^*)$ is the covariance of the index data X_i^* and X_j^* after processing. $D(X_i^*)$ and $D(X_j^*)$ are the variances of the processed index data X_i^* and X_j^*, respectively. By solving **Formula (4)**, the eigenvectors λ_1, λ_2, …, λ_p and the corresponding eigenvectors γ_1, γ_2, …, γ_p are obtained.

3.2.2.3 Determining Principal Components by Calculating the Principal Component Contribution Rate and the Cumulative Contribution Rate

$$P_t = \frac{\lambda_t}{\sum_{j=1}^{p}\lambda_j} \left(t = 1, 2, \cdots, p\right) \tag{5}$$

$$P = \sum_{t=1}^{m} P_t \tag{6}$$

In these formulas, P_t is the contribution rate of the main components, p is the cumulative contribution rate, and λ_t is the eigenvalue corresponding to the first m principal components when the cumulative contribution rate reaches the requirement.

3.2.2.4 Calculating the Score of the Groundwater Chemical Composition Evolution Factors

$$x = \sum_{t=1}^{m}\sum_{j=1}^{p} \gamma_{tj} X_{tj}^{*} p_t \tag{7}$$

In the formula, x is the score of the factors affecting the evolution of the groundwater chemical composition and γ_{tj} is the principal component load, which is the tth component of the eigenvector r_j.

3.2.2.5 Determining the Evaluation Level of Each Main Control Factor Score

The principal component scores of the two main factors affecting the groundwater chemical composition were evaluated. According to the data characteristics of the score values and referring to existing data, the evaluation grade standards of the score values of the impact factors were determined as follows:

$$\left\{ s_{gj} \middle| g = 1, 2, 3;\ j = 1, 2 \right\} \tag{8}$$

In the formula, s_{gi} represents the critical value of the evaluation level of each impact factor. g is the evaluation level (Levels 1–3) and j represents the jth influencing factor in sample i, representing natural and human factors, respectively.

$$\left\{ x_{ij} \middle| i = 1, 2, 3, \cdots, n;\ j = 1, 2 \right\} \tag{9}$$

In the formula, x_{ij} represents the score value of the jth index of the ith sample. i is the evaluation sample and n is the number of samples.

3.2.2.6 Calculating the Connection Number of Each Main Control Factor Score About Each Sample

The relationship between the principal component score of the jth index about the evaluation sample i and the index value of the evaluation standard was calculated.

If the indicator is a positive indicator $x_{ij} \le s_{1j}$ or a reverse indicator $x_{ij} \ge s_{1j}$,

$$u_{ij1} = \begin{cases} 1 \\ 1 - 2\dfrac{x_{ij} - s_{1j}}{s_{2j} - s_{1j}} \\ -1 \end{cases} \tag{10}$$

If the indicator is a positive indicator $s_{1j} < x_{ij} \le s_{2j}$ or a reverse indicator $s_{1j} > x_{ij} \ge s_{2j}$,

$$u_{ij2} = \begin{cases} 1 - 2\dfrac{s_{1j} - x_{ij}}{s_{1j} - s_{0j}} \\ 1 \\ 1 - 2\dfrac{x_{ij} - s_{2j}}{s_{3j} - s_{2j}} \end{cases} \tag{11}$$

If the indicator is a positive indicator $s_{2j} < x_{ikj} \le s_{3j}$ or a reverse indicator $s_{2j} > x_{ikj} \ge s_{3j}$,

$$u_{ij3} = \begin{cases} -1 \\ 1 - 2\dfrac{s_{2j} - x_{ij}}{s_{2j} - s_{1j}} \\ 1 \end{cases} \tag{12}$$

In the above formulas, u_{ij1}, u_{ij2}, u_{ij3} represent the number of index connections within each level for the jth index of sample i, respectively. s_{1j} and s_{2j} are the limit values of Grades 1 and 2 and Grades 2 and 3, respectively. s_{0j} is the minimum value of Grade 1, and s_{3j} is the maximum value of Grade 3.

The identity, difference and opposition of the jth principal component score index about sample i are transformed into relative membership. The calculation process is as follows:

$$v_{ijg}^{''} = 0.5 + 0.5u_{ijg} \tag{13}$$

$$v_{ijg}^{'} = v_{ijg}^{''} \Big/ \sum_{g=1}^{3} v_{ijg}^{''} \tag{14}$$

$$u_{ij} = v_{ij1}^{'} + v_{ij2}^{'} I + v_{ij3}^{'} J \tag{15}$$

In the above formulas, u_{ij} represents the degree of identity ($v_{ij1}^{'}$), degree of difference ($v_{ij2}^{'}$) and degree of opposition ($v_{ij3}^{'}$) of the jth indicator about sample i. $v_{ijg}^{''}$ is the calculation process.

3.2.2.7 Calculating the Partial Linkages of Influencing Factors

The support degree of each grade was calculated using the second-order partial connection number. The calculation formulas are shown in **(16)**–**(18)**:

$$S_1 = a \cdot \left(1 + \partial^{+} a + \partial^{2+} a\right) \tag{16}$$

$$S_2 = b \cdot \left(\partial^{-} b + 1 + \partial^{+} b\right) \tag{17}$$

$$S_3 = c \cdot \left(\partial^{2-} c + \partial^{-} c + 1\right) \tag{18}$$

In the above formulas, S_1, S_2, and S_3 represent Level 1, Level 2, and Level 3 support, respectively.

By comparing the sizes of S_1, S_2, and S_3, the depth evolution trend of the evaluation level of the research object can be determined. $\partial^{+} a$ and $\partial^{2+} a$ represent the positive evolution rates from b and c to a, respectively. $\partial^{-} b$ represents the negative evolution rate of a to b, and $\partial^{+} b$ represents the positive evolution rate of c to b. $\partial^{2-} c$ and $\partial^{-} c$ represent the negative evolution rates from a and b to c, respectively.

The calculation formulas of the evolution rate of the connection number are shown in Formulas **(19)**–**(24)**:

$$\partial^{+} a = \frac{a}{a + b} \tag{19}$$

$$\partial^{2+} a = \frac{a}{a + b} \Big/ \left(\frac{a}{a + b} + \frac{b}{b + c} \right) \tag{20}$$

$$\partial^{-} b = \frac{b}{a + b} \tag{21}$$

$$\partial^{+} b = \frac{b}{b + c} \tag{22}$$

$$\partial^{2-} c = \frac{c}{b + c} \Big/ \left(\frac{b}{a + b} + \frac{c}{b + c} \right) \tag{23}$$

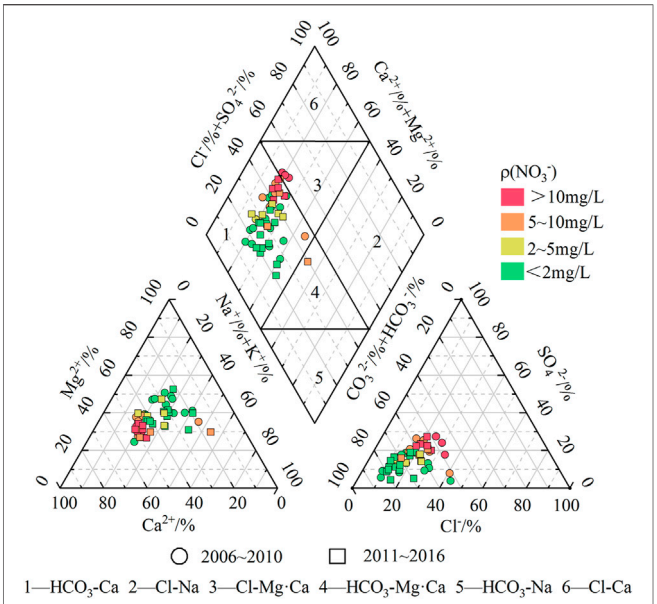

FIGURE 3 | The Piper trilinear diagram of conventional ions of the shallow groundwater in different periods.

$$\partial^{-}c = \frac{c}{b+c} \tag{24}$$

4 RESULTS AND DISCUSSION

4.1 Evolution of Groundwater Chemical Characteristics

4.1.1 Content and Evolution of Chemical Components in Water

The collected shallow groundwater samples were divided into two groups according to time: 2006–2010 and 2011–2016. The hydrochemical data of each group were averaged for each period. Overall, the total concentration of cations and anions in the shallow groundwater increased over time. From 2006 to 2010 and 2011 to 2016, the order of the average cation concentration was $Ca^{2+} > Na^{+} > Mg^{2+} > K^{+}$, and Ca^{2+}, Na^{+} and Mg^{2+} increased by 7.94, 20.88, and 2.69%, respectively. In contrast, K^{+} decreased by 2.56%. For the anions, the order of the anion average concentration in the two periods changed from $HCO_3^{-} > Cl^{-} > SO_4^{2-}$ to $HCO_3^{-} > SO_4^{2-} > Cl^{-}$, which was mainly due to the decrease in the Cl^{-} concentration from 95.75 to 88.77 mg/L and the increase in that of SO_4^{2-} from 88.52 to 99.62 mg/L. Because of the increase in cation and anion concentrations, the TDS and TH increased. TDS increased from 760.96 to 786.36 mg/L, and TH increased from 489.73 to 509.84 mg/L. The NO_3^{-} concentration increased from 4.86 to 4.89 mg/L. Although the average concentration of NO_3^{-} in 2011–2016 only increased by 0.03 mg/L compared with that in 2006–2010, the number of water quality monitoring cases with NO_3^{-} concentrations over 10 mg/L increased from three to five, indicating that the range of the NO_3^{-} pollution of the groundwater tended to increase. The pH decreased slightly from 7.5 to 7.4, indicating an alkaline-to-acidic trend.

The variation coefficients of the main components from 2011 to 2016 were lower than those from 2006 to 2010, and the largest reduction was that of Cl^{-}. From the average coefficient of the variation of each ion, the maximum coefficient of variation was that of NO_3^{-}, with an average variation coefficient of 1.48, indicating that NO_3^{-} is mainly affected by human factors (Zhai et al., 2015; Xiao et al., 2017; Yin et al., 2019). It is followed by Cl^{-} and SO_4^{2-}, with an average variation coefficient of about 0.5. The smaller coefficients of variation were those of HCO_3^{-}, TDS, TH, and Mg^{2+}, and the average coefficient of variation was about 0.2. The smallest coefficient of variation was that of HCO_3^{-}, with an average of 0.19, indicating that HCO_3^{-} was mainly affected by natural factors (Zhai et al., 2015; Yin et al., 2019).

4.1.2 Evolution of Groundwater Chemical Types

The groundwater chemical types are affected by natural conditions and human activities. The Piper three-line diagram was used to analyse the hydrochemical types in 2006–2010 and 2011–2016 to analyse the evolution characteristics of the hydrochemical types in the two periods.

As shown in **Figure 3**, 2006–2010 is similar to 2011–2016. Most water quality monitoring sites were located in Area 1, indicating that alkaline earth metals (Ca^{2+} and Mg^{2+}) exceeded alkaline metals (K^{+} and Na^{+}) and weak acids (HCO_3^{-}) exceeded strong acids (Cl^{-} and SO_4^{2-}) in most water quality monitoring sites in the study area. Therefore, the water of this region is mainly HCO_3–Ca-type water. In 2011–2016, compared with 2006–2010, part of the Cl–Mg·Ca-type water changed into HCO_3–Ca-type water, whereas a small amount of HCO_3–Ca-type water changed into HCO_3–Na·Mg-type water. The change of Cl–Mg·Ca-type water into HCO_3–Ca-type water may have been caused by the migration of Cl^{-} to the deep groundwater and thus the decrease of the concentration of Cl^{-} in the shallow groundwater. The conversion of HCO_3–Ca to HCO_3–Na·Mg may be related to the dissolution of silicate on the one hand. According to the monitoring data of the groundwater level in the study area, the average groundwater level decreased from 11.89 to 17.60 m from 2000 to 2016. The recharge path of groundwater was lengthened, which led to the increase in Na^{+} dissolution in silicate during the recharge process. This resulted in the transformation of HCO_3–Ca into HCO_3–Na·Mg. On the other hand, it may be related to human inputs of Na^{+}.

In addition, the Piper trilinear diagram (**Figure 3**) shows that with the increase in NO_3^{-} concentration, the main trend of the water chemistry type evolved from HCO_3–Ca-type water to Cl–Mg·Ca-type water. At the same time, with the increase in NO_3^{-} concentration, the main cation and anion components also change accordingly. For the cations, with the increase in NO_3^{-} concentration, the ratio of Ca^{2+} and Na^{+} increased, whereas that of Mg^{2+} decreased. For the anions, with the increase in NO_3^{-} concentration, the proportions of Cl^{-} and SO_4^{2-} increased, whereas the proportion of HCO_3^{-} decreased. This indicates that the change in the NO_3^{-} concentration profoundly affected the component evolution of the groundwater. **Table 1** shows that

TABLE 1 | Calculation results of the chemical components and coefficients of variation of the shallow groundwater in the study area (unit: mg/L).

Time	Name	K^+	Na^+	Ca^{2+}	Mg^{2+}	Cl^-	SO_4^{2-}	HCO_3^-	TDS	TH	NO_3^-	PH
2006–2010	Content of each component	2.03	71.58	95.37	59.61	95.75	88.52	448.29	760.96	489.73	4.86	7.5
	Coefficient of variation	0.4	0.45	0.35	0.3	0.67	0.53	0.21	0.27	0.24	1.6	0.02
2011–2016	Content of each component	1.97	86.53	102.94	61.21	88.77	99.62	552.07	786.36	509.84	4.89	7.4
	Coefficient of variation	0.35	0.38	0.32	0.23	0.38	0.45	0.16	0.19	0.19	1.36	0.02
2006–2016	Content of each component	2.00	79.06	99.16	60.41	92.26	94.07	500.18	773.66	499.79	4.88	7.45
	Coefficient of variation	0.38	0.42	0.34	0.27	0.53	0.49	0.19	0.23	0.22	1.48	0.02

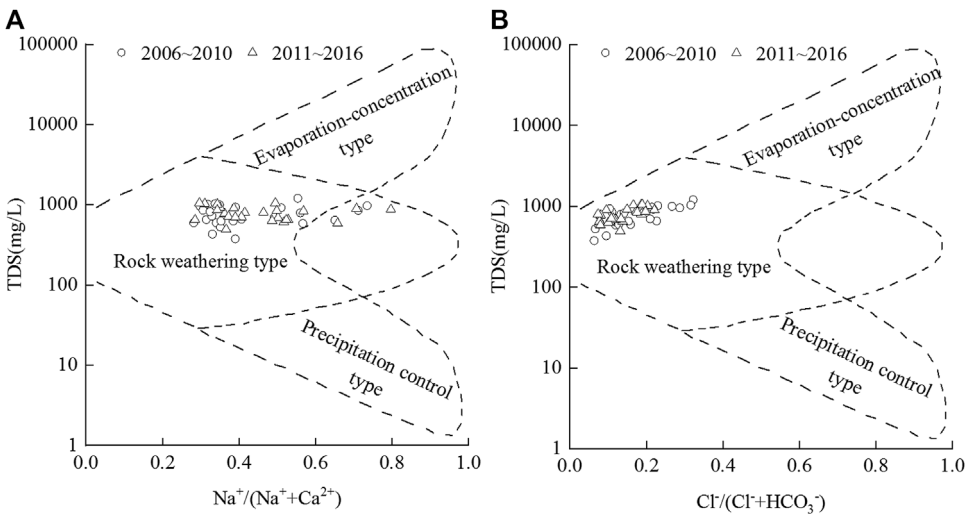

FIGURE 4 | Gibbs diagram for different periods in the study area.

the variation coefficient of NO_3^- is very large compared with those of the other main ions. Thus, it can be considered that NO_3^- is mainly caused by human factors; that is, human factors have a great impact on groundwater components.

4.2 Source Evolution of Groundwater Chemical Components

4.2.1 Evolution of Water–Rock Interaction

The Gibbs graphical method can be used to identify the sources of chemical components in natural water. The natural origin control mode of water chemical compositions can be divided into three types: evaporation–concentration type, rock weathering type and precipitation control type. The relationships between TDS and $Na^+/(Na^+ + Ca^{2+})$, $Cl^-/(Cl^- + HCO_3^-)$ in 2006–2010 and 2011–2016 were drawn using the Gibbs diagram method. **Figure 4** shows that the natural origin control mode of the shallow groundwater chemical composition in the study area is mainly rock weathering type.

From 2006 to 2010, the average value of $Na^+/(Na^+ + Ca^{2+})$ was 0.42, and the TDS was 760.96 mg/L. From 2011 to 2016, the average value of $Na^+/(Na^+ + Ca^{2+})$ was 0.45, and the TDS was 786.36 mg/L. Both $Na^+/(Na^+ + Ca^{2+})$ and the TDS increased. However, the TDS values of the two periods showed a stable trend with increasing $Na^+/(Na^+ + Ca^{2+})$, indicating that the cation components were mainly controlled by rock weathering and that the other natural types had little effect on the cation components. At the same time, the $Na^+/(Na^+ + Ca^{2+})$ values greater than 0.6 of some water quality

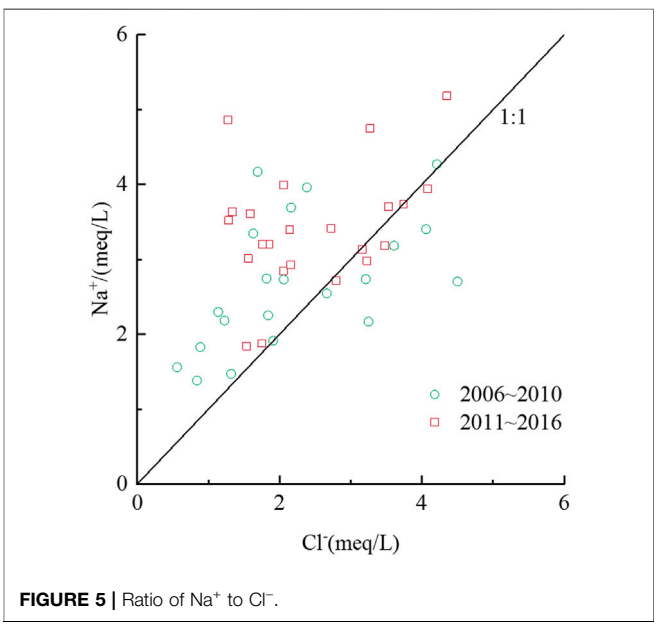

FIGURE 5 | Ratio of Na^+ to Cl^-.

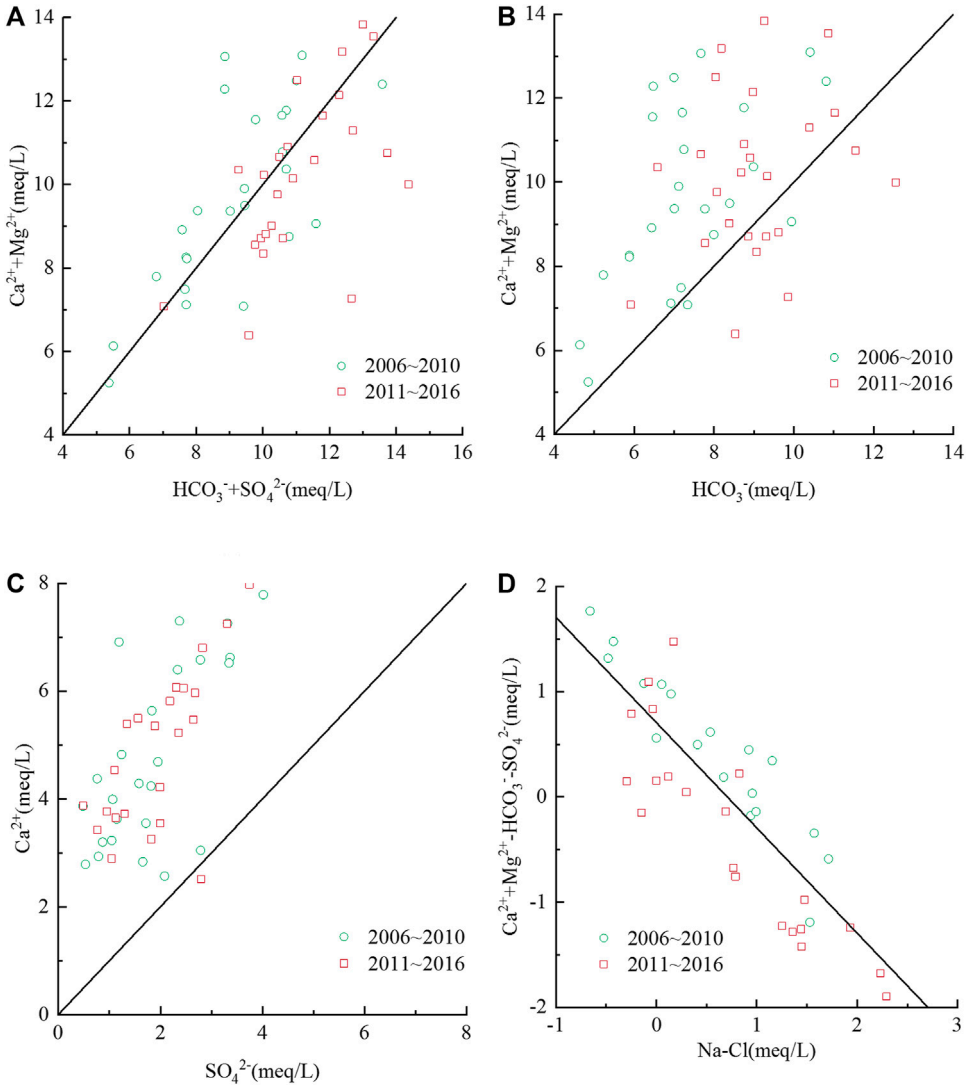

FIGURE 6 | Ratio diagram of the ions in the water chemical components in the study area.

monitoring points indicate that the cation components in these regions may have been affected by human factors.

The average value of $Cl^-/(Cl^- + HCO_3^-)$ was 0.14, slightly lower than 0.18 in 2006–2010. The $Cl^-/(Cl^- + HCO_3^-)$ ratio was less than 0.4 in both periods, indicating that water–rock interactions play a major role in the determination of the anion components. In addition, **Figure 4B** shows that the TDS value increased with increasing $Cl^-/(Cl^- + HCO_3^-)$, indicating that, in addition to water–rock interactions, natural and human factors also affected the anion components and TDS.

4.2.2 Analysis Based on the ion Combination Ratio

The ion ratio relationship was used to reveal the source of the main ions to further analyse the chemical evolution of the groundwater. The Na^+/Cl^- ratio was used to reflect the sources of Na^+ and Cl^-. **Figure 5** shows that the water quality monitoring points are scattered on both sides of the 1:1 line, and the points above the 1:1 line are significantly more than those below. Compared with that in 2006–2010, the average ratio of Na^+/Cl^- increased from 1.44 to 1.67 in 2011–2016, resulting in more points above the 1:1 line in 2011–2016 than those in 2006–2010. On the one hand, this indicates that the source of Na^+ is not only rock salt dissolution but also silicate dissolution. On the other hand, the source of Na^+ may also be related to ion exchange reactions or artificial inputs of Na^+. According to the simulated value SI of the mineral saturation index (**Supplementary Table S1**), the values of rock salt mineral saturation in 2006–2010 and 2011–2016 were −6.70 and −6.73, respectively, which are less than 0. This indicates that the rock salt minerals were unsaturated and that part of Na^+ came from rock salt. The dissolution formulas of rock salt and silicate minerals are shown in **Eqs 25**, **26**, respectively:

$$NaCl \rightarrow Na^{+}+Cl^{-} \quad (25)$$

$$2NaAlSi_3O_8+2CO_2+11H_20 \rightarrow Al_2Si_2O_5(OH)_4+4H_4SiO_4+2Na^{+}+2HCO_3^{-} \quad (26)$$

In addition, a small number of water quality monitoring points are located below 1:1, deviating from the 1:1 line, indicating that there may be an increase in the Cl^{-} concentration caused by anthropogenic inputs of chloride.

In the analysis of the sources of Ca^{2+}, the relationship between $Ca^{2+} + Mg^{2+}$ and $HCO_3^{-} + SO_4^{2-}$ (**Figure 6A**) shows that the water quality monitoring points are located on both sides of the 1:1 line, indicating that the sources of Ca^{2+} and Mg^{2+} are mainly carbonate and sulphate. At the same time, in further tracing the sources of Ca^{2+} and Mg^{2+}, it can be known from the ratio of $Ca^{2+} + Mg^{2+}$ to HCO_3^{-} (**Figure 6B**) that most of the water quality monitoring points are above the 1:1 line. According to the simulation results in **Supplementary Table S1**, the mineral saturation values of calcite and dolomite in 2006–2010 and 2011–2016 were 0.14, 0.25 and 0.43, 0.62, respectively. These values are greater than 0, indicating that the two carbonate minerals are in a saturated state. Therefore, the sources of Ca^{2+} and Mg^{2+} are not carbonates. In further tracing the source of Ca^{2+}, the relationship between Ca^{2+} and SO_4^{2-} was plotted. **Figure 6C** shows that the ratio of Ca^{2+} to SO_4^{2-} is basically greater than one. At the same time, according to the simulation results in **Supplementary Table S1**, the mineral saturation values of anhydrite and gypsum were −1.92 and −1.70 from 2006 to 2010 and −1.86 and −1.64 from 2011 to 2016, respectively. These values are all less than 0, indicating that sulphate dissolution was an important source of Ca^{2+}. However, the Ca^{2+}/SO_4^{2-} ratio is higher than the 1:1 line, indicating that, in addition to sulphate, Ca^{2+} was derived from other exogenous inputs. The dissolution equations of anhydrite and gypsum are shown in **Eqs 27**, **28**, respectively.

$$CaSO_4 \rightarrow Ca^{2+}+SO_4^{2-} \quad (27)$$

$$CaSO_4 \cdot 2H_2O \rightarrow Ca^{2+}+SO_4^{2-}+2H_2O \quad (28)$$

In exploring whether ion exchange reactions occurred between Na^{+} and Ca^{2+}, Mg^{2+}, the ratio of $Ca^{2+} + Mg^{2+}$–HCO_3^{-}–SO_4^{2-} to Na^{+}–Cl^{-} (**Figure 6D**) is around −1, indicating that ion exchange reactions occurred. Meanwhile, the relationship between $Ca^{2+} + Mg^{2+}$ and $HCO_3^{-} + SO_4^{2-}$ shows that the average ratios of $Ca^{2+} + Mg^{2+}$ and $HCO_3^{-} + SO_4^{2-}$ in 2006–2010 and 2011–2016 are 1.05 and 0.92, respectively. The water quality monitoring points have a downward trend to 1:1, indicating that the exchange reaction of Ca^{2+} and Mg^{2+} in 2011–2016 has an increasing trend compared with that in 2006–2010.

4.3 The Spatiotemporal Evolution Trend of the Influence Degrees

A principal component analysis of the shallow groundwater in the study area was conducted to further analyse the dominant factors of the water chemistry evolution in the study area. On the basis of Formulas **(1)**–**(3)**, the correlation coefficient matrix of the shallow groundwater hydrochemical data was obtained using the SPSS software. As shown in **Supplementary Table S2**, Ca^{2+} and SO_4^{2-} had high positive correlations with NO_3^{-}; the correlation coefficients were more than 0.6, indicating that the concentrations of NO_3^{-} and Ca^{2+}, SO_4^{2-} increased or decreased. The higher correlation with HCO_3^{-}, Na^{+}, and Mg^{2+} featured correlation coefficients greater than 0.6, indicating that the NO_3^{-} and Ca^{2+}, SO_4^{2-}, HCO_3^{-}, and Na^{+}, Mg^{2} concentrations increased or decreased.

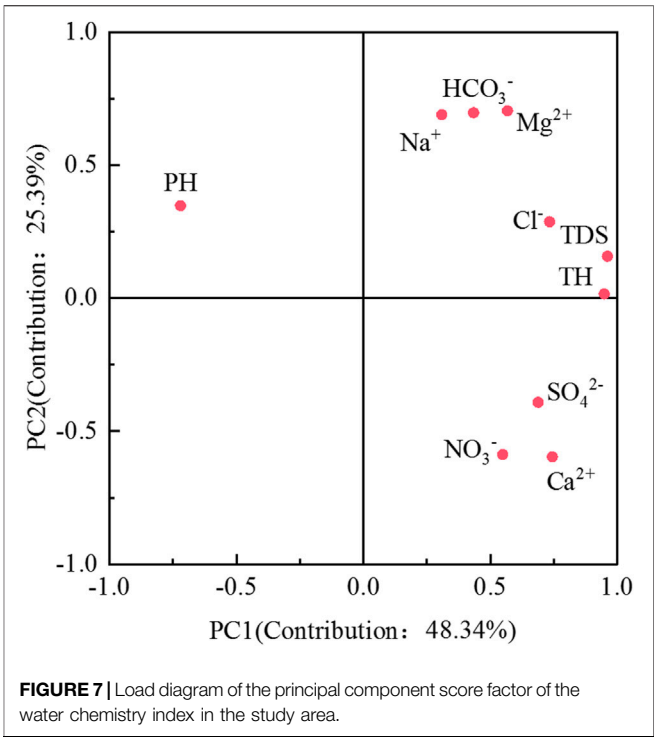

FIGURE 7 | Load diagram of the principal component score factor of the water chemistry index in the study area.

The principal component analysis of the shallow groundwater in the study area was performed using Formulas **(4)**–**(7)**. Two principal components (PC1 and PC2) with eigenvalues greater than one were extracted, and their contribution rates were 48.34 and 25.39%, respectively, and the cumulative contribution rate was 73.73%. The load of the principal component score factor is shown in **Figure 7**. The Piper plot (**Figure 1**) shows that the anions in the study area are mainly HCO_3^{-}, accounting for more than 70% of the anion concentration equivalent, and the minimum spatial variation coefficient is 0.19. Therefore, HCO_3^{-} can be used as the dominant factor for identifying natural factors. The spatial variation coefficient of NO_3^{-} was the largest relative to those of other indicators, reaching 1.48. With increasing NO_3^{-}, the groundwater hydrochemical type and anion and cation components also changed accordingly. So, NO_3^{-} can be used as the dominant factor in identifying human factors.

According to the principal component score factor load diagram (**Figure 7**), the maximum positive load scores of PC1 are TDS, TH and Ca^{2+}. Given the two indicators HCO_3^{-} and NO_3^{-}, the positive load score of PC1 can be used as a

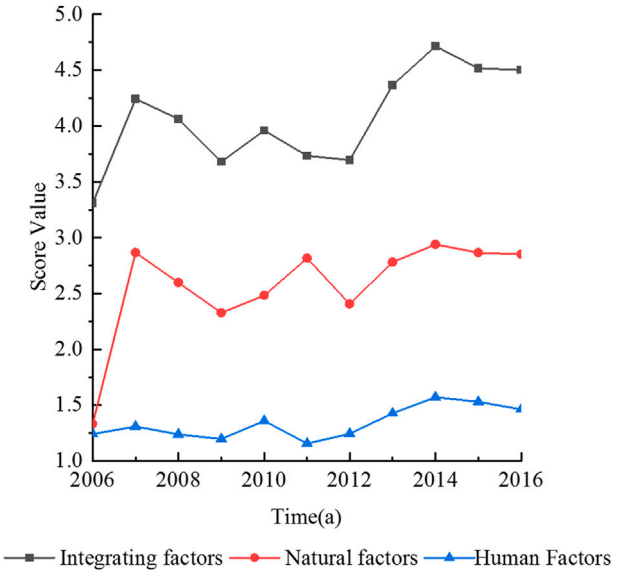

FIGURE 8 | Evolution of the principal component scores with time affected by various factors.

comprehensive index of natural and human factors. HCO_3^-, Mg^{2+}, and Na^+ with the highest score of the PC2 positive load chart can be used as the evaluation index for the influence degrees of natural factors. The maximum scores of the PC2 negative load diagram are NO_3^- and Ca^{2+}, which can be used as evaluation indices for the influence degree of human factors.

According to the identification results of the influencing factors of the hydrochemical evolution, **Formula (7)** was used to calculate the scores of the human, natural and natural–human factors. The PC2 load was processed positively and the evolution process of the principal component scores with time under the guidance of such three factors was drawn (**Figure 8**) to facilitate the comparison of data. The score of the comprehensive effect was always greater than that of the natural and human factors, indicating that the evolution process of the water's chemical components in the study area was always affected by human and natural factors. The scores of the natural and human influences were 2.56 and 1.34, respectively, indicating that the evolution of the groundwater components was always dominated by natural influences. At the same time, the score of the comprehensive effect increased from 3.73 in 2011 to 4.50 in 2016. From 2011 to 2016, the role of natural factors was basically stable. Moreover, the score always fluctuated around 2.80. The score under human influence rose from 1.16 in 2011 to 1.46 in 2016, indicating that the impact of human factors on groundwater chemical composition increased.

The partial connection number method was used to calculate the support degree of the principal component scores of the natural and human factors for each grade to reflect the deep evolution trend of natural and human factors. The classification of the score evaluation grades is shown in **Table 2**.

According to the anthropogenic impact on the spatial distribution of the human influence degree on groundwater chemical components (**Figure 9**), the northern region with greater influence is mainly located in the Huangcun–Xihongmen–Jiugong–Yizhuang–Yinghai area, which is close to the central urban area of Beijing. In addition, the study area had high degrees of urbanisation and a dense population (Zhai et al., 2015). Furthermore, regional sewage channels such as the Xinfeng River Liangshui River and other rivers in the northern region may have caused groundwater pollution. In contrast, the central and southern regions mainly involve agriculture, so they were relatively less affected by humans.

According to the calculations of the support degree of each grade under the influence of the partial connection number on human factors (**Figure 10**), the support degree of Grade 2 was always in a dominant position compared with Grades 1 and 3, indicating that the influence degree of human factors on the groundwater chemical components in the region was basically stable. Besides, the support of Grade 1 is higher than that of Grade 3, but the distance between the support curve of Grade 3 and that of Grade 1 had a decreasing trend since 2012, indicating that the degree of human influence may be further enhanced.

From a spatial perspective (**Figure 11**), the influence of natural factors on the chemical composition of the groundwater in the Yufa, Lixian, Anding, and Caiyu areas in the southern region is greater than those in the northern region and part of the central region. According to the support degree of the partial connection number under the natural influence (**Figure 12**), the support degree of Grade 2 was much higher than those of Grades 1 and 3, indicating that the influence of natural factors is the same as that of human factors, and it is basically stable. From 2007 to 2012, the Grades 1 and 3 support were basically in a balanced state. Since 2012, the support degree of Grade 3 has been significantly greater than that of Grade 1, indicating that the natural impact has increased. It may have been caused by the continuous overexploitation of groundwater in the study area and the continuous decline of the water level, which has changed the regional groundwater environment.

TABLE 2 | Principal component score evaluation level under the guidance of various factors.

Serial number	Evaluating indicator	Limits and levels of the evaluation index					
		Index limits	Index levels	Index limits	Index levels	Index limits	Index levels
1	PC2 positive load (natural factors)	≤2.10	Level I	≤3.02	Level II	≤7.02	Level III
2	PC2 negative Load* (human Factors)	≤0.77	Level I	≤1.55	Level II	≤5.21	Level III

**The PC2 negative load is the index value after the positive treatment.*

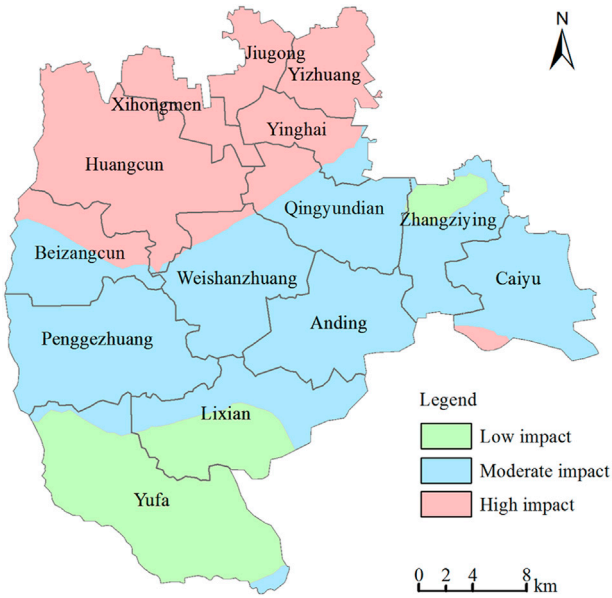

FIGURE 9 | Spatial distribution of the influence degree of human factors on the groundwater chemical composition.

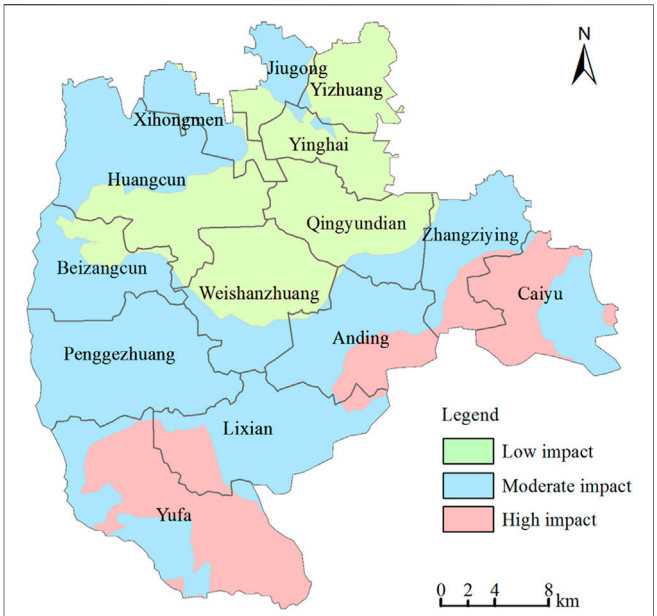

FIGURE 11 | Spatial distribution of the natural factors' influence degree on the groundwater chemical composition.

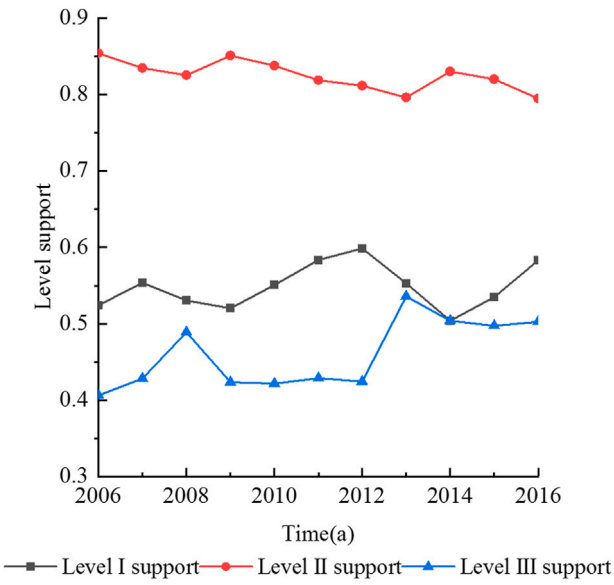

FIGURE 10 | Evolution curve of each grade's support degree under human influence.

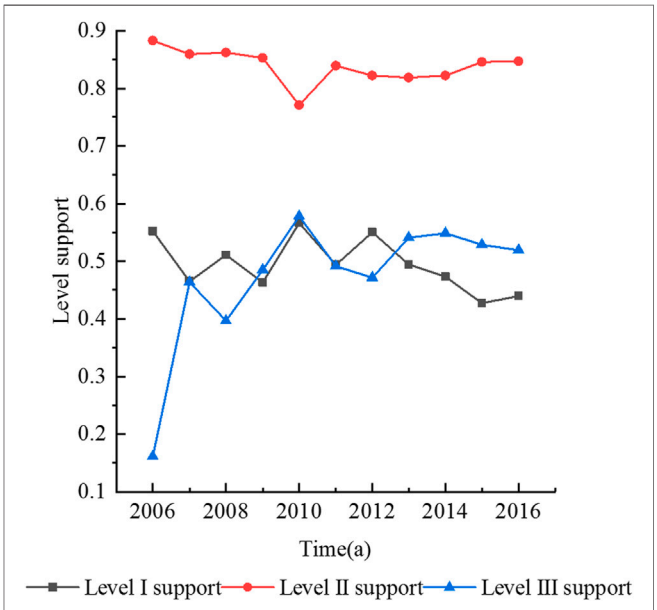

FIGURE 12 | Evolution curve of the support degree under natural factors.

On the one hand, the longer supply path of atmospheric precipitation leads to mineral intensification leaching in the vadose zone. On the other hand, with the decline of the water level, some aquifers become aeration zones, and the redox environment in the strata changes greatly. Some insoluble substances become soluble substances because of the increase in oxygen content, which leads to the deterioration of the groundwater environment.

5 CONCLUSION

In order to understand the effects of natural and human factors on the chemical composition of groundwater in the process of rapid urbanization. The Daxing District, a typical area in the Beijing Plain, was taken as the research object in this paper. By

collecting monitoring data on the shallow groundwater quality from 2006 to 2016, the spatiotemporal evolution trend of the groundwater's chemical characteristics and influencing factors were studied using the Piper three-line diagram, Gibbs diagram, ion combination ratio method, variation coefficient method, principal component–partial correlation method and other methods. The main conclusions are as follows:

1) From 2006 to 2016, the total cation concentration, total anion concentration, TDS and TH of the shallow groundwater in the study area showed an upward trend over time. The average concentration of NO_3^- had a little change, but NO_3^- in the groundwater pollution range had an increasing trend. At the same time, according to the calculation results of each ion variation coefficient, the maximum coefficient of variation was that of NO_3^- (1.48), indicating that it was mainly affected by human factors. The variation coefficient of HCO_3^- was 0.19, which indicated that it was mainly affected by natural factors.
2) The water chemical types in the study area from 2006 to 2016 were still mainly HCO_3–Ca water. However, with the increased NO_3^- concentrations, the main cation and anion components changed accordingly, showing an evolution trend from HCO_3–Ca-type to Cl–Mg·Ca-type. The change in the NO_3^- concentration profoundly affected the component evolution of the groundwater.
3) The regions greatly affected by natural factors were those in the south, whereas the northern and central regions were relatively less affected by natural factors. The areas most affected by human factors were those in the north, mainly in areas with higher urbanisation, followed by the central and southern regions. The influence of human and natural factors on the groundwater chemical composition was highly correlated with regional urbanisation and industrial distribution. The southern region was mainly dominated by agricultural planting, whereas the northern region was relatively developed in industry and commerce with a high degree of urbanisation.

In the process of urbanisation, human factors greatly impact the groundwater environment, especially regarding the input of NO_3^- into shallow groundwater. This leads to the increase in NO_3^- concentrations in aquifers, which profoundly affects the evolution of water chemical components and types. Therefore, corresponding measures should be taken to ensure the safety of the regional water supply.

1) Aiming at areas with high regional permeability or shallow groundwater depth, engaging in polluting industries must be strictly forbidden. The regional municipal sewage drainage facilities should be further improved. For example, domestic sewage should be collected and treated. Meanwhile, the direct discharge of domestic sewage into surface water must be prohibited. Because of the lack of surface water in the southern plains of Beijing, the water in the existing rivers is basically from treated reclaimed water in the central urban area. The concentration of NO_3^- and salt in the reclaimed water is higher than that in natural water, which also affects the groundwater in the region (Xiao et al., 2017; Yin et al., 2019). Therefore, relevant departments must strictly follow relevant standards in treating urban sewage to reduce its impact on groundwater aquifers.
2) According to the spatial distribution of the main controlling factors affecting the evolution of the groundwater components, corresponding groundwater protection measures and industrial layout schemes should be formulated. The groundwater quality in the region is affected by both domestic sewage and industrial wastewater due to the high degree of urbanisation. Domestic pollution sources show an increasing trend with increasing population, but the main pollution source is still industrial pollution. Thus, heavy-groundwater-pollution industries and high-water-consumption industries should be gradually withdrawn to give way to the construction, expansion and technical transformation of industrial industries that meet the requirements for the prevention and control of groundwater pollution to prevent enterprises with serious groundwater pollution from moving to rural areas and control groundwater pollution from the source. On another note, agricultural planting is the main factor for regions where natural factors have great influence. Therefore, the efficient utilisation and recycling of agricultural resources such as chemical fertilisers, pesticides, straws and livestock manure should be comprehensively promoted to encourage cleaner agricultural production and reduce the impacts on groundwater quality.

DATA AVAILABILITY STATEMENT

The original contributions presented in the study are included in the article/**Supplementary Materials**, further inquiries can be directed to the corresponding author.

AUTHOR CONTRIBUTIONS

Conceptualization, S-YY and B-HM; methodology, CL; software, CL; validation, CL; for-mal analysis, CL; investigation, CL; resources, CL; data curation, CL; writing—original draft preparation, CL; writing—review and editing, CL; visualization, CL; supervision, B-HM and S-YY; project administration, S-YY and B-HM; funding acquisition, S-YY; All authors have read and agreed to the published version of the manuscript.

FUNDING

This work was supported by the Central University Fund of China (2019MS028) and the National Key Research and Development Program of China (2016YFC0401406).

ACKNOWLEDGMENTS

Thanks for the support of the above funding and the laboratory of College of water re-sources and hydropower engineering, North China Electric Power University.

SUPPLEMENTARY MATERIAL

The Supplementary Material for this article can be found online at: https://www.frontiersin.org/articles/10.3389/fenvs.2022.913542/full#supplementary-material

REFERENCES

Adimalla, N., and Qian, H. (2019). Groundwater Quality Evaluation Using Water Quality Index (WQI) for Drinking Purposes and Human Health Risk (HHR) Assessment in an Agricultural Region of Nanganur, South India. *Ecotoxicol. Environ. Saf.* 176, 153–161. doi:10.1016/j.ecoenv.2019.03.066

Adimalla, N., and Li, P. (2019). Occurrence, Health Risks, and Geochemical Mechanisms of Fluoride and Nitrate in Groundwater of the Rock-Dominant Semi-arid Region, Telangana State, India. *Hum. Ecol. Risk Assess. Int. J.* 25 (1-2SI), 81–103. doi:10.1080/10807039.2018.1480353

Arunprakash, M., Giridharan, L., Krishnamurthy, R. R., and Jayaprakash, M. (2014). Impact of Urbanization in Groundwater of South Chennai City, Tamil Nadu, India. *Environ. Earth Sci.* 71 (2), 947–957. doi:10.1007/s12665-013-2496-7

Baojing, G., Ying, G., Scott, X. C., Weidong, L., and Jie, C. (2013). Nitrate in Groundwater of China: Sources and Driving Forces. *Glob. Environ. Change* 23 (5), 1112–1121. doi:10.1016/j.gloenvcha.2013.05.004

Busico, G., Kazakis, N., Cuoco, E., Colombani, N., Tedesco, D., Voudouris, K., et al. (2020). A Novel Hybrid Method of Specific Vulnerability to Anthropogenic Pollution Using Multivariate Statistical and Regression Analyses. *Water Res.* 171, 115386. doi:10.1016/j.watres.2019.115386

Diamantopoulou, P., and Voudouris, K. (2008). Optimization of Water Resources Management Using SWOT Analysis: the Case of Zakynthos Island, Ionian Sea, Greece. *Environ. Geol.* 54 (1), 197–211. doi:10.1007/s00254-007-0808-5

He, X., Qian, J., Liu, Z., Lu, Y., Ma, L., Zhao, W., et al. (2017). Temporal-spatial Evolution of Groundwater Nitrogen Pollution over Seven Years in a Highly Urbanized City in the Southern China. *Bull. Environ. Contam. Toxicol.* 99 (6), 753–759. doi:10.1007/s00128-017-2187-2

Hu, L., Dai, K., Xing, C., Li, Z., Tomás, R., Clark, B., et al. (2019). Land Subsidence in Beijing and its Relationship with Geological Faults Revealed by Sentinel-1 InSAR Observations. *Int. J. Appl. Earth Obs. Geoinf.* 82, 101886. doi:10.1016/j.jag.2019.05.019

Huang, G., Sun, J., Zhang, Y., Chen, Z., and Liu, F. (2013). Impact of Anthropogenic and Natural Processes on the Evolution of Groundwater Chemistry in a Rapidly Urbanized Coastal Area, South China. *Sci. Total Environ.* 463-464, 209–221. doi:10.1016/j.scitotenv.2013.05.078

Huang, Y., Nian, P., and Zhang, W. (2015). The Prediction of Interregional Land Use Differences in Beijing: A Markov Model. *Environ. Earth Sci.* 73 (8), 4077–4090. doi:10.1007/s12665-014-3693-8

Ji, Y., Wu, J., Wang, Y., Elumalai, V., and Subramani, T. (2020). Seasonal Variation of Drinking Water Quality and Human Health Risk Assessment in Hancheng City of Guanzhong Plain, China. *Expo. Health* 12 (3SI), 469–485. doi:10.1007/s12403-020-00357-6

Ji, Z., Cui, Y., Zhang, S., Chao, W., and Shao, J. (2021). Evaluation of the Impact of Ecological Water Supplement on Groundwater Restoration Based on Numerical Simulation: A Case Study in the Section of Yongding River, Beijing Plain. *Water* 13 (21), 3059. doi:10.3390/W13213059

Jia, Z., Bian, J., and Wang, Y. (2018). Impacts of Urban Land Use on the Spatial Distribution of Groundwater Pollution, Harbin City, Northeast China. *J. Contam. Hydrol.* 215, 29–38. doi:10.1016/j.jconhyd.2018.06.005

Li, J., Shi, Z., Wang, G., and Liu, F. (2020a). Evaluating Spatiotemporal Variations of Groundwater Quality in Northeast Beijing by Self-Organizing Map. *Water* 12 (5), 1382. doi:10.3390/w12051382

Li, J., Wang, Y., Zhu, C., Xue, X., Qian, K., Xie, X., et al. (2020b). Hydrogeochemical Processes Controlling the Mobilization and Enrichment of Fluoride in Groundwater of the North China Plain. *Sci. Total Environ.* 730, 138877. doi:10.1016/j.scitotenv.2020.138877

Li, M. Z., Zhai, Y. Z., Zhou, J., and Wang, J. S. (2013). Hydrochemical Characteristics and Water Quality Assessment of Groundwater in Daxing District of Beijing, China. *Appl. Mech. Mater.* 295-298, 696–700. doi:10.4028/www.scientific.net/AMM.295-298.696

Li, P., He, X., and Guo, W. (2019). Spatial Groundwater Quality and Potential Health Risks Due to Nitrate Ingestion through Drinking Water: A Case Study in Yan'an City on the Loess Plateau of Northwest China. *Hum. Ecol. Risk Assess.* 25 (1-2SI), 11–31. doi:10.1080/10807039.2018.1553612

Li, P., Wu, J., Qian, H., Zhang, Y., Yang, N., Jing, L., et al. (2016). Hydrogeochemical Characterization of Groundwater in and Around a Wastewater Irrigated Forest in the Southeastern Edge of the Tengger Desert, Northwest China. *Expo. Health* 8 (3), 331–348. doi:10.1007/s12403-016-0193-y

Li, Z., Jin, J., Cui, Y., Zhang, L., Wu, C., Ning, S., et al. (2022). Dynamic Evaluation of Regional Water Resources Carrying Capacity Based on Set Pair Analysis and Partial Connection Number. *Water Supply* 22 (3), 2407–2423. doi:10.2166/ws.2021.371

Lianne, M., Lalita, B., Tasha, E., Cheryl, L. W., and Yu-Pin, L. (2017). Use of Principal Components Analysis and Kriging to Predict Groundwater-Sourced Rural Drinking Water Quality in Saskatchewan. *Int. J. Environ. Res. Public Health* 14 (9), 1065. doi:10.3390/ijerph14091065

Liu, J., Jin, D., Wang, T., Gao, M., Yang, J., and Wang, Q. (2019). Hydrogeochemical Processes and Quality Assessment of Shallow Groundwater in Chenqi Coalfield, Inner Mongolia, China. *Environ. Earth Sci.* 78 (12), 347. doi:10.1007/s12665-019-8355-4

Ma, Z., Fang, Z., Xie, X., Chai, F., and Zhang, Q. (2015). Study on Feature Storage and Storage Capacity of Underground Reservoir Based on GMS in MHS Area of Beijing, China. *Arab. J. Geosci.* 8 (12), 10359–10369. doi:10.1007/s12517-015-1990-5

Maria, L. C., Eduardo, D. A. C., Aníbal, D. F. S., Rodrigo, D. A. C., and Marcos, D. F. M. S. (2012). Evaluation of the Influence of Natural and Antrhopogenic Processes on Water Quality in Karstic Region. *Water Air Soil Pollut.* 223 (5), 2157–2168. doi:10.1007/s11270-011-1012-5

Martín, D. C. M. A., Esteller, M. V., Expósito, J. L., and Hirata, R. (2014). Impacts of Urbanization on Groundwater Hydrodynamics and Hydrochemistry of the Toluca Valley Aquifer (Mexico). *Environ. Monit. Assess.* 186 (5), 2979–2999. doi:10.1007/s10661-013-3595-3

Podgorski, J., and Berg, M. (2020). Global Threat of Arsenic in Groundwater. *Science* 368 (6493), 845–850. doi:10.1126/science.aba1510

Qin, H., Andrews, C. B., Tian, F., Cao, G., Luo, Y., Liu, J., et al. (2018). Groundwater-pumping Optimization for Land-Subsidence Control in Beijing Plain, China. *Hydrogeol. J.* 26 (4), 1061–1081. doi:10.1007/s10040-017-1712-z

Qin, H. (2021). Numerical Groundwater Modeling and Scenario Analysis of Beijing Plain: Implications for Sustainable Groundwater Management in a Region with Intense Groundwater Depletion. *Environ. Earth Sci.* 80 (15), 499. doi:10.1007/s12665-021-09795-0

Rao, P. N., Prasad, K. M., Madhusudhan, B. J., Krishna, V., Anand, A., and Madhnure, P. (2016). Impact of Urbanization on Groundwater Quality in Vijayawada Urban Agglomeration, the New Capital Region of Andhra Pradesh, India–A Baseline Study. *J. Geol. Soc. India* 87 (5), 539–552. doi:10.1007/s12594-016-0428-3

Sarkar, A., Shekhar, S., and Rai, S. P. (2017). Assessment of the Spatial and Temporal Hydrochemical Facies Variation in the Flood Plains of North-West Delhi Using Integrated Approach. *Environ. Earth Sci.* 76 (19), 665. doi:10.1007/s12665-017-7019-5

Shang, F., Ren, S., Yang, P., Li, C., Xue, Y., and Huang, L. (2016). Modeling the Risk of the Salt for Polluting Groundwater Irrigation with Recycled Water and Ground Water Using HYDRUS-1 D. *Water Air Soil Pollut.* 227 (6), 189. doi:10.1007/s11270-016-2875-2

Shi, Y., Zheng, X. Q., Sun, Y. B., and Jia, Z. R. (2014). Intra-Urban Migration Patterns in the Perspective of Improved Radiation Model - A Case Study of

Beijing. *Adv. Mat. Res.* 869-870, 110–116. doi:10.4028/www.scientific.net/AMR.869-870.110

Wang, L., and He, Q. (2015). The Evaluation of Groundwater Resources Value of Beijing Based on Emergy Theory. *Adv. Mater. Sci. Eng.* 2015, 1–9. doi:10.1155/2015/743136

Wu, H., Hu, L., Yang, S., Fan, W., Tian, D., Ren, H., et al. (2019). "Remote Sensing of the Immigration Community Variation in Daxing District, Beijing," in IGARSS 2019 - 2019 IEEE International Geoscience and Remote Sensing Symposium, Yokohama, Japan, 28 July-2 Aug. 2019, 6352–6355. doi:10.1109/IGARSS.2019.8898878

Xiang, W.-Q., Yang, X.-H., and Li, Y.-Q. (2021). A Set Pair Analysis Model for Suitability Evaluation of Human Settlement Environment. *Therm. Sci.* 25 (3), 2109–2116. doi:10.2298/TSCI191001095X

Xiao, Y., Gu, X., Yin, S., Pan, X., Shao, J., and Cui, Y. (2017). Investigation of Geochemical Characteristics and Controlling Processes of Groundwater in a Typical Long-Term Reclaimed Water Use Area. *Water* 9 (10), 800. doi:10.3390/w9100800

Yang, H., and Zhao, K. (2019). The Calculation and Application of Partial Connection Numbers[J]. *CAAI Trans. Intelligent Syst.* 14 (05), 865–876. doi:10.11992/tis.201810022

Yang, P., Wang, Y., Wu, X., Chang, L., Ham, B., Song, L., et al. (2020). Nitrate Sources and Biogeochemical Processes in Karst Underground Rivers Impacted by Different Anthropogenic Input Characteristics. *Environ. Pollut.* 265, 114835. doi:10.1016/j.envpol.2020.114835

Yang, Y., Wang, H., Zhao, W., and Yan, J. (2021). Evaluation Model of W Ater Resources Carrying Capacity Based on Set Pair Potential and Partial Connection Number. *Adv. Eng. Sci.* 53 (03), 99–105. doi:10.15961/j.jsuese.202000629

Yin, S., Xiao, Y., Gu, X., Hao, Q., Liu, H., Hao, Z., et al. (2019). Geostatistical Analysis of Hydrochemical Variations and Nitrate Pollution Causes of Groundwater in an Alluvial Fan Plain. *Acta Geophys.* 67 (4), 1191–1203. doi:10.1007/s11600-019-00302-5

Zhai, Y., Lei, Y., Zhou, J., Li, M., Wang, J., and Teng, Y. (2015). The Spatial and Seasonal Variability of the Groundwater Chemistry and Quality in the Exploited Aquifer in the Daxing District, Beijing, China. *Environ. Monit. Assess.* 187 (2), 143. doi:10.1007/s10661-014-4249-9

Zhang, M., Hu, L., Yao, L., and Yin, W. (2018a). Numerical Studies on the Influences of the South-To-North Water Transfer Project on Groundwater Level Changes in the Beijing Plain, China. *Hydrol. Process.* 32 (12), 1858–1873. doi:10.1002/hyp.13125

Zhang, X., Sun, M., Wang, N., Huo, Z., and Huang, G. (2016). Risk Assessment of Shallow Groundwater Contamination under Irrigation and Fertilization Conditions. *Environ. Earth Sci.* 75 (7), 603. doi:10.1007/s12665-016-5379-x

Zhang, X., Wu, X., Zhao, R., Mu, W., and Wu, C. (2022). Identifying the Facts and Driving Factors of Deceleration of Groundwater Table Decline in Beijing during 1999-2018. *J. Hydrol.* 607, 127475. doi:10.1016/j.jhydrol.2022.127475

Zhang, Y., Wu, J., and Xu, B. (2018b). Human Health Risk Assessment of Groundwater Nitrogen Pollution in Jinghui Canal Irrigation Area of the Loess Region, Northwest China. *Environ. Earth Sci.* 77 (7), 273. doi:10.1007/s12665-018-7456-9

Zhou, L., Guo, J. M., and Li, X. (2015). "Monitoring and Analyzing Surface Subsidence Based on SBAS-InSAR in Beijing Region, China," in International conference on Intelligent Earth Observing and Applications, Guilin, December 2015, 9808, 98081Y. doi:10.1117/12.2208803

Zhou, Y., Xiao, W., Wang, J., Zhao, Y., Huang, Y., Tian, J., et al. (2016). Evaluating Spatiotemporal Variation of Groundwater Depth/Level in Beijing Plain, a Groundwater-Fed Area from 2001 to 2010. *Adv. meteorology* 2016, 1–11. doi:10.1155/2016/8714209

Conflict of Interest: The authors declare that the research was conducted in the absence of any commercial or financial relationships that could be construed as a potential conflict of interest.

Publisher's Note: All claims expressed in this article are solely those of the authors and do not necessarily represent those of their affiliated organizations, or those of the publisher, the editors and the reviewers. Any product that may be evaluated in this article, or claim that may be made by its manufacturer, is not guaranteed or endorsed by the publisher.

frontiers | Frontiers in Environmental Science

ORIGINAL RESEARCH
published: 13 June 2022
doi: 10.3389/fenvs.2022.917416

Groundwater Flow Modeling of a Near-Surface Disposal Repository for Low- and Intermediate-Level Radioactive Waste in Southwest China

Huang Zhang[1], Qiulan Zhang[1], Yunli Chen[2], Jingli Shao[1], Yali Cui[1], Wenyi Wan[1] and Shangqi Han[1]*

[1]China University of Geosciences, Beijing, China, [2]CNNC Everclean Environmental Engineering Co. Ltd, Beijing, China

The influence and function of engineering facilities were increasingly concerned about the safety analysis of low- and intermediate-level radioactive waste (LILW). In terms of near-surface disposal, many artificial facilities were set down, such as drainage facilities, covering layers, and disposal units. To analyze the long-term impact of these artificial facilities on groundwater in the disposal site area, we built four time-continuing models by setting the time nodes of parameter or boundary changes using FEFLOW code, considering the possible aging and degradation state of these facilities. According to the models, the site area's groundwater level situations for long-term safety assessment were predicted. The results showed the different regulating abilities of drainage facilities affected the groundwater level of the disposal site in different degradation states, which also reflected the necessity of artificial facilities simulation in groundwater modeling. In addition, the Monte Carlo method and surrogate model were adopted to analyze the influence of the uncertainty of model parameters on the output of groundwater flow models. This study could help in further understanding the groundwater flow modeling for long-term safety assessment of near-surface disposal engineering.

Keywords: long-term safety assessment, sensitivity analysis, and uncertainty analysis, drainage facilities, FEFLOW software, groundwater level prediction

OPEN ACCESS

Edited by:
Lichun Wang,
Tianjin University, China

Reviewed by:
Xuan Yu,
Sun Yat-sen University, China
Muhammad Imran,
COMSATS University, Pakistan

****Correspondence:***
Qiulan Zhang
qlzhang919@cugb.edu.cn

Specialty section:
This article was submitted to Freshwater Science, a section of the journal Frontiers in Environmental Science

Received: *11 April 2022*
Accepted: *28 April 2022*
Published: *13 June 2022*

Citation:
Zhang H, Zhang Q, Chen Y, Shao J, Cui Y, Wan W and Han S (2022) Groundwater Flow Modeling of a Near-Surface Disposal Repository for Low- and Intermediate-Level Radioactive Waste in Southwest China. Front. Environ. Sci. 10:917416. doi: 10.3389/fenvs.2022.917416

1 INTRODUCTION

Radioactive waste disposal has been being studied by countries that own the nuclear power industry all the time (Yim and Simonson, 2000; Darda et al., 2021). Many experts and scholars worldwide conducted studies and developed international cooperation to find out the best way to store and keep various radioactive wastes in the recent 30 years (Watson et al., 2018; Birkholzer et al., 2019; Deng et al., 2020). Along with looking for suitable disposal methods (Michie, 1998; Bracke and Fischer-Appelt, 2015; Bracke et al., 2019; Chapman, 2019), performance assessment and safety assessment became the important evaluation parts. However, the disposal methods were different for radioactive wastes with different activities, then the evaluation methods and procedures were also different. The International Atomic Energy Agency (IAEA, 1994) established a waste classification and disposal options system to identify disposal options appropriate for each waste class. In the announcement, the radioactive wastes were categorized into exempt radioactive waste, low- and intermediate-level radioactive waste (LILW), short-lived radioactive waste, long-lived radioactive waste, and high-level radioactive waste, depending on the activity level of the radioactive wastes. It also stipulated the main

storage approach LILW was near-surface disposal and geological disposal. Near-surface disposal demonstrated a greater diversity of disposal system designs, a wider variety in hydrogeological settings, and waste that was more heterogeneous in nature and more difficult to characterize than typical waste streams intended for geological disposal (Kozak, 2017). These differences have led to diverse philosophy and technical approaches in near-surface and geological disposal safety assessments. Building public confidence in radioactive waste disposal in the long term was a critical issue that researchers were concerned about (Jeong et al., 2018; Klein et al., 2021). Groundwater played an essential role in radioactive transfer to the biosphere in most radioactive waste disposal for its primary flow passage function (Lee and Kim, 2017; Li et al., 2020). Groundwater flow modeling was the primary and widely-used method to recognize the groundwater level conditions, calculate the flow rate, and make future predictions. Therefore, a sufficient understanding of the disposal processes and disposal facilities' effects must be attained in modeling (Yi et al., 2012; Jeong et al., 2018; Birkholzer et al., 2019).

For near-surface disposal, the degeneration of drainage facilities, vaults, packages, and the covering layer of the repository were inevitable processes. These researches did not make a detailed analysis of the functions of artificial facilities in the regional-scale groundwater model. Some researchers used multi-scale hydrogeological models to clearly understand the groundwater flow movement from deposit vaults to the biosphere, including regional scale, site scale, and vault scale (LLWR, 2011; SKB, 2013; SKB, 2014). The regional-scale model usually provided the groundwater boundaries for the smaller scale models. However, in some cases, only the small-scale model like the vault scale model would consider details of the geometry of the disposal facilities and material properties in simulations. Ignoring the effect of artificial facilities on a regional scale would affect the accuracy of water level simulation results. For the numerical tools used to create groundwater flow models, mature commercial software and codes like MODFLOW, FEFLOW, POREFLOW, TOUGH3, and HydroGeoSphere (Cornelissen et al., 2016; Welch et al., 2019; De Caro et al., 2020; Santos et al., 2020; Parameswaran et al., 2021) was mainly adopted. Software and codes were generally selected by site conditions and research objectives. For near-surface disposal facilities, many researchers modeled the groundwater flow using finite element and subsurface flow systems FEFLOW software (Ashraf and Ahmad, 2008; Bugai et al., 2012; Geetha Manjari and Sivakumar Babu, 2017). It is a valuable and mature tool to simulate the pore continuum groundwater flow and is suitable for building groundwater flow models and analyzing artificial facilities' effects and groundwater flow regime.

In this research, our research objective was a near-surface disposal repository for low-and intermediate-level radioactive waste (LILW) in Southwest China. A series of groundwater flow models at the same regional scale was constructed, considering the evolution and state update of the repository facilities using FEFLOW software for analyzing the groundwater condition in the long term. The models can reveal the possible change of groundwater level and flow field condition on a millennial scale under the aging and degradation of artificial facilities. Moreover, the Monte Carlo method (Fu and Gómez-Hernández, 2009; Jafari et al., 2016; Sreekanth et al., 2020) and surrogate model were used to analyze the effect of model parameters' uncertainties on the groundwater level of disposal site in the year of 2,150, 2,350, and 3,050. The study could support evaluating the influence of near-surface disposal engineering facilities on groundwater levels and the safety assessment of waste disposal.

2 STUDY AREA

The study area was located in Sichuan Province, Southwest China, as shown in **Figure 1**. The site's elevation was 487–1,080 m above mean sea level, and the shortest distance between the site and the river was only about 2.5 km. LILW disposal repository was built on a hillside with an altitude of 606 m. About 180,000 m^3 of LILW would be emplaced by 2050.

2.1 Geological and Hydrogeological Conditions

The disposal site was a classic example of hilly topography at an elevation about 606 m above mean sea level, underlain by shale base rock of the Silurian age. The geological drilling survey data of the study area showed that the site area's stratigraphy was relatively simple. The argillaceous shale of the Early Jurassic and Middle-Late Silurian ages widely existed, with thin Quaternary deposits overlying in local places (**Figure 1A**). The previous detailed drilling data showed the strata could be divided into five sub-layers. They were Quaternary Holocene silty clay (collapse slope deposit), completely weathered argillaceous shale, highly weathered argillaceous shale, moderately weathered argillaceous shale, and slightly weathered argillaceous shale top-down (**Table 1**). In weathered argillic shale, fractures developed pretty well. According to the near-surface survey of fractures, the main characteristics of fractures in the site were small joints with steep dip angles.

In contrast with 35 types of fractured rock masses classified by the International Society for Rock Mechanics (Lili, 2011), fractures developed in weathered argillic shale of this study area mainly belonged to Low Ductility and Medium Interval type, followed by Medium Ductility and Medium Interval type. Lili (2011), Zhang et al. (2017) once used FractureToKarst software to analyze the existence and size of REV of the 35 types of fractured rock according to the criterion that the permeability coefficient does not change dramatically with the change of the study range. The REV of the Low Ductility and Medium Interval and Medium Ductility and Medium Interval type fractured rocks were 30.0 m × 15.0 m and 10.0 m × 5.0 m.

The site's groundwater was mainly weathered fissure water with a depth of 5–30 m, distributed in a plane shape and controlled by landform. The primary groundwater sources were atmospheric precipitation recharge, surface trench water, and groundwater recharge from the overlying quaternary aquifer of local places. They discharged to surface streams, Bailong River or Pingxi River.

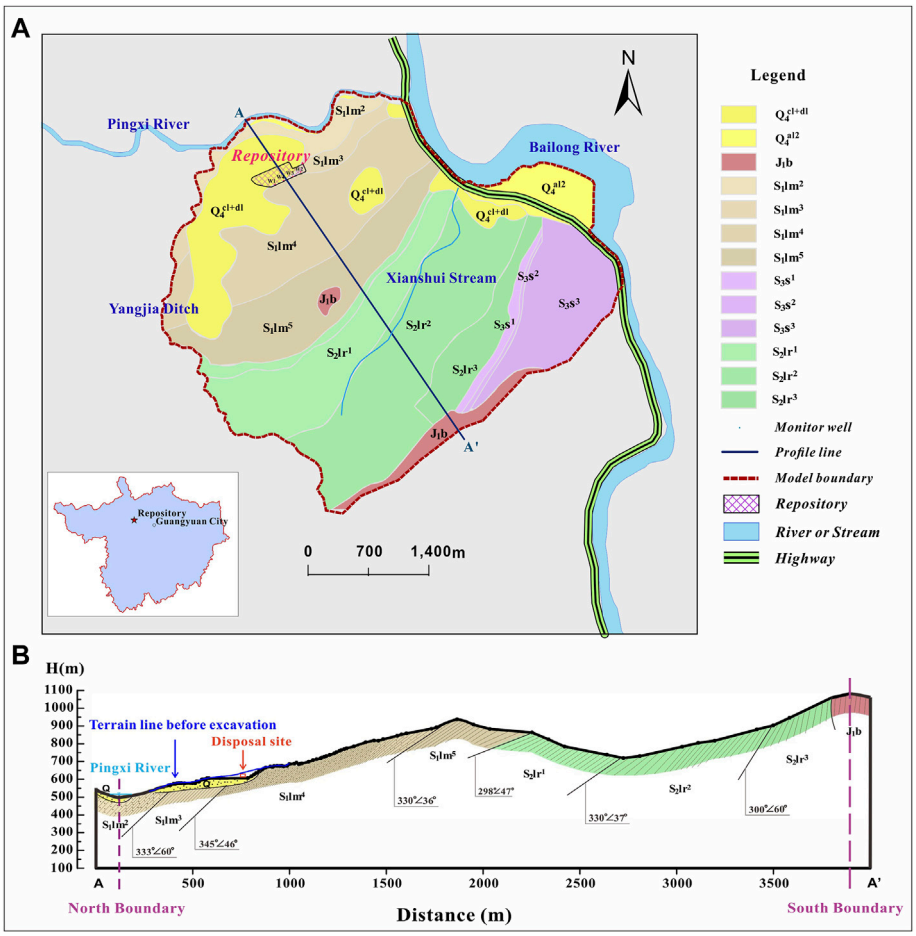

FIGURE 1 | (A) Geologic map of the LILW repository study area. **(B)** Northwest geological section of the study area.

TABLE 1 | Hydraulic conductivity of layers calculated from previous tests (unit: m/s).

Layers	Depth(m)	Pumping test	Borehole pressure test	Model range
Artificial fill, Quaternary alluvium	0–30	8.10E-07–1.33E-06	7.64E-08–6.48E-07	4.17E-07–1.16E-06
Highly weathered argillaceous shale	0–40	1.75E-09–1.18E-07	7.69E-08–4.281E-07	1.16E-08–2.31E-07
Moderately weathered argillaceous shale	25–70	1.09E-09–1.31E-09	1.50E-11–1.79E-10	5.70E-10–5.79E-09
Slightly weathered argillaceous shale	50–250	—	6.414E-11–6.92E-10	1.16E-10–5.794E-10
Unweather argillaceous shale	200–550	—	—	1.16E-11–1.16E-10

2.2 Artificial Facilities

In this research, artificial facilities like covering layers and drainage facilities were the main components considered in groundwater flow modeling. In this study, the covering layers of the disposal units consisted of four sub-layers, which were the vegetable layer (VL), the water-retaining layer (WRL), the clay layer (CL), and the local soil layer (LSL), respectively (**Figure 2A**).In addition, several seepage ditches had been set around the site, and inclined drainage holes had been arranged along the slope (**Figure 2B**). Moreover, as time goes by, the drainage hole could be blocked by sands and gravel, and the seepage ditches would be deformed and damaged due to geological processes and bio disturbance. Therefore, three states describe their aging and failure processes were defined. The first was the sound state, which means these artificial facilities work normally and drain smoothly. The second state was an altered state. In this state, some of these facilities had problems gradually, and drain occurred difficultly. The last state was called the degraded state, where all of these facilities were invalided and drained void. In this study, the 2,150 and 2,350 were supposed to be the time nodes according to the lifetime of these installations (**Figure 3**). After 2,150, half of the drainage installations were assumed lost efficacy. Then, by 2,350, the drainage system was ultimately out of work. These states were essential references for subsequent multi-stage modeling.

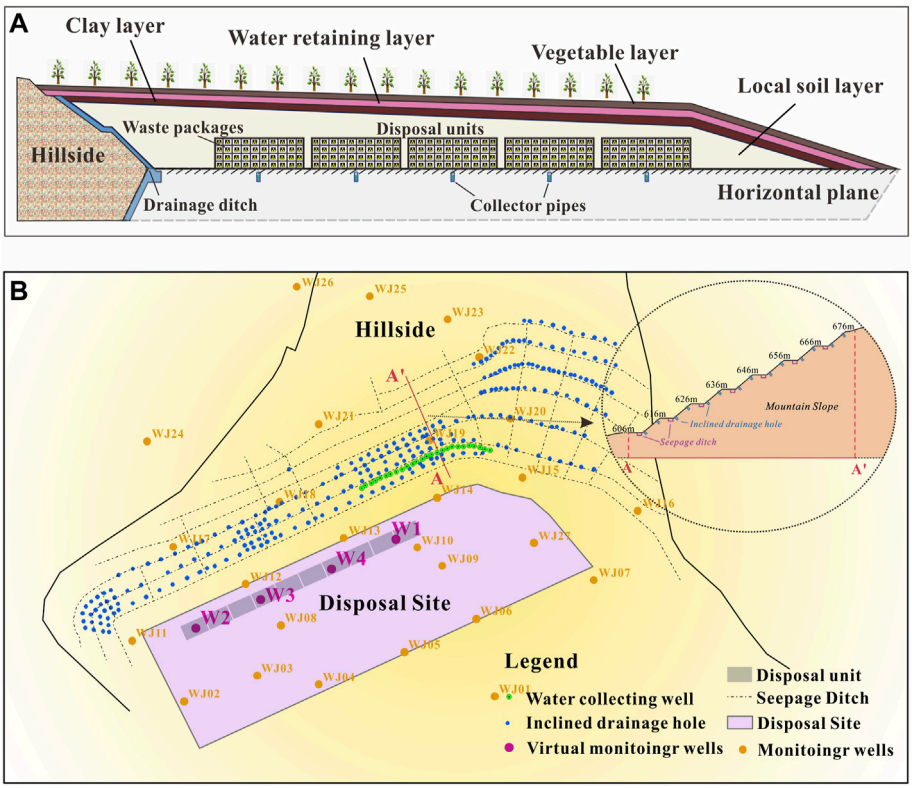

FIGURE 2 | (A) The disposal units' generalized structure of the LILW repository. **(B)**. Schematic diagram of artificial drainage facilities.

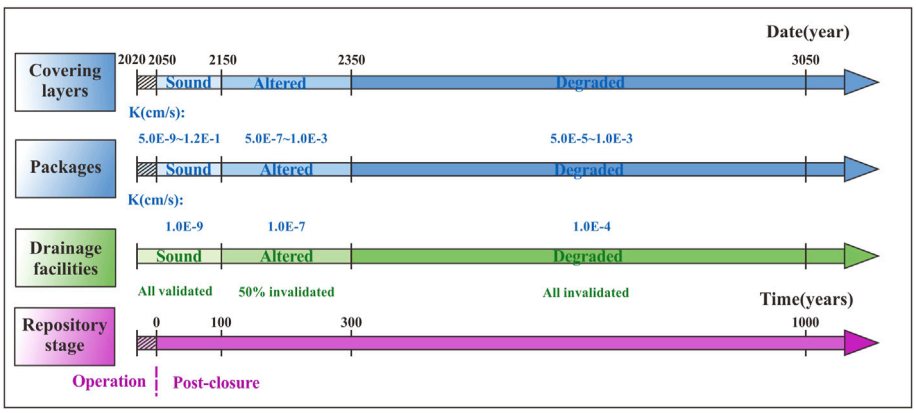

FIGURE 3 | Time phase and states of main facilities components in simulations.

3 MODELING METHOD AND SETTING

In total four time-continuous groundwater flow models were established following the state's changes to the disposal repository. The first flow model was the current flow model, which aimed to simulate the flow dynamics from operation to closure of the disposal repository. The covering layer was not formed in this period. The second one was called the sound stage flow model. Because of the addition of the covering layer, the model structure needed to be adjusted. In this period, the drainage facilities ran smoothly, and the lithology of the covering layer and disposal unit was also stable. Hence, the hydraulic parameters were at their original value in simulation. The third flow model was defined as the altered state flow model. Due to the degradation of the artificial facilities and disposal materials, the drainage structures, hydraulic

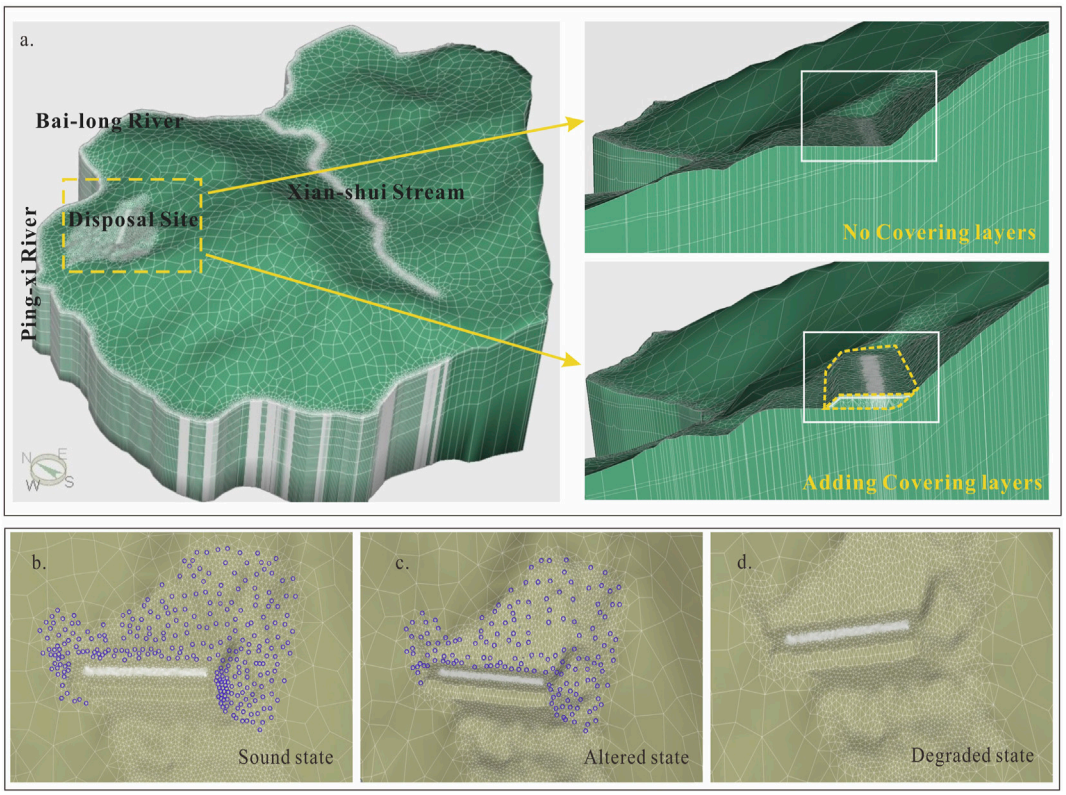

FIGURE 4 | (A) Schematic graphs of space discretization before and after adding covering layers. **(B–D)**: Simulation of drainage facilities under different states.

parameters of the disposal unit, and covering layer were needed to make the corresponding adjustments. The last was the degraded state model, with artificial drainage facilities failing; the covering layer and disposal unit materials were wholly degraded and homogenized. The hydraulic parameters should be adjusted along with the change of the artificial facilities states in simulations. The specific and critical model settings were described as follows:

3.1 Model Scope and Boundary Conditions

The extent of the regional model was decided by the hydrological conditions of the mountain area. Pingxi river in the north of the disposal site flowed into the Bailong River from west to east. The inlet was at the northeast corner of the disposal site. Therefore, the two fixed head boundaries were determined by a north river and a river in the northeast. In addition, it was surrounded by a natural surface ditch and ridge along the west and south boundaries, which made the region an essentially isolated hydrogeologic unit (**Figure 1A**). A high hill in the south could be considered an impermeable boundary (**Figure 1B**). The west boundary was determined by a natural ditch called Yangjia Ditch as a mixed boundary (**Figure 1A**). The primary river Pingxi River, from west to east, was simulated as a head-dependent flow boundary. A stream named Xianshui Stream was in the middle of the study area (**Figure 1A**). It was treated as a drainage ditch boundary in simulations because it didn't exist a stable water level all along. After being recharged by precipitation, the groundwater flowed from the hilly area to the foot of the hills and discharged mainly into the Pingxi River, and then flowed out through the Bailong River.

3.2 Grid Structure and Seepage Boundary

According to the lithology of the study area, the whole model was vertically divided into nine layers. Grid encryption was carried out in the disposal site area and the rivers. Cells' size (side length) was generally 50–100 m in most study areas and was encrypted in the disposal area by less than 15 m. Moreover, the model structure changed when adding the covering layers above the disposal units. Showed in **Figure 4A**, after adding the covering layers, the covering layer's cells needed to overlay the disposal unit's cells in the model structure.

Seepage boundaries were used to simulate the drainage facilities, and they would change along with three different states. In the sound state, the seepage boundaries were set at all the locations of drain holes (**Figure 4B**). The drainage facilities were supposed to lose efficacy at an altered state, so there were half holes being chosen uniformly and randomly to keep seepage boundaries (**Figure 4C**). In the degraded state, the drainage facilities were assumed to be invalid. Therefore, we canceled the seepage boundaries in this period, as shown in **Figure 4D**.

TABLE 2 | Hydraulic conductivity of covering sub-layers and packages under different states (unit: m/s).

States	Time (year)	Sub-layer number						Packages (E)
		VL (E)	WRL (E)			CL (E)	LSL (E)	
		1	2	3	4	5	6	
Sound state	**2050–2,150**	1.0–5	1.0E-8	1.20E-3	5.0E-11	1.0–9	1.0–7	5.0E-13
Altered state	**2,151–2,350**	3.0–5	1.0E-7	1.0E-3	5.0E-10	5.0–9	1.2–7	5.0E-11
	2,351–2,550	5.0–5	5.0E-7	5.0E-5	5.0E-8	1.0–8	3.5–7	5.0E-9
Degraded state	**2,551–3,050**	1.0–6	1.0E-6	1.0E-5	5.0E-7	1.0–6	1.0–6	5.0E-6

3.3 Hydraulic Conductivities

The mathematical models for groundwater flow in fractured media mainly included the following:

- The equivalent continuous media model
- Discrete fracture network model
- Dual media model
- Coupling model

Each one had its applicable conditions. If REV (Representative Element Volume) existed in the study fracture area and was small enough compared with the scale of the study area, the equivalent continuum model can be used to describe the groundwater movement in this fractured media (Zhifang, 2007). According to this, we contrasted the range of study areas and the REV of weathered argillic shale. The REV was less than 30 m × 15 m based on Lili Zhang's research (Lili, 2011), and the study area was about 13.1 km^2, more than two orders of magnitude both in width and length. Therefore, an equivalent continuous medium was used to generalize fractured media in this study. The whole study area was generalized into the heterogeneous, three-dimensional, and transient groundwater flow system.

Therefore, the rock, soils, and artificial disposal facilities in the site area were generalized as the equivalent continuous isotropic medium in this study. **Table.1** showed the value range assigned for the dirt and rock layers according to the rock hydraulic properties and previous field hydraulic testing results by the preliminary site investigation from the Beijing Research Institute of Uranium Geology (BRIUG). Also,these parameters were regarded as invariant over time.

Considering the covering layers' designed structure and possible future degradation for artificial facilities, the covering layers were subdivided into six layers for different filling materials based on four sub-layers (**Figure 2A**). Three aging states (**Figure 3**) were assumed. Six layers, including one vegetable layer (VL), three water-retaining layers (WRL), one clay layer (CL), and one local soil layer (LSL). Three aging states included sound state, altered state, and degraded state. The material parameters in every state were uniform and steady in simulations. So, different hydraulic conductivity values were assigned to characterize its hydraulic properties and aging state at various future times according to the material's property (**Table 2**).

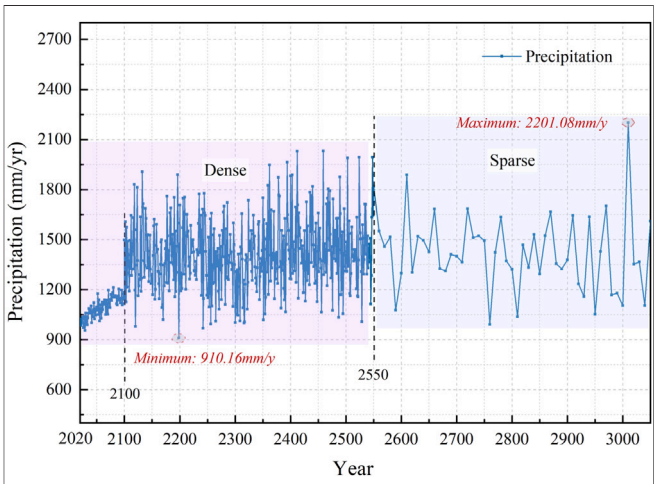

FIGURE 5 | Predicted precipitation curve in Rcps4.5 (Low GHG emissions condition of Representative Concentration Pathway Climate Scenario) by Institute of Earth Environment, Chinese Academy of Sciences.

3.4 Precipitation

The primary recharge source of groundwater in the study area was atmospheric precipitation infiltration. According to the different outcropping lithology and the influence of topographic slope, the annual rainfall recharge in the study area was divided and calculated by giving different infiltration coefficients. For a long-term assessment with a thousand-year scale, more factors could affect the climate and precipitation. According to a peer meteorological particular study had been conducted by the Institute of Earth Environment, four Representative Concentration Pathways Climate Scenarios (RCPs) were designed based on multiple earth system models: RCP2.6, RCP4.5, RCP6.0, and RCP8.5, corresponding to very low, low, moderate, and high greenhouse gas (GHG) emissions conditions, respectively. In each RCPs climate scenario, there was a corresponding precipitation curve over time. The RCPs4.5 climate scenario was the most usual and comparatively conservative scenario therein. Thus, the rainfall under RCPs 4.5 climate scenario was chosen in future prediction simulations. As **Figure 5** showed, the precipitation had an overall increasing trend in the future. Before 2,100, the rainfall rose sharply, and after 2,100, the amount of rain fluctuated remarkably, ranging from 910.16 to 2,201.08 mm/y. After 2,550, the precipitation value became sparse, with one per

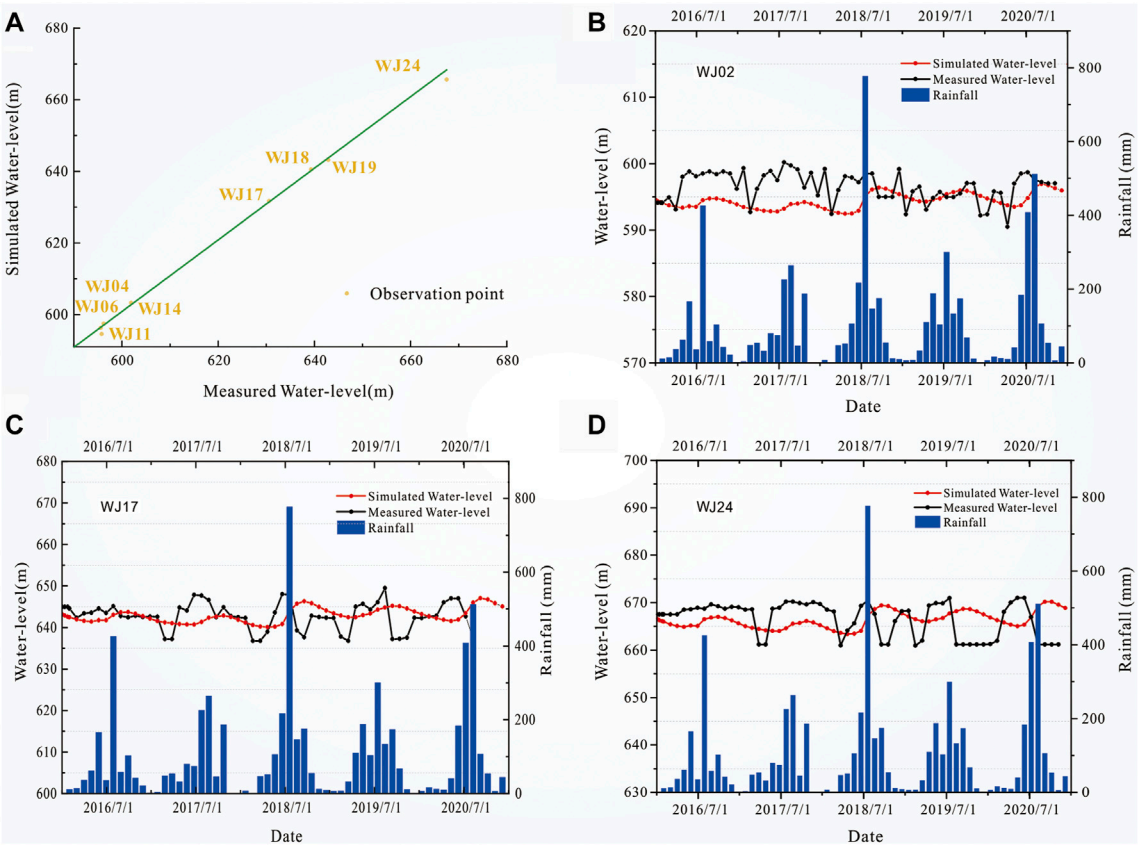

FIGURE 6 | (A) Fitting diagram of groundwater observation wells in steady flow. **(B–D)** Fitting diagram of groundwater observation wells WJ02, WJ17, and WJ24 in transient flow.

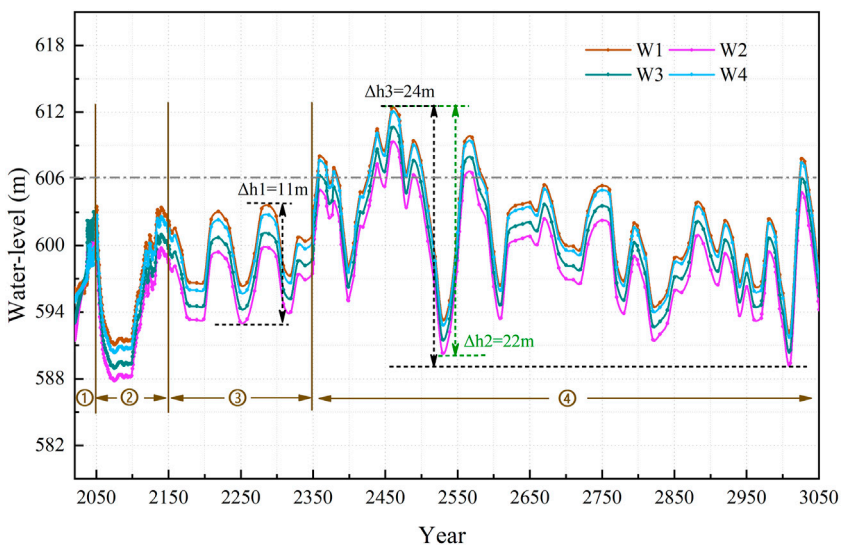

FIGURE 7 | Variation curves of groundwater levels of LILW repository from 2,020 to 3,050.

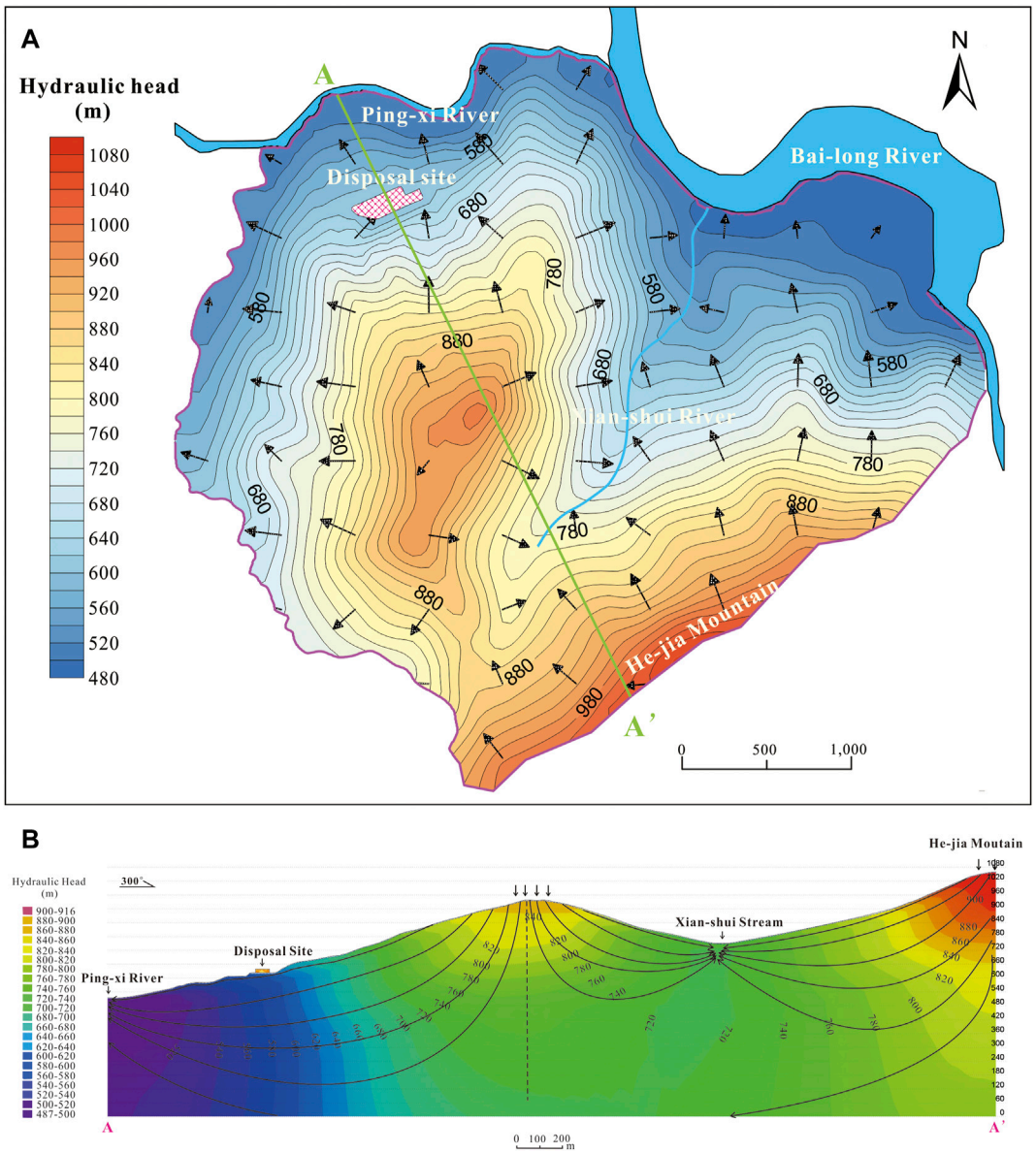

FIGURE 8 | (A) Flow field diagram of the study area in 2,150. **(B)** Flow field profile in the northwest direction in 2,150.

decade. Hence, the rainfall values were supposed to be the same every decade during simulations.

4 RESULTS AND DISCUSSION

4.1 Model Calibration

The flow equilibrium analysis and the fitting comparison between the actual and simulated hydraulic head of boreholes were used to identify and calibrate the current mode. After numerous adjusting parameters, the current model had an equilibrium in recharge and discharge, and the water levels fitted well. The benchmark data of the steady flow groundwater level fitting was the average value of the stable water levels in the dry and wet seasons from 2016 to 2020. Nine representative monitor boreholes located near the disposal site were analyzed. The mean absolute error was 1.5 m and the square of correlation coefficient $R^2 = 0.99 \approx 1$, which means the simulated water levels were very close to the actual situation. **Figure 6A** showed the fitting diagram of measured and observed values, and each point was very close to the line, indicating that the simulation value made a pretty good agreement with the measured data.

After the calibration of transient flow, the groundwater flow model can better simulate the dynamic change of groundwater in the study area and reproduce the response process of groundwater to rainfall. The monitoring water level data from 2016 to 2020 were used for identification and verification. **Figures 6B–D** showed the dynamic fitting results of water level of observation wells WJ02, WJ17, and WJ24. The variation trends of simulated and observed

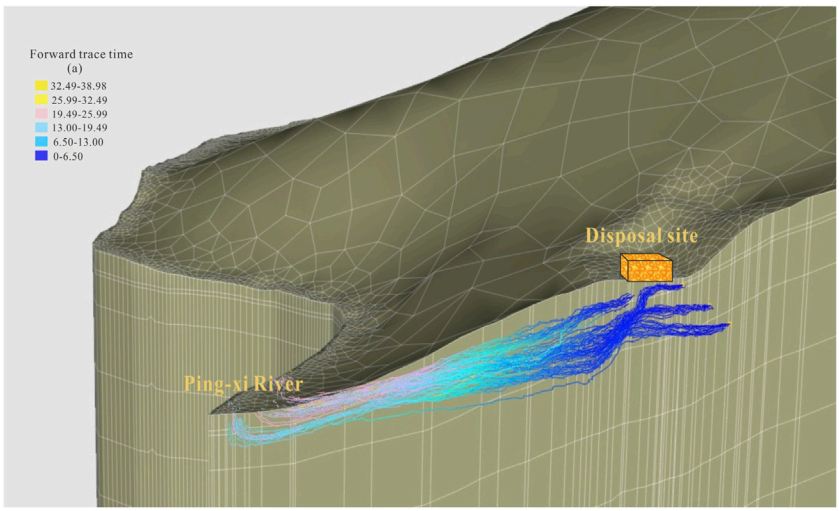

FIGURE 9 | Particles' travel lines from the aquifer beneath the repository to the Pingxi River.

water levels were the same by comparing the process line of simulated and measured water levels. The fluctuations of unreal water levels were basically in accord with the changes in rainfall. In conclusion, the steady and unsteady water level fitting results reached the general fitting goals.

4.2 Groundwater Level Prediction and Analysis

4.2.1 Groundwater Level

To better understand groundwater levels of the disposal units, four virtual monitoring points in disposal units were set (locations of W1, W2, W3, and W4 can be seen in **Figure 2B**). As the variation curves showed, the change of hydraulic head had a linear increase in the operation stage (years 2020–2050) of the disposal units (**Figure 7**①, which is in accordance with the change in rainfall.

In 2,050, the disposal units will be manually covered. The sound state was defined from 2050 to 2,150 while all artificial facilities were under regular operation (covering layers and waste packages were not degraded, and drainage facilities are fully operational). As a result, the groundwater levels dropped rapidly in this period (**Figure 7**②). It was possible because the small waterproof space formed as the instantly adding covering layers during simulation. That would bring less infiltration. However, as the rainfall increased and the surrounding continuous groundwater recharge, groundwater began to recover gradually, and by 2,150, it nearly reached the level before adding the covering layers.

After that, the artificial facilities were supposed to come into an altered stage (from 2,150 to 2,350, **Figure 3**). In this stage, half of the drain facilities stochastically occurred plugging or blocking after more than 100 years' use. The covering layers and packages' material hydraulic properties had aging problems (**Figure 3**). The resulting curve showed the groundwater appeared to have a similar fluctuation shape variation to the precipitation change, and the range of fluctuation was 11 m (**Figure 7**③, $\Delta h1$).

After 2,350, all artificial facilities were assumed under the complete degradation stage, which means the drainage facilities completely failed. It can be seen that the change in water level had a more significant fluctuation than that in the altered stage by a fluctuation range of 24 m (**Figure 7**④, $\Delta h3$).

Above all, it can be concluded that the groundwater level of the disposal unit was basically controlled by precipitation, especially the drainage facilities had a particular regulating effect on the groundwater level, which can cut down the fluctuation impact brought by rainfall's fluctuation to some degree by lowering the maximum amplitude of groundwater level variation at the disposal site from 22 m (**Figure 7**, $\Delta h2$) to 11 m (**Figure 7**③, $\Delta h1$) under roughly the same rainfall fluctuation (**Figure 5**, year 2,150–2,550). The huge water level fluctuations came from the more significant change in rainfall, the biggest difference was up to 1,290.92 mm. According to the predicted results, the groundwater level would not be beyond the bottom of the repository before 2,350. After 2,350, when the rainfall was more remarkable than 1950 mm/y for 10 years, the groundwater level would be beyond the bottom of the repository, but there will be no immersion phenomenon.

4.2.2 Flow Field

In the region flow, shallow water generally flowed from south to north, controlled by rainfall and topography, and drained into rivers and gullies from the top places of the terrain. According to the plane, the flow field shown in **Figure 8A**, Pingxi River, Bailong River, Xianshui Stream, and Yangjia Ditch were discharge sites. The groundwater flow direction was north for the disposal area, flowing from the south slope to the Pingxi River. It can be seen from the northwest section flow field (**Figure 8B**) that there were double groundwater flow systems in the study area: the local and regional groundwater flow systems. The groundwater in the disposal area participated in a local groundwater flow

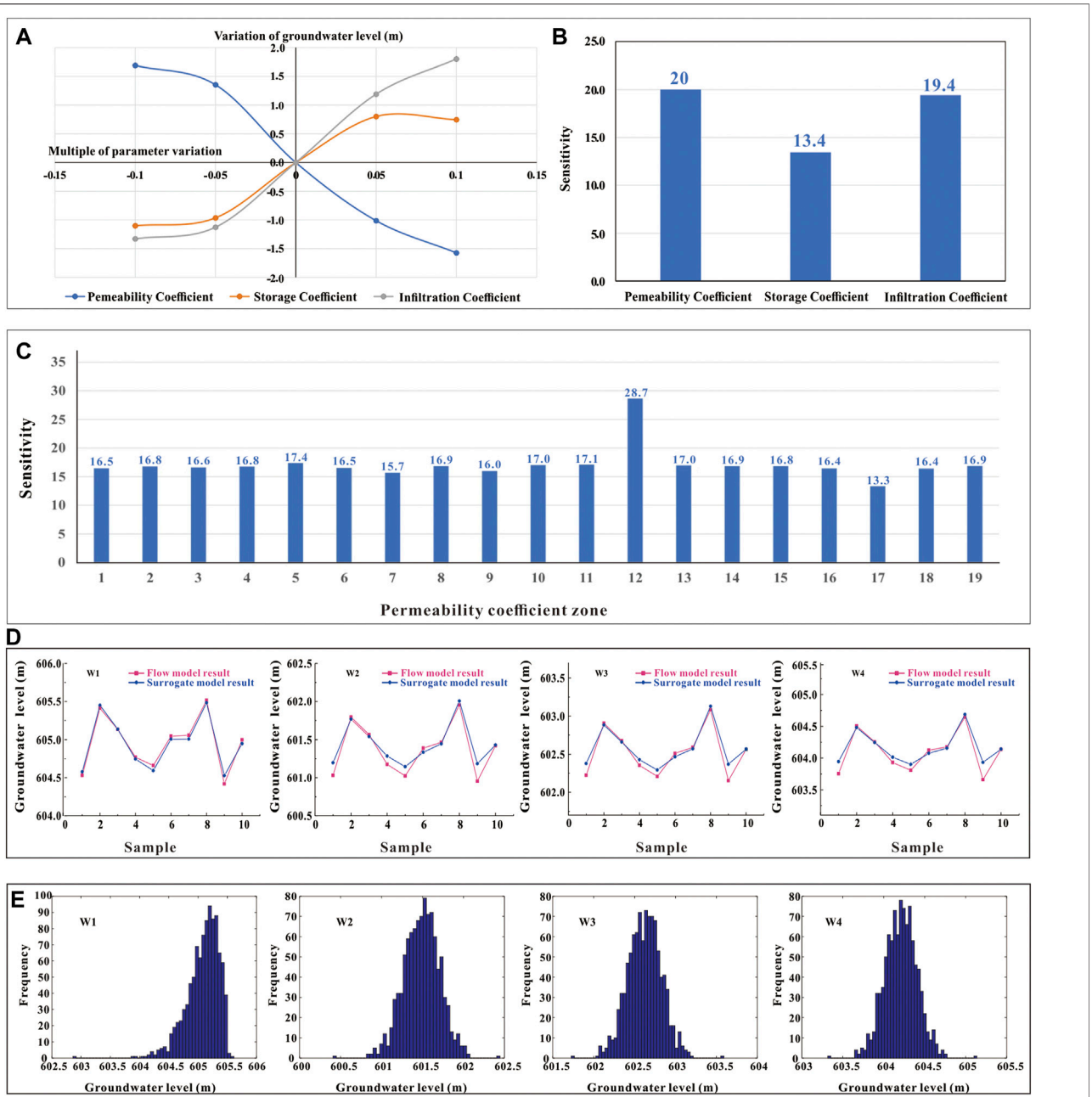

FIGURE 10 | (A,B). Groundwater level variation diagram and sensitivity histogram. **(C)**. Sensitivity histogram of all permeability coefficient zones. **(D)**. Fitting results of groundwater levels of four virtual monitoring holes (W1, W2, W3, W4) between the 2,150 years' surrogate model and groundwater flow model. **(E)**. Frequency distributions of groundwater level terms by the 2150-years surrogate model.

system circulation, which was mainly supplied by the rainfall on the high places of the adjacent slope and flowed into the Pingxi River along the north, and the circulation depth was shallow (depth less than 300 m). In addition, the Xianshui Stream, as the main outlet, belonged to another local groundwater flow system. Groundwater flowed from both sides of higher places to it. The rainfall in the Hejia Mountain area would also flow deep underground (minimum depth of over 500 m) and drained into the Pingxi River, forming a regional groundwater flow system.

4.2.3 Particle-Tracking Test

To know the time groundwater flowing from the disposal site to Pingxi River would spend, some water particles in the aquifer under the disposal units were set to figure out the possible runoff path and the travel time flowing to outlets based on the current model. The results showed the particles would flow north into the

TABLE 3 | Water level errors between surrogate models and groundwater flow models.

Well number	Surrogate Model					
	2,150 (year)		2,350 (year)		3,050 (year)	
	MSE	R^2	MSE	R^2	MSE	R^2
W1	0.0003	0.9772	0.0026	0.9652	0.0027	0.9653
W2	0.0015	0.9406	0.002	0.9291	0.0022	0.9386
W3	0.0012	0.9368	0.0032	0.907	0.0025	0.9161
W4	0.0016	0.9206	0.0035	0.9286	0.0047	0.9221

Pingxi River, and the whole process took less than 25.99 years. The fastest particle took less than 19.49 years (**Figure 9**). Along with these path lines, the depth of the groundwater level was getting smaller and smaller. Also, the range of the depths is mainly in the top two layers, ranging from 0 to 45 m.

4.3 Uncertainty Analysis of Groundwater Flow Model Parameters

Due to the uncertainty of the input parameters of the flow model, the sensitive parameters of groundwater level and the change ranges and characteristics of groundwater level caused by the possible variety of the sensitive parameters were further analyzed.

4.3.1 Sensitivity Analysis

The factor transformation method of a local sensitivity analysis method was used to determine sensitive parameters and partition parameters in the groundwater flow models. In models, permeability coefficient, rainfall infiltration coefficient, and water storage coefficient were the main considered parameters. As shown in **Figures 10A,B**, the sensitivity of the permeability coefficient was the highest, the sensitivity of the infiltration coefficient was the second, and the sensitivity of the water storage coefficient was the lowest. And the most significant sensitivity area of the three corresponding parameters was chosen as the sensitive variable for the subsequent uncertainty analysis. Taking the permeability coefficient, for example (**Figure 10C**), the 12th permeability coefficient partition had the most considerable sensitive value, so the permeability coefficient in the 12th partition was determined to be the sensitive variable. The same method determined the most sensitive infiltration and water storage coefficient zones.

4.3.2 Surrogate Models

Due to the time-consuming operation of the four flow models, it would take a lot of time to conduct thousands of simulations. Therefore, to save calculation time, three surrogate models were built to analyze groundwater levels condition in 2,150, 2,350, and 3,050 years, respectively. The surrogate models' construction process included: 1) Generation of 50 samples for each surrogate model. The procedures involved using the Latin Hypercube Sampling method (Zhang and Pinder, 2003) to obtain 50 groups of model parameters and then inserting them into the groundwater numerical model to get the water level results in four virtual monitoring wells of the disposal site. 2) Using the Support Vector Regression (SVR) method (Bozorg-Haddad et al., 2020) to train the surrogate model based on the randomly chosen 40 groups of model parameters and the running result values in the 50 groups of samples. 3) Surrogate model testing. The remaining ten groups of sample parameters and running results were used to verify the accuracy of the surrogate models. Taking the 2150-year surrogate model as an example, shown in **Figure 10D**, the results of the groundwater level of four virtual monitoring holes fitted well with the surrogate model. The mean square error MSE was small, the maximum was not more than 0.0016, and the determinate coefficients R2 were above 0.92. These data indicated the established support vector regression model had high precision and met the requirements of calculation, which can approximately replace the function of groundwater flow models. The 2350-and 3050-years surrogate models fitted well with the flow models as well, and the accuracy calculation results of the three surrogate models were shown in **Table 3**.

4.3.3 Uncertainty Analysis Results

Using the Latin Hypercube Sampling method to obtain 1,000 samples according to the probability distribution characteristics of random variables, three surrogate models were used to calculate the groundwater level results. After that, the SPSS software was used to conduct the K-S test for the prediction results. The statistical indexes result can see in **Table 4**. The frequency distribution characteristics of groundwater levels in 2,150, 2,350, and 3,050 years showed in **Figure 10E**. The frequency distributions of groundwater levels were Skewed and

TABLE 4 | Frequency distributions characteristics of groundwater level terms predicted by three time period surrogate models.

Well number	Groundwater level											
	2,150 (year)				2,350 (year)				3,050 (year)			
	W1	W2	W3	W4	W1	W2	W3	W4	W1	W2	W3	W4
Mean	605.08	601.49	602.62	604.21	605.45	602	603.11	604.62	603.95	600.7	601.51	603.02
SD	0.28	0.22	0.21	0.2	0.08	0.11	0.12	0.09	0.08	0.11	0.12	0.09
Max	605.61	602.45	603.59	605.14	605.61	602.25	603.38	604.81	604.11	600.95	601.78	603.21
Min	602.86	600.41	601.73	603.32	605.21	601.75	602.84	604.39	603.71	600.45	601.24	602.79
Skewness	-1.33	-0.13	-0.02	-0.02	-0.08	0.38	0.39	0.2	-0.08	0.34	0.43	0.21
Distribution	Skewed	Normal	Normal	Normal	Normal	Skewed	Skewed	Skewed	Normal	Skewed	Skewed	Skewed

TABLE 5 | Confidence interval of groundwater levels in 2,150, 2,350, and 3,050.

Well number	Groundwater level								
	2,150 (year)			2,350 (year)			3,050 (year)		
	95%	80%	60%	95%	80%	60%	95%	80%	60%
W1	604.61–605.54	604.84–605.32	605.01–605.15	605.31–605.58	605.38–605.52	605.43–605.47	603.81–604.08	603.88–604.02	603.93–603.97
W2	601.13–601.85	601.31–601.67	601.43–601.55	601.82–602.17	601.91–602.09	601.97–602.03	600.52–600.87	600.61–600.79	600.67–600.73
W3	602.28–602.96	602.45–602.80	602.57–602.68	602.92–603.30	603.01–603.20	603.08–603.14	601.32–601.70	601.41–601.60	601.48–601.54
W4	603.89–604.53	604.04–604.37	604.16–604.26	604.48–604.76	604.55–604.69	604.60–604.64	602.88–603.16	602.95–603.09	603.00–603.04

Normal distribution. And the confidence interval and the range of groundwater level variation can be calculated according to these frequency distributions.

As **Table.5** showed, in 2,150, the groundwater level of four virtual observation wells had a 95% probability of being between 601.13 and 605.54 m. In 2,350, the water levels of four virtual observation well had a 95% probability of being between 601.82 and 605.58 m. In 3,050, the water level of virtual observation wells was between 600.52 and 604.08 m, which was all lower than the elevation of the disposal platform.

5 CONCLUSION

In this study, a set of groundwater flow models at the regional scale was constructed to analyze and predict the possible change in groundwater within a millennial scale. The models considered the artificial facilities' function and potential alterations, including the adequate, partial failure, and complete failure drainage facilities, the addition of the covering layer, and the degradation of disposal unit materials over time. The results showed groundwater level of the disposal unit was basically controlled by precipitation, especially the drainage facilities had a particular regulating effect on the groundwater level, which can cut down the fluctuation impact brought by rainfall fluctuation to the degree of lowering the maximum amplitude of groundwater level variation at the disposal site from 22 to 11 m under roughly the same rainfall fluctuation. Therefore, the drainage facilities can protect the disposal units from soaking groundwater. Keeping them effective can help store radioactive waste. From the perspective of store safety in radioactive waste and groundwater, we made sensitivity and uncertainty analysis to predict the groundwater level range and probability in 2,150, 2,350, and 3,050. Also, we assessed the groundwater circulation process and expected the groundwater migration time from the disposal site to the discharge area by the current model. The main conclusions from this study include:

Long-term flow models showed that groundwater levels would not be beyond the bottom of the repository before 2,350. But after 2,350, when the rainfall was more significant than 1950 mm/y for 10 years, all the drainages lost efficacy, and the groundwater level would be higher than the bottom surface of the disposal units. The uncertainty analysis results showed that in 2,150, the groundwater levels of four virtual observation wells had a 95% probability of being between 601.13 and 605.54 m. In 2,350, the groundwater levels of virtual observation wells had a 95% probability of being between 601.82 and 605.58 m. In 3,050, the groundwater levels of virtual observation wells were between 600.52 and 604.08 m, all lower than the elevation of the disposal platform with a height of 606 m. The groundwater in the disposal area participated in a local groundwater flow system circulation, which was mainly supplied by the rainfall on the high places of the adjacent slope and flowed into the Pingxi River along the north, and the circulation depth was shallow (depth less than 300 m). Particle-tracking numerical tests showed the particles

would flow north into the Pingxi River, and the whole process took less than 25.99 years. The fastest particle took less than 19.49 years.

This work was a critical regional groundwater flow modeling case for the long-term safety assessment of a particular LILW near-surface disposal repository. These results can provide a basis for further analysis of radioactive waste migration range and time, and also provide references for regional flow modeling processes in near-surface disposal engineering. Besides, there were some deficiencies in this work. In the time nodes given, they were subjectively defined according to the service life of artificial facilities, but the time is uncertain. Therefore, how to deal with the uncertainties is a meaningful research topic for radioactive disposal safety in the future.

DATA AVAILABILITY STATEMENT

The original contributions presented in the study are included in the article/Supplementary Material; further inquiries can be directed to the corresponding author.

AUTHOR CONTRIBUTIONS

HZ: drafting the manuscript. QZ: revising and editing the manuscript. YuC: data collection and provision of the study area. JS: development or design of the methodology. YaC: site survey and data analysis. WW: building flow models. SH: uncertainty analysis.

FUNDING

This work was supported by the project of Systematic Analysis of the whole safety process of Low and Medium Radioactive Solid Waste Disposal Site in Fei-feng Mountain.

ACKNOWLEDGMENTS

The authors are grateful to the peer climate studies by the Institute of Earth Environment, Chinese Academy of Sciences, and fracture and hydraulic test results data from Nuclear Industry Southwest Geotechnical Investigation and Design Institute Co., Ltd.

REFERENCES

Ashraf, A., and Ahmad, Z. (2008). Regional Groundwater Flow Modelling of Upper Chaj Doab of Indus Basin, Pakistan Using Finite Element Model (Feflow) and Geoinformatics. *Geophys. J. R. Astronomical Soc.* 173 (1), 17–24. doi:10.1111/j.1365-246X.2007.03708.x

Birkholzer, J. T., Tsang, C.-F., Bond, A. E., Hudson, J. A., Jing, L., and Stephansson, O. (2019). 25 Years of DECOVALEX - Scientific Advances and Lessons Learned from an International Research Collaboration in Coupled Subsurface Processes. *Int. J. Rock Mech. Min. Sci.* 122 (122), 103995. doi:10.1016/j.ijrmms.2019.03.015

Bozorg-Haddad, O., Delpasand, M., and Loáiciga, H. A. (2020). Self-optimizer Data-Mining Method for Aquifer Level Prediction. *Water supply* 20 (2), 724–736. doi:10.2166/ws.2019.204

Bracke, G., and Fischer-Appelt, K. (2015). Methodological Approach to a Safety Analysis of Radioactive Waste Disposal in Rock Salt: An Example. *Prog. Nucl. Energy* 84, 79–88. doi:10.1016/j.pnucene.2015.01.012

Bracke, G., Kudla, W., and Rosenzweig, T. (2019). Status of Deep Borehole Disposal of High-Level Radioactive Waste in Germany. *Energies* 12, 2580. doi:10.3390/en12132580

Bugai, D., Skalskyy, A., Dzhepo, S., Kubko, Y., Kashparov, V., Van Meir, N., et al. (2012). Radionuclide Migration at Experimental Polygon at Red Forest Waste Site in Chernobyl Zone. Part 2: Hydrogeological Characterization and Groundwater Transport Modeling. *Appl. Geochem.* 27 (27), 1359–1374. doi:10.1016/j.apgeochem.2011.09.028

Chapman, N. (2019). Who Might Be Interested in a Deep Borehole Disposal Facility for Their Radioactive Waste? *Energies* 12, 1542. doi:10.3390/en12081542

Cornelissen, T., Diekkrüger, B., and Bogena, H. (2016). Using High-Resolution Data to Test Parameter Sensitivity of the Distributed Hydrological Model Hydrogeosphere. *Water* 8 (5), 202. doi:10.3390/w8050202

Darda, S. A., Gabbar, H. A., Damideh, V., Aboughaly, M., and Hassen, I. (2021). A Comprehensive Review on Radioactive Waste Cycle from Generation to Disposal. *J. Radioanal. Nucl. Chem.* 329 (1), 15–31. doi:10.1007/s10967-021-07764-2

De Caro, M., Crosta, G. B., and Previati, A. (2020). Modelling the Interference of Underground Structures with Groundwater Flow and Remedial Solutions in Milan. *Eng. Geol.* 272, 105652. doi:10.1016/j.enggeo.2020.105652

Deng, D., Zhang, L., Dong, M., Samuel, R. E., Ofori-Boadu, A., and Lamssali, M. (2020). Radioactive Waste: A Review. *Water Environ. Res.* 92, 1818–1825. doi:10.1002/wer.1442

Fu, J., and Gómez-Hernández, J. (2009). Uncertainty Assessment and Data Worth in Groundwater Flow and Mass Transport Modeling Using a Blocking Markov Chain Monte Carlo Method. *J. hydrology* 364 (3-4), 328–341. doi:10.1016/j.jhydrol.2008.11.014

Geetha Manjari, K., and Sivakumar Babu, G. L. (2017). Probabilistic Analysis of Groundwater and Radionuclide Transport Model from Near Surface Disposal Facilities. *Georisk Assess. Manag. Risk Eng. Syst. Geohazards* 12, 60–73. doi:10.1080/17499518.2017.1329538

IAEA (1994). *Siting of Near Surface Disposal Facilities*. Vienna: International Atomic Energy Agency. IAEA Safety Series No. 111-G-3.1.

Jafari, F., Javadi, S., Golmohammadi, G., Mohammadi, K., Khodadadi, A., and Mohammadzadeh, M. (2016). Groundwater Risk Mapping Prediction Using Mathematical Modeling and the Monte Carlo Technique. *Environ. Earth Sci.* 75 (6), 491. doi:10.1007/s12665-016-5335-9

Jeong, J., Kown, M., and Park, E. (2018). Safety Assessment of Near Surface Disposal Facility for Low-And Intermediate-Level Radioactive Waste (LILW) through Multiphase-Fluid Simulations Based on Various Scenarios. *Econ. Environ. Geol.* 2 (51), 131–147. doi:10.9719/EEG.2018.51.2.131

Klein, E., Hardie, S. M. L., Kickmaier, W., and McKinley, I. G. (2021). Testing Repository Safety Assessment Models for Deep Geological Disposal Using Legacy Contaminated Sites. *Sci. Total Environ.* 776, 145949. doi:10.1016/j.scitotenv.2021.145949

Kozak, M. W. (2017). "Safety Assessment for Near-Surface Disposal of Low and Intermediate Level Wastes," in *Geological Repository Systems for Safe Disposal of Spent Nuclear Fuels and Radioactive Waste*. Second Edition, 475–498. doi:10.1016/b978-0-08-100642-9.00016-5

Lee, S., and Kim, J. (2017). Post-closure Safety Assessment of Near Surface Disposal Facilities for Disused Sealed Radioactive Sources. *Nucl. Eng. Des.* 313, 425–436. doi:10.1016/j.nucengdes.2017.01.001

Li, X., Li, D., Xu, Y., and Feng, X. (2020). A DFN Based 3D Numerical Approach for Modeling Coupled Groundwater Flow and Solute Transport in Fractured Rock Mass. *Int. J. Heat Mass Transf.* 149, 119179. doi:10.1016/j.ijheatmasstransfer.2019.119179

Lili, Z. (2011). *Determining the Representative Elementary Volumes of Fracture Rock Mass Based on Permeability Analysis*. Beijing: China university of geoscience, 20–111. (in Chinese).

LLWR (2011). *The 2011 ESC: Hydrogeology*. LLWR/ESC/R(11)10022.

Michie, U. M. (1998). Deep Geological Disposal of Radioactive Waste A Historical Review of the UK Experience. *Interdiscip. Sci. Rev.* 23 (2), 242–257. doi:10.1179/isr.1998.23.3.242

Parameswaran, T. G., Anusree, N., Sughosh, P., Sivakumarbabu, G. L., and Deepagoda, T. K. K. C. (2021). Suitability of Mechanically Biologically Treated Waste for Landfill Covers. *Lect. Notes Civ. Eng.* 144, 511–519. doi:10.1007/978-981-16-0077-7_44

Santos, J. E., Xu, D., Jo, H., Landry, C. J., Prodanović, M., and Pyrcz, M. J. (2020). Poreflow-net: A 3D Convolutional Neural Network to Predict Fluid Flow through Porous Media. *Adv. Water Resour.* 138, 103539. doi:10.1016/j.advwatres.2020.103539

SKB (2013). *Flow Modelling on the Repository Scale for the Safety Assessment. SDM-PSU Forsmark*. Stockholm: Svensk Kärnbränslehantering AB. SKB TR-13-08.

SKB (2014). *Flow and Transport Modelling on the Vault Scale. SDM-PSU Forsmark*. Stockholm: Svensk Kärnbränslehantering AB. SKB TR-14-14.

Sreekanth, J., Crosbie, R., Pickett, T., Cui, T., Peeters, L., Slatter, E., et al. (2020). Regional-scale Modelling and Predictive Uncertainty Analysis of Cumulative Groundwater Impacts from Coal Seam Gas and Coal Mining Developments. *Hydrogeol. J.* 28 (1), 193–218. doi:10.1007/s10040-019-02087-9

Watson, C., Wilson, J., Savage, D., and Norris, S. (2018). Coupled Reactive Transport Modelling of the International Long-Term Cement Studies Project Experiment and Implications for Radioactive Waste Disposal. *Appl. Geochem.* 97, 134–146. doi:10.1016/j.apgeochem.2018.08.014

Welch, E. M., Dulai, H., El-Kadi, A., and Shuler, C. K. (2019). Submarine Groundwater Discharge and Stream Baseflow Sustain Pesticide and Nutrient Fluxes in Faga'alu Bay, american samoa. *Front. Environ. Sci.* 7, 162. doi:10.3389/fenvs.2019.00162

Yi, S., Ma, H., Zheng, C., Zhu, X., Wang, H. a., Li, X., et al. (2012). Assessment of Site Conditions for Disposal of Low- and Intermediate-Level Radioactive Wastes: A Case Study in Southern China. *Sci. Total Environ.* 414, 624–631. doi:10.1016/j.scitotenv.2011.10.060

Yim, M.-S., and Simonson, S. A. (2000). Performance Assessment Models for Low Level Radioactive Waste Disposal Facilities: a Review. *Prog. Nucl. Energy* 36 (1), 1–38. doi:10.1016/S0149-1970(99)00015-3

Zhang, L., Xia, L., and Yu, Q. (2017). Determining the REV for Fracture Rock Mass Based on Seepage Theory. *Geofluids* 2017, 1–8. doi:10.1155/2017/4129240

Zhang, Y., and Pinder, G. (2003). Latin Hypercube Lattice Sample Selection Strategy for Correlated Random Hydraulic Conductivity Fields. *Water Resour. Res.* 39 (8), SBH 11. doi:10.1029/2002WR001822

Zhifang, Z. (2007). *Theory on Dynamics of Fluids in Fractured Medium*. Beijing: Higher Education Press, 24–80. (in Chinese).

Conflict of Interest: Author YC was employed by CNNC Everclean Environmental Engineering Co., Ltd.

The remaining authors declare that the research was conducted in the absence of any commercial or financial relationships that could be construed as a potential conflict of interest.

Publisher's Note: All claims expressed in this article are solely those of the authors and do not necessarily represent those of their affiliated organizations, or those of the publisher, the editors, and the reviewers. Any product that may be evaluated in this article, or claim that may be made by its manufacturer, is not guaranteed or endorsed by the publisher.

frontiers | Frontiers in Environmental Science

ORIGINAL RESEARCH
published: 21 June 2022
doi: 10.3389/fenvs.2022.926866

Effect of Large-Scale Mining Drainage on Groundwater Hydrogeochemical Evolution in Semi-Arid and Arid Regions

Ankun Luo[1,2,3], *Guangcai Wang*[1], *Shuning Dong*[2,3], *Hao Wang*[2,3], *Zheming Shi*[1]*, *Zhongkui Ji*[2,3] *and Jiankun Xue*[2,3]

[1]Key Laboratory of Groundwater Conservation of MWR, China University of Geosciences, Beijing, China, [2]Xi'an Research Institute of China Coal Technology and Engineering Group Corp, Xi'an, China, [3]Shaanxi Key Laboratory of Prevention and Control Technology for Coal Mine Water Hazard, Xi'an, China

Groundwater evolution and circulation in coal mining areas will be significantly affected by natural processes and human activities. However, the impacts of large-scale mining drainage on groundwater hydrochemistry are unclear in the semi-arid and arid inland coalfields in northwest China. In particular, for shallow buried areas, the spontaneous combustion of coal seam outcrops forms burnt rock that is rich in fractures. Being a strong water-yield aquifer after receiving recharge, burnt rock has become a potential source of mine water inrush hazards. Therefore, drainage from this aquifer is necessary to eliminate potential hazards, which also leads to the deterioration of the local ecological diversity and sustainability. The hydrogeochemical method is an effective way to study the source and evolution of groundwater in mining areas and to determine the long-term cumulative effect of mining and drainage on the hydrogeochemical evolution of burnt rock areas. It is, however, still poorly understood. In this study, we employed the hydrochemical and isotope (^{2}H, ^{3}H, and ^{18}O) to investigate the long-term effects of drainage on the hydrogeochemical evolution in the coalfield of southern Xinjiang, China. The results showed that the hydrochemical environment became more complex as the effect of recharge of different tritium-based groundwater ages in multiple-layered aquifer system and leads to the changes in the concentration of the chemical components. Before large-scale mining drainage, groundwater flowed from west to east and was finally discharged into the Kuqa River. The major water–rock interactions that occurred were the dissolution of halite, carbonate and gypsum dissolution, cation exchange, and dedolomitization. After large-scale and long-term mining drainage from the burnt rock aquifer, the groundwater flow field had changed, and the Kuqa river turned to recharge into the burn rock aquifer, the hydrochemical evolution also changed from water–rock interaction to mixture. This was caused by the significant decline in the groundwater level and changes in groundwater circulation in the mining area, which further led to the loss of valuable surface water resources in this arid area. Based on the characteristics and recharge conditions of burnt rock, we suggested that grouting can effectively cut off the hydraulic connection between the river and burnt rock and thus protect water resources.

Keywords: groundwater, large-scale mining drainage, burnt rock aquifer, hydrogeochemistry, semi-arid and arid regions

OPEN ACCESS

Edited by:
Yong Xiao,
Southwest Jiaotong University, China

Reviewed by:
Lishuang Guo,
Ministry of Emergency Management, China
Zhi Chen,
China Earthquake Administration, China

***Correspondence:**
Zheming Shi
szm@cugb.edu.cn

Specialty section:
This article was submitted to Freshwater Science, a section of the journal Frontiers in Environmental Science

Received: *23 April 2022*
Accepted: *13 May 2022*
Published: *21 June 2022*

Citation:
Luo A, Wang G, Dong S, Wang H, Shi Z, Ji Z and Xue J (2022) Effect of Large-Scale Mining Drainage on Groundwater Hydrogeochemical Evolution in Semi-Arid and Arid Regions. Front. Environ. Sci. 10:926866. doi: 10.3389/fenvs.2022.926866

INTRODUCTION

Spontaneous combustion is commonly observed in coal seam outcrops all around the world (Oren and Sensogut, 2010; Song et al., 2017; Kruszewski et al., 2018; Onifade and Genc, 2018; Zhang et al., 2020). During spontaneous combustion, heat spreads upwards, which causes the overlying rocks to heat up and transform into a suite of thermally metamorphosed rocks (named burnt rock) through a process known as combustion metamorphism (Shi et al., 2021). As a result, the color and structure of the burnt rock change significantly (Huang et al., 2008) and eventually turn reddish and rich in fractures. Previous studies have mostly focused on the petrology and mineralogy of burnt rocks to describe mineral and textural transformations during spontaneous combustion (Baboolal et al., 2018; Laita et al., 2019). However, the burnt rock becomes a strong water-yield aquifer after receiving recharge due to fractures created by the combustion metamorphism processes, affecting the safety of the underground coal mining process. In northwest China, burnt rocks are widely formed in the coal outcrop area as the shallow buried Jurassic strata (Ma et al., 2021). Yuan et al. (2019) have documented that the structure of the burnt rock is damaged with a large number of pores and fractures, which is one of the key factors of instability in the surrounding rock. Xue et al. (2021) employed the AHP and entropy-weight method to evaluate the water abundance of BRA and to avoid the recurrence of water inrush during coal mining. Because of the strong water yield, a water inrush from BRA occurred in the underground coal mine of Yongxin, causing a tunnel flooding incident that killed two people (Xue et al., 2021). In order to avoid such hazards, it is necessary to drain water from the overlying aquifer before mining (Dong et al., 2021). Secondary problems such as groundwater pollution (Wang et al., 2021b), ground subsidence (Zeng et al., 2020), and soil salinization (Zhang et al., 2007) may also occur. Furthermore, excessive drainage may change the flow path of the groundwater (Dimitrova-Petrova et al., 2020), which can complicate the hydrogeological condition of the mining area. The hydrogeochemical process and evolution of groundwater can reflect the flow process (Carrillo-Rivera et al., 2007; Xiao et al., 2022a), and the hydrogeochemical characteristics can change significantly in the mining area after excessive drainage. Therefore, it is necessary to study the hydrogeochemistry of BRA under the influence of large-scale mining drainage, which is poorly understood.

The hydrochemical and stable isotope analysis can be used to investigate the groundwater circulation, hydraulic connection, and water–rock interaction (Keita and Tang, 2017; Emvoutou et al., 2018; Meyzonnat et al., 2021). By combining the Piper diagram, Durov plot, and Gibbs plot, groundwater hydrogeochemical processes can be studied (Salameh et al., 2018). Stable isotopes and radioactive isotopes are used to identify the source and age of groundwater (Huang et al., 2017; Wang et al., 2021a). With the help of multivariate statistical analysis (MSA), such as hierarchical cluster analysis (HCA) (Barzegar et al., 2017), principal component analysis (PCA) (Dehghanzadeh et al., 2015; Xiao et al., 2022b), and correlation analysis (CA) (Qiao et al., 2019), a more reasonable explanation for the hydrogeochemical changes can be obtained (Qu et al., 2021).

In this study, the integration of hydrogeochemistry and isotope (^{2}H,^{18}O, and ^{3}H) analysis, MSA, hydrogeological condition, and coal mine exploitation was employed to identify the origins of groundwater and hydrogeochemical evolution under the influence of mining drainage in a typical arid coalfield located in southern Xinjiang that is affected by BRA in China. This work aimed to 1) identify the key factors controlling hydrogeochemical origin and evolution, 2) reveal the effect of large-scale mining drainage on the hydrogeochemistry for BRA in the coalfield, and 3) propose reasonable suggestions for water resource protection and mine safety production.

STUDY AREA

The A-ai coalfield is located in southern Xinjiang, China (**Figure 1**), which has a total area of 32 km^2. It is dominated by a continental arid climate, characterized by strong evaporation, low precipitation, and frequent droughts (Sabit et al., 2008), with an average annual precipitation of 90.09 mm and mean annual pan evaporation of 2,219 mm. Approximately, 85% of the annual precipitation occurs between June and September (Li et al., 2011). The landform is influenced by wind erosion with surface elevations varying from +1840 m to +2005 m, and the topography of the A-ai coalfield is generally a basin with high surroundings and a low middle. In addition, four gullies are perpendicular to this basin from the north to the south. The Kuqa River is the only perennial river in the region that acts as the main source of drinking water. A syncline runs through this area and stretches 12 km wide from west to east and has a length of 2–4 km from south to north. No other large faults are found here. The coal seam spreads along the two wings of the syncline and is exposed on the surface. Due to the subsurface spontaneous combustion of the coal seam, sandstone and mudstone on the roof have changed the appearance and petrologic characters into burnt rock with a great number of fractures (**Figure 2**). Therefore, the A-ai coalfield is bounded by gully Ⅰ in the west, the Kuqa river in the east, and the coal seam and burnt rock outcrop in the north and south (**Figure 1**).

The sedimentary sequence above coal-bearing strata in the study area is shown in **Figure 3**. From top to bottom, the strata are Quaternary and Jurassic. According to the microscopic features of typical samples from Jurassic, quartz, feldspar, mica, carbonate, and gypsum account for more than 90% (Liu et al., 2011). The quaternary aquifer (QA) is only deposited near gullies and the Kuqa river and has a thickness of 0–40 m. The Jurassic Ahe Group (J_{1a}) is dominated by fine sandstone and mudstone but is poor in water. The Jurassic Taliqike Group (J_{1t}) is the coal-bearing stratum, and above the coal seam is a sandstone confined aquifer (SCA). In the coal outcrop areas, the overlying rock of the coal seam gradually turns to melted or honeycombed forms, generating plenty of cracks and fractures during the

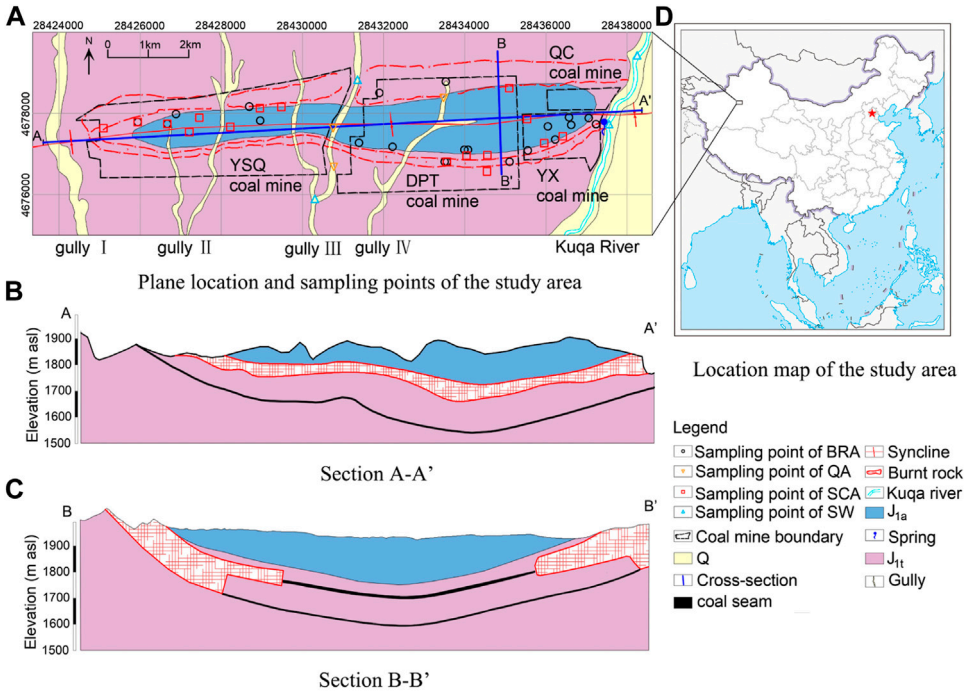

FIGURE 1 | General information about the study area and water sampling site **(A)** the plane location and sampling points of the study area; **(B)** the section A-A'; **(C)** the section B-B'; **(D)** the location map of the study area.

FIGURE 2 | (A) Burnt rock block and **(B)** outcrop.

combustion of coal. Burnt rocks can easily receive recharges from precipitation and become a strong water-yield aquifer. The drilling unit water inflow (q) is a generally accepted index in China to evaluate the water yield of an aquifer (Qiao et al., 2017). According to the pumping test, the average hydraulic conductivity (K) and q value (flow rate when the water level drops 10 m for a 91 mm borehole) of the SCA are 0.049 m/d and 0.017 L/(sm), respectively, indicating a weak permeability and water yield. Therefore, this aquifer has little impact on coal mining. In contrast, the burnt rock aquifer (BRA) is distributed at the outcrops of coal seams on both sides of the syncline with great permeability and a very strong wateryield (with an average K of 17.874 m/d and q of 11.434 L/(sm), indicating that BRA is the main water-filled aquifer and the primary threat to coal mining safety. Under natural conditions or before large-scale coal mining, the groundwater recharge sources are precipitation and surface water (SW) from gullies in the rainy season. The direction of groundwater flow is from the west to the east, which then gets discharged to the Kuqa River in the east in the form of spring and direct contact.

Four coal mines are distributed in this area, namely, Yushuquan (YSQ), Dapingtan (DPT), Yongxin (YX), and Qiuci (QC). From 2012 to 2014, due to the production of new mines and upgrades in the mining technology (from the

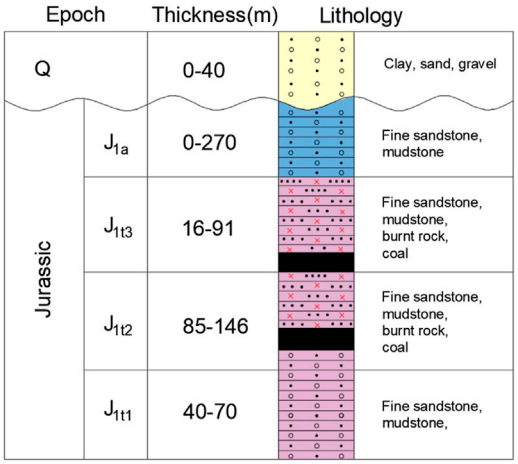

FIGURE 3 | Stratigraphic column of the study area.

pillar mining method to the comprehensive mechanized mining method), the amount of coal production increased sharply from 0.12 to 1.59 million tons per year and has since been maintained to date. Several water inrush disasters have occurred in this area, causing the deaths of 10 people and the flooding of several tunnels in the A-ai coalfield. Therefore, with an increase in mining output, the large-scale drainage of BRA has been carried out by drilling holes in an effort to avoid disasters such as that which occurred in 2015.

MATERIAL AND METHODS

Groundwater Sampling and Analytical Techniques

In this study, 46 water samples from groundwater and surface water were obtained from the A-ai coalfield from the years 2007–2021. The data included 22 samples from the BRA (including 1 sample from the spring), 17 samples from the SCA, 3 samples from QA, and 4 samples from SW (2 samples from the Kuqa river and 2 samples from the gully Ⅲ). Sampling locations were recorded using a portable GPS device and displayed in **Figure 1**. All of the groundwater samples were taken from springs or boreholes. Water samples were mainly analyzed at the Shaanxi Key Laboratory of Prevention and Control Technology for Coal Mine Water Hazard. The concentrations of Na^++K^+, Mg^{2+}, Ca^{2+}, SO_4^{2-}, and Cl^- ions were measured by ion chromatography, while the concentrations of HCO_3^- and CO_3^{2-} were measured by the traditional titrimetric method. The total dissolved solids (TDS) were calculated based on all the ion concentrations determined previously (**Table 1**). pH was measured *in situ* with a portable pH meter, and tritium (^3H) was determined on electrolytically enriched water samples by liquid scintillation spectrometry. For the reliability of the chemical data (Chen et al., 2015), the error of the charge balance error (CBE) was calculated as follows:

$$\mathrm{CBE} = \frac{\left|\sum cations - \sum anions\right|}{\left|\sum cations + \sum anions\right|} \times 100,$$

where all ions are measured in meq/L. The calculated results of the CBE showed that the uncertainty was less than ±5%, which is acceptable for this study. The stable isotopes of $\delta^{18}O$ and δ^2H were measured by using a liquid water isotope analyzer (LGR LWIA-24d) and compared with the Vienna standard mean ocean water standard, which had precisions of 0.21‰ and 0.04‰, respectively.

Pumping tests were conducted to obtain the aquifer hydraulic conductivity. A total of 10 single-hole steady-flow pumping tests were carried out in the study area in the past 10 years.

Multivariate Statistical Analysis

Multivariate statistical analysis has been widely used to extract valuable information from large hydrogeochemical datasets (Khanoranga and Khalid, 2019; Liu et al., 2020). In this study, hierarchical cluster analysis (HCA), principal component analysis (PCA), and correlation analysis (CA) were employed to analyze the hydrogeochemical classification and the temporal and spatial variation. The Ward linkage method and the Euclidean distance were performed in the HCA of this study, and a dendrogram was used to graphically show clusters of the datasets and their proximity (Cloutier et al., 2008). PCA is used to explain the majority of variance by extracting the eigenvalues from the correlation between the chemical variables (Singh et al., 2017), while CA can reveal a statistical relationship between two or more variables (Nagaraju et al., 2016). All statistical calculations were performed in SPSS software version 20.0 for Windows.

RESULTS

General Hydrogeochemical Properties

The variation of hydrogeochemical composition in coalfields is affected by many factors, such as hydrogeological condition, lithology, mineral composition, precipitation, temperature, and also by mining and other human activities (Zhang et al., 2021). In **Table 1**, all the water samples were classified by the sampling location and arranged by the sampling time. The pH of all samples ranged from 7.11 to 8.88, with a mean of 7.82, which is slightly alkaline. It was closely related to alkaline mineral sources in the aquifer system, especially samples 40 and 41 from the Kuqa River (8 and 8.19, respectively) indicating the close relationship with soil salinization (Xuemei et al., 2009). The TDS reflects the strength of water–rock interaction and the hydraulic connection between multi-aquifers (Shvartsev et al., 2016; Hao et al., 2020). The TDS values of BRA ranged from 505.53 mg/L to 2,124.90 mg/L with a mean of 1570.23 mg/L, while those of SCA ranged from 1394.93 mg/L to 7058.26 mg/L with a mean of 3331.89 mg/L. The ion concentrations in both BRA and SCA were all obviously larger than those in SW and QA. Since the

TABLE 1 | Hydrogeochemical data from the study area.

No.	Year	Sample location	Ca^{2+} (mg/L)	Mg^{2+} (mg/L)	$Na^{+}+K^{+}$ (mg/L)	HCO_3^{-}(mg/L)	SO_4^{2-} (mg/L)	Cl^{-}(mg/L)	Water chemical type	TDS (mg/L)	pH	CBE	^{3}H (TU)	δD	$\delta^{18}O$	$SI_{Calcite}$	$SI_{Dolomite}$	SI_{Gypsum}	SI_{Halite}
1	2007	Spring	147.13	73.19	442.96	233.4	496.27	640.94	Na-Cl-SO_4	1928.83	-	-1.77%	-	-	-	-	-	-	-
2	2010	BRA	131.34	76.40	509.52	378.87	554.70	611.03	Na-Cl-SO_4	2072.43	7.40	-2.56%	-	-56.44	-9.12	0.38	0.81	-0.96	-5.15
3	2010	BRA	115.49	59.09	358.32	301.62	409.85	451.23	Na-Cl-SO_4	1544.79	7.70	-2.39%	-	-54.12	-8.74	0.57	1.13	-1.07	-5.42
4	2011	BRA	92.02	32.01	472.17	347.72	430.43	433.39	Na-Cl-SO_4	1659.99	-	-1.42%	8.96	-55.4	-7.45	-	-	-	-
5	2011	BRA	106.05	67.07	362.39	297.29	403.27	446.80	Na-Mg-Ca-Cl-SO_4	1555.12	-	-1.06%	3.03	-61.8	-8.23	-	-	-	-
6	2011	BRA	87.53	64.01	279.52	233.58	346.48	368.61	Na-Cl-SO_4	1273.38	-	-1.43%	5.54	-58.4	-8.15	-	-	-	-
7	2011	BRA	87.53	53.46	271.49	201.73	348.95	356.32	Na-Cl-SO_4	1229.06	-	-2.43%	-	-57.7	-8.29	-	-	-	-
8	2012	BRA	158.72	70.89	492.82	296.01	620.95	627.64	Na-Cl-SO_4	2,124.90	-	-2.88%	-	-	-	-	-	-	-
9	2012	BRA	136.67	98.98	479.04	277.89	564.99	638.28	Na-Cl-SO_4	2,108.84	7.90	-0.24%	-	-	-	0.75	1.65	-0.94	-5.16
10	2012	BRA	123.45	38.79	495.67	187.27	446.89	670.19	Na-Cl-SO_4	1876.13	-	-3.42%	-	-	-	-	-	-	-
11	2012	BRA	114.63	58.85	287.07	241.64	373.23	378.71	Na-Ca-Cl-SO_4	1823.45	7.90	-0.78%	-	-	-	0.69	1.36	-1.08	-5.58
12	2012	BRA	98.89	61.58	357.68	251.63	400.58	411.00	Na-Cl-SO_4	1455.55	7.84	0.56%	-	-	-	0.57	1.22	-1.13	-5.46
13	2012	BRA	92.58	52.17	292.53	193.31	346.89	404.24	Na-Cl-SO_4	1288.20	-	-2.73%	-	-	-	-	-	-	-
14	2018	BRA	127	62.66	370.62	317.18	433.44	429.14	Na-Cl-SO_4	1581.45	7.6	0.03%	-	-	-	0.53	1.03	-1.02	-5.43
15	2019	BRA	89.06	54	479.77	376.44	443.01	450.03	Na-Cl-SO_4	1704.09	7.75	0.02%	-	-	-	0.59	1.24	-1.16	-5.3
16	2019	BRA	135.83	64.72	379.43	331.28	424.46	453.06	Na-Cl-SO_4	1630.46	8.05	0.48%	-	-	-	1.01	1.98	-1.01	-5.39
17	2020	BRA	118.53	93.66	385.44	423.67	485.72	453.36	Na-Mg-Cl-SO_4	1758.06	8.77	-1.33%	-	-	-	1.66	3.52	-1.06	-5.39
18	2020	BRA	124.95	80.81	369.49	380.63	486.77	463.96	Na-Cl-SO_4	1716.30	7.91	-3.10%	-	-	-	0.88	1.86	-1.00	-5.4
19	2020	BRA	55.03	31.81	426.03	435.83	263.78	346.47	Na-Cl-HCO_3	1341.04	7.8	0.09%	-	-	-	0.54	1.12	-1.51	-5.45
20	2021	BRA	95.38	66.37	493.69	347.37	467.98	439.78	Na-Cl-SO_4	1736.89	7.75	3.71%	-	-	-	0.51	1.07	-1.1	-5.29
21	2021	BRA	46.94	31.89	137.64	219.92	231.79	72.49	Na-Mg-SO_4-HCO_3	630.71	7.87	0.01%	-	-	-	0.32	0.75	-1.51	-6.59
22	2021	BRA	61.9	30.4	72.17	176.71	191.00	61.7	Na-Ca-Mg-SO_4-HCO_3	505.53	7.84	-0.76%	-	-56.73	-8.96	0.34	0.65	-1.45	-6.93
23	2007	SCA	107.84	52.95	633.12	248.66	632.89	675.51	Na-Cl-SO_4	2,255.48	-	-1.70%	-	-	-	-	-	-	-
24	2007	SCA	145.33	53.03	552.78	184.95	656.75	671.68	Na-Cl-SO_4	2,172.05	-	-2.73%	-	-	-	-	-	-	-
25	2010	SCA	76.36	45.48	2,580.23	163.11	373.64	3893.51	Na-Cl	7058.26	-	-4.06%	-	-	-	-	-	-	-
26	2010	SCA	235.51	134.66	704.67	423.36	938.22	957.14	Na-Cl-SO_4	3181.88	7.20	-2.30%	0.36	-55.34	-8.9	0.4	0.84	-0.62	-4.84
27	2010	SCA	233.71	141.25	591.33	373.69	889.66	863.13	Na-Cl-SO_4	2,905.93	7.20	-2.10%	0.34	-54.36	-8.67	0.36	0.78	-0.63	-4.96
28	2010	SCA	122.28	53.59	484.38	323.16	497.92	564.03	Na-Cl-SO_4	1883.78	7.30	-2.70%	0.39	-56	-9.03	0.2	0.32	-1.00	-5.2
29	2010	SCA	133.61	67.33	424.14	670.98	457.59	358.93	Na-HCO_3-Cl-SO_4	1777.09	7.50	-2.43%	0.28	-56.77	-8.87	0.75	1.47	-1.01	-5.45
30	2011	SCA	85.85	43.58	618.56	156.61	337.43	880.19	Na-Cl	2054.36	-	-2.64%	-	-60.1	-8.84	-	-	-	-
31	2012	SCA	132.66	72.45	653.96	415.48	705.88	580.68	Na-Cl-SO_4	2,353.37	7.43	1.15%	-	-	-	0.43	0.87	-0.88	-5.07
32	2018	SCA	154.47	158.98	1431.09	846.14	56.1	2,233.79	Na-Cl	4457.50	7.39	0.06%	-	-	-	0.72	1.75	-2.05	-4.18
33	2019	SCA	232.28	149	566.06	289.43	717.3	951.38	Na-Mg-Ca-Cl-SO_4	2,760.74	7.48	0.03%	-	-	-	0.54	1.17	-0.71	-4.93
34	2019	SCA	139.78	71.11	757.42	430.92	821.48	672.71	Na-Cl	2,677.96	7.43	0.01%	-	-	-	0.44	0.86	-0.83	-4.95
35	2020	SCA	29.23	14.6	2077.98	1161.08	41.22	2,201.75	Na-Cl	5059.17	8.38	2.31%	-	-	-	1.07	2.15	-2.89	-4.03
36	2020	SCA	227.75	114.43	1158.29	288.65	976.07	1492.13	Na-Cl-SO_4	4113.00	7.22	0.03%	-	-	-	0.22	0.42	-0.65	-4.45
37	2020	SCA	92.28	90.47	858.5	648.08	85.5	1291.08	Na-Cl-HCO_3	2,754.24	8.48	-2.49%	-	-	-	1.49	3.27	-1.96	-4.61
38	2021	SCA	60.53	50.56	2,512.05	668.41	1104.56	2,905.7	Na-Cl	6967.61	8.15	-3.65%	-	-	-	0.85	1.9	-1.27	-3.85
39	2021	SCA	98.98	66.48	1315.96	486.07	1253.95	1168.27	Na-Cl-SO_4	4146.68	7.72	-3.03%	-	-	-	0.55	1.21	-0.9	-4.5
40	2012		48.5	24.08	8.71	120.82	62.14	55.32		259.16	8	-0.82%	10.37	-46.9	-7.36	0.31	0.59	-1.93	-7.87

(Continued on following page)

TABLE 1 | (*Continued*) Hydrogeochemical data from the study area.

No.	Year	Sample location	Ca^{2+} (mg/L)	Mg^{2+} (mg/L)	$Na^{+}+K^{+}$ (mg/L)	HCO_3^- (mg/L)	SO_4^{2-} (mg/L)	Cl^- (mg/L)	Water chemical type	TDS (mg/L)	pH	CBE	^3H (TU)	δD	$\delta^{18}O$	$SI_{Calcite}$	$SI_{Dolomite}$	SI_{Gypsum}	SI_{Halite}
		Kuqa River							Ca-Mg-HCO_3-Cl-SO_4										
41	2021	Kuqa River	79.9	28.6	33.14	185.91	170	43.1	Ca-Mg-SO_4-HCO_3	447.70	8.19	-0.83%	-	-54.04	-8.22	0.82	1.47	-1.38	-7.42
42	2011	Gully III	91.06	29.74	31.26	149.07	201.64	55.53	Ca-Mg-SO_4-HCO_3	488.03	-	0.26%	7.11	-54.2	-6.52	-	-	-	-
43	2021	Gully III	52.62	39.89	102.01	200.51	215.46	78.69	Na-Mg-Ca-SO_4-HCO_3	588.93	7.55	0.01%	-	-	-	0.02	0.2	-1.49	-6.68
44	2012	QA	77.94	44.12	230.83	239.3	178.86	316.74	Na-Cl	968.14	8.26	0.57%	-	-	-	0.92	1.88	-1.48	-5.74
45	2012	QA	99.20	65.54	124.69	223.52	302.04	212.76	Na-Mg-Ca-SO_4-Cl	924.60	-	-1.94%	-	-	-	-	-	-	-
46	2012	QA	39.68	32.10	177.01	144.98	241.55	191.48	Na-Cl-SO_4	764.47	-	-4.47%	-	-	-	-	-	-	-

spontaneous combustion of coal seams leads to a significant increase in the fractures in BRA, there will be a good hydraulic connection and thus lead to a small standard deviation in the ion concentrations, the TDS, and pH in the aquifer.

Figure 4 shows that several main hydrogeochemical types could be identified in all samples. The water samples from BRA and SCA showed a similar hydrogeochemical type but were different in mineralization. SCA samples were presented as a highly saline Na-Cl-SO_4 type. Although the major hydrogeochemical type in SCA was dominated by Na-Cl-SO_4, the average concentration of SO_4 was just slightly excess 25%, while the concentrations of both Na and Cl exceeded 55%. Meanwhile, the standard deviation of TDS in SCA was 1667.68 mg/L, which gives an indication of the heterogeneity. A total of 22 water samples from BRA are Na-Cl-SO_4 water chemical type with a lower TDS, including a sample from the spring near the Kuqa River (the spring is origin from the BRA at a flow rate of 0.69 L/s in 2007 but stopped flowing in 2015, when large-scale mining drainage began). In contrast, mixed water chemical types were observed in samples from the surface water and QA with low mineralization (ranging from 259.16 to 968.14 with a mean of 634.43). As a local drinking water source, two samples from the Kuqa River over 10 years met the WHO guidelines for both drinking and irrigation. The samples of QA were collected from different gullies with the weak hydraulic connections.

Relationships Among Major Ions by Multivariate Statistical Analysis

Six major ions were classified by the R-mode HCA process, while the Ward method and squared Euclidian distances were employed to measure the similarity between them. As shown in **Figure 5**, these ions could be classified into two clusters. Ca, Mg, SO_4, and HCO_3 were classified into cluster I, suggesting the dissolution of carbonate. Cluster comprised Na and Cl, indicating the dissolution of halite.

The Pearson correlation coefficients are presented in **Table 2**, which shows that the TDS correlates strongly with Cl and Na (greater than 0.9), indicating that the dissolution of halite plays an important role in the increment of TDS. In addition, Ca correlated strongly with Mg (0.846), indicating the dissolution of dolomite.

We further used the principal component analysis to investigate the hydrochemical processes in this area. The principal components were extracted from the correlation matrix from the seven parameters (Ca, Mg, Na, HCO_3, SO_4, Cl, and TDS). The Kaiser criterion is such that only the components with eigenvalues greater than one are retained (Yilmaz and Buyukyildiz, 2015). **Table 3** shows the principal component loadings and their separate variances explained. The result shows that the first two components extracted have eigenvalues greater than one and account for 80.61% of the total variance in the dataset. Component 1 is characterized by highly positive loadings in Na, Cl, and TDS (all higher than 0.9) with 52.28% of the explained variance. Component 2 is characterized by highly positive loadings in Ca, Mg, and SO_4. The loadings of the chemical parameters can be defined by descriptive terms according to the position in the plane

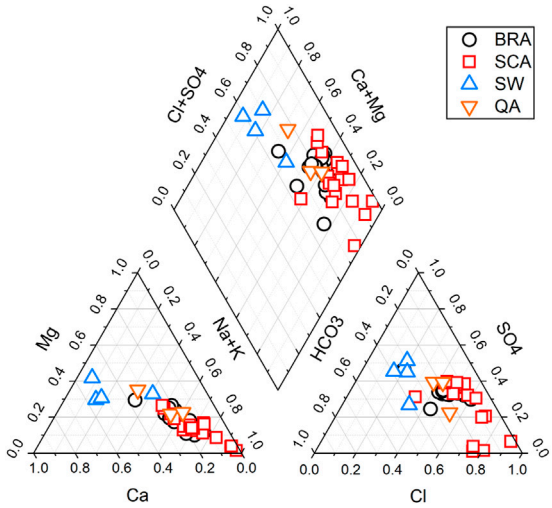

FIGURE 4 | Piper diagram of all water samples.

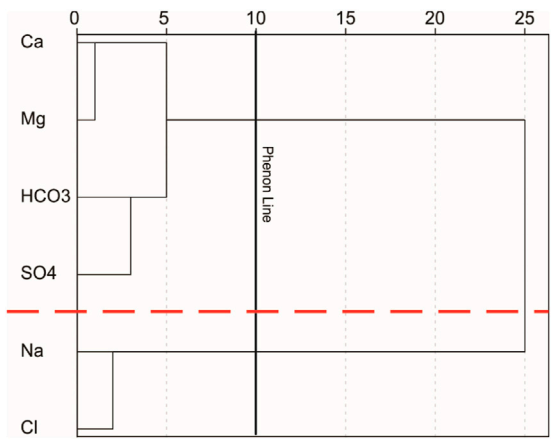

FIGURE 5 | Dendrogram of HCA results.

(**Figure 6**). Component 1 was defined as the salinity component because of the close relationship of Na, Cl, and TDS, while component 2 was defined as the hardness component because of the association of Ca and Mg, which was used to calculate hardness. The factors that cause these high loads will be discussed in a later section.

The results of the multivariate statistical methods (HCA, PCA, and CA), Na, Cl, and TDS are dominant in cluster 1 and those of Ca, Mg, and SO_4 are dominant in cluster 2. This means that the natural processes dominate the evolution of groundwater hydrogeochemistry in this study.

Relationship Between the Hydraulic Conductivity and TDS

The hydraulic conductivity K can reflect the residence time by affecting the seepage velocity (Loaiciga, 2004), while the length of residence time can reflect the degree of water–rock interaction, which causes changes in the characteristics of the hydrogeochemistry, especially TDS (Jia et al., 2019). Ten pumping tests were conducted to assess the hydraulic conductivity of BRA and SCA in the study area (**Figure 7**). The values of K and TDS in BRA ranged from 3.11 to 27.86 m/d and 505.53–2,121.90 mg/L, with averages of 17.874 m/d and 1570.23 mg/L, respectively. In contrast, the values of K and TDS in SCA ranged from 0.0001 to 0.14 m/d and 1394.93–7058.26 mg/L, with averages of 0.0049 m/d and 3331.89 mg/L, respectively. Similarly, the values of q in SCA ranged from 0.00001 to 0.047 L/(m s) with an average of 0.017 L/(m s), while the values of q in BRA ranged from 2.13 to 27.226 L/(m s) with an average of 11.434 L/(m s). Obviously, the K and q values of BRA are significantly larger than those of SCA, while the TDS is lower in BRA than in SCA. The pumping test in the three boreholes (including samples 2 and 26 from the same borehole but in different aquifers, and samples 3 and 28, 6 and 30), the difference are shown in K and TDS values of the two aquifers. The four water samples (samples 2 and 3 from BRA and samples 26 and 28 from SCA) showed the same water chemical type but with difference in mineralization, while two samples (samples 6 and 30) from these two aquifers showed different chemical types. In addition, sample 25 showed the highest TDS but the lowest K. Under the same hydraulic gradient, the smaller value of K provided more sufficient residence time and a wider range of water–rock

TABLE 2 | Pearson correlation matrix of the major chemical parameters in groundwater.

	Ca	Mg	Na	HCO_3	SO_4	Cl	TDS
Ca	1	**0.846****	0.019	-0.004	0.597**	0.087	0.212
Mg		1	0.146	0.225	0.439**	0.234	0.318*
Na			1	0.568**	0.334*	**0.970****	**0.978****
HCO_3				1	0.030	0.467**	0.534**
SO_4					1	0.249	0.466**
Cl						1	**0.963****
TDS							1

TABLE 3 | Principal component loadings and explained variance for two components.

Parameter	Component 1	Component 2
Ca	-0.053	**0.963**
Mg	0.118	**0.883**
Na	**0.987**	0.079
HCO_3	0.670	0.004
SO_4	0.237	**0.734**
Cl	**0.949**	0.123
TDS	**0.950**	0.277
Eigenvalue	3.66	1.98
Explained variance (%)	52.28	28.33
Cumulative % of variance	52.28	80.61

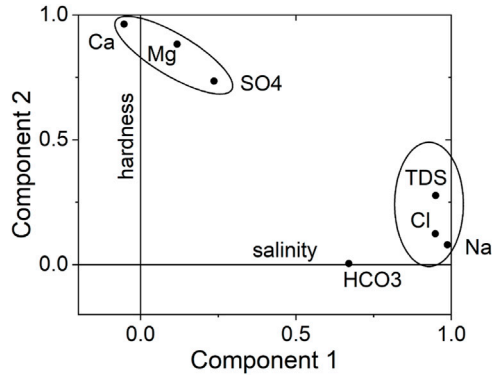

FIGURE 6 | Loadings for the two components with Varimax normalized rotation.

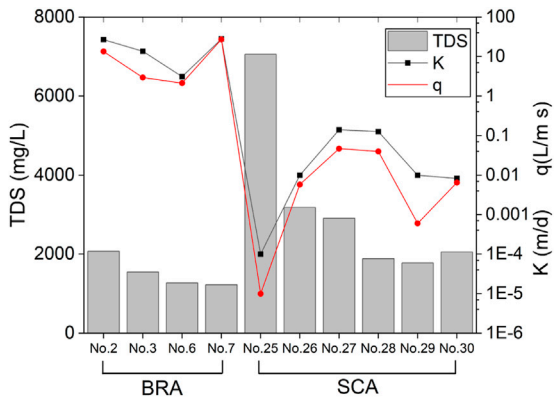

FIGURE 7 | TDS, hydraulic conductivity, and water yield of groundwater in BRA and SCA.

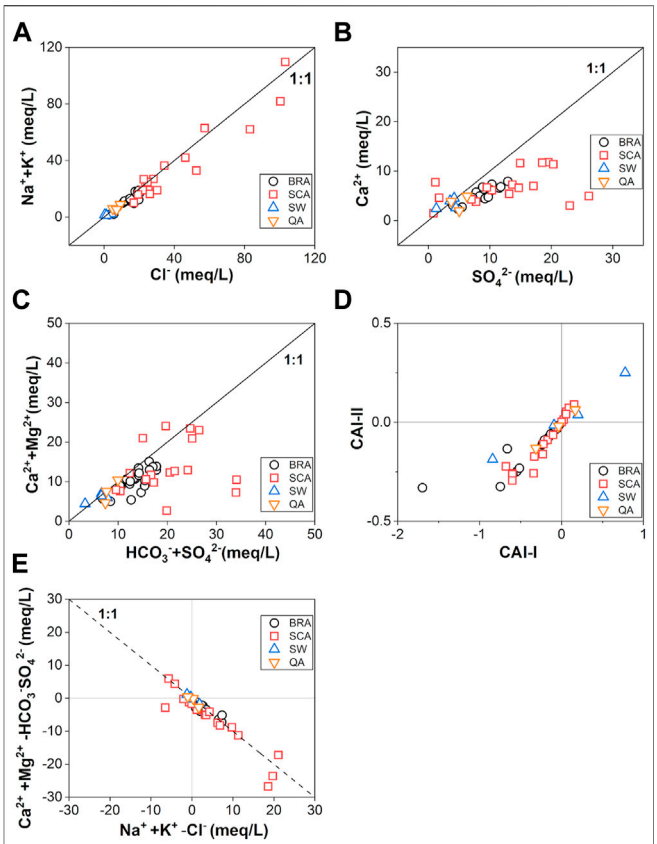

FIGURE 8 | Scatter plots of some pairs of ions **(A)** Cl^- and Na^++K^+; **(B)** SO_4^{2-} and Ca^{2+}; **(C)** HCO_3^-+SO_4^{2-} and Ca^{2+}+Mg^{2+}; **(D)** CAI-I and CAI-II; **(E)** Na^++K^+-Cl^- and Ca^{2+}+Mg^{2+}-HCO_3^--SO_4^{2-}.

interaction. As a result, the high velocity of the groundwater flow results in low concentrations of ions in BRA.

DISCUSSION

Geogenic Sources of Chemical Compositions in Groundwater

The source of groundwater and the process of hydrogeochemistry can be identified by the ratio coefficient of the major ions (Li et al., 2016). Combined with MSA, more valuable information about the relationship between hydrogeochemical components can be found.

The ideal ratios of Cl and Na would be one, if such ions are released by halite dissolution (Ettazarini, 2005). Meanwhile, because of the close relationship between Na and Cl calculated by MSA, scatter plots of Na and Cl are drawn in **Figure 8A**. Most samples are plotted along the 1:1 line, indicating that the dissolution of halite could be the main hydrogeochemical process in this area. This result is consistent with the principal component analysis, and both refer to the salinity component. Similar to the dissolution line of halite, carbonate and gypsum dissolution have the decided ratio relationship (**Eqs. 1–3**).

$$CaCO_3 + H_2O + CO_2 = Ca^{2+} + 2HCO_3^-, \quad (1)$$

$$CaMg(CO_3)_2 + 2H_2O + 2CO_2 = Ca^{2+} + Mg^{2+} + 4HCO_3^-, \quad (2)$$

$$CaSO_4 \cdot 2H_2O = Ca^{2+} + SO_4^{2-} + 2H_2O. \quad (3)$$

As the main parameter for calculating hardness, the relationship between Ca and Mg also indicates the hardness component in PCA. Considering the significant correlations between Ca, Mg, and SO_4, most water samples were below the 1:1 line of gypsum dissolution (**Figure 8B**) and above the 2:1 line of carbonate dissolution (**Figure 8C**), which point toward cation exchange. Therefore, the Schoeller indices (CAI-I and CAI-II) and the relationship between (Na-Cl) and (Ca + Mg-HCO_3-SO_4) (**Figures 8D,E**) were employed to verify that the cation exchange is one of the hydrogeochemical processes. CAI-I and CAI-II were calculated according to the following **Eqs 4**, **5**, where ions are expressed in meq/L.

$$CAI - I = [Cl^- - (Na^+ + Cl^-)]/Cl^-, \quad (4)$$

$$CAI - II = [Cl^- - (Na^+ + Cl^-)]/(HCO_3^- + SO_4^{2-} + CO_3^{2-} + NO_3^-), \quad (5)$$

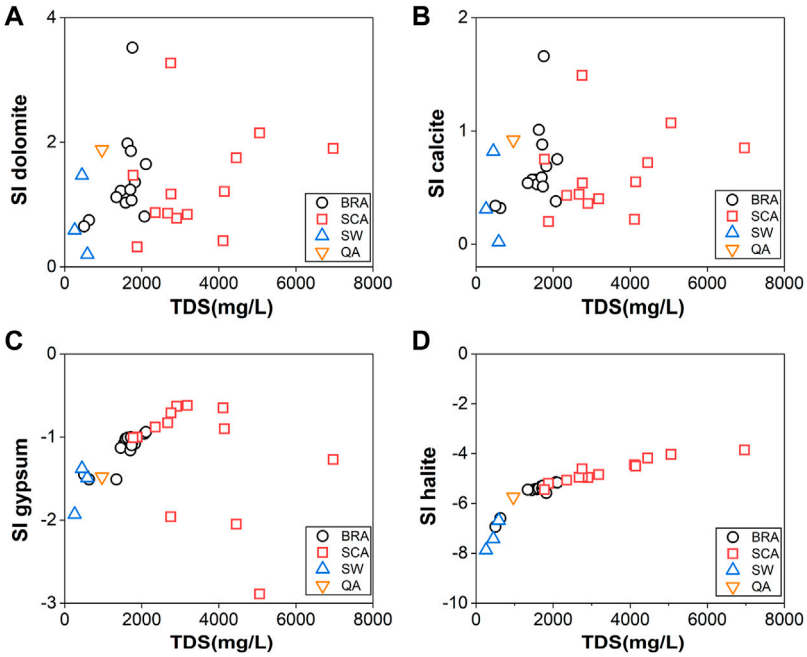

FIGURE 9 | Scatterplots of saturation indices of **(A)** dolomite, **(B)** calcite, **(C)** gypsum, and **(D)** halite against TDS.

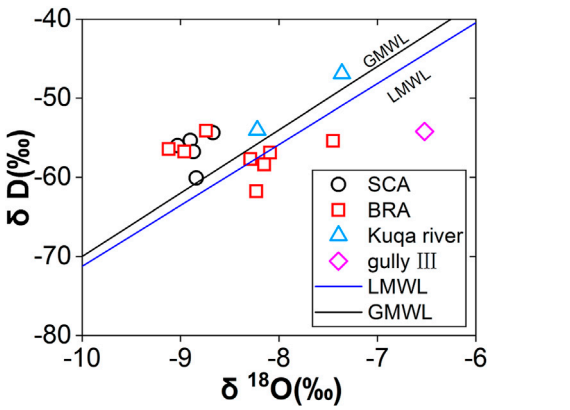

FIGURE 10 | Relationship between δD and $\delta^{18}O$ isotopic concentrations.

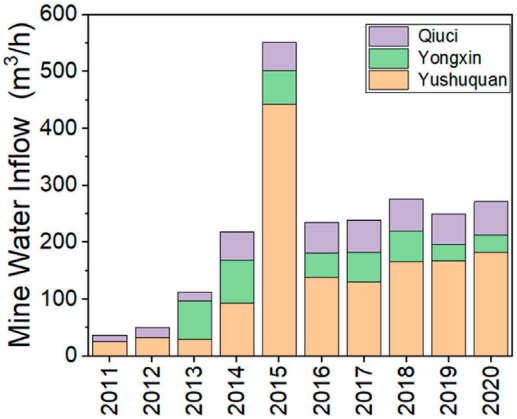

FIGURE 11 | Annual average mine water inflow from 2011 to 2020 in coal mines.

If cation exchange has a significant impact on hydrogeochemical evolution, the water samples should fall in the third quadrant in **Figure 8D** with negative CAI values and linear with a slope of −1 in **Figure 8E** (Fisher and Iii, 1997). Thus, most samples exhibit cation exchange plays an important role in this area. Furthermore, the slightly negative correlation between HCO_3 and Ca (-0.004 in **Table 2**) indicates the possible dedolomitization process. With the increase in the Ca concentration caused by the dissolution of gypsum, the dissolution of dolomite will also lead to a decrease in HCO_3 with the precipitation of calcite. The process could be simplified as follows (Zang et al., 2015).

$$2CaSO_4 + CaMg(CO_3)_2 \rightarrow 2CaCO_3 \downarrow + Ca^{2+} + Mg^{2+} + SO_4^{2-}, \quad (6)$$

Therefore, halite, carbonate and gypsum dissolution, cation exchange, and dedolomitization significantly affect the variation of the major cations in the groundwater of the A-ai coalfield.

The saturation index (SI) of minerals can be calculated from the equation: $SI = \log (K_{IAP}/K_{SP})$, where K_{IAP} is the ion activity

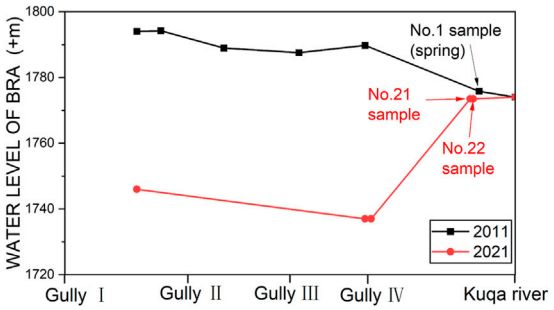

FIGURE 12 | Borehole water level variation in 2011 and 2021.

product for the mineral equilibrium reaction, and K_{SP} is the solubility product. The results of the SI suggest a trend of mineral equilibrium and water–rock interaction, which was calculated by the PHREEQC program and is shown in **Table 1**. The relationship between SI and TDS for each aquifer is shown in **Figure 9**. The halite and gypsum concentrations for all groundwater samples have negative SI values, while a positive trend with TDS can be seen in **Figures 8C,D**. This indicates that the mineral will be continuously weathered by the groundwater and cause increments of TDS. However, it should be noted that water samples from low permeability in SCA have a higher saturation index than those from the high permeability BRA and surface water. In contrast, the SI values of dolomite and calcite from all samples were greater than zero, indicating that these samples were oversaturated with carbonate minerals. The precipitation of calcite and dolomite in groundwater may be related to low rainfall and strong evaporation (Kumar and Singh, 2015).

Origin of Groundwater

Using stable isotopes of δD and $\delta^{18}O$ is an effective method to analyze groundwater circulation and origin (Craig, 1961). In this study, the local meteoric water line (LMWL) was used as a baseline, where $\delta D = 7.70\delta^{18}O+5.74$ (Wang and Zhang, 2017). The global meteoric water line (GMWL, $\delta D = 8\delta^{18}O+10$, Craig, 1961) is also plotted in **Figure 10**. The difference in the slope and intercept of LMWL can reflect the vapor sources and climatic conditions in different regions. Through comparison of the two lines, the slope and intercept of the LMWL (7.70, 5.74) are significantly smaller than those of the GMWL (8, 10), indicating the dry climate and strong evaporation in this area (Wu et al., 2010).

All groundwater samples are distributed close to the GMWL and LMWL, indicating that meteoric origin is the major recharge source. In addition, the deviation of groundwater isotope values from the meteoric waterline may be caused by the secondary evaporation of precipitation before infiltration (Peng et al., 2004). Meanwhile, most SCA water samples deviate significantly from LWML compared to BRA water samples, indicating that the longer water–rock interaction in SCA than that of BRA. Due to the low flow rate and the long flow path, the surface water from Gully III experienced more intense evaporation and deviated from LMWL more than that from the Kuqa River.

According to the identification method from USGS (Lindsey et al., 2019), the tritium-based age of groundwater could be classified into the modern (post-1950s) and premodern (pre-1950s) thresholds. Groundwater with a tritium content of less than 0.5 TU is classified as premodern groundwater, while larger than 0.5 TU is classified as a modern one. As shown in **Table 1**, the ^{3}H concentrations of water samples from SCA range from 0.28 to 0.39 TU with a mean value of 0.34 TU, indicating that the age of groundwater from SCA is earlier than in the 1950s. In contrast, the ^{3}H concentrations from BRA (ranging from 3.03 to 8.96 TU with a mean value of 5.84) and surface water (ranging from 7.11 to 10.37 TU with a mean value of 8.74) are significantly higher than the threshold. Combined with the results of stable isotopes, one can conclude that the water in BRA is recharged since the 1950s. Furthermore, although the origins of

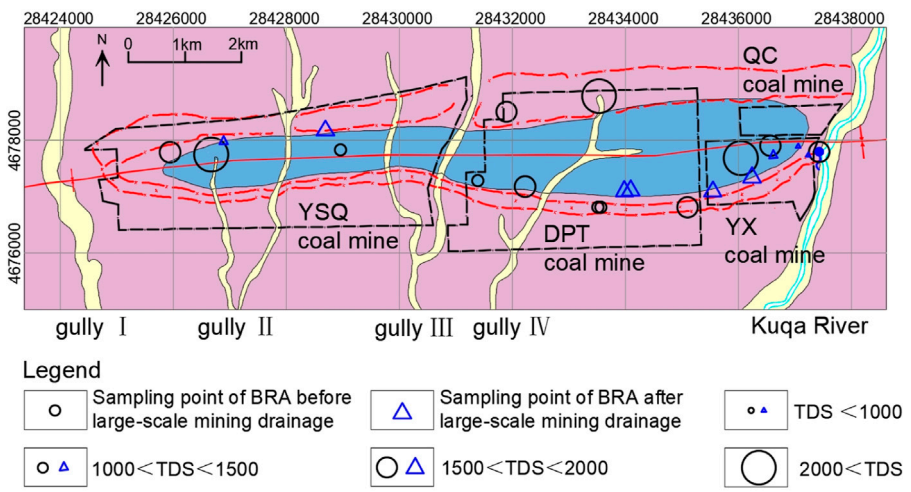

FIGURE 13 | Planar graph of the relationship between sampling location, time, and TDS in the BRA.

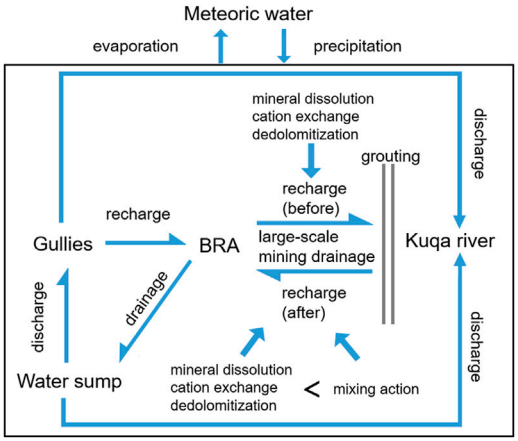

FIGURE 14 | Origin and evolution of hydrogeochemistry and hydrogeology in the BRA.

groundwater are all from precipitation through rock outcrops, the circulation condition of BRA is better than SCA, which is consistent with the results of stable isotopic of δD and $\delta^{18}O$.

Effect of Large-Scale Mining Drainage on Hydrogeochemistry

According to the previous discussion, BRA is superior to SCA in terms of the recharge conditions, K, and flow velocity. Therefore, BRA is the main aquifer in the A-ai coalfield and has been drained by boreholes during the mining process. With increases in coal production, the average annual mine water inflow also increases (**Figure 11**), which mainly comes from BRA (it should be noted that because the DPT coal mine has not been produced, only three mines are included). In particular, in the YSQ coal mine, large-scale mining drainage was carried out in 2015, and the spring was cut off in this year. This year is considered to be the start of large-scale mining drainage. Due to the lack of long-term and continuous water level observation data, the water level of BRA boreholes along the syncline in 2011 and 2021 is shown in **Figure 12**. Under natural conditions or before large-scale mining drainage in 2011, groundwater in BRA flowed from the west to the east and discharged into the Kuqa River. In contrast, after large-scale mining drainage for many years, the water level of BRA declined sharply by almost 50 m. The water level of the Kuqa River is significantly higher than that of BRA and may cause the discharge of the river to the BRA.

In order to further study the influence of water level decline on hydrogeochemical characteristics, the water samples of BRA were divided into two clusters, according to the sampling time (before or after the start year of large-scale mining drainage in 2015), as shown on the planar graph (**Figure 13**), where the diameter of the circle represents the value of TDS. First, sampling locations near the outcrop area are easier to receive recharge from meteoric water thus with lower TDS. Second, the water chemical types of these two clusters are different and the concentration of HCO_3 slightly increased in the second cluster, indicating that additional origin or water–rock interaction occurs in these samples. In the YX coal mine area, the TDS of the second cluster samples is significantly lower than the first cluster, and TDS gradually increases from the east to the west. More attention should be paid to samples 21 and 22 from BRA with approximately 300 m away from the Kuqa River. These two samples were collected from underground boreholes in YX coal mine, which have similar hydrogeochemical characteristics and quite a low TDS (630.71 and 505.53 mg/L, respectively). Obviously, the decline of the water level resulted in changes in the groundwater circulation condition. Low mineralization surface water flowed into the BRA through outcrop from the Kuqa River, and thus, this river has transferred from the recharge boundary to the discharge boundary. Therefore, the major hydrogeochemical process of BRA near the Kuqa river is mixing. As drainage continues, this variation will spread more widely.

Comprehensive Analysis and Water Resource Protection

Combined with the aforementioned discussions, the origin and evolution of hydrogeochemistry and hydrogeology in the BRA of the A-ai coalfield is summarized in **Figure 14**. Before large-scale mining drainage, seasonal flow in gullies of surface water will directly recharge to BRA; then, groundwater flows from the west to the east and recharges to the Kuqa River. During this process, mineral dissolution, such as halite, carbonate and gypsum, cation exchange, and dedolomitization play a pivotal role in the hydrogeochemical evolution. With large-scale mining drainage, the spring is disappearing, and the groundwater in the BRA start receiving recharge from the Kuqa River. At this point, the effect of the mixing action is markedly stronger than in other hydrogeochemical processes. Meanwhile, much groundwater flowed into the coal mine water sump and was discharged to the gullies or the Kuqa River after treatment and purification. Finally, a greater amount of low mineralization surface water will enter into the aquifer. As a result, the hydrogeochemistry of the aquifer will be changed in a wider range. On the other hand, clean and valuable surface water resources would be contaminated continuously in this area.

Drainage is inevitable during the mining process, so obstructing the source of recharge to protect water resources is a better approach. Considering the dry climate and less effect of precipitation, cutting off the flow path from the Kuqa River to the BRA is a preferred method. According to the hydrogeological characteristic of the burnt rock, the high permeability provides a good foundation for grouting. On the east side of the YX and QC coal mine, which is along the Kuqa River, cement could be injected into the BRA through boreholes to construct an underground curtain to effectively separate the Kuqa River and BRA. After that, only limited storage in the BRA and little recharge from precipitation is necessary for drainage. This not only decreases the cost of drainage but also protects the water

resource. More importantly, coal mines in the A-ai coalfield will not be threatened by the water hazards of the BRA and would avoid casualties related to tunnel flooding.

CONCLUSION

In this study, we analyzed the effect of large-scale mining drainage on the regional characteristics of hydrogeochemistry in an arid coalfield by analyzing hydrogeochemical (major ions, ^{3}H, and stable isotopes of δD and $\delta^{18}O$) and hydrogeological data (pumping tests, annual average mine water inflow, and water level). The results showed that precipitation is the main recharge source of groundwater and surface water. In addition, the SCA is dominated by the Na-Cl-SO_4 type with higher TDS but has poor permeability and water yield. The significantly low concentrations of ^{3}H and high mineralization in SCA indicate the old water age and the weak hydraulic connection with other aquifers. In contrast, as the main risk factor for coal mine water hazards, the BRA has a young age and similar water chemical type with SCA but with a lower TDS. Spontaneous combustion of the coal seam caused a remarkable increase in permeability and the good recharge condition caused the strong water yield, which resulted in casualties and tunnel flooding events. Under natural or small-scale mining drainage conditions, groundwater flowed from the west to the east under the water–rock interaction of dissolution of halite, carbonate and gypsum, cation exchange, and dedolomitization, and they were finally discharged to the Kuqa River. After the perennial large-scale mining drainage, the water level of the BRA decreased sharply, causing changes to the hydrogeological condition. Furthermore, the main hydrogeochemical process in the BRA gradually changed from being a water–rock interaction into a mixing action. The influence range will gradually expand with continuous drainage. On the basis of the high permeability of the BRA, we proposed practical advice for the sustainable development and protection of surface water resources by grouting. By doing so, we could avoid the loss of surface water caused by prolonged drainage.

Similar to other coalfield areas, long-term mining activities have largely destroyed the original groundwater circulation pattern and produced a large amount of acid mine water. The results of this study provided a comprehensive analysis of groundwater evolution for the A-ai coalfield and also could serve as a template for other coalfields in northwest China to enhance the awareness of water resource protection (Huang et al., 2017).

DATA AVAILABILITY STATEMENT

The original contributions presented in the study are included in the article/supplementary material; further inquiries can be directed to the corresponding author.

AUTHOR CONTRIBUTIONS

AK, SZ, WG, and WH contributed to the conception and design of the study. AK, JZ, and XJ organized the database. AK and DS performed the statistical analysis. AK and SZ wrote the first draft of the manuscript. All authors contributed to manuscript revision, read, and approved the submitted version.

FUNDING

This work was financially supported by the Chinese 13th Five-Year Key Research and Development Program (Grant No. 2017YFC0804100).

REFERENCES

Baboolal, A. A., Knight, J., and Wilson, B. (2018). Petrography and Mineralogy of Pyrometamorphic Combustion Metamorphic Rocks Associated with Spontaneous Oxidation of Lignite Seams of the Erin Formation, Trinidad. *J. S. Am. Earth Sci.* 82, 181–192. doi:10.1016/j.jsames.2018.01.002

Barzegar, R., Moghaddam, A. A., Tziritis, E., Fakhri, M. S., and Soltani, S. (2017). Identification of Hydrogeochemical Processes and Pollution Sources of Groundwater Resources in the Marand Plain, Northwest of Iran. *Environ. Earth Sci.* 76 (7), 16. doi:10.1007/s12665-017-6612-y

Carrillo-Rivera, J. J., Varsanyi, I., Kovacs, L., and Cardona, A. (2007). Tracing Groundwater Flow Systems with Hydrogeochemistry in Contrasting Geological Environments. *Water Air Soil Pollut.* 184 (1-4), 77–103. doi:10.1007/s11270-007-9400-6

Chen, Z., Zhou, X., Du, J., Xie, C., Liu, L., Li, Y., et al. (2015). Hydrochemical Characteristics of Hot Spring Waters in the Kangding District Related to the Lushan <i>M</i>_S = 7.0 Earthquake in Sichuan, China. *Nat. Hazards Earth Syst. Sci.* 15 (6), 1149–1156. doi:10.5194/nhess-15-1149-2015

Cloutier, V., Lefebvre, R., Therrien, R., and Savard, M. M. (2008). Multivariate Statistical Analysis of Geochemical Data as Indicative of the Hydrogeochemical Evolution of Groundwater in a Sedimentary Rock Aquifer System. *J. Hydrology* 353 (3-4), 294–313. doi:10.1016/j.jhydrol.2008.02.015

Craig, H. (1961). Isotopic Variations in Meteoric Waters. *Science* 133 (3465), 1702–1703. doi:10.1126/science.133.3465.1702

Dehghanzadeh, R., Safavy Hir, N., Shamsy Sis, J., and Taghipour, H. (2015). Integrated Assessment of Spatial and Temporal Variations of Groundwater Quality in the Eastern Area of Urmia Salt Lake Basin Using Multivariate Statistical Analysis. *Water Resour. Manage* 29 (4), 1351–1364. doi:10.1007/s11269-014-0877-7

Dimitrova-Petrova, K., Geris, J., Wilkinson, M. E., Lilly, A., and Soulsby, C. (2020). Using Isotopes to Understand the Evolution of Water Ages in Disturbed Mixed Land-Use Catchments. *Hydrol. Process.* 34 (4), 972–990. doi:10.1002/hyp.13627

Dong, S. N., Zhou, W. F., and Wang, H. (2021). Introduction to Special Issue on Mine Water Inrushes: Risk Assessment, Mitigation, and Prevention. *Mine Water Environ.* 40 (2), 321–323. doi:10.1007/s10230-021-00782-2

Emvoutou, H. C., Tandia, B. K., Nkot, S. N. B., Ebonji, R. C. S., Nlend, Y. B., Ekodeck, G. E., et al. (2018). Geologic Factors Controlling Groundwater Chemistry in the Coastal Aquifer System of Douala/Cameroon: Implication for Groundwater System Functioning. *Environ. Earth Sci.* 77 (5), 23. doi:10.1007/s12665-018-7400-z

Ettazarini, S. (2005). Processes of Water-Rock Interaction in the Turonian Aquifer of Oum Er-Rabia Basin, Morocco. *Environ. Geol.* 49 (2), 293–299. doi:10.1007/s00254-005-0088-x

Fisher, R. S., and Mullican, III, W. F. (1997). Hydrochemical Evolution of Sodium-Sulfate and Sodium-Chloride Groundwater beneath the Northern Chihuahuan Desert, Trans-Pecos, Texas, USA. *Hydrogeology J.* 5 (2), 4–16. doi:10.1007/s100400050102

Hao, C.-M., Huang, Y., Ma, D.-J., and Fan, X. (2020). Hydro-geochemistry Evolution in Ordovician Limestone Water Induced by Mountainous Coal Mining: A Case Study from North China. *J. Mt. Sci.* 17 (3), 614–623. doi:10.1007/s11629-019-5485-9

Huang, L., Liu, C. Y., Yang, L., Zhao, J. F., and Fang, J. J. (2008). Petrologic and REE Geochemical Characters of Burnt Rocks. *Acta Geol. sin.-engl. Ed.* 82 (2), 392–398. doi:10.1111/j.1755-6724.2008.tb00589.x

Huang, T., Pang, Z., Li, J., Xiang, Y., and Zhao, Z. (2017). Mapping Groundwater Renewability Using Age Data in the Baiyang Alluvial Fan, NW China. *Hydrogeol. J.* 25 (3), 743–755. doi:10.1007/s10040-017-1534-z

Jia, H., Qian, H., Qu, W., Zheng, L., Feng, W., and Ren, W. (2019). Fluoride Occurrence and Human Health Risk in Drinking Water Wells from Southern Edge of Chinese Loess Plateau. *Int. J. Environ. Res. Public Health* 16 (10), 1683. doi:10.3390/ijerph16101683

Keita, S., and Zhonghua, T. (2017). The Assessment of Processes Controlling the Spatial Distribution of Hydrogeochemical Groundwater Types in Mali Using Multivariate Statistics. *J. Afr. Earth Sci.* 134, 573–589. doi:10.1016/j.jafrearsci.2017.07.023

Khanoranga, K., and Khalid, S. (2019). An Assessment of Groundwater Quality for Irrigation and Drinking Purposes Around Brick Kilns in Three Districts of Balochistan Province, Pakistan, through Water Quality Index and Multivariate Statistical Approaches. *J. Geochem. Explor.* 197, 14–26. doi:10.1016/j.gexplo.2018.11.007

Kruszewski, Ł., Fabiańska, M. J., Ciesielczuk, J., Segit, T., Orłowski, R., Motyliński, R., et al. (2018). First Multi-Tool Exploration of a Gas-Condensate-Pyrolysate System from the Environment of Burning Coal Mine Heaps: An *In Situ* FTIR and Laboratory GC and PXRD Study Based on Upper Silesian Materials. *Sci. Total Environ.* 640-641, 1044–1071. doi:10.1016/j.scitotenv.2018.05.319

Kumar, A., and Singh, C. K. (2015). Characterization of Hydrogeochemical Processes and Fluoride Enrichment in Groundwater of South-Western Punjab. *Water Qual. Expo. Health* 7 (3), 373–387.

Laita, E., Bauluz, B., and Yuste, A. (2019). High-Temperature Mineral Phases Generated in Natural Clinkers by Spontaneous Combustion of Coal. *Minerals* 9 (4), 17. doi:10.3390/min9040213

Li, X., Jiang, F., Li, L., and Wang, G. (2011). Spatial and Temporal Variability of Precipitation Concentration Index, Concentration Degree and Concentration Period in Xinjiang, China. *Int. J. Climatol.* 31 (11), 1679–1693. doi:10.1002/joc.2181

Li, P., Zhang, Y., Yang, N., Jing, L., and Yu, P. (2016). Major Ion Chemistry and Quality Assessment of Groundwater in and Around a Mountainous Tourist Town of China. *Expo. Health* 8 (2), 239–252. doi:10.1007/s12403-016-0198-6

Lindsey, B., Jurgens, B. C., and Belitz, K. (2019). *Tritium as an Indicator of Modern, Mixed, and Premodern Groundwater Age*.

Liu, L., Zhang, C., He, D., Wei, B., and Li, C. (2011). Chemical Compositions of Detrital Feldspars and Micas within the Late Triassic and Early Jurassic Sequences of Northern Kuqa Basin, Xinjiang and Their Implications to Provenance Tectonics. *Acta Petrol. Sin.* 27 (1), 310–320.

Liu, F., Zhao, Z., Yang, L., Ma, Y., Xu, Y., Gong, L., et al. (2020). Geochemical Characterization of Shallow Groundwater Using Multivariate Statistical Analysis and Geochemical Modeling in an Irrigated Region along the Upper Yellow River, Northwestern China. *J. Geochem. Explor.* 215, 106565. doi:10.1016/j.gexplo.2020.106565

Loáiciga, H. A. (2004). Residence Time, Groundwater Age, and Solute Output in Steady-State Groundwater Systems. *Adv. Water Resour.* 27 (7), 681–688. doi:10.1016/j.advwatres.2004.05.004

Ma, D. Y., Ruan, R. H., Li, Y. D. A., Zhang, L., Wang, X. B., Zi, J. B., et al. (2021). Characteristics of Fine Particle Formation during Combustion of Xinjiang High-Chlorine-Sodium Coal. *Fuel* 297, 10. doi:10.1016/j.fuel.2021.120772

Meyzonnat, G., Barbecot, F., Alvarado, J. C., Pinti, D. L., Lauzon, J. M., and McCormack, R. (2021). Depth-Sequential Investigation of Major Ions, Delta O-18, Delta H-2 and Delta C-13 in Fractured Aquifers of the St. Lawrence Lowlands (Quebec, Canada) Using Passive Samplers. *Water* 13 (13), 25. doi:10.3390/w13131806

Nagaraju, A., Thejaswi, A., and Sreedhar, Y. (2016). Assessment of Groundwater Quality of Udayagiri Area, Nellore District, Andhra Pradesh, South India Using Multivariate Statistical Techniques. *Earth Sci. Res. J.* 20 (4), E1–E7. doi:10.15446/esrj.v20n4.54555

Onifade, M., and Genc, B. (2018). Spontaneous Combustion of Coals and Coal-Shales. *Int. J. Min. Sci. Technol.* 28 (6), 933–940. doi:10.1016/j.ijmst.2018.05.013

Oren, O., and Sensogut, C. (2010). Spontaneous Combustion Liability of Kutahya (Turkey) Region Lignites. *Energy Sources, Part A Recovery, Util. Environ. Eff.* 32 (10), 877–885. doi:10.1080/15567031003587605

Peng, H., Mayer, B., Harris, S., and Krouse, H. R. (2004). A 10-yr Record of Stable Isotope Ratios of Hydrogen and Oxygen in Precipitation at Calgary, Alberta, Canada. *Tellus B Chem. Phys. Meteorology* 56 (2), 147–159. doi:10.3402/tellusb.v56i2.16410

Qiao, W., Li, W., Li, T., Chang, J., and Wang, Q. (2017). Effects of Coal Mining on Shallow Water Resources in Semiarid Regions: A Case Study in the Shennan Mining Area, Shaanxi, China. *Mine Water Environ.* 36 (1), 104–113. doi:10.1007/s10230-016-0414-4

Qiao, W., Li, W., Zhang, S., and Niu, Y. (2019). Effects of Coal Mining on the Evolution of Groundwater Hydrogeochemistry. *Hydrogeol. J.* 27 (6), 2245–2262. doi:10.1007/s10040-019-01969-2

Qu, S., Shi, Z. M., Liang, X. Y., Wang, G. C., and Jin, X. M. (2021). Origin and Controlling Factors of Groundwater Chemistry and Quality in the Zhiluo Aquifer System of Northern Ordos Basin, China. *Environ. Earth Sci.* 80 (12), 15. doi:10.1007/s12665-021-09735-y

Sabit, M., JiangLing, H. U., and Ismail, D. (2008). Climatic Change Characteristics of Kuqa River-Weigan River Delta Oasis during Last 40 Years. *Sci. Geogr. Sin.* 28 (4), 518–524. doi:10.3724/SP.J.1047.2008.00014

Salameh, E., Toll, M., and Al Raggad, M. (2018). Hydrogeochemical Prospecting for Evaporate and Clay Deposits in Harrat Ash Shaam Basalts, Jordan. *J. Geochem. Explor.* 186, 243–255. doi:10.1016/j.gexplo.2017.12.017

Shi, B. B., Wang, Z. Y., Liu, P., Zhou, F. B., and Peng, C. Y. (2021). Pozzolanicity Verification of Combustion Metamorphic Rocks from Coalfield Fire Zones in China. *J. Loss Prev. Process Ind.* 69, 7. doi:10.1016/j.jlp.2021.104390

Shvartsev, S., Shen, Z. L., Sun, Z. X., Wang, G. C., Soldatova, E., and Guseva, N. (2016). Evolution of the Groundwater Chemical Composition in the Poyang Lake Catchment, China. *Environ. Earth Sci.* 75 (18), 1239. doi:10.1007/s12665-016-6065-8

Singh, C. K., Kumar, A., Shashtri, S., Kumar, A., Kumar, P., and Mallick, J. (2017). Multivariate Statistical Analysis and Geochemical Modeling for Geochemical Assessment of Groundwater of Delhi, India. *J. Geochem. Explor.* 175, 59–71. doi:10.1016/j.gexplo.2017.01.001

Song, Y., Jiang, B., Mathews, J. P., Yan, G., and Li, F. (2017). Structural Transformations and Hydrocarbon Generation of Low-Rank Coal (Vitrinite) during Slow Heating Pyrolysis. *Fuel Process. Technol.* 167, 535–544. doi:10.1016/j.fuproc.2017.08.003

Wang, S., and Zhang, M. (2017). SPATIO-TEMPORAL CHARACTERISTICS AND INFLUENCING FACTORS OF STABLE ISOTOPES IN PRECIPITATION ACROSS THE CHINESE TIANSHAN MOUNTAINS. *Quat. Sci.* 37 (5), 1119–1130.

Wang, J. J., Liang, X., Ma, B., Liu, Y. F., Jin, M. G., Knappett, P. S. K., et al. (2021a). Using Isotopes and Hydrogeochemistry to Characterize Groundwater Flow Systems within Intensively Pumped Aquifers in an Arid Inland Basin, Northwest China. *J. Hydrology* 595, 14. doi:10.1016/j.jhydrol.2021.126048

Wang, X. J., Di, J. Z., Liang, B., Yang, Y., Dong, Y. R., and Wang, M. X. (2021b). Study on Treatment of Acid Mine Drainage by Nano Zero-Valent Iron Synergistic with SRB Immobilized Particles. *Environ. Eng. Res.* 26 (5), 13. doi:10.4491/eer.2020.333

Wu, J., Ding, Y., Ye, B., Yang, Q., Zhang, X., and Wang, J. (2010). Spatio-temporal Variation of Stable Isotopes in Precipitation in the Heihe River Basin, Northwestern China. *Environ. Earth Sci.* 61 (6), 1123–1134. doi:10.1007/s12665-009-0432-7

Xiao, Y., Hao, Q., Zhang, Y., Zhu, Y., Yin, S., Qin, L., et al. (2022a). Investigating Sources, Driving Forces and Potential Health Risks of Nitrate and Fluoride in Groundwater of a Typical Alluvial Fan Plain. *Sci. Total Environ.* 802, 149909. doi:10.1016/j.scitotenv.2021.149909

Xiao, Y., Liu, K., Hao, Q., Xiao, D., Zhu, Y., Yin, S., et al. (2022b). Hydrogeochemical Insights into the Signatures, Genesis and Sustainable Perspective of Nitrate Enriched Groundwater in the

Piedmont of Hutuo Watershed, China. *CATENA* 212, 106020. doi:10.1016/j.catena.2022.106020

Xue, J. K., Shi, L., Wang, H., Ji, Z. K., Shang, H. B., Xu, F., et al. (2021). Water Abundance Evaluation of a Burnt Rock Aquifer Using the AHP and Entropy Weight Method: a Case Study in the Yongxin Coal Mine, China. *Environ. Earth Sci.* 80 (11), 12. doi:10.1007/s12665-021-09703-6

Xuemei, W., Zhongping, C., Tashpolat, T., and Aijin, G. (2009). Analysis on the Characteristics of Soil Salinization in the Northern Margin of Tarim BasinA Case Study in the Delta Oasis of Weigan and Kuqa Rivers. *J. Arid Land Resour. Environ.* 23 (9), 134–138.

Yilmaz, V., and Buyukyildiz, M. (2015). FACTOR ANALYSIS OF SURFACE WATER QUALITY PARAMETERS FOR THE RIVERS OF TURKEY. *Fresenius Environ. Bull.* 24 (1), 113–123.

Yuan, Y., Liu, Z. H., Zhu, C., Yuan, C. F., and Wang, S. Z. (2019). The Effect of Burnt Rock on Inclined Shaft in Shallow Coal Seam and its Control Technology. *Energy Sci. Eng.* 7 (5), 1882–1895. doi:10.1002/ese3.398

Zang, H., Zheng, X., Jia, Z., Chen, J., and Qin, Z. (2015). The Impact of Hydrogeochemical Processes on Karst Groundwater Quality in Arid and Semiarid Area: a Case Study in the Liulin Spring Area, North China. *Arab. J. Geosci.* 8 (9), 6507–6519. doi:10.1007/s12517-014-1679-1

Zeng, Q., Shen, L., and Yang, J. (2020). Potential Impacts of Mining of Super-thick Coal Seam on the Local Environment in Arid Eastern Junggar Coalfield, Xinjiang Region, China. *Environ. Earth Sci.* 79 (4), 15. doi:10.1007/s12665-020-8806-y

Zhang, J. Y., Guo, L. W., Gong, J. L., Zhu, L. Q., and Gong, X. M. (2007). *Analysis on Impacting the Soil Environment of the Underground Coal Mining*. Jiaozuo, PEOPLES R CHINA: Science Press Beijing, 1966–1969.

Zhang, Y., Zhang, X. Q., Hower, J. C., and Hu, S. R. (2020). Mineralogical and Geochemical Characteristics of Pyrometamorphic Rocks Induced by Coal Fires in Junggar Basin, Xinjiang, China. *J. Geochem. Explor.* 213, 11. doi:10.1016/j.gexplo.2020.106511

Zhang, J., Chen, L. W., Hou, X. W., Lin, M. L., Ren, X. X., Li, J., et al. (2021). Multi-isotopes and Hydrochemistry Combined to Reveal the Major Factors Affecting Carboniferous Groundwater Evolution in the Huaibei Coalfield, North China. *Sci. Total Environ.* 791, 148420. doi:10.1016/j.scitotenv.2021.148420

Conflict of Interest: The authors declare that the research was conducted in the absence of any commercial or financial relationships that could be construed as a potential conflict of interest.

Publisher's Note: All claims expressed in this article are solely those of the authors and do not necessarily represent those of their affiliated organizations, or those of the publisher, the editors, and the reviewers. Any product that may be evaluated in this article, or claim that may be made by its manufacturer, is not guaranteed or endorsed by the publisher.

frontiers | Frontiers in Environmental Science

ORIGINAL RESEARCH
published: 24 June 2022
doi: 10.3389/fenvs.2022.941726

Dynamic Relationship Between Water Resources and New Urbanization Based on a Vector Autoregressive Model: A Case Study of Hebei Province, China

Shule Li[1], *Jingjing Yan*[1]*, *Qiuming Pei*[2]*, *Jinghua Sha*[1] *and Fei Liu*[3]

[1]School of Economics and Management, China University of Geosciences, Beijing, China, [2]Faculty of Geosciences and Environmental Engineering, Southwest Jiaotong University, Chengdu, China, [3]Institute of Mountain Hazards and Environment, Chinese Academy of Sciences, Chengdu, China

Overly rapid urban expansion in the past has significantly changed water resources, resulting in an imbalance between water resources and the sustainable development of new urbanization. To facilitate the sustainable development and utilization of water resources and promote the high-quality development of new urbanization, this study constructs evaluation index systems for water resources and new urbanization. The analytic hierarchy process, entropy method and projection pursuit method are used to determine the weight of each index, and Hebei Province is taken as an example for empirical analysis. The results indicate an upward trend for water resources in Hebei during the 2000–2019 period, while the water resources support capacity and water environmental pollution showed trends of gradual improvement but changed greatly, the water ecological carrying capacity gradually increased, and the negative impact of water disaster damage on the comprehensive situation of regional water resources gradually increased. Meanwhile, a qualitative breakthrough has been made in the development of new urbanization. Based on their evaluation results data, the long-term equilibrium relationship between water resources and new urbanization as well as the dynamics are empirically analyzed using a vector autoregressive model with a variable cointegration test, generalized impulse responses, and a decomposition prediction method using evaluation result data for the 2000–2019 period. There is indeed a supporting and inhibiting dynamic relationship between new urbanization and water resources as well as its components. At the early stage of urbanization, the endowment of water resources, the background value of the water environment, the ecological capacity of water and man-made water disasters were not fully considered, which led to the sharp contradiction between water resources and new urbanization. For a period, the decline in water resource support capacity and serious water environmental pollution have gradually become important factors limiting new urbanization in Hebei, and the constraining effects of the reduced water ecological carrying capacity and water disaster damage have gradually decreased. For future development, decision makers in Hebei should take measures such as adjusting the economic growth mode, improving resource utilization efficiency and technical level, and fully considering the positive role of new urbanization in promoting water resources and water

OPEN ACCESS

Edited by:
Venkatramanan Senapathi, Alagappa University, India

Reviewed by:
Qili Hu, Chengdu University of Technology, China
Hongji Wang, Southwestern University of Finance and Economics, China

***Correspondence:**
Jingjing Yan
yanjingjing312@hotmail.com
Qiuming Pei
pqm@swjtu.edu.cn

Specialty section:
This article was submitted to Freshwater Science, a section of the journal Frontiers in Environmental Science

Received: *11 May 2022*
Accepted: *06 June 2022*
Published: *24 June 2022*

Citation:
Li S, Yan J, Pei Q, Sha J and Liu F (2022) Dynamic Relationship Between Water Resources and New Urbanization Based on a Vector Autoregressive Model: A Case Study of Hebei Province, China. Front. Environ. Sci. 10:941726. doi: 10.3389/fenvs.2022.941726

environments. At the same time, Hebei Province should reduce the rate of water resource consumption by strengthening water conservation measures, optimizing the water utilization structure, and increasing investments in water pollution prevention and control to enhance the stability of water environments to realize the coordinated development of water resources and new urbanization.

Keywords: water resources, new urbanization, Hebei Province, vector autoregression, dynamic relationship

1 INTRODUCTION

Urbanization is the inevitable trend of social and economic development and an important symbol of national modernization (Castells-Quintana 2017; Ahmad et al., 2019). Since the reform and opening up in 1978, urbanization in China has developed rapidly, with the urbanization rate of the resident population increasing by nearly three times, the urban population increasing by four times, and the actual built-up area expanding by more than 20 times, resulting in a drastic change in the urban landscape (Su et al., 2016, Guan et al., 2018a; Chen et al., 2019a). As the world's second largest economy, China's urbanization process has become a major event affecting the process of mankind in the 21st century, which has a significant impact on the development of China and even the world (Chen et al., 2013; Tan et al., 2016). China is now a primarily urban society in terms of urban population and spatial morphology. However, in terms of lifestyle as well as unbalanced regional and urban-rural development, there are still large gaps regarding standards for urban society in China (Wei and Zhang 2017, Guan et al., 2018b; Fang et al., 2019b). According to the law of urbanization development in developed countries, China will still be in the stage of rapid development with a growth rate of 30%–70% in the next 10–15 years (Wang et al., 2015; Chen et al., 2016). It is imperative to apply scientific and reasonable research methods to systematically analyze urbanization and comprehensively improve the level of urbanization both quantitatively and qualitatively. Therefore, in 2014, the Chinese government clearly put forward the strategic task of promoting the development of new-type urbanization (Fang et al., 2015; Taylor 2015), which involves not only the fundamental issue of coordinated development of the national economy but also the sustainable development of rational utilization and long-term protection of resources and environment (Chan 2014; Zeng et al., 2020). In recent years, with the steady advancement of China's new urbanization, relevant academic research has gradually stepped into the stage of steady deepening. The research hotspots mainly include the following aspects: the theoretical connotation and development framework of new urbanization (Yang and Jiang 2018), the evaluation system of new urbanization (Cobbinah et al., 2015; Anwar et al., 2017; Zhong et al., 2020), the impact effect of new urbanization (Shang et al., 2018), the coupling and coordination between new urbanization and ecological environment (Liu et al., 2018, Wang J. et al., 2019), population urbanization and the equalization of basic public services (Chen et al., 2019b; Li and Liu 2021), the integration of new urbanization and rural revitalization (Fang et al., 2015; Li et al., 2018), and ecological civilization and sustainable development (Wang and Chen 2019; Zhao et al., 2019).

Water resources, as the material on which human beings depend for survival, support the development of society and economy (Wang H. et al., 2020; Liu H. et al., 2022). The understanding of hydrogeochemical characteristics such as nitrogen, fluoride, and major ions analysis could help to evaluate the risk of groundwater to human health (Ahmed and Ali 2011; Wang W. et al., 2020; Xiao et al., 2022). In recent work, fuzzy comprehensive quantitative evaluation, Drosophila optimization algorithm and Monte Carlo simulation method were used to evaluate hydrogeological risk and predict water quality evolution (Ouelhazi et al., 2014; Shojaei et al., 2015; Wang X. et al., 2019; Ruan et al., 2021), which could avoid the degradation of groundwater quality, improve the fragility of water resource systems and water ecological conditions, and improve the sustainable utilization capacity of regional water resources. Meanwhile, the coordinated development of water resources, economy and society has gradually attracted much attention (Ma et al., 2018; Song et al., 2018; Mou et al., 2019). Through multi-index dynamic comprehensive analysis and evaluation of water resources carrying capacity, including principal component analysis, system dynamics, ecological footprint, modeling studies can estimate the maximum development capacity and supporting capacity of regional water resources (Leeuwen and Sjerps 2015; Magri and Berezowska-Azzag 2019; Wang et al., 2018; Mou et al., 2020). Furthermore, in order to maintain a good ecological environment in the process of water resources development and utilization, and reduce flood and drought disasters, most studies focused on water resources security supply, water resources security evaluation and water resources security early warning system by using the DPSIR conceptual framework, artificial neural network, water footprint and other methods (Malzer et al., 2010; Kot et al., 2015; Roeger and Tavares 2018; Rickert et al., 2019).

With the continuous advancements in urbanization, excessive urban expansion has significantly altered water resources, making it difficult to balance the relationship of urban size and population growth with water resources (Du et al., 2006; Fang et al., 2021; Tang et al., 2021). Every 1% increase in China's urbanization rate leads to a 0.58% increase in total water consumption (Barron et al., 2013; Shen et al., 2014). Population agglomeration, urban expansion, and economic development have caused damage and pose threats to water resource supplies and water environmental protection, and water resources are not aligned with the sustainable development of new urbanization. In some studies, researchers studied the restrictive effects of water resources on

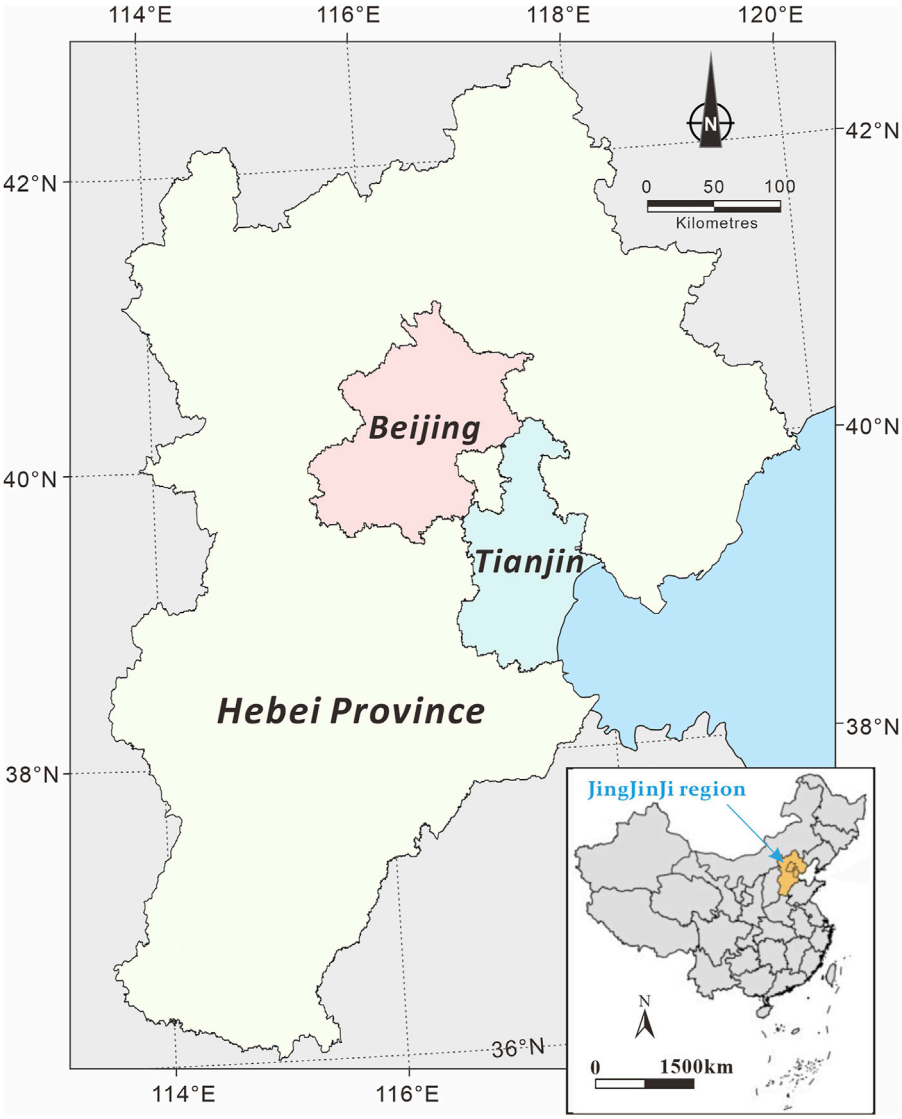

FIGURE 1 | Geographical location of Hebei Province. The map is modified from (Yao 2017).

production, life and ecology in the development of urbanization through quantitative and qualitative analysis methods such as entropy method and spatial spillover effect (Meinzen-Dick and Appasamy 2002; Tiffen 2003; Bao and Fang 2012). In contrast, some scholars use multivariate statistical techniques, multi-objective analysis and spatial spillover effects to analyze the impact of urbanization on water resources (Panagopoulos, 2014; Dong et al., 2016; Bao and Chen 2017; Zhang et al., 2018, Wang H. et al., 2020, Liu S. K.et al., 2022). In addition, there are also studies that focus on the two independent systems of water resources and urbanization from the perspective of systems (Liu et al., 2018). In their work, a system coordinated development degree model was established to analyze the interaction and coupling effect of water resources and urbanization (Wu et al., 2017; Zhang et al., 2019). Currently, there is a comprehensive understanding of water resources including resources, environment, ecology and disasters (Wang et al., 2018); hence, this study constructs comprehensive evaluation index systems for multifactor water resources and new urbanization, empirically tests the process and extent of their interaction using a vector autoregressive model and explores the idea of the coordinated development of new urbanization and water resources in Hebei Province, China, as an example.

2 STUDY AREA AND DATA

2.1 Study Area

Hebei surrounds the capital of Beijing and the municipality of Tianjin in a semi-ring shape, is the only province in China that encompasses two major municipalities, and has unique location advantages (**Figure 1**). Despite development guidance through

the Beijing-Tianjin-Hebei (JingJinJi) integration, the economic growth and urbanization of Hebei have been slower than those of other major economic provinces in the country. In 2019, Hebei dropped from sixth place to 13th place in the national GDP ranking of provinces, and the urbanization rate for the permanent population ranked 19th and below the national average (Fang et al., 2019a; Li et al., 2019; Liang et al., 2019).

Hebei is located in the Haihe River Basin, which experiences the most water scarcity in China. As a province with extreme water shortages, in 2019, the per capita water resources in Hebei were 149.9 m^3, only 7% of the national per capita water resources. The cumulative amount of groundwater overdraft is approximately 180 billion m^3, forming the world's largest groundwater funnel, which is the main cause of ground subsidence in the JingJinJi area, producing a series of water environment and ecological issues, such as vegetation degradation and soil salinization that seriously endanger human life and production (Xie et al., 2017; Xie et al., 2018). In the long term, if water resource constraints are not fully considered, the aforementioned water resource problems will seriously limit the scale of urbanization in Hebei because of economic growth, spatial expansion, population agglomeration, and the increase in consumption (Ma et al., 2020).

2.2 Data Sources and Normalization

China formally began compiling data for and releasing the China Water Resources Bulletin in 1997, followed soon after by Hebei compiling data for and releasing the Hebei Water Resources Bulletin. For this reason, the sample interval for the present study is 2000–2019, considering the availability and reliability of other data. The data are mainly derived from the statistical data and field survey data reported in the *China Statistical Yearbook*, *China Urban Statistical Yearbook*, *China Urban and Rural Construction Statistical Yearbook*, and *Hebei Statistical Yearbook* for the corresponding years.

The data of indexes included in the water resource and new urbanization evaluation index systems cannot be directly compared due to the differences in value ranges caused by factors such as units of measure, dimensional processing, and positive and negative index values. To eliminate the differences in indexes and make the indexes comparable under statistical standards, the index values are normalized using min-max normalization. The indexes are divided into two categories: positive (+) and negative (−). The larger the value of a positive index is, the greater the positive contribution to the system; in contrast, the smaller the value of a negative index is, the greater the negative contribution to the system. With m evaluation indexes $x_1, x_2, \ldots, x_m$ and the raw index data of n cities x_{ij} ($i = 1, 2, \ldots, n$; $j = 1, 2, \ldots, m$), the specific equations are as follows:

Normalization for positive index:

$$B_{ij} = \frac{x_{ij} - min\, x_{ij}}{max\, x_{ij} - min\, x_{ij}} \quad (1)$$

Normalization of negative index:

$$B_{ij} = \frac{max\, x_{ij} - x_{ij}}{max\, x_{ij} - min\, x_{ij}} \quad (2)$$

where B_{ij} is the normalized data, min x_{ij} is the minimum value, and max x_{ij} is the maximum value.

3 METHODS

3.1 Construction of a Water Resource Evaluation Index System

Due to the difference in research direction, the connotation explanation and research content of water resources are different. Based on the existing research results this study sorted out the "four water issues" in the process of water resource development in China, such as the declining support capacity for water resources, serious pollution of water environments, a reduction in the water ecological carrying capacity, and serious damage from water disasters (Larsen Tove et al., 2016; Xia et al., 2017; Schellenberg et al., 2020). A water resource evaluation index system consisting of four primary indexes, nine secondary indexes, and 33 tertiary indexes is constructed (**Table 1**). The problem-oriented evaluation index system can not only simplify the number of indicators but also make the independence and importance of indicators clearer, which is conducive to the development of water resource potential and the alleviation of the contradiction between people and resources. The four primary indicators are described as follows:

1) Water resource support capacity (WRSC). The WRSC is mainly manifested in the current level of scientific and technological development, as well as the supporting limit of regional water resources to the development population, society and economy. However, with the rapid development of urbanization, the demand for water resources is increasing daily, and the contradiction between supply and demand is prominent. WRSC has difficulty supporting urban development, and even becomes the bottleneck restricting social development. The evaluation of the WRSC mainly includes *water resource quantity*, *water supply problem* and *water consumption problem.* Among them, the water resource quantity mainly reflects the endowment of regional water resources. The water supply problem reflects the degree of water resources development and utilization and the perfection of basic water supply facilities. The water consumption problem mainly reflects the regional water consumption level, the degree of water structure optimization and the comprehensive water use efficiency.
2) Water environmental pollution (WEP). Because of the irreplaceable nature of water resources, the quality of the water environment has direct and indirect influences on the ecological environment, atmospheric environment, soil environment and even the social environment. The WEP evaluation is mainly carried out from three aspects: *water quality improvement*, *pollution emission* and *sewage treatment.* Pollution emissions include agricultural pollution emissions, urban pollution emissions and industrial pollution emissions. Sewage treatment includes urban sewage treatment capacity and sewage resource utilization.

TABLE 1 | Water resources evaluation index system.

Primary indexes	Secondary indexes	Tertiary indexes	Categories
Water Resource Support Capacity (WRSC)	Water Resource Quantity	Total water resources (10^8m^3)	+
		Per capita water resources (m^3/person)	+
		Water production coefficient	+
		Runoff modulus (10^4 m^3/km^2)	+
		Total urban water supply (10^8m^3)	+
	Water Supply Problem	Development and utilization rate of water resources (%)	−
		Development and utilization rate of surface water (%)	−
		Development and utilization rate of Groundwater (%)	−
		Length of urban water supply pipeline (km)	+
	Water Consumption Problem	Total water consumption (10^8m^3)	−
		Agricultural irrigation water ratio (%)	−
		Industrial water ratio (%)	+
		Domestic water consumption (m^3/person)	+
		Per capita water consumption (m^3/person)	−
		Irrigation water consumption per mu (m^3/Mu)	−
		Water consumption of 10000 yuan industrial added value (m^3)	−
Water Environmental Pollution (WEP)	Water Quality Improvement	Proportion of water quality of river I ~ III (%)	+
		Standard rate of urban centralized drinking water source (%)	+
	Pollution Emission	Fertilizer application amount per unit cultivated area (ton/km^2)	−
		Livestock and poultry production per unit land area	−
		Urban domestic sewage discharge (10^4t)	−
		Ammonia nitrogen discharge of domestic sewage (10^4t)	−
		Industrial wastewater discharge (10^4t)	−
		Industrial chemical oxygen demand emissions (10^4t)	−
	Sewage Treatment	Total sewage treatment (10^4t)	+
		Daily urban sewage treatment capacity (10^4t)	+
		industrial water use recycling rate (%)	+
Water Ecological Carrying Capacity (WECC)	Aquatic Habitat	River connectivity	+
		Forest and grass coverage (%)	+
		Proportion of water area (%)	+
Water Disaster Damage (WDD)	Flood Disaster	Flood death toll (person)	−
		Proportion of flood economic loss in GRP (%)	−
	Drought Disaster	Drought affected area (10^4km^2)	−

3) Water ecological carrying capacity (WECC). With the development of the social economy, the threat of human activities to water ecosystem is increasing, and the function of the water ecosystem is seriously degraded. The sustainability of the WECC can be reflected by three aquatic habitat indicators: *river connectivity*, *forest and grass coverage* and *proportion of water are*a.
4) Water disaster damage (WDD). Water disasters generally refer to the fact that too much or too little water affects or destroys human production and life. The evaluation of WDD is mainly carried out through two aspects: *flood disaster*s caused by too much water and *drought disasters* caused by too little water.

3.2 Construction of a New Urbanization Evaluation Index System

In the context of complex and severe domestic and international situations, the level of urbanization in the new era can no longer be reflected using a single index, i.e., population urbanization rate (Li et al., 2018; Gu 2019). The "new" of new urbanization is defined as that with China's development entering the transition period; its development mode, the driving force and the target are different from the traditional extensive urbanization development (Shen et al., 2015; Lu and Ke 2018; Nong et al., 2018; Yu 2021). In other words, it has a connotative economic growth mode, harmonious social development mode, intensive resource utilization mode, innovative science and technology driving ability and the principle of coordinated urban-rural planning. Therefore, for new urbanization, its measurement standard also needs to adopt the comprehensive evaluation method of multiple indicators to grasp the achievements, difficulties and challenges in the process of urbanization, and promote healthy and sustainable development. On this basis, the present study establishes a new urbanization evaluation index system consisting of five primary indexes, 12 secondary indexes, and 48 tertiary indexes (**Table 2**), which can more clearly reflect the achievements, difficulties and challenges in the process of urbanization development.

3.3 Weight Calculation of Evaluation Index Systems

In the above index selection process, because of the different degrees of influence of indexes on the overall system, the final

TABLE 2 | New urbanization evaluation index system.

Primary indexes	Secondary indexes	Tertiary indexes	Categories
Economic Growth Mode (EGM)	Economic Basic Level	Per capital GDP (Ten thousand yuan)	+
		Per capita local general budget revenue (Ten thousand yuan)	+
		Per capita fixed asset investment (Ten thousand yuan)	+
		Foreign direct investment (Thousands of dollars)	+
	Characteristics of Economic Structure	The proportion of added value of the secondary industry in GDP (%)	+
		The proportion of added value of the tertiary industry in GDP (%)	+
		Proportion of industrial added value in GDP (%)	+
	Economic Development Benefits	Growth rate of regional GDP (%)	+
		Interest rate on output	+
		Whole-society-productivity (Yuan/person)	+
Quality of Social Development (QSD)	Human Development	Permanent population urbanization rate (%)	+
		Proportion of secondary industry employees (%)	+
		Proportion of tertiary industry employees (%)	+
		urban registered unemployment rate (%)	−
		Urban Engel coefficient	−
	Infrastructure	Urban population density (Person/km^2)	−
		Highway passenger capacity (Ten thousand people)	+
		Public transport vehicles per 10,000 people	+
		Internet penetration rate (%)	+
		Harmless treatment rate of domestic waste (%)	+
		Sewage treatment rate (%)	+
	Public Service	Hospital beds per 10000 people	+
		Coverage rate of basic endowment insurance for urban permanent residents (%)	+
		The teacher-student ratio in primary and secondary schools	+
		Public library collection per 10000 people (Volume)	+
Resource Utilization Pattern (RUP)	Economic And Social Efficiency	GDP realized by unit fixed asset investment	+
		GDP realized per unit built-up area	+
		Urban population absorbed per unit built-up area (Ten thousand people/km^2)	+
	Ecological Resource Efficiency	Urban per capita public green space (m^2/person)	+
		Energy intensity per GDP (Tons of standard coal/ten thousand yuan)	−
		Water Consumption per Unit of GDP (m^3/Yuan)	−
		SO_2 emissions per unit of GDP (Ton/ten thousand yuan)	−
		Electricity consumption per unit of GDP (KWh/ten thousand yuan)	−
Scientific and Technological Innovation Capacity (STIC)	Innovation Input	R&D personnel equivalent to full-time equivalent	+
		R&D expenditure (ten thousand yuan)	+
		Local financial expenditure on science and technology (100 million yuan)	+
		Education expenditure (Ten thousand yuan)	+
	Innovation Output	Number of domestic patent applications accepted (Piece)	+
		Number of domestic patent applications granted (Piece)	+
		Proportion of scientific research employees in the total employed population	+
Harmonious Relationship Between Urban and Rural Areas (HRBUR)	Social Security Differences	Per capita GDP difference between urban and rural areas	−
		Differences in registered unemployment between urban and rural areas	−
		Ratio of teachers to students in urban and rural primary and secondary schools	−
		Ratio of books collected in urban and rural public libraries	−
		Ratio of hospital beds in urban and rural areas	−
	Difference in Living Standards	Ratio of per capita disposable income of urban and rural residents	−
		Per capita consumption expenditure ratio of urban and rural residents	−
		Engel coefficient difference between urban and rural areas	−

selection results directly affect the feasibility and accuracy of the final evaluation results for water resources and the new urbanization development level. Therefore, it is particularly important to choose an appropriate method to handle the index weights. Considering that each weighting method has certain limitations, to reduce the differences caused by different weighting methods, the subjective weighting analytic hierarchy process, the objective weighting entropy method, and the projection pursuit method, which can identify multiple-index, multiyear high-dimensional evaluation indexes, are selected to determine the index weights, and the comprehensive weight obtained by calculating their mean values reduces, to a certain

extent, the limitations and drawbacks of individual weighting methods (Liu et al., 2018).

3.4 Vector Autoregressive Model

The VAR model is an econometric model that has been widely used in economic research in recent years for the comprehensive analysis of multiple mutual economic variables. It is usually used to predict interconnected time series systems and analyze the dynamic impact of random disturbances on variable systems (Sun 2017; Schulterbrandt Gragg et al., 2018) and to model the relationship between variables through an unstructured approach. It is expressed in **Eq. 1**:

$$\boldsymbol{y}_t = \boldsymbol{A}_1\boldsymbol{y}_{t-1} + \boldsymbol{A}_2\boldsymbol{y}_{t-2} + \cdots + \boldsymbol{A}_p\boldsymbol{y}_{t-p} + \boldsymbol{B}\boldsymbol{x}_t + \varepsilon_t \; t = 1, 2, \cdots, T \quad (3)$$

where y_t is the k-dimensional vector of endogenous variables; x_t is the d-dimensional vector of exogenous variables; x_t is the k-dimensional error vector, which is a white noise process and is not correlated with its own lagged value; p is the lag order; T is the number of samples; and $A_1, A_2, \cdots, A_p$ and B are the coefficient matrices to be estimated for y_t and x_t, respectively.

The principle of the VAR model is to construct the model by taking each endogenous variable as a function of all endogenous variables in the system. Therefore, to analyze the relationship between water resources and new urbanization, this study is based on the evaluation index systems constructed in **Sections 2.1**, **2.2**. The obtained evaluation results for water resources and new urbanization are used as empirical analysis data in the VAR model. This avoids the problem that a single index cannot fully reflect the endogenous variable of the water resources and new urbanization system.

4 RESULTS AND DISCUSSION

4.1 Analysis of the Evaluation Results for Water Resources

The weights of evaluation indexes for water resources in Hebei are calculated according to Subsection 2.3; the results are shown in **Supplementary Table S1**. The data for Hebei from 2000 to 2019 are processed to calculate the scores for each water resource dimension. The values are greater than 0 and not greater than 1, and the larger the value is, the better the comprehensive situation for water resources. As seen in **Figure 2**, the comprehensive evaluation results for water resources in Hebei increase from 0.302 in 2000 to 0.587 in 2019, exhibiting an overall upward trend, with fluctuations. Among them, there was a downward trend in 2004–2006 and 2012–2014. During this period, the change in water resources may be due to the rapid development of the secondary industry and the improvement of living standards, resulting in difficulties in supporting water resources and the deterioration of the water environment.

Specifically, the average evaluation score of the WESC in Hebei Province from 2000 to 2019 accounted for 40%, which is the basis of urban water resource development potential, shows a phased upward trend but with large fluctuations. According to the calculation, the fluctuation of *water resource quantity* in the WESC dimension is large, indicating that the load carried by the natural endowment of water resources in Hebei, a region with poor water resources, has exhibited an increasing trend year by year as the economic aggregates and population density grow and the demand for water resources increases continuously. However, the evaluation scores of *water supply problem* and *water use problem* are on the rise, which indicates that due to the gradual shortage of water resources, people attach great importance to water resources and begin to implement stricter measures to limit the development and protection policies of water resources to ensure the sustainability of water resources.

The WEP dimension is also an important factor affecting water resources in Hebei. Among them, with the development of the decision-making and deployment of special actions to promote water quality improvement and comprehensive treatment in Hebei, the *water quality improvement* increased from 0.01 in 2000 to 0.61 in 2019, and the water quality of centralized drinking water sources was comprehensively improved. In terms of *pollution emission* and *sewage treatment*, when the urbanization level transits from development to maturity, the development mode of extensive economy in the traditional stage of urbanization will result in a large amount of pollution discharge, and the pollution discharge score will also drop. When the level of urbanization reaches a certain level, the pressure on the environment gradually decreases and the WEP score fluctuates upward as Hebei promotes the implementation of special actions for improving water quality and the comprehensive management of water quality.

Focusing on the WECC, Hebei in recent years has implemented a number of measures, such as long-term recuperation mechanisms, protection and management, ecological replenishment, and comprehensive prevention and control of soil erosion to treat and restore ecologically overloaded rivers and lakes. As a result, the degraded ecological spaces of rivers and lakes as well as the water ecological situation continued to improve, and the WECC score increased from 0.029 in 2000 to 0.091 in 2019.

Regarding the WDD dimension, the rapid economic development and urban construction have increased the vulnerability of the ecological environment, and the WDD score decreased from 0.072 in 2000 to 0.026 in 2019. The proportion of WDD also dropped from 24% to 4%, which gradually reduced the positive impact on water resources in Hebei Province. This may even lead to the frequent occurrence of extreme natural disasters in the future.

4.2 Analysis of the Evaluation Results for New Urbanization

The weights of the evaluation indexes for new urbanization in Hebei are calculated based on Subsection 2.3, and the results are provided in **Supplementary Table S2**.

The data for Hebei from 2000 to 2019 are processed to calculate the comprehensive score for new urbanization and the score for each dimension; the results are shown in **Figure 3**. The overall development level of new urbanization

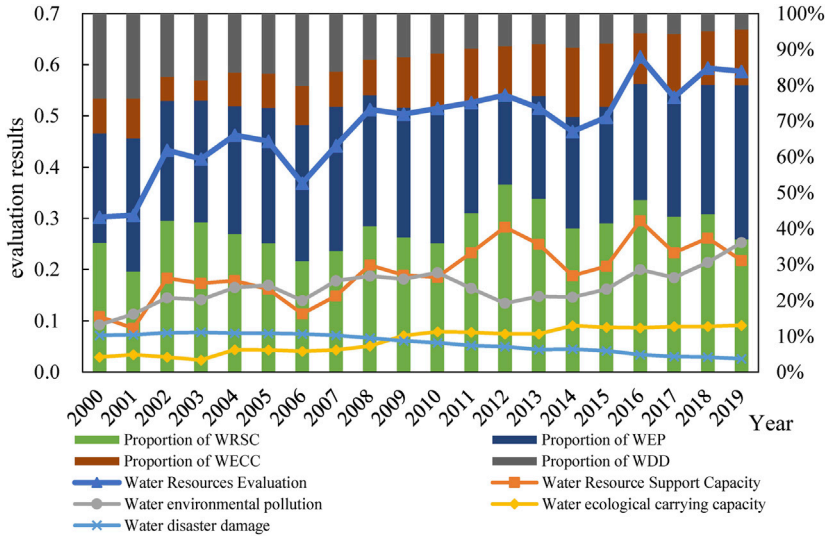

FIGURE 2 | Comprehensive evaluation results of water resources in Hebei Province from 2000 to 2019.

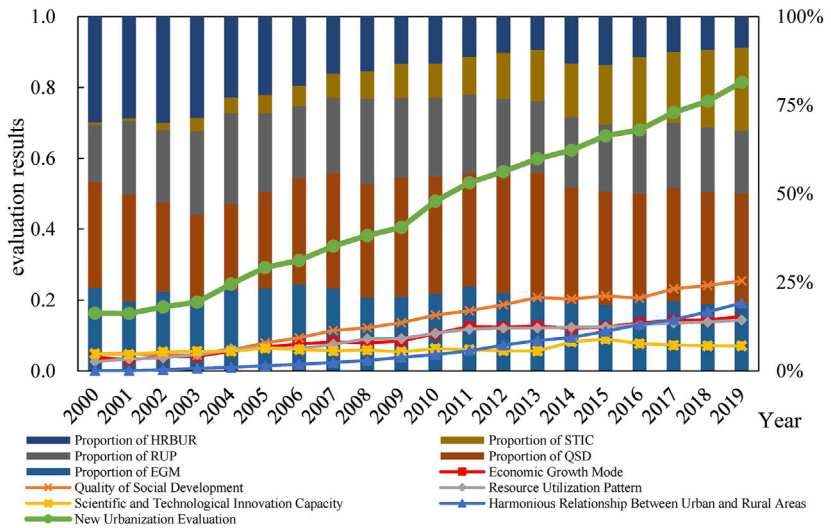

FIGURE 3 | Comprehensive evaluation results of new urbanization in Hebei Province from 2000 to 2019.

in Hebei shows a fluctuating upward trend, from 0.164 in 2000 to 0.815 in 2019. Except for the coordinated urban-rural relationship, which shows an increasing and then decreasing trend, the economic growth mode, social development quality, resource utilization mode, and technological innovation capacity all show steady growth trends.

Specifically, first, the evaluation score of the QSD from 2000 to 2019 accounted for 31%, which made the largest contribution to the development level of new urbanization. This shows that in recent years, Hebei has paid attention to the "people-oriented" social infrastructure construction and improvement of the public service system, and its role has been gradually enhanced. Second, the STIC increased from the lowest score among the five dimensions in 2000 to second in 2019, reflecting the undeniable role and status of the STIC in promoting the rapid development of new urbanization. However, through calculation, it can be seen that the development of the STIC is mainly manifested in the investment of *innovation input*, while the *innovation output* ability is relatively weak. Third, the EGM exhibits a fluctuating upward trend, and its contribution to the level of urbanization is consistently third among the five dimensions. Although Hebei has a good economic basic level, its role in economic and efficient development and continuous

TABLE 3 | ADF unit roots test of variable series.

Variable	T statistic	1% critical value	5% critical value	10% critical value	*p* value	Test results
R1	−2.3591	−3.8315	−3.0300	−2.6552	0.1654	nonstationary
R2	−0.3165	−3.9591	−3.0810	−2.6813	0.9009	nonstationary
R3	−0.8579	−3.8315	−3.0300	−2.6552	0.7787	nonstationary
R4	1.4907	−3.8315	−3.0300	−2.6552	0.9985	nonstationary
U	1.3017	−3.8315	−3.0300	−2.6552	0.9975	nonstationary
DR1	−4.5692	−3.8868	−3.0522	−2.6666	0.0026	stationary
DR2	−2.3664	−2.7283	−1.9663	−1.6050	0.0219	stationary
DR3	−4.1394	−3.8574	−3.0404	−2.6606	0.0056	stationary
DR4	−4.8576	−3.9204	−3.0656	−2.6735	0.0017	stationary
DU	−4.2163	−3.8574	−3.0404	−2.6606	0.0048	stationary

optimization of industrial institutions is not obvious enough. Fourth, the RUP shows an upward trend of fluctuating, with a relatively stable share. During the whole research period, the RUP remained in fourth place, with relatively little development compared with that for the first three dimensions, especially the weight of *economic and social efficiency* of 0.053, which was much lower than the *ecological resource efficiency* of 0.104. Finally, the HRBUR decreases from first among the five dimensions in 2000 to last, reflecting the widening of the urban-rural income gap and the gradual increase in urban-rural conflicts, which may affect the sustainable development of new urbanization in the future.

4.3 Analysis of the Dynamic Relationship

Because the present study mainly examines whether the "four water issues" in Hebei has an impact on new urbanization, only the relationships between WRSC, WEP, WECC, and WDD, and the development of new urbanization are analyzed; the five dimensions of new urbanization are not discussed in detail. For ease of discussion, the water resource support capacity, water environment pollution, water ecological carrying capacity, and water disaster damage in the comprehensive situation of water resources are denoted by R1, R2, R3, and R4, respectively, and new urbanization is denoted by U.

4.3.1 Establishing and Testing the VAR Model

4.3.1.1 Stationarity Test

Before cointegration analysis, to avoid pseudo-regression, it is first necessary to perform the augmented Dickey-Fuller (ADF) stationarity test on the time series data of the variables. Nonstationary data need to be differenced to become stationary.

The test results are shown in **Table 3**. For the sample interval at the 5% significance level, the hypothesis that all variables have unit roots does not pass the significance test; therefore, the five series are all nonstationary. After the first-order difference, the null hypotheses for DR3, DR4, and DU at the 5% significance level are rejected, and hence, the series are stationary. These results indicate that the first-order difference of each series from 2000 to 2019 is stationary and integrated in the same order, satisfying the precondition of the cointegration test.

4.3.1.2 Cointegration Test

The cointegration test refers to the stationarity of the series obtained from a certain linear combination of two or more nonstationary variable series. The obtained results are analyzed using EViews 9.0 software and provided in **Table 4**. The trace statistic and the maximum eigenvalue are both greater than the critical value of 5%; therefore, there is a cointegration relationship between R1, R2, R3, R4, and U.

4.3.1.3 VAR Modeling

The optimal lag order is an important precondition of the VAR model. Only when the lag order is determined can the form of the VAR model be decided. To determine the order of vector autoregression, the results of six tests are used in the present study for comprehensive judgment, and all support an optimal lag order of 2.

The cointegration analysis results indicate that there is a cointegration relationship between the two variables, that is, there is a long-term equilibrium relationship between the two variables. However, to examine the short-term causal relationship between the two, the tested stationary series are substituted into the model based on the previous test results and the selected lag period, the model parameters are estimated using the least squares method, and the coefficient matrix of the VAR model is fitted using **Eq. 3**. The model estimation results are shown in **Table 5**. The degree of influence and significance of each variable and its lagged term on that variable as well as the fitting effect of the regression equation all pass the test of independent and identical distribution of residuals.

4.1.3.4 Stability Test

The modules of all roots obtained by EViews 9.0 software were used to analyze the stability of the model. If the model is unstable, the results are not credible. As seen in **Table 6**, the modules of the roots are all less than 1, indicating that the four VAR models established between R1, R2, R3, R4, and U in the present study are stable and that the various tests based on this model are valid.

4.3.2 Analysis of the Impulse Response

As determined from the earlier test and analysis, there is indeed a causal relationship between water resources and

TABLE 4 | J-J cointegration test.

Cointegration relationship	Hypothesized				
	No. of CE (s)	Eigenvalue	Trace statistic	0.05 critical value	Prob.**
R1 and U	None *	0.1181	15.8353	15.4947	0.0444
	At most 1	0.0085	1.0020	3.8415	0.3168
R2 and U	None *	0.1145	19.5742	15.4947	0.0115
	At most 1 *	0.0433	5.2284	3.8415	0.0222
R3 and U	None *	0.1196	19.2473	15.4947	0.0129
	At most 1 *	0.0351	4.2119	3.8415	0.0401
R4 and U	None *	0.1180	15.7982	15.4947	0.0450
	At most 1	0.0083	0.9846	3.8415	0.3211

TABLE 5 | VAR model estimation results.

	R1	U	R2	U	R3	U	R4	U
R1/R2/R3/R4 (–1)	0.080746	0.030997	0.791051	0.189651	0.63229	0.986759	0.633524	–1.33098
	(0.2364)	(0.1167)	(0.2875)	(0.1932)	(0.2874)	(0.5703)	(0.2531)	(2.2707)
	(0.34163)	(0.26573)	(2.75152)	(0.98163)	(2.20042)	(1.73012)	(2.50262)	(–0.58616)
R1/R2/R3/R4 (–2)	–0.41365	0.134523	0.037909	0.303279	–0.43947	–0.93793	–0.14744	1.447852
	(0.2362)	(0.1166)	(0.2788)	(0.1873)	(0.3139)	(0.6231)	(0.1952)	(1.7511)
	(–1.75167)	(1.15425)	(0.13600)	(1.61901)	(–1.39992)	(–1.50529)	(–0.75527)	(0.82684)
U (–1)	0.571075	0.955199	–0.62002	0.686869	0.077627	0.919607	–0.02801	0.951503
	(0.4970)	(0.2453)	(0.3676)	(0.2471)	(0.1322)	(0.2624)	(0.0289)	(0.2591)
	(1.14905)	(3.89425)	(–1.68654)	(2.78029)	(0.58713)	(3.50427)	(–0.96965)	(3.67184)
U (–2)	–0.34339	0.0235	0.661808	0.29929	0.012148	0.09394	–0.02132	0.062838
	(0.5016)	(0.2475)	(0.3656)	(0.2457)	(0.1192)	(0.2366)	(0.0337)	(0.3025)
	(–0.68463)	(0.09493)	(1.81022)	(1.21820)	(0.10193)	(0.39712)	(–0.63219)	(0.20775)
C	0.153861	0.014977	0.039202	–0.02671	0.012053	0.027082	0.048936	0.021714
	(0.0385)	(0.0190)	(0.0384)	(0.0258)	(0.0060)	(0.0119)	(0.0140)	(0.1254)
	(3.99594)	(0.78811)	(1.02119)	(–1.03527)	(2.01549)	(2.28159)	(3.50024)	(0.17315)
R-squared	0.585488	0.99453	0.593285	0.995859	0.912759	0.995394	0.9912	0.994222
Adj. R-squared	0.457946	0.992847	0.468141	0.994585	0.885916	0.993976	0.988492	0.992444
Sum sq. resids	0.015521	0.00378	0.006337	0.002862	0.000808	0.003184	4.96E-05	0.003994
S.E. equation	0.034553	0.017053	0.022079	0.014837	0.007885	0.01565	0.001954	0.017527
F-statistic	4.590546	590.9449	4.740847	781.6457	34.00313	702.2814	366.0712	559.2277
Log likelihood	37.96259	50.67363	46.02397	53.17872	64.559	52.21932	89.66957	50.17993
Akaike AIC	–3.66251	–5.07485	–4.55822	–5.35319	–6.61767	–5.24659	–9.40773	–5.01999
Schwarz SC	–3.41518	–4.82752	–4.31089	–5.10587	–6.37034	–4.99927	–9.1604	–4.77267
Mean dependent	0.205815	0.489233	0.172502	0.489233	0.065853	0.489233	0.054891	0.489233
S.D. dependent	0.046932	0.201637	0.030275	0.201637	0.023344	0.201637	0.018215	0.201637

TABLE 6 | Stability test results of VAR model.

R1 and U		R2 and U		R3 and U		R4 and U	
Roots	Modules	Roots	Modules	Roots	Modules	Roots	Modules
0.9959	0.9959	0.9896	0.9896	0.9303	0.9303	0.9953	0.9953
0.7406	0.7406	0.8696	0.8696	0.7420	0.7420	0.7404	0.7404
–0.0965	0.0965	0.7327	0.7327	–0.1558	0.1558	0.0956	0.0956
0.0943	0.0943	0.1179	0.1179	0.1091	0.1091	–0.0950	0.0950

new urbanization. To further investigate the relationship, the present study introduces the impulse response function (IRF) to describe the response of an endogenous variable to errors, that is, the trajectory of the influence of an information impact with the standard deviation added to the disturbance term on the current and future values of endogenous variables can visually depict the dynamic interaction between water resources and new urbanization as well as its effect. It is expressed as follows:

$$\boldsymbol{Y}_{t+s} = \boldsymbol{U}_{t+s} + \boldsymbol{\psi}_{t1}\boldsymbol{U}_{t+s-1} + \boldsymbol{\psi}_2\boldsymbol{U}_{t+s-2} + \cdots + \boldsymbol{\psi}_s\boldsymbol{U}_t + \cdots \mathbf{t} = 1, 2, \cdots, \mathbf{T}$$

$$\boldsymbol{\psi}_s = \frac{\vartheta \boldsymbol{Y}_{t+s}}{\vartheta \boldsymbol{U}_t} \tag{4}$$

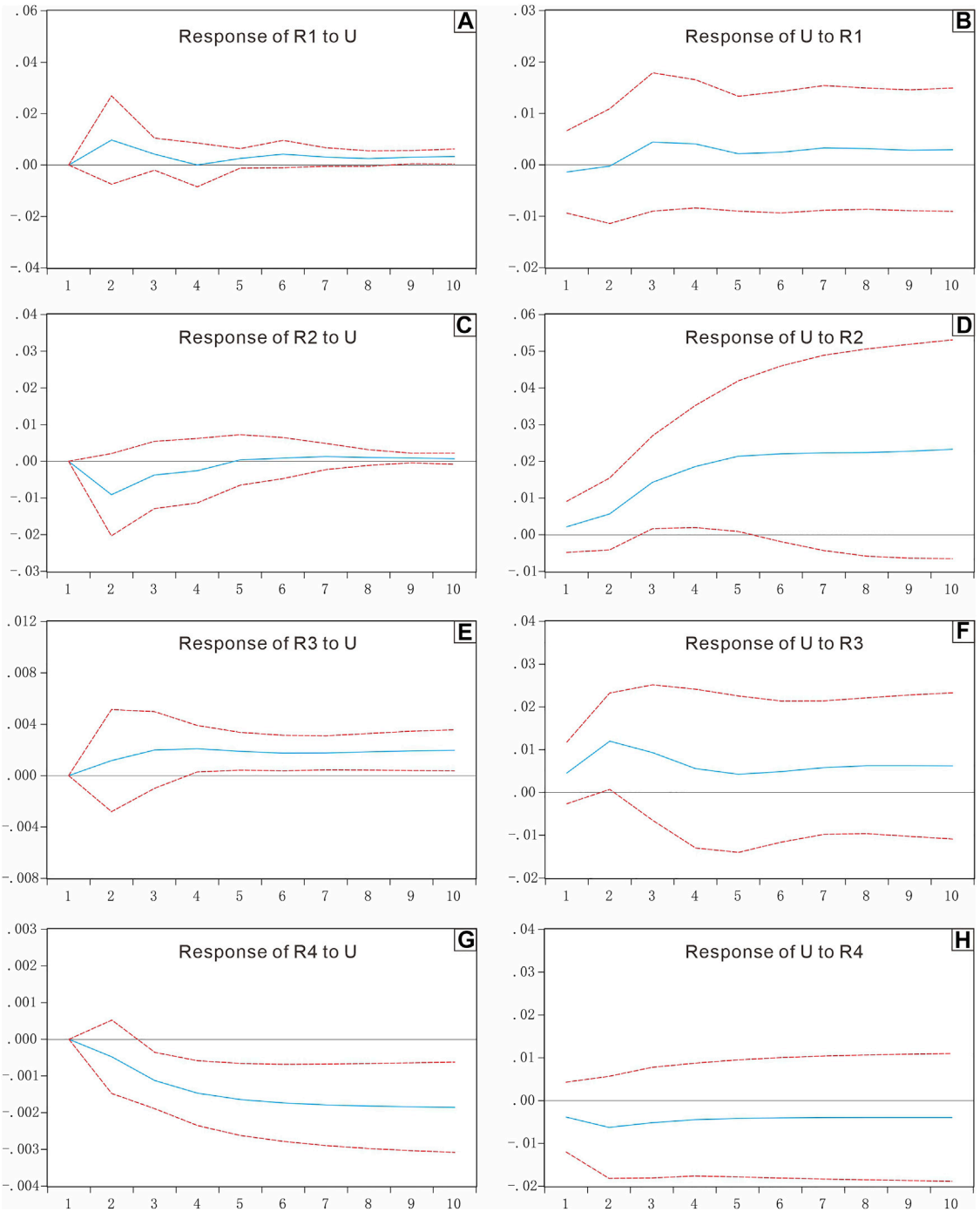

FIGURE 4 | Diagrams show impulse response of water resources and new urbanization for R1 to U **(A)**, U to R1 **(B)**, R2 to U **(C)**, U to R2 **(D)**, R3 to U **(E)**, U to R3 **(F)**, R4 to U **(G)** and U to R4 **(H)**.

where Y_{t+s} is the endogenous vector; U_t is the error term; ψ_s is the error response vector; and ϑ is the standard error result of the vector.

Figures 4A,B shows two indexes, i.e., R1 and U, and their mutual impact effect as well as the dynamic response of the system. First, the influence of the impact of one standard deviation to U on R1 is generally positive, increasing gradually in the first two periods, reaching a maximum in the second period and then starting to decline, decreasing to 0 in the fourth period, and then increasingly slightly but basically close to the X-axis.

Second, the influence of the impact of adding one standard deviation to R1 on U is negative in the first period, then begins to increase, reaching a maximum in the third period and then starting to decline and basically remaining stable after the sixth period. These results indicate that the rapid growth of urbanization in Hebei in the short term leads to a gradual increase in the development and utilization of water resources and a decrease in the WESC; however, when urbanization reaches a certain level, the rapid consumption of water resources and serious water supply shortages can be alleviated with the popularization of economical and intensive water use.

As seen from **Figures 4C,D**, the influence of one standard deviation to U on R2 starts to be negative, the first period is 0, the second period reaches the minimum value, then it starts to rise, and it becomes positive convergence on the X-axis from the fifth period. In contrast, the influence of the impact of one standard deviation on R2 on U is the smallest in the first period, and then gradually increases. This indicates that in the short term, the WEP increases with advancements in urbanization. In other words, current urbanization development occurs at the expense of water environments, but it gradually weakens and tends to be rationalized in the long term.

As shown in **Figures 4E,F**, the influence of one standard deviation to U on R3 is generally positive. The impact in the first period is 0, then it starts to rise, and the fourth period reaches its maximum, and then changes steadily. Second, the influence of the impact of one standard deviation to R3 on U is generally positive, which is the smallest value in the first period, then gradually increasing, and the largest in the second period, then decreasing. In the short term, the stronger is the WECC of a city, the faster is its urbanization development. However, as urbanization advances, the requirements for the WECC become increasingly higher, and the stresses on the WECC become increasingly more obvious.

In **Figures 4G,H**, the influence of the impact of one standard deviation to U on R4 is generally negative. The influence of the first period is 0, and then it begins to decline. Similarly, the influence of the impact of one standard deviation to R4 on U is generally negative, with the maximum in the first period, then a slight decrease, the minimum in the second period, and then a slow increase. In the short term, with the advancement of urbanization in Hebei, the expansion of cities and towns encroaching on farmland and the three-dimensional development of urban space, the regional flood control and drainage capacity will decline, which will lead to certain water disasters. However, the WDD has a stable and destructive effect on urbanization. The greater the degree of WDD in a city is, the slower its urbanization development).

4.3.3 Process Analysis of the Effect

Unlike the IRF method, VAR variance decomposition decomposes the prediction mean square error (MSE) of the endogenous variable in the model into m parts associated with each equation according to its cause, so that it can be decomposed into subvariables associated with the random disturbance terms. By analyzing the relative importance of endogenous variables in the model to the impact of each information set, the relative contribution of each variable is calculated to understand the relative importance of each information set to the endogenous variables of the model. This study uses the VAR variance decomposition method to investigate the degree of influence of water resources and new urbanization in Hebei. The prediction error of the VAR model in the first s periods is given as follows.

$$\boldsymbol{M}_s = \boldsymbol{\varepsilon}_{t+s} + \boldsymbol{\lambda}_1\boldsymbol{\varepsilon}_{t+s-1} + \boldsymbol{\lambda}_2\boldsymbol{\varepsilon}_{t+s-2} + \cdots + \boldsymbol{\lambda}_{s-1}\boldsymbol{\varepsilon}_{t-1} \tag{5}$$

where λ_{s-1} is the lag response for period s-1. The variance in the two variable factors is decomposed by EViews 9.0 software.

From the perspective of R1, the contribution of U to the fluctuation in R1 increases from 0% in the first period to 10.69% in the 10th period; the contribution of R1 to the fluctuation in U increases from 0.67% in the first period to 2.83% in the 10th period (**Figure 5A**). This result indicates that the decrease in WRSC in the initial stage is mainly influenced by Hebei's own resource endowment; however, with the development of urbanization, the massive consumption of resources affects the role of water resources in guaranteeing the development of urbanization. The amount of water resources is sufficient, and the increase in the level of urbanization is mainly affected by urban development itself. However, when the demand for water resources gradually exceeds the upper limit of the regional water resource endowment, it is difficult for water resources to support urban development and will play a constraining role in urbanization development.

Figure 5B for the variance decomposition result. The contribution of U to the fluctuation in R2 increases from 0% in the first period to 10.5% in the tenth period; the contribution of R2 to the fluctuation in U increases from 2.11% in the first period to 84.98% in the tenth period. WEP is more influenced by its own environmental capacity endowment in the early stage of urbanization development, but urbanization produces increasingly more disturbance to the regional water environment. The level of urbanization development is less affected by WEP in the early stage, but when environmental pollution exceeds the natural endowment of the environmental capacity, water pollution gradually constrains urbanization in Hebei.

The difference in WECC is that the contribution of U to the fluctuation in R3 increases from 1% in the first period to 24.17% in the 10th period; the contribution of R3 to the fluctuation in U increases from 8.5% in the first period to 28.41% in the second period and decreases to 15.19% in the 10th period, which is still higher than that in the first period (**Figure 5C**). This result indicates that the changes in water ecology in the early stage of urban development are mainly influenced by itself but that the increase in the level of urbanization gradually affects the carrying capacity of regional water ecology. The initial development of urbanization does cause a decrease in the WECC, which in turn inhibits the sustainable development of urbanization through feedback effects. However, with continuous improvements in water ecology, the serious constraints on urbanization are reduced but a certain inhibiting effect remains.

As shown in **Figure 5D**, the contribution of U to the fluctuation in R4 increases from 0% in the first period to 74.63% in the 10th

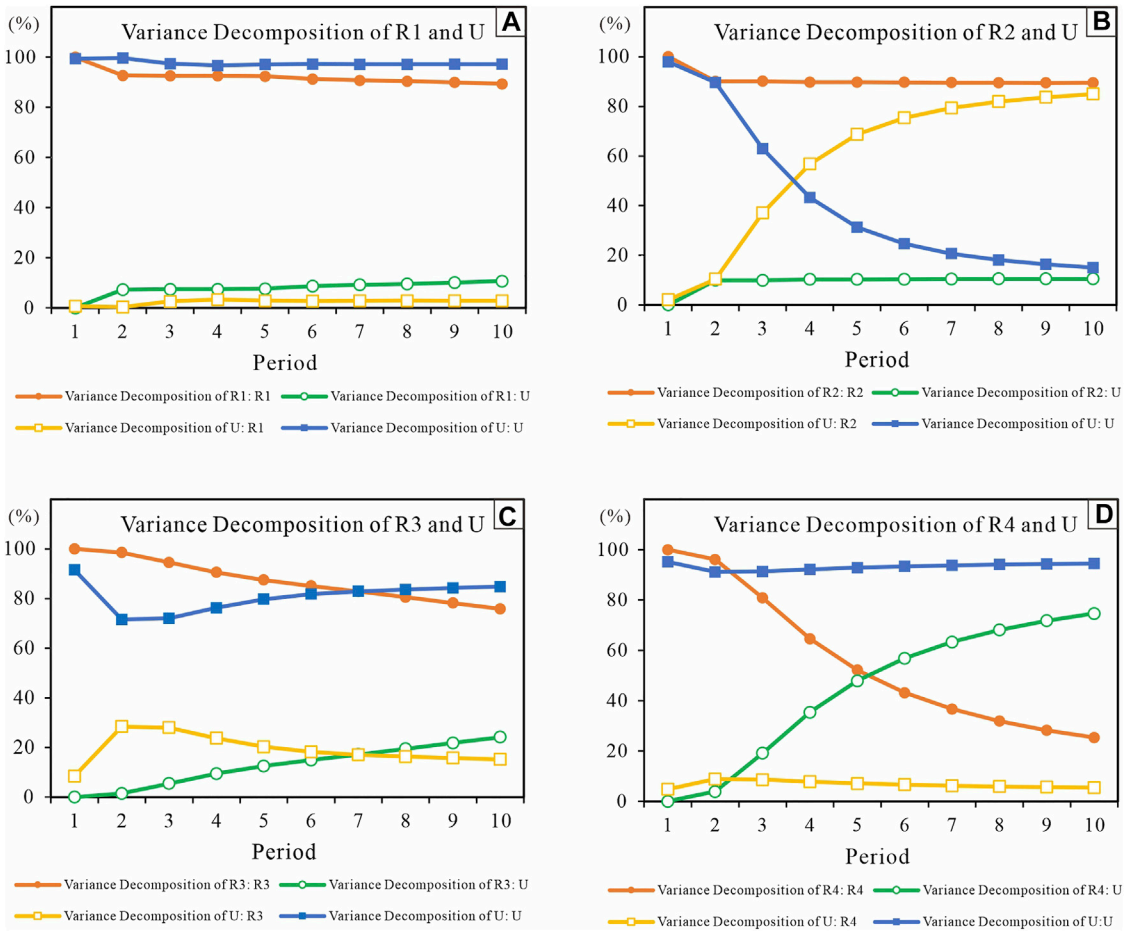

FIGURE 5 | Diagrams show variance decomposition of water resource and new urbanization for R1 and U **(A)**, R2 and U **(B)**, R3 and U **(C)** and U to R4 **(D)**. Data are given in **Supplementary Table S3**.

period; the contribution of R4 to the fluctuation in U increases from 4.83% in the first period to 8.85% in the second period and decreases to 5.47% in the 10th period. In terms of WDD, urban development is more influenced by natural factors during the early stages, but urbanization indeed causes water disaster events, which in turn affect the progress of urban development. However, with continuous improvements in the water disaster prevention and control system in Hebei, the constraints of the WDD on urbanization gradually decrease, but there is still a certain inhibiting effect compared with the initial stage of development.

5 CONCLUSION AND RECOMMENDATIONS

Based on the time series data of evaluation results for water resources and new urbanization in Hebei from 2000 to 2019, this study establishes a VAR model for water resources and new urbanization to analyze the dynamic response relationship between the two. The following conclusions and recommendations are provided.

1) During the 2000–2019 period, the comprehensive evaluation results for water resource in Hebei Province showed a fluctuating upward trend, reflecting gradual improvement in the comprehensive situation of water resource. In particular, water resource support capacity and water environment pollution have changed significantly. The average proportion of water resources support capacity and water environmental pollution in water resources evaluation results is as high as 75%, although they show a trend of gradual improvement. If the constraints of resources and environmental capacity are not fully considered, when resource consumption and pollution discharge reach a certain limit, the self-recovery function of resources and environmental elements in urban areas will be destroyed, thus inhibiting the sustainable and healthy development of water resources. Through the same evaluation results, the water ecological carrying capacity gradually increases, while

the negative impact of water disasters on the comprehensive situation of regional water resources gradually increases. Therefore, in the future, it is necessary to continuously strengthen and improve the comprehensive water disaster prevention and control system in Hebei Province, and promote emergency observation, early warning, disaster investigation and evaluation of various disasters.

2) As China's economy is changing from high-speed development to high-quality development under the new normal, the corresponding urbanization development is also changed from rapid growth in the medium term to quality improvement in the later period. By constructing a new urbanization evaluation index system of "connotation, harmony, intensive, innovation and coordination", the evaluation score of new urbanization in Hebei increases from 0.164 in 2000 to 0.815 in 2019, and urbanization development achieved a qualitative breakthrough. However, the development of new urbanization is an extremely complicated development complex process that is influenced by many factors. Therefore, the development of new urbanization in Hebei Province still needs to solve the challenges and problems faced by water resources, and reveal the interaction and feedback mechanism between water resources and new urbanization.
3) Based on the perspective of the relationship between water resources and new urbanization, this study applies a cointegration test to verify the long-term dynamic relationship between water resources and new urbanization in Hebei Province. By introducing the IRF, it is shown that there is a supporting and inhibiting dynamic relationship between water resources as well as their components and new urbanization in Hebei. This shows that in the early stage of urbanization, influencing factors such as water resource endowment, water environment background value, water ecological capacity and man-made water disasters were not fully considered, which led to the sharp contradiction between water resources and new urbanization. Therefore, it is suggested that in the future development of new urbanization in Hebei, measures such as adjusting the economic growth mode, improving resource utilization efficiency, and upgrading the technical level should be taken to reduce urbanization's consumption of water resources, interference of water environment, degradation of water ecology, and human factors of water disasters to achieve the healthy and sustainable development of water resources in Hebei Province.
4) The results of the variance decomposition model further indicate that the declining support for water resources and the serious pollution of water environments have gradually become important factors limiting new urbanization in Hebei and that the constraining effects of the declining water ecological carrying capacity and water disaster damage on urbanization gradually decrease. While developing and utilizing water resources for new urbanization in Hebei, it is recommended that in the real-world context of poor water resources and serious water environment pollution, investments in water conservancy projects, such as the South-North Water Diversion Project, the intensive use of resources, and water pollution prevention and control should be increased, and the positive role of new urbanization in promoting water resources and water environments should be fully considered, as should slowing the consumption rate of water resources, optimizing the water use structure, and improving the stability of water environments.

DATA AVAILABILITY STATEMENT

The original contributions presented in the study are included in the article/**Supplementary Material**, further inquiries can be directed to the corresponding authors.

AUTHOR CONTRIBUTIONS

SL and JS conceived of the original idea and helped to supervise this study. SL took the lead in the calculation and writing of the publication. SL and QP contributed to the calculation of data and the writing of the publication. FL and JY assisted in calculations through interviews and review of the publication. All authors listed have made a substantial, direct and intellectual contribution to the work and approved it for publication.

FUNDING

This research was jointly supported by Western China Young Scholars Program of the Chinese Academy of Sciences, The Second Tibetan Plateau Scientific Expedition and Research (SQ2019QZKK2203) and National Natural Science Foundation of China (Nos. 41971258, 42101215).

ACKNOWLEDGMENTS

We thank the editor and reviewers for their helpful comments. We are grateful to Yufang Ma, Ziyao An, Siyu Mou, and Xiaoxiao Hao for the assistance in data collection.

SUPPLEMENTARY MATERIAL

The Supplementary Material for this article can be found online at: https://www.frontiersin.org/articles/10.3389/fenvs.2022.941726/full#supplementary-material

REFERENCES

Ahmad, M., Zhao, Z.-Y., and Li, H. (2019). Revealing Stylized Empirical Interactions Among Construction Sector, Urbanization, Energy Consumption, Economic Growth and CO2 Emissions in China. *Sci. Total Environ.* 657, 1085–1098. doi:10.1016/j.scitotenv.2018.12.112

Ahmed, A. A., and Ali, M. H. (2011). Hydrochemical Evolution and Variation of Groundwater and its Environmental Impact at Sohag, Egypt. *Arabian J. Geosciences* 4 (3), 339–352. doi:10.1007/s12517-009-0055-z

Anwar, B., Xiao, Z., Akter, S., and Rehman, R.-U. (2017). Sustainable Urbanization and Development Goals Strategy through Public-Private Partnerships in a South-Asian Metropolis. *Sustainability* 9 (11), 1940. doi:10.3390/su9111940

Bao, C., and Chen, X. (2017). Spatial Econometric Analysis on Influencing Factors of Water Consumption Efficiency in Urbanizing China. *J. Geogr. Sci.* 27 (12), 1450–1462. doi:10.1007/s11442-017-1446-9

Bao, C., and Fang, C.-l. (2012). Water Resources Flows Related to Urbanization in China: Challenges and Perspectives for Water Management and Urban Development. *Water Resour. Manage* 26 (2), 531–552. doi:10.1007/s11269-011-9930-y

Barron, O. V., Barr, A. D., and Donn, M. J. (2013). Effect of Urbanisation on the Water Balance of a Catchment with Shallow Groundwater. *J. Hydrology* 485, 162–176. doi:10.1016/j.jhydrol.2012.04.027

Castells-Quintana, D. (2017). Malthus Living in a Slum: Urban Concentration, Infrastructure and Economic Growth. *J. Urban Econ.* 98, 158–173. doi:10.1016/j.jue.2016.02.003

Chan, K. W. (2014). China's Urbanization 2020: a New Blueprint and Direction. *Eurasian Geogr. Econ.* 55 (1), 1–9. doi:10.1080/15387216.2014.925410

Chen, M., Gong, Y., Lu, D., and Ye, C. (2019a). Build a People-Oriented Urbanization: China's New-type Urbanization Dream and Anhui Model. *Land Use Policy* 80, 1–9. doi:10.1016/j.landusepol.2018.09.031

Chen, M., Liu, W., and Lu, D. (2016). Challenges and the Way Forward in China's New-type Urbanization. *Land Use Policy* 55, 334–339. doi:10.1016/j.landusepol.2015.07.025

Chen, M., Liu, W., and Tao, X. (2013). Evolution and Assessment on China's Urbanization 1960-2010: Under-urbanization or Over-urbanization? *Habitat Int.* 38, 25–33. doi:10.1016/j.habitatint.2012.09.007

Chen, M., Ye, C., Lu, D., Sui, Y., and Guo, S. (2019b). Cognition and Construction of the Theoretical Connotations of New Urbanization with Chinese Characteristics. *J. Geogr. Sci.* 29 (10), 1681–1698. doi:10.1007/s11442-019-1685-z

Cobbinah, P. B., Erdiaw-Kwasie, M. O., and Amoateng, P. (2015). Africa's Urbanisation: Implications for Sustainable Development. *Cities* 47, 62–72. doi:10.1016/j.cities.2015.03.013

Dong, F., Liu, Y., Su, H., Liang, Z., Zou, R., and Guo, H. (2016). Uncertainty-Based Multi-Objective Decision Making with Hierarchical Reliability Analysis under Water Resources and Environmental Constraints. *Water Resour. Manage* 30 (2), 805–822. doi:10.1007/s11269-015-1192-7

Du, H., Zhang, X., and Wang, B. (2006). Co-adaptation between Modern Oasis Urbanization and Water Resources Exploitation: A Case of Urumqi. *Chin. Sci. Bull.* 51 (1), 189–195. doi:10.1007/s11434-006-8225-9

Fang, C., Cui, X., Li, G., Bao, C., Wang, Z., Ma, H., et al. (2019a). Modeling Regional Sustainable Development Scenarios Using the Urbanization and Eco-Environment Coupler: Case Study of Beijing-Tianjin-Hebei Urban Agglomeration, China. *Sci. Total Environ.* 689, 820–830. doi:10.1016/j.scitotenv.2019.06.430

Fang, C., Liang, L., and Wang, Z. (2019b). Quantitative Simulation and Verification of Upgrade Law of Sustainable Development in Beijing-Tianjin-Hebei Urban Agglomeration. *Sci. China Earth Sci.* 62 (12), 2031–2049.

Fang, C., Liu, H., and Wang, S. (2021). The Coupling Curve between Urbanization and the Eco-Environment: China's Urban Agglomeration as a Case Study. *Ecol. Indic.* 130, 108107. doi:10.1016/j.ecolind.2021.108107

Fang, C., Ma, H., and Wang, J. (2015). A Regional Categorization for "New-type Urbanization" in China. *PLOS ONE* 10 (8), e0134253. doi:10.1371/journal.pone.0134253

Gu, C. (2019). Urbanization: Processes and Driving Forces. *Sci. China Earth Sci.* 62 (9), 1351–1360. doi:10.1007/s11430-018-9359-y

Guan, X., Wei, H., Lu, S., Dai, Q., and Su, H. (2018a). Assessment on the Urbanization Strategy in China: Achievements, Challenges and Reflections. *Habitat Int.* 71, 97–109.

Guan, X., Wei, H., Lu, S., and Su, H. (2018b). Mismatch Distribution of Population and Industry in China: Pattern, Problems and Driving Factors. *Appl. Geogr.* 97, 61–74. doi:10.1016/j.apgeog.2018.05.021

Kot, M., Castleden, H., and Gagnon, G. A. (2015). The Human Dimension of Water Safety Plans: a Critical Review of Literature and Information Gaps. *Environ. Rev.* 23 (1), 24–29.

Larsen, T. A., Hoffmann, S., Lüthi, C., Truffer, B., and Maurer, M. (2016). Emerging Solutions to the Water Challenges of an Urbanizing World. *Science* 352 (6288), 928–933. doi:10.1126/science.aad8641

Li, L., and Liu, D. (2021). Exploring the Bidirectional Relationship between Urbanization and Rural Sustainable Development in China since 2000: Panel Data Analysis of Chinese Cities. *J. Urban Plann. Dev.* 147 (3), 05021024. doi:10.1061/(asce)up.1943-5444.0000721

Li, M., Shi, Y., Duan, W., Chen, A., Wang, N., and Hao, J. (2019). Spatiotemporal Decoupling of Population, Economy and Construction Land Changes in Hebei Province. *Sustainability* 11. doi:10.3390/su11236794

Li, Y., Jia, L., Wu, W., Yan, J., and Liu, Y. (2018). Urbanization for Rural Sustainability - Rethinking China's Urbanization Strategy. *J. Clean. Prod.* 178, 580–586. doi:10.1016/j.jclepro.2017.12.273

Liang, L., Wang, Z., and Li, J. (2019). The Effect of Urbanization on Environmental Pollution in Rapidly Developing Urban Agglomerations. *J. Clean. Prod.* 237, 117649.

Liu, H., Wei, L., Chen, C., and Wang, Z. (2022). The Impact of Consumption Patterns and Urbanization on the Cross-Regional Water Footprint in China: A Decomposition Analysis. *Front. Environ. Sci.* 9. doi:10.3389/fenvs.2021.792423

Liu, N., Liu, C., Xia, Y., and Da, B. (2018). Examining the Coordination between Urbanization and Eco-Environment Using Coupling and Spatial Analyses: A Case Study in China. *Ecol. Indic.* 93, 1163–1175. doi:10.1016/j.ecolind.2018.06.013

Liu, S.-K., Lin, Z.-E., and Chiueh, P.-T. (2022). Improving Urban Sustainability and Resilience with the Optimal Arrangement of Water-Energy-Food Related Practices. *Sci. Total Environ.* 812, 152559. doi:10.1016/j.scitotenv.2021.152559

Lu, X.-h., and Ke, S.-g. (2018). Evaluating the Effectiveness of Sustainable Urban Land Use in China from the Perspective of Sustainable Urbanization. *Habitat Int.* 77, 90–98. doi:10.1016/j.habitatint.2017.10.007

Ma, T., Sun, S., Fu, G., Hall, J. W., Ni, Y., He, L., et al. (2020). Pollution Exacerbates China's Water Scarcity and its Regional Inequality. *Nat. Commun.* 11 (1), 650. doi:10.1038/s41467-020-14532-5

Ma, Y., Yan, J., Sha, J., He, G., Song, C., Fan, S., et al. (2018). Dynamic Simulation of the Atmospheric Environment Improved by a Focus on Clean Energy Utilization of Resource-Based Cities in China. *J. Clean. Prod.* 192, 396–410. doi:10.1016/j.jclepro.2018.04.247

Magri, A., and Berezowska-Azzag, E. (2019). New Tool for Assessing Urban Water Carrying Capacity (WCC) in the Planning of Development Programs in the Region of Oran, Algeria. *Sustain. Cities Soc.* 48, 101316. doi:10.1016/j.scs.2018.10.040

Mälzer, H.-J., Staben, N., Hein, A., and Merkel, W. (2010). Identification, Assessment, and Control of Hazards in Water Supply: Experiences from Water Safety Plan Implementations in Germany. *Water Sci. Technol.* 61 (5), 1307–1315. doi:10.2166/wst.2010.026

Meinzen-Dick, R., and Appasamy, P. P. (2002). *Urbanization and Intersectoral Competition for Water*. Woodrow Wilson International Center for Scholars Environmental Change and Security Project (ed.) Finding the Source: The Linkages Between Population and Water. Washington, DC: The Woodrow Wilson Institute, 27–51.

Mou, S., Yan, J., Sha, J., Deng, S., Gao, Z., Ke, W., et al. (2020). A Comprehensive Evaluation Model of Regional Water Resource Carrying Capacity: Model Development and a Case Study in Baoding, China. *Water* 12 (9), 2637.

Mou, S., Yan, J., Sha, J., Li, S., Ma, Y., He, G., et al. (2019). Dynamic Simulation of the Optimal Allocation of Water Resources via the Introduction of Integrated Water Environmental Policies in Baoding, China. *Environ. Sci. Pollut. Res.* 26 (26), 27516–27533. doi:10.1007/s11356-019-05537-9

Nong, D. H., Lepczyk, C. A., Miura, T., and Fox, J. M. (2018). Quantifying Urban Growth Patterns in Hanoi Using Landscape Expansion Modes and Time Series Spatial Metrics. *PLOS ONE* 13 (5), e0196940. doi:10.1371/journal.pone.0196940

Ouelhazi, H., Lachaal, F., Charef, A., Challouf, B., Chaieb, H., and Horriche, F. J. (2014). Hydrogeological Investigation of Groundwater Artificial Recharge by Treated Wastewater in Semi-arid Regions: Korba Aquifer (Cap-Bon Tunisia). *Arab. J. Geosci.* 7 (10), 4407–4421. doi:10.1007/s12517-013-1090-3

Panagopoulos, G. P. (2014). Assessing the Impacts of Socio-Economic and Hydrological Factors on Urban Water Demand: A Multivariate Statistical Approach. *J. Hydrology* 518, 42–48. doi:10.1016/j.jhydrol.2013.10.036

Rickert, B., van den Berg, H., Bekure, K., Girma, S., and de Roda Husman, A. M. (2019). Including Aspects of Climate Change into Water Safety Planning: Literature Review of Global Experience and Case Studies from Ethiopian Urban Supplies. *Int. J. Hyg. Environ. Health* 222 (5), 744–755. doi:10.1016/j.ijheh.2019.05.007

Roeger, A., and Tavares, A. F. (2018). Water Safety Plans by Utilities: A Review of Research on Implementation. *Util. Policy* 53, 15–24. doi:10.1016/j.jup.2018.06.001

Ruan, S., Hong, Y., and Zhuang, Y. (2021). Evolution and Restoration of Water Quality in the Process of Urban Development: a Case Study in Urban Lake, China. *Environ. Monit. Assess.* 193 (7), 407. doi:10.1007/s10661-021-09182-z

Schellenberg, T., Subramanian, V., Ganeshan, G., Tompkins, D., and Pradeep, R. (2020). Wastewater Discharge Standards in the Evolving Context of Urban Sustainability–The Case of India. *Front. Environ. Sci.* 8. doi:10.3389/fenvs.2020.00030

Schulterbrandt Gragg, R., Anandhi, A., Jiru, M., and Usher, K. M. (2018). A Conceptualization of the Urban Food-Energy-Water Nexus Sustainability Paradigm: Modeling from Theory to Practice. *Front. Environ. Sci.* 6. doi:10.3389/fenvs.2018.00133

Shang, J., Wang, Z., Li, L., Chen, Y., and Li, P. (2018). A Study on the Correlation between Technology Innovation and the New-type Urbanization in Shaanxi Province. *Technol. Forecast. Soc. Change* 135, 266–273. doi:10.1016/j.techfore.2018.04.029

Shen, L., Zhou, J., Skitmore, M., and Xia, B. (2015). Application of a Hybrid Entropy–McKinsey Matrix Method in Evaluating Sustainable Urbanization: A China Case Study. *Cities* 42, 186–194.

Shen, Y., Oki, T., Kanae, S., Hanasaki, N., Utsumi, N., and Kiguchi, M. (2014). Projection of Future World Water Resources under SRES Scenarios: an Integrated Assessment. *Hydrological Sci. J.* 59 (10), 1775–1793. doi:10.1080/02626667.2013.862338

Shojaei, M., Nazif, S., and Kerachian, R. (2015). Joint Uncertainty Analysis in River Water Quality Simulation: a Case Study of the Karoon River in Iran. *Environ. Earth Sci.* 73 (7), 3819–3831. doi:10.1007/s12665-014-3667-x

Song, C., Yan, J., Sha, J., He, G., Lin, X., and Ma, Y. (2018). Dynamic Modeling Application for Simulating Optimal Policies on Water Conservation in Zhangjiakou City, China. *J. Clean. Prod.* 201, 111–122.

Su, H., Wei, H., and Zhao, J. (2016). Density Effect and Optimum Density of the Urban Population in China. *Urban Stud.* 54 (7), 1760–1777. doi:10.1177/0042098015624839

Sun, Q. (2017). Empirical Research on Coordination Evaluation and Sustainable Development Mechanism of Regional Logistics and New-type Urbanization: a Panel Data Analysis from 2000 to 2015 for Liaoning Province in China. *Environ. Sci. Pollut. Res.* 24 (16), 14163–14175. doi:10.1007/s11356-017-8980-y

Tan, Y., Xu, H., and Zhang, X. (2016). Sustainable Urbanization in China: A Comprehensive Literature Review. *Cities* 55, 82–93. doi:10.1016/j.cities.2016.04.002

Tang, P., Huang, J., Zhou, H., Fang, C., Zhan, Y., and Huang, W. (2021). Local and Telecoupling Coordination Degree Model of Urbanization and the Eco-Environment Based on RS and GIS: A Case Study in the Wuhan Urban Agglomeration. *Sustain. Cities Soc.* 75, 103405. doi:10.1016/j.scs.2021.103405

Taylor, J. R. (2015). The China Dream Is an Urban Dream: Assessing the CPC's National New-type Urbanization Plan. *J Chin Polit Sci* 20 (2), 107–120. doi:10.1007/s11366-015-9341-7

Tiffen, M. (2003). Transition in Sub-saharan Africa: Agriculture, Urbanization and Income Growth. *World Dev.* 31 (8), 1343–1366. doi:10.1016/s0305-750x(03)00088-3

Van Leeuwen, C. J., and Sjerps, R. M. A. (2015). The City Blueprint of Amsterdam: An Assessment of Integrated Water Resources Management in the Capital of the Netherlands. *Water Sci. Technol. Water Supply* 15 (2), 404–410. doi:10.2166/ws.2014.127

Wang, H., Huang, J., Zhou, H., Deng, C., and Fang, C. (2020). Analysis of Sustainable Utilization of Water Resources Based on the Improved Water Resources Ecological Footprint Model: A Case Study of Hubei Province, China. *J. Environ. Manag.* 262, 110331. doi:10.1016/j.jenvman.2020.110331

Wang J, J., Zhou, W., Pickett, S. T. A., Yu, W., and Li, W. (2019). A Multiscale Analysis of Urbanization Effects on Ecosystem Services Supply in an Urban Megaregion. *Sci. Total Environ.* 662, 824–833. doi:10.1016/j.scitotenv.2019.01.260

Wang, W., Chen, Y., and Wang, W. (2020b). Groundwater Recharge in the Oasis-Desert Areas of Northern Tarim Basin, Northwest China. *Hydrology Res.* 51 (6), 1506–1520. doi:10.2166/nh.2020.071

Wang X, X., Zhou, Y., Zhao, Z., Wang, L., Xu, J., and Yu, J. (2019). A Novel Water Quality Mechanism Modeling and Eutrophication Risk Assessment Method of Lakes and Reservoirs. *Nonlinear Dyn.* 96 (2), 1037–1053. doi:10.1007/s11071-019-04837-6

Wang, X.-R., Hui, E. C.-M., Choguill, C., and Jia, S.-H. (2015). The New Urbanization Policy in China: Which Way Forward? *Habitat Int.* 47, 279–284. doi:10.1016/j.habitatint.2015.02.001

Wang, X., and Chen, X. (2019). An Evaluation Index System of China's Development Level of Ecological Civilization. *Sustainability* 11 (8), 2270. doi:10.3390/su11082270

Wang, Y., Cheng, H., and Huang, L. (2018). Water Resources Carrying Capacity Evaluation of a Dense City Group: a Comprehensive Water Resources Carrying Capacity Evaluation Model of Wuhan Urban Agglomeration. *Urban Water J.* 15 (7), 615–625. doi:10.1080/1573062x.2018.1529805

Wei, H., and Zhang, Y. (2017). Analysis of Impact of Urbanization on Environmental Quality in China. *CHINA & WORLD Econ.* 25 (2), 85–106. doi:10.1111/cwe.12195

Wu, X., Xu, C., and Pang, Q. (2017). Analysis on Driving Effect of the Urbanization Development Speed on Water Resources Conflict. *Math. Problems Eng.* 2017, 6810120. doi:10.1155/2017/6810120

Xia, J., Zhang, Y., Xiong, L., He, S., Wang, L., and Yu, Z. (2017). Opportunities and Challenges of the Sponge City Construction Related to Urban Water Issues in China. *Sci. China Earth Sci.* 60 (4), 652–658. doi:10.1007/s11430-016-0111-8

Xiao, Y., Hao, Q., Zhang, Y., Zhu, Y., Yin, S., Qin, L., et al. (2022). Investigating Sources, Driving Forces and Potential Health Risks of Nitrate and Fluoride in Groundwater of a Typical Alluvial Fan Plain. *Sci. Total Environ.* 802, 149909. doi:10.1016/j.scitotenv.2021.149909

Xie, H., Cheng, L., and Lu, H. (2018). Farmers' Responses to the Winter Wheat Fallow Policy in the Groundwater Funnel Area of China. *Land Use Policy* 73, 195–204. doi:10.1016/j.landusepol.2018.02.003

Xie, H., Cheng, L., and Lv, T. (2017). Factors Influencing Farmer Willingness to Fallow Winter Wheat and Ecological Compensation Standards in a Groundwater Funnel Area in Hengshui, Hebei Province, China. *Sustainability* 9 (5), 839. doi:10.3390/su9050839

Yang, W., and Jiang, X. (2018). Evaluating Sustainable Urbanization of Resource-Based Cities Based on the McKinsey Matrix: Case Study in China. *J. Urban Plann. Dev.* 144 (1), 05017020. doi:10.1061/(asce)up.1943-5444.0000423

Yu, B. (2021). Ecological Effects of New-type Urbanization in China. *Renew. Sustain. Energy Rev.* 135, 110239. doi:10.1016/j.rser.2020.110239

Zeng, L., Wang, J., Zhang, J., Lv, J., and Cui, W. (2020). New Urbanization Paths in Mineral Resource Abundant Regions in China: A Three-Dimensional Cube Framework. *Resour. Policy* 68, 101709. doi:10.1016/j.resourpol.2020.101709

Zhang, K., Shen, J., He, R., Fan, B., and Han, H. (2019). Dynamic Analysis of the Coupling Coordination Relationship between Urbanization and Water Resource Security and its Obstacle Factor. *Ijerph* 16 (23), 4765. doi:10.3390/ijerph16234765

Zhang, W., Yu, Y., Zhou, X., Yang, S., and Li, C. (2018). Evaluating Water Consumption Based on Water Hierarchy Structure for Sustainable Development Using Grey Relational Analysis: Case Study in Chongqing, China. *Sustainability* 10 (5), 1538. doi:10.3390/su10051538

Zhao, Y., Sheng, X., Yang, P., and Zhu, L. (2019). Evaluation of Ecological Civilization in Megacities. *Appl. Ecol. Environ. Res.* 17 (4), 8527–8540. doi:10.15666/aeer/1704_85278540

Zhong, L., Li, X., Law, R., and Sun, S. (2020). Developing Sustainable Urbanization Index: Case of China. *Sustainability* 12 (11), 4585. doi:10.3390/su12114585

Conflict of Interest: The authors declare that the research was conducted in the absence of any commercial or financial relationships that could be construed as a potential conflict of interest.

Publisher's Note: All claims expressed in this article are solely those of the authors and do not necessarily represent those of their affiliated organizations, or those of the publisher, the editors and the reviewers. Any product that may be evaluated in this article, or claim that may be made by its manufacturer, is not guaranteed or endorsed by the publisher.

frontiers | Frontiers in Environmental Science

ORIGINAL RESEARCH
published: 01 July 2022
doi: 10.3389/fenvs.2022.946112

Impact of a Low-Permeability Layer on the Pumping Efficiency Under Threats of Saltwater Up-Coning

Zhenyu Wu[1], *Maozhu Tang*[2], *Edoardo Daly*[2] *and Chunhui Lu*[1]*

[1]State Key Laboratory of Hydrology-Water Resources and Hydraulic Engineering, Hohai University, Nanjing, China, [2]Department of Civil Engineering, Monash University, Clayton, VIC, Australia

Previous studies on saltwater up-coning are mostly based on the assumption of a homogeneous aquifer and neglect the effect of heterogeneity. A numerical study was carried out to explore the impact of a low-permeability (*k*) layer on the pumping efficiency under threats of saltwater up-coning. It is found that the presence of the low-*k* layer could impede up-coning of saltwater, thereby improving significantly pumping efficiency, as expected. For the cases adopted, when the permeability of the 2 m thick low-*k* layer is three orders of magnitude less than that of the corresponding homogeneous aquifer, the pumping duration (i.e., the time before the salinity of pumped water reaches 2%) can be up to about 10 times longer than that of the homogeneous aquifer case. Additionally, a sound linear relationship could be developed between the normalized pumping duration of the layered case (*E*) (defined as the difference of the pumping duration between layered and homogeneous cases relative to the pumping duration in the homogeneous case) and the permeability of the homogeneous aquifer relative to that of the low-*k* layer (β). However, a short low-*k* layer may lead to the failure of this linear relationship. Moreover, a thicker low-*k* layer leads to a larger *E* when all other conditions are unchanged. When varying the location of the low-*k* layer, the large *E* occurs for the low-*k* layer located below and near the well bottom. The results obtained in the current study offer significant implications for preventing saltwater up-coning and improving the pumping efficiency through natural and artificial barriers.

Keywords: low-permeability layer, up-coning, numerical modelling, pumping efficiency, groundwater

OPEN ACCESS

Edited by:
Lichun Wang,
Tianjin University, China

Reviewed by:
Tianyuan Zheng,
Ocean University of China, China
Xuejing Wang,
Southern University of Science and Technology, China

***Correspondence:**
Chunhui Lu
clu@hhu.edu.cn

Specialty section:
This article was submitted to Freshwater Science, a section of the journal Frontiers in Environmental Science

Received: *17 May 2022*
Accepted: *13 June 2022*
Published: *01 July 2022*

Citation:
Wu Z, Tang M, Daly E and Lu C (2022) Impact of a Low-Permeability Layer on the Pumping Efficiency Under Threats of Saltwater Up-Coning. Front. Environ. Sci. 10:946112. doi: 10.3389/fenvs.2022.946112

1 INTRODUCTION

Coastal aquifers represent a vital component of freshwater resources in many countries worldwide. However, the overexploitation of the coastal aquifer has resulted in seawater intrusion, causing the degradation of groundwater resources and ecological systems (Werner et al., 2013). The existence of fresh groundwater overlaying saltwater in groundwater systems is ubiquitous in most coastal aquifers as well as in many inland aquifers (e.g., Schmorak and Mercado, 1969). The utilization of freshwater resources in those regions is therefore highly constrained by the presence of saltwater up-coning (i.e., the vertical rise of saline water into a production well), which may occur when groundwater is extracted through a partially penetrating well installed in the freshwater zone above a layer of intruded saltwater. It usually takes a long time for the up-coned saltwater to migrate back to the original position prior to pumping, indicating that once a pumping well is abandoned due to salinization, it can be reused for groundwater utilization after a long time (Zhou et al., 2005). Different skimming well

options, such as scavenger wells and skimming tube wells, have been introduced to control saltwater up-coning and to enhance the freshwater extraction efficiency (Saeed et al., 2002).

Saltwater up-coning have been receiving attention for several decades, being studied using analytical, numerical, and experimental methods (Werner et al., 2013). These studies revealed that the rate and extent of saltwater up-coning rely on many factors, such as hydraulic properties of the aquifer, pumping rate and duration, initial interface position, density contrast between freshwater and saltwater, and regional flow. Additional factors affecting saltwater up-coning are dispersion and sorption effects, groundwater recharge, and the well and aquifer geometries (e.g., Reilly and Goodman, 1987; Saeed et al., 2002; Hamza, 2006; Werner et al., 2009).

Diersch et al. (1984) were among the first to use numerical models to analyse dispersive processes during saltwater up-coning and found through sensitivity analysis that the salinity at the pumping well is strongly affected by dispersion. Zhou et al. (2005) explored the effect of longitudinal and transversal dispersivities on the pumping duration defined as the time before the salinity of pumped water reaches a specified value. Their numerical simulation results showed that the smaller the dispersivities, the longer the well pumps freshwater. In addition, the effect of the density difference between the freshwater and saltwater on the up-coning process was investigated in their study. The results indicated that the density effect could retard the solute transport toward the pumping well and prolong the pumping duration prior salinization.

Jakovovic et al. (2012) studied the effect of dye tracer (Rhodamine WT) adsorption on saltwater up-coning based on sand-tank experiments and numerical modelling. The results revealed that under low pumping rates, the spatial variability of the velocity is pronounced, increasing from the centre of the plume towards the interface. The dye tracer could be retarded relative to the salt and be preferentially transported along the higher-velocity paths towards the well forming double-peaked up-coning patterns. However, high pumping rates made the adsorption effect insignificant.

Recently, Jakovovic et al. (2016) investigated the problem of saltwater up-coning by analysing the saltwater up-coning zone of influence (SUZI). The SUZI is defined as the region around a pumping well within which significant rise in the saltwater-freshwater interface occurs. They found through both numerical and analytical methods that the SUZI was dependent on the relative magnitudes of pumping, regional flow, distance of the well from the coast, and position of the well above the interface. Moreover, the results of the three-dimensional coastal setting simulations showed an asymmetric shape of the lateral extent of the SUZI, which is largest in the direction parallel to the coast. The occurrence of this phenomenon is attributed to that the ocean and the inland extent of the seawater wedge limit the propagation of the SUZI perpendicular to the coast.

While significant studies have been conducted, there is very limited research investigating the impact of aquifer heterogeneity on the saltwater up-coning processes. Interface up-coning in stratified aquifers has been examined analytically by Dagan and Zeitoun (1998), where the hydraulic conductivity was modelled as a stationary random function of the vertical coordinate. By contrast, a significant number of studies have been carried out to explore the impact of aquifer heterogeneity on seawater intrusion (e.g., Kim et al., 2006; Liu et al., 2014; Strack and Ausk, 2015). Taking an example, Lu et al. (2013) investigated the steady-state mixing zone in stratified coastal aquifers based on laboratory experiments and numerical modelling and observed that a low-permeability (k) layer exerts a high impact on the mixing-zone development. Accordingly, we hypothesize that the presence of a low-k layer would highly affect saltwater up-coning dynamics.

The main aim of this study is to investigate the impact of a low-k layer on saltwater up-coning processes using a variable-density flow and solute transport numerical model, as a first step to analyse the effects of aquifer heterogeneity on the generation and dynamics of saltwater up-coning. The pumping duration, the same definition as in Zhou et al. (2005), will serve as the main indicator for assessing the impact of the low-k layer on the pumping efficiency. The results of layered aquifers and corresponding homogeneous aquifers will be compared to reveal the importance of the low-k layer on controlling groundwater flow and salt transport. More importantly, quantitative relationships between the pumping duration and the k magnitude of the low-k layer are obtained; these provide a simple tool for developing natural and artificial barriers to prevent saltwater up-coning and enhance the pumping efficiency.

2 METHODS

2.1 Conceptual Model and Parameter Values

The conceptual model in Zhou et al. (2005), modified from the saltwater up-coning problem presented by Reilly and Goodman (1987) and Voss and Souza (1987), is further modified in our study and is used as a reference case, since the aquifer is homogeneous (**Figure 1**). An axisymmetric, anisotropic, and confined aquifer is considered; the domain with a radius of 3,000 m and 150 m thickness, initially consists of three zones identified by different concentrations. The upper zone is the freshwater zone (C_f = 0 kg m^{-3}) and 98 m thick, while a 50 m thick saltwater zone is located at the bottom of the aquifer with the concentration C_s = 35 kg m^{-3}. A 2 m thick mixing zone separates these two zones with a concentration equal to C_s/2. The origin of the coordinate system is located at the bottom left of the model domain. In comparison with the conceptual model used in Zhou et al. (2005), the thickness of the saltwater zone is increased from 20 to 50 m, and the radius of the model is increased from 2000 to 3,000 m. These modifications were necessary to assure that the saltwater zone was deep enough to be able to supply water for length of all simulations. A smaller domain would have caused the concentrations of the water near the bottom boundary to become lower than C_s, this affecting the pumping times.

An extraction well was located at the center of the axisymmetric domain at the top of the freshwater zone with a constant pumping rate Q_w = 2,400 m^3 d^{-1} and a well screen length d_f = 20 m. The initial hydraulic head is set as 10 m above the aquifer top. Recharge of freshwater and saltwater occurred along the external radial boundary with fixed-head and fixed concentration boundary conditions. Note that the fixed concentration is used in our solute boundary condition, while in Zhou et al. (2005), a concentration gradient of zero is prescribed normal to the

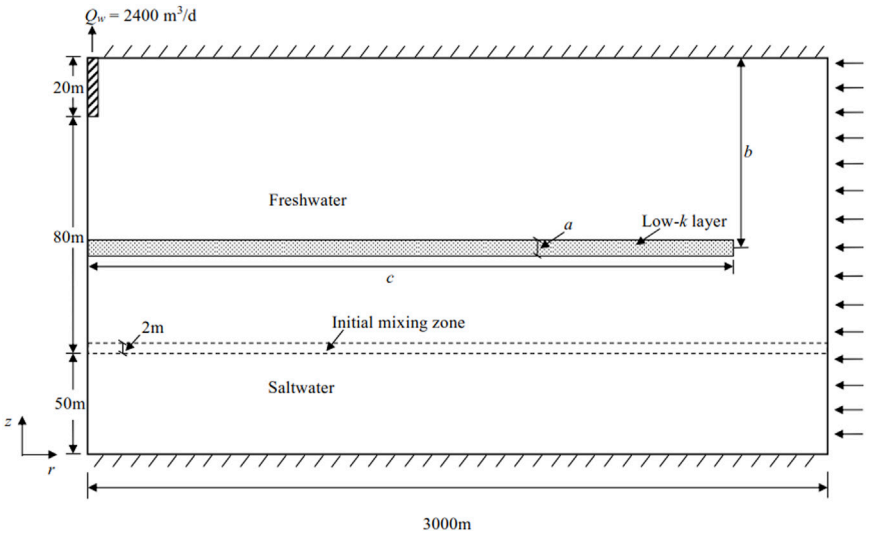

FIGURE 1 | Conceptual model of a saltwater up-coning problem (modified from Figure 1 in Zhou et al. (2005).

TABLE 1 | Values of parameters in the homogeneous case.

Parameter	Symbol	Value	Unit
Porosity	θ	0.2	-
Permeability in the horizontal direction	k_x	2.56×10^{-11}	m^2
Permeability in the vertical direction	k_z	1.0×10^{-11}	m^2
Dynamic viscosity	μ	1.0×10^{-3}	kg m^{-1} s^{-1}
Pumping rate	Q_w	2400	m^3 d^{-1}
Freshwater density	ρ_f	1,000	kg m^{-3}
Saltwater density	ρ_s	1,025	kg m^{-3}
Longitudinal dispersivity	α_L	1	m
Transverse dispersivity	α_T	0.5	m
Molecular diffusion coefficient	D_m	0	m^2 s^{-1}

boundary, and therefore salt can enter from this boundary only through advection. After pumping, saline water beneath the well is gradually drawn upward and the concentration of the extracted water gradually increases. Like in Zhou et al. (2005), it is assumed that, once the concentration of the extracted water reaches 2% of the saltwater concentration (i.e., C_s), the well is shut off.

For the base homogenous case, permeability in the horizontal and vertical directions (k_x and k_z) are 2.56×10^{-11} and 1.0×10^{-11} m^2, respectively. A constant value of 1×10^{-3} kg m^{-1} s^{-1} is used for dynamic viscosity (μ). The porosity (θ) of the aquifer is 0.2. The densities of the freshwater (ρ_w) and saltwater (ρ_s) are 1,000 and 1,025 kg m^{-3}, the latter approximately equaling to a common density of seawater. The longitudinal and transversal dispersivities (α_L and α_T) are 1 and 0.5 m, respectively. Molecular diffusion is neglected. The values of the parameters in the homogeneous case, listed in **Table 1**, are as those assumed for Case A in Zhou et al. (2005).

To study the effect of layered aquifer heterogeneity on saltwater up-coning, a horizontal low-k layer is considered with a thickness of a, distance between the center of the low-k layer and the top of aquifer of b, and extent from the well c. By varying the values of a, b, and c, nine scenarios are designed to test their sensitivity. Three different values of a (2, 4, and 8 m) are selected. For b, five values (6, 20, 32, 46, and 50 m) are chosen; when b = 6 m, the extraction well penetrates the low-k layer. Six values of c (100, 500, 1,000, 1,500, 2000, and 3,000 m) are assumed, where c = 3,000 m means that the low-k layer extended to the entire length of the domain. Moreover, to examine the sensitivity of the k magnitude of the low-k layer, values ranging from one to three orders of magnitude lower than the value in the homogeneous case are adopted. The highest values of k correspond to sands and the lowest values silts (Verruijt, 1970). When varying the value of k, the anisotropic ratio is fixed.

2.2 Numerical Implementation

Numerical simulations are implemented by SEAWAT-2000, a code based on the finite-difference method and developed by USGS for simulating variable-density flow and solute transport in porous media (Langevin et al., 2003). The code SEAWAT-2000 is developed by combining MODFLOW and MT3DMS into a single program that solves the coupled flow and solute transport equations. The governing equations are not shown here for the sake of conciseness and can be found in many references (e.g., Langevin et al., 2003). These three computer programs are originally based on the Cartesian coordinate system. Langevin (2008) showed that axisymmetric flow and transport can be simulated by these programs by adjusting several input parameters to account for the increase in flow area with radial distance from the well. In addition, the logarithmic weighting of interblock transmissivity that is a standard option in MODFLOW can be used for axisymmetric models to represent the linear change in hydraulic conductance within a single finite-difference cell.

For the reference case, the entire domain is discretized into 75 layers and 307 columns, resulting in 23025 cells in total. Each layer is 2 m thick, while the columns are variably spaced with 0.25 m horizontal resolution near the well expanding to 25 m horizontal resolution at the radial boundary. This discretization scheme is similar to that used in Langevin (2008).

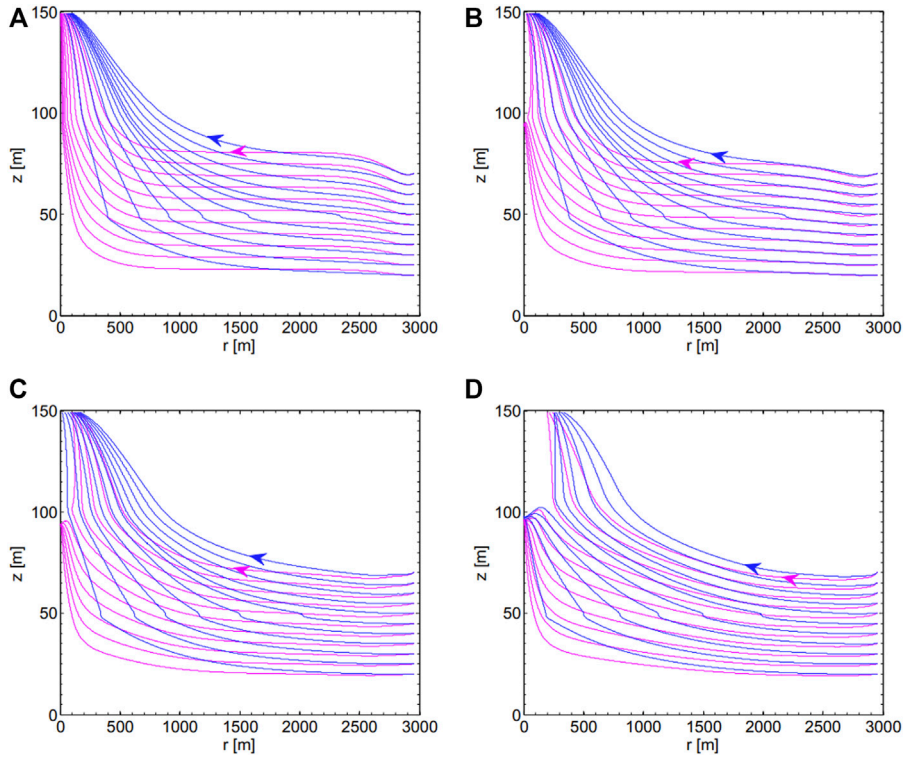

FIGURE 2 | Streamlines developed in the homogeneous case (magenta) and the layered case (blue) after **(A)** 1 year, **(B)** 2 years, **(C)** 5 years, and **(D)** 20 years.

2.3 Quantitative Indicators

As mentioned above, the salt concentration distribution (C) and the pumping duration (T) before the salinity of pumped water reaches a specified value (2% in the current study) are taken as quantitative indicators. Here, we define two dimensionless variables based on these two indicators:

$$w = \frac{C}{C_s} \tag{1}$$

and

$$E = \frac{(T_L - T_H)}{T_H} \tag{2}$$

in which T_L and T_H are the pumping durations when the salinity of pumped water reaches 2% in layered and homogeneous cases, respectively. E quantifies the efficiency of well pumping under the threats of saltwater up-coning. In addition, a dimensionless parameter β is defined to reflect the relative magnitude of k of the low-k layer to that in the homogenous case:

$$\beta = \frac{k_H}{k_L} \tag{3}$$

in which k_H and k_L are permeability of the homogenous case and the low-k layer in the horizontal direction, respectively. Since the anisotropy ratio of the aquifer is maintained the same for all cases, the value of β is constant for a given low-k layer regardless of the direction of permeability.

3 RESULTS AND DISCUSSION

3.1 Impact on the Flow Field

Figure 2 shows the streamlines developed in the homogeneous aquifer case and layered aquifer case after 1, 2, 5, and 20 years, in which the layered aquifer has the parameters a = 2 m, b = 50 m, c = 3,000 m, and β = 1,000. The streamlines start from the external boundary with the vertical coordinates between 20 and 70 m. The streamlines in both cases change with the time, and the presence of the low-k layer alters significantly their direction. Initially, the streamlines near the external boundary in the homogeneous case are higher than in the layered case (see **Figure 2A**). With time the relative locations of the streamlines near the external boundary in the two cases are gradually altered (see **Figures 2B–D**). On the other hand, the presence of the low-k layer cause the streamlines to go up earlier than the counterparts in the homogeneous case. It is interesting that at larger pumping times, the lower streamlines in both cases tend to arrive at the vertical axis with z = 95 m, though this occurs in the homogeneous case earlier.

Figure 3 shows the development of the flow regime in the homogeneous aquifer case and layered aquifer case (the same case as in **Figure 2**). Similar to the findings in Zhou et al. (2005), who used a smaller domain, flow recirculation regimes are developed in both cases at the bottom-left saltwater zone during pumping though they occur at different times. Comparison with additional simulation results (not shown here) shows that the enlarged model domain used here results in the later occurrence of flow recirculation. The flow

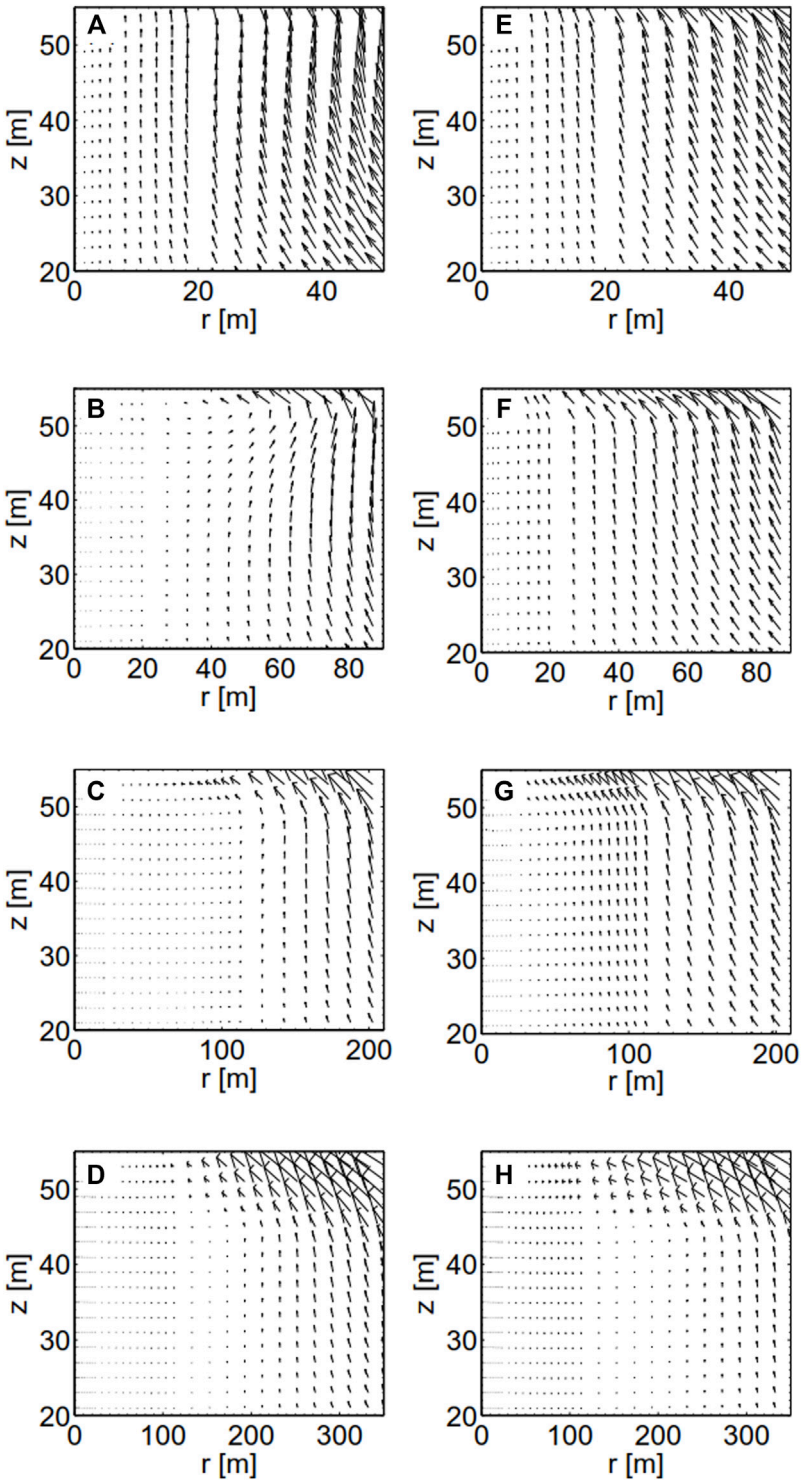

FIGURE 3 | The development of the flow regime after 1, 2, 5, and 20 years in the bottom-left saltwater zone in the homogeneous case **(A–D)** and layered case **(E–H)**.

recirculation beneath the pumping well prevents the high concentration of saltwater in the mixing zone from migrating upward to the well (i.e., up-coning). It is shown that the flow recirculation regime in the homogeneous aquifer case is developed earlier than that in the layered aquifer case. On the other hand, the area of the flow recirculation regime in both cases grows with the time.

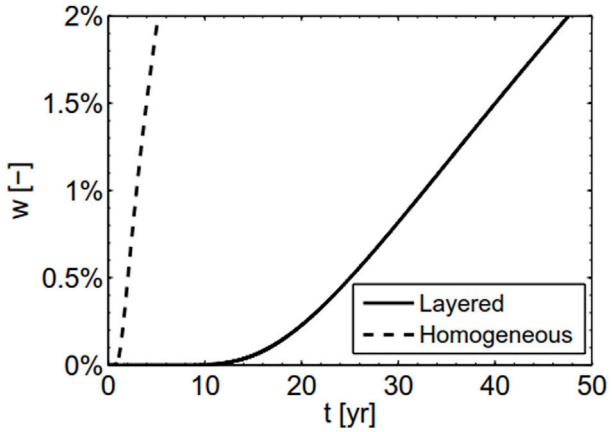

FIGURE 4 | The breakthrough curves of pumped water in the homogeneous (dashed line) and layered (solid line) cases. The layered case is the same case as in **Figure 2**.

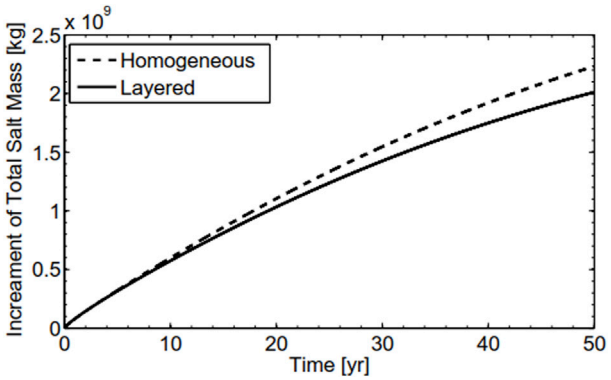

FIGURE 5 | The transient increment of the total mass within the model domain for the homogeneous (dashed line) and layered (solid line) cases. The layered case is the same case as in **Figure 2**.

3.2 Impact on Breakthrough Curves of Pumped Water

Figure 4 shows the breakthrough curves of pumped water for the homogeneous case and layered aquifer case (the same case as in **Figure 2**). As shown, the rate of saltwater up-coning in the homogenous case is significantly faster than that in the layered case. For the layered aquifer case, during about the first 10 yrs, there is no obvious response of the concentration of pumped water to well pumping, while only about 300 days are found for this phase in the homogeneous aquifer case. The values of T_H = 5.2 yrs and T_L = 47.6 yrs result in a value of E = 8.2 (**Eq. (2)**). The value of T_H in the current study is smaller than 5.6 yrs in Langevin (2008). With the larger model, saltwater is supplied by the aquifer near the well leading to lower pumping times. With the size of the domain used by Zhou et al. (2005) and Langevin (2008), the saltwater layer at the bottom of the aquifer is not enough to deep and salty water is thus replenished from the external lateral boundary on the right (**Figure 1**) leading to longer pumping times.

3.3 Impact on the Increment of the Total Salt Mass

Figure 5 shows the transient increment of the total salt mass within the model domain for the homogeneous case and layered aquifer case (the same case as in **Figure 2**). During approximately the initial 6 years, the two curves in the figure are almost overlapping, indicating that the increment of the total salt mass for the two cases are very close, despite of the significant difference of the average salt concentration of pumping water in the two cases (see **Figure 4**). In other words, the impact of the low-k layer on the increment of the total mass within the model domain during this initial stage is not significant. After that, the curve of the homogeneous aquifer case deviates from that of the layered aquifer case, representing that the increment of the total salt mass in the former case is obviously larger than that in the latter case.

3.4 Impact on the Salt Concentration Distribution

Figure 6 shows transient salt concentration distributions after 1, 3, 5.2, and 47.6 years of pumping in the homogeneous case and layered aquifer case (the same case as in **Figure 2**). The salt concentration distributions are characterized by five contour lines of the normalized mass fraction (w = 0.02, 0.2, 0.5, 0.8, and 0.98). One can find from these figures that the concentration contour line w = 0.98 is very close to the concentration contour line w = 0.8 and only slightly lower than its initial position even at large pumping times; this indicates that the thickness of the saltwater layer adopted is sufficient to replenish the up-coned saltwater. This would not occur with the domain used in Zhou et al. (2005) and Langevin (2008) (not shown here).

After 1 year of pumping, the salt concentration distribution below the pumping well in the homogeneous case is visibly affected, while negligible effects on the layered aquifer case are found; this shows that the low-k layer exerts a significant impact on preventing saltwater up-coning (**Figures 6A,E**), as expected. When the well has pumped for 3 years, the mixing zone (defined as the zone between the concentration contour lines of w = 0.02 and 0.98) in the homogeneous case is widened significantly and the concentration contour line of w = 0.02 enters the well (**Figure 6B**). However, the average concentration of pumped water has not reached the criterion of well shut-off. At the same moment, by contrast, the mixing zone is slightly widened and the salt concentration distribution starts to ascend in the layered aquifer case (**Figure 6F**).

When the well has pumped for about 5.2 years, in the homogeneous case, the mixing-zone thickness is remained similar and the four concentration contour lines of w = 0.02, 0.5, 0.8, and 0.98 are at similar locations, in comparison to those developed after 3 years of pumping (**Figure 6C**). However, the concentration contour line of w = 0.2 has been elevated significantly, causing the average concentration of pumped water to reach the well shut-off criterion (i.e., T_H = 5.2 years). At this time, in the layered aquifer case four concentration contour lines are still below the low-k layer, although

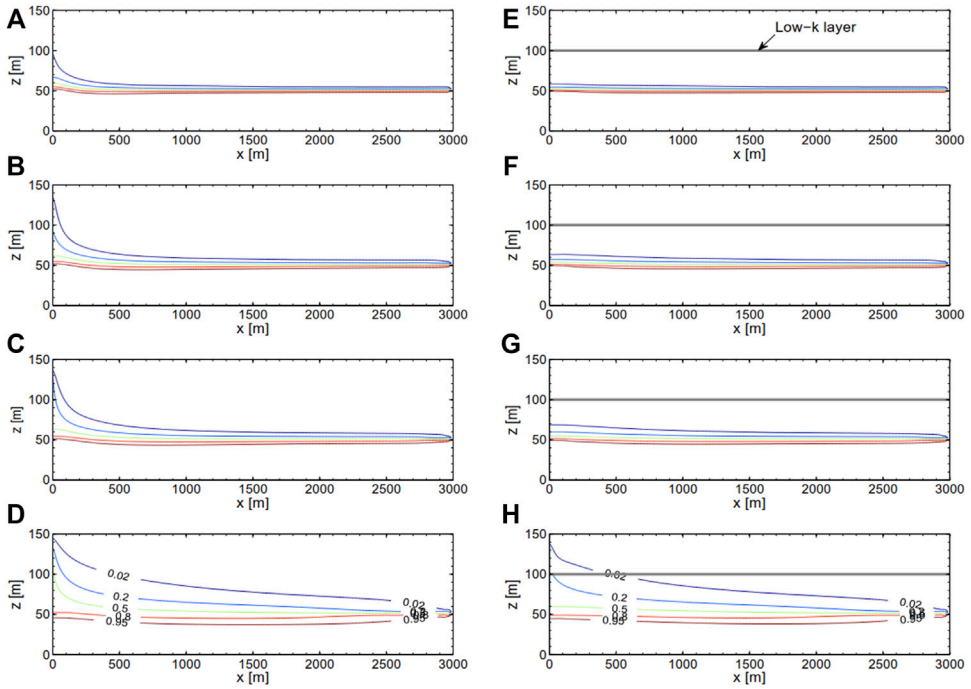

FIGURE 6 | Transient salt concentration distributions after 1, 3, 5.2, and 47.6 years of pumping in the homogeneous case **(A–D)** and layered case **(E–H)**. The layered case is the same case as in **Figure 2**.

the thickness of the mixing zone is increased noticeably (**Figure 6G**). This indicates that the presence of the low-*k* layer slows dramatically the saltwater up-coning rate, and results in a longer allowable pumping time. The concentration of pumped water in the layered aquifer case reaches the well shut-off criterion when the well has pumped for about T_L = 47.6 years (**Figure 6H**). If the well shut-off criterion does not apply to the homogeneous aquifer case, the up-coning of saltwater is extensive and the aquifer is highly contaminated by saltwater (**Figure 6D**). Interestingly, at large pumping times, the highest concentration contour lines (i.e., $w = 0.98$) could be below the initial condition in both cases, further widening the mixing zone.

3.5 Sensitivity Analysis

3.5.1 Sensitivity to *a* and β

Figure 7 shows that the sensitivity of E to β for a = 2, 4, and 8 m, with b = 50 m and c = 3,000 m. Sound linear relationships are found for different values of a, with R^2 all equal to or larger than 0.988. A larger thickness of the low-*k* layer results in a higher value of E, as expected. In other words, a thicker low-*k* layer would facilitate preventing saltwater up-coning and increasing the pumping efficiency (i.e., E). When the low-*k* layer is 8 m thick and its permeability is three orders of magnitude less than that of the homogeneous aquifer, the allowable pumping duration is about 22 times higher than that of the homogeneous aquifer case (i.e., E = 22).

3.5.2 Sensitivity to *b* and β

Figure 8 shows the sensitivity of E to β for b = 6, 20, and 50 m, and the sensitivity of E to b when β = 10, 100, 500, and 1,000, in which

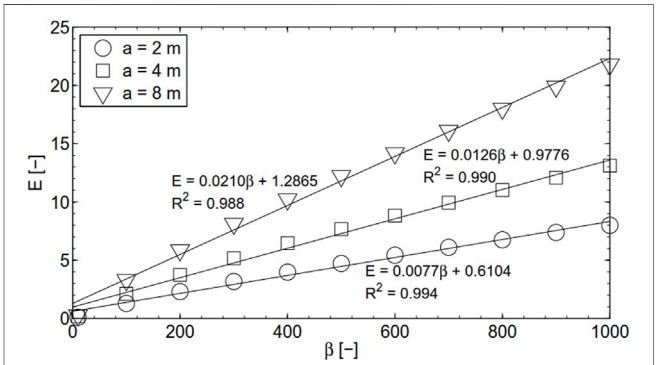

FIGURE 7 | Sensitivity of E to β for a = 2, 4, and 8 m, with b = 50 m and c = 3000 m.

a = 2 m and c = 3,000 m. Good linear relationships are constructed between E and β for three different values of b (**Figure 8A**). It is clearly shown that E is not a monotonic function of $b$and the largest E occurs when the low-k layer is below and near the bottom of the well. By contrast, when the low-*k* layer penetrates the well, E decreases significantly with decreasing b. On the other hand, when b > 30 m, E decreases gradually with increasing b. In particular, when $b \geq$ 100 m (i.e., the low-*k* layer is located in the initial mixing zone or saltwater zone), the effect of the low-*k* layer on saltwater up-coning could be neglected.

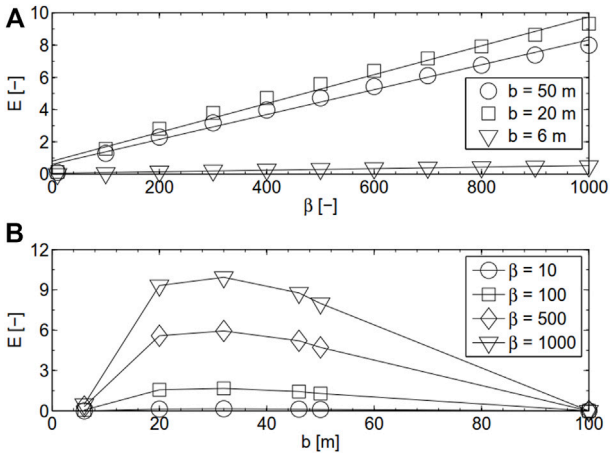

FIGURE 8 | (A) Sensitivity of E to β for b = 6, 20, and 50 m, and **(B)** sensitivity of E to b for β = 10, 100, 500, and 1,000.

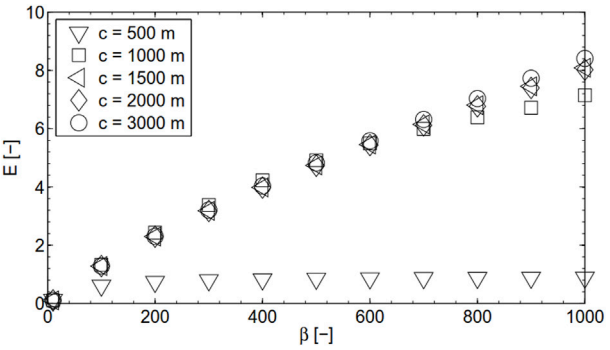

FIGURE 9 | Sensitivity of E to β for c varying between 500 and 3,000 m, in which a = 2 m and b = 50 m.

3.5.3 Sensitivity to c and β

Figure 9 shows the sensitivity of E to β for c varying between 500 and 3,000 m, with a = 2 m and b = 50 m. When c is equal to or larger than 1,500 m, as shown, the differences of E among different cases are considerably small, i.e., the length effect is negligible. For c = 1,000 m, the length effect is negligible for a large range of β, but remarkable for β larger than 700, resulting in a smaller E and the failure of the linear relationship between E and β. For c = 500 m, the length effect is significant and the impact of β on E is highly weakened.

3.5 Implications

To control the saltwater up-coning under pumping wells, skimming wells have been used in practice, as mentioned above. The results obtained in the current study indicate that a geology-based way could be used to improve pumping efficiency. When there is an aquitard in the subsurface, it is suggested that the partially penetrating well does not reach this natural barrier. Otherwise, the efficiency of the well could be significantly lowered. On the other hand, one could develop an artificial barrier below the well bottom to improve pumping efficiency. The technique of developing a plate-shaped stratum capable of offering significant hydraulic resistance is now available (Strack and Ausk, 2016). The obtained linear relationship between β and E together with the understanding of the effects of a, b, and c on E could assist in the design of an artificial barrier.

4 CONCLUSION

We used a numerical model to explore the impact of a horizontal low-k layer within a homogeneous aquifer on saltwater up-coning. Two main conclusions can be withdrawn as follows:

1) The low-k layer could alter significantly the flow patterns and thus reduce or impede saltwater up-coning. A sound linear relationship can be found between β and E, if the radius of the low-k layer is large enough. A thicker low-k layer leads to a larger E under otherwise the same conditions.
2) The maximum E occurs as the low-k layer is located below and near the well bottom. When the low-k layer penetrates the well, E decreases sharply with decreasing b. When the low-k layer is located below this critical location, by contrast, E decreases relatively gently with increasing b.

Despite that the model is highly simplified and neglects many other factors such as regional flow and unsteady pumping conditions, the results developed could provide significant implications for improving pumping efficiency under the threats of saltwater up-coning through natural and artificial barriers.

DATA AVAILABILITY STATEMENT

The original contributions presented in the study are included in the article/Supplementary Material, further inquiries can be directed to the corresponding author.

AUTHOR CONTRIBUTIONS

ZW and MT performed the numerical modelling and theortical analysis, and wrote the first draft of the manuscript. ED and CL contributed to conception.

FUNDING

CL acknowledges the National Key Research and Development Project (2021YFC3200500), National Natural Science Foundation of China (51879088), Fundamental Research Funds for the Central Universities (B200204002), and Natural Science Foundation of Jiangsu Province (BK20190023). Funds received for open access publication fees from Hohai University.

REFERENCES

Dagan, G., and Zeitoun, D. G. (1998). Free-surface Flow toward a Well and Interface Upconing in Stratified Aquifers of Random Conductivity. *Water Resour. Res.* 34 (11), 3191–3196. doi:10.1029/98wr02039

Diersch, H.-J., Prochnow, D., and Thiele, M. (1984). Finite-element Analysis of Dispersion-Affected Saltwater Upconing below a Pumping Well. *Appl. Math. Model.* 8, 305–312. doi:10.1016/0307-904x(84)90143-4

Hamza, K. I. (2006). "Numerical Analysis of Saltwater Upconing beneath a Pumping Well," in The 10th International Water Technology Conference (IWTC-2006), Alexandria, Egypt, March 23–25, 2006. (IWTC10).

Jakovovic, D., Post, V. E. A., Werner, A. D., Männicke, O., Hutson, J. L., and Simmons, C. T. (2012). Tracer Adsorption in Sand-Tank Experiments of Saltwater Up-Coning. *J. Hydrology* 414-415, 476–481. doi:10.1016/j.jhydrol.2011.11.024

Jakovovic, D., Werner, A. D., De Louw, P. G. B., Post, V. E. A., and Morgan, L. K. (2016). Saltwater Upconing Zone of Influence. *Adv. Water Resour.* 94, 75–86. doi:10.1016/j.advwatres.2016.05.003

Kim, K. Y., Seong, H., Kim, T., Park, K. H., Woo, N. C., Park, Y. S., et al. (2006). Tidal Effects on Variations of Fresh-Saltwater Interface and Groundwater Flow in a Multilayered Coastal Aquifer on a Volcanic Island (Jeju Island, Korea). *J. Hydrology* 330, 525–542. doi:10.1016/j.jhydrol.2006.04.022

Langevin, C. D. (2008). Modeling Axisymmetric Flow and Transport. *Groundwater* 46 (4), 579–590. doi:10.1111/j.1745-6584.2008.00445.x

Langevin, C. D., Shoemaker, W. B., and Guo, W. (2003). MODFLOW-2000, the U.S. Geological Survey Modular Ground-Water Model--Documentation of the SEAWAT-2000 Version with the Variable-Density Flow Process (VDF) and the Integrated MT3DMS Transport Process (IMT). U.S. Geological Survey Open-File Report 03-426, 43.

Liu, Y., Mao, X., Chen, J., and Barry, D. A. (2014). Influence of a Coarse Interlayer on Seawater Intrusion and Contaminant Migration in Coastal Aquifers. *Hydrol. Pross.* 28, 5162–5175. doi:10.1002/hyp.10002

Lu, C., Chen, Y., Zhang, C., and Luo, J. (2013). Steady-state Freshwater-Seawater Mixing Zone in Stratified Coastal Aquifers. *J. Hydrology* 505, 24–34. doi:10.1016/j.jhydrol.2013.09.017

Reilly, T. E., and Goodman, A. S. (1987). Analysis of Saltwater Upconing beneath a Pumping Well. *J. Hydrology* 89, 169–204. doi:10.1016/0022-1694(87)90179-x

Saeed, M. M., Bruen, M., and Asghar, M. N. (2002). A Review of Modelling Approaches to Simulate Saline-Upconing under Skimming Wells. *Nord. Hydrol.* 33, 165–188. doi:10.2166/nh.2002.0021

Schmorak, S., and Mercado, A. (1969). Upconing of Fresh Water - Sea Water Interface below Pumping Wells, Field Study. *Water Resour. Res.* 5 (6), 1290–1311.

Strack, O. D. L., and Ausk, B. K. (2015). A Formulation for Vertically Integrated Groundwater Flow in a Stratified Coastal Aquifer. *Water Resour. Res.* 51, 6756–6775. doi:10.1002/2015wr016887

Verruijt, A. (1970). *Theory of Groundwater Flow*. London: Macmillan.

Voss, C. I., and Souza, W. R. (1987). Variable Density Flow and Solute Transport Simulation of Regional Aquifers Containing a Narrow Freshwater-Saltwater Transition Zone. *Water Resour. Res.* 23 (10), 1851–1866. doi:10.1029/wr023i010p01851

Werner, A. D., Bakker, M., Post, V. E. A., Vandenbohede, A., Lu, C., Ataie-Ashtiani, B., et al. (2013). Seawater Intrusion Processes, Investigation and Management: Recent Advances and Future Challenges. *Adv. Water Resour.* 51, 3–26. doi:10.1016/j.advwatres.2012.03.004

Werner, A. D., Jakovovic, D., and Simmons, C. T. (2009). Experimental Observations of Saltwater Up-Coning. *J. Hydrology* 373, 230–241. doi:10.1016/j.jhydrol.2009.05.004

Zhou, Q., Bear, J., and Bensabat, J. (2005). Saltwater Upconing and Decay beneath a Well Pumping above an Interface Zone. *Transp. Porous Med.* 61 (3), 337–363. doi:10.1007/s11242-005-0261-4

Conflict of Interest: The authors declare that the research was conducted in the absence of any commercial or financial relationships that could be construed as a potential conflict of interest.

frontiers | Frontiers in Environmental Science

ORIGINAL RESEARCH
published: 12 July 2022
doi: 10.3389/fenvs.2022.917103

Sensitivity Analysis for Modeling of Cr(VI) Transfer From Soil to Surface Runoff

Xiujie Wu[1,2], *Zhongyuan Xu*[3]*, *Juxiu Tong*[4] *and Bill X. Hu*[5]

[1]College of Environment and Civil Engineering, Chengdu University of Technology, Chengdu, China, [2]State Key Laboratory of Geohazard Prevention and Geoenvironment Protection, Chengdu University of Technology, Chengdu, China, [3]Faculty of Geosciences and Environmental Engineering, Southwest Jiaotong University, Chengdu, China, [4]Key Laboratory of Groundwater Circulation and Evolution, China University of Geosciences (Beijing), Ministry of Education, Beijing, China, [5]School of Water Conservancy and Environment, University of Jinan, Jinan, China

Heavy metal contamination in soil has become a serious environmental problem in China, and chromium is one of the major threats to human health. In order to better understand the transfer pattern of heavy metal hexavalent chromium from polluted sites into surface water, the influencing factors that affect solute transfer from soil into the surface runoff with linear and nonlinear adsorption equations based on a two-layer incomplete mixing model were analyzed in this study. The Quasi-Newton method was used to optimize model parameters by fitting with the experimental laboratory data of chromium (Cr(VI)) in surface runoff. The local sensitivity analysis and the Morris global sensitivity analysis approaches were used to assess the parameter importance of rainfall intensity p, the thickness of the mixing layer h_{mix}, incomplete mixing parameter α and γ, the soil adsorption parameters, and the initial soil water content θ_0. The study results showed that the optimized nonlinear models were better consistent with the experimental results than the linear adsorption equation model. The results of global sensitivity indicated that rainfall intensity p was the main factor influencing Cr(VI) transport from the soil into surface runoff. The h_{mix} and the α in the two-layer model were vital parameters that influenced such transport processes. Moreover, the soil adsorption properties and the θ_0 had the lowest effects on runoff Cr(VI) loss. The results indicate that for controlling pollution migration in surface runoff, it is essential to focus on the analysis of precipitation conditions and soil properties that control the thickness of the mixing layer and the degree of mixing.

Keywords: surface runoff, sensitive analysis, Cr(VI), adsorption, incomplete mixing model

OPEN ACCESS

Edited by:
Haiyan Liu,
East China University of Technology, China

Reviewed by:
Chenglong Yu,
China University of Geosciences Wuhan, China
Xiaolong Geng,
National Oceanographic and Atmospheric Administration, United States

***Correspondence:**
Zhongyuan Xu
zyxufsu@gmail.com

Specialty section:
This article was submitted to Freshwater Science, a section of the journal Frontiers in Environmental Science

Received: *10 April 2022*
Accepted: *09 May 2022*
Published: *12 July 2022*

Citation:
Wu X, Xu Z, Tong J and Hu BX (2022) Sensitivity Analysis for Modeling of Cr(VI) Transfer From Soil to Surface Runoff. Front. Environ. Sci. 10:917103. doi: 10.3389/fenvs.2022.917103

INTRODUCTION

Due to the rapid development of industrialization and urbanization, heavy metal contamination in soil has become an essential aspect of global environmental pollution (Yang et al., 2018). Heavy metals (e.g., Cd, Cr, and Hg) in water bodies that originate either from contaminated soil or from the soil with natural heavy metal content may pose a threat to human health (Chen et al., 2021). Among them, hexavalent chromium (Cr^{6+}) has received much attention due to its easy movement with stable

Abbreviations: LSA, local sensitivity analysis; GSA, global sensitivity analysis.

and soluble properties (Sarkar et al., 2010) and its extensive sources from human activities, such as printing and dyeing, iron and steel manufacturing, leather tanning, chemical production, and fertilizers (Thangam et al., 2018). As a non-point pollution source, high content of chemicals in the soil migrate to the surface water and groundwater through the rainfall-runoff process, which is a crucial process of heavy metal pollution (Xiao et al., 2022). Therefore, it is of great significance to study the soil Cr(VI) loss and transfer into the rainfall-induced surface runoff.

The variations of Cr(VI) content in groundwater are usually characterized by convection, dispersion, adsorption, and reduction processes (Gorny et al., 2016). Various numerical methods depend on the lumped mixing layer approach (Donigian et al., 1977) and the diffusion approach (Wallach and van Genuchten 1990), and these approaches have been developed to analyze and illustrate experimental results. The mixing layer approach has gained more popularity than the diffusion approach by the ability to account for the influence of raindrops in the rainfall process (Li et al., 2017). It depends on the assumption that soil water mixes with surface runoff instantaneously and rainwater completely or incompletely in a thin layer below the soil surface without any contribution from the soil part under this mixing layer. Therefore, the thickness of the mixing layer determines the total amount of solutes transfer into the surface runoff (Ahuja and Lehman 1983; Tian et al., 2011a). Also, previous studies have found that the number of solutes in the soil entering surface runoff water when the subsurface drainage decreases exponentially with depth (Ahuja et al., 1981). However, the complete mixing method assumes that the soil water, surface water, and solute concentrations in rainwater within the mixed layer are the same during precipitation, which differs from the actual situation under subsurface drainage conditions. Hence, the complete mixing approach has been modified, and an incomplete mixing approach that considers the infiltration process has been developed (Wang et al., 1998). Both the complete mixing cell and incomplete uptake models were used to evaluate the transfer of soil-applied pesticide into the runoff in the field test (Young and Fry 2019). The result showed that the incomplete model provides more intuitive and reasonable results than the complete mixing model. Furthermore, it reported that the complete mixing cell model, as well as the refined equivalent model, facilitated the use of simplified parameters when describing the runoff process of solute transport to loess lands, while the incomplete mixed model was more suitable for practical situations (Yang et al., 2016). Tong et al. (2010) developed a two-layer incomplete mixing model to analyze the chemical components transported from soil to surface runoff water, which considers the surface runoff-ponding layer, soil mixing layer, and the lower layer below is regarded as the whole study system. This model is based on the assumption that the surface of the soil is (nearly) horizontal and the thickness of the mixing layer is considered constant, without considering lateral or return flows in the soil. The results of chemical components transfer from soil to the runoff in the unsaturated soil experiments were well explained by the simple two-layer incomplete mixing model, which verified model is reliable and reasonable (Wu et al., 2015; Tong et al., 2010).

Adsorption is an essential part of interpreting the transfer process, especially for heavy metal solutes, and solute transport models are usually combined with adsorption equations to analyze solute transport patterns. Laboratory test data was used to examine the modeling works with linear isotherm adsorption equation (Henry equation) by Wang (2012) and nonlinear isotherm adsorption equation (Langmuir and Temkin equation) by Wu et al. (2014, 2015). In addition, the selection impact of different adsorption models on the Cr(VI) loss simulation has been evaluated, and it suggested the Langmuir model is preferable (Xia et al., 2018). The model under each adsorption assumption is accompanied by a set of uncertain/unknown parameters. It is vital for model prediction accuracy to verify these uncertain parameters. Usually, we use the best-fit method to determine the parameters. Meanwhile, it is efficient to order the parameters' priority in the prediction of solute concentration in the surface runoff before each parameter calibration (Song et al., 2015).

The sensitivity analysis (SA) aims to give intuitive and quantitative importance results for a specific parameter or a group of parameters that affect model performance (Saltelli et al., 2004), and it plays an important role in the model verification, parameterization, optimization, and uncertainty quantification (Song et al., 2015). Fundamental analysis of the parameter sensitivity in a model indicates how significant the simulation result relies on a single parameter, which is local sensitivity analysis (LSA). However, the parameters may relate to each other, which means one changing parameter may drive other parameters to change. Therefore, the result of local sensitivity is unreasonable. At this point, the global sensitivity analysis (GSA) is vital for investigating the effects of parameters systematically and the uncertainty of simulation results, thereby enhancing the interpretation of the system (Saltelli and Annoni 2010). A variety of GSA techniques have been applied to hydrogeological models, such as the screening method (Saltelli et al., 2008), regression analysis (Tiscareno-Lopez et al., 1993), meta-modeling method (Petropoulos et al., 2009), variance-based method (Xia et al., 2018), etc. Based on sensitivity analysis of fitting parameters in the two-layer incomplete mixing model (Tong et al., 2010) with different adsorption equations (such as α, γ, h_{mix}, k_d, K, S_{max}, and N). It suggested that the most important influencing factor is h_{mix}, and the sensitivity of adsorption parameters in the model gradually increases with time (Wu et al., 2015; Xia et al., 2018).

Many researchers have developed treatment processes to remediate Cr(VI) (Bansal et al., 2009; Lu et al., 2021). In contrast, few researchers devoted to the adsorptive solute of Cr(VI) transfer from soil into the surface runoff, especially, quantitative comparative analysis has not been carried out on the important influencing of multiple environmental factors, which is the main study in this article. As multi-factor analysis requires a large number of experiments, considering the toxicological damage of Cr(VI) to experimenters, this study was limited to the test results under a single environmental condition and relied on model simulation for analysis. In

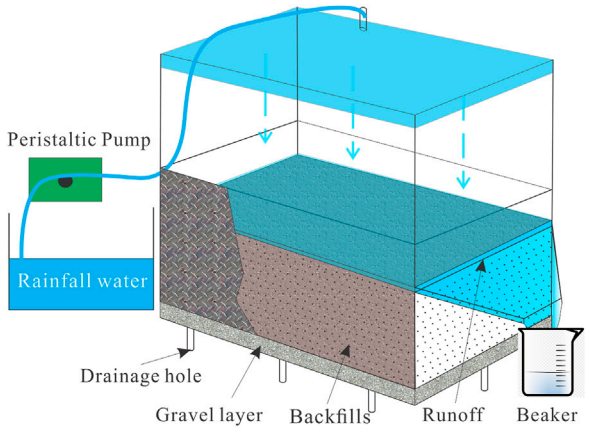

FIGURE 1 | Schematic of the experimental apparatus (Tong et al., 2010).

particular, some factors are interactive with each other, such as rainfall intensity and the thickness of the mixing layer (Tian et al., 2011a). Therefore, a comprehensive sensitivity analysis of various factors needs to be carried out. In this study, the model involves two sets of parameters, and in order to quantitatively examine the sensitivity of different models to their parameters, a series of sensitivity analyses were conducted. Among the GSA methods, the screening method is identifying the significance of input variables contributing to the output uncertainty in high-dimensionality models than exactly quantifying sensitivity (Saltelli et al., 2008), which reduces amounts of computation greatly. The Morris screening GSA method is widely used to solve the multi-parameter analysis due to its higher interpretability and practicability (Shin et al., 2013; Tian 2013). For analyzing the process of chemical transfer, the Henry and Langmuir adsorption equation was used in the modeling. The ODE45 method was applied to do the optimization of the parameters by using MATLAB. The LSA and Morris GSA were performed to evaluate the contribution and uncertainty of parameters to the variations in soil Cr(VI) released to surface runoff. These two sensitivity analysis methods performed well in the contaminant prediction and water science (Herman et al., 2013; Xu et al., 2018, 2019). In this study, the sensitivity of two adsorption models was compared to further understand the adsorption effect on heavy metal solute loss in the rainfall-runoff process.

METHODS

Laboratory Experiment of Cr(VI) Loss

The experiment was implemented with a sandbox of 100 cm in length, 30 cm in width, and 40 cm in height in **Figure 1** (Tong et al., 2010). A sand-gravel layer was laid at the bottom as a filter layer, and drainage holes were set in the middle of the bottom. The soil thickness is 23cm, and the maximum depth of ponding water h_p (t_r) is 1.1 cm. The chemical content of the water is nearly zero since distilled water was used in the rainfall. The drainage outlet was put 23 cm higher than the box bottom. The soil is collected from the background area, which can be regarded as soil without chromium. The initial soil concentration was set to 300 mg/kg, and it was ground, 2 mm screened dried silty sand. Then the calculated proportions of soil and potassium dichromate solution were well mixed. After standing for about 30 min, the sandbox was filled in layers. Surface runoff was collected approximately every 2 min, and the solute concentration of the water samples was determined using an Atomic Absorption Spectrometer (ContrAA-700, Analytic Jena AG). This experiment was conducted in 2012 and was duplicated twice in 2013. All of the experimental physical parameters are listed in **Table 1**.

Mathematical Model

A brief description of the prediction model and laboratory experiments of solid solute transfer into the surface runoff is given in this paper, and more details were described in Tong et al. (2010). The two-layer system model (**Figure 2**) was applied to investigate the Cr(VI) transfer from soil into surface runoff under the Henry and Langmuir adsorption equations, where soil particles were ignored in the surface runoff process. There are two sections in the model. The upper section comprises the mixing layer and ponding-runoff layer, and the lower layer is the soil below the mixing layer. The equation of solute mass in the saturated mixing layer is

$$\boldsymbol{M_w = C_w[\alpha(h_w - h_{mix}\cdot\theta_s) + h_{mix}\cdot\theta_s]}, \quad (1)$$

where M_w is the chemical mass dissolved in the water per unit area [μg/cm^2]; h_w is the depth of net water in the mixing layer and ponding-runoff layer [cm]; θ_s is saturated volumetric water content [cm^3/cm^3]; h_{mix} is the thickness of the mixing layer, where the solute concentration is evenly distributed [cm]; C_w is the concentration of the mixing layer and ponding-runoff layer [μg/cm^3] = [μg/mL]; α ($0<\alpha \leq 1$) is the incomplete mixing parameter of solute between the soil water in the mixing layer and the ponding-runoff water.

The soluble chemical mass flows away via ponding-runoff and infiltration water. Hence, the following equation based on mass conservation is obtained:

$$\boldsymbol{\frac{dM_w(t)}{dt} = -\gamma\cdot i\cdot C_w(t) - \alpha\cdot q\cdot C_w(t)}, \quad (2)$$

where γ ($0<\gamma \leq 1$) is the incomplete mixing parameter of the solute between infiltration water and the soil water in the mixing layer; q is the flow rate per unit area of surface runoff [cm/min]; i is the infiltration flux [cm/min].

The increasing process of ponding water on the soil surface before runoff was considered, and the rainfall-induced runoff event can be divided into four stages, as shown in **Figure 3**.

Period I: from the beginning of rainfall to the soil reaches saturation in the mixing layer and ponding-runoff layer, *0*~*t*sa; period II: from saturation state in mixing layer and ponding-runoff layer to surface ponding occurred, $t_{sa} \sim t_p$; period III: from ponding to surface runoff occurred, tp ~ t$_r$1; period IV: from surface runoff start to the end of rainfall; according to the

TABLE 1 | Experimental and simulation parameters used in this test.

Experiment	Initial volumetric water content θ_0	Saturated volumetric water content Ts	Rainfall intensity p/ [cm/min]	Initiation time of ponding t_p/min
1	0.35	0.49	0.0925	10
2	0.30	0.49	0.0978	25
3	0.30	0.49	0.0963	2

Initiation time of runoff t_r/min	Initiation time of steady runoff t_s/min	Initial solute concentration in soil S0/ [mg/kg]	Bulk density ρ/[g/cm3]
32	34.5	300	1.35
52	55	300	1.35
23	25.5	300	1.35

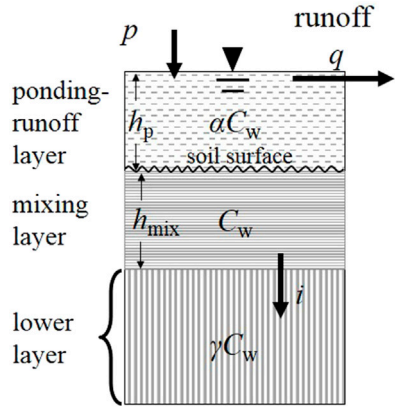

FIGURE 2 | Simple two-layer incomplete mixing model (Non-actual size) (Tong et al., 2010).

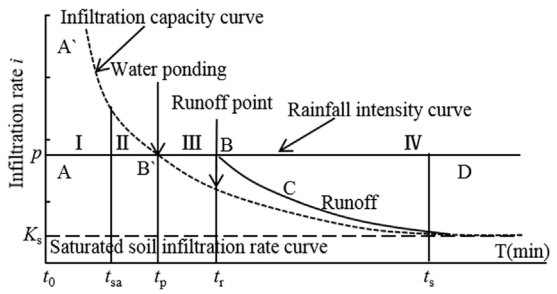

FIGURE 3 | The curve of soil infiltration rate changes with time during a rainfall event (Mein and Larson 1973).

different characteristics of soil infiltration rate, this period can be divided into two sub-periods:

o Sub-period I: soil infiltration linearly changes with time, t_{r1}~t_{r2}

o Sub-period II: soil infiltration rate reaches a stable state, t_{r2}~t_s

The solution variations in the experiment are divided into several different stages. Thus different equations were used for these stages in the mixing layer and ponding-runoff layer. α and γ are regarded as constants in the process of Cr(VI) loss from the soil into surface runoff and infiltration.

In this process, adsorption is a significant factor influencing the Cr(VI) loss. Two kinds of adsorption equations were used to describe this relationship.

Langmuir adsorption equation (Langmuir 1918):

$$\frac{C_w}{S} = \frac{1}{KS_{max}} + \frac{C_w}{S_{max}}, \tag{3}$$

where S is the capacity of equilibrium adsorption [mg/Kg], S_{max} is the single molecular layer adsorption saturated adsorption capacity [mg/Kg], K is a constant that describes the reaction energy, it links with the adsorption-desorption equilibrium constant for a reversible reaction [L/mg].

Henry Adsorption Equation

$$s = k_d C_w, \tag{4}$$

where k_d is the linear absorption coefficient [L/kg].

The Langmuir adsorption equation in the mixing model:

$$M_w = C_w[\alpha(h_w - h_{mix} \cdot \theta_s) + h_{mix} \cdot \theta_s] + h_{mix} \cdot \rho_s \cdot \frac{C_w}{BC_w + C}, \tag{5}$$

where $B = \frac{1}{S_{max} \frac{1}{K \cdot S_{max}}}$.

The Henry adsorption equation in the mixing model:

$$M_w = C_w[\alpha(h_w - h_{mix} \cdot \theta_s) + h_{mix} \cdot (\theta_s + k_d \rho_s)]. \tag{6}$$

The ODE equations used in the numerical calculation are shown in **Supplementary Text S1**.

Optimization

The experimental data were applied to calibrate the mathematical model with the Langmuir and Henry adsorption equations. Some parameters in the equations above were not obtained by the experiment test directly. The Quasi-Newton optimization method was used to calculate parameters of γ, α, h_{mix}, k_d in the Henry equation and γ, α, h_{mix}, B, C in the Langmuir equation by fitting experimental results. The application of the Quasi-Newton method was shown in **Supplementary Text S2**.

Sensitivity Analysis

Local Sensitivity Analysis

In this work, the forward difference approximation was used to calculate the sensitivity of ith observation concerning jth parameter (Hill and Tiedeman 2007):

$$\left(\frac{\partial y_i^{'}}{\partial b_j}\right)\Big|_{b} \approx \frac{y_i^{'}(\boldsymbol{b}+\boldsymbol{\Delta b}) - y_i^{'}(\boldsymbol{b})}{\Delta b_j}, \tag{7}$$

where $y_i^{'}$ is the calculated result of ith observation; b_j is the jth estimated parameter; b is the vector of parameter values; Δb is a vector of zero except that the jth parameter is Δb_j, Δb_j should be 1–5% of b_j (Saltelli et al., 2000).

Different parameters had different units, and for adequate comparing sensitivity of different parameters, approximations were converted to a dimensionless scaled form (Hill 1992; Hill. 1998):

$$dss_{ij} = \left(\frac{\partial y_i^{'}}{\partial b_j}\right)\Big|_{b} |b_j| \omega_{ii}^{1/2}, \tag{8}$$

where dss_{ij} is dimensionless scaled sensitivity of ith observation with respect to jth parameter; ω_{ii} is the weight in the ith simulation.

The total effect of different observations for one parameter is reflected in composite scaled sensitivity. It was calculated by the following equation (Hill 1992; Hill 1998):

$$css_j = \sum_{i=1}^{N}\left(\frac{dss_{ij}^2}{N}\right)^{1/2}, \tag{9}$$

where css_j is composite scaled sensitivity (CSS) of jth parameter; N is the number of observations.

Global Sensitivity Analysis With the Morris Method

In the modeling, variations of some parameters may influence each other on the local estimation. GSA thoroughly considers the significance of one parameter under interactions with other parameters. In this study, the Morris method (Morris 1991; Saltelli et al., 2004) was implemented in calculating the global sensitivities of parameters. The Morris method is a one-at-a-time experiment. It is based on the element effect, which is the effect of changing one parameter at a time. The trajectory sampling was used in the Morris method to compute m parameters (m+1) simulations were calculated with a random start sampling point in one trajectory, the input space of each parameter is discretized into n levels, and the whole calculation contains r trajectories. The element effect of changing ith parameter in jth trajectory is

$$d_{ij} = \frac{y(x_j + e_i\Delta) - y(x_j)}{\Delta}, \tag{10}$$

where $x_j = (x_1, x_2, ..., x_m)$ of jth trajectory; $\Delta = 1/(n-1)$; e_i is a vector of zeros but with a unit at its ith component.

Once computations were completed, the average (μ) of one parameter in r trajectories reflects an estimation of the total-order effect, and the standard deviation (σ) described the variability of parameter space and the extent of parameter interactions (Herman et al., 2013).

$$\mu_i = \frac{1}{r}\sum_{j=1}^{r} d_{ij}, \tag{11}$$

$$\sigma_i = \sqrt{\frac{1}{r}\sum_{j=1}^{r}(d_{ij} - u_i)^2}. \tag{12}$$

The specified value in local analysis and estimation ranges in the global analysis of seven parameters are listed in **Table 2**.

RESULTS AND DISCUSSION

Experiment and Optimization Results

There are three categories of parameters in the optimization, including the two incomplete mixing parameters α and γ, the mixed layer thickness h_{mix} related to precipitation conditions (Ahuja et al., 1981), and the parameters of adsorption equations. Five and four parameters are involved in the modeling with corresponding Langmuir and Henry adsorption equations. The results of Quasi-Newton optimization are expressed in **Figure 4**, and the observed data (Experiment 1 is cited by Wang 2012; and Experiment 3 is cited by Wu et al., 2014) are presented as black squares. The simulations fit the experimental results quite well under both adsorption equations. The R-square of Langmuir adsorption and Henry adsorption ranged from 0.84 to 0.99. The results of the three experiments show that the initial concentration of Cr(VI) in the surface runoff was different between the three experiments, from 1.7 mg/L to 20 mg/L, and they reduced with time. In the early stage of the experiments, the concentration of soil heavy metal solutes was high, and the main factors affecting the solute concentration in runoff water were dissolution, mixing, and dilution. As the precipitation time extended, the density of surface soil pollutants decreased, and the concentration of solutes entering the surface runoff water also decreased rapidly. Surface pollutants precipitated from the soil, the influence of adsorption is strengthened, and deep pollutants contribute to the solute concentration in runoff water through convection, diffusion, and other effects.

The optimization results for all parameters are within a reasonable range which is from previous studies (**Table 2**). The γ is much larger than the α, which is consistent with the observations, and the solute concentration in surface runoff water (0.0 mg/L~1.7 mg/L) is much smaller than that in subsurface drainage water (139.3 mg/L~234.3 mg/L) in the experiment. Therefore, controlling subsurface drainage would be a practical approach to limit Cr(VI) migration

TABLE 2 | The value ranges for local and global sensitivity analysis of all parameters. L and H represent Langmuir and Henry. EX1, EX1, and EX3 are short for the three experiments, 1, 2, and 3.

Parameter	Specified value			Range	Unit	References
	EX1 1	EX 2	EX3			
h_{mix}_L	0.37	0.76	0.48	0–1	Cm	Ahuja et al. (1981) Ahuja and Lehman, (1983) Wallach et al. (1988) Havis et al. (1992) Nofziger and Wu (2005) Walter et al. (2007) Shi et al. (2011) Tian et al. (2011a)
h_{mix}_H	0.40	0.78	0.64			
γ_L	0.6	0.41	0.67	0–1	-	Tong et al. (2010)
γ_H	0.55	0.24	0.35			
α_L	0.14	0.34	0.32	0–1	-	
α_H	0.08	0.02	0.02			
S_{max}	57.1	68.73	63.21	22.9–200	mg/kg	Khan et al. (2010) Fernández-Pazos et al. (2013) Tewari and Vivekanand (2013)
K	0.02	0.19	0.07	0.00078–0.428	L/mg	
k_d	0.2	0.51	0.2	0–2.5	L/kg	Fernández-Pazos et al. (2013)

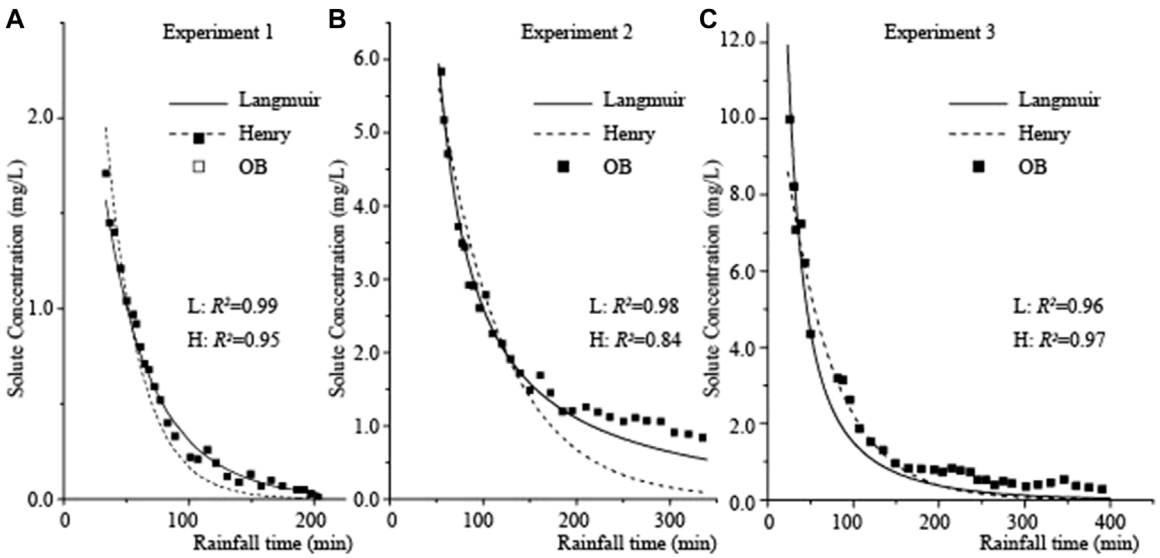

FIGURE 4 | Comparison of experimental data and optimized models within Langmuir and Henry equation. Note: OB was for the Observation data.

from contaminated soils. In addition, this phenomenon is the same as in the case of fertilizer components loss in surface runoff from the soil with sandbox experiments (Tong et al., 2010). However, according to experiment and simulation results under the free subsurface drainage condition, the h_{mix} is one magnitude degree lower than the h_{mix} in this study (Tian et al., 2011a). Meanwhile, the soil was designed to be initially saturated without ponding depth, causing a much shorter runoff starting time than unsaturated soil (Tian et al., 2011b). Therefore, the deeper mixing layer is reasonable, considering the longer interaction time between soil and runoff water. The h_{mix} is close to the result of the experiment (0.356 cm), in which the water table was controlled to be 0 cm below the soil surface during the rainfall process (Tian et al., 2011b).

Local Sensitivity

For the LSA, the CSS of Cr(VI) concentration in surface runoff was calculated under each parameter's Langmuir and Henry adsorption equations. Moreover, the value ranges of the parameters are listed in **Table 2**. In general, a larger CSS value represents more significance of such parameter to the simulated Cr(VI) concentration in surface runoff. The results of the LSA are shown in **Figure 5**.

As shown in **Figures 5A,B**, the model is more sensitive to the parameters in the early stage, and the sensitivity gradually decreases over time. Based on the results of the local sensitivity analysis of the three experimental results, it can be seen that the overall nonlinear adsorption model is more sensitive to parameters the mixing layer depth h_{mix}, the rainfall intense p and incomplete mixing parameter γ, and the remaining parameters including both parameters in the Langmuir adsorption equation are less sensitive (**Figure 5C**). However, the model with a linear adsorption equation is sensitive to all of the parameters except the initial water content (**Figure 5D**). The results illustrate that Cr(VI) transport and releasing are more influenced by the thickness of the mixing layer and ponding-runoff layer. These LSA results of the three experiments are not

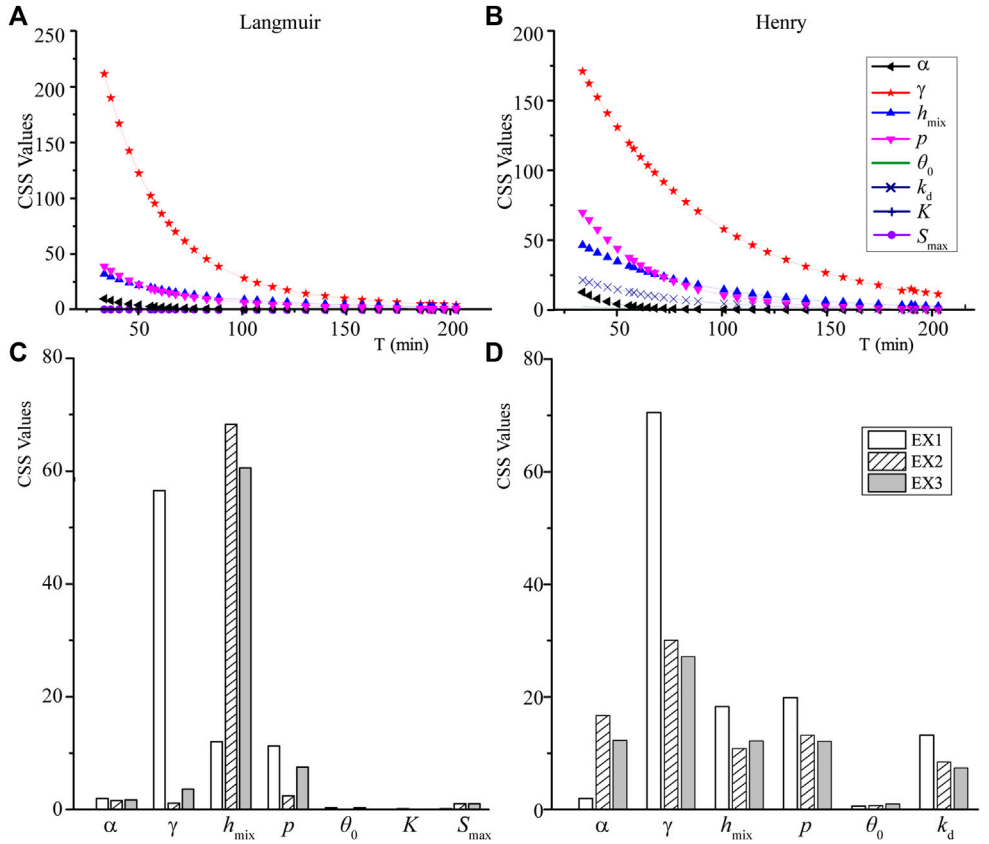

FIGURE 5 | CSS values of Langmuir **(A)** and Henry **(B)** models along time during the rainfall-runoff process; **(C)** and **(D)** represent the mean values of CSS at different times for each parameter in the model with Langmuir and Henry equations, respectively.

showing a similar trend but are not precisely consistent with each other, which indicates that the result of the LSA method varies with the calculated parameters and/or the experimental conditions.

Global Sensitivity

Unlike LSA, GSA considers the existence of correlations between parameters and gives a more comprehensive perspective of the sensitivity of different parameters. All parameters in LSA were examined in the GSA. The Morris trajectory method was applied for less computational cost than using the variance-based method. A simulation with level $n = 4$ and path $r = 10$ is good enough for most cases (Saltelli et al., 2004). Therefore, the Morris trajectory high-density sampling methods, where level $n = 5$ and path $r = 10$ in this study, were used to obtain more reliable results, and the results were plotted in **Figure 6**.

The model's sensitivity to different parameters over time shows that the trend resembled the LSA, where the model is more sensitive to parameter changes in the early stage and gradually decreases with time (**Figures 6** (a) and (b)). From the absolute mean values of element effect for each parameter abs(μ), the simulated results show that Cr(VI) concentration in surface runoff water is most sensitive to parameter p, followed by h_{mix}, α, γ, adsorption parameters, and θ_0, which are significantly different from the results of the LSA. This means that the model is most sensitive to p considering the interaction of the parameters, with which h_{mix} was also an essential parameter for the model. Overall, the model is fairly sensitive to the two incomplete parameters of α and γ in the simple two-layer model. The α has a more substantial effect on Cr(VI) loss in the surface runoff than γ, which is also different from the results of the LSA. Both from the LSA and GSA results, the parameters in the adsorption equations as well as θ_0 have relatively small effects on the results of Cr(VI) loss in surface runoff. The impact on the simulation results of adsorption parameters in the Henry linear equation is relatively more significant than that of the parameters in the Langmuir nonlinear adsorption equation. This is most likely due to the nonlinear adsorption equation having a more complex form and one more parameter, which decentralize the calculation, and when the parameters are compared individually, neither one has a significant effect on the simulation results.

The results of the LSA are significantly different from the results of the GSA. According to the GSA method, it is known that the result includes two parameters, one is the mean (μ) value of elemental effects, and the other is the standard

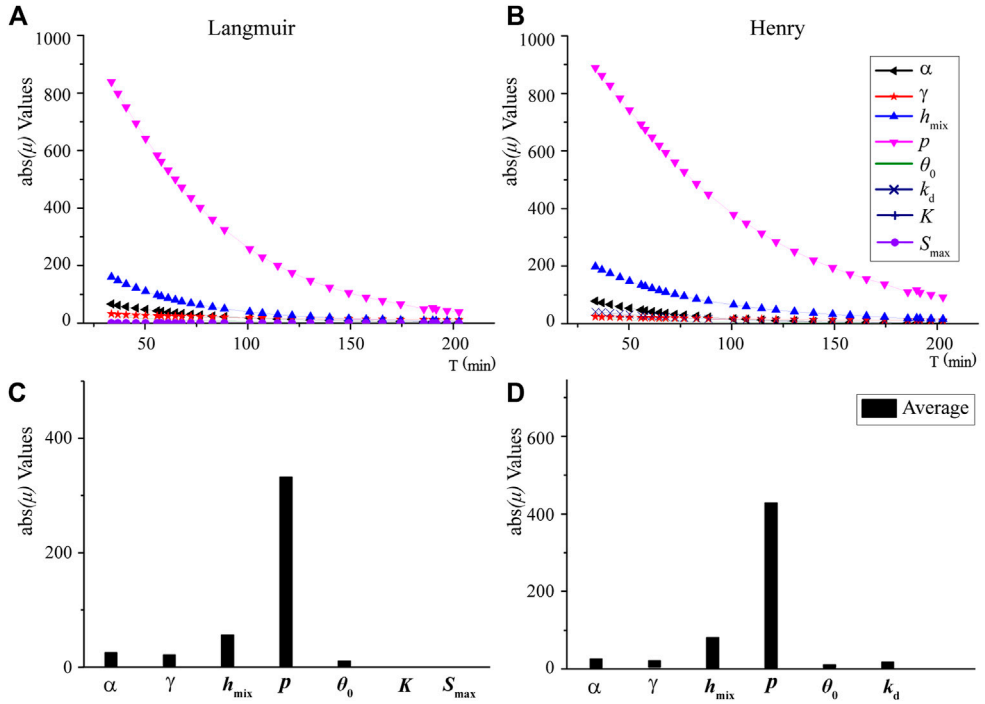

FIGURE 6 | (A) and **(B)** represent that the absolute mean values of the element effect of each parameter abs(μ) are changing with time in the model with Langmuir and Henry equations; **(C)** and **(D)** is the average of elemental effects at different times for each parameter.

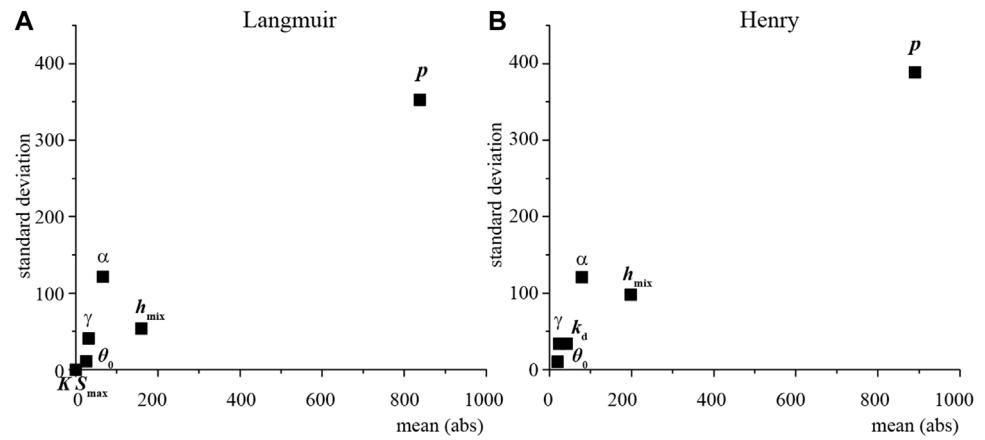

FIGURE 7 | The absolute mean versus standard deviation of element effect for each parameter at the runoff start time.

deviation (σ) value of elemental effects. The value μ represents a general estimate of the sensitivity of a given input, and σ is a proxy for the input interaction and/or the non-linearity amount. The higher the value of σ represents less reliability of the sensitivity in the LSA (van Engelen et al., 2021). The absolute mean of the element effects and the standard deviation values are combined to analyze the model's sensitivity to the parameters (**Figure 7**).

As shown in **Figure 7**, p is the most critical factor controlling Cr(VI) loss in surface runoff. Meanwhile, both h_{mix} and α are essential to the model, but γ is less important. Under the linear adsorption equation condition, the adsorption coefficient k_d is more crucial to the model, while under the nonlinear adsorption assumption, all the parameters associated with the adsorption equation have little effect on the simulation results. The θ_0 has a minor effect on both models. According to experimental results the θ_0 is a vital parameter to the solutes concentrations in the surface runoff. It has been shown that the higher θ_0 is the greater runoff volume per unit time and higher solute concentration in the runoff, but less sediment mass in the runoff (Dong et al.,

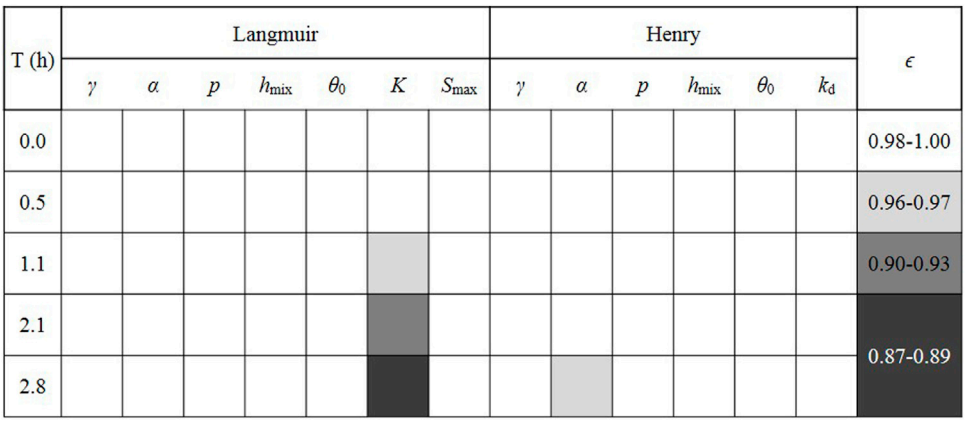

FIGURE 8 | The ϵ values of each parameter in the simulation during the rainfall process.

2018). The difference between the results of this study and the previous study is that the θ_0 was used only for the calculation of the ponding time but is less relevant to the subsequent calculation of the solute concentration in the surface runoff. The parameter h_{mix} gradually increases with p (Tian et al., 2011a), which enhances the impact of rainfall variability on the model. The γ is vital to the simulation result due to the high σ value resulting from the interaction of the strong parameters. Despite the parameter p, the GSA results are consistent with the previous study with the variance-based GSA (Xia et al., 2018). Therefore, it shows that the low computational effort of the Morris trajectory method is able to give reasonable results for the model in this study.

The mean of the absolute value of elementary effects ($\mu*$) is calculated to show non-monotonous effects (Campolongo et al., 2007). The two elementary effects parameters allow us to estimate a measure of non-monotonicity, ϵ, for each parameter:

$$\varepsilon = \frac{abs(\mu)}{\mu^*}. \tag{14}$$

An ϵ approaching one represents the elementary effect of the input is quite monotonous. The sign of the model's response to changes in the input is always equal, regardless of the other input configurations. In contrast, close to zero means it is highly non-monotonous. As shown in **Figure 8**, only the nonlinear adsorptive parameter K variation showed a relatively high non-monotonicity for the simulation results with different model parameters. The rest of the parameter effects were monotonic. However, the sensitivity of the model to K was deficient in both the LSA and GSA and had little effect on the simulated results of Cr(VI) concentration in surface runoff.

CONCLUSION

In order to better understand the Cr^{6+} transfer from contaminated fields under precipitation with subsurface drainage conditions, the main influencing factors of Cr(VI) loss in surface runoff under the two adsorption assumptions were explored on the basis of a previous experimental study. The numerical model was used in the calculation to solve the complex equations. The optimization with the Quasi-Newton method was applied to determine several vital parameters, such as γ, α, h_{mix}, k_d, K, and S_{max}. Then, the LSA and GSA were carried out on the significant parameters, such as p, γ, α, h_{mix}, θ_0, k_d, K, and S_{max}, in the model to investigate the effect of different parameters on the simulated Cr(VI) concentration in surface runoff. The main conclusions were obtained as follows:

- Quasi-Newton optimization performs very well in this study, and the optimization results well fit with the experimental data. In addition, the parameters determined from optimization were reasonable.
- The sensitivity of the model to all parameters gradually decreased as precipitation proceeded.
- The local sensitivity of the model to the parameters in descending order is γ, p, h_{mix}, and α. The sensitivity of the model to the parameters in the adsorption equations and the θ_0 was inferior.
- The GSA of the models shows that the models are also more sensitive to p, h_{mix}, and α, while not γ, θ_0, and parameters related to the adsorption equation.

In summary, this study supplemented the influence of environmental factors on runoff loss of adsorptive heavy metal chromium. The effects of rainfall intensity, the model mixing parameters, the thickness of the mixing layer, and adsorption conditions on the migration of hexavalent Chromium were quantitatively compared using a low computing cost GSA method. It turns out that the most important factors influencing the Cr(VI) transfer from soil into surface runoff during precipitation were the p, h_{mix}, α, and γ. θ_0 and the adsorption properties had a minor effect on the simulated Cr(VI) concentration in surface runoff. However, it should be mentioned that the θ_0 is a significant condition to the concentration variations in the surface runoff.

DATA AVAILABILITY STATEMENT

The raw data supporting the conclusion of this article will be made available by the authors, without undue reservation.

AUTHOR CONTRIBUTIONS

XW was responsible for the main manuscript writing and data analysis; ZX completed the writing of the model program and analysis of the results; JT was responsible for providing the experimental data; and BH participated in the conclusion analysis.

FUNDING

This work was partly supported by the National Natural Science Foundation of China (Grant 42072271) and the Fundamental Research Funds for the Central Universities (Grant Nos. 2682022CX036 and 2652018179).

SUPPLEMENTARY MATERIAL

The Supplementary Material for this article can be found online at: https://www.frontiersin.org/articles/10.3389/fenvs.2022.917103/full#supplementary-material

REFERENCES

Ahuja, L. R., and Lehman, O. R. (1983). The Extent and Nature of Rainfall-soil Interaction in the Release of Soluble Chemicals to Runoff. *J. Environ. Qual.* 12 (1), 34–40. doi:10.2134/jeq1983.00472425001200010005x

Ahuja, L. R., Sharpley, A. N., Yamamoto, M., and Menzel, R. G. (1981). The Depth of Rainfall-Runoff-Soil Interaction as Determined by 32 P. *Water Resour. Res.* 17 (4), 969–974. doi:10.1029/WR017i004p00969

Bansal, M., Singh, D., and Garg, V. K. (2009). A Comparative Study for the Removal of Hexavalent Chromium from Aqueous Solution by Agriculture Wastes' Carbons. *J. Hazard. Mater.* 171, 83–92. doi:10.1016/j.jhazmat.2009.05.124

Campolongo, F., Cariboni, J., and Saltelli, A. (2007). An Effective Screening Design for Sensitivity Analysis of Large Models. *Environ. Model. Softw.* 22 (10), 1509–1518. doi:10.1016/j.envsoft.2006.10.004

Chen, R., Zhang, Q., Chen, H., Yue, W., and Teng, Y. (2021). Source Apportionment of Heavy Metals in Sediments and Soils in an Interconnected River-Soil System Based on a Composite Fingerprint Screening Approach. *J. Hazard. Mater.* 411, 125125. doi:10.1016/j.jhazmat.2021.125125

Dong, W., Cao, C., Meng, X., Wang, Q., and Fu, Q. (2018). Experimental Studies on the Transfer of Dissolved Solutes from Soil into Surface Runoff on Loess Slopes in China. *Appl. Water Sci.* 8 (6). 10. doi:10.1007/s13201-018-0832-5

Donigian, A. S., Jr., Beyerlein, D. C., Davis, H. H., and Crawford, N. H. (1977). *Agricultural Runoff Management (ARM) Model, Version II; Refinement and Testing*. Athens, Ga: Environ. Res. Lab. U.S. EPA.

Fernández-Pazos, M. T., Garrido-Rodriguez, B., Nóvoa-Muñoz, J. C., Arias-Estévez, M., Fernández-Sanjurjo, M. J., Núñez-Delgado, A., et al. (2013). Cr(VI) Adsorption and Desorption on Soils and Biosorbents. *Water Air Soil Pollut.* 224 (1), 1–12. doi:10.1007/s11270-012-1366-3

Gao, B., Todd Walter, M., Steenhuis, T. S., HogarthParlange, W. L. J. Y., and Parlange, J.-Y. (2004). Rainfall Induced Chemical Transport from Soil to Runoff: Theory and Experiments. *J. Hydrology* 295 (1-4), 291–304. doi:10.1016/j.jhydrol.2004.03.026

Gorny, J., Billon, G., Noiriel, C., Dumoulin, D., Lesven, L., and Madé, B. (2016). Chromium Behavior in Aquatic Environments: a Review. *Environ. Rev.* 24 (4), 503–516. doi:10.1139/er-2016-0012

Havis, R. N., Smith, R. E., and Adrian, D. D. (1992). Partitioning Solute Transport between Infiltration and Overland Flow under Rainfall. *Water Resour. Res.* 28, 2569–2580. doi:10.1029/92WR01366

Heathman, G. C., Ahuja, L. R., and Lehman, O. R. (1985). The Transfer of Soil Surface-Applied Chemicals to Runoff. *Trans. ASAE* 28 (6), 1909–1915. doi:10.13031/2013.32540

Herman, J. D., Kollat, J. B., Reed, P. M., and Wagener, T. (2013). Technical Note: Method of Morris Effectively Reduces the Computational Demands of Global Sensitivity Analysis for Distributed Watershed Models. *Hydrol. Earth Syst. Sci.* 17 (7), 2893–2903. doi:10.5194/hess-17-2893-2013

Hill, M. C. (1992). A Computer Program (MODFLOWP) for Estimating Parameters of a Transient, Three-Dimensional Ground-Water Flow Model Using Nonlinear Regression. *U.S. Geol. Surv. Open-File Rep.* 91, 1–358. doi:10.3133/ofr91484

Hill, M. C. (1998). Methods and Guidelines for Effective Model Calibration. U.S. Geological Survey Water-Resources Investigations Report 98 –4005 AvaliableAt: http://pubs.water. usgs.gov/wri984005/.

Hill, M. C., and Tiedeman, C. R. (2007). *Effective Groundwater Model Calibration: With Analysis of Data, Sensitivities, Predictions, and Uncertainty*. Wiley-Interscience, 46–47.

Khan, A. A., Muthukrishnan, M., and Guha, B. K. (2010). Sorption and Transport Modeling of Hexavalent Chromium on Soil Media. *J. Hazard. Mater.* 174 (1-3), 444–454. doi:10.1016/j.jhazmat.2009.09.073

Langmuir, I. (1918). The Adsorption of Gases on Plane Surfaces of Glass, Mica and Platinum. *J. Am. Chem. Soc.* 40, 1361–1403. doi:10.1021/ja02242a004

Li, J., Tong, J., Xia, C., Hu, B. X., Zhu, H., Yang, R., et al. (2017). Numerical Simulation and Experimental Study on Farmland Nitrogen Loss to Surface Runoff in a Raindrop Driven Process. *J. Hydrology* 549, 754–768. doi:10.1016/j.jhydrol.2017.01.035

Lu, S.-F., Wu, Y.-L., Chen, Z., Li, T., Shen, C., Xuan, L.-K., et al. (2021). Remediation of Contaminated Soil and Groundwater Using Chemical Reduction and Solidification/stabilization Method: a Case Study. *Environ. Sci. Pollut. Res.* 28 (10), 12766–12779. doi:10.1007/s11356-020-11337-3

Mein, R. G., and Larson, C. L. (1973). Modeling Infiltration during a Steady Rain. *Water Resour. Res.* 9 (2), 384–394. doi:10.1029/WR009i002p00384

Morris, M. D. (1991). Factorial Sampling Plans for Preliminary Computational Experiments. *Technometrics* 33 (2), 161–174. doi:10.2307/126904310.1080/00401706.1991.10484804

Nofziger, D. L., and Wu, J. (2005). *CHEMFLO™-2000 User's Manual: Interactive Software for Simulating Water and Chemical Movement in Unsaturated Soils Stillwater[Z]*. OK: Oklahoma State University.

Petropoulos, G., Wooster, M. J., Carlson, T. N., Kennedy, M. C., and Scholze, M. (2009). A Global Bayesian Sensitivity Analysis of the 1d SimSphere Soil-Vegetation-Atmospheric Transfer (SVAT) Model Using Gaussian Model Emulation. *Ecol. Model.* 220, 2427–2440. doi:10.1016/j.ecolmodel.2009.06.006

Ren, A., Guo, B., Liu, S., and Zhou, B. (2000). Study on the Migration of Chromium in Soil. *URBAN Environ. Urban Ecol.* 13 (2), 54–56.

Saltelli, A., and Annoni, P. (2010). How to Avoid a Perfunctory Sensitivity Analysis. *Environ. Model. Softw.* 25 (12), 1508–1517. doi:10.1016/j.envsoft.2010.04.012

Saltelli, A., Chan, K., and Scott, E. M. (2000). *Sensitivity Analysis*. Hoboken, NJ: Wiley.

Saltelli, A., Ratto, M., Andres, T., Campolongo, F., Cariboni, J., Gatelli, D., et al. (2008). *Global Sensitivity Analysis: The Primer*. Chichester: John Wiley & Sons.

Saltelli, A., Tarantola, S., Campolongo, F., and Ratto, M. (2002). "Sensitivity Analysis in Practice," in *Sensitivity Analysis in Practice: A Guide to Assessing Scientific Models*. Editor A. Saltelli. 1st ed. (Chichester, England: John Wiley & Sons). doi:10.1002/0470870958

Sarkar, B., Xi, Y., Megharaj, M., Krishnamurti, G. S. R., Rajarathnam, D., and Naidu, R. (2010). Remediation of Hexavalent Chromium through Adsorption by Bentonite Based Arquad 2HT-75 Organoclays. *J. Hazard. Mater.* 183 (1-3), 87–97. doi:10.1016/j.jhazmat.2010.06.110

Shi, X., Wu, L., Chen, W., and Wang, Q. (2011). Solute Transfer from the Soil Surface to Overland Flow: A Review. *Soil Sci. Soc. Am. J.* 75 (4), 1214–1225. doi:10.2136/sssaj2010.0433

Shin, M.-J., Guillaume, J. H. A., Croke, B. F. W., and Jakeman, A. J. (2013). Addressing Ten Questions about Conceptual Rainfall-Runoff Models with Global Sensitivity Analyses in R. *J. Hydrology* 503, 135–152. doi:10.1016/j.jhydrol.2013.08.047

Song, X., Zhang, J., Zhan, C., Xuan, Y., Ye, M., and Xu, C. (2015). Global Sensitivity Analysis in Hydrological Modeling: Review of Concepts, Methods, Theoretical Framework, and Applications. *J. Hydrology* 523, 739–757. doi:10.1016/j.jhydrol.2015.02.013

Tewari, H., and Vivekanand (2013). Removal of Heavy Metals from Industrial Effluent Using Pinus Roxburghii Leaves as Biosorbent: Equilibrium Modelling. *Water Sci. Technol. A J. Int. Assoc. Water Pollut. Res.* 67 (9), 1894–1900. doi:10.2166/wst.2013.034

Thangam, T. E. D., Kumar, V. N., and Vasline, Y. A. (2018). Decontamination of Hexavalent Chromium by Geo Chemical Fixation Method in a Hazardous Dump Site, Ranipet, Tamil Nadu, India. *J. Eng. Appl. Sci.* 13 (1), 208–212. doi:10.36478/jeasci.2018.208.212

Tian, K., Huang, C. H., Tian, P., Wang, G. Q., Fu, X. D., and Guo, H. D. (2011b). Movement of Soil Solute under Simulated Rainfall Runoff. *Trans. CSAE* 27 (4), 81–87. doi:10.3969/j.issn.1002-6819.2011.04.014

Tian, K., Huang, C. H., Tian, P., Wang, G. Q., and Fu, X. D. (2011a). Simulated Experiment of Mixing Zone Depth under Rainfall-Runoff Conditions. *Trans. Chin. Soc. Agric. Eng.* 27 (11), 188–192.

Tian, W. (2013). A Review of Sensitivity Analysis Methods in Building Energy Analysis. *Renew. Sustain. Energy Rev.* 20, 411–419. doi:10.1016/j.rser.2012.12.014

Tiscareno-Lopez, M., Lopes, V. L., Stone, J. J., and Lane, L. J. (1993). Sensitivity Analysis of the WEPP Watershed Model for Rangeland Applications I: Hillslope Processes. *Trans. ASAE* 36 (6), 1659–1672. doi:10.13031/2013.28509

Tong, J.-X., Yang, J.-Z., Hu, B. X., and Bao, R.-c. (2010). Experimental Study and Mathematical Modelling of Soluble Chemical Transfer from Unsaturated/saturated Soil to Surface Runoff. *Hydrol. Process.* 24 (21), 3065–3073. doi:10.1002/hyp.7722

van Engelen, J., Bierkens, M. F. P., Delsman, J. R., and Oude Essink, G. H. P. (2021). Factors Determining the Natural Fresh-Salt Groundwater Distribution in Deltas. *Water Res.* 57 (1), e2020WR027290. doi:10.1029/2020WR027290

Wallach, R., Jury, W. A., and Spencer, W. F. (1988). Transfer of Chemicals from Soil Solution to Surface Runoff: A Diffusion-Based Soil Model. *Soil Sci. Soc. Am. J.* 52 (3), 612–618. doi:10.2136/sssaj1988.03615995005200030002x

Wallach, R., and van Genuchten, M. T. (1990). A Physically Based Model for Predicting Solute Transfer from Soil Solution to Rainfall-Induced Runoff Water. *Water Resour. Res.* 26 (9), 2119–2126. doi:10.1029/WR026i009p02119

Walter, M. T., Gao, B., and Parlange, J.-Y. (2007). Modeling Soil Solute Release into Runoff with Infiltration. *J. Hydrology* 347 (3-4), 430–437. doi:10.1016/j.jhydrol.2007.09.033

Wang, Q. J., Wang, W. Y., Shen, B., and Shao, M. A. (1998). Interacting Depth of Rainfall-Runoff-Soil Solute. *J. Soil Eros. Soil Water Conservation* 4 (2), 41–46.

Wang, Y. (2012). Study on the Adsorptive Solute (Cr6+) Transfer from Soil to the Surface Runoff, Dissertation. Beijing: China University of Geosciences, 13–14. Thesis.

Wu, J., Ran, Z. M., Liu, H. Q., and Du, J. (1997). Absorption Behavior of Chromium (VI) in Red Soils. *Chongqing Environ. Sci.* 19 (6), 22–26.

Wu, X. J., Tong, J. X., and Tan, C. Q. (2015). Experiment and Simulation on Soil Cr(VI) Loss to Surface Runoff under Condition of Nonlinear Langmuir Adsorption. *Trans. Chin. Soc. Agric. Eng. Trans. CSAE)* 31 (1), 146–152.

Wu, X. J., Tong, J. X., Tan, C. Q., Hu, B. X., and Yang, J. Z. (2014). Study on the Adsorptive Solute Cr(VI) Loss from Soil to Surface Runoff with Temkin Adsorption. *AMM* 641-642, 209–216. doi:10.4028/www.scientific.net/amm.641-642.209

Xia, C.-A., Tong, J., Hu, B. X., Wu, X., and Guadagnini, A. (2018). Assessment of Alternative Adsorption Models and Global Sensitivity Analysis to Characterize Hexavalent Chromium Loss from Soil to Surface Runoff. *Hydrol. Process.* 32 (20), 3140–3157. doi:10.1002/hyp.13233

Xiao, Y., Liu, K., Hao, Q., Xiao, D., Zhu, Y., Yin, S., et al. (2022). Hydrogeochemical Insights into the Signatures, Genesis and Sustainable Perspective of Nitrate Enriched Groundwater in the Piedmont of Hutuo Watershed, China. *CATENA* 212, 106020. doi:10.1016/j.catena.2022.106020

Xu, Z., Hu, B. X., Xu, Z., and Wu, X. (2019). Simulating Seawater Intrusion in a Complex Coastal Karst Aquifer Using an Improved Variable-Density Flow and Solute Transport-Conduit Flow Process Model. *Hydrogeol. J.* 27, 1277–1289. doi:10.1007/s10040-018-1903-2

Xu, Z., Hu, B. X., and Ye, M. (2018). Numerical Modeling and Sensitivity Analysis of Seawater Intrusion in a Dual-Permeability Coastal Karst Aquifer with Conduit Networks. *Hydrol. Earth Syst. Sci.* 22, 221–239. doi:10.5194/hess-22-221-2018

Yang, Q., Li, Z., Lu, X., Duan, Q., Huang, L., and Bi, J. (2018). A Review of Soil Heavy Metal Pollution from Industrial and Agricultural Regions in China: Pollution and Risk Assessment. *Sci. Total Environ.* 642, 690–700. doi:10.1016/j.scitotenv.2018.06.068

Yang, T., Wang, Q., Liu, Y., Zhang, P., and Wu, L. (2016). A Comparison of Mathematical Models for Chemical Transfer from Soil to Surface Runoff with the Impact of Rain. *CATENA* 137, 191–202. doi:10.1016/j.catena.2015.09.014

Young, D. F., and Fry, M. M. (2019). Field-scale Evaluation of Pesticide Uptake into Runoff Using a Mixing Cell and a Non-uniform Uptake Model. *Environ. Model. Softw.* 122, 104055. doi:10.1016/j.envsoft.2017.09.007

Zhang, Z., Liu, J., Feng, L., and Zou, W. (2011). A Prediction Model Based on Langmuir Theory for Equilibrium Adsorption Amount. *J. Northeast. Univ. Nat. Sci.* 32 (5), 749–751.

Conflict of Interest: The authors declare that the research was conducted in the absence of any commercial or financial relationships that could be construed as a potential conflict of interest.

Publisher's Note: All claims expressed in this article are solely those of the authors and do not necessarily represent those of their affiliated organizations, or those of the publisher, the editors and the reviewers. Any product that may be evaluated in this article, or claim that may be made by its manufacturer, is not guaranteed or endorsed by the publisher.

frontiers | Frontiers in Environmental Science

ORIGINAL RESEARCH
published: 22 July 2022
doi: 10.3389/fenvs.2022.950098

Using an Improved SWAT Model to Simulate Karst Sinkholes: A Case Study in Southwest China

Yan Zhou[1], *Liangjie Zhao*[2]*, *Jianwen Cao*[2] *and Yaru Wang*[3]

[1]China University of Geosciences, Beijing, China, [2]Institute of Karst Geology, Chinese Academy of Geological Sciences, Guilin, China, [3]Hebei Hydrological Engineering Geological Survey Institute Co, Ltd., Shijiazhuang, China

Hydrological simulation of the karst area is significant for assessing water resources accurately and exploring the relationship in the hydrologic cycle. However, the existence of sinkholes causes the spatial heterogeneity of aquifers and changes the distribution of surface water as well as groundwater, which makes the traditional hydrogeological model difficult to quantitatively characterize the hydrological processes of the sinkhole. Hence, improving the hydrological model for the karst area is a necessary direction at present. The soil and water assessment tool (SWAT) is one of the most widely used semi-distributed hydrological models right now in the world. In this study, we focused on the upper course of the South Panjiang River and used the pond module of the SWAT model to simulate karst sinkholes, modifying the source code to realize the rapid response to the recharge in karst sinkholes. After the improvement, the surface runoff, especially the peak value of the Xiqiao Hydrological Station at the outlet, has been reduced, while the baseflow of modified subbasins has been increased and the water yield is under a state of water balance. In addition, the model evaluation factor R^2 was strengthened from 0.76 to 0.83 and NSE was strengthened from 0.66 to 0.79 of the Xiqiao Hydrological Station during the validation period. The improved model was used to analyze the spatial distribution of hydrological components. Also, it was found there are spatial relations between runoff modulus–slope and baseflow–surface runoff–land use types. The analysis demonstrated that the improved SWAT model could effectively change the hydrological components and simulate the rapid replenishment of karst sinkholes.

Keywords: karst area, sinkhole, semi-distributed model SWAT, surface runoff, baseflow

OPEN ACCESS

Edited by:
Yong Xiao,
Southwest Jiaotong University, China

Reviewed by:
Zhonghua Tang,
China University of Geosciences, China
Yuanzheng Zhai,
Beijing Normal University, China

***Correspondence:**
Liangjie Zhao
zhaoliangjie@mail.cgs.gov.cn

Specialty section:
This article was submitted to Freshwater Science, a section of the journal Frontiers in Environmental Science

Received: *22 May 2022*
Accepted: *22 June 2022*
Published: *22 July 2022*

Citation:
Zhou Y, Zhao L, Cao J and Wang Y (2022) Using an Improved SWAT Model to Simulate Karst Sinkholes: A Case Study in Southwest China. Front. Environ. Sci. 10:950098. doi: 10.3389/fenvs.2022.950098

INTRODUCTION

Karst is a special landscape shape, which can be classified into carbonate karst, evaporate karst, and sandstone karst according to the constituting material (Veress 2020). It develops mainly with groundwater solution of the carbonate rocks when groundwater flows, which exports the products of dissolution, creating underground voids, and the processes can develop a hydraulic continuum from the surface to spring (Bakalowicz 2005). Karst is widely distributed in Southwest China, and a lot of research on karst has been carried out in these areas, including determining the output characteristics of fissure flows (Li et al., 2020), estimating groundwater storage and detecting anomalies in karstic regions (Huang et al., 2019), and investigating the influence of climatic variability on solute dynamics (Liu et al., 2020).

The karst aquifer and epikarst are indispensable parts of the karst area. The karst aquifer constitutes an important source of water supply. Ford and Williams, (2007) estimated that 7–10% of the planet is karst and roughly 20–25% of the global population depends largely or entirely on groundwater obtained from them. Typical epikarst phenomena such as spring, cave, sinkhole, and depression are present under the erosion of water flow. Among them, sinkholes develop where the rock in the karstic area undergoes chemical weathering or dissolution through groundwater movement and infiltration of surface water or precipitation (Cahalan and Milewski 2015).

However, modeling karst systems is still a complex task and has been the subject of continuing research globally. A difficulty is that the geometry of fractures, the position of conduits, and the interactions between different types of flows are unknown in many cases (Salerno and Tartari 2009). As an important method, the hydrological model emerges as time requires. Three types of mathematical hydrological models can be applied for the karst flow simulation: theoretical or physical models, conceptual models, and empirical or black-box models (Deni-Juki and Juki 2003). The simplest way to model karst hydrology is the application of "black-box" models. They transfer input to output without the explicit representation of any physical processes and ignore the complexity of the aquifer geometry (Halihan and Wicks 1998). The KAGIS model, artificial neural network model, and regression model were used to simulate and predict the hydrodynamic behavior of karst aquifers (Felton and Currens 1994; Lallahem et al., 2005; Hu et al., 2008; Valdes-Abellan et al., 2018; Nhu et al., 2020). However, the results lose their reliability outside the range of conditions they were calibrated for (Hartmann et al., 2014). Moreover, it requires long time series of input data, which is difficult for the data-starved area (Meng and Wang 2010).

The conceptual model is based on a set of equations transferring input to output, conceptually representing physical processes, and it is widely used in karst modeling due to easy implementation (Hartmann et al., 2012). The Hydrological Model for Karst Environment (HYMKE) (Rimmer and Salingar 2006; Samuels et al., 2010), Génie Rural à 4 paramètres Journalier (GR4J) (Sezen et al., 2019), and Karst Simulation Simplified (K sim^2) model (Makropoulos et al., 2008) are successfully applied in the karst area. However, this kind of model often discards details in the system dynamics to simplify the model, and it is difficult to be applied to large-scale basins (Meng and Wang 2010). For the quantitative spatial simulation in large-scale watersheds, conceptual models are less advantageous than physical models (Martínez-Santos and Andreu 2010).

The physics-based numerical model generally ignores the complexity of karst aquifer geometry and interprets the response with mathematical techniques and empirical assumptions. These approaches can also simplify the conduit geometry and interpret the response that the system will generate (Halihan and Wicks 1998). Karst areas usually lack data and have a complex structure, and the distributed and semi-distributed models have advantages. This kind of model allows grid refinement, and its structure allows for adding and removing flexible mechanisms. It not only considers the temporal and spatial variation of hydrological elements but also reflects the spatial distribution characteristics of basins. Among them, the semi-distributed model SWAT became popular in the last decades to specifically address anthropogenic challenges related to hydrology, nutrient transport, sediment transport, and crop growth in diverse climatic, physiographic, and socioeconomic settings (Piniewski et al., 2019). It has strong applicability in predicting future changes in water resources, and it is convenient to use the spatial information provided by remote sensing technology or computer technology to simulate the hydrological effects in many different scenarios (Shang et al., 2019). Therefore, the SWAT model has been used in many areas, like Minnesota, Michigan, and Colombia of the United States (Schomberg et al., 2005; Villamizar et al., 2019), San Pedro watershed of Mexico (Nie et al., 2011), Amur River Basin of Asia (Zhou et al., 2020), and Ganga River Basin of India (Anand et al., 2018).

The research methods based on SWAT in the karst area can be divided into two categories: the unmodified SWAT model and the modified SWAT model. The research studies which applied an unmodified model have been carried out in Kenya (Baker and Miller 2013), China (Xie et al., 2021), Spain (Martínez-Salvador and Conesa-García 2020), Greece (Malagò et al., 2016), and other countries. But some prerequisites are generally required for the application of an unmodified SWAT model to simulate the karst hydrology. For example, the geological survey in the study area tends to be thorough and detailed, and the karst hydrogeological parameters affecting flow prediction such as infiltration rate and drainage area can be determined accurately, or researchers conduct tracing experiments to obtain the actual flow of the karst underground river and combine the experimental results with the SWAT model (Amatya et al., 2011; Lauber et al., 2014). However, the geological surveys in karst areas are often inadequate, some scholars focus on the improvement of numerical model performance in the karst area, and there have been many related explorations and breakthroughs. Baffaut and Benson, (2009) proposed a way to present the quick movement of water from the ground surface to the aquifer in sinkholes by distinguishing the delay time of seepage from soil and infiltrations from ponds, which attempt to simulate the karst flow process and pollutant transport better. Mohammed et al. (Rahman et al., 2016) incorporated a wetland geometric formula into SWAT to overcome the limitation of morphometric properties and scale and shape parameters. This research method to implant the improved formula into the model to simulate karst morphology is a way of karst simulation, and the improvement of the karst hydrologic formula is worth learning. Palanisamy and Workman, (2014) conceptualized the sinkholes in the karst watershed as orifices, and flow through these orifices was modeled as a function of sinkhole diameter, incorporating the flow components in the SWAT model; this applies to karst basins dominated by sinkholes. Wang et al. (2019) combined the lumped model–reservoir model and semi-distributed hydrologic model SWAT model

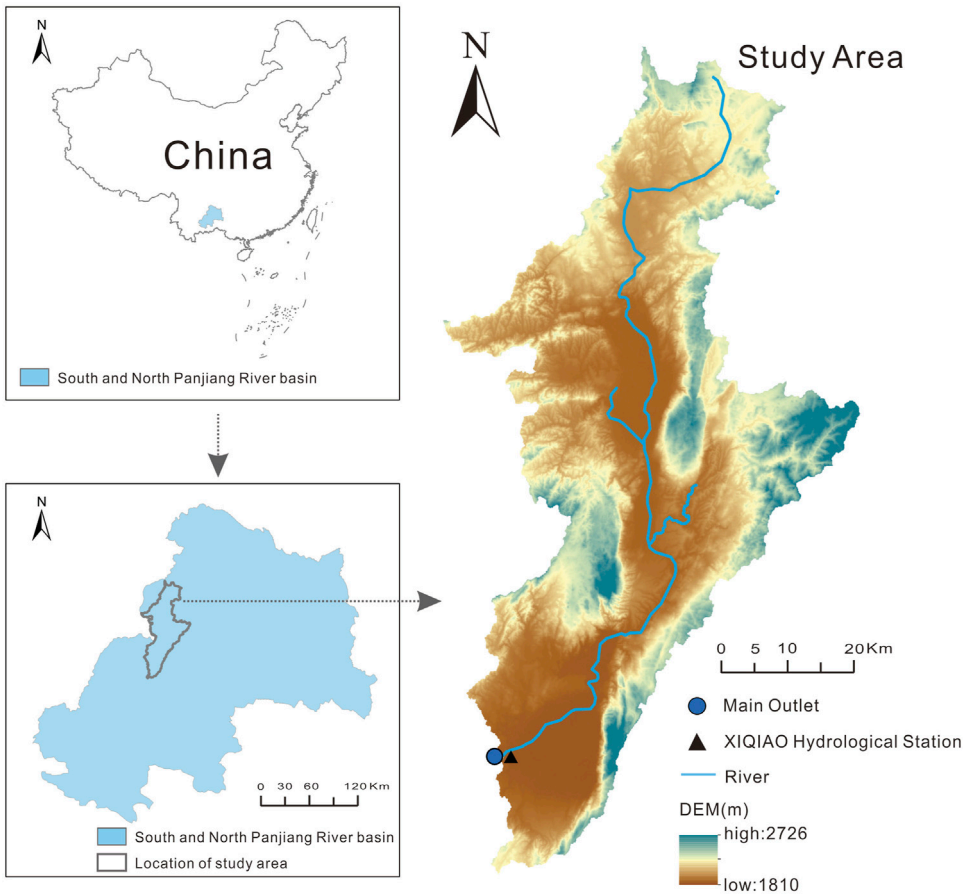

FIGURE 1 | Location of the study area.

to simulate the water cycle in Xianghualing karst watershed in southern China, and they used a reservoir to generalize the recharge from depressions.

Previous efforts have been made to improve the SWAT model, but there has been little quantitative analysis of karst sinkhole simulation, particularly for Southwest China. A systematic understanding of how sinkholes affect karst flow is still lacking. Baffaut and Benson, (2009) proposed a method to modify the pond subroutines SWAT to account for a higher infiltration rate in sinkholes in southwest Missouri. In this study, we applied the same method in the source area of South and North Panjiang River basin (SNPB) of Southwest China. We used the improved SWAT model (version 2012) to simulate the hydrology process of rapid response in the karst area and proved the applicability of the improved model in the study area.

METHODS

Study Area

SNPB is located in Southwest China and on the upper reaches of the Pearl River watershed. The basin slopes from southwest to northeast, the western region is a natural mountain barrier, and the eastern part is on the southeast slope of the Yunnan–Guizhou Plateau. The South Panjiang River and North Panjiang River are the two rivers in the watershed, which originate in the same place—Maxiong Mountains of Yunnan Province.

This study focuses on the source area of the South Panjiang River, which lies between latitude 25° to 26°N and longitude 103° to 104° with an area of 2,762 km^2 (as shown in **Figure 1**). The climate of the study area is a typical subtropical humid monsoon climate with an average annual temperature of 19.7°C and a relative humidity of the atmosphere ranging from 76 to 82%. The warm and wet period from June to September is distinguishable, with an average precipitation of 1, 279.4 mm, equivalent to 66% of the total annual precipitation. Except for a small area of stratified bedrock in the west, the rest of the distribution lithology is carbonate such as limestone and dolomite. Under the influence of climatic characteristics, karst topography is well-developed. The karst drainage network is distributed tightly and ranges between 11.1 and 15.9 km/km^2. A large number of karst sinkholes formed under the action of long-term water flow erosion and weathering erosion. These sinkholes are basically cylindrical and show a closed state.

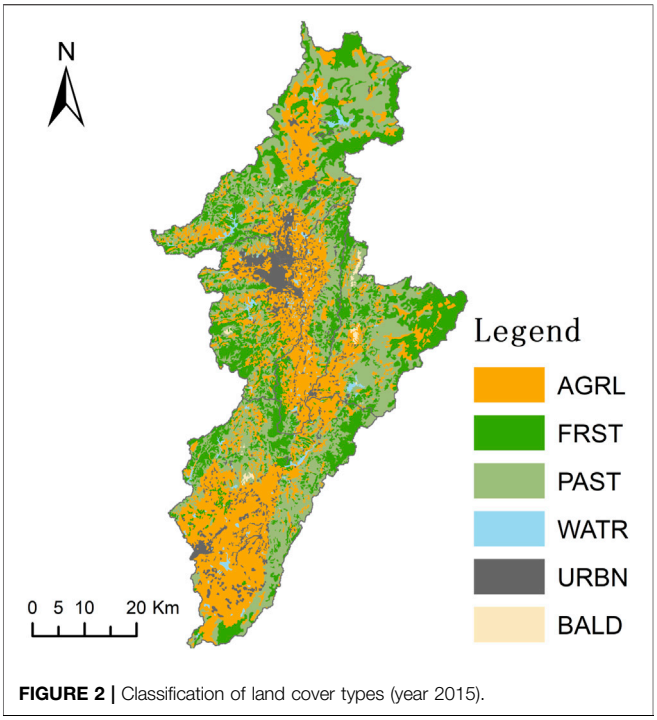

FIGURE 2 | Classification of land cover types (year 2015).

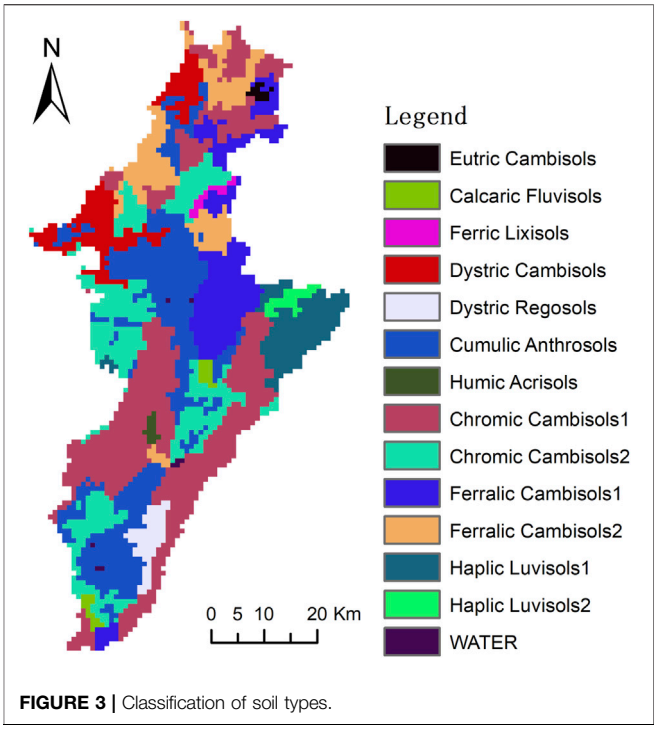

FIGURE 3 | Classification of soil types.

Data Source

DEM Data

Digital elevation data (DEM) was acquired from the Geospatial Data Cloud (http://www.gscloud.cn/) with 30 m × 30 m resolution (**Figure 1**). It shows the spatial distribution of regional geomorphology. DEM data were used to analyze topography and slope, extract river network and sinkholes, make mask processing, and so on. Moreover, a watershed can be divided into multiple subbasins based on the river network and DEM in the SWAT model.

Land Use Type

The land use map of the year 2015 was obtained from the Resource and Environment Science and Data Center Platform (http://www.resdc.cn/) with 1000 m resolution (**Figure 2**). We reclassified the initial land use map and got six land use types: farmland (AGRL), forest land (FRST), grassland (PAST), lakes and other bodies of water (WATR), urban construction land (URBN), and unused bare land (BALD). "AGRL," "FRST," and "PAST" are the three main land use types of the study area, and the areas are 823 km^2 (30%), 778 km^2 (28%), and 925 km^2 (34%), respectively. The farmland near the river channel is mainly used for aquatic crops such as rice, and some irrigated farmland is used for crops such as corn and vegetables. Forestland types are mainly evergreen broad-leaved forest, deciduous broad-leaved forest, and coniferous forest. Grassland type is mainly natural grasslands with medium coverage.

Soil Type

Soil data were obtained from the Harmonized World Soil Database (HWSD) established by the United Nations Food and Agriculture Organization (FAO) and the International Institute for Applied Systems (IIASA) in Vienna, which linked to the soil characteristic database with a resolution of 1000 m × 1000 m. Each soil type contains physical and chemical properties. Thus, it plays an important role in the hydrological cycle in hydrological response units (HRUs) and affects the movement of water in the soil profile. We calculated the properties of the soil through the HWSD database, mathematical formula, and soil water characteristics module from SPAW software (Rao and Saxton 1995). The soil types which had the same soil names and properties were defined as the same one, and the final soil properties were made as a database in SWAT. mdb. The soil data were reclassified into 14 types as shown in **Figure 3**.

Meteorological Database

The meteorological data used in the model were taken from The China Meteorological Assimilation Datasets for the SWAT model (CMADS) developed by Prof. Dr. Xianyong Meng (Meng and Wang 2017) from China Agricultural University (CAU). The CMADS data set has been modified as a format that the SWAT model can recognize and use the data set without any format conversion. The data include daily precipitation, maximum and minimum temperatures, solar radiation, relative humidity, and wind speed, from the year 2010 to 2015 at the 20 meteorological stations.

Hydrological Data

The calibration and verification data are the streamflow data of hydrological stations from the Institute of Karst Geology Chinese Academy of Geological Sciences. Average monthly streamflow data from the year 2012 to 2015 of the Xiqiao station from research institutes were used to calibrate the SWAT model. In

addition, the daily streamflow data of the same station from 28 July 2015 to 4 October 2015 were also obtained. The location of the hydrological station mentioned previously is shown in **Figure 1**.

Improved SWAT Model

SWAT hydrological model simulation is divided into the overland flow phase and channel flow phase. The first phase controls the flow of water, sediment, and pollutants into the channel within the subbasin. The second phase is the process in which the flows from the first phase migrate to the outlet. The hydrologic processes simulated by the SWAT model mainly include surface runoff, soil infiltration, evapotranspiration, interflow, and return flow. The hydrology circulation system is based on the water balance equation (Arnold et al., 1998; HAO et al., 2006).

The aquifer constructed according to the regular SWAT model will be generalized as a loose homogeneous medium, and the infiltration delay days of soil profiles in karst areas are the same as in other areas in the traditional SWAT code. However, karst sinkholes have a phenomenon of rapid vertical replenishment, and the exchange rate of surface water and groundwater is much faster than that of other areas, which the regular model cannot accurately depict. In order to solve this problem, in this study, we used the pond module in SWAT to conceptualize the karst sinkholes and modified the algorithm to distinguish the rapid vertical replenishment hydrological process of the sinkholes.

Pond can receive a portion of the water from the subbasin, and its water storage is a function of daily inflow and outflow, including infiltration and evaporation. The outflow of the pond is simulated according to storage capacity and changes according to the soil moisture content and the flood season. The water balance equation of the pond in SWAT is shown in **Formula (1)**:

$$V = V_{stored} + V_{flowin} - V_{flowout} + V_{pcp} - V_{evap} - V_{seep}, \quad (1)$$

where V is the amount of water stored at the end of a day, m^3; V_{stored} is the amount of water stored at the beginning of a day, m^3; V_{flowin} is the amount of water that flows into on a given day, m^3; $V_{flowout}$ is the amount of water that flows out on a given day, m^3; V_{pcp} is the amount of precipitation over the water body on a given day, m^3; V_{evap} is the amount of evaporation of the water body on a given day, m^3; and V_{seep} is the amount of water leakage on a given day, m^3.

The formula for controlling the pond hydrologic process in SWAT is as follows (Neitsch et al., 2002):

$$SA = \beta_{sa} \cdot V^{exsa}, \quad (2)$$

$$exsa = \frac{\log_{10}(SA_{em}) - \log_{10}(SA_{pr})}{\log_{10}(V_{em}) - \log_{10}(V_{pr})}, \quad (3)$$

$$\beta_{sa} = \left(\frac{SA_{em}}{V_{em}}\right)^{exsa}, \quad (4)$$

where SA is the initial surface area of ponds, β_{sa} is a coefficient, V is the initial volume of water stored in the pond, $exsa$ is an exponential, SA_{em} is the surface area of ponds when filled to emergency spillway, V_{em} is the volume of water stored in ponds when filled to the emergency spillway, SA_{pr} is the surface area of ponds when filled to the principal spillway, and V_{pr} is the volume of water stored in ponds when filled to the principal spillway.

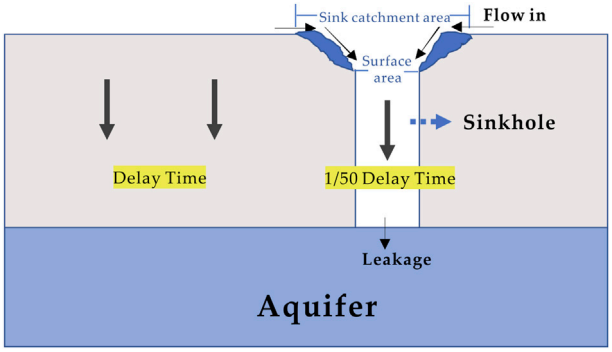

FIGURE 4 | Karst sinkhole simulated by the pond module in the modified version of SWAT.

The pond module needs to be added at the subbasin scale, and all sinkholes are generalized with one pond for each subbasin. The pond was represented in the model by some specific parameter variables: a fraction of subbasin area that drains into ponds (PND_FR) and hydraulic conductivity through the bottom of ponds (PND_K). The parameters V, SA_{em}, V_{em}, SA_{pr}, and V_{pr} in the aforementioned formula are also variables that control the pond in the input interface of the model. The total area of the sinks in each subbasin is the value of these two parameters: SA_{em} and SA_{pr}. Through weighted statistics, one can obtain the average depth of the depression and then figure out the volume value: V_{em} and V_{pr} of the pond. The initial volume of water stored in the pond was set close to 0 m^3. The bottom of the pond was endowed with a large hydraulic conductivity coefficient (10,000), making all the water flowing into the pond infiltrate and recharge the groundwater. The catchment area corresponds to the existing depression refers to the precipitation area of water flowing in the sinkhole. Hydrological analysis can obtain the catchment area of depressions in each area and the ratio of this area to the entire subbasin. Then, the ratio was characterized by setting the PND_FR parameter in the SWAT model.

In order to realize the change of water transfer speed and quantity in the vertical direction and rapid recharge of groundwater aquifer in sinkholes, we modified the original algorithm of the SWAT model. In the original model code (shown as **Eq. 5**), the amount of water from ponds (rchrgkarst) and percolation from the bottom of the soil profile in HRU [sepbtm(j)] use the same delay time variable which represents the duration of water leaving the bottom of the root zone to reach the shallow aquifer. With improvement, recharge is divided into two parts: leakage recharge of the soil profile and rapid recharge of karst sinkholes. The water passing through the pond was taken out separately, using a specific delay time variable. According to the empirical coefficient of previous models we built, the delay time variable of pond leakage was set to 1/50 of the initial value (as shown in **Figure 4**). After the

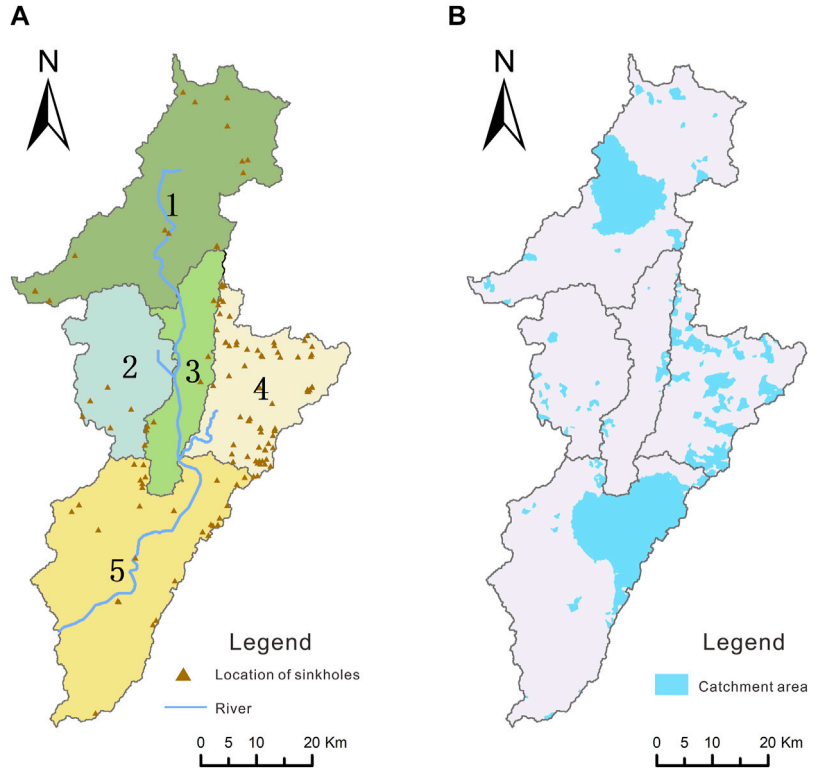

FIGURE 5 | Division of watershed and location of sinkholes **(A)**. Catchment area of the sinkholes in each subbasin **(B)**.

modification of the SWAT code, the formula for calculating the daily recharge of the karst aquifer is given as **Eq. 6**:

$$rchrg(j) = (1. - exp(-1/delay)) * \left(sepbtm(j) + gwq_{ru(j)} + rchrg_{karst}\right) + exp(-1/delay) * rchrg1, \quad (5)$$

$$rchrg(j) = (1. - exp(-1/delay)) * \left(sepbtm(j) + gwq_{ru(j)}\right) + (1. - exp(-1/(delay/50))) * rchrg_{karst} + exp(-1/delay) * rchrg1, \quad (6)$$

where $rchrg(j)$ is the amount of water entering the shallow aquifer on the current day, mm; $delay$ is the groundwater delay (time required for water leaving the bottom of the root zone to reach the shallow aquifer), days; $sepbtm(j)$ is the percolation from the bottom of the soil profile for the day, mm; $gwq_{ru(j)}$ is the groundwater contribution to streamflow on the current day, mm; $rchrg_{karst}$ is the amount of water from ponds, mm; and $rchrg1$ is the amount of water entering the shallow aquifer on the previous day, mm.

Numerical Model

Model Setup

In the process of setting up the improved SWAT model, the DEM data were used to generate rivers and calculate the direction of flow. Then, the threshold value of the minimum area in the study catchment was set at 30000 Ha and generated the river network. Based on the river network and outlets, the study area was divided into five subbasins. The soil map and land use map were added to establish SWAT, and the corresponding index tables were imported to connect the map properties with the SWAT database. For slope classification, we selected the multiple slope method and divided slope into three levels: 0~15, 15~25, and 25~9,999. After defining HRU and setting the minimum generative area ratio of land use, soil, and slope at 15, 15, and 10%, respectively, the SWAT model finally generated 833 HRUs (hydrological response units) in five subbasins.

We built two sets of models, which are called the original model and the improved model. No pond module was added to the original model, but in the improved model, we added the pond module to simulate karst sinkholes and the code of the pond was modified at the same time. In the improved model, the pond module was set in No. 1, No. 4, and No. 5 subbasins (as shown in **Figure 5**). Then, the surface area, initial volume, and volume of ponds when filled to spillway were, respectively, input into the model to complete the characterization of the pond.

In this study, we modified the SWAT source code in the Windows platform application development environment Visual Studio 2010. The subroutine gwmod. f was modified, and after modification and successful compilation, we replaced the original Swat. exe executable.

TABLE 1 | Parameter characteristics of sinkholes in five subbasins.

Subbasin no.	Subbasin area (ha)	Sinkhole number	Sinkhole area (ha)	Sinkhole depth(m)	Fraction of the pond catchment area
1	90,316	15	20.25	14.83	0.21
2	30,849	7	5.67	12.3	0.05
3	25,723	5	4.05	12.63	0.04
4	35,054	69	109.35	14.43	0.47
5	93,990	28	114.21	14.04	0.36

Model Calibration and Validation

The SWAT model was calibrated using monthly streamflow data from 1 January 2012 to 31 December 2013 at Xiqiao stations in the study area. The Xiqiao Hydrological Station was chosen because the study area is an independent hydrogeological unit, and the Xiqiao Hydrological Station is located at the outlet of the whole basin. The warm up period was from 1 January 2010 to 31 December 2011. The validation period was from 1 January 2014 to 31 December 2015. During the simulation period, the maximum precipitation was 1171 mm, and the minimum precipitation was 402 mm, including the wet year and dry year. Model sensitivity analysis and calibration were carried out using the Sequential Uncertainty Fitting version 2 (SUFI-2) approach using the SWAT-CUP interface developed by Abbaspour (2015). Sensitivity analysis can determine the parameters that have a greater impact on the model and improve the simulation efficiency. The sensitivity of the parameter is determined by t factor and p factor, and the t factor is positively correlated with sensitivity, but p is negatively correlated. Model performance was evaluated based on statistical parameters of the coefficient of determination (R^2) and Nash–Sutcliffe efficiency (NSE) (Moriasi et al., 2007). R^2 and NSE are calculated as follows:

$$R^2 = \frac{\left[\sum_{i=1}^{n}\left(Q_{m,i} - Q_{m,avg}\right)\left(Q_{s,i} - Q_{s,avg}\right)\right]^2}{\sum_{i=1}^{n}\left(Q_{m,i} - Q_{m,avg}\right)^2 \sum_{i=1}^{n}\left(Q_{s,i} - Q_{s,avg}\right)^2}, \quad (7)$$

$$NSE = 1 - \frac{\sum_{i=1}^{n}\left(Q_{m,i} - Q_{s,i}\right)^2}{\sum_{i=1}^{n}\left(Q_{m,i} - Q_{m,avg}\right)^2}, \quad (8)$$

where $Q_{m,i}$ and $Q_{s,i}$ are the ith observed and simulated stream flows, respectively, $Q_{m,avg}$ and $Q_{s,avg}$ are the mean of the observed and simulated data, and n is the total number of observations.

RESULTS

Sinkhole and River Characteristics

We used the hydrologic analysis tool in ArcGIS to identify negative terrain, calculate negative terrain depth, and generate catchment areas of the sinkholes. The field survey shows that the depth of sinkholes in the area is usually between 10 and 20 m, so we take negative terrain with this depth range as sinkholes. Because sinkholes are not only negative terrain but also have closed features, we identified contour lines and removed unclosed sinkholes. **Figure 5** shows the location and catchment area of the sinkholes. In each subbasin, the area of all sinkholes was taken as the surface area of the pond and the average depth of all sinkholes was taken as the depth of the pond. The fraction of the subbasin area that drains into ponds (PND_FR) was the proportion of the catchment area of sinkholes to the subbasin area. Sinkhole parameters are shown in **Table 1**. It can be seen that the numbers of sinkholes in subbasins No. 2 and No. 3 are seven and five, respectively, and PND_FR is less than 0.05. It indicates that sinkholes are not widely distributed in these two subbasins compared with other subbasins. Therefore, the pond module was set in subbasins No. 1, No. 4, and No. 5. When extracting the river, a real river network map was added for guidance, and the "burn-in" algorithm in SWAT lowered the elevation of the river in DEM to generate a near-real river. The extracted river is shown in **Figure 5**.

TABLE 2 | Parameter sensitivity ranking and parameter fitted value range.

Rank	Parameter	Initial value	Fitted value
1	CN2	35–98	60–62
2	ALPHA_BF	0–1	0.9–0.96
3	GW_DELAY	0–500	0–30
4	PND_VOL	0–30	10–24
5	REVAPMN	0–750	650–700
6	RCHRG_DP	0–1	0–0.005
7	GWQMN	0–5,000	300–350
8	GW_REVAP	0.01–0.2	0.01–0.012

Improved Model Evaluation

During the calibration process, eight parameters were selected and 200 iterations were carried out in the hydrological stations. The parameter sensitivity, value ranges, and the final values are shown in **Table.2**, and rank stands for the sensitivity sequence. Soil conservation service curve number CN2 mainly affects surface runoff. Baseflow alpha factor ALPHA_BF affects the redistribution of groundwater runoff. Groundwater delay time GW_DELAY affects the groundwater delay. The three parameters are very sensitive, which is closely related to the hydrological process affected by a pond. Other parameters, such as the depth of water for return flow GWQMN, affect the generation of baseflow. The deep aquifer percolation fraction RCHRG_DP is the percolation fraction of the deep aquifer and describes the characteristics of the deep aquifer. The groundwater "revap" coefficient GW_REVAP and depth of water for

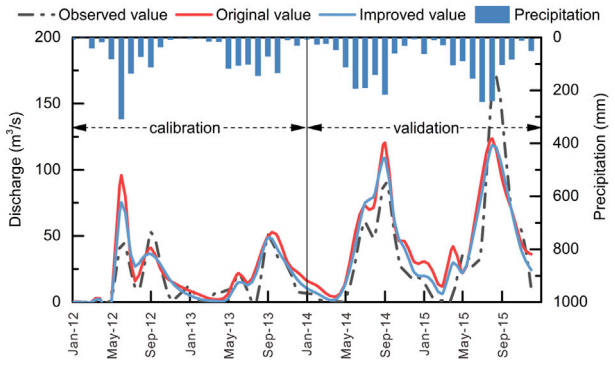

FIGURE 6 | Monthly discharge during the calibration period (2012–2013) and the validation period (2014–2015) before and after model improvement.

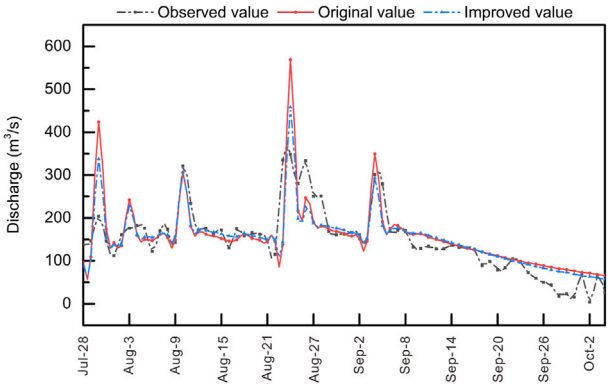

FIGURE 7 | Daily discharge during the flood season in the year 2015 before and after model improvement.

evaporation REVAPMN affect the generation of baseflow by altering the evaporation of a shallow aquifer. PND_VOL affects the initial volume of the pond. All parameters were adjusted by replace, and the parameters identified in this study are consistent with those related studies (Moreira et al., 2018; Thavhana et al., 2018; Liang et al., 2020).

Comparison of the Performance of the Original and Improved Models

The streamflow data of the Xiqiao Hydrological Station were compared to assess the accuracy and applicability of the improved model (as shown in **Figure 6**). We used the same set of parameters before and after the model improvement, so that the change of the model only comes from the addition and improvement of the pond. The results show that for the original model, the value of R^2 is 0.70 and NSE is 0.35 in the calibration period, while the value of R^2 is 0.74 and NSE is 0.61 as simulated by the improved model. For the original model, R^2 and NSE values are 0.76 and 0.66, respectively, in the validation period, while the value of R^2 is 0.83 and NSE is 0.79 as obtained from the improved model. Both the linear correlation and model reliability have been strengthened with the improvements we proposed. In order to show the difference before and after improvement in more detail, we selected the flood season of the year 2015, July 28–October 4, and conducted daily simulation (as shown in **Figure 7**), and the result shows the decrease in peak flow and the increase in baseflow, especially in August, the simulated peak value and normal flow value are obviously closer to the measured data.

Change of Hydrological Components After Model Improvement

According to the output. sub files obtained by the improved SWAT model, we calculated the average annual surface runoff depth and baseflow depth of No. 1, No. 4, and No. 5 subbasins. Compared with the improved model and original model (**Table.3**), the surface runoff depth was reduced by 9.2, 13.5, and 21.4 mm and the reduction rate was 21, 47, and 36%, respectively. Corresponding with the coefficient PND_FR that had been set in each subbasin, this result indicates that the subbasins with the pond let part of surface runoff flow into the pond, and the proportion of water flow in the pond was the value of the PND_FR parameter. Corresponding to the decrease in surface runoff, the baseflow depth of each subbasin increased. In the subbasins of No. 1, No. 4, and No. 5, the baseflow was increased by 16.4, 20.3, and 16.1 mm, respectively, which reflected the recharge of surface runoff to baseflow.

Compared with the original model, in the improved model, the lateral flow depth was reduced from 22.5 to 18.8 mm in subbasin No. 1, from 12.2 to 7.5 mm in subbasin No. 4, and 8.0 to 7.1 mm in subbasin No. 5. The water yield is composed of surface runoff, baseflow, and lateral flow. In the original model, the water yield of subbasins No. 1, No. 4, and No. 5 was 262.4, 186.6, and 316.6 mm, respectively, and the total water yield was 765.6 mm. In the improved model, the water yield of subbasins No. 1, No. 4, and No. 5 was 265.8, 188.7, and 310.6 mm, respectively, and the total water yield was 765.1 mm. The water yield was basically under a state of water balance. It can be seen that the recharge of surface runoff to baseflow caused a decrease in lateral flow, and a part of the lateral flow was directly converted into the baseflow to recharge the river.

Spatial Distribution of Hydrological Components

According to the results of SWAT, we analyzed the spatial distribution of river discharge, runoff modulus, surface runoff depth, and baseflow depth. **Figure 8** shows that the rivers in the subbasins No. 1, No. 2, and No. 4 are located in the upstream and tributaries, and the annual average discharge is 7.2 m^3/s, 8.4 m^3/s, and 6.8 m^3/s, respectively. The rivers in subbasins No. 3 and No. 5 are located in the downstream and the mainstream, and the annual average discharge is 19.0 m^3/s and 33.6 m^3/s, respectively. The discharge of the river shows the distribution characteristics of increasing gradually from upstream to downstream and from tributaries to mainstreams.

TABLE 3 | Changes in surface runoff depth, baseflow depth, and lateral flow depth in the subbasins No. 1, No. 4, and No. 5 (unit: mm).

Subbasin no.	Surface runoff			Baseflow			Lateral flow		
	Initial	Improve	Decrease	Initial	Improve	Increase	Initial	Improve	Decrease
1	43.9	34.7	9.2	195.9	212.3	16.4	22.5	18.8	3.7
4	28.8	15.3	13.5	145.6	165.9	20.3	12.2	7.5	4.7
5	59.0	37.8	21.4	249.6	265.7	16.1	8.0	7.1	0.9

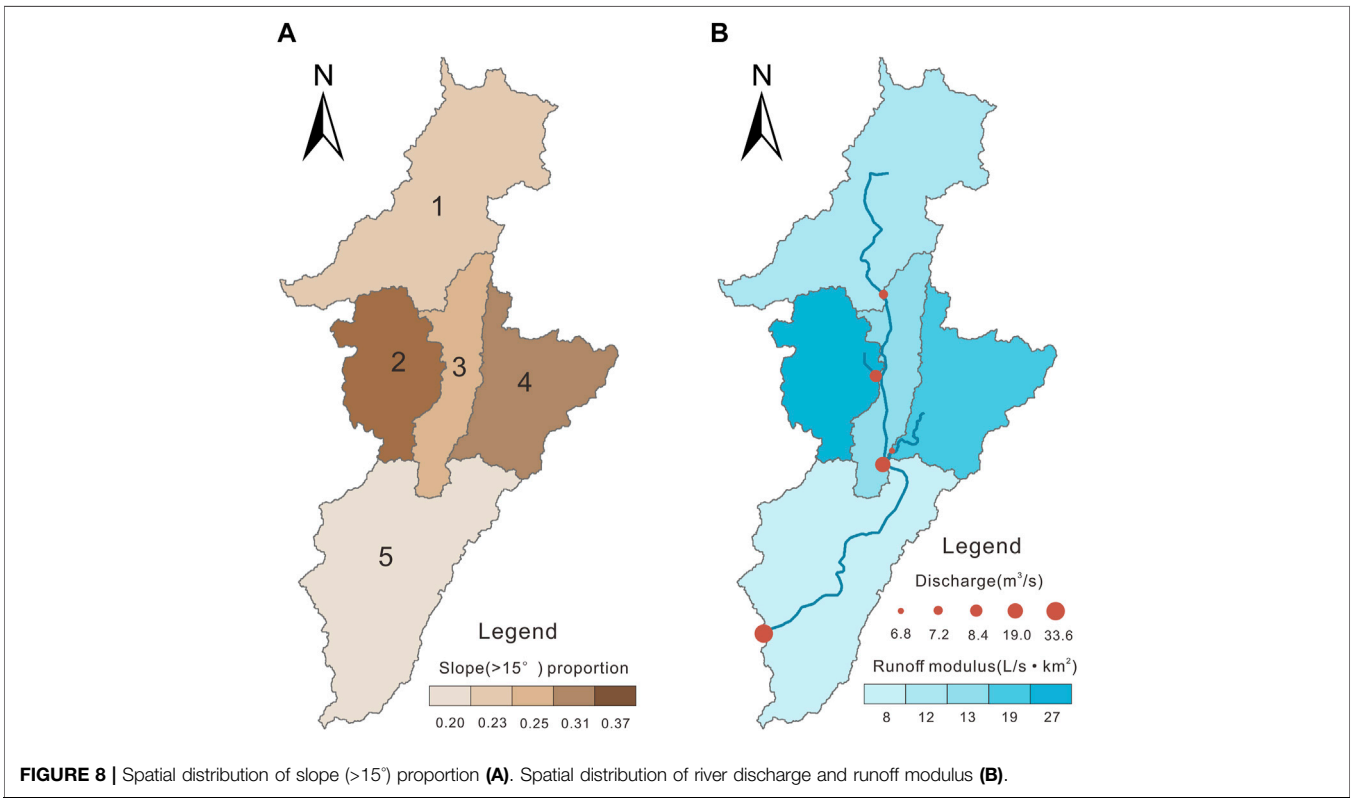

FIGURE 8 | Spatial distribution of slope (>15°) proportion **(A)**. Spatial distribution of river discharge and runoff modulus **(B)**.

A runoff modulus is a basic hydrogeological parameter, which can compare runoff in different subbasins. The slope is a land feature, and the slope above 15° is classified as a steep slope. We calculated the runoff modulus and the proportion of slope above 15° for each subbasin (as shown in **Figure 8**). In subbasin No. 2, the runoff modulus is 27 L/s·km^2, the slope ratio is 0.37, and both the parameters are the largest. In subbasin No. 5, the runoff modulus is 8 L/s·km^2, the slope ratio is 0.20, and both the parameters are the smallest. Comparing the runoff modulus with the slope distribution in **Figure 8**, the larger the proportion of steep slopes, the larger the runoff modulus. As the slope increases, the velocity of surface runoff becomes faster, the duration of runoff generation on the slope is short, and the infiltration amount is small. On the contrary, the runoff is large.

The distribution of hydrological components is influenced by land use. The land use types are mainly farmland (AGRL), forest land (FRST), and grassland (PAST) in the study area. The surface runoff depth and baseflow depth generated by these three land use types in each subbasin were calculated. **Figure 9** shows that for surface runoff depth, AGRL > FRST > PAST. However,

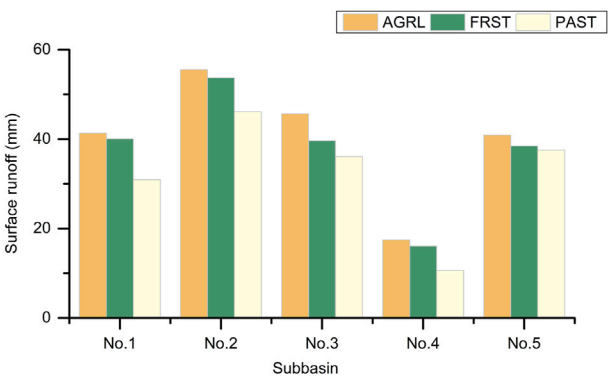

FIGURE 9 | Average annual surface runoff depth in each subbasin under different land use types.

Figure 10 shows that for baseflow depth, FRST > PAST > AGRL. It can be seen that the surface runoff and baseflow are related to the land use types. Farmland is more likely to produce

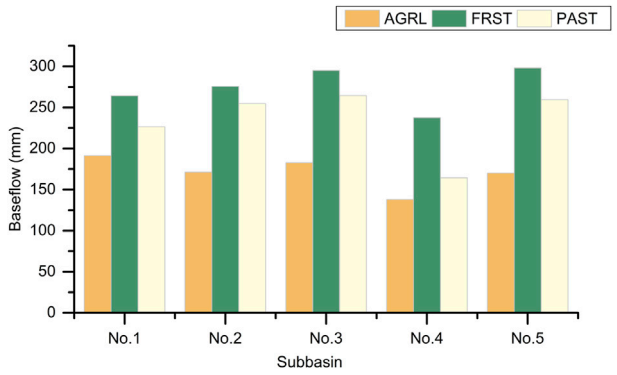

FIGURE 10 | Average annual baseflow depth in each subbasin under different land use types.

surface runoff, and forest land produces more baseflow due to water conservation of vegetation. The root system of crops is underdeveloped and cannot consolidate the soil well. The surface runoff will wash the surface soil of farmland and generate more runoff. The phenomenon of soil physical crusting often occurs on the surface of overcultivated land, which will also increase the runoff. The forest root system is very developed, and forest soil has a good structure and porosity; so the infiltration velocity is fast, which plays the role of intercepting surface runoff and generating baseflow.

DISCUSSION

For the traditional hydrological process, streamflow is the sum of surface flow, lateral flow, and baseflow, but in our study area, the unique karst topography differentiates the process and a part of water enters the deep aquifer through high-permeability channels and forms preferential flow (Rimmer and Salingar 2006). Using the model to accurately show the surface runoff and baseflow in karst areas is useful for analyzing the quick and large response of groundwater discharge to rainfall events, karst underground floods, the transport of sediment, and organic material.

In this study, we used the pond module in SWAT to simulate sinkholes. After improvement, the indicators of NSE and R^2 have been strengthened in the 2012–2015 monthly scale simulation. In the improved model, the simulated flow line is closer to the observed data, especially the decrease can be observed at the peak value of the surface runoff at the Xiqiao Hydrological Station. For subbasins No. 1, No. 4, and No. 5, the surface runoff was relatively decreased and baseflow was relatively increased after improvement. This change was due to the addition of the pond module, which made a part of surface water to quickly replenish groundwater through karst sinkholes. Moreover, in the steady stage of the flood season, the flow process line rises, which reflects that the baseline was elevated. It can be concluded that the addition of pond module and characterization of karst morphology will change the amount of surface water and groundwater resource allocation in the modified subbasin, the flow distribution between surface runoff and baseflow was changed, and the improved model outperformed the original model in terms of both the model fitting effect and model quality and enabled to simulate the recharge process and the hydrologic cycle of the sinkholes.

During the simulation, R^2 and NSE in the validation period were better than the calibration period because R^2 and NSE are sensitive to the peak value of river discharge. However, the simulated peak value in June 2012 was much greater than the observed value. Although the improved model weakened the surface runoff, it still overpredicted this value, so R^2 and NSE in the calibration period are smaller than the validation period. The reason for this phenomenon is the heavy rainfall in June 2012, which reached 325 mm. The SWAT model is sensitive to rainfall, and the simulated curve reflects this peak value of discharge caused by heavy rainfall. But, before six months, this heavy rainfall is the dry season, with an average of only 22 mm of rainfall per month. The heavy rainfall recharged the soil water and karst fissures first so that the observed value did not show a peak value of discharge.

The karst area simulation is still in the exploration stage, especially the application results of the SWAT model to depict karst morphology are not abundant. In Southwest China, some scholars exposed the karst underground river to the surface and some scholars generated HRUs according to karst characteristics, but these studies did not involve the hydrologic process of sinkholes (Yu et al., 2012; Zhang et al., 2020). Outside of Southwest China, Palanisamy and Workman, (2014) proposed KarstSWAT to simulate sinkholes located on the streambed in the Cane Run watershed. They simulated the horizontal hydrologic process of flow from the stream channel into the deep aquifer through sinkholes and then transferred from karst conduits to spring. But in our study, sinkholes are located all over the watershed, and we focused on the vertical hydrologic process of sinkholes rapidly diverting the surface water to the shallow aquifer through large hydraulic conductivity and short delay time. We used the pond module in SWAT to simulate sinkholes as same as Baffaut and Benson, (2009), and their study specifically analyzed the flow simulation characteristic of the improved SWAT model in southwest Missouri. In our study, we further defined a specific value of delay time in the pond and compared the quantity changes of hydrology components surface runoff depth and baseflow depth before and after improvement and analyzed the water balance relationship. This method is suitable for any karst area with sinkholes because the area and volume of sinkholes can be obtained by remote sensing interpretation or field investigation in any study area, and the pond module can generalize the sinkhole characteristics and describe the vertical connection between the surface and underground. We successfully simulated sinkholes in Southwest China, which also proved that this method can be applied to karst landscapes in different regions. In addition, field investigation of karst sinkholes is an arduous task (Bakalowicz 2005; Zisman et al., 2013). We applied the sinkhole parameters analyzed by DEM to the model and obtained good results, which provided a method for the simulation of karst areas with few field investigation data. We aimed at the source area of the

South Panjiang River in this study. It is necessary to further analyze the distribution situation of the sinkholes in the whole SNPB and popularize this method to describe the karst characteristic in more detail.

CONCLUSION

In this study, we conceptualized the sinkholes as the pond with large hydraulic conductivity at the bottom, and the fast recharge response of karst was realized by modifying the groundwater delay time of the algorithm with the SWAT model. The improved model was fitted with the measured data of the Xiqiao Hydrological Station, and it was verified that R^2 and NSE can achieve satisfactory results. The surface runoff of karst subbasins No. 1, No. 4, and No. 5 with the pond module was significantly decreased by 21, 47, and 36% corresponding to the PND_FR values 0.21, 0.47, and 0.36, respectively. The baseflow of the subbasins was increased significantly, and the pond module also made a portion of lateral flow become baseflow. After the improvement, the evaluation factor R^2 of the Xiqiao station increased from 0.70 to 0.74 and NSE increased from 0.35 to 0.61 during the calibration period. In the validation period, the R^2 increased from 0.76 to 0.83 and NSE increased from 0.66 to 0.79. Using the improved model to explore the spatial distribution of hydrological components, it was found the runoff modulus in the study area has a positive correlation related to the slope (>15°) proportion, the baseflow depth and surface runoff depth are related to the land use types, farmland produces more surface runoff, and forest land produces more baseflow. This study proved that the improved model simulates sinkholes successfully and has a better effect than the original model. This method can describe the preferential flow of the karst sinkhole and the reallocation of surface water and groundwater.

DATA AVAILABILITY STATEMENT

The original contributions presented in the study are included in the article/supplementary material, further inquiries can be directed to the corresponding author.

AUTHOR CONTRIBUTIONS

YZ: drafting the manuscript. LZ: supervision and data curation. JC: investigation and data collection of the study area. YW: creation of models.

FUNDING

This study was supported by the "Study on nonlinear Features of Water Exchange between Conduit and Matrix in Karst dual Water-bearing Medium" from "The National Science Fund for Distinguished Young Scholars" (42102296).

REFERENCES

Abbaspour, K. C. (2015). *SWAT-CUP: SWAT Calibration and Uncertainty Programs*. Switzerland: EAWAG: Dübendorf, 130.

Anand, J., Gosain, A. K., and Khosa, R. (2018). Prediction of Land Use Changes Based on Land Change Modeler and Attribution of Changes in the Water Balance of Ganga Basin to Land Use Change Using the SWAT Model. *Sci. Total Environ.* 644 (dec.10), 503–519. doi:10.1016/j.scitotenv.2018.07.017

Arnold, J. G., Srinivasan, R., Muttiah, R. S., and Williams, J. R. (1998). Large Area Hydrologic Modeling and Assessment Part I: Model Development. *JAWRA J. Am. Water Resour. Assoc.* 34 (1), 1–17. doi:10.1111/j.1752-1688.1998.tb05961.x

Bakalowicz, M. (2005). Karst Groundwater: a Challenge for New Resources. *Hydrogeol. J.* 13 (1), 148–160. doi:10.1007/s10040-004-0402-9

Baker, T. J., and Miller, S. N. (2013). Using the Soil and Water Assessment Tool (SWAT) to Assess Land Use Impact on Water Resources in an East African Watershed. *J. Hydrology* 486, 100–111. doi:10.1016/j.jhydrol.2013.01.041

Cahalan, M. D., and Milewski, A. M. (2015). Sinkhole Formation Mechanisms and Geostatistical-Based Prediction Analysis in a Mantled Karst Terrain. *Catena* 165, 333–344.

C. Baffaut, C., and V. W. Benson, V. W. (2009). Modeling Flow and Pollutant Transport in a Karst Watershed with SWAT. *Trans. ASABE* 52 (2), 469–479. doi:10.13031/2013.26840

Deni-Juki, V., and Juki, D. (2003). Composite Transfer Functions for Karst Aquifers. *J. Hydrology* 274 (1-4), 0–94.

D. M. Amatya, D. M., M. Jha, M., A. E. Edwards, A. E., D. R. Hitchcock, T. M., and Hitchcock, D. R. (2011). Swat-Based Streamflow and Embayment Modeling of Karst-Affected Chapel Branch Watershed, South Carolina. *Trans. Asabe* 54 (4), 1311–1323. doi:10.13031/2013.39033

D. N. Moriasi, D. N., J. G. Arnold, J. G., M. W. Van Liew, M. W. V., R. L. Bingner, R. L., T. L. Veith, R. D., and Veith, T. L. (2007). Model Evaluation Guidelines for Systematic Quantification of Accuracy in Watershed Simulations. *Trans. Asabe* 50 (3), 885–900. doi:10.13031/2013.23153

Felton, G. K., and Currens, J. C. (1994). Peak Flow Rate and Recession-Curve Characteristics of a Karst Spring in the Inner Bluegrass, Central Kentucky. *J. Hydrology* 162 (1–2), 99–118. doi:10.1016/0022-1694(94)90006-x

Ford, D., and Williams, P. (2007). *Karst Hydrogeology and Geomorphology*. American Geophysical Union.

Halihan, T., and Wicks, C. M. (1998). Modeling of Storm Responses in Conduit Flow Aquifers with Reservoirs. *J. Hydrology* 208 (1-2), 82–91. doi:10.1016/s0022-1694(98)00149-8

Hao, F. H., Cheng, H. G., and Yang, S. T. (2006). *Non-point Source Pollution Model*. Beijing: China Environ Science Press.

Hartmann, A., Goldscheider, N., Wagener, T., Lange, J., and Weiler, M. (2014). Karst Water Resources in a Changing World: Review of Hydrological Modeling Approaches. *Rev. Geophys.* 52 (No.3), 218–242. doi:10.1002/2013rg000443

Hartmann, A., Lange, J., Weiler, M., Arbel, Y., and Greenbaum, N. (2012). A New Approach to Model the Spatial and Temporal Variability of Recharge to Karst Aquifers. *Hydrology Earth Syst. Sci.* 16 (No.7), 2219–2231. doi:10.5194/hess-16-2219-2012

Hu, C., Hao, Y., Yeh, T.-C. J., Pang, B., and Wu, Z. (2008). Simulation of Spring Flows from a Karst Aquifer with an Artificial Neural Network. *Hydrol. Process.* 22 (5), 596–604. doi:10.1002/hyp.6625

Huang, Z., Yeh, P. J.-F., Pan, Y., Jiao, J. J., Gong, H., Li, X., et al. (2019). Detection of Large-Scale Groundwater Storage Variability over the Karstic Regions in Southwest China. *J. Hydrology* 569, 409–422. doi:10.1016/j.jhydrol.2018.11.071

Lallahem, S., Mania, J., Hani, A., and Najjar, Y. (2005). On the Use of Neural Networks to Evaluate Groundwater Levels in Fractured Media. *J. Hydrology* 307 (1-4), 92–111. doi:10.1016/j.jhydrol.2004.10.005

Lauber, U., Ufrecht, W., and Goldscheider, N. (2014). Spatially Resolved Information on Karst Conduit Flow from In-Cave Dye-Tracing. *Hydrology Earth Syst. Sci. Discuss.* 10 (9), 11311–11335. doi:10.5194/hess-18-435-2014

Li, G., Rubinato, M., Wan, L., Wu, B., Fang, J. J., and Zhou, J. (2020). Preliminary Characterization of Underground Hydrological Processes under Multiple Rainfall Conditions and Rocky Desertification Degrees in Karst Regions of Southwest China. *Water* 12 (2), 594. doi:10.3390/w12020594

Liang, G., Qin, X., Cui, Y., Chen, S., and Huang, Q. (2020). Improvement and Application of a Distributed Hydrological Model in Karst Regions. *Hydrogeology Eng. Geol.* 47 (2), 60–67.

Liu, J., Ding, H., Xiao, M., Xu, Z.-Y., Su, Y. Z.-H., Zhao, L., et al. (2020). Climatic Variabilities Control the Solute Dynamics of Monsoon Karstic River: Approaches from C-Q Relationship, Isotopes, and Model Analysis in the Liujiang River. *Water* 12 (3), 862. doi:10.3390/w12030862

Makropoulos, C., Koutsoyiannis, D., Stanić, M., Djordjević, S., Prodanović, D., Dašić, T., et al. (2008). A Multi-Model Approach to the Simulation of Large Scale Karst Flows. *J. Hydrology* 348 (3–4). doi:10.1016/j.jhydrol.2007.10.011

Malagò, A., Efstathiou, D., Bouraoui, F., Nikolaidis, N. P., Franchini, M., Bidoglio, G., et al. (2016). Regional Scale Hydrologic Modeling of a Karst-Dominant Geomorphology: The Case Study of the Island of Crete. *J. Hydrology* 540, 64–81.

Martínez-Salvador, A., and Conesa-García, C. (2020). Suitability of the SWAT Model for Simulating Water Discharge and Sediment Load in a Karst Watershed of the Semiarid Mediterranean Basin. *Water Resour. Manag.* 34 (2), 785–802.

Martínez-Santos, P., and Andreu, J. M. (2010). Lumped and Distributed Approaches to Model Natural Recharge in Semiarid Karst Aquifers. *J. Hydrology* 388 (3), 389–398.

Meng, H., and Wang, L. (2010). Advance in Karst Hydrological Model. *Prog. Geogr.* 29 (11), 1311–1318.

Meng, X. Y., and Wang, H. (2017). Significance of the China Meteorological Assimilation Driving Datasets for the SWAT Model (CMADS) of East Asia. *Water* 9 (10), 5. doi:10.3390/w9100765

Moreira, L. L., Schwamback, D., and Rigo, D. (2018). Sensitivity Analysis of the Soil and Water Assessment Tools (SWAT) Model in Streamflow Modeling in a Rural River Basin. *Revista Ambiente Água* 13 (6), e2221. doi:10.4136/ambi-agua.2221

Neitsch, S. L., Arnold, J. G., Kiniry, J. R., Williams, J. R., and King, K. W. (2002). *Soil and Water Assessment Tool Theoretical Documentation*. version 2000.

Nhu, V. H., Rahmati, O., Falah, F., Shojaei, S., Al-Ansari, N., Shahabi, H., et al. (2020). Mapping of Groundwater Spring Potential in Karst Aquifer System Using Novel Ensemble Bivariate and Multivariate Models. *Water* 12 (4), 25. doi:10.3390/w12040985

Nie, W., Yuan, Y., Kepner, W., Nash, M. S., Jackson, M., and Erickson, C. (2011). Assessing Impacts of Landuse and Landcover Changes on Hydrology for the Upper San Pedro Watershed. *J. Hydrology* 407 (1-4), 105–114. doi:10.1016/j.jhydrol.2011.07.012

Palanisamy, B., and Workman, S. R. (2014). Hydrologic Modeling of Flow through Sinkholes Located in Streambeds of Cane Run Stream, Kentucky. *J. Hydrologic Eng.* 20 (5), 04014066.

Piniewski, M., Bieger, K., and Mehdi, B. (2019). Advancements in Soil and Water Assessment Tool (SWAT) for Ecohydrological Modelling and Application. *Ecohydrol. Hydrobiology* 19, 179–181. doi:10.1016/j.ecohyd.2019.05.001

Rahman, M. M., Thompson, J. R., and Flower, R. J. (2016). An Enhanced SWAT Wetland Module to Quantify Hydraulic Interactions between Riparian Depressional Wetlands, Rivers and Aquifers. *Environ. Model. Softw.* 84, 263–289. doi:10.1016/j.envsoft.2016.07.003

Rao, A. S., and Saxton, K. E. (1995). Analysis of Soil Water and Water Stress for Pearl Millet in an Indian Arid Region Using the SPAW Model. *J. Arid Environ.* 29 (2), 155–167. doi:10.1016/s0140-1963(05)80086-2

Rimmer, A., and Salingar, Y. (2006). Modelling Precipitation-Streamflow Processes in Karst Basin: The Case of the Jordan River Sources, Israel. *J. Hydrology* 331 (3-4), 524–542. doi:10.1016/j.jhydrol.2006.06.003

Salerno, F., and Tartari, G. (2009). A Coupled Approach of Surface Hydrological Modelling and Wavelet Analysis for Understanding the Baseflow Components of River Discharge in Karst Environments. *J. Hydrology* 376 (1–2), 295–306. doi:10.1016/j.jhydrol.2009.07.042

Samuels, R., Rimmer, A., Hartmann, A., Krichak, S., and Alpert, P. (2010). Climate Change Impacts on Jordan River Flow: Downscaling Application from a Regional Climate Model. *J. Hydrometeorol.* 11 (4), 860–879. doi:10.1175/2010jhm1177.1

Schomberg, J. D., Host, G., Johnson, L. B., and Richards, C. (2005). Evaluating the Influence of Landform, Surficial Geology, and Land Use on Streams Using Hydrologic Simulation Modeling. *Aquat. Sci.* 67 (4), 528–540. doi:10.1007/s00027-005-0785-2

Sezen, C., Bezak, N., Bai, Y., and Šraj, M. (2019). Hydrological Modelling of Karst Catchment Using Lumped Conceptual and Data Mining Models. *J. Hydrology* 576, 98–110. doi:10.1016/j.jhydrol.2019.06.036

Shang, X., Jiang, X., Jia, R., and Wei, C. (2019). Land Use and Climate Change Effects on Surface Runoff Variations in the Upper Heihe River Basin. *Water* 11 (2), 344. doi:10.3390/w11020344

Thavhana, M. P., Savage, M. J., and Moeletsi, M. E. (2018). SWAT Model Uncertainty Analysis, Calibration and Validation for Runoff Simulation in the Luvuvhu River Catchment, South Africa. *Phys. Chem. Earth, Parts A/B/C* 105, 115–124. doi:10.1016/j.pce.2018.03.012

Villamizar, S. R., Pineda, S. M., and Carrillo, G. A. (2019). The Effects of Land Use and Climate Change on the Water Yield of a Watershed in Colombia. *Water* 11 (2), 285. doi:10.3390/w11020285

Valdes-Abellan, J., Pla, C., Fernandez-Mejuto, M., and Andreu, J. M. (2018). Validating the KAGIS Black-Box GIS-Based Model in a Mediterranean Karst Aquifer: Case of Study of Mela Aquifer (SE Spain). *Hydrol. Process.* 32 (16), 2584–2596. doi:10.1002/hyp.13215

Veress, M. (2020). Karst Types and Their Karstification. *J. Earth Sci.* 31 (3), 621–634. doi:10.1007/s12583-020-1306-x

Wang, Y., Shao, J., Su, C., Cui, Y., and Zhang, Q. (2019). The Application of Improved SWAT Model to Hydrological Cycle Study in Karst Area of South China. *Sustainability* 11 (18), 5024. doi:10.3390/su11185024

Xie, K., Chen, H., Qiu, Y., Kim, J.-S., Yoon, S.-K., Lin, Y., et al. (2021). Exploring and Predicting the Individual, Combined, and Synergistic Impact of Land-Use Change and Climate Change on Streamflow, Sediment, and Total Phosphorus Loads. *Front. Environ. Sci.* 9, 726793. doi:10.3389/fenvs.2021.726793

Yu, D., Sun, L., Yu, J., and Wang, Z. (2012). Simulation on Soil Erosion and Streamflow in Maotiaohe Watershed of Guizhou Province Based on SWAT Model. *Chin. Agric. Sci. Bull.* 28 (17), 256–261.

Zhang, C., Zhang, F., Geng, X., Ji, J., and Chen, Y. (2020). Generalization Method of Karst Underground River in SWAT:An Example of the Daotian River Watershed in Bijie, Guizhou. *Carsologica Sin.* 39 (5), 665–672.

Zhou, S., Zhang, W., and Guo, Y. (2020). Impacts of Climate and Land-Use Changes on the Hydrological Processes in the Amur River Basin. *Water* 12 (1), 76.

Zisman, E. D., Wightman, M., and Kestner, J. (2013). Sinkhole Investigation Methods: the Next Step after Special Publication No. 57. *Carbonates Evaporites* 28 (1-2), 103–109. doi:10.1007/s13146-013-0145-6

Conflict of Interest: YW was employed by the company Hebei Hydrological Engineering Geological Survey Institute Co, Ltd.

The remaining authors declare that the research was conducted in the absence of any commercial or financial relationships that could be construed as a potential conflict of interest.

frontiers | Frontiers in Environmental Science

ORIGINAL RESEARCH
published: 10 August 2022
doi: 10.3389/fenvs.2022.946914

Regional Groundwater Water Quality Assessment and Contamination Source Identification by a Self-Organizing Map and Entropy Method in Pinggu Basin, Northeast Beijing

Shaojie Lv[1], Zongwen Zhang[2], Ning Sun[2], Zheming Shi[1,3]*, Jia Li[1] and Shen Qu[1]*

[1]MOE Key Laboratory of Groundwater Circulation and Environmental Evolution, China University of Geosciences, Beijing, China, [2]Chinese Academy of Environmental Planning, Beijing, China, [3]School of Water Resources and Environment, China University of Geosciences, Beijing, China

OPEN ACCESS

Edited by:
Yong Xiao,
Southwest Jiaotong University, China

Reviewed by:
Shiyang Yin,
North China Electric Power University, China
Qichen Hao,
Chinese Academy of Geological Sciences, China

***Correspondence:**
Zongwen Zhang
zhangzw@caep.org.cn
Zheming Shi
szm@cugb.edu.cn

Specialty section:
This article was submitted to Freshwater Science, a section of the journal Frontiers in Environmental Science

Received: 18 May 2022
Accepted: 21 June 2022
Published: 10 August 2022

Citation:
Lv S, Zhang Z, Sun N, Shi Z, Li J and Qu S (2022) Regional Groundwater Water Quality Assessment and Contamination Source Identification by a Self-Organizing Map and Entropy Method in Pinggu Basin, Northeast Beijing. Front. Environ. Sci. 10:946914. doi: 10.3389/fenvs.2022.946914

Groundwater quality assessment is important for understanding the suitability of groundwater resources for various purposes. Although many different methods have been proposed for this purpose, few methods have considered the spatial variation of groundwater components during the assessments. In this study, we proposed to combine the self-organizing map (SOM) and entropy-based weight determining method to assess groundwater quality. Totally, 955 water samples taken from 58 wells during 2010–2017 were used in the study. 22 hydrochemical components (K^+, Na^+, Ca^{2+}, Mg^{2+}, NH_4^+, Cl^-, SO_4^{2-}, F^-, NO_3^-, Fe^{2+}, Fe^{3+}, Al, etc.) were used in the assessment for each sample. These sampling points can be classified into five clusters, which may be affected by four different sources: landfill sources (cluster 3), industrial and agricultural sources (cluster 5), and domestic sewage discharge sources (clusters 1, 2, and 4). The scores of the water quality of the five clusters that were calculated by the entropy method are 0.2658, 0.2634, 0.5737, 0.2608, and 0.5718, indicating that the groundwater affected by domestic sewage discharge sources (clusters 1, 2, and 4) are better than other two sources (clusters 3 and 5) in the study area. The results of this study provide insights for the protection of groundwater resources and the treatment of groundwater pollution in the future.

Keywords: self-organizing map (SOM), entropy method, water quality, groundwater, contamination

1 INTRODUCTION

Groundwater is the key water source for food, energy, and ecosystems especially in arid or semi-arid area (Gleeson et al., 2016). As part of the North China Plain, Beijing suffers from the semi-arid climate and is highly dependent on the groundwater as its water supply (Li et al., 2020b). In order to cope with the water resource shortage in Beijing, multiple emergency groundwater supply sources have been constructed in the phreatic aquifer in the Pinggu Basin, northeast of Beijing (Li et al., 2020a). Thus, groundwater resource protection is especially important in the Pinggu Basin. However,

rapid urbanization and industrialization in recent years in this area have put a serious threat on the groundwater quality and the groundwater supply. Only a few studies have investigated the hydrochemical characteristics and the groundwater quality in these areas (Jiang et al., 2017; Li et al., 2020a). Jiang et al. (2017) studied the major ions of groundwater in the shallow aquifer of the Pinggu Basin and found that water–rock interaction was the dominated process that controlled the hydrochemical evolution. Recently, Li et al. (2020a) investigated the spatial and temporal evolutions of groundwater hydrochemical monitoring data by the SOM method and found that Cl^-, SO_4^{2-}, NO_3^-, and NH_4^+ increased in 2017 compared with that of 2014, but the groundwater quality around this area has not been evaluated in an integrative way.

Assessing groundwater quality usually needs to deal with a large dataset as there are complex chemical components in the groundwater (Sanchez-Martos et al., 2002) and multiple factors need to be considered when performing the assessment (Li et al., 2014). The Water Quality Index (WQI) method is an efficient way of assessing the influence of individual parameters on the overall groundwater quality, and thus has become the popular method for groundwater quality assessment (Vasanthavigar et al., 2010; Li et al., 2014). However, the determination of the weight in this method is somewhat subjective which may affect the result of the groundwater quality (Amiri et al., 2014). In order to solve this issue, an information entropy-based weight determining method was proposed in the assessment (Li et al., 2011). Multivariate statistical analysis methods have also been widely used in the groundwater quality assessment as they are powerful in dimension reduction and classification (Omo-Irabor et al., 2008). However, such methods do not consider the spatial and temporal variations of the groundwater components and the randomicity, complexity, and non-linearity in the environment issues (Bodrud-Doza et al., 2016). Artificial intelligence (AI) algorithms such as self-organizing maps (SOM) have been introduced into the groundwater quality assessment recently and they have shown that they can be used in the groundwater quality assessment effectively (Gharibi et al., 2012; Nguyen et al., 2015). However, only individual weight was considered in the SOM method, while missing the integrative impact on the overall quality.

In this study, we proposed to combine both the information entropy-based weight determining method and the SOM method to assess the groundwater quality in the Pinggu Basin during 2010–2017. Such a method considered both the overall quality by individual parameters and individual wells, and also integrated the spatial and temporal variations, thus, we consider it is useful in assessing the regional groundwater quality, especially when the dataset is large.

2 MATERIALS AND METHODS

2.1 Study Area and Data

As one of the districts of Beijing, the Pinggu Basin is located on the transitional area of the Yanshan Mountains and the North China Plain (116°58′37″-117°18′42″N, 40°2′19″-40°11′48″E). The basin is a rifted-basin with a distance of 32 km across east to west and 15 km across north to south, and it has an area of 402 km^2 (**Figure 1**). The basin is an individual intermontane basin hydrogeological unit with a limestone aquifer as the major aquifer in the mountain area and a Quaternary sediment pore aquifer in the plain area. Groundwater is mainly recharged by meteoric precipitation, surface water leakage, and lateral flow. The major flow direction is consistent with the river direction–flow from north to south or from northeast to southwest. Groundwater recharge sources in the study area are mainly composed of atmospheric precipitation infiltration recharge, surface water infiltration recharge such as river channels, and a lateral replenishment of the piedmont zone. Moreover, leakage from the Haizi Reservoir, flood infiltration, and return infiltration of canals are also important sources of supply. Groundwater is mainly discharged by human exploitation.

The aquifers in the plain area can be divided into four different aquifers. The lower boundary of the first layer has a depth of 51.9 m, the second aquifer has a depth of 100 m, 180 m for the third aquifer, and below that is the fourth aquifer. 58 groundwater-monitoring wells are constructed in the basin (**Figure 1**): 32 wells located in the first layer of the phreatic aquifer, 14 wells located in the second aquifer, 8 wells located in the third aquifer, and 4 wells in the fourth aquifer. Water samples were collected and analyzed by the Beijing Institute of Hydrogeology and Engineering Geology every 3 months from October 2010 to June 2017. These water samples were used to analyze the following 22 parameters: K^+, Na^+, Ca^{2+}, Mg^{2+}, NH_4^+, HCO_3^-, CO_3^{2-}, Cl-, SO_4^{2-}, F^-, NO_3^-, TDS, CO_2, Fe^{2+}, Fe^{3+}, oxygen consumption, Al, nitrite, total hardness, pH, electrical conductivity (EC), and total alkalinity. For these ions with concentrations below the limit of detection, we do not involve them in the further study. As for the other ions, we compared them with the environmental background value and chose those parameters for the further study. Before sampling, the *in-situ* measurements of pH, TDS, CO_2, oxygen consumption, and electrical conductivity were performed by portable meters. Sample bottles (clean polyethylene bottles) were rinsed by the same groundwater 2–3 times, and all samples were filtered with 0.45 m filter membranes and collected in the sample bottles. And, nitric acid was added to the sample used to test cations to pH < 2. After that, all samples were stored in ice boxes at 4°C until the laboratory analysis. An inductively coupled plasma spectrometer (ICP-9100) was used to analyze the concentrations of ions (K^+, Na^+, Ca^{2+}, and Mg^{2+}). Ion chromatography (ICS-2500) was used to determine the concentrations of Cl^-, SO_4^{2-}, F^-, and NH_4^+. The concentrations of Fe^{2+}, Fe^{3+}, NH_4^+, and NO_3^- and nitrite were measured by using a hash reagent. The concentrations of HCO_3^- were determined by acid–base titration **Figure 2**.

2.2 Materials and Method

SOM was employed to classify the groundwater samples. The classification results of the groundwater samples and the concentration distribution of various ions in each water sample were obtained, which were then used to identify pollution sources. Then, the entropy method was used to

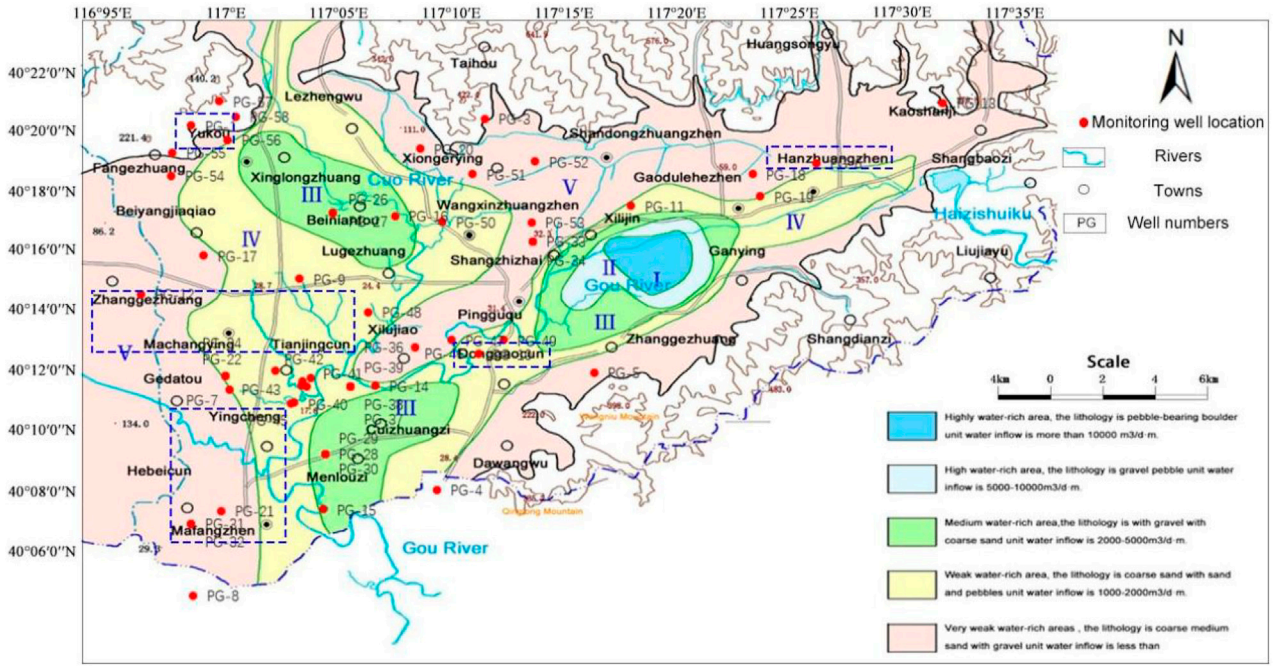

FIGURE 1 | Hydrogeologcial setting of the Pinggu Basin and location of the monitoring wells.

calculate the groundwater quality scores of all the water samples, and the water quality scores of the water samples were obtained statistically. Combined with the results of SOM and the entropy method, the water quality evaluation and pollution source identification analysis were carried out.

2.2.1 Entropy Method

Many different chemical parameters need to be considered in an overall groundwater quality assessment, and different water samples should also be considered in the spatial groundwater quality assessment. Thus, the weight of each parameter and water sample should be determined in the calculation. Currently, weight is usually given by the experts (Li et al., 2011) or calculated from the standard-exceeding rate. Those methods are either too subjective or miss the processes of interaction between multiple parameters. The information entropy method is an effective way to determine the weight in a complex, large dataset and also have been used in groundwater quality assessments. The concept of information entropy was first proposed by Shannon (Shannon, 1948), and it can be used as a measure of information or uncertainty. Thus, it is an efficient way of providing uncertainty and probability. Unlike the fuzzy synthetic evaluation methods that focus on the spatial characteristics of the groundwater quality, the entropy method can deal with both spatial and temporal groundwater quality data.

The algorithm of the entropy method can be realized by MATLAB programming. It can be realized by the following steps:

1) selecting n water samples (i = 1,2,. . .,n) and m chemical parameters (j = 1,2, . . . ,m),x_{ij} represents the j_{th} groundwater quality parameter of the i_{th} water sample.

2) Normalization of the chemical parameters. Because of the different units of chemical parameters, before using them to calculate the comprehensive index, we first do the normalization. That is, transform the absolute value of the index into the relative value, so as to solve the homogenization problem caused by different chemical parameter concentrations. Moreover, because of the different meanings of the positive index and negative index values, we use different algorithms to normalize the data for high and low indexes, the detail steps are as follow:

For the positive index:

$$x_{ij}^{'} = \frac{x_j - \mathbf{x}_{\min}}{x_{\max} - \mathbf{x}_{\min}} \tag{1}$$

For the negative index:

$$x_{ij}^{'} = \frac{\mathbf{x}_{\max} - x_j}{x_{\max} - \mathbf{x}_{\min}} \tag{2}$$

where x_j is the index value of j_{th} chemical parameter, $x_{\max}$ is the maximum for indicator j, $x_{\min}$ is the minimum for indicator j, and x_{ij}' is the standardized values.

3) Calculating the weight of the i_{th} water sample of j_{th} chemical parameters:

$$p_{ij} = \frac{x_{ij}^{'}}{\sum_{i=1}^{n} x_{ij}^{'}} \tag{3}$$

4) Calculation of entropy for the j_{th} chemical parameters:

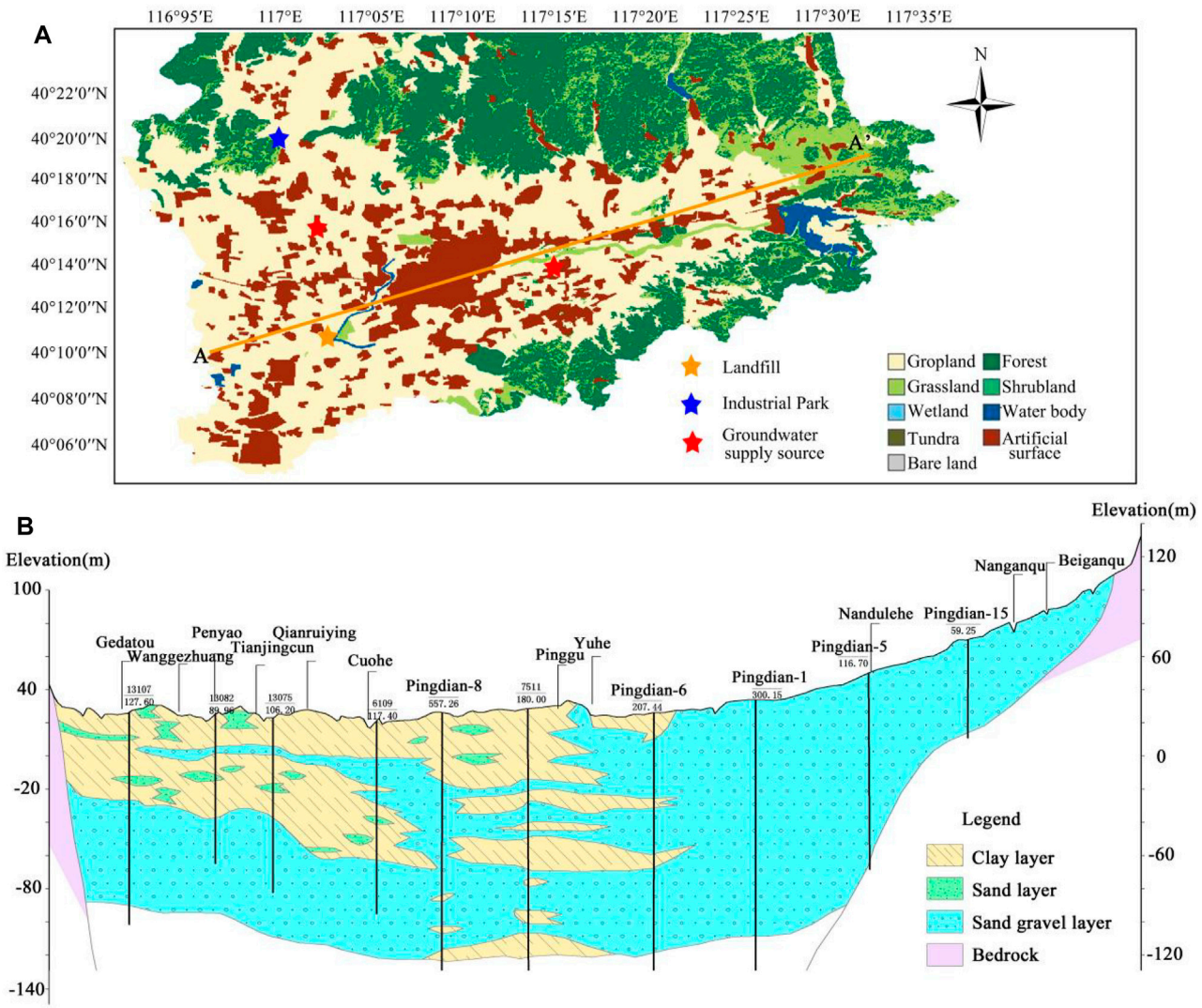

FIGURE 2 | (A) Land-use map of the Pinggu District, and A-A′ is the location of the geological profile; **(B)**The geological profile of the Pingu area, and the position is shown in **Figure 2A** (AA′).

$$e_j = -k\sum_{i=1}^{n} p_{ij}\ln\left(p_{ij}\right),\ k = \frac{1}{\ln(n)}, \tag{4}$$

n is the number of water samples, and p_{ij} is the specific weight of the chemical parameters.

5) Calculation of entropy redundancy for the chemical parameters:

$$d_j = 1 - e_j \tag{5}$$

The greater the difference of the index value j, the greater the left and right of the evaluation of the scheme, the smaller the entropy value, and the definition of the difference coefficient;

6) Weight evaluation:

$$W_j = \frac{d_j}{\sum_{j=1}^{m} d_j},\ j = 1, 2\cdots m \tag{6}$$

7) Computing a comprehensive score for each water sample:

$$S_i = \sum_{j=1}^{m} W_j \times p_{ij}\quad (i = 1, 2, \cdots n) \tag{7}$$

2.2.2 Self-Organizing Map (SOM)

The SOM method is an unsupervised neutral network algorithm proposed by Kohonen (Kohonen, 1995). It can project high-dimensional, complex data into a low-dimensional, regularly arranged map based on the data similarity (Jin et al., 2011).

Thus, it is an effective linear dimensionality reduction method (Choi et al., 2014) that has been widely used in data mining, classification, etc. One of the key purposes of the SOM method is to obtain the informative and physically explainable reference vectors (also known as weight vectors, prototype vectors, and code-book vectors). The map size determines the accuracy of the pattern recognition; however, topographical adjacency is further among the clusters. Thus, one should use the optimal size both for the pattern recognition and topographical proximity of the clusters (Nguyen et al., 2015). Here, we follow the previous study of the heuristic rule of $m = 5\sqrt{n}$ to determine the node of SOM (Li et al., 2020a), where n is the number of input data, m is the number of SOM node. And the ratio of the number of rows and columns can be determined by the square root of the ratio between the two biggest eigenvalues of the transformed data (Garcı´a and González, 2004). Thus, the structure of the SOM is determined, and the reference vector can also be obtained. The SOM algorithm can be carried out by using the MATLAB software, which usually consists of the following steps:1) setting variables and parameters, including input vectors $X(n)$, number of iterations N and time step; 2)Setting the initial value of the weight vector $W_i(n)$ and learning the initial value of the rate η_0, and normalizing the weight vector and the inputting vector; 3) Constructing the structure and selecting the training water sample X; 4) From the input layer to calculate the domain function $e^{-d^2/2\sigma^2}$ ($\sigma = \sigma_0 e^{-t/2}$) and the Euclidean distance between W_i and X ; 5) According to the Euclidean minimum principle, finding the best matching unit of the input water sample (BMU):

$$\|X - W_p\| = \min\|X - W_i\| = \min[d_i] \quad i = 1, 2, ..., m \tag{8}$$

Choosing the winning neuron p through competitive learning.6) Updating the BMU and its adjacent neurons to the input water sample and calculating the weight vectors for each time step as follows:

$$W(t) = W(t-1) + \eta e^{-d^2/2\sigma^2}\left(X(i) - W(j)\right) \tag{9}$$

7) Iteration learning rate $\eta = \eta_0 e^{-t/1000}$ and topology fields, and re-specify the weights after learning; check if the number of iterations n exceeds N, if exceeded, return to step 3, otherwise, end of the processes.

2.2.3 Evaluation Method of Water Quality Combined With SOM and the Entropy Method

The monitoring wells are distributed in different areas of the Pinggu Basin, thus the results obtained directly by clustering cannot verify their rationality. Here, we evaluated the water quality of all the water samples first, and then clustered the hydrochemical characteristics and classification of the water samples by the SOM method. Through the analysis of water quality and hydrochemical characteristics, the rationality of the method and the accuracy of the results are verified.

First, all water samples 955) were screened for outliers or missing data, and we compared them with the background values of each chemical component. If five or more chemical components in each water sample were below the background value, the water sample data were excluded. Because the Cr^{6+}, manganese, arsenic, mercury, volatile phenol, cyanide and nitrite, volatile phenol, cyanide, and nitrite in many water samples are all below the background value, we ignored these water samples in the study in order to ensure the weight value of the important chemical components. As a result, 533 samples were selected from 955 water samples.

Among the 533 water samples, many of them were sampled quarterly from the same monitoring well in the same year, while some monitoring wells only had one water sample in that year. In order to prevent the duplication and superposition of the samples, the average value of a single monitoring well data for each year (the average of quarterly data for that year) was taken, and totally, 270 sample data were processed.

The entropy method is used to evaluate the groundwater quality of a single well. The weight of each chemical parameter in the calculation process is determined by the magnitude of change. The water quality score of each water sample is calculated by this method. The score is weighted by the numerical contribution of each pollution component. The higher the score, the greater the fraction of each pollution group or the contribution of the components, and the worse the water quality. The entropy method is calculated at the individual level, thus the whole situation of the water samples can be obtained by classifying 270 water samples by using the SOM method. The 270 water samples can be divided into multiple groups and distributed in the grid. The similar locations in the grids may indicate the same or similar hydrochemical types and the similar source of pollutants. After that, we compared the cluster result with the water quality score. Finally, the 270 water samples were classified into multiple clusters based on the SOM results, and the average score of the water samples in each large cluster was also calculated. The calculation process is shown in **Figure 3**.

3 RESULT

3.1 Assessment of the Water Quality in Individual Monitoring Wells

The entropy method determines the index weight according to the variation degree of each index value, and the deviation caused by human factors can be avoided. The result of the entropy method for the 58 wells is shown in **Table 1**. In **Table 1**, the score of each well stands for the water quality S_i of each well, with a higher score meaning worse water quality.

The scores of the monitoring well can be divided equally by using the entropy method. According to the distribution of monitoring wells in **Figure 1**, monitoring wells are roughly distributed in the northwest, west, south, east, and central areas of the study area. The scores could be divided into five clusters at equal intervals (**Table 2**). It can be found that the scores of PG-43 and PG-45 in the water quality of monitoring wells were much higher than those of other wells, and other values were all within the normal range.

According to **Table 1**, the group of groundwater wells (PG-45, 43, 27, 48, 56, 42, 26, 41, 40, and 58) shows the highest score. The

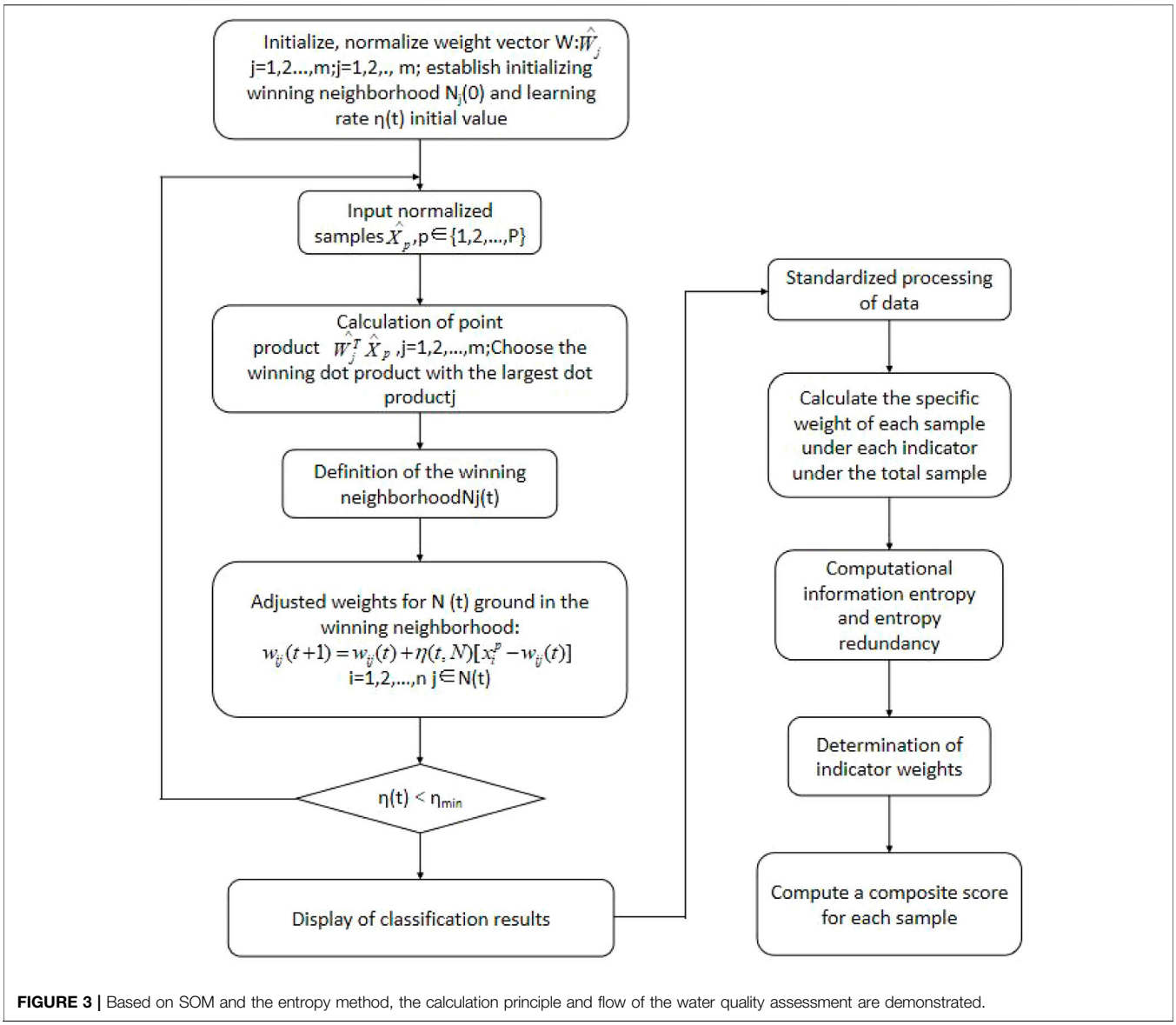

FIGURE 3 | Based on SOM and the entropy method, the calculation principle and flow of the water quality assessment are demonstrated.

smallest group of scores includes PG-47, 50, 16, 17, 10, 20, and 9 wells. The first group's wells PG-45, 43, 27, 48, 42, 26, 41, and 40 are located near the landfill (**Figures 1**, **2**), and PG-56 and 58 monitoring wells are mainly located near Yukou town. PG-10, 47, and 50 monitoring wells are located in the middle of the study area. PG-16, 17, 20, and 9 monitoring wells are located in the southern part of the study area. From the ranking of the water quality scores, the spatial distribution of the monitoring wells with similar water qualities is relatively concentrated.

Since we only evaluate the water quality of each single well, the overall water quality in the study area needs to be further studied. We analyzed the overall water quality by using a self-organizing mapping neural network (SOM) in the next section.

3.2 SOM Results

22 chemical parameters from 270 samples were used in the SOM analysis. Based on the aforementioned method, the number of SOM nodes is set as 100, the number of rows and columns are 10 and 10, respectively. This SOM method is used for the standard cluster analysis of groundwater chemical monitoring data. **Figure 3** shows the SOM mapping of 22 components and finally gets the training process. Each map represents a reference vector of 100 SOM nodes, where the reference vectors are standardized using color visualization graphs. The node representing a high value is crimson and a low value is dark blue, comparing each component of the SOM by color gradient, the correlation among each component could be identified.

The classification results of the water samples (**Figure 4**) and the topology results of each index (**Figure 5**) were obtained through the SOM analysis of the 270 water samples.

SOM combines the k-means clustering algorithm. The DB index (DBI for short) is the maximum value of the ratio between the inner distance and the distance between the classes, which is used to judge the clustering results. The smaller DBI value

TABLE 1 | Evaluation of the monitoring wells' quality.

Well number	S_i	Well number	S_i
PG-1	0.237	PG-29	0.343
PG-2	0.168	PG-30	0.382
PG-3	0.182	PG-31	0.246
PG-4	0.206	PG-32	0.271
PG-5	0.35	PG-33	0.51
PG-6	0.252	PG-34	0.439
PG-7	0.154	PG-35	0.419
PG-8	0.268	PG-36	0.459
PG-9	0.19	PG-37	0.491
PG-10	0.161	PG-38	0.459
PG-11	0.21	PG-39	0.364
PG-12	0.245	PG-40	0.642
PG-13	0.23	PG-41	0.709
PG-14	0.291	PG-42	0.725
PG-15	0.28	PG-43	1.673
PG-16	0.155	PG-45	3.2
PG-17	0.161	PG-47	0.128
PG-18	0.254	PG-48	0.803
PG-19	0.214	PG-49	0.433
PG-20	0.178	PG-50	0.142
PG-21	0.248	PG-51	0.328
PG-22	0.294	PG-52	0.506
PG-23	0.59	PG-53	0.404
PG-24	0.628	PG-54	0.254
PG-25	0.5	PG-55	0.271
PG-26	0.71	PG-56	0.769
PG-27	0.837	PG-57	0.369
PG-28	0.246	PG-58	0.637

indicates the smaller distance within the class, while the larger DBI value indicates the larger distance between the classes. This also shows that the clustering results are better.

In order to select the best number of clusters, the DBI value based on the k-means clustering algorithm is employed, and the clusters of 5 show the minimum DBI.

Figure 4 shows a pattern classification of five clusters. According to the SOM classification results, 270 water samples can be divided into five clusters: cluster 1: PG-2, 7, 9, 10, 16, 17, 20, 21, 22, 36, 37, and 38. This cluster of monitoring wells is basically distributed in the second and third aquifers; cluster 2: PG-1, 4, 8, 12, 15, 28, 31, 32, 37, 38, 39, 47, 49, 50, and 54; cluster 3: PG-22, 23, 24, 29, 30, 31, 32, 40, 41, 42, 43, and 48; cluster 4: PG-4, 5, 6, 11, 13, 18, 19, 20, 33, and 34; cluster 5: PG-1, 4, 5, 13, 14, 26, 27, 33, 34, 35, 51, 52, 53, 56, 57, and 58. The monitoring wells of clusters 1, 2, 3, and 4 are mostly distributed in the first and second aquifers, while the PG-1, 2, 17, 36 monitoring wells are in the fourth aquifer.

SOM classification results show that the five clusters are distributed roughly in five regions: southern, central, eastern, southwest, and northwest of the study area (**Figure 5**). In the southern region, the number of monitoring wells in layers 1 to 4 is 9, 7, 5, and 3, respectively. The monitoring wells are located in cluster 1 and cluster 3. In the east, the number of monitoring wells in layers 1 to 4 is 6, 6, 2, and 1, respectively. The monitoring wells are mainly located in cluster 2. In the northern region, the number of monitoring wells in layers 1 to 4 is 6, 3, 1, and 0, and the monitoring wells are mainly located in cluster 4. In the west, the number of monitoring wells in layers 1 to 4 is 9, 4, 2, and 1, respectively. The monitoring wells are located in cluster 5. It can be seen that the block distribution of the monitoring wells in **Figure 5** is consistent with the SOM classification results.

TABLE 2 | Grade division of the water quality scores.

cluster	Score interval	Grade
I	0.128-0.2698	Better
II	0.2699-0.4116	Good
III	0.4117-0.5534	General
IV	0.5535-0.6952	Bad
VI	0.6953-3.2	Worse

Figure 6 shows the SOM mapping of the 22 chemical components, each map representing a reference vector with 100 SOM nodes, where the reference vectors are normalized using a color visualization map. Dark red indicates the high values and dark blue indicates the low values. Each grid in **Figure 6** corresponds to **Figure 4** one by one, and the depth of the color represents the corresponding ion concentration of the monitoring well at that position.

On this aforementioned principle, SOM calculated the concentration distribution of each ion in the water sample group in **Figure 6**. Combining the results of **Figure 4** and **Figure 6**, we can see that in cluster 1, the higher contents are K^+ and CO_3^{2-}, and Na^+, Cl^- dominated in cluster 2; The higher contents in cluster 3 are Na^+, Ca^{2+}, NH_4^+, $HCO3^-$, F^-, TDS, free CO_2, Fe^{2+}, oxygen consumption, total hardness, EC, and total alkalinity; cluster 4 contains: CO_3^{2-}, NO_3^-; The higher contents in cluster 5 are: Ca^{2+}, Cl^-, SO_4^{2-}, NO_3^-, TDS, free CO_2, Fe^{3+},nitrite, oxygen consumption, total hardness, EC, and total alkalinity. **Figure 6** shows the corresponding distribution of each ion on the SOM classification results. On the other hand, groundwater samples in nodes with relatively low ion concentrations are located in the upper left and upper right corners of each SOM diagram.

The groundwater data were analyzed by using the SOM method. 100 (10 × 10) output neurons were selected (**Figure 5**), and the sampling points were divided into 5 clusters (**Figure 4**). Neurons use color coding to display the weight vector value of each neuron. Blue and red correspond to the parameters with low and high concentrations, respectively. Therefore, the interdependence of the variables can be identified by comparing the color of the neurons. As can be seen from **Figure 5**, HCO_3^-, Na^+, and Mg^{2+} have similar color gradients, Cl^- and NO_3^- have similar gradients, and Al and nitrite have similar gradients, indicating that they may be controlled by the same hydrochemical process. Cl^-, SO_4^{2-}, and NO_3^- are negatively correlated with HCO_3^-, Na^+, and Mg^{2+} by an inverse color gradient, indicating that Cl^-, SO_4^{2-}, NO_3^-, and HCO_3^-, Na^+, and Mg^{2+} are controlled by different sources. Fe^{3+}, Fe^{2+}, and NH_4^+ have obvious similarities in color gradient, indicating that they undergo common hydrochemical processes such as REDOX reactions.

3.3 Assessment of Water Quality of the Five Clusters of the Monitoring Wells

If the water quality scores of a single monitoring well are compared, some errors may occur. Therefore, the score of a single monitoring well is calculated and the outliers in each cluster and each cluster of

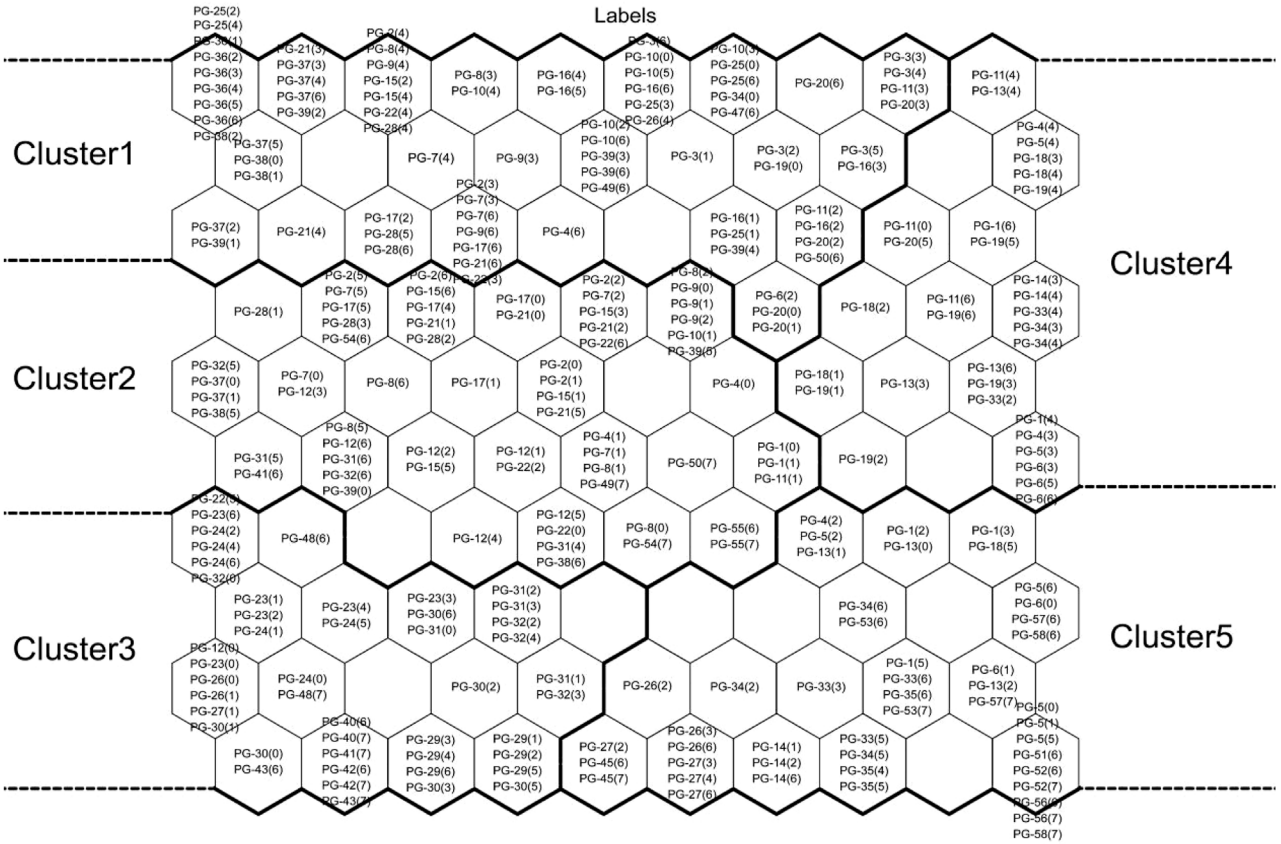

FIGURE 4 | Pattern classification map of the seven clusters by the SOM method. The number in the node represents the number of each well, and the area name is referred to as monitoring well number year (Pinggu area + year + quarter).

water quality are eliminated, so the score obtained is more persuasive and credible. The removal of the outliers is very important for water quality evaluation, and the entropy method can be very convenient in carrying out this step, but the comprehensive evaluation method is very difficult to carry out this step.

The average score and ranking of the five types of water quality data after pretreatment are obtained in **Table 3**:

The score obtained by the entropy method is obtained by the information contribution of various pollution components to water quality. The higher the score, the worse the water quality, and vice versa. After removing the outliers, the average score of each monitoring well was calculated, and the modified score was used as the final score of the monitoring well. The best water quality is located cluster 4, followed by cluster 1 and cluster 2 with close scores; the fourth and fifth are clusters 5 and 3, respectively.

4 DISCUSSION

4.1 Evaluation of Water Quality in the Five Clusters

The minimum DBI corresponding to the most appropriate number of clusters is 5. And the box diagram of the water quality score for the five clusters is shown in **Figure 7**. From **Figure 7**, we could find that the water quality in cluster 3 is the worst, followed by cluster 5.

According to the classification of SOM, the wells of clusters 1, 2, and 4 are highly similar, and those of clusters 3 and 5 are highly similar. Combined with **Figure 3**, it can be seen that cluster 2 is located in the central and eastern areas of the study area and belongs to the living area, while cluster 3 is distributed in the southeast area of the study area and near the QianRuiying landfill site. The scores of the two are 0.2634 and 0.5737, respectively. Although clusters 2 and 3 are very close, there is a large difference in the water quality, indicating the large effect of different pollution sources on the water quality of the aquifer. Cluster 1 is distributed in the south of the study area, located in the area of Zhanggezhuang–Machangying–Tianjingcun, which is away from the urban, and thus made the relative goodness of the water quality. Cluster 4 is mainly distributed in the northeastern side of the Pinggu Basin, and also the upstream of the region, thus with low score and good water quality. The water quality scores of cluster 1 and 2 are very similar. Cluster 5 is distributed in the southwest region of the study area, including Yukou Town Industrial Park and a large area of farmlands (**Figure 2A**), with industrial pollution and agricultural pollution, with a score of 0.5718 and thus indicating bad water quality. The scores of cluster 5 and cluster 3 are very similar, both of which have persistent pollution.

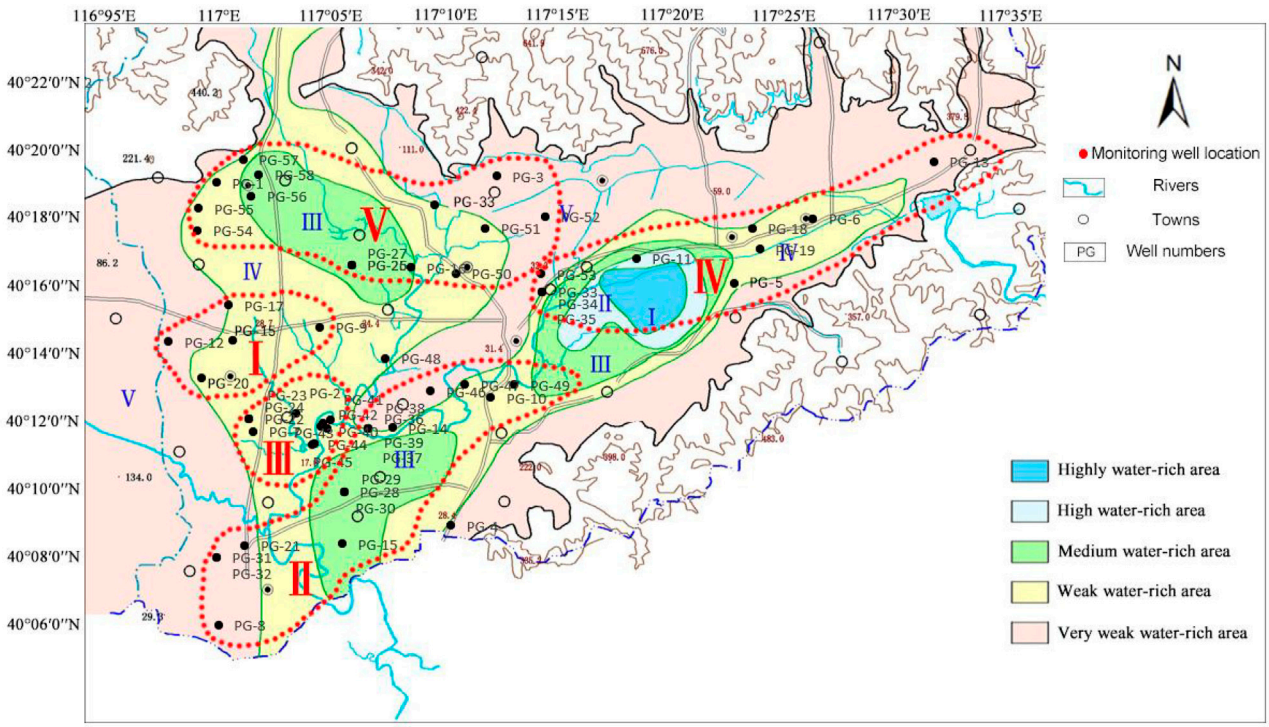

FIGURE 5 | Classification of the monitoring wells obtained through SOM.

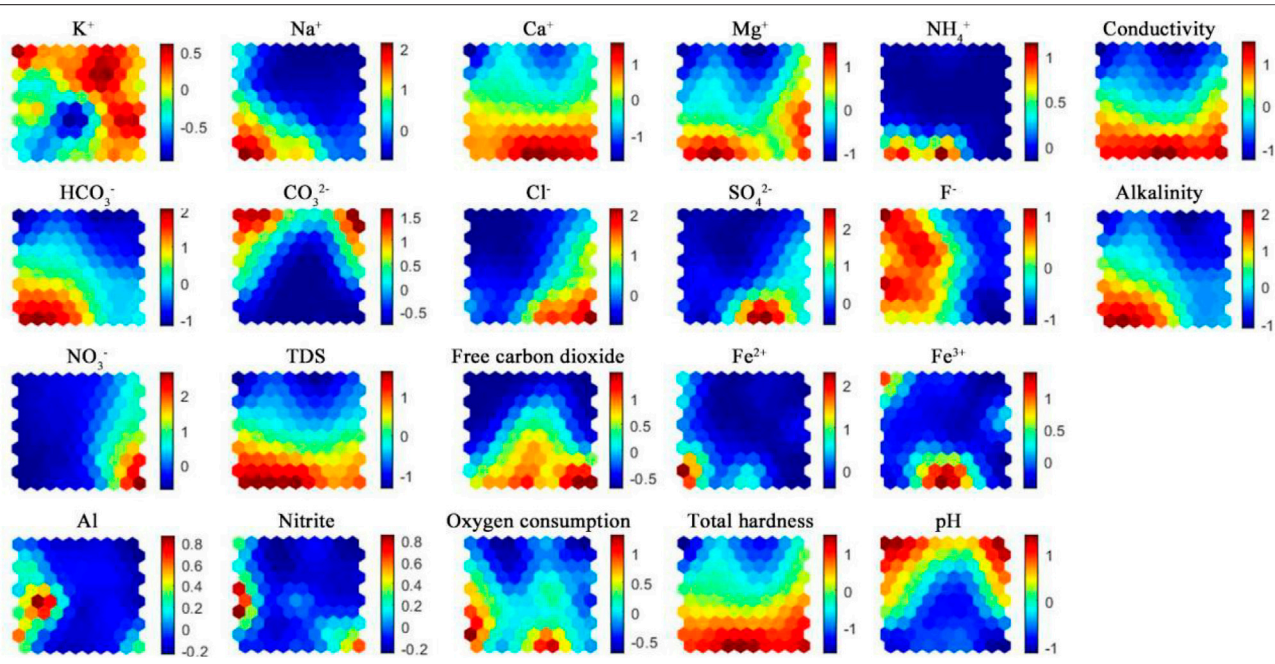

FIGURE 6 | Visualize gradients for each component.

4.2 Spatial Distribution of Each Clusters

By using the entropy method, we obtained the weight value and average concentration of the corresponding chemical components of each groundwater sample (**Table 4**). The weight value of each chemical component is important for the water quality assessment, and it explains the importance of

TABLE 3 | Average score of the 5 water quality clusters.

cluster	1	2	3	4	5
Average score	0.2658	0.2634	0.5737	0.2608	0.5718
Ranking	2	3	5	1	4
Grade	Better	Better	Bad	Better	Bad

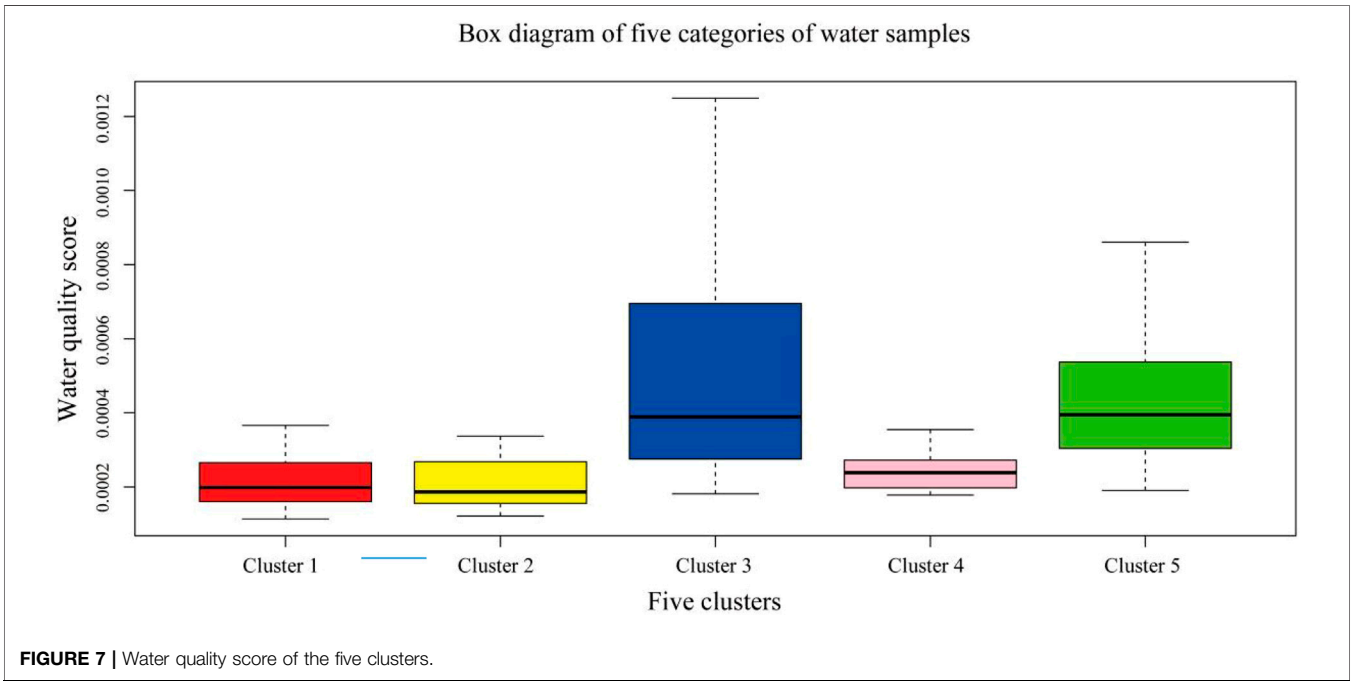

FIGURE 7 | Water quality score of the five clusters.

TABLE 4 | Average concentrations of cluster 1 to cluster 5 calculated by the entropy method.

Ionizing ions	Weight	1	2	3	4	5
K^+	0.0098	1.817	1.376	1.237	1.622	1.735
Na^+	0.0282	10.524	22.234	28.087	9.153	15.746
Ca^{2+}	0.0058	44.467	58.715	73.850	58.188	81.145
Mg^{2+}	0.0082	22.599	25.729	33.443	30.750	31.840
NH_4^+	0.1776	0.011	0.005	0.126	0.001	0.104
HCO_3^-	0.0128	226.323	302.782	426.052	229.078	307.494
CO_3^{2-}	0.0676	11.818	3.655	2.165	13.163	0.383
Cl^-	0.0363	5.938	6.702	10.678	21.741	33.381
SO_4^{2-}	0.0290	8.176	9.783	13.226	20.428	36.506
F^-	0.0226	0.519	1.621	0.722	0.230	0.186
NO_3^-	0.0539	8.093	6.539	2.359	32.216	41.134
TDS	0.0111	340.266	428.121	591.848	413.531	549.681
free CO_2	0.0686	0.271	1.779	2.467	0.288	3.851
Fe^{2+}	0.0960	0.294	0.183	1.001	0.164	0.334
Fe^{3+}	0.1022	0.349	0.137	0.427	0.224	0.499
Al	0.0924	0.096	0.156	0.143	0.048	0.107
Nitrite	0.1364	0.003	0.006	0.007	0.002	0.009
Oxygen consumption	0.0145	0.387	0.496	0.590	0.405	0.545
Total hardness	0.0053	204.228	252.652	322.130	272.031	333.702
pH	0.0072	8.145	7.922	7.845	8.159	7.791
Conductivity	0.0032	408.696	493.621	659.717	526.353	678.085
Alkalinity	0.0114	205.139	254.212	352.717	209.594	252.638

various chemical components that should be chosen for monitoring. And the components with the largest weight could be selected for monitoring if multiple components exist. The columns 3 to 7 showed the average concentration of the five levels of the groundwater. If such a classification could be corresponding to the result of SOM, then we could conclude that our model is reasonable and could be further used in the water quality classification and assessment.

Through the calculation of water quality, the weight value of each ion and the average concentration of each ion in the 5 types of monitoring wells were obtained. The ions with higher weights are respectively: NH_4^+, Nitrite, Fe^{3+}, Fe^{2+}, Al, free CO_2, CO_3^{2-}, NO_3^-, and Cl^-, and other ions have a relatively low proportion. In addition, the average concentration and source of each ion in cluster 1 to cluster 5 are discussed below.

For the monitoring wells of cluster 1, they are distributed in the south side of the study area, mainly in the Zhanggezhuang–Machangying–Tianjingcun areas (The blue dotted box is shown in **Figure 1**). The distribution of the monitoring wells is relatively concentrated. PG-20 is located in the first layer aquifer, PG-9, 10, 15, and 37 are located in the second aquifer, PG-7 and 22 are located in the third aquifer, and PG-2 and 14 are located in the forth layer of the aquifer. As can be seen from the SOM topology, the CO_3^{2-} is most similar with pH, and it is contrary to the trend of free CO_2. Combined with **Table 4**, it can be seen that the average concentration of each component is relatively low in the five types of waters. The reasons may be as follow: It is possible that these groundwater samples are all outside the town, with a certain distance from downtown. The second reason maybe that there are only very few monitoring wells that are distributed in the first layer. Thus the groundwater is difficult to be contaminated. As can be seen from the SOM topology in **Figure 4**, the upper-left corner (cluster 1) is dark, indicating the low concentration of each chemical component. The average score of the water quality in cluster 1 was 0.2658, showing good quality comparing with cluster 3 and cluster 5.

For cluster 2, the distribution of the monitoring wells is slightly scattered, but they are mainly distributed in the eastern and central areas of the study area. PG-28, 29, and 30 are located in the same place which monitors layer 3, layer 2, and layer 1 aquifer. And the PG-36 to PG-39 monitoring wells are located in layer 4, layer 3, layer 2, and layer 1. PG-28, 29, and 30 are classified in cluster 3 with the worst water quality. The PG-28, 36, 37, 38, 39, 46, 48, and 50 wells are located in the middle of the study area. Among them, the PG-39, 46, 48, and 50 wells are located in the first layer. The distribution of the latter three wells is relatively scattered, and the distribution of the PG-28, 36, 37, 38, and 39 wells is relatively concentrated. The area is located in the main urban area, which has suffered from the effect of human activities. The PG-8, 21, 31, 32 wells are near the Yingcheng and Ma Fang towns (The blue dotted box is shown in **Figure 1**), which are distributed at the edge of the study area and the east with a sparse population. Therefore, the groundwater is less polluted by human activities and the concentration of chemical components is low. Among the calculated average concentration, the contents of Na^+ and F^- (Xiao et al., 2022) are very high, with 22.234 mg/l and 1.621 mg/l, respectively, which is consistent with the results of SOM topology in **Figure 4**. The average score of cluster 2's water quality is 0.2634, which is very close to cluster 1. Thus, the water quality in cluster 2 is also good.

For cluster 3, these monitoring wells are located in the southeast of the central part of the study area. It can be seen from the SOM gray topology that the concentrations of Na^+, Mg^{2+}, HCO_3^-, NH_4^+, F^-, TDS, Fe^{2+}, total hardness, electrical conductivity, and total alkalinity are relatively high. This result can also be matched with the average concentration in **Table 3**. This cluster is mainly located near the Pinggu landfill, and it is found that there are reductive garbage leachates in the area without oxidation that enter into the groundwater in a relatively closed accumulation environment, resulting in strong reducibility. Here, the concentrations of SO_4^{2-} and NO_3^- are 13.226 mg/L and 2.359 mg/L, respectively. The sources of pollution from the monitoring wells near the dump site include ammonia nitrogen, nitrate (Xiao et al., 2021; Yong et al., 2022), and nitrite. Therefore, the measured concentrations of NH_4^+ and nitrite are 0.126 mg/L and 0.007 mg/L, respectively. The PG-22, 23, and 24 wells are located in the same place, and monitoring layer 3, layer 2, and layer 1, respectively. The PG-40, 41, 42, and 43 wells are located in the first layer and are very concentrated. Therefore, the horizon distribution of cluster I's monitoring wells, the concentration of the same pollution component in cluster 3's water quality must be higher. In addition, due to the impact of a landfill plant, the relatively high concentration of the pollution component is reasonable. Among the ion weights calculated by the entropy method, the weights of NH_4^+ and nitrite are the largest, which are 0.1776 and 0.1364, respectively, which shows that the aforementioned inference is reasonable. The calculated score of this kind of water quality is 0.5737, which is the highest among the five kinds of water qualities, indicating that this kind of water quality is the worst.

For cluster 4, the SOM gray topology shows that CO_3^{2-}, K^+ concentrations in this kind of water are relatively high, with a high mean concentration, high CO_3^{2-}, K^+, and NO_3^- concentrations. The concentrations of other chemical components are lower than those of cluster 3 and cluster 5. These monitoring wells are distributed in the Donggao Village–Hanzhuang Town–Ruoshanji area (The blue dotted box is shown in **Figure 1**). Some of the areas are rural areas, without large factories and a large amount of domestic wastewater pollution, so the ion concentration is relatively low. The PG-6, 11, 13, 18, and 19 wells are located in the first aquifer, and the PG-5, 33, and 34 wells are located in the second and third aquifers. And the score of the water quality is 0.2608, which is lowest among the five clusters of groundwater, indicating the best water quality in the study area.

For the wells in cluster 5, Ca^{2+}, Cl^-, SO_4^{2-}, NO_3^-, TDS, Fe^{3+}, nitrite, total hardness, and electrical conductivity, and the average concentration showed in high value which is consistent with the results shown in the SOM topology diagram (**Figure 3**). As shown in **Figure 1**, the study area is in the southwest, with Yu Kou Town Industrial Park (The blue dotted box is shown in **Figure 1**) and a large area of farmlands. The PG-27, 51, 52, 53, 57, and 58 wells are located in the first aquifer, where the PG-26 and 1 wells are

located in the second and third aquifers. The possible pollution source from industrial wastewater discharge and pesticide use in this area may lead to the poor quality of water. And the water quality score of cluster 5 is 0.5718, which is close to cluster 3.

In summary, the cluster grouped by the combination of self-organizing map (SOM) and entropy-based weight determining method is quite in agreement with the distribution of the contamination sources in the study area. This also indicates that the methods proposed in this study are useful in groundwater quality assessment and possible contamination identification.

5 CONCLUSION

In this study, we used entropy-based weight determining method, in combination with the SOM method to evaluate the water quality and to identify the possible sources of these different clusters. Five clusters were grouped by based on the water quality score and the SOM result.

The cluster 1 is dominant with K^+ and CO_3^{2-}, and these monitoring wells are distributed in the south of the study area. Cluster 2 is dominant with Na^+ and Cl^-, and these monitoring wells are mainly distributed in the eastern and central areas of the study area. Cluster 3 is dominant with Na^+, Ca^{2+}, NH_4^+, HCO_3^-, F^-, TDS, free CO_2, Fe^{2+}, oxygen consumption, total hardness, EC, and total alkalinity, and these monitoring wells are located in the southeast region of the central part of the study area. The cluster 4 is dominant with CO_3^{2-}, NO_3^-, and these monitoring wells are distributed in the Donggao Village–Hanzhuang Town–Ruoshanji area as well as some of the rural areas. The cluster 5 is dominant with Ca^{2+}, Cl^-, SO_4^{2-}, NO_3^-, TDS, free CO_2, Fe^{3+}, nitrite, oxygen consumption, total hardness, EC, and total alkalinity, and these monitoring wells are distributed in the southwest region of the study area.

Our results show that large-scale farming and intensive industrial activities in the southwest region of the study area increased the concentrations of Ca^{2+}, Cl^-, SO_4^{2-}, NO_3^-, TDS, Fe^{3+}, and nitrite in the groundwater. In the southeast region of the study area, the concentrations of Mg^{2+}, HCO_3^-, NH_4^+, F^-, TDS, and Fe^{2+} were mainly caused by landfill activities. The areas affected by domestic sewage discharge are the southern, central, eastern, and northwest regions of the study area. The Na^+, F^- concentrations in the central and eastern regions are higher, and the K^+, NO_3^- concentrations in the northwest region are higher.

Based on the SOM classification results, the entropy method was used to calculate the ranking of the five types of water quality: cluster 4 > cluster 1 > cluster 2 > cluster 5 > cluster 3. The pollution of the monitoring wells of clusters 1, 2, and 4 in the water is low, and the pollution of the monitoring wells of clusters 3 and 5 in the water is high. According to the water quality score and the influence of surrounding pollution, the influence degree can be inferred as follows: Industrial and farmland > landfill > living quarters. Industrial wastewater, pesticides, garbage, and other polluting components will infiltrate into the aquifer and cause water pollution. Therefore, water quality monitoring is conducive to the control of industrial wastewater treatment, rational use of pesticides, and proper disposal of garbage, which can protect the groundwater to a certain extent and prevent it from further pollution.

SOM classification results correspond to water quality calculation results of the entropy method, which also shows the reliability and applicability of these two models. SOM can provide groups for the calculation of the entropy method and improve the accuracy of the calculation results of the entropy method. At the same time, the entropy method is used to evaluate water quality based on the SOM classification results, and the data are further calculated and analyzed. In addition, based on the research results of this article, it is shown that the combination of these two models can be used to search and distinguish groundwater pollution sources, and these provide a new way for groundwater protection and purification.

Based on the aforementioned analysis, this model evaluates the water quality of monitoring wells from two aspects: spatial distribution of the pollution components and water sample evaluation. The results are consistent with those reported in Pinggu and with the research results of other scholars. It shows that this model is suitable for water quality assessment of multiple monitoring wells, and the effect is good.

DATA AVAILABILITY STATEMENT

The raw data supporting the conclusions of this article will be made available by the authors, without undue reservation.

AUTHOR CONTRIBUTIONS

SL, ZZ, and ZS contributed to conception and design of the study. SL, NS, SQ, and JL organized the database, SL and NS performed the statistical analysis. SL, ZZ, NS, SQ, and ZS wrote the first draft of the manuscript. All authors contributed to the manuscript revision, read, and approved the submitted version.

REFERENCES

Amiri, V., Rezaei, M., and Sohrabi, N. (2014). Groundwater Quality Assessment Using Entropy Weighted Water Quality Index (EWQI) in Lenjanat, Iran. *Environ. Earth Sci.* 72 (9), 3479–3490. doi:10.1007/s12665-014-3255-0

Bodrud-Doza, M., Islam, A. R. M. T., Ahmed, F., Das, S., Saha, N., and Rahman, M. S. (2016). Characterization of Groundwater Quality Using Water Evaluation Indices, Multivariate Statistics and Geostatistics in Central Bangladesh. *Water Sci.* 30 (1), 19–40. doi:10.1016/j.wsj.2016.05.001

Choi, B.-Y., Yun, S.-T., Kim, K.-H., Kim, J.-W., Kim, H. M., and Koh, Y.-K. (2014). Hydrogeochemical Interpretation of South Korean Groundwater Monitoring Data Using Self-Organizing Maps. *J. Geochem. Explor.* 137, 73–84. doi:10.1016/j.gexplo.2013.12.001

Garcı´a, H. L., and González, I. M. (2004). Self-Organizing Map and Clustering for Wastewater Treatment Monitoring. *Eng. Appl. Artif. Intell.* 17 (3), 215–225. doi:10.1016/j.engappai.2004.03.004

Gharibi, H., Mahvi, A. H., Nabizadeh, R., Arabalibeik, H., Yunesian, M., and Sowlat, M. H. (2012). A Novel Approach in Water Quality Assessment Based on Fuzzy Logic. *J. Environ. Manage.* 112, 87–95. doi:10.1016/j.jenvman.2012.07.007

Gleeson, T., Befus, K. M., Jasechko, S., Luijendijk, E., and Cardenas, M. B. (2016). The Global Volume and Distribution of Modern Groundwater. *Nat. Geosci.* 9 (2), 161–167. doi:10.1038/ngeo2590

Jiang, T., Qu, C., Wang, M., and Hu, B. (2017). Hydrochemical Characteristics of Shallow Groundwater and the Origin in the Pinggu Plain, Beijing. *J. Arid Land Resour. Environ.* 31 (11), 122–127.

Jin, Y.-H., Kawamura, A., Park, S.-C., Nakagawa, N., Amaguchi, H., and Olsson, J. (2011). Spatiotemporal Classification of Environmental Monitoring Data in the Yeongsan River Basin, Korea, Using Self-Organizing Maps. *J. Environ. Monit.* 13 (10), 2886–2894. doi:10.1039/c1em10132c

Kohonen, T. (1995). "Self-Organizing Maps," in *Series in Information Sciences* (Heidelberg: Springer), 30. doi:10.1007/978-3-642-97610-0

Li, J., Shi, Z., Wang, G., and Liu, F. (2020a). Evaluating Spatiotemporal Variations of Groundwater Quality in Northeast Beijing by Self-Organizing Map. *Water* 12 (5), 1382. doi:10.3390/w12051382

Li, J., Wang, Y., Zhu, C., Xue, X., Qian, K., Xie, X., et al. (2020b). Hydrogeochemical Processes Controlling the Mobilization and Enrichment of Fluoride in Groundwater of the North China Plain. *Sci. Total Environ.* 730, 138877. doi:10.1016/j.scitotenv.2020.138877

Li, P.-Y., Qian, H., and Wu, J.-H. (2011). Application of Set Pair Analysis Method Based on Entropy Weight in Groundwater Quality Assessment-A Case Study in Dongsheng City, Northwest China. *E-Journal Chem.* 8, 879683. doi:10.1155/2011/879683

Li, P., Wu, J., Qian, H., Lyu, X., and Liu, H. (2014). Origin and Assessment of Groundwater Pollution and Associated Health Risk: A Case Study in an Industrial Park, Northwest China. *Environ. Geochem Health* 36 (4), 693–712. doi:10.1007/s10653-013-9590-3

Nguyen, T. T., Kawamura, A., Tong, T. N., Nakagawa, N., Amaguchi, H., and Gilbuena, R. (2015). Clustering Spatio-Seasonal Hydrogeochemical Data Using Self-Organizing Maps for Groundwater Quality Assessment in the Red River Delta, Vietnam. *J. Hydrology* 522, 661–673. doi:10.1016/j.jhydrol.2015.01.023

Omo-Irabor, O. O., Olobaniyi, S. B., Oduyemi, K., and Akunna, J. (2008). Surface and Groundwater Water Quality Assessment Using Multivariate Analytical Methods: A Case Study of the Western Niger Delta, Nigeria. *Phys. Chem. Earth Parts A/B/C* 33 (8-13), 666–673. doi:10.1016/j.pce.2008.06.019

Sanchez-Martos, F., Aguilera, P. A., Garrido-Frenich, A., Torres, J. A., and Pulido-Bosch, A. (2002). Assessment of Groundwater Quality by Means of Self-Organizing Maps: Application in a Semiarid Area. *Environ. Manag.* 30 (5), 0716–0726. doi:10.1007/s00267-002-2746-z

Shannon, C. E. (1948). A Mathematical Theory of Communication. *Bell Syst. Tech. J.* 27 (3), 3270–3423. doi:10.1002/j.1538-7305.1948.tb01338.x

Vasanthavigar, M., Srinivasamoorthy, K., Vijayaragavan, K., Ganthi, R. R., Chidambaram, S., Anandhan, P., et al. (2010). Application of Water Quality Index for Groundwater Quality Assessment: Thirumanimuttar Sub-Basin, Tamilnadu, India. *Environ. Monit. Assess.* 171 (1-4), 595–609. doi:10.1007/s10661-009-1302-1

Xiao, Y., Hao, Q., Zhang, Y., Zhu, Y., Yin, S., Qin, L., et al. (2021). Investigating Sources, Driving Forces and Potential Health Risks of Nitrate and Fluoride in Groundwater of a Typical Alluvial Fan Plain. *Sci. Total Environ.* 802, 149909. doi:10.1016/j.scitotenv.2021.149909

Xiao, Y., Liu, K., Hao, Q., Li, Y., Xiao, D., and Zhang, Y. (2022). Occurrence, Controlling Factors and Health Hazards of Fluoride-Enriched Groundwater in the Lower Flood Plain of Yellow River, Northern China. *Expo. Health* 14, 345–358. doi:10.1007/s12403-021-00452-2

Yong, X., Kla, B., Qh, C., Dx, A., Yz, C., Sy, D., et al. (2022). Hydrogeochemical insights into the signatures, genesis and sustainable perspective of nitrate enriched groundwater in the piedmont of Hutuo watershed, China. *CATENA* 222, 106020. doi:10.1016/j.catena.2022.106020

Conflict of Interest: The authors declare that the research was conducted in the absence of any commercial or financial relationships that could be construed as a potential conflict of interest.

Publisher's Note: All claims expressed in this article are solely those of the authors and do not necessarily represent those of their affiliated organizations, or those of the publisher, the editors, and the reviewers. Any product that may be evaluated in this article, or claim that may be made by its manufacturer, is not guaranteed or endorsed by the publisher.

frontiers | Frontiers in Environmental Science

TYPE Review
PUBLISHED 06 September 2022
DOI 10.3389/fenvs.2022.968546

OPEN ACCESS

EDITED BY
Chengcheng Li,
China University of Geosciences
Wuhan, China

REVIEWED BY
Jian Liu,
Southwest Jiaotong University, China
Vhahangwele Masindi,
Council for Scientific and Industrial
Research (CSIR), South Africa
Yiqing Liu,
Southwest Jiaotong University, China

*CORRESPONDENCE
Hong Li,
lihong0910@126.com

SPECIALTY SECTION
This article was submitted to Freshwater
Science,
a section of the journal
Frontiers in Environmental Science

RECEIVED 14 June 2022
ACCEPTED 08 August 2022
PUBLISHED 06 September 2022

CITATION
Li H and Liu Q (2022), Reaction medium
for permeable reactive barrier
remediation of groundwater polluted by
heavy metals.
Front. Environ. Sci. 10:968546.
doi: 10.3389/fenvs.2022.968546

Reaction medium for permeable reactive barrier remediation of groundwater polluted by heavy metals

Hong Li[1]* and Qingmei Liu[2]

[1]Luzhou Vocational and Technical College, Luzhou, China, [2]Chengdu Academy of Enviromental Sciences, Chengdu, China

Heavy metal pollution of groundwater has a serious impact on human health, which has become a key issue in the field of water resources and water environment. Permeable reactive barrier (PRB) is an *in-situ* remediation technology for passive groundwater pollution, with the advantages of economy and efficiency. The reaction material in the PRB wall is the key to the whole system, which can intercept or degrade heavy metals to achieve the removal of pollutants. Among a wide variety of reaction materials, PRB has been successfully used to remove various heavy metal contaminants. In this paper, reaction materials are classified into three broad categories, namely single material, mixed material, and composite material. On this basis, the action mechanism of various materials to remove heavy metal pollutants is analyzed, and the screening method of reaction medium is summarized. Finally, the deficiencies and development directions of PRB reaction medium materials in the removal of heavy metals in groundwater are pointed out, providing reference for the subsequent development and application of PRB reaction medium.

KEYWORDS

reaction medium, permeable reactive barrier, heavy metals, removal mechanism, groundwater

1 Introduction

Approximately 2.5 billion people depend directly on groundwater for drinking water on a global scale (Li et al., 2021). In addition, more than half of agricultural irrigation water relies on groundwater (Famiglietti, 2014). In this case, the excessive consumption of groundwater makes it a research hotspot in this field (Jarvis, 2021). In general, heavy metals refer to metals and metalloids with a density greater than 5 g cm^{-3} or an atomic number greater than 20 in the periodic table, including cadmium, mercury, copper, arsenic, chromium, etc., (Barceló and Poschenrieder, 1990). Sources of heavy metals in groundwater include natural and anthropogenic sources (Hashim et al., 2011). Heavy metals widely present in the earth's crust can dissolve in groundwater through natural weathering, erosion, or changes in soil pH value (Fedoročková et al., 2021). Moreover, landfill leachate, sewage, mine tailings leachate, deep well treatment liquid waste,

industrial waste seepage or industrial leakage may all cause elevated concentrations of heavy metals in groundwater (Ali et al., 2019). Since heavy metals cannot be degraded, their continuous accumulation poses a threat to drinking water safety and human and animal health (Mukherjee et al., 2020). Long-term direct or indirect exposure to heavy metal-contaminated groundwater may lead to the accumulation of heavy metals in various organs, leading to diseases such as osteoporosis, respiratory diseases, skin problems, cardiovascular, and cerebrovascular diseases, and reproductive diseases (Khan et al., 2013). For example, cadmium can cause symptoms such as acute respiratory failure in humans. cadmium, lead, and mercury can damage the kidneys of human body (Salman et al., 2011). As a hidden water source, the discovery of groundwater pollution is delayed (MacDonald and Kavanaugh, 1994).

Groundwater treatment technology is mainly divided into *in-situ* treatment technology and *ex-situ* treatment technology. PRB technology and pump-treat technology are typical representatives of groundwater *in-situ* and *ex-situ* remediation technologies, respectively. Compared with traditional pump-treat technology, PRB technology relies on underground active reaction medium materials to remove dissolved pollutants in polluted water, which neither requires additional power systems nor damages natural environments such as soil and groundwater. Therefore, it has the advantages of simple operation, reasonable cost and ideal processing effect, which is considered as a promising processing technology (Obiri-Nyarko et al., 2014). However, PRB technology also has some disadvantages. For example, when the media material loses activity or becomes blocked due to precipitation, the media material should be replaced in time, which makes the cost difficult to quantify (Wilkin et al., 2009). During operation, treatment effects need to be closely monitored to ensure PRB effectiveness (Faisal et al., 2018). Moreover, PPR technology is greatly affected by geological conditions and site characteristics (Obiri-Nyarko et al., 2014). As shown in Figure 1, PRB technology is to build a reactive wall in the vertical direction of the groundwater pollution plume, and fill the wall with reactive substances. When the plume flows through the wall, the pollutants undergo a series of physical, chemical or biological reactions with the active reactive substance, thereby intercepting or converting the pollutants into non-toxic substances. According to reports, there have been more than 200 engineering application cases of PRB technology to deal with groundwater pollution around the world.

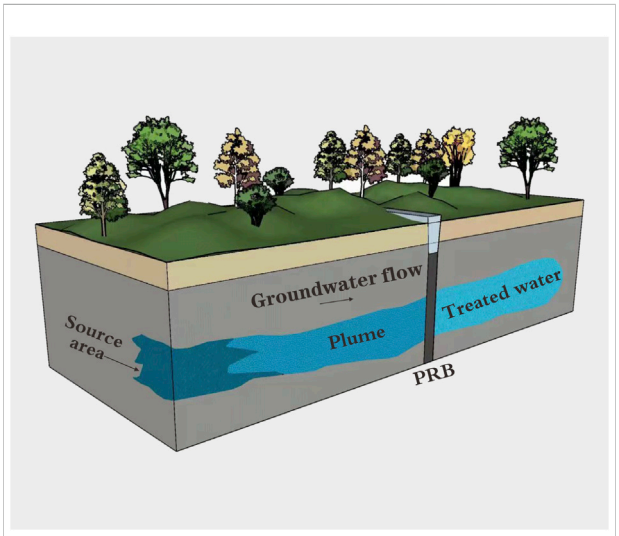

FIGURE 1
Working principle of PRB technology (Day et al., 1999).

The key to PRB technology to deal with groundwater pollution is the active medium material filled in the wall. In more detail, the reactivity, cost, and lifetime of materials can have a direct impact on the stability, economy, and safety of PRB systems. The choice of reaction medium material mainly depends on the reaction mechanism between pollutants and medium material. In addition, it is also affected by hydrogeological conditions such as pH. Before 2000, the medium material was traditional zero-valent iron (ZVI). Since then, the research focus has turned to the development of new medium materials. According to the structural characteristics of medium material, there are three categories: single material, mixed material and composite material.

Under ideal conditions, the reaction medium should have the following characteristics. 1) The filling material should have stable structure and uniform particle size. In addition, the particle size should not be too small to ensure that the permeability coefficient is higher than the surrounding area. 2) The pollution component can fully react with the filler and be removed. 3) The filling material should be stable and active enough to ensure that the PRB system has a long-term stable treatment effect on pollutants (Asokbunyarat et al., 2017). 4) The product after the interaction between the reaction material and the pollution component should be non-toxic and free from secondary pollution (Jeen et al., 2011). 5) The reaction product is not easy to block the system (Blowes et al., 2000). 6) The filling material is cheap and readily available (Liu et al., 2020).

Scherer et al. (2000) summarized the types and properties of PRB reaction materials, and discussed the feasibility and long-term efficacy of PRB technology. However, some new materials have been developed and applied within the last 20 years (Obiri-Nyarko et al., 2014) reported the application of ZVI, zeolite, activated carbon, apatite and other materials in groundwater remediation, without introducing the application of mixed materials and composite materials (Wu et al., 2020) detailed the application of ZVI as a reactive material in the treatment of heavy metal pollution in groundwater (Song J. et al., 2021) reviewed the PRB technique for remediation of heavy metal-contaminated media materials, but did not indicate the process for

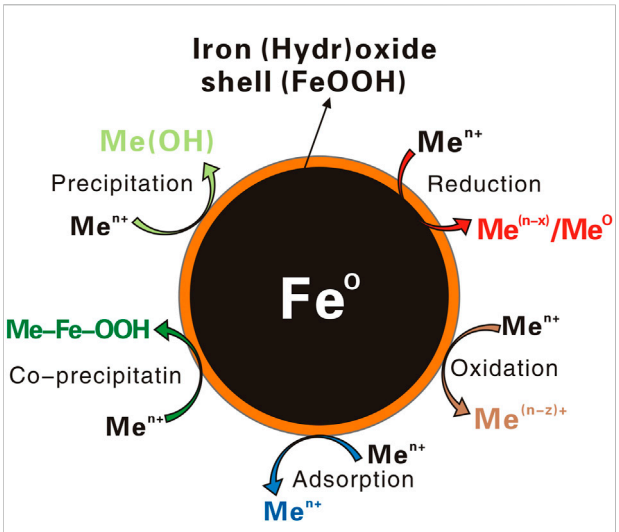

FIGURE 2
Schematic illustration of reaction mechanism of ZVI [modified from (Fu et al., 2014)].

screening reactive materials. In this study, reaction materials are classified into three main categories, namely single material, mixed material, and composite material. The research status of various media materials in the treatment of heavy metal pollution in groundwater is summarized, including the types of heavy metals, experimental scale and removal effect. On this basis, the main mechanism of heavy metal removal by reaction materials is revealed and the experimental methods for screening dielectric materials are summarized. Finally, the development direction of reaction materials is pointed out.

2 Materials and methods

2.1 Single material

2.1.1 Zero-valent iron

With strong electronegativity, high reactivity and fast reaction, ZVI has a good removal effect on heavy metals such as Cr, U, V, Ni, Pb, Cd, Hg, and Cu. ZVI has been used in many practical projects. ZVI easily reacts with oxygen to form FeO(OH) or $Fe(OH)_3$ solids, thus causing the clogging of the reaction medium. Usually, highly permeable substances (such as sand and gravel) are added to the reaction wall to increase the permeability and prolong the service life (Jeen et al., 2011). As shown in Figure 2, the main mechanism of ZVI removal of heavy metals lies in redox, precipitation, adsorption, etc. With the removal of Cr(VI) by ZVI as an example, the reaction equation is as follows (Dries et al., 2005; Lai and Lo, 2008; Soto et al., 2015):

$$2Fe^0 + Cr_2O_7^{2-} + 7H_2O \rightarrow 2Cr^{3+} + 2Fe^{2+} + 14OH^-$$
$$Cr^{3+} + 3OH^- \rightarrow Cr(OH)_3(s)$$
$$2Cr^{3+} + 6OH^- \rightarrow Cr_2O_3 + 3H_2O$$
$$Fe^{3+} + 3OH^- \rightarrow 3Fe(OH)_3$$
$$2Fe^{3+} + 6OH^- \rightarrow 3Fe_2O_3 + 3H_2O$$
$$(1-x)Fe^{3+} + xCr^{3+} + 3OH^- \rightarrow (Cr_xFe_{1-x})(OH)_3$$

ZVI may have bio-stimulatory effects on the PRB system and downstream microorganisms (Xu et al., 2017). According to (Wang et al., 2022), ZVI promotes the biological reduction of Cr(VI).

Compared with ZVI, nanoscale zero-valent iron (nZVI) has smaller particle size, larger specific surface area and surface energy, one to three orders of magnitude higher reactivity (Jiang et al., 2018), and stronger transport capacity in soil. nZVI can be directly injected into underground aquifers (Mystrioti et al., 2020), which has good application prospects. However, the high reactivity makes nZVI susceptible to oxidation, the magnetic properties make it easy to agglomerate and cause clogging. The modification of nZVI is an important research direction to develop new reaction medium.

2.1.2 Carbonaceous material

A large number of hydroxyl, phenol and carboxyl groups are distributed on the surface of activated carbon (AC), and the internal pores are well developed (Li et al., 2010). Therefore, activated carbon has excellent adsorption and chemical stability (Dong et al., 2016), which is a commonly used material in the early stage of PRB. Moreover, it is widely used in the removal of heavy metals (Hornig et al., 2008). However, the heavy metal removal effect of activated carbon is easily affected by pH (Di Natale et al., 2007). The increase in pH would enhance the binding of water molecules to activated carbon and decrease the adsorption capacity of activated carbon (Obiri-Nyarko et al., 2014). The groundwater component affects the performance of activated carbon. For example, anions such as chloride and sulfate will compete with pollutants for reaction sites, thereby reducing the adsorption capacity of activated carbon (Namasivayam and Sangeetha, 2006).

Another type of carbonaceous material is biochar (BC), with abundant internal pores and negative charges on the surface (Lou et al., 2016). This is prepared from various types of biowaste materials under low pyrolysis temperature and anoxic conditions (Liang et al., 2021). Compared with AC, BC is cheaper to produce and has a stronger affinity. However, the adsorption capacity of BC for Ni, Pb, Cr, and Cd is lower than that of modified AC (Wilson et al., 2006). By loading organic functional groups (Zhou et al., 2013), minerals (Han Y. et al., 2016) and nZVI (Zhou et al., 2014) or activated by acid and alkali solutions, the adsorption capacity of BC can be significantly improved. The heavy metal removal mechanisms include physical adsorption, ion exchange,

electrostatic interaction, etc. Typically, the entire removal process is a combination of different mechanisms (Shakoor et al., 2020). The materials used in the preparation of BC are of various types and sources, which have important application value in the restoration of heavy metals in groundwater.

2.1.3 Mineral material

2.1.3.1 Iron-bearing mineral

Iron-bearing minerals have become a new type of reaction material for PRB systems, including iron sulfide mineral and iron oxide minerals (Aredes et al., 2012). The removal mechanism of heavy metal ions by natural iron oxide minerals is mainly (irreversible) chemisorption, and to a lesser extent (reversible) physisorption. As a good arsenic removal material, laterite can stably adsorb arsenic in water in the pH range of 4–11 (Aredes et al., 2012). Due to their abundant reserves, low price, and non-toxicity to the environment, iron sulfide mineral is usually used to remove heavy metals in polluted water (Abdul et al., 2019). The effect of groundwater composition on removal efficiency should be fully considered. When humic acid (HA) is contained in, for example, groundwater, HA competes with Cr(VI) for pyrite surface sites, resulting in the reduction of Cr(VI) removal (Kantar et al., 2017). In addition, the heat treatment method can also affect the removal effect of pyrite on heavy metal contaminants. The adsorption capacity of Hg(II) by natural pyrite is 0.19 mg g^{-1}, which could be increased to 54.44 mg g^{-1} by calcination under nitrogen atmosphere (Zhu et al., 2020). Under acidic conditions, the removal mechanism of Cr(VI) by pyrite is as follows (Gong et al., 2016):

$$FeS + H^{+} \rightarrow Fe^{2+} + HS^{-}$$
$$3Fe^{2+} + Cr^{6+} \rightarrow Cr^{3+} + 3Fe^{3+}$$
$$3S^{2-} + 2Cr^{6+} \rightarrow 2Cr^{3+} + 3S$$
$$xCr^{3+} + (1-x)Fe^{3+} + 3H_2O \rightarrow (Cr_xFe_{1-x})(OH)_3(s) + 3H^{+}$$

2.1.3.2 Channel/lamellar structural mineral

Minerals such as zeolite and apatite have channel or lamellar (chain lamellar) structure inside, with good adsorption performance and ion exchange performance, which can remove a variety of heavy metal ions (Kumara and Kawamoto, 2021). Zeolite is a hydrated framework-like aluminosilicate mineral composed of tetrahedra of AlO_4 and SiO_4 (Maharana and Sen, 2021), with abundant internal channels (Bailey et al., 1999), as well as catalytic ability and molecular sieving ability (Cerjan Stefanović et al., 2007). It has a negative surface charge (Abdelrahman et al., 2021), and a cation exchange capacity of 2–4 meg g^{-1} (Liu et al., 2020). With strong adsorption on Cu(II), Pb(II), Cd(II), Ni(II), and Zn(II), and low price, zeolite is considered to be an ideal material for heavy metals removal (Wang and Peng, 2010). At low pH values, an excess of protons can compete effectively with the heavy metal ions for binding sites on zeolite surface (Faisal and Hmood, 2015). The higher the degree of groundwater mineralization, the better the removal efficiency of heavy metal ions by zeolite (Jarvis et al., 2006). Heavy metal cation contaminants can be adsorbed or exchanged into the internal channel structure of channel/lamellar (chain lamellar) structured minerals. Therefore, the voids between the medium material particles are not blocked, thereby maintaining high permeability and extending service life. This feature is of great significance in the practical application of PRB engineering.

Because of its wide source, non-toxic, cheap, and simple preparation process, apatite, a common phosphate material, is often used to remove divalent heavy metal ions. Dong et al. (2013), which is considered as a high-quality inorganic ion lattice adsorption and exchange material. When the environmental pH is neutral or weakly acidic, hydroxyl apatite (HAP) can remove heavy metal contaminants through surface adsorption and ion exchange. When the environmental pH is less than 4, apatite removes heavy metal pollutants through dissolution-precipitation reactions and other pathways (Oliva et al., 2010; Elkady et al., 2018; Nijhawan et al., 2018).

Due to the abundant channels, synthetic HAP is often used in the removal of target pollutants (Asri et al., 2010). HAP is the main inorganic component of animal bones, and the content can reach 70%. Therefore, HAP obtained from discarded animal bones has a cost advantage (Ngueagni et al., 2020). Studies have shown that HAP prepared from animal bones such as fish bones and bovine bones are mostly used for remediation of heavy metals in industrial wastewater and soil (Hernández-Cocoletzi et al., 2020; Wang et al., 2021). It is necessary to research biological HAP as PRB reaction materials. HAP can form stable minerals with metal cations, with high stability under oxidative or reducing conditions (Wellman et al., 2008). Without considering the coexistence of other anions and cations, the reaction between HAP and uranium has the following three main mechanisms: 1) Dissolution and precipitation. Under acidic conditions, hydroxyapatite dissolves part of Ca^{2+} and PO_4^{3-}, and precipitate with UO_2^{2+}. New species are formed, such as Ca $[(UO_2)(PO_4)]_2{\cdot}nH_2O$ and H_2 $[(UO_2)(PO_4)]_2{\cdot}nH_2O$ (Kong et al., 2019). 2) Ion exchange. Divalent metal ions in solution are prone to ion exchange reaction with hydroxyapatite. Calcium sites on the surface of HAP can ion-exchange with uranium ions (Stötzel et al., 2009). 3) Adsorption. UO_2^{2+} achieves the adsorption of uranium by occupying surface active sites on hydroxyapatite (Simon et al., 2008).

Permeable concrete is a highly porous special concrete prepared from cement slurry and coarse aggregate (particle size greater than 4.75 mm) (Alighardashi, 2018; Wijeyawardana et al., 2022). The innovative development of mineral materials is to act as a reactive barrier to remove heavy metals and nitrates in groundwater (Shabalala et al., 2017; Alighardashi, 2018). The heavy metals removal mechanism of permeable concrete is mainly to generate metal hydroxide precipitation (Holmes et al., 2017). In addition, microbial action and adsorption also

facilitate the removal of heavy metals (Yousefi and Matavos-Aramyan, 2018).

2.1.4 Ion exchange resin

Ion exchange resin has the characteristics of high adsorption capacity, long-lasting activity and fast reaction rate, which is often used for the removal of heavy metal ions in sewage (Vilensky et al., 2002; Ahmad and Sharma, 2019). Through continuous research on resin modification, selective adsorption and regeneration are significantly improved, which increases the possibility of application in groundwater remediation technology. As a promising PRB reaction medium, ion exchange resin is often used to treat uranium in groundwater, where the treatment process is not easily disturbed by groundwater components (Stucker et al., 2011; Zawierucha and Nowik-Zajac, 2019). With PHREEQE geochemical software (Barton et al., 2004), predicted the existence of uranium in groundwater under different pH conditions. On this basis, they proposed that H^+ on the cation exchange resin can be replaced by cations (Na^+, K^+, Ca^{2+}, and Mg^{2+}) in groundwater, thereby reducing the pH of groundwater and promoting the formation of UO_2^{2+} and adsorption on the resin. However, the main removal mechanism of uranium by anion resins is electrostatic action. However, ion exchange resins are not suitable for treating wastewater with excessively high concentrations of pollutants. Expensive price is the main reason to limit its application. In this regard, the development of inexpensive ion exchange resins becomes an important research direction.

2.1.5 Solid waste

In recent years, solid waste have been used in the reaction medium, which plays a role in reducing the hazard of heavy metals in groundwater, as well as the cost of solid waste treatment and PRB operation. Solid waste such as waste sludge (Chien et al., 2021), fly ash (Yang et al., 2020), and recycled concrete (Indraratna et al., 2010) etc., has become a popular research object for the development of new reaction media. Solid waste in line with the concept of sustainable development is selected as the medium material. However, the composition of solid waste is complex, which may increase the risk of secondary pollution. For the development of solid waste reaction media, the removal capacity and removal mechanism of the material, and the stability of the generated product are important concerns (Faisal et al., 2018). Basic oxygen furnace sludge (BOFS) is rich in ZVI and iron oxides such as FeO and Fe_3O_4 (Omran et al., 2020). BOFS has small particle size, large specific surface area, and positive charge on the surface, which is conducive to the adsorption of CrO_4^{2-} and $Cr_2O_7^{2-}$ in groundwater (Frade et al., 2018). In addition, co-precipitation can occur between $Cr^{3+}$and Fe^{3+} (Blowes et al., 2000). Therefore, the removal mechanisms of Cr(VI) in groundwater by BOFS are mainly adsorption, reduction and co-precipitation. The possible reaction processes are as follows (Wilkin and Puls, 2003; Puls, 2006; Han C. et al., 2016):

$$Cr_2O_7^{2-} + 3Fe(0) + 14H^+ \rightarrow 2Cr^{3+} + 3Fe^{2+} + 7H_2O$$
$$HCrO_4^- + 3Fe^{2+} + 7H^+ \rightarrow Cr^{3+} + 3Fe^{3+} + 4H_2O$$
$$(1-x)Fe^{3+} + Cr^{3+} + 2H_2O \rightarrow Fe_{(1-x)}CrOOH(s) + 3H^+$$

For example, (Frade et al., 2018), found that steelmaking converter sludge is rich in iron oxides such as ZVI and FeO. At pH 5.5, its adsorption capacity for Cr (VI) is 0.213 mg g^{-1}. Calcium content in BOFS is up to 13.9% (w/w). Calcium can promote the release of OH^- the increase of pH, and the precipitation of $Cr(OH)_3$. However, high pH is not conducive to the reduction of Cr(VI). In addition (Araujo et al., 2019), also confirmed that BOFS and ZVI have similar removal effects on high concentrations of arsenic in acidic wastewater.

The advantages and disadvantages of single reaction medium used within PRB have been summed up in Table 1.

2.2 Mixed material

Although there are many types of single media and are widely used in groundwater heavy metal pollution control, it is difficult to meet complex environmental conditions. Two or more of ZVI, mineral material and carbonaceous material are mixed in a certain proportion to form the mixed material, which can enhance the penetration ability of the reaction medium, the type of removal mechanism, the removal rate and the service life.

2.2.1 Mixed material with zero-valent iron

2.2.1.1 Zero-valent iron and mineral material

When ZVI is used as a single active substance, it is easy to cause passivation and blockage. The mixing of ZVI and mineral material can not only increase the permeability coefficient of the PRB system, but also effectively reduce the aggregation of ZVI. When ZVI is mixed with inert mineral materials such as sand and gravel, the permeability coefficient inside the PRB system is improved. In the study by (Wang et al., 2022), a mixed material consisting of ZVI (20%), gravel (20%), and sand (60%) was treated as a PRB filler for Cr(VI). At this time, the concentration of Cr(VI) can be reduced from 27.29–242.65 mg L^{-1} to below 0.1 mg L^{-1}. In addition, this study also found that ZVI could induce changes in the structure and composition of the downstream native microbial community, thereby promoting the biological reduction of Cr(VI).

Pumice and trass have the advantages of abundant channels and large specific surface area, which are often used as adsorbents or filter media for sewage treatment.

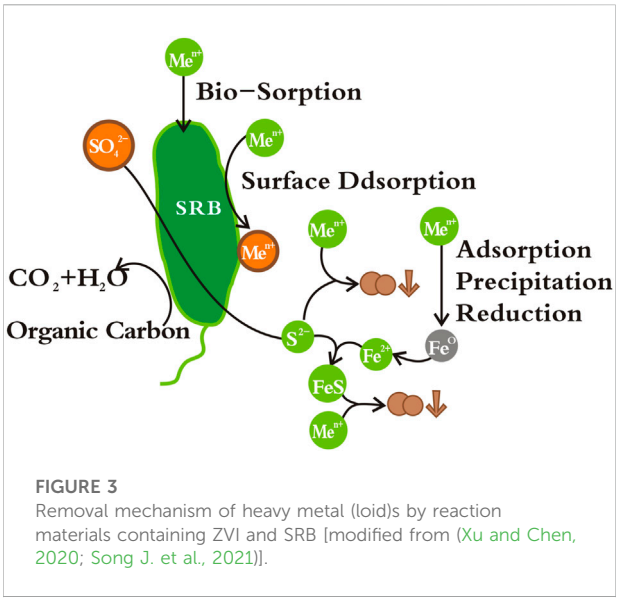

FIGURE 3
Removal mechanism of heavy metal (loid)s by reaction materials containing ZVI and SRB [modified from (Xu and Chen, 2020; Song J. et al., 2021)].

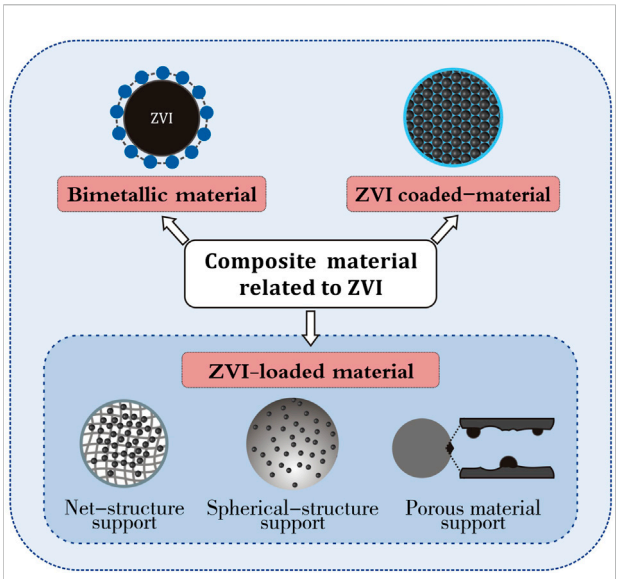

FIGURE 4
Classification of composite materials related to ZVI [modified from (Qu et al., 2017) (Zhang et al., 2021)].

The mixing of ZVI with porous minerals not only increases the permeability coefficient, but also solves the blocking problem of PRB walls. According to the study of (Faisal et al., 2020), when the initial concentration of nickel is 8 mg L^{-1}, the life expectancy of the PRB system with ZVI/pumice mixed material as the reaction medium is more than 26 months, while the life expectancy of the PRB system with only ZVI as the reaction medium is only 3.6 months. In addition, the pyrite/ZVI mixed material as a reaction medium can inhibit the increase of pH, promote the regeneration of Fe(II), and prolong the service life (Lü et al., 2018).

2.2.1.2 Zero-valent iron and compost

Subterranean environment is rich in microorganisms. Bioremediation is an important technology for remediation of soil and groundwater. Compost materials have attracted much attention due to their rich microbial species and high cation exchange capacity (Cancelo-González et al., 2017). Most heavy metal sulfides have low solubility. Sulfate reduction is often used to solve the problem of heavy metal pollution in mining wastewater. This provides a basis for the application of sulfate reducing bacteria (SRB) in PRB technology, and its removal mechanism of heavy metals is shown in Figure 3 (Wilopo et al., 2008) used ZVI, sheep manure, compost and sawdust as fillers to study the removal of arsenic and manganese by PRB. Inoculated SRB may promote the precipitation of part of arsenic in the form of Fe-As-S, but it is not conducive to the solidification of manganese. Inoculation with SRB increases the lifespan of PRB to 15.76 years, which is much higher than that of PRB without SRB (6.74 years). Appropriate pH is a necessary condition for microbial growth. Good permeability is conducive to the normal operation of the PRB system (Gibert et al., 2013) constructed a field-scale PRB system with calcite, plant compost, ZVI, and sludge as fillers, with over 98% heavy metal removal. However, the complex media composition easily leads to the inhomogeneity of the filling material, which can produce clogging and preferential flow channel phenomena. The particle size distribution of the filling material is adjusted to improve this by adding inert materials such as sand and stones.

The growth of microorganisms requires a suitable growth environment. Therefore, suitable pH range and temperature and sufficient nutrients are beneficial to enhance the microbial action in the PRB system. Moreover, the toxic effects of the constituents of the pollutants on microorganisms need to be taken into account.

2.2.2 Mixed material without zero-valent iron

The cost of ZVI-containing fillers is relatively high. In order to improve the economics of PRB technology, solid wastes from agricultural or industrial production processes can be used as precursors to prepare PRB reaction medium (Faisal et al., 2020) mixed waste foundry sand (WFS) with a mass ratio of 82% and filter sand (FS) with a mass ratio of 18% as a reaction medium to treat wastewater containing lead and nickel. Among them, the removal mechanism of the former is mainly chemical adsorption, with the maximum adsorption capacities of 13.966 and 4.227 mg g^{-1}. In order to reduce the secondary pollution, more and more attention has been paid

TABLE 1 Analysis of the advantages and disadvantages of single reaction medium to remove heavy metals.

Mixed reaction media		Mechanism	Advantages	Disadvantages	References
ZVI/nZVI		(a) Adsorption (b) Reduction (c) Precipitation (d) Co-precipitation	(a) Strong reduction ability (b) A variety of heavy metals can be treated (c) Large specific surface area (d) Fast reaction rate	(a) Prone to passivation (b) Easy to cause clogging (c) Prone to agglomeration	Turner et al. (2005), Faisal et al. (2015), Pawluk et al. (2015)
carbonaceous material	Activated carbon	(a) Physical sorption (b) Ion-exchange (c) Complexation (d) Precipitation (e) Electrostatic interaction	(a) Good adsorption properties (b) Steady chemical property	(a) Greatly affected by pH (b) High production cost	Li et al. (2010); Dong et al. (2016)
	Biochar		(a) Good adsorption properties (b) Steady chemical property (c) low cost	Low mechanical strength	Paranavithana et al. (2016); Xiang et al. (2021)
mineral material	Iron-bearing mineral	(a) Sorption	(a) Strong selective adsorption (b) Favorable ion exchange capacity (c) Low cost	(a) Easy to passivate when pH increases (b) Low penetrability (c) Complex chemical composition (d) Potential secondary pollution	Aredes et al. (2012); Liu et al. (2015)
	Channel/lamellar structural mineral	(b) Ion exchange (c) Precipitation	(a) High permeability (b) High mechanical strength (c) Low cost	(a) Complex chemical composition (b) Potential secondary pollution (c) Difficult to recycle (d) Limited processing efficiency	Dong et al. (2013); Faisal and Abd Ali. (2016)
Ion exchange resin		Ion exchange	(a) Large exchange capacity (b) Strong selective (c) Fast reaction rate (d) Low risk of secondary pollution	(a) Not suitable for removal of high-concentration heavy metals (b) High cost	Barton et al. (2004), Flint et al. (2021)
Solid waste		(a) Sorption (b) Ion exchange (c) Precipitation	(a) Materials from a wide range of sources (b) Green development (c) Low cost	(a) Complex chemical composition (b) Limited processing efficiency (c) Potential secondary pollution	Faisal and Abd Ali. (2016), Araujo et al. (2019), Ali Alyaa and Abd Ali Ziad. (2020), Chien et al. (2021)

to the research and development of environmentally friendly materials (Fan et al., 2018) developed a new type of environmentally friendly filler, with corn straw, fly ash, synthetic zeolite, loess ferromanganese nodules and other mixed materials as active media. Its removal mechanism is mainly complexation and electrostatic attraction, with greater than 90% removal rate of Pb(II) and Cd(II).

In contrast, the preparation of mixed material is simpler than that of composite material. The key step in the preparation of mixed material lies in the selection and addition of a variety of single materials. As shown in Table 2, there are differences in the heavy metal treatment capacity and removal mechanism of the reaction medium composed of different types of materials. The selection of active materials should fully consider the removal mechanism of target pollutants. In order to reasonably construct the reaction medium of the PRB, it is necessary to take into account the environmental conditions such as groundwater component and permeability of the surrounding soil.

2.3 Composite material

2.3.1 Composite material related to zero-valent iron

2.3.1.1 Bimetallic material

The ZVI surface is plated with another metal with high reduction potential (such as copper, platinum, and nickel) to

TABLE 2 Application of mixed reaction medium in PRB treatment of groundwater heavy metals.

Mixed reaction media	Heavy metals	Type of experiment	Initial concentration ($mg·L^{-1}$)	Reaction time	Removal efficiency (%)	Adsorption capacity ($mg·g^{-1}$)	Mechanism	References
ZVI and sand	Cr(VI)	Field-scale	27.29–242.65	6 months	Close to 100%		Reduction; precipitation	Wang et al. (2022)
ZVI, pyrite and sand	Ni	Batch and column	20	120 min	>90%		Reduction; precipitation	Nicola et al. (2017)
ZVI and lapillus	Cu(II)	Column	500				Adsorption; co-precipitation	Bilardi et al. (2019)
	Ni(II)		50					
	Zn(II)		50					
ZVI, sheep manureetc.	As(III)	Batch and column	50	48 h	98.9	30.96	Reduction; adsorption; precipitation	Wilopo et al. (2008)
calcite, vegetal compostetc.	Al	Field-scale	15	3 years	>96		Reduction; adsorption; precipitation	Gibert et al. (2013)
	Zn		20		>95			
	Cu		1.2		>98			
BC and soil	Cd(II)	Batch	333	60 min	99.99	30.1	Adsorption	Paranavithana et al. (2016)
	Pb(II)		325		92.5	46.7		
WFS and FS	Pb(II)	Batch and column	50	60 min	>95	13.966	Adsorption; ion exchanges; precipitation	Faisal et al. (2020)
	Ni(II)		50			4.227		
AC and WFS	Zn(II)	Batch	155	3 h	>75		Adsorption	Naji et al. (2020)
Cement kiln dust and FS	Cu(II)	Column	100	99 days	98		Adsorption	Sulaymon et al. (2015)
	Zn(II)				99			
Corn straw, fly ashetc.	Pb(II)	Column	5	12 h	>90		Adsorption	Fan et al. (2018)
	Cd(II)		0.5					
leaf/yard compost, ZVIetc.	As	Pilot	206	30 months	>99		Adsorption; precipitation	Ludwig et al. (2009)
	Pb		2.02					
	Cd		0.324					
	Zn		1060					
	Ni		2.12					

form bimetallic material, which act as galvanic cells during the reaction to speed up the reaction rate. The bimetallic system composed of nZVI can reduce the agglomeration between nZVI and the activation energy during the reaction, thereby increasing the reduction rate (Maamoun et al., 2021). Shubair et al. (2018) demonstrated that the removal mechanism of cesium by nZVI and nZVI/Cu is mainly chemical adsorption, with a removal rate of more than 99%. In contrast, the reaction rate of nZVI/Cu is faster (Xie et al., 2021) synthesized nZVI/Pt bimetallic particles, which showed good removal of heavy metals and chlorophenols (Zhu et al., 2017) demonstrated that nZVI/Ni bimetallic material can reduce the effect of agglomeration, with 99% Cr(VI) removal rate. Copper can promote the electron transfer of Fe^0 and the generation of Fe^{2+}, thereby accelerating Cr(VI) removal. With the remove of Cr(VI) by the bimetallic system composed of nZVI/Cu as an example, the chemical reaction formula is as follows (Maamoun et al., 2021):

$$3Fe^0 + Cr_2O_7^{2-} + 14H^+ \rightarrow Cr^{3+} + 3Fe^{2+} + 7H_2O$$
$$6Fe^{2+} + Cr_2O_7^{2-} + 14H^+ \rightarrow 2Cr^{3+} + 6Fe^{2+} + 7H_2O$$
$$Fe^0 + Cu^{2+} + 14H^+ \rightarrow Cu^0 + Fe^{2+}$$
$$3Cu^0 + Cr_2O_7^{2-} + 14H^+ \rightarrow 2Cr^{3+} + 3Cu^{2+} + 7H_2O$$
$$Cr^{3+} + 3OH^- \rightarrow 3Cr(OH)_3(s)\downarrow$$
$$Fe^{2+} + Cr^{3+} + 8OH^- \rightarrow FeCr_2O_4(s)\downarrow + 4H_2O$$

Moreover, copper can inhibit the oxidation of Fe^0 and increase the electrons obtained by Cr(VI). As shown in Table 3, The research on removing heavy metals from groundwater with ZVI bimetal as reaction media is still in the laboratory stage. It has extensive removal of heavy metals, and its removal mechanism mainly consists of adsorption and reduction. Compared with ZVI and nZVI, bimetallic particles have a faster reaction rate and overcome the disadvantage of easy agglomeration. However, its preparation process is complicated. In addition, some metals are expensive (such as silver and platinum) or cause secondary pollution to the environment

TABLE 3 Application of bimetallic material in PRB treatment of heavy metals in groundwater.

Reaction media	Heavy metals	Type of experiment	Initial concentration (mg L^{-1})	Reaction time	Removal efficiency (%)	Adsorption capacity (mg g^{-1})	Mechanism	References
Cu/Fe	Cr(VI)	Batch and column	20	3 h	85	17.94	Reduction; precipitation	Maamoun et al. (2021)
Si/Fe	Ni(II)	Batch	150	60 min	65.90	55	Adsorption	Abdelrahman and Hegazey. (2019)
	Cu(II)				65.83	56		
	Zn(II)				62.53	53		
Fe/Al	Hg	Batch	32.5	90 min	99.74		Reduction; adsorption	Aghaei et al. (2021)
	As		9.3		99.80			
	Cu		53.4		98.20			
	Pb		91.4		95.50			
Cu/Fe	As(V)	Batch	50	4 h	55		Reduction; adsorption	Rajendran and Thangavelu. (2021)
Ce/Fe	As(V)	Batch and column	10	24 h	Nearly 100	164.94	Reduction; adsorption	Wen et al. (2018)
	Cr(VI)		10		>90	127.42		
Fe/Ni	Zn(II)	Batch	20	240 min	>90	149.25	adsorption	Abukhadra et al. (2018)
	Co(II)			240 min		106.4		
	Cu(II)			120 min		147.5		
Fe/Co.	Cr(VI)	Batch	8	12 h	99	1.6	Reduction; adsorption	Qin et al. (2016)
Fe/Al	U(VI)	Batch	100	24 h	99	575	Reduction; adsorption	Xiang et al. (2018)

(copper and nickel). These factors above limit the application of bimetallic materials.

2.3.1.2 ZVI-loaded material

In order to overcome the shortcoming of easy agglomeration in nZVI, a series of ZVI-loaded solid materials were developed. Reported loaded materials include pyrite (Lü et al., 2018), zeolite (Tasharrofi et al., 2020), bentonite (Zhang et al., 2012), clay (Jia et al., 2011), montmorillonite (Jia and Wang, 2013), activated carbon (Wang M. et al., 2019), biochar (Liu Y. et al., 2019), and graphene (Xing et al., 2016). The application of ZVI-loaded material has been summed up in Table 4.

Magnetite and pyrite alone can be used as reaction medium for PRB system, or loaded material for ZVI. Magnetite is an octahedral crystal rich in Fe_3O_4 and having strong magnetism. Magnetite can attach nZVI to its surface, thereby effectively preventing nZVI from agglomerating. The results of (Wu et al., 2009) showed that when Fe_3O_4:Fe^0 is 40:1, the reaction rate of composite material and Cr(VI) is the fastest. Furthermore, the reaction rate is related to the pH in the solution. Alkaline conditions are not conducive to the removal of Cr(VI). Pyrite is rich in FeS_2, with strong electron transfer ability and reducibility (Min et al., 2021) prepared a ZVI-loaded pyrite composite material (ZVI/FeS_2) using pyrite and ZVI as raw materials by ball milling, with over 99% Cr(VI) removal rate and long-term stability.

Silicon-containing minerals such as zeolite and clay are important heavy metal adsorbents for water. Natural zeolite has high internal porosity and surface active sites, which is suitable as a loaded material for nZVI to eliminate aggregation of nZVI (Li et al., 2018). Clay minerals such as kaolinite, illite, pyrophyllite and montmorillonite can overcome the disadvantage of easy agglomeration in nZVI (Ezzatahmadi et al., 2017). (Bhowmick et al., 2014) prepared a nZVI-loaded montmorillonite, which has a maximum adsorption capacity of 59.9 and 45.5 mg L^{-1} for As(III) and As(V) in a wide pH range (4–8). As(V) and As(III) form complexes on the surface of composites. As(III) is all oxidized to As(V), but As(V) is not reduced. NaOH solution (0.1 M) can be used for the regeneration of composites. After five cycles of test, the properties of composites don't change significantly. Therefore, it is considered an ideal reaction medium for handling arsenic containing groundwater.

BC and AC are porous organic carbonaceous materials with various functional groups on their surfaces. With their large heavy metal adsorption capacity, they are often used as remediation materials for heavy metal pollution in the environment. The ZVI-containing composite material with BC and AC as loaded materials has good removal effect on arsenic, strontium, chromium, and lead (Mandal et al., 2020) prepared nZVI-loaded green tea biochar. The stabilizing effect of Pb(II) is sorted as nZVI-loaded green tea biochar > pristine nZVI > green tea biochar. The load of ZVI to BC is greater than AC. ZVI affects the redox process of target heavy metals. With the removal of selenium as an example, the removal effect of ZVI-loaded BC on

TABLE 4 Application of ZVI-loaded materials in PRB treatment of heavy metals in groundwater.

Reaction media	Heavy metals	Type of experiment	Initial concentration (mg L^{-1})	Reaction time	Removal efficiency (%)	Adsorption capacity (mg g^{-1})	Mechanism	Reference
nZVI-loaded magnetite	As(III) As(V)	Batch	10	1 h	Nearly 100		Reduction; co-precipitation	Wu et al. (2009)
ZVI/FeS2-loaded natural pyrite	Cr(VI)	Batch	448.1 mg kg−1 (soil)	7 d	99.5		Reduction; co-precipitation	Min et al. (2021)
ZVI-loaded pyrite (FeS2)	Sb(V)	Batch	100	180 min	99.18	248.1	Adsorption	He et al. (2020)
ZVI-loaded HAP	U(VI)	Batch	10	100 min	93.8	46.9	Adsorption; precipitation	Zeng et al. (2019)
nZVI-loaded modified zeolite	Cd(II)	Batch	50	90 min		20.6	Adsorption; precipitation; ion exchange	Tasharrofi et al. (2020)
microscale ZVI-loaded zeolite	Pb (II) Cd(II)	Batch and column	50			154.61 63.14	Adsorption; precipitation; ion exchange	Kong et al. (2017)
nZVI-loaded attapulgite	Cr(VI)	Batch	40	12 h	90.6	266.65	Reduction; adsorption	Zhang et al. (2019)
nZVI-loaded AC	Pb(II)	Batch	10	5 min	95	59.35	Adsorption	Liu et al. (2019a)
nZVI-loaded BC	Cr(VI)	Batch	20	8 h	99	40.0	Reduction; adsorption	Qian et al. (2017)
nZVI-loaded exhausted coffee grounds	Pb(II)	Batch	10	1 h		164.1	Reduction; adsorption	Park et al. (2019)
	Cd(II)			24 h		112.5		
	As(III)			1 h		23.5		
	As(V)			1 h		9.3		
nZVI-loaded GO	Cr(VI)	Batch	50	12 h		26.39	Adsorption; reduction; precipitation	Yang et al. (2021)

TABLE 5 Application of nZVI coated-material in PRB treatment of groundwater heavy metals.

Reaction media	Heavy metals	Type of experiment	Initial concentration (mg L^{-1})	Reaction time	Removal efficiency (%)	Adsorption capacity (mg g^{-1})	Mechanism	References
Double surfactant-modified nZVI	Cr(VI)	Batch	80	2 min	99	231.75	Adsorption; reduction; precipitation	Li et al. (2020)
CMC- wrapped nZVI	Cu(II)	Batch	100	2 min		99.7	Adsorption; precipitation	Lou et al. (2019)
	Ni(II)			5 min		84.7		
APAM-modified nZVI	Ni(II)		100	2 h	>80		Adsorption; precipitation	Liu et al. (2016)
Chitosan nanospheres-encapsulated ZVI	As(III)	Batch	2	3 h		94 ± 1.5	adsorption	Gupta et al. (2012)
	As(V)					119 ± 2.6		
CMC-wrapped nZVI	U(VI)	Batch and column	25	29.9 min	Nearly 100%		Adsorption; reduction; precipitation	Zhao et al. (2020)

Se(IV) and Se(VI) is higher than that of ZVI-loaded AC. In addition, pH significantly affected the removal of Se(IV) and Se(VI) by ZVI-loaded BC and ZVI-loaded AC (Tan et al., 2019). Although the nZVI-loaded BC has an ideal removal effect of heavy metals, the preparation procedure is complicated (Zhang et al., 2022) prepared composite materials with biochar and nZVI

using a one-step pyrolysis method, enabling large-scale commercial applications. Furthermore, the activated carbon fiber (Qu et al., 2017) and graphene oxide (GO) (Yang et al., 2021) can also be used as the loaded material of ZVI.

With carbonaceous material as ZVI loading material, the ZVI-loaded BC and AC have more negative charges than the BC and AC surfaces, which has stronger adsorption capacity for cations. The main heavy metal removal mechanism is adsorption. As support material, GO can reduce ZVI aggregation. The abundant functional groups on its surface can well adsorb heavy metals. For Cr(VI) and As(V) in aqueous solution, the another main removal mechanism is reduction. With magnetite and pyrite as ZVI support materials, the main mechanisms for removing heavy metals are adsorption and reduction. HAP is rich in phosphate, and its main mechanism for heavy metal removal is adsorption and precipitation. When zeolite with abundant internal pores is used as ZVI support material, the main mechanisms of heavy metal removal are adsorption, precipitation and ion exchange.

2.3.1.3 Zero-valent iron coated-material

As shown in Table 5, ZVI can also be coated by other materials, which has a good removal effect on heavy metals in groundwater. Surfactants, natural or synthetic polymers can be used to coat the surface of nZVI, which can effectively overcome the agglomeration phenomenon by changing the surface charge of the particles (Reginatto et al., 2020). The nZVI coated by surfactant has good dispersion and transport, fast reaction rate, and wide application range. In addition to continuous reactive walls, injectable suspensions can be used to remediate groundwater (Truex et al., 2011). According to Li et al. (2020), two surfactants polyvinylpyrrolidone (PVP) and sodium oleate (NaOA) were used to coat nZVI. The two active materials exhibited a synergistic effect on Cr(VI) removal.

Surfactant and nZVI are easily desorbed in complex groundwater environments. Polyelectrolytes such as sodium carboxymethyl cellulose (CMC) (Yu et al., 2020), polyacrylic acid (PAA) (Jiemvarangkul et al., 2011), and polyacrylamide (APAM) (Liu et al., 2016) can exist stably for a long time (Zhao et al., 2020). prepared a CMC-wrapped ZVI composite material. When the initial concentration of U(VI) was 25 mg L^{-1} and the pH was 6, the removal rate was close to 100%. According to the XPS spectra of uranium-loaded nanoparticles CMC-ZVI, U(IV) and U(VI) coexist on the surface of the composite material. The main removal mechanisms are reduction, adsorption and precipitation. Bicarbonate extraction is used to extract the precipitated and adsorbed U(VI). The removal mechanism of uranium by composite materials is as follows:

$$UO_2^{2+} + 2H_2O + 2OH^- \leftrightarrow UO_3 \cdot 3H_2O(s)$$

$$UO_2^{2+} + 2 > Fe - OH \leftrightarrow \left[(> Fe - O)_2 UO_2 \right]_{ads} + 2H^+$$

$$Fe^0 + 1.5UO_2^{2+} + 6H^+ \rightarrow Fe^{3+} + 1.5U^{4+} + 3H_2O$$

$$2Fe^{2+}_{structural} + UO_2^{2+} + 6H^+ \rightarrow U^{4+} + 2Fe^{3+}_{structural} + 2H_2O$$

In summary, the classification of composite material related to ZVI is shown in Figure 4.

2.3.2 Mineral-related composite material

The removal effect of a single mineral medium on different pollutants has a huge difference. Many researchers have used nanoparticles-loaded mineral, surfactant modification, and polymer-encapsulated minerals to prepare composite materials to remove complex groundwater pollution (Zeng et al., 2020) made an environmentally friendly and economical SiO_2/FeC_2O_4 composite material using biotite as raw material by one-step synthesis. When the initial concentration was 20 mg L^{-1}, the removal rate of Cr(VI) was close to 100% in the pH range of 2–10 (Wang et al., 2020) modified bentonite with cetyltrimethylammonium bromide (CTMAB), which increased the maximum adsorption capacity for Cr(VI) to 19-fold compared to before modification. In addition, the feasibility of its application in PRB was demonstrated by column experiments (Bambaeero and Bazargan-Lari, 2021) prepared a HAP/chitosan composite material from shrimp shell, bovine bone and snail shell, which has good adsorption capacity for Zn(II) and Cu(II) (Vahdat et al., 2019) loaded Fe_3O_4 on the surface of HAP prepared from chicken thigh bone, and successfully prepared a nano composite material, which has adsorption capacity on lead as high as 109.89 mg g^{-1}. According to the desorption experiment, EDTA solution (0.001 M) is an ideal desorption reagent, and its adsorption capacity to composites only decreases by 19% after five cycles.

Microorganisms are abundant in nature. For example, both SRB and iron-reducing bacteria have been shown to have the ability to reduce Fe(III) to Fe(II) (Cao et al., 2010). Co-processing of heavy metal pollution in groundwater with mineral composite materials and microorganisms has become an important research direction. In the study of (Xu et al., 2022), SRB were used to synthesize biogenic FeS kaolin composite material, which has ideal adsorption effect on various heavy metals such as Pb(II), Sb(III), and Cd(II). The introduction of microorganisms can often save costs. During the operating life cycle of PRB, it is necessary to strengthen the control of environmental factors such as pH, redox potential and toxin substance.

As shown in Table 6, mineral-related composites can extensively remove heavy metal ions from groundwater. There are differences in the removal mechanisms of heavy metals by composites prepared from different substances and mineral materials. In general, clay has strong adsorption and ion exchange capacities. Zeolite has ideal adsorption, ion exchange and catalytic capabilities. Apatite can provide sufficient phosphate. Mineral materials can improve the comprehensive properties of materials while retaining the advantages of carrier materials, which can not only be embedded in polymers, but also

TABLE 6 Application of mineral-related composite materials in PRB treatment of groundwater heavy metals.

Reaction media	Heavy metals	Type of experiment	Initial concentration (mg L^{-1})	Reaction time	Removal efficiency (%)	Adsorption capacity (mg g^{-1})	Mechanism	References
FeS-loaded sand	As(III)	Batch	5	2 days		41.7	Precipitation; reduction; adsorption	Han et al. (2011)
Mackinawite-loaded sand	Cr(VI)	Batch	5	3 days	100	0.187	Reduction; precipitation; adsorption	Park et al. (2018)
Nano-FeC_2O_4-loaded SiO_2	Cr(VI)	batch and column	20	90 min	95.45		Reduction; precipitation; complexation	Zeng et al. (2020)
Fe_3O_4-loaded HAP	Fe(II)		50	1 h	98	4.9	Adsorption; ion exchange	Vahdat et al. (2019)
	Mn(II)		50		95	4.8	precipitation;	
Chitosan-immobilized HAP	Zn(II)	Batch	3	95 min	60	25.78	Adsorption; precipitation	Bambaeero and Bazargan-Lari, (2021)
	Cu(II)		3	220 min	90	20.394		
Chitosan immobilized bentonite	Cu(II)	Column	500	24 h	85.57	14.92	Adsorption; ion exchange	Futalan et al. (2011)
CMC-stabilized FeS	Cr(VI)	Batch	50	150 min	92.5	1046.1	Adsorption; reduction; co-precipitation	Wang et al. (2019b)
CMC-stabilized FeS	U(VI)	batch	10	1 h	>90		Reduction; adsorption	Duan et al. (2020)
TMAB-modified bentonite	Cr(VI)	batch and column	100	40 min		7.227	Adsorption; ion exchange	Wang et al. (2020)
Biogenic FeS-loaded Kaolin	Cd	batch	250	360 min		71.71	Reduction; adsorption	Xu et al. (2022)
	Pb		250			133.54		
	Cu		250			51.90		
	Zn		250			54.41		
	As		250			38.71		
	Sb		250			96.38		

be used as support materials for nanoparticles such as FeC_2O_4, FeS, and Fe_3O_4.

2.3.3 Carbon-related composite material

Carbon composite material is another important medium material. The application of the carbon composite material have been summed up in Table 7. AC and BC have high porosity and large specific surface area, which are ideal loaded materials (Shapira and Zucker, 2022) loaded MoS_2 on AC, which achieved an adsorption capacity for mercury of 1280 mg g^{-1}. In addition, this kind of composite material has a good recycling effect (Song X. et al., 2021) prepared biochar by microwave *in-situ* synthesis with reed as raw material and modified it by nano-magnetite. The maximum adsorption capacity of Cr(VI) by the modified composite material was 9.92 mg g^{-1}, which was higher than that of unmodified biochar (8.03 mg g^{-1}).

In general, polymers such as surfactant and polyelectrolyte are rich in functional groups. Such substances can be used to modify AC and BC (Inyang et al., 2016). Chen et al. (2022) loaded chitosan on the surface of BC to synergize the hydroxyl groups of chitosan with the carbonyl groups of pristine BC, thereby enhancing the adsorption capacity for Sb(III). According to the research of (Yi et al., 2019), chitosan-coated AC has broad prospects in the treatment of groundwater and soil cadmium pollution remediation.

With large specific surface area, abundant functional groups, and strong hydrophilicity, GO can efficiently adsorb heavy metals. However, the characteristics of easy aggregation and difficult separation limit its scope of application. In addition to composite materials such as magnetic GO and ZVI-loaded GO, composite materials such as chitosan-coated GO (Yang et al., 2014), alginate-modified GO, silica-loaded GO (GO-SiO_2), and thiol-modified GO have potential application value of removing heavy metals from groundwater (Zhang et al., 2020). Alginate is a hydrophilic biosorbent material rich in carboxylic acid groups. Despite its poor stability in the environment, it can be hydrogen-bonded with GO to prepare three-dimensional porous composite materials (Pan et al., 2018). The gel properties of alginate can

TABLE 7 Application of carbon-related composite materials in PRB treatment of groundwater heavy metals.

Reaction media	Heavy metals	Type of experiment	Initial concentration (mg·L-1)	Reaction time	Removal efficiency (%)	Adsorption capacity ($mg·g^{-1}$)	Mechanism	References
nano-Fe_3O_4-loaded BC	Cr(VI)	Batch				9.92	Adsorption; reduction	Song et al. (2021b)
Fe_3O_4-loaded BC	As(V)	Batch and column	5	24 h	>90	7.41	Adsorption	Zhang et al. (2016)
Chitosan-loaded BC	Sb(III)	Batch	40	24 h		17.2	Adsorption	Chen et al. (2022)
Nano-zirconia-loaded BC	As(V)	Batch	10	12 h		7.867	Ion exchange; adsorption	Liu et al. (2021)
Ce-doped AC	Cd(II)	Batch	1.85	150 min	51.24	5.88	Adsorption	Kouotou et al. (2022)
4-vinylpyridine-coated AC	Cr(VI)	Batch	18.1	24 h		53.7	Adsorption; reduction; ion exchange	Fang et al. (2007)
Calcium alginate-coated GO	Pb(II)		310.8	40 min		368.2	Adsorption	Pan et al. (2018)
	Cu(II)		95.32			98.1		
	Cd(II)		168.8			183.6		
EDTA-modified GO	Pb(II)		100	20 min		479 ± 46	Adsorption	Madadrang et al. (2012)
NH_2-functionalized GO-SiO_2	Cu(II)	Batch	12.71–158.88	4 h		158.9	Adsorption	Yang et al. (2016)

ensure that the composite material is separated from the water environment, thereby avoiding secondary pollution of the water body (Pan et al., 2019). The composite of two novel materials, GO and SiO_2, can complement each other's advantages (Yang et al., 2016) introduced amino groups into the GO-SiO_2, which showed an adsorption capacity of up to 158.9 mg g^{-1} for Cu(II) under the optimal adsorption conditions. On the one hand, the GO composite material has strong adsorption capacity for heavy metals. On the other hand, it has the disadvantages of complicated process and high cost. Therefore, it is necessary to develop new fabrication processes to reduce costs.

Carbonaceous material is light in weight and high in strength, and its large surface area can effectively disperse nanoparticles (such as MoS_2 and nano-magnetite). The surface properties and electron distribution of carbonaceous materials have positive effect on electron migration. In more detail, the electron transfer of heavy metal pollutants and their intermediates is effectively promoted during the adsorption process. Due to its environmental friendliness, it is considered as an ideal material for PRB reaction media.

In summary, there are differences in the removal mechanism and removal effect of heavy metals by different reaction media. Reasonable selection of medium materials should be based on actual conditions, such as groundwater quality and geological conditions. The advantages and disadvantages of the three types of reaction media are compared in Table 8.

3 Screening of reaction medium

The removal effect of PRB on heavy metals in groundwater mainly depends on the reaction medium filled inside. Under reaction medium adsorption, ion exchange, and chemical reaction, heavy metals can be converted into low-toxic substances or fixed in PRB, so as to achieve the purpose of reducing toxic effects. Thus, the key to PRB technology lies in the choice of reaction medium. The screening of reaction medium mainly has three stages, including static batch test, dynamic column test, and simulated slot test. The removal ability and principle, permeability, long-term effect and other properties of the reaction medium were studied.

3.1 Batch test

The static batch test mainly explores the removal ability of the reaction medium to target pollutants through a series of condition control experiments, and obtains the preferred medium (Tasharrofi et al., 2020) carried out batch tests for the removal of Cd(II) from native zeolite and different modified zeolites. According to the research results, sodium zeolite had the most ideal adsorption effect on Cd(II) with an initial concentration of 50 mg L^{-1}, with a maximum adsorption capacity of 22 mg g^{-1}, which was selected as the adsorbent for subsequent experiments.

TABLE 8 Comparison of advantages and disadvantages of three types of reaction media.

Reaction media	Advantages	Disadvantages
Single material	Simple reaction mechanism and high removal efficiency of characteristic pollutants	Limited effect on complex groundwater pollution control
Mixed materials	(a) Mechanical mixing of two or more materials, and simple preparation process	(a) Limited removal efficiency
	(b) Good effect on complex groundwater pollution	(b) Improper material particle size combination is prone to preferential flow or clogging
	(c) Reasonable combination between different materials, and good hydraulic conditions	(c) Multiple chemical reaction processes and poor controllability
Composite materials	(a) Cooperative work, and high removal efficiency (b) Good effect on complex groundwater pollution (c) Multiple reaction mechanism	(a) Complex preparation process, and high cost (b) Potential secondary pollution

After completing the preliminary screening, batch test can be used to determine the optimal reaction conditions and reaction principle, thus providing a basis for later dynamic experiments (Chattanathan et al., 2013) prepared HAP from catfish bone. The results of batch test showed that the medium was ideal for the removal of U(VI) when the pH was in the range of 5.5–7. In addition, the smaller the particle size and the larger the surface area, the higher the removal rate of U(VI) (Liu et al., 2014) conducted a batch test study of arsenic removal from ox bone spodium. The adsorption behavior fits the Langmuir isotherm, with an R^2 of 0.97. Its main adsorption mechanism is monolayer chemisorption.

3.2 Column test

The dynamic column test mainly studies the effect of the medium on the removal of pollutants by the reaction medium under hydrodynamic conditions. Through a 9-months Column test, (Liu and Lo, 2011) found that HA could promote the removal of Cr(VI) in a PRB with ZVI as the reaction medium. In addition, calcium in the groundwater component affects the action of HA. Calcium in groundwater would cause precipitates to easily aggregate on the ZVI surface, thereby inhibiting electron transfer and affecting Cr(VI) removal. Second, column tests are often used to simulate the longevity of PRB when aquiclude runs. The long-term study of the reaction medium mainly involves the change of the activity of the reaction medium and the blockage of the medium pores during the service period of the PRB. According to the findings of (Kuma et al., 2016), in the PRB system with ZVI as the reaction medium, the reason that affects the long-term effect of PRB is the blockage of the medium pores caused by the precipitation of secondary minerals. In addition, the column test can study the long-term effect of the medium, as well as the influence of the initial concentration of heavy metals, hydraulic retention time, flow rate, dissolved oxygen content, and organic matter content on the operation effect of PRB (Huang et al., 2020) carried out column tests with SGO/Fe-Mn as the reaction medium to study the removal ability and influencing factors of mercury. According to the research results, the higher initial concentration of mercury, the lower pore velocity, and the lower dissolved organic matter and dissolved oxygen content in the groundwater, the stronger removal ability. On the basis of column experiments, (Obiri-Nyarko et al., 2015) simulated the behavior of Pb^{2+} with the help of PHREEQC, which confirmed that zeolite is an effective media material for the removal of lead contamination in groundwater.

3.3 Pilot-scale test

According to the hydraulic characteristics, the column test simulates a 1D groundwater flow situation. The pilot-scale test can reflect the removal effect of the reaction medium on target pollutants under 3D water flow, with a more realistic simulation effect. Unlike batch and column experiments, the Pilot-scale test can reveal pollutant removal mechanisms in complex field environments, especially the effects of subsurface microorganisms (Beak and Wilkin, 2009). Therefore, pilot-scale test is necessary. Through Geochemist's Workbench and X-ray absorption spectroscopy, (Beak and Wilkin, 2009) found that the removal mechanism of arsenic by PRB with zero-valent iron as the reaction medium is more complicated than the results of previous laboratory simulation studies. Sulfate is reduced to sulfide under the action of microorganisms in the subterranean environment. The formation of FeS provides more mineral surface for arsenic removal (Rhee et al., 2010)conducted a pilot-scale test using ZVI-loaded zeolite as the reaction medium. According to the test results, ZVI-loaded zeolite can efficiently remove Cd(II) and Cr(VI), which is an ideal active

medium for processing complex groundwater polluted by heavy metals (Ludwig et al., 2009) conducted a 30-months experiment with leaf compost and ZVI as the active media for the PRB pilot-scale test to explore the removal effect of As, Pb, Cd, Zn, and Ni and other pollutants in groundwater. The test results show that the removal rate of each pollutant is more than 99%. The cycle of batch and column tests is too short to accurately predict the lifetime of the reaction medium and the long-term performance of the PRB.

The above three types of tests are widely used in the screening process of PRB reaction medium materials. The exploration of the reaction mechanism of the reaction medium and contaminants and the long-term performance of the reaction medium is advanced through the combination with numerical simulation.

4 Conclusion and outlook

PRB is a cost-effective remediation technology for heavy metal pollution in groundwater, in which the reaction medium is an important component. The development of cheap, efficient and environmentally friendly new reaction medium materials has far-reaching significance for the treatment of groundwater and soil heavy metal pollution. Despite extensive research on reaction medium materials, there are still some deficiencies, which hamper the application of PRB technology.

(1) Most of the development of mixed material and composite material reaction medium for dealing with heavy metal pollution revolves around ZVI. The choice of reaction medium is relatively small. The development and research of a single new material is an important direction.
(2) The types of active materials containing natural ore materials and industrial and agricultural solid waste are increasing. Despite good economics, the composition of such materials is complex. Besides the difficulty in controlling the reaction rate between active materials and heavy metals, there is unclear reaction mechanism as well as potential risk of environmental pollution.
(3) The introduction of microbial action can enhance the long-term effect of PRB. The co-treatment of groundwater and soil heavy metal pollution with active materials and microorganisms is beneficial for cost savings. In addition, it is necessary to strengthen the control of pH, redox potential, toxin substance and other environmental factors.
(4) For composite materials, the complex preparation process and high cost will limit the application of PRB technology. The development of composite materials with simple preparation process, strong adsorption capacity, good chemical stability, and easy recycling will be the main development direction of reaction medium materials, especially nano-composite materials.
(5) At present, the research on the treatment of heavy metal pollution in groundwater with reaction medium mainly relies on indoor batch test and column test. The pilot-scale test should be paid attention to, which can more accurately examine the removal effect of the reaction material on the target pollutant. In addition, geochemical numerical modelling is worth researchers' attention, which can more accurately analyze the removal mechanism, evaluate the service life and potential environmental risks of the reaction material, and determine the potential and limitations of use.

Author contributions

HL and QL contributed to the writing of the manuscript. HL reviewed and edited the manuscript.

Funding

This research was funded by Research Fund for high-level talents of Luzhou Vocational and Technical College (ZLYGCC202101).

Acknowledgments

Wei Du of Luzhou Vocational and Technical College, was of great assistance during data collection.

Conflict of Interest

The authors declare that the research was conducted in the absence of any commercial or financial relationships that could be construed as a potential conflict of interest.

Publisher's note

References

Abdelrahman, E. A., Abou El-Reash, Y. G., Youssef, H. M., Kotp, Y. H., and Hegazey, R. M. (2021). Utilization of rice husk and waste aluminum cans for the synthesis of some nanosized zeolite, zeolite/zeolite, and geopolymer/zeolite products for the efficient removal of Co(II), Cu(II), and Zn(II) ions from aqueous media. *J. Hazard. Mater.* 401, 123813. doi:10.1016/j.jhazmat.2020.123813

Abdelrahman, E. A., and Hegazey, R. M. (2019). Exploitation of Egyptian insecticide cans in the fabrication of Si/Fe nanostructures and their chitosan polymer composites for the removal of Ni(II), Cu(II), and Zn(II) ions from aqueous solutions. *Compos. Part B Eng.* 166, 382–400. doi:10.1016/j.compositesb.2019.02.027

Abdul, N., Abdul-Talib, S., and Amir, A. (2019). Nano-pyrite as a reductant to remove chromium in groundwater. *KSCE J. Civ. Eng.* 23, 992–999. doi:10.1007/s12205-019-1034-x

Abukhadra, M. R., Dardir, F. M., Shaban, M., Ahmed, E. A., and Soliman, M. F. (2018). Superior removal of Co2+, Cu2+ and Zn2+ contaminants from water utilizing spongy Ni/Fe carbonate–fluorapatite; preparation, application and mechanism. *Ecotoxicol. Environ. Saf.* 157, 358–368. doi:10.1016/j.ecoenv.2018.03.085

Aghaei, E., Wang, Z., Tadesse, B., Tabelin, C. B., Quadir, Z., and Alorro, R. D. (2021). Performance evaluation of Fe-Al bimetallic particles for the removal of potentially toxic elements from combined acid mine drainage-effluents from refractory gold ore processing. *Minerals* 11 (6), 590. doi:10.3390/min11060590

Ahmad, W., and Sharma, S. (2019). Synthesis, characterisation and ion exchange properties of hybrid organic–inorganic composite material: Polyacrylamide zirconium (IV) iodosulphosalicylate. *Int. J. Environ. Anal. Chem.* 99 (15), 1604–1614. doi:10.1080/03067319.2019.1628950

Ali Alyaa, F., and Abd Ali Ziad, T. (2020). Sustainable use of concrete demolition waste as reactive material in permeable barrier for remediation of groundwater: Batch and continuous study. *J. Environ. Eng. New. York.* 146 (7), 04020048. doi:10.1061/(ASCE)EE.1943-7870.0001714

Ali, H., Khan, E., and Ilahi, I. (2019). Environmental chemistry and ecotoxicology of hazardous heavy metals: Environmental persistence, toxicity, and bioaccumulation. *J. Chem.* 2019, 1–14. doi:10.1155/2019/6730305

Alighardashi, A., Mehrani, M. J., and Ramezanianpour, A. M. (2018). Pervious concrete reactive barrier containing nano-silica for nitrate removal from contaminated water. *Environ. Sci. Pollut. Res.* 25, 29481–29492. doi:10.1007/s11356-018-3008-9

Araujo, S. F., Caldeira, C. L., Ciminelli, V. S. T., Silva, A., and Amorim, C. C. (2019). Versatility of iron-rich steel waste for the removal of high arsenic and sulfate concentrations in water. *Environ. Sci. Pollut. Res.* 26 (5), 4266–4276. doi:10.1007/s11356-018-3168-7

Aredes, S., Klein, B., and Pawlik, M. (2012). The removal of arsenic from water using natural iron oxide minerals. *J. Clean. Prod.* 29-30, 208–213. doi:10.1016/j.jclepro.2012.01.029

Asokbunyarat, V., Lens, P. N. L., and Annachhatre, A. (2017). "Permeable reactive barriers for heavy metal removal," in *Environmental chemistry for a sustainable world*, 65–100.

Asri, S. E., Laghzizil, A., Coradin, T., Saoiabi, A., Alaoui, A., and M'hamedi, R. (2010). Conversion of natural phosphate rock into mesoporous hydroxyapatite for heavy metals removal from aqueous solution. *Colloids Surfaces A Physicochem. Eng. Aspects* 362 (1), 33–38. doi:10.1016/j.colsurfa.2010.03.036

Bailey, S. E., Olin, T. J., Bricka, R. M., and Adrian, D. D. (1999). A review of potentially low-cost sorbents for heavy metals. *Water Res.* 33 (11), 2469–2479. doi:10.1016/S0043-1354(98)00475-8

Bambaeero, A., and Bazargan-Lari, R. (2021). Simultaneous removal of copper and zinc ions by low cost natural snail shell/hydroxyapatite/chitosan composite. *Chin. J. Chem. Eng.* 33, 221–230. doi:10.1016/j.cjche.2020.07.066

Barceló, J., and Poschenrieder, C. (1990). Plant water relations as affected by heavy metal stress: A review. *J. Plant Nutr.* 13 (1), 1–37. doi:10.1080/01904169009364057

Barton, C. S., Stewart, D. I., Morris, K., and Bryant, D. E. (2004). Performance of three resin-based materials for treating uranium-contaminated groundwater within a PRB. *J. Hazard. Mater.* 116 (3), 191–204. doi:10.1016/j.jhazmat.2004.08.028

Beak, D. G., and Wilkin, R. T. (2009). Performance of a zerovalent iron reactive barrier for the treatment of arsenic in groundwater: Part 2. Geochemical modeling and solid phase studies. *J. Contam. Hydrology* 106 (1), 15–28. doi:10.1016/j.jconhyd.2008.12.003

Bhowmick, S., Chakraborty, S., Mondal, P., Van Renterghem, W., Van den Berghe, S., Roman-Ross, G., et al. (2014). Montmorillonite-supported nanoscale zero-valent iron for removal of arsenic from aqueous solution: Kinetics and mechanism. *Chem. Eng. J.* 243, 14–23. doi:10.1016/j.cej.2013.12.049

Bilardi, S., Calabrò, P. S., and Moraci, N. (2019). The removal efficiency and long-term hydraulic behaviour of zero valent iron/lapillus mixtures for the simultaneous removal of Cu2+, Ni2+ and Zn2+. *Sci. Total Environ.* 675, 490–500. doi:10.1016/j.scitotenv.2019.04.260

Blowes, D. W., Ptacek, C. J., Benner, S. G., McRae, C. W. T., Bennett, T. A., and Puls, R. W. (2000). Treatment of inorganic contaminants using permeable reactive barriers11Disclaimer: The U. S. Environment Protection Agency through its Office of Research and Development partially funded and collaborated in the research described here under assistance agreement number CR-823017 to the University of Waterloo. *J. Contam. Hydrology* 45 (1), 123–137. doi:10.1016/s0169-7722(00)00122-4

Cancelo-González, J., Martiñá-Prieto, D., Hernández-Huerta, D., and Barral, M. T. (2017). Metal removal by pine bark compost using a permeable reactive barrier device at laboratory scale. *Environ. Chem.* 14 (5), 310–318. doi:10.1071/EN17028

Cao, F., Li, F. B., Liu, T. X., Huang, D. Y., Wu, C. Y., Feng, C. H., et al. (2010). Effect of aeromonas hydrophila on reductive dechlorination of DDTs by zero-valent iron. *J. Agric. Food Chem.* 58 (23), 12366–12372. doi:10.1021/jf102902f

Cerjan Stefanović, Š., Zabukovec Logar, N., Margeta, K., Novak Tušar, N., Arčon, I., Maver, K., et al. (2007). Structural investigation of Zn2+ sorption on clinoptilolite tuff from the Vranjska Banja deposit in Serbia. *Microporous Mesoporous Mater.* 105 (3), 251–259. doi:10.1016/j.micromeso.2007.04.033

Chattanathan, S. A., Clement, T. P., Kanel, S. R., Barnett, M. O., and Chatakondi, N. (2013). Remediation of uranium-contaminated groundwater by sorption onto hydroxyapatite derived from catfish bones. *Water Air Soil Pollut.* 224 (2), 1429. doi:10.1007/s11270-012-1429-5

Chen, H., Gao, Y., El-Naggar, A., Niazi, N. K., Sun, C., Shaheen, S. M., et al. (2022). Enhanced sorption of trivalent antimony by chitosan-loaded biochar in aqueous solutions: Characterization, performance and mechanisms. *J. Hazard. Mater.* 425, 127971. doi:10.1016/j.jhazmat.2021.127971

Chien, S.-W. C., Li, Y.-P., and Liu, C.-C. (2021). Permeable reactive barrier of waste sludge from wine processing utilized to block a metallic mixture plume in a simulated aquifer. *Water Sci. Technol.* 84 (9), 2472–2485. doi:10.2166/wst.2021.440

Day, S. R., O'Hannesin, S. F., and Marsden, L. (1999). Geotechnical techniques for the construction of reactive barriers. *J. Hazard. Mater.* 67 (3), 285–297. doi:10.1016/S0304-3894(99)00044-8

Di Natale, F., Lancia, A., Molino, A., and Musmarra, D. (2007). Removal of chromium ions form aqueous solutions by adsorption on activated carbon and char. *J. Hazard. Mater.* 145 (3), 381–390. doi:10.1016/j.jhazmat.2006.11.028

Dong, L., Liu, W., Jiang, R., and Wang, Z. (2016). Study on the adsorption mechanism of activated carbon removing low concentrations of heavy metals. *Desalination Water Treat.* 57 (17), 7812–7822. doi:10.1080/19443994.2015.1100140

Dong, L., Zhu, Z., Qiu, Y., and Zhao, J. (2013). Advance in research of heavy metals removal by hydroxyapatite and its composite. *Chem. Bull./ Huaxue Tongbao* 76, 405–410.

Dries, J., Bastiaens, L., Springael, D., Agathos, S. N., and Diels, L. (2005). Combined removal of chlorinated ethenes and heavy metals by zerovalent iron inbatch and continuous flow column systems. *Environ. Sci. Technol.* 39 (21), 8460–8465. doi:10.1021/es050251d

Duan, J., Ji, H., Zhao, X., Tian, S., Liu, X., Liu, W., et al. (2020). Immobilization of U(VI) by stabilized iron sulfide nanoparticles: Water chemistry effects, mechanisms, and long-term stability. *Chem. Eng. J.* 393, 124692. doi:10.1016/j.cej.2020.124692

Elkady, M., Shokry, H., and Hamad, H. (2018). Microwave-assisted synthesis of magnetic hydroxyapatite for removal of heavy metals from groundwater. *Chem. Eng. Technol.* 41 (3), 553–562. doi:10.1002/ceat.201600631

Ezzatahmadi, N., Ayoko, G. A., Millar, G. J., Speight, R., Yan, C., Li, J., et al. (2017). Clay-supported nanoscale zero-valent iron composite materials for the remediation of contaminated aqueous solutions: A review. *Chem. Eng. J.* 312, 336–350. doi:10.1016/j.cej.2016.11.154

Faisal, A. A. H., Abbas, T. R., and Jassam, S. H. (2015). Removal of zinc from contaminated groundwater by zero-valent iron permeable reactive barrier. *Desalination Water Treat.* 55 (6), 1586–1597. doi:10.1080/19443994.2014.928908

Faisal, A. A. H., and Abd Ali, Z. T. (2016). Groundwater protection from lead contamination using granular dead anaerobic sludge biosorbent as permeable reactive barrier. *Desalination Water Treat.* 57 (9), 3891–3903. doi:10.1080/19443994.2014.990928

Faisal, A. A. H., Al-Ridah, Z. A., Naji, L. A., Naushad, M., and El-Serehy, H. A. (2020). Waste foundry sand as permeable and low permeable barrier for restriction of the propagation of lead and nickel Ions in groundwater. *J. Chem.* 2020, 1–13. doi:10.1155/2020/4569176

Faisal, A. A. H., and Hmood, Z. A. (2015). Groundwater protection from cadmium contamination by zeolite permeable reactive barrier. *Desalination Water Treat.* 53 (5), 1–10. doi:10.1080/19443994.2013.855668

Faisal, A. A. H., Sulaymon, A. H., and Khaliefa, Q. M. (2018). A review of permeable reactive barrier as passive sustainable technology for groundwater remediation. *Int. J. Environ. Sci. Technol. (Tehran).* 15 (5), 1123–1138. doi:10.1007/s13762-017-1466-0

Famiglietti, J. S. (2014). The global groundwater crisis. *Nat. Clim. Chang.* 4 (11), 945–948. doi:10.1038/nclimate2425

Fan, C., Gao, Y., Zhang, Y., Dong, W., and Lai, M. (2018). Remediation of lead and cadmium from simulated groundwater in loess region in northwestern China using permeable reactive barrier filled with environmentally friendly mixed adsorbents. *Environ. Sci. Pollut. Res.* 25 (2), 1486–1496. doi:10.1007/s11356-017-0587-9

Fang, J., Gu, Z., Gang, D., Liu, C., Ilton, E. S., and Deng, B. (2007). Cr(VI) removal from aqueous solution by activated carbon coated with quaternized poly(4-vinylpyridine). *Environ. Sci. Technol.* 41 (13), 4748–4753. doi:10.1021/es061969b

Fedoročková, A., Raschman, P., Sučik, G., Švandová, M., and Doráková, A. (2021). Reactive, sparingly soluble calcined magnesia, tailor-made as the reactive material for heavy metal removal from contaminated groundwater using permeable reactive barrier. *Minerals* 11 (11), 1153. doi:10.3390/min11111153

Flint, L. C., Arias-Paić, M. S., and Korak, J. A. (2021). Removal of hexavalent chromium by anion exchange: Non-target anion behavior and practical implications. *Environ. Sci. Water Res. Technol.* 7 (12), 2397–2413. doi:10.1039/D1EW00382H

Frade, P. R., Notini, L., Santos, S. V., Moreira, R. F. P. M., Leão, M. M. D., and Amorim, C. C. (2018). Feasibility study of the use of basic oxygen furnace sludge in a permeable reactive barrier. *J. Hazard. Mater.* 351, 188–195. doi:10.1016/j.jhazmat.2018.02.035

Fu, F., Dionysiou, D. D., and Liu, H. (2014). The use of zero-valent iron for groundwater remediation and wastewater treatment: A review. *J. Hazard. Mater.* 267, 194–205. doi:10.1016/j.jhazmat.2013.12.062

Futalan, C. M., Kan, C., Dalida, M. L., Pascua, C., and Wan, M. (2011). Fixed-bed column studies on the removal of copper using chitosan immobilized on bentonite. *Carbohydr. Polym.* 83 (2), 697–704. doi:10.1016/j.carbpol.2010.08.043

Gibert, O., Cortina, J. L., de Pablo, J., and Ayora, C. (2013). Performance of a field-scale permeable reactive barrier based on organic substrate and zero-valent iron for *in situ* remediation of acid mine drainage. *Environ. Sci. Pollut. Res.* 20 (11), 7854–7862. doi:10.1007/s11356-013-1507-2

Gong, Y., Tang, J., and Zhao, D. (2016). Application of iron sulfide particles for groundwater and soil remediation: A review. *Water Res.* 89, 309–320. doi:10.1016/j.watres.2015.11.063

Gupta, A., Yunus, M., and Sankararamakrishnan, N. (2012). Zerovalent iron encapsulated chitosan nanospheres – a novel adsorbent for the removal of total inorganic Arsenic from aqueous systems. *Chemosphere* 86 (2), 150–155. doi:10.1016/j.chemosphere.2011.10.003

Han, C., Jiao, Y., Wu, Q., Yang, W., Yang, H., and Xue, X. (2016a). Kinetics and mechanism of hexavalent chromium removal by basic oxygen furnace slag. *J. Environ. Sci.* 46, 63–71. doi:10.1016/j.jes.2015.09.024

Han, Y., Cao, X., Ouyang, X., Sohi, S. P., and Chen, J. (2016b). Adsorption kinetics of magnetic biochar derived from peanut hull on removal of Cr (VI) from aqueous solution: Effects of production conditions and particle size. *Chemosphere* 145, 336–341. doi:10.1016/j.chemosphere.2015.11.050

Han, Y. S., Jeong, H. Y., Demond, A. H., and Hayes, K. F. (2011). X-ray absorption and photoelectron spectroscopic study of the association of As(III) with nanoparticulate FeS and FeS-coated sand. *Water Res.* 45 (17), 5727–5735. doi:10.1016/j.watres.2011.08.026

Hashim, M. A., Mukhopadhyay, S., Sahu, J. N., and Sengupta, B. (2011). Remediation technologies for heavy metal contaminated groundwater. *J. Environ. Manag.* 92 (10), 2355–2388. doi:10.1016/j.jenvman.2011.06.009

He, X., Min, X., Peng, T., Ke, Y., Zhao, F., Sillanpää, M., et al. (2020). Enhanced adsorption of antimonate by ball-milled microscale zero valent iron/pyrite composite: Adsorption properties and mechanism insight. *Environ. Sci. Pollut. Res.* 27 (14), 16484–16495. doi:10.1007/s11356-020-08163-y

Hernández-Cocoletzi, H., Salinas, R. A., Águila-Almanza, E., Rubio-Rosas, E., Chai, W. S., Chew, K. W., et al. (2020). Natural hydroxyapatite from fishbone waste for the rapid adsorption of heavy metals of aqueous effluent. *Environ. Technol. Innovation* 20, 101109. doi:10.1016/j.eti.2020.101109

Holmes, R. R., Hart, M. L., and Kevern, J. T. (2017). Removal and breakthrough of lead, cadmium, and zinc in permeable reactive concrete. *Environ. Eng. Sci.* 35 (5), 408–419. doi:10.1089/ees.2017.0160

Hornig, G., Northcott, K., Snape, I., and Stevens, G. (2008). Assessment of sorbent materials for treatment of hydrocarbon contaminated ground water in cold regions. *Cold Regions Sci. Technol.* 53 (1), 83–91. doi:10.1016/j.coldregions.2007.08.004

Huang, Y., Wang, M., Gong, Y., and Zeng, E. Y. (2020). Efficient removal of mercury from simulated groundwater using thiol-modified graphene oxide/Fe–Mn composite in fixed-bed columns: Experimental performance and mathematical modeling. *Sci. Total Environ.* 714, 136636. doi:10.1016/j.scitotenv.2020.136636

Indraratna, B., Regmi, G., Nghiem Long, D., and Golab, A. (2010). Performance of a PRB for the remediation of acidic groundwater in acid sulfate soil terrain. *J. Geotech. Geoenviron. Eng.* 136 (7), 897–906. doi:10.1061/(ASCE)GT.1943-5606.0000305

Inyang, M. I., Gao, B., Yao, Y., Xue, Y., Zimmerman, A., Mosa, A., et al. (2016). A review of biochar as a low-cost adsorbent for aqueous heavy metal removal. *Crit. Rev. Environ. Sci. Technol.* 46 (4), 406–433. doi:10.1080/10643389.2015.1096880

Jarvis, A. P., Moustafa, M., Orme, P. H. A., and Younger, P. L. (2006). Effective remediation of grossly polluted acidic, and metal-rich, spoil heap drainage using a novel, low-cost, permeable reactive barrier in Northumberland, UK. *Environ. Pollut.* 143 (2), 261–268. doi:10.1016/j.envpol.2005.11.028

Jarvis, T. (2021). Global groundwater: Source, scarcity, sustainability, security, and solutions. *Groundwater* 59, 479–480. doi:10.1111/gwat.13113

Jeen, S. W., Gillham, R. W., and Przepiora, A. (2011). Predictions of long-term performance of granular iron permeable reactive barriers: Field-scale evaluation. *J. Contam. Hydrology* 123 (1), 50–64. doi:10.1016/j.jconhyd.2010.12.006

Jia, H., Gu, C., Boyd, S. A., Teppen, B. J., Johnston, C. T., Song, C., et al. (2011). Comparison of reactivity of nanoscaled zero-valent iron formed on clay surfaces. *Soil Sci. Soc. Am. J.* 75 (2), 357–364. doi:10.2136/sssaj2010.0080nps

Jia, H., and Wang, C. (2013). Comparative studies on montmorillonite-supported zero-valent iron nanoparticles produced by different methods: Reactivity and stability. *Environ. Technol.* 34 (1), 25–33. doi:10.1080/09593330.2012.679698

Jiang, D., Zeng, G., Huang, D., Chen, M., Zhang, C., Huang, C., et al. (2018). Remediation of contaminated soils by enhanced nanoscale zero valent iron. *Environ. Res.* 163, 217–227. doi:10.1016/j.envres.2018.01.030

Jiemvarangkul, P., Zhang, W.-x., and Lien, H.-L. (2011). Enhanced transport of polyelectrolyte stabilized nanoscale zero-valent iron (nZVI) in porous media. *Chem. Eng. J.* 170 (2), 482–491. doi:10.1016/j.cej.2011.02.065

Kantar, C., Bulbul, M. S., and Keskin, S. (2017). Role of humic substances on Cr(VI) removal from groundwater with Pyrite. *Water Air Soil Pollut.* 228 (1), 48. doi:10.1007/s11270-016-3233-0

Khan, K., Lu, Y., Khan, H., Ishtiaq, M., Khan, S., Waqas, M., et al. (2013). Heavy metals in agricultural soils and crops and their health risks in Swat District, northern Pakistan. *Food Chem. Toxicol.* 58, 449–458. doi:10.1016/j.fct.2013.05.014

Kong, L., Ruan, Y., Zheng, Q., Su, M., Diao, Z.-H., Chen, D., et al. (2019). Uranium extraction using hydroxyapatite recovered from phosphorus containing wastewater. *J. Hazard. Mater.* 382, 120784. doi:10.1016/j.jhazmat.2019.120784

Kong, X., Huang, G., Han, Z., Xu, Y., Zhu, M., and Zhang, Z. (2017). Evaluation of zeolite-supported microscale zero-valent iron as a potential adsorbent for Cd2+ and Pb2+ removal in permeable reactive barriers. *Environ. Sci. Pollut. Res.* 24 (15), 13837–13844. doi:10.1007/s11356-017-8974-9

Kouotou, D., Gharibi, E. K., Bailón-García, E., and Ghalit, M. (2022). Improved Cd (II) ions removal performance from aqueous solution using cerium doped activated carbon. *Mater. Today Proc.* 51, 1957–1965. doi:10.1016/j.matpr.2021.04.298

Kuma, N., Millot, R., Battaglia-Brunet, F., Omoregie, E., Chaurand, P., Borschneck, D., et al. (2016). Microbial and mineral evolution in zero valent iron-based permeable reactive barriers during long-term operations. *Environ. Sci. Pollut. Res.* 23 (6), 5960–5968. doi:10.1007/s11356-015-5712-z

Kumara, G. M. P., and Kawamoto, K. (2021). Use of natural zeolite and its mixtures to refine high-concentrated heavy metal-contaminated wastewater: An investigation of simultaneous removal of Cd (II) and Pb (II) by batch Adsorption method. *Water Air Soil Pollut.* 232 (11), 463. doi:10.1007/s11270-021-05420-9

Lai, K. C. K., and Lo, I. M. C. (2008). Removal of chromium (VI) by acid-washed zero-valent iron under various groundwater geochemistry conditions. *Environ. Sci. Technol.* 42 (4), 1238–1244. doi:10.1021/es071572n

Li, J., Fan, M., Li, M., and Liu, X. (2020). Cr(VI) removal from groundwater using double surfactant-modified nanoscale zero-valent iron (nZVI): Effects of materials in different status. *Sci. Total Environ.* 717, 137112. doi:10.1016/j.scitotenv.2020.137112

Li, P., Karunanidhi, D., Subramani, T., and Srinivasamoorthy, K. (2021). Sources and consequences of groundwater contamination. *Arch. Environ. Contam. Toxicol.* 80 (1), 1–10. doi:10.1007/s00244-020-00805-z

Li, Y., Du, Q., Wang, X., Zhang, P., Wang, D., Wang, Z., et al. (2010). Removal of lead from aqueous solution by activated carbon prepared from Enteromorpha prolifera by zinc chloride activation. *J. Hazard. Mater.* 183 (1), 583–589. doi:10.1016/j.jhazmat.2010.07.063

Li, Z., Wang, L., Meng, J., Liu, X., Xu, J., Wang, F., et al. (2018). Zeolite-supported nanoscale zero-valent iron: New findings on simultaneous adsorption of Cd(II), Pb(II), and As(III) in aqueous solution and soil. *J. Hazard. Mater.* 344, 1–11. doi:10.1016/j.jhazmat.2017.09.036

Liang, M., Lu, L., He, H., Li, J., Zhu, Z., and Zhu, Y. (2021). Applications of biochar and modified biochar in heavy metal contaminated soil: A descriptive review. *Sustainability* 13 (24), 14041. doi:10.3390/su132414041

Liu, H., Liao, L., Lu, G., Wang, L., Mei, L., and Guo, Q. (2020). Research progresses of the application of mineral materials as reactive media in the permeable reactive barrier technology. *Acta mineral. sin.* 40, 274–280. doi:10.16461/j.cnki.1000-4734.2020.40.119

Liu, J., Huang, X., Liu, J., Wang, W., Zhang, W., and Dong, F. (2014). Adsorption of arsenic(V) on bone char: Batch, column and modeling studies. *Environ. Earth Sci.* 72 (6), 2081–2090. doi:10.1007/s12665-014-3116-x

Liu, J., Liu, A., and Zhang, W.-x. (2016). The influence of polyelectrolyte modification on nanoscale zero-valent iron (nZVI): Aggregation, sedimentation, and reactivity with Ni(II) in water. *Chem. Eng. J.* 303, 268–274. doi:10.1016/j.cej.2016.05.132

Liu, M., Sun, F., Lv, Y., Xu, Y., Li, M., Wang, Y., et al. (2021). Remediation of arsenic-contaminated soil by nano-zirconia modified biochar. *Environ. Sci. Pollut. Res.* 28 (48), 68792–68803. doi:10.1007/s11356-021-15362-8

Liu, T., and Lo, I. M. C. (2011). Influences of humic acid on Cr(VI) removal by zero-valent iron from groundwater with various constituents: Implication for long-term PRB performance. *Water Air Soil Pollut.* 216 (1), 473–483. doi:10.1007/s11270-010-0546-2

Liu, X., Lai, D., and Wang, Y. (2019a). Performance of Pb(II) removal by an activated carbon supported nanoscale zero-valent iron composite at ultralow iron content. *J. Hazard. Mater.* 361, 37–48. doi:10.1016/j.jhazmat.2018.08.082

Liu, Y., Mou, H., Chen, L., Mirza, Z. A., and Liu, L. (2015). Cr(VI)-contaminated groundwater remediation with simulated permeable reactive barrier (PRB) filled with natural pyrite as reactive material: Environmental factors and effectiveness. *J. Hazard. Mater.* 298, 83–90. doi:10.1016/j.jhazmat.2015.05.007

Liu, Y., Sohi, S. P., Liu, S., Guan, J., Zhou, J., and Chen, J. (2019b). Adsorption and reductive degradation of Cr(VI) and TCE by a simply synthesized zero valent iron magnetic biochar. *J. Environ. Manag.* 235, 276–281. doi:10.1016/j.jenvman.2019.01.045

Lou, K., Rajapaksha, A. U., Ok, Y. S., and Chang, S. X. (2016). Pyrolysis temperature and steam activation effects on sorption of phosphate on pine sawdust biochars in aqueous solutions. *Chem. Speciat. Bioavailab.* 28 (1-4), 42–50. doi:10.1080/09542299.2016.1165080

Lou, Y., Cai, Y., Tong, Y., Hsieh, L., Li, X., Xu, W., et al. (2019). Interaction between pollutants during the removal of polychlorinated biphenyl-heavy metal combined pollution by modified nanoscale zero-valent iron. *Sci. Total Environ.* 673, 120–127. doi:10.1016/j.scitotenv.2019.04.064

Lü, Y., Li, Z., Li, J., Chen, K., Dong, H., Shou, J., et al. (2018). Synergetic effect of pyrite on Cr(VI) removal by zero valent iron in column experiments: An investigation of mechanisms. *Chem. Eng. J.* 349, 522–529. doi:10.1016/j.cej.2018.05.133

Ludwig, R. D., Smyth, D. J. A., Blowes, D. W., Spink, L. E., Wilkin, R. T., Jewett, D. G., et al. (2009). Treatment of arsenic, heavy metals, and acidity using a mixed ZVI-compost PRB. *Environ. Sci. Technol.* 43 (6), 1970–1976. doi:10.1021/es802394p

Maamoun, I., Falyouna, O., Eljamal, R., Bensaida, K., and Eljamal, O. (2021). Optimization modeling of nFe0/Cu-PRB design for Cr(VI) removal from groundwater. *Int. J. Environ. Sci. Dev.* 12, 131–138. doi:10.18178/ijesd.2021.12.5.1330

MacDonald, J. A., and Kavanaugh, M. C. (1994). Restoring contaminated groundwater: An achievable goal? *Environ. Sci. Technol.* 28 (8), 362A–368A. doi:10.1021/es00057a001

Madadrang, C. J., Kim, H. Y., Gao, G., Wang, N., Zhu, J., Feng, H., et al. (2012). Adsorption behavior of EDTA-graphene oxide for Pb (II) removal. *ACS Appl. Mat. Interfaces* 4 (3), 1186–1193. doi:10.1021/am201645g

Maharana, M., and Sen, S. (2021). Magnetic zeolite: A green reusable adsorbent in wastewater treatment. *Mater. Today Proc.* 47, 1490–1495. doi:10.1016/j.matpr.2021.04.370

Mandal, S., Pu, S., Shangguan, L., Liu, S., Ma, H., Adhikari, S., et al. (2020). Synergistic construction of green tea biochar supported nZVI for immobilization of lead in soil: A mechanistic investigation. *Environ. Int.* 135, 105374. doi:10.1016/j.envint.2019.105374

Min, X., Li, Q., Zhang, X., Liu, L., Xie, Y., Guo, L., et al. (2021). Characteristics, kinetics, thermodynamics and long-term effects of zerovalent iron/pyrite in remediation of Cr(VI)-contaminated soil. *Environ. Pollut.* 289, 117830. doi:10.1016/j.envpol.2021.117830

Mukherjee, A., Guo, H., Langan, S., Mckenzie, A., and Aureli, A. (2020). *Global groundwater: Source, scarcity, sustainability, security, and solutions*.

Mystrioti, C., Ntrouka, A., Thymi, S., Papassiopi, N., and Xenidis, A. (2020). Effect of limestone grain size on the mobility of green nanoiron suspension. *Appl. Geochem.* 122, 104759. doi:10.1016/j.apgeochem.2020.104759

Naji, L. A., Faisal, A. A. H., Rashid, H. M., Naushad, M., and Ahamad, T. (2020). Environmental remediation of synthetic leachate produced from sanitary landfills using low-cost composite sorbent. *Environ. Technol. Innovation* 18, 100680. doi:10.1016/j.eti.2020.100680

Namasivayam, C., and Sangeetha, D. (2006). Removal and recovery of vanadium(V) by adsorption onto ZnCl2 activated carbon: Kinetics and isotherms. *Adsorption* 12 (2), 103–117. doi:10.1007/s10450-006-0373-3

Ngueagni, P. T., Kumar, P. S., Woumfo, E. D., and Prasanth, S. M. (2020). "Adsorption of Pb(II) and Cd(II) ions onto modified biogenic slaughterhouse waste: Equilibrium and kinetic analysis," in *International journal of environmental analytical chemistry*, 1–20. doi:10.1080/03067319.2020.1784409

Nicola, M., Stefania, B., and Calabro, P. S. (2017). Fe0/pumice mixtures: From laboratory tests to permeable reactive barrier design. *Environ. Geotech.* 4 (4), 245–256. doi:10.1680/jenge.15.00002

Nijhawan, A., Butler, E., and Sabatini, D. (2018). Hydroxyapatite ceramic adsorbents: Effect of pore size, regeneration, and selectivity for Fluoride. *J. Environ. Eng. New. York.* 144, 04018117. doi:10.1061/(ASCE)EE.1943-7870.0001464

Obiri-Nyarko, F., Grajales-Mesa, s., and Malina, G. (2014). An overview of permeable reactive barriers for *in situ* sustainable groundwater remediation. *Chemosphere* 111, 243–259. doi:10.1016/j.chemosphere.2014.03.112

Obiri-Nyarko, F., Kwiatkowska-Malina, J., Malina, G., and Kasela, T. (2015). Geochemical modelling for predicting the long-term performance of zeolite-PRB to treat lead contaminated groundwater. *J. Contam. Hydrology* 177-178, 76–84. doi:10.1016/j.jconhyd.2015.03.007

Oliva, J., De Pablo, J., Cortina, J.-L., Cama, J., and Ayora, C. (2010). The use of Apatite II™ to remove divalent metal ions zinc(II), lead(II), manganese(II) and iron(II) from water in passive treatment systems: Column experiments. *J. Hazard. Mater.* 184 (1), 364–374. doi:10.1016/j.jhazmat.2010.08.045

Omran, M., Fabritius, T., Yu, Y., and Chen, G. (2020). Thermal and mass spectroscopic analysis of BF and BOF sludges: Study of their behavior under air and inert atmosphere. *Metals* 10 (3), 397. doi:10.3390/met10030397

Pan, L., Wang, Z., Yang, Q., and Huang, R. (2018). Efficient removal of lead, copper and cadmium ions from water by a porous calcium alginate/graphene oxide composite aerogel. *Nanomaterials* 8 (11), 957. doi:10.3390/nano8110957

Pan, L., Wang, Z., Zhao, X., and He, H. (2019). Efficient removal of lead and copper ions from water by enhanced strength-toughness alginate composite fibers. *Int. J. Biol. Macromol.* 134, 223–229. doi:10.1016/j.ijbiomac.2019.05.022

Paranavithana, G. N., Kawamoto, K., Inoue, Y., Saito, T., Vithanage, M., Kalpage, C. S., et al. (2016). Adsorption of Cd2+ and Pb2+ onto coconut shell biochar and biochar-mixed soil. *Environ. Earth Sci.* 75 (6), 484. doi:10.1007/s12665-015-5167-z

Park, M. H., Jeong, S., Lee, G., Park, H., and Kim, J. Y. (2019). Removal of aqueous-phase Pb(II), Cd(II), As(III), and As(V) by nanoscale zero-valent iron supported on exhausted coffee grounds. *Waste Manag.* 92, 49–58. doi:10.1016/j.wasman.2019.05.017

Park, M., Park, J., Kang, J., Han, Y.-S., and Jeong, H. Y. (2018). Removal of hexavalent chromium using mackinawite (FeS)-coated sand. *J. Hazard. Mater.* 360, 17–23. doi:10.1016/j.jhazmat.2018.07.086

Pawluk, K., Fronczyk, J., and Garbulewski, K. (2015). Reactivity of nano zero-valent iron in permeable reactive barriers. *Pol. J. Chem. Technol.* 17 (1), 7–10. doi:10.1515/pjct-2015-0002

Puls, R. W. (2006). "Long-term performance of permeable reactive barriers: Lessons learned on design, contaminant treatment, longevity, performance monitoring and cost - an overview," in *Soil and water pollution monitoring, protection and remediation*.

Qian, L., Zhang, W., Yan, J., Han, L., Chen, Y., Ouyang, D., et al. (2017). Nanoscale zero-valent iron supported by biochars produced at different temperatures: Synthesis mechanism and effect on Cr(VI) removal. *Environ. Pollut.* 223, 153–160. doi:10.1016/j.envpol.2016.12.077

Qin, N., Zhang, Y., Zhou, H., Geng, Z., Liu, G., Zhang, Y., et al. (2016). Enhanced removal of trace Cr(VI) from neutral and alkaline aqueous solution by FeCo bimetallic nanoparticles. *J. Colloid Interface Sci.* 472, 8–15. doi:10.1016/j.jcis.2016.03.025

Qu, G., Kou, L., Wang, T., Liang, D., and Hu, S. (2017). Evaluation of activated carbon fiber supported nanoscale zero-valent iron for chromium (VI) removal from groundwater in a permeable reactive column. *J. Environ. Manag.* 201, 378–387. doi:10.1016/j.jenvman.2017.07.010

Rajendran, M., and Thangavelu, D. (2021). Removal of As(V) from water using galvanically coupled sacrificial metals. *J. Hazard. Mater.* 409, 124564. doi:10.1016/j.jhazmat.2020.124564

Reginatto, C., Cecchin, I., Salvagni Heineck, K., Thomé, A., and Reddy, K. R. (2020). Influence of nanoscale zero-valent iron on hydraulic conductivity of a residual clayey soil and modeling of the filtration parameter. *Environ. Sci. Pollut. Res.* 27 (9), 9288–9296. doi:10.1007/s11356-019-07197-1

Rhee, S.-S., Lee, S., and Park, J. (2010). Simultaneous removal of Cd and Cr(VI) in the subsurface using permeable reactive barrier filled with Fe-loaded zeolite: Soil box experiment. *J. Korean Geotechnical Soc.* 26, 61–68.

Salman, M., Rehman, R., Mahmud, T., Zaman, W., Shafique, U., and Ali, S. (2011). Assessment of concentration of lead, cadmium, chromium and selenium in blood serum of cancer and diabetic patients of Pakistan. *J. Chem. Soc. Pak.* 33, 869–873.

Scherer, M. M., Richter, S., Valentine, R. L., and Alvarez, P. J. J. (2000). Chemistry and microbiology of permeable reactive barriers for *in situ* groundwater clean up. *Crit. Rev. Microbiol.* 26 (4), 221–264. doi:10.1080/10408410091154237

Shabalala, A. N., Ekolu, S. O., Diop, S., and Solomon, F. (2017). Pervious concrete reactive barrier for removal of heavy metals from acid mine drainage – column study. *J. Hazard. Mater.* 323, 641–653. doi:10.1016/j.jhazmat.2016.10.027

Shakoor, M. B., Ali, S., Rizwan, M., Abbas, F., Bibi, I., Riaz, M., et al. (2020). A review of biochar-based sorbents for separation of heavy metals from water. *Int. J. Phytoremediation* 22 (2), 111–126. doi:10.1080/15226514.2019.1647405

Shapira, K., and Zucker, I. (2022). Emerging investigator series: Molybdenum disulfide-enabled activated carbon - a multifunctional adsorbent for practical water treatment applications. *Environ. Sci. Nano* 9 (2), 477–488. doi:10.1039/D1EN00897H

Shubair, T., Eljamal, O., Khalil, A. M. E., Tahara, A., and Matsunaga, N. (2018). Novel application of nanoscale zero valent iron and bimetallic nano-Fe/Cu particles for the treatment of cesium contaminated water. *J. Environ. Chem. Eng.* 6 (4), 4253–4264. doi:10.1016/j.jece.2018.06.015

Simon, F. G., Biermann, V., and Peplinski, B. (2008). Uranium removal from groundwater using hydroxyapatite. *Appl. Geochem.* 23 (8), 2137–2145. doi:10.1016/j.apgeochem.2008.04.025

Song, J., Huang, G., Han, D., Hou, Q., Gan, L., and Zhang, M. (2021a). A review of reactive media within permeable reactive barriers for the removal of heavy metal(loid)s in groundwater: Current status and future prospects. *J. Clean. Prod.* 319, 128644. doi:10.1016/j.jclepro.2021.128644

Song, X., Zhang, Y., Cao, N., Sun, D., Zhang, Z., Wang, Y., et al. (2021b). Sustainable chromium (VI) removal from contaminated groundwater using nano-magnetite-modified biochar via rapid microwave synthesis. *Molecules* 26 (1), 103. doi:10.3390/molecules26010103

Soto, C., Nakano, K., Leon Romero, M., Aikawa, Y., Arai, S., and Nishimura, O. (2015). Differences in the removal mechanisms of Undaria pinnatifida and Phragmites australis as biomaterials for lead removal. *Water Sci. Technol.* 72, 1226–1233. doi:10.2166/wst.2015.334

Stötzel, C., Müller, F. A., Reinert, F., Niederdraenk, F., Barralet, J. E., and Gbureck, U. (2009). Ion adsorption behaviour of hydroxyapatite with different crystallinities. *Colloids Surfaces B Biointerfaces* 74 (1), 91–95. doi:10.1016/j.colsurfb.2009.06.031

Stucker, V., Ranville, J., Newman, M., Peacock, A., Cho, J., and Hatfield, K. (2011). Evaluation and application of anion exchange resins to measure groundwater uranium flux at a former uranium mill site. *Water Res.* 45 (16), 4866–4876. doi:10.1016/j.watres.2011.06.030

Sulaymon, A. H., Faisal, A. A. H., and Khaliefa, Q. M. (2015). Cement kiln dust (CKD)-filter sand permeable reactive barrier for the removal of Cu(II) and Zn(II) from simulated acidic groundwater. *J. Hazard. Mater.* 297, 160–172. doi:10.1016/j.jhazmat.2015.04.061

Tan, G., Mao, Y., Wang, H., Junaid, M., and Xu, N. (2019). Comparison of biochar- and activated carbon-supported zerovalent iron for the removal of Se(IV) and Se(VI): Influence of pH, ionic strength, and natural organic matter. *Environ. Sci. Pollut. Res.* 26 (21), 21609–21618. doi:10.1007/s11356-019-05497-0

Tasharrofi, S., Rouzitalab, Z., Maklavany, D. M., Esmaeili, A., Rabieezadeh, M., Askarieh, M., et al. (2020). Adsorption of cadmium using modified zeolite-supported nanoscale zero-valent iron composites as a reactive material for PRBs. *Sci. Total Environ.* 736, 139570. doi:10.1016/j.scitotenv.2020.139570

Truex, M. J., Vermeul, V. R., Mendoza, D. P., Fritz, B. G., Mackley, R. D., Oostrom, M., et al. (2011). Injection of zero-valent iron into an unconfined aquifer using shear-thinning fluids. *Ground Water Monit. remediat.* 31 (1), 50–58. doi:10.1111/j.1745-6592.2010.01319.x

Turner, M., Sogorka, A., Dave, N., Duchene, M., Dwyer, B., Hubble, D., et al. (2005). *Technical/regulatory guidelines : Permeable reactive barriers: Lessons learned/new directions*.

Vahdat, A., Ghasemi, B., and Yousefpour, M. (2019). Synthesis of hydroxyapatite and hydroxyapatite/Fe3O4 nanocomposite for removal of heavy metals. *Environ. Nanotechnol. Monit. Manag.* 12, 100233. doi:10.1016/j.enmm.2019.100233

Vilensky, M., Berkowitz, B., and Warshawsky, A. (2002). *In situ* remediation of groundwater contaminated by heavy- and transition-metal ions by selective ion-exchange methods. *Environ. Sci. Technol.* 36, 1851–1855. doi:10.1021/es010313+

Wang, F., Xu, W., Xu, Z., and Liu, H. (2020). CTMAB-modified bentonite–based PRB in remediating Cr(VI) contaminated groundwater. *Water Air Soil Pollut.* 231 (1), 20. doi:10.1007/s11270-019-4386-4

Wang, H., Yan, K., Xing, H., Chen, J., and Lu, R. (2021). Effective removal of Cu2+ from aqueous solution by synthetic abalone shell hydroxyapatite microspheres adsorbent. *Environ. Technol. Innovation* 23, 101663. doi:10.1016/j.eti.2021.101663

Wang, M., Cheng, W., Wan, T., Hu, B., Zhu, Y., Song, X., et al. (2019a). Mechanistic investigation of U(VI) sequestration by zero-valent iron/activated carbon composites. *Chem. Eng. J.* 362, 99–106. doi:10.1016/j.cej.2018.12.138

Wang, Q., Song, X., Wei, C., Jin, P., Chen, X., Tang, Z., et al. (2022). *In situ* remediation of Cr(VI) contaminated groundwater by ZVI-PRB and the corresponding indigenous microbial community responses: A field-scale study. *Sci. Total Environ.* 805, 150260. doi:10.1016/j.scitotenv.2021.150260

Wang, S., and Peng, Y. (2010). Natural zeolites as effective adsorbents in water and wastewater treatment. *Chem. Eng. J.* 156 (1), 11–24. doi:10.1016/j.cej.2009.10.029

Wang, T., Liu, Y., Wang, J., Wang, X., Liu, B., and Wang, Y. (2019b). *In-situ* remediation of hexavalent chromium contaminated groundwater and saturated soil using stabilized iron sulfide nanoparticles. *J. Environ. Manag.* 231, 679–686. doi:10.1016/j.jenvman.2018.10.085

Wellman, D. M., Glovack, J. N., Parker, K., Richards, E. L., and Pierce, E. M. (2008). Sequestration and retention of uranium(VI) in the presence of hydroxylapatite under dynamic geochemical conditions. *Environ. Chem.* 5 (1), 40–50. doi:10.1071/en07060

Wen, Z., Ke, J., Xu, J., Guo, S., Zhang, Y., and Chen, R. (2018). One-step facile hydrothermal synthesis of flowerlike Ce/Fe bimetallic oxides for efficient As(V) and Cr(VI) remediation: Performance and mechanism. *Chem. Eng. J.* 343, 416–426. doi:10.1016/j.cej.2018.03.034

Wijeyawardana, P., Nanayakkara, N., Gunasekara, C., Karunarathna, A., Law, D., and Pramanik, B. K. (2022). Improvement of heavy metal removal from urban runoff using modified pervious concrete. *Sci. Total Environ.* 815, 152936. doi:10.1016/j.scitotenv.2022.152936

Wilkin, R., and Puls, R. (2003). *Capstone report on the application, monitoring, and performance of permeable reactive barriers for ground-water remediation*.

Wilkin, R. T., Acree, S. D., Ross, R. R., Beak, D. G., and Lee, T. R. (2009). Performance of a zerovalent iron reactive barrier for the treatment of arsenic in groundwater: Part 1. Hydrogeochemical studies. *J. Contam. Hydrology* 106 (1), 1–14. doi:10.1016/j.jconhyd.2008.12.002

Wilopo, W., Sasaki, K., Hirajima, T., and Yamanaka, T. (2008). Immobilization of arsenic and manganese in contaminated groundwater by permeable reactive barriers using zero valent iron and sheep manure. *Mat. Trans.* 49 (10), 2265–2274. doi:10.2320/matertrans.M-MRA2008827

Wilson, K., Yang, H., Seo, C. W., and Marshall, W. E. (2006). Select metal adsorption by activated carbon made from peanut shells. *Bioresour. Technol.* 97 (18), 2266–2270. doi:10.1016/j.biortech.2005.10.043

Wu, Y., Guan, C.-Y., Griswold, N., Hou, L.-y., Fang, X., Hu, A., et al. (2020). Zero-valent iron-based technologies for removal of heavy metal(loid)s and organic pollutants from the aquatic environment: Recent advances and perspectives. *J. Clean. Prod.* 277, 123478. doi:10.1016/j.jclepro.2020.123478

Wu, Y., Zhang, J., Tong, Y., and Xu, X. (2009). Chromium (VI) reduction in aqueous solutions by Fe3O4-stabilized Fe0 nanoparticles. *J. Hazard. Mater.* 172 (2), 1640–1645. doi:10.1016/j.jhazmat.2009.08.045

Xiang, G., Long, S., Liu, H., and Wu, X. (2021). Cd(II) removal from aqueous solutions by pomelo peel derived biochar in a permeable reactive barrier: Modelling, optimization and mechanism. *Mat. Res. Express* 8 (11), 115508. doi:10.1088/2053-1591/ac386b

Xiang, S., Cheng, W., Nie, X., Ding, C., Yi, F., Asiri, A. M., et al. (2018). Zero-valent iron-aluminum for the fast and effective U(VI) removal. *J. Taiwan Inst. Chem. Eng.* 85, 186–192. doi:10.1016/j.jtice.2018.01.039

Xie, J., Lei, C., Chen, W., Xie, Q., Guo, Q., and Huang, B. (2021). Catalytic properties of transition metals modified nanoscale zero-valent iron for simultaneous removal of 4-chlorophenol and Cr(VI): Efficacy, descriptor and reductive mechanisms. *J. Hazard. Mater.* 403, 123827. doi:10.1016/j.jhazmat.2020.123827

Xing, M., Xu, L., and Wang, J. (2016). Mechanism of Co(II) adsorption by zero valent iron/graphene nanocomposite. *J. Hazard. Mater.* 301, 286–296. doi:10.1016/j.jhazmat.2015.09.004

Xu, R., Li, Q., Yang, Y., Jin, S., Liao, L., Wu, Z., et al. (2022). Removal of heavy metal(loid)s from aqueous solution by biogenic FeS–kaolin composite: Behaviors and mechanisms. *Chemosphere* 299, 134382. doi:10.1016/j.chemosphere.2022.134382

Xu, Y.-N., and Chen, Y. (2020). Advances in heavy metal removal by sulfate-reducing bacteria. *Water Sci. Technol.* 81 (9), 1797–1827. doi:10.2166/wst.2020.227

Xu, Y., Wang, C., Hou, J., Wang, P., You, G., Miao, L., et al. (2017). Application of zero valent iron coupling with biological process for wastewater treatment: A review. *Rev. Environ. Sci. Biotechnol.* 16 (4), 667–693. doi:10.1007/s11157-017-9445-y

Yang, L., Hu, J., Wu, W., Tang, J., Ding, K., and Li, J. (2016). *In situ* NH2-functionalized graphene oxide/SiO2 composites to improve Cu(II) removal from ammoniacal solutions. *Chem. Eng. J.* 306, 77–85. doi:10.1016/j.cej.2016.07.035

Yang, X., Hu, L., Bai, J., Mao, X., Chen, X., Wang, X., et al. (2021). Increased structural defects of graphene oxide compromised reductive capacity of ZVI towards hexavalent chromium. *Chemosphere* 277, 130308. doi:10.1016/j.chemosphere.2021.130308

Yang, Y., Wu, W., Zhou, H., Huang, Z., Ye, T., Liu, R., et al. (2014). Adsorption behavior of cross-linked chitosan modified by graphene oxide for Cu(II) removal. *J. Cent. South Univ.* 21 (7), 2826–2831. doi:10.1007/s11771-014-2246-3

Yang, Z., Dong, Y., and Li, Z. (2020). "Acid mine drainage remediation with simulated permeable reactive barrier filled with fly ash and its composite materials as reactive media," in *Energy sources, Part A: Recovery, utilization, and environmental effects*, 1–14. doi:10.1080/15567036.2020.1801901

Yi, N., Wu, Y., Fan, L., and Hu, S. (2019). Remediating Cd-contaminated soils using natural and chitosan-introduced zeolite, bentonite, and activated carbon. *Pol. J. Environ. Stud.* 28 (3), 1461–1468. doi:10.15244/pjoes/89577

Yousefi, A., and Matavos-Aramyan, S. (2018). Mix design optimization of silica fume-based pervious concrete for removal of heavy metals from wastewaters. *Silicon* 10 (4), 1737–1744. doi:10.1007/s12633-017-9663-5

Yu, Q., Guo, J., Muhammad, Y., Li, Q., Lu, Z., Yun, J., et al. (2020). Mechanisms of enhanced hexavalent chromium removal from groundwater by sodium carboxymethyl cellulose stabilized zerovalent iron nanoparticles. *J. Environ. Manag.* 276, 111245. doi:10.1016/j.jenvman.2020.111245

Zawierucha, I., and Nowik-Zajac, A. (2019). Evaluation of permeable sorption barriers for removal of Cd(II) and Zn(II) ions from contaminated groundwater. *Water Sci. Technol.* 80 (3), 448–457. doi:10.2166/wst.2019.288

Zeng, H., Lu, L., Gong, Z., Guo, Y., Mo, J., Zhang, W., et al. (2019). Nanoscale composites of hydroxyapatite coated with zero valent iron: Preparation, characterization and uranium removal. *J. Radioanal. Nucl. Chem.* 320 (1), 165–177. doi:10.1007/s10967-019-06451-7

Zeng, Q., Huang, Y., Huang, L., Hu, L., Xiong, D., Zhong, H., et al. (2020). Efficient removal of hexavalent chromium in a wide pH range by composite of SiO2 supported nano ferrous oxalate. *Chem. Eng. J.* 383, 123209. doi:10.1016/j.cej.2019.123209

Zhang, F., Wang, X., Xionghui, J., and Ma, L. (2016). Efficient arsenate removal by magnetite-modified water hyacinth biochar. *Environ. Pollut.* 216, 575–583. doi:10.1016/j.envpol.2016.06.013

Zhang, J., Yang, X., Shi, J., Zhao, M., Yin, W., Wang, X., et al. (2022). Carbon matrix of biochar from biomass modeling components facilitates electron transfer from zero-valent iron to Cr(VI). *Environ. Sci. Pollut. Res.* 29 (16), 24309–24321. doi:10.1007/s11356-021-17713-x

Zhang, Q., Hou, Q., Huang, G., and Fan, Q. (2020). Removal of heavy metals in aquatic environment by graphene oxide composites: A review. *Environ. Sci. Pollut. Res.* 27 (1), 190–209. doi:10.1007/s11356-019-06683-w

Zhang, W., Dong, Y., Wang, H., Guo, Y., Zeng, H., and Zan, J. (2021). Removal of uranium from groundwater using zero-valent-iron coated quartz sands. *J. Radioanal. Nucl. Chem.* 327 (1), 1–12. doi:10.1007/s10967-020-07523-9

Zhang, W., Qian, L., Ouyang, D., Chen, Y., Han, L., and Chen, M. (2019). Effective removal of Cr(VI) by attapulgite-supported nanoscale zero-valent iron from aqueous solution: Enhanced adsorption and crystallization. *Chemosphere* 221, 683–692. doi:10.1016/j.chemosphere.2019.01.070

Zhang, Y., Li, Y., Li, J., Sheng, G., Zhang, Y., and Zheng, X. (2012). Enhanced Cr(VI) removal by using the mixture of pillared bentonite and zero-valent iron. *Chem. Eng. J.* 185-186, 243–249. doi:10.1016/j.cej.2012.01.095

Zhao, X., Liu, W., Cai, Z., Fu, J., Duan, J., Zhao, D., et al. (2020). Reductive immobilization of uranium by stabilized zero-valent iron nanoparticles: Effects of stabilizers, water chemistry and long-term stability. *Colloids Surfaces A Physicochem. Eng. Aspects* 604, 125315. doi:10.1016/j.colsurfa.2020.125315

Zhou, Y., Gao, B., Zimmerman, A. R., Chen, H., Zhang, M., and Cao, X. (2014). Biochar-supported zerovalent iron for removal of various contaminants from aqueous solutions. *Bioresour. Technol.* 152, 538–542. doi:10.1016/j.biortech.2013.11.021

Zhou, Y., Gao, B., Zimmerman, A. R., Fang, J., Sun, Y., and Cao, X. (2013). Sorption of heavy metals on chitosan-modified biochars and its biological effects. *Chem. Eng. J.* 231, 512–518. doi:10.1016/j.cej.2013.07.036

Zhu, F., Li, L., Ren, W., Deng, X., and Liu, T. (2017). Effect of pH, temperature, humic acid and coexisting anions on reduction of Cr(VI) in the soil leachate by nZVI/Ni bimetal material. *Environ. Pollut.* 227, 444–450. doi:10.1016/j.envpol.2017.04.074

Zhu, Y., Peng, S., Lu, P., Chen, T., and Yang, Y. (2020). Mercury removal from aqueous solutions using modified pyrite: A column experiment. *Minerals* 10 (1), 43. doi:10.3390/min10010043

frontiers | Frontiers in Environmental Science

TYPE Original Research
PUBLISHED 11 October 2022
DOI 10.3389/fenvs.2022.1024797

OPEN ACCESS

EDITED BY
Chengcheng Li,
China University of Geosciences
Wuhan, China

REVIEWED BY
Zhuanxi Luo,
Huaqiao University, China
Zheng Zhang,
China University of Mining and
Technology, China
Yimin Sang,
Beijing Institute of Petrochemical
Technology, China

*CORRESPONDENCE
Herong Gui,
guiherong@163.com

SPECIALTY SECTION
This article was submitted to Freshwater
Science,
a section of the journal
Frontiers in Environmental Science

RECEIVED 22 August 2022
ACCEPTED 26 September 2022
PUBLISHED 11 October 2022

CITATION
Hao C, Wang Y, He K and Gui H (2022),
Seasonal distribution of deep
groundwater fluoride, geochemical
factors and ecological risk for irrigation
in the Shendong mining area, China.
Front. Environ. Sci. 10:1024797.
doi: 10.3389/fenvs.2022.1024797

Seasonal distribution of deep groundwater fluoride, geochemical factors and ecological risk for irrigation in the Shendong mining area, China

Chunming Hao[1,2,3], Yantang Wang[3], Kaikai He[3] and Herong Gui[2]*

[1]State Key Laboratory of Coal Resources and Safe Mining, Beijing, China, [2]Key Laboratory of Mine Water Resource Utilization of Anhui Higher Education Institutes, Suzhou University, Suzhou, China, [3]North China Institute of Science and Technology, Sanhe, China

High-fluoride (F^-) deep groundwater in the vicinity of mining areas poses severe ecological risks. In this study, we aimed to characterize and reveal the seasonal distribution and influencing factors of elevated F^- concentrations in the deep groundwater in the Shendong mining area, Shaanxi and Inner Mongolia province, China. In addition, the ecological risks associated with F^- concentrations in irrigation water were assessed. During the wet and dry seasons, the F^- concentrations in mine water samples ranged between 0.12 and 13.92 mg/L (mean: 4.24 mg/L) and between 0.20 and 17.58 mg/L (mean: 4.59 mg/L), respectively. The F^- content of mine water was clearly higher during the dry season than that during the wet season. F^- concentrations in deep groundwater exhibited consistent spatial distributions during both the dry and wet seasons, with an evident increase from southeast to northwest. The dissolution and precipitation of F^--bearing and calcium minerals, cation exchange, competitive adsorption, evaporation, and anthropogenic activities during both the wet and dry seasons were identified as important factors influencing F^- concentrations in deep groundwater. In addition, the ecological assessment revealed that 100% and 88.89% of low-F^- deep groundwater samples were suitable for practices during the dry and wet seasons, respectively. In contrast 84.00% and 84.62% of high-F^- deep groundwater samples were unsuitable for irrigation practices during the dry and wet seasons, respectively. This research provided useful prevention policies of deep groundwater extraction to mitigate environment problems associated with excessive F^- irrigation.

KEYWORDS

fluoride, seasonal distribution, geochemical factors, ecological assessment, deep groundwater

Introduction

Fluorine (F), one of the lightest halogen elements in the environment, is difficult to precipitate under normal temperature and pressure conditions and typically occurs as fluoride (F^-) in natural water (Ali et al., 2018). For emerging countries such as China and India, potable groundwater is the primary source of F^- consumption (Aghapour et al., 2018; Ali et al., 2018; Adeyeye et al., 2021; Araya et al., 2022). It is well known that the concentration of F^- has an effect on human health. F^- concentrations in natural water sources are typically less than 1.00 mg/L (Laxmankumar et al., 2019; LaFayette et al., 2020). Long-term consumption of potable groundwater containing F^- concentrations greater than 1.00 mg/L and 4.00 mg/L can cause dental and skeletal fluorosis, respectively (Kumar et al., 2018; LaFayette et al., 2020). In addition, a high concentration (>10.00 mg/L) of F^- is commonly associated with carcinogenic effects, including arthritis, neurological disorders, thyroid cancer, infertility, and hypertension (Ali et al., 2018; Toolabi et al., 2021; Chicas et al., 2022; Hao et al., 2022). Hence, it is safe to consume potable groundwater with F^- concentration below 1.00 mg/L, which is the maximum permissible F^- concentration for drinking water in China (He J et al., 2013; Hao et al., 2021a). Prior to consumption, the pre-treatment processes that regulate the F^- concentration in groundwater are considered essential. Groundwater is also the primary source of irrigation water in arid and semi-arid regions around the world, ensuring specific crop yields (Kumar et al., 2018; Kumar et al., 2019; Li et al., 2021).

The two principal sources of F^- in groundwater are anthropogenic (Borzi et al., 2015; Mamatchi et al., 2019; Su et al., 2021; Yadav et al., 2021; Zango et al., 2021; Huang et al., 2022) and geogenic in origin (Currell et al., 2011; He X et al., 2013; Xiao et al., 2015; Dehbandi et al., 2018; Hao et al., 2021b; Duggal and Sharma, 2022). Previous studies have found that geogenic processes are frequently responsible for elevated F^- concentrations in groundwater (Dehbandi et al., 2018; Emenike et al., 2018; Rashid et al., 2018; Hao et al., 2021c; Duggal and Sharma, 2022; Huang et al., 2022). Importantly, F-bearing minerals in rock strata, including fluorite, fluorapatite, and cryolite, are typically identified as the most important geogenic sources of F^- (He J et al., 2013; Mondal et al., 2014; Olaka et al., 2016; Laxmankumar et al., 2019; Hao et al., 2021d; Duggal and Sharma, 2022; Rehman et al., 2022). In addition, specific water-rock interactions play a very important role in the fluoride enrichment of groundwater, such as evaporation (Dehbandi et al., 2018; Li et al., 2018; Chicas et al., 2022; Rehman et al., 2022), competitive adsorption (Li et al., 2018; Ali et al., 2019; Rehman et al., 2022), and ion exchange effects (Li et al., 2015; Ali et al., 2018; Huang et al., 2022; Nizam et al., 2022). Anthropogenic sources, such as application of phosphate fertilisers and pesticides, use of aluminum smelting, glass and brick industries, the burning of coal, and processing of mining activities, also contribute excessive amounts of fluoride into groundwater (Li et al., 2018; Rashid et al., 2018; Ali et al., 2019; Hao et al., 2022; Zhang et al., 2022). Furthermore, numerous geochemical ions may affect the presence of F^- in groundwater. For instance, high-F^- groundwater often have neutral to alkaline pH and they are typically Na-HCO_3 dominant with low concentrations of Ca^{2+} and Mg^{2+} (Li et al., 2018; LaFayette et al., 2020; Huang et al., 2022; Nizam et al., 2022).

The exploitation of underground coal resources is always accompanied by the drainage of vast quantities of mine water (Yang et al., 2019; Yuan et al., 2022). Excessive mining activities and their associated mine water drainage are unavoidable sources of several geogenic elements such as F^- and other pollutants (Jeong et al., 2018; Blasco et al., 2019; Yadav et al., 2021). F^- has been previously detected in coal and categorized as a toxic element (He J et al., 2013; Yadav et al., 2021; Hao et al., 2022) and coal mines activities usually incorporate toxic elements into mine water (Yadav et al., 2021). The discharge of untreated F^--containing mine water from coal mines typically contaminates the surrounding groundwater system and leads to environmental degradation (Yadav et al., 2021; Zhang et al., 2021; Zhang et al., 2022). Due to various geochemical factors, the seasons influence the F^- concentrations in groundwater differently (Orland et al., 2014; Najamuddin et al., 2016; Sahu et al., 2020). Owing to the negative effects of high-F^- mine water, it is of the utmost importance to monitor the seasonal quality of groundwater in arid and water-scarce areas from an ecological perspective. As one of the eight largest coalfields in the world, the Shendong mining area annually discharges approximately 106 million tons of mine (Hao et al., 2021a; Xu et al., 2021; Zhang et al., 2021). Several studies have indicated that the F^- concentration in mine water of part of the Shendong mining area exceeds 1.00 mg/L, which unquestionably poses environmental risks (Hao et al., 2021b; Guo et al., 2021; Zhang et al., 2021; Hao et al., 2022). The large amount of groundwater with high fluoride is not suitable for domestic water, due to lack appropriate treatment technology and adequate funding (Gu, 2014; Gu et al., 2021). Hence, the high-F^- groundwater primarily guarantees the water supply for ecological irrigation for the natural fragilely ecological conditions (Gu, 2014; Gu et al., 2021) and for landscape water after simple purification treatment (Song et al., 2020), which doubtlessly brings potential crises for the ecological environment of the mining area. Although the spatial distribution, geochemical behavior, and formation mechanisms for elevated F^- in mine water in the Shendong mining areas have been investigated (Hao et al., 2021c; Zhang et al., 2021; Hao et al., 2022), the impact of high-F^- mine water, seasonal effects, and ecological irrigation risks of F^- concentrations on the surrounding deep groundwater have received limited attention. Moreover, assessing the F^- concentrations in deep groundwater during the dry and wet seasons is beneficial for analyzing the seasonal concentration changes and determining the ecological irrigation risks.

In this study, we aimed to 1) further investigate the spatial characteristics and influencing factors of deep groundwater F^- in the vicinity of the Shendong mining area during the dry and wet seasons; and 2) assess the ecological irrigation risks associated with F^- concentrations in deep groundwater using the sodium adsorption ratio (SAR) and sodium percentage (Na%). The results of this study contributed to a comprehensive understanding of the seasonal distribution and geochemical factors of F^- in deep groundwater affected by mining activities, thereby preventing ecological impacts associated with excessive F^- irrigation in the Shendong mine area.

Geological background

The Shendong mining area (geographical coordinates: 111°04′–111°11′ N and 39°20′–39°30′ E) is located in a mountainous region and spans a surface area of 3481 km^2 (Figure 1). This region has a typical warm-temperate and semi-arid continental monsoon climate and recorded an average annual precipitation rate of approximately 437.2 mm and an average annual evaporation rate of 2065.1 mm between 1949 and 2012. The average temperature is 9.9°C. As a component of the Ulan Mulun River system, no major rivers transect the mining area.

The overall geological structure of the Shendong mining area is a monocline dipping towards the SW with a dip angle of 1–8°. Faults are rare in the mining areas and the geologic structure is identified as simple (Zhang et al., 2021; Hao et al., 2022). Usually, Yanchang Formation (T_{3y}) of the Upper Triassic, Fuxian Formation (J_{1f}) of the Lower Jurassic, Yanan Formation ($J_{1\text{-}2y}$) of the Middle and Lower Jurassic, Zhiluo Formation (J_{2z}) and Anding Formation (J_{2a}) of the Middle Jurassic, Cenozoic (K_z) and Salawusu Formation (Q_{3s}) are the main geological strata from bottom to top in the Shendong mining area (Zhang et al., 2021). The Q_{3s} phreatic (shallow groundwater) and $J_{1\text{-}2y}$ deep groundwater (deep groundwater) aquifers are the main aquifers in the mining area. Owing to their thickness (119.09–227.12 m, mean: 174.93 m) and relative abundance of water, deep groundwater aquifers are an essential source of potable and irrigation water in the area. The lithology of the deep groundwater aquifers is predominantly medium-coarse sandstones with a small amount of siltstone. There are extensive amounts of F^- and silicate minerals in the rock stratum and the fractures are poorly developed. The deep groundwater has hydraulic conductivity from 0.002 to 0.016 m/d, and belongs to a weak water-rich aquifer. Unpolluted water aquifers principally have hydrochemical facies of Na-HCO_3 and Na-HCO_3-Cl. Deep groundwater is primarily recharged through precipitation infiltration and partially recharged through shallow groundwater leakages.

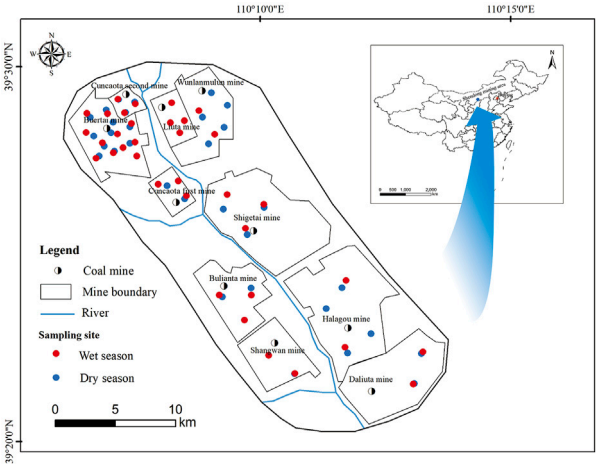

FIGURE 1
Location of Shendong mining area in China and distribution of deep groundwater sampling sites.

Groundwater flows from south to north *via* sandstone fissures and mainly drains out through springs and burnt rocks aquifer.

The deep groundwater aquifer contains abundant coal reserves, and the recoverable coal seams consist of No. 1^{-2}, 2^{-2}, 3^{-1}, 4^{-2}, and 5^{-2} coal seams with an average thickness of 4–6 m (Xu et al., 2021; Zhang et al., 2021; Hao et al., 2022). The surface of the mining area is covered by scattered surface materials, sparse vegetation, a dry environment, and windblown sand, with a thickness of 20–50 m (Zhang et al., 2021). In the mining area, water erosion and wind erosion are widespread and intense, and soil and water loss are severe issues (Xiao et al., 2020). Agriculture is uncommon in the Shendong mine area, where psammophytes and xerophytes are the dominant ecological plants.

Materials and methods

Sample collection

A total of 35 deep groundwater samples were collected from drilling holes and monitoring wells in the dry (December 2020) and wet (August 2020) seasons (Figure 1). Before collection, brown ampoules were washed 2–3 times, first with distilled and then with sample water. The sample water was then filtered *via* 0.45 μm glass fiber membranes prior to collection. Two 500 ml samples were collected from each sampling location for cation and anion analyses. Meanwhile, 5.00 ml of F^- recovery indicator (1.00 mg/L) was added to and mixed with the cation

TABLE 1 The classification statistics of SAR and Na% irrigation suitability.

Parameter	Range	Grade
Sodium adsorption ratio (SAR)	<10	Low (suitable)
	10–18	Medium (more suitable)
	19–26	High (not suitable)
	>26	Very high (not suitable)
Sodium percentage (Na%)	<20	Low (suitable)
	20–40	Medium (more suitable)
	40–60	High (not suitable)
	>60	Very high (not suitable)

analysis sample. Total dissolved solids (TDS) and pH values were measured *in situ*.

Sample analysis

Calcium, magnesium, sodium, and potassium concentrations were measured using inductively coupled plasma-atomic emission spectrometry (ICP-OES; Agilent 7900, United States). The concentrations of F^-, chloride, and sulfate were determined by ion chromatography (Dionex Integrion IC, Thermo Fisher, United States). Nitrates and ammonia-nitrogen were determined by spectrophotometry (Multiskan SkyHigh, United States). The concentrations of bicarbonate and carbonate were determined using acid-base titration. The pH and TDS values were obtained using a portable pH meter (HANNA H18424, Italy) and a portable electrical conductivity meter (HANNA H1833, Italy), respectively.

Each reported value was the average of three test results, with a relative standard deviation below 10%. The detection limit of bicarbonate and carbonate analyses was 0.1 mg/L, whereas all other ion analyses had a detection limit of 0.01 mg/L. Recovery rates of 95%–105% for F^- concentration were determined. The absolute ionic balance errors of the analyzed water samples were generally around 5%. Moreover, approximately 20% of the water samples were randomly re-analyzed to ensure that the relative deviation qualification rate exceeded 90%.

Assessment of irrigation water quality

The quality of deep groundwater for irrigation was evaluated using the SAR and Na% methods.

The SAR and Na% were estimated using Eqs 1, 2:

$$\mathbf{SAR} = \mathbf{Na^+} \Big/ \sqrt{\mathbf{Ca^{2+}} + \mathbf{Mg^{2+}}} \quad (1)$$

$$\mathbf{Na\%} = (\mathbf{Na^+} + \mathbf{K^+}) \Big/ (\mathbf{Ca^{2+}} + \mathbf{Mg^{2+}} + \mathbf{Na^+} + \mathbf{K^+}) \times \mathbf{100} \quad (2)$$

where each ion was measured in meq/L. Table 1 displays the classification statistics for the SAR and Na% irrigation suitability of deep groundwater.

Statistical analysis

Origin 2021 software was used for data description and statistical analysis. Piper and Gibbs diagrams were used to elucidate the hydrogeochemical facies and processes. The spatial variance of F^- in groundwater was evaluated using the inverse distance weight method within ArcGIS 9.3. The geochemical model PHREEQC was used to calculate the

TABLE 2 Geochemistry data in deep groundwater for wet and dry season.

Types	mg/L											pH
	F^-	Cl^-	HCO_3^-	SO_4^{2-}	NO_3^-	K^+	Ca^{2+}	Mg^{2+}	Na^+	NH_4^+	TDS	
Wet season (n = 35)												
Min	0.12	5.52	135.2	3.05	0.00	0.10	1.03	0.46	8.90	0.00	198	7.02
Max	13.92	969.00	1460.0	1035.60	8.10	11.50	104.15	52.70	1754.20	2.11	3842	9.70
Mean	4.40	171.33	492.4	171.53	1.25	3.95	29.63	6.54	335.01	0.20	1021	8.12
SD	3.72	186.41	348.1	252.67	1.48	2.83	26.68	10.07	310.83	0.38	666	0.58
Dry season (n = 35)												
Min	0.20	6.07	155.2	6.04	0.00	0.12	0.58	0.61	5.01	0.00	182	7.05
Max	17.58	425.70	1526.5	910.10	8.17	13.00	72.82	29.86	998.30	2.57	2874	8.50
Mean	4.94	157.00	617.2	184.54	1.42	4.57	22.54	8.05	385.68	0.26	1351	7.86
SD	4.18	137.28	337.6	178.56	1.77	3.30	23.79	7.71	243.10	0.56	721	0.45

Values less than LOD (limit of detection) were set to zero for statistical purposes.

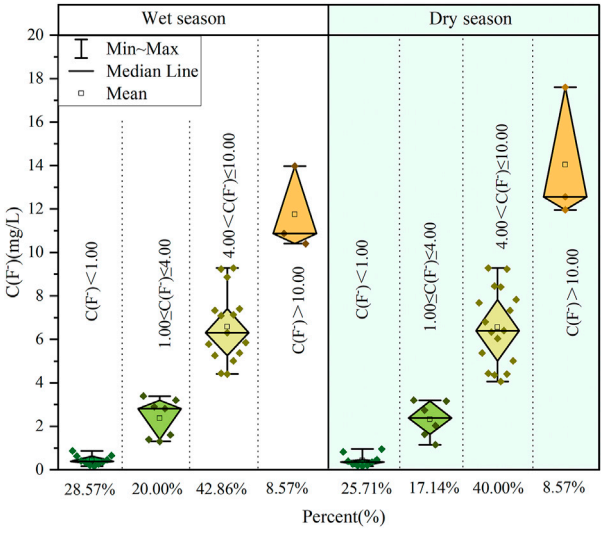

FIGURE 2
The percent boxplots of F^- content during the wet and dry seasons.

saturation index (SI) values to assess the degree of equilibrium between the water and minerals. The geochemical data for deep groundwater are contained in Table 2.

Results

Fluoride concentration of deep groundwater

The F^- concentrations in deep groundwater ranged between 0.12 and 13.92 mg/L (mean: 4.40 ± 3.72 mg/L) in the wet season (Table 2). Approximately 65.71% of deep groundwater samples exhibited F^- concentrations that exceeded the drinking water guidelines in China (i.e., 1.00 mg/L). Deep groundwater had higher F^- concentrations during the dry season than those during the wet season, ranging from 0.20 to 17.58 mg/L (mean: 4.94 ± 4.18 mg/L). Notably, 74.29% of the deep groundwater samples had F^- concentrations exceeding 1.00 mg/L. The mean F^- concentration of deep groundwater during the dry season was 1.12 times that during the wet season, suggesting that inhabitants who consume this water face a greater risk of developing fluorosis during the dry season.

Considering the drinking water guidelines in China and the health risk of fluorosis (Toolabiet al., 2021; Hao et al., 2022), the deep groundwater samples were divided into four groups: below 1.00 mg/L (low-F^- deep groundwater), 1.00–4.00 mg/L, 4.00–10.00 mg/L, and above 10.00 mg/L. All the F^- concentrations recorded in deep groundwater that exceeded 1.00 mg/L were designated as high-F^- deep groundwater. The

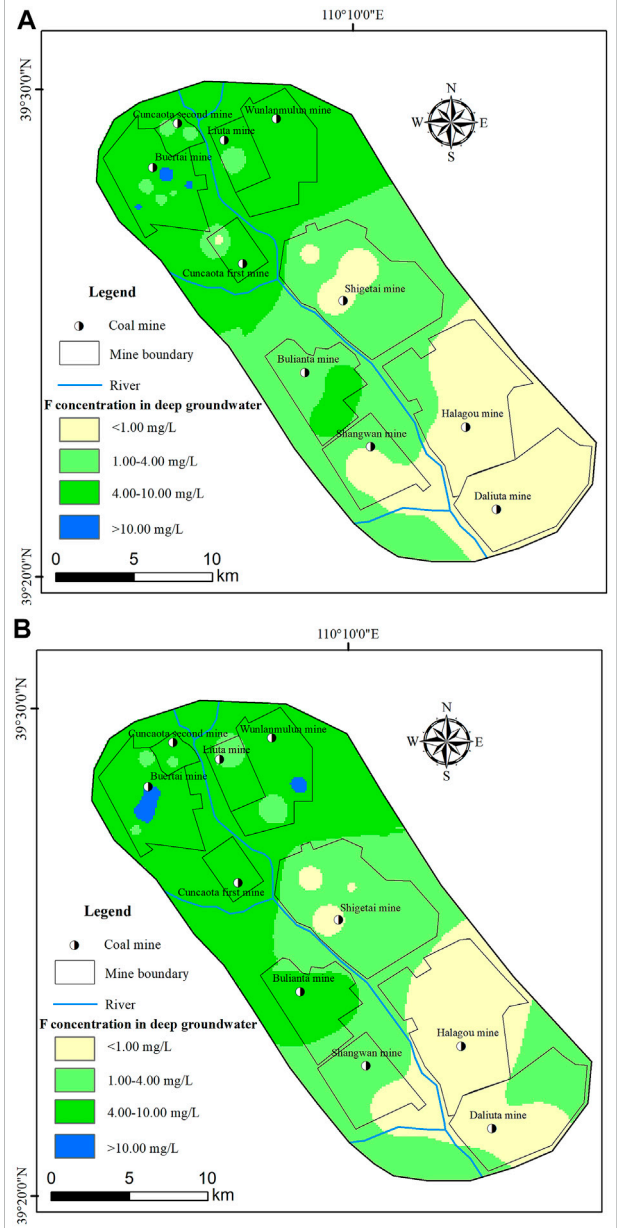

FIGURE 3
Distribution of F^- content in deep groundwater samples of the studied areas **(A)** during the wet season; **(B)** during the dry season.

range of F^- concentrations for deep groundwater samples with below 1.00 mg/L, 1.00–4.00 mg/L and 4.00–10.00 mg/L were identical in both wet and dry seasons (Figure 2). Compared with wet season, the F^- concentration was markedly increased in the deep groundwater with F^- concentrations above 10.00 mg/L and the mean F^- concentration was 1.21 times during the dry season, indicating that seasonal variation played a significant role in the enrichment of F^- in deep groundwater samples with F^- concentrations above 10.00 mg/L.

The mapping of F^- concentrations in deep groundwater revealed consistent spatial variations between the dry and wet seasons, with the fluoride concentrations of mine waters clearly increasing from the southeast to northwest (Figure 3). In particular, the Buertai mine area had the highest F^- concentrations in deep groundwater, measuring 13.92 mg/L during the wet season and 17.58 mg/L during the dry season. The results were identical to the studies of the spatial distribution of mine water reported by Hao (2022) and Zhang (2021), indicating that the F^- concentrations of deep groundwater may be significantly impacted by coal mining activities.

Geochemical characterization

As shown in Table 2, pH values of the deep groundwater in the Shendong mining area ranged from 7.02 (i.e., neutral) to 9.70 (i.e., alkaline), with a mean of 8.12 ± 0.58 in the wet season. Moreover, the pH values ranged from 7.05 to 8.50, with an average of 7.86 ± 0.45, in the dry season. TDS values of deep groundwater exceeded the acceptable limit for drinking water of 1000 mg/L by approximately 40.00% and 54.29% in the wet and dry seasons, respectively. The mean TDS concentration of deep groundwater during the dry season was higher than that during the wet season, indicating that the water-rock interaction process in deep groundwater was relatively stronger (Guo and Wang, 2005; Jakóbczyk-Karpierz et al., 2017; Hao et al., 2021a).

Deep groundwater samples in the study area were mainly located in the bottom right of the piper diagram, with the predominant hydrochemical types being the Na-HCO_3-Cl (52.00%) and Na-HCO_3-SO_4 (28.00%) types in the wet season, and Na-HCO_3-Cl (53.85%) and Na-HCO_3-SO_4 (30.77%) types in the dry season (Supplementary Figure S1). In addition, the high-F^- deep groundwaters were either the Na-HCO_3-Cl or Na-HCO_3-SO_4 types, with Na-types constituting the overwhelming majority. The low- F^- deep groundwaters had various proportions of Ca-HCO_3, Ca-SO_4-Cl, Na-HCO_3, and Na-HCO_3-Cl types, with 56% Ca-type and 44% Na-type. The results demonstrated that the transition from Ca-types to Na-types was advantageous for the enrichment of F^- concentrations in deep groundwater (Liu et al., 2021; Zhang et al., 2021).

Geochemical factors controlling fluoride in deep groundwater

Generally, understanding the relationship between F^- and geochemical elements in deep groundwater is essential to gain deeper insight into fluoride behavior (Li et al., 2015; Laxmankumar et al., 2019; Liu et al., 2021; Toolabi et al., 2021).

In Figure 4, deep groundwater F^- had a strongly negative correlation with Mg^{2+} (R^2 = −0.66) and Ca^{2+} (R^2 = −0.84), and a significantly positive correlation with pH (R^2 = 0.82), Cl^- (R^2 = 0.85),

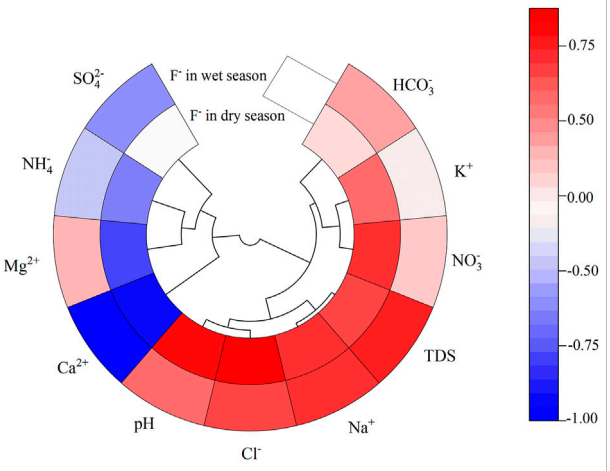

FIGURE 4
Relationships between F^- content and the geochemical elements in deep groundwater during the wet and dry seasons.

Na^+ (R^2 = 0.72), TDS (R^2 = 0.69), and NO_3^- (R^2 = 0.74), in the dry season. However, high TDS (R^2 = 0.86), Na^+ (R^2 = 0.77), Cl^- (R^2 = 0.68) and low Ca^{2+} (R^2 = −0.87) concentrations were the primary limiting geochemical factors for F^- during the wet season. Notably, the similar effect relationship between F^- and Ca^{2+}, Na^+, TDS, and Cl^- during both the dry and wet seasons indicated that Ca^{2+}, Na^+, TDS, and Cl^- had a significant effect on F^- concentrations in deep groundwater in the study area. However, the effect of pH, Mg^{2+}, and NO_3^- on F^- concentrations may have explained why F^- content increased more during the dry season than during the wet season.

Discussion

As shown in Figure 5A, there was a significantly negative correlation between F^- and Ca^{2+} during the wet and dry seasons in the Shendong mining area, indicating that the dissolution of F-bearing minerals was one of the major factors influencing the enrichment of F^- in deep groundwater (Hao et al., 2021b; Chen et al., 2021; Noor et al., 2022). All deep groundwater samples collected during the wet and dry seasons were distributed towards the saturated dissolution line of fluorite (K_{SP} = $10^{-10.6}$), further demonstrating that the dissolution of fluorite had a substantial effect on the appearance of high-F^- deep groundwater. Therefore, as the Ca^{2+} content rapidly increased, the F^- content would accelerate the reduction. The dissolution process of fluorite minerals was as follows:

$$\mathbf{CaF_2 \rightarrow Ca^{2+} + 2F^-} \quad (3)$$

The geology of the study area, as defined by Zhao and Wei, 2020; Duan et al., 2021, includes extensive F-bearing minerals

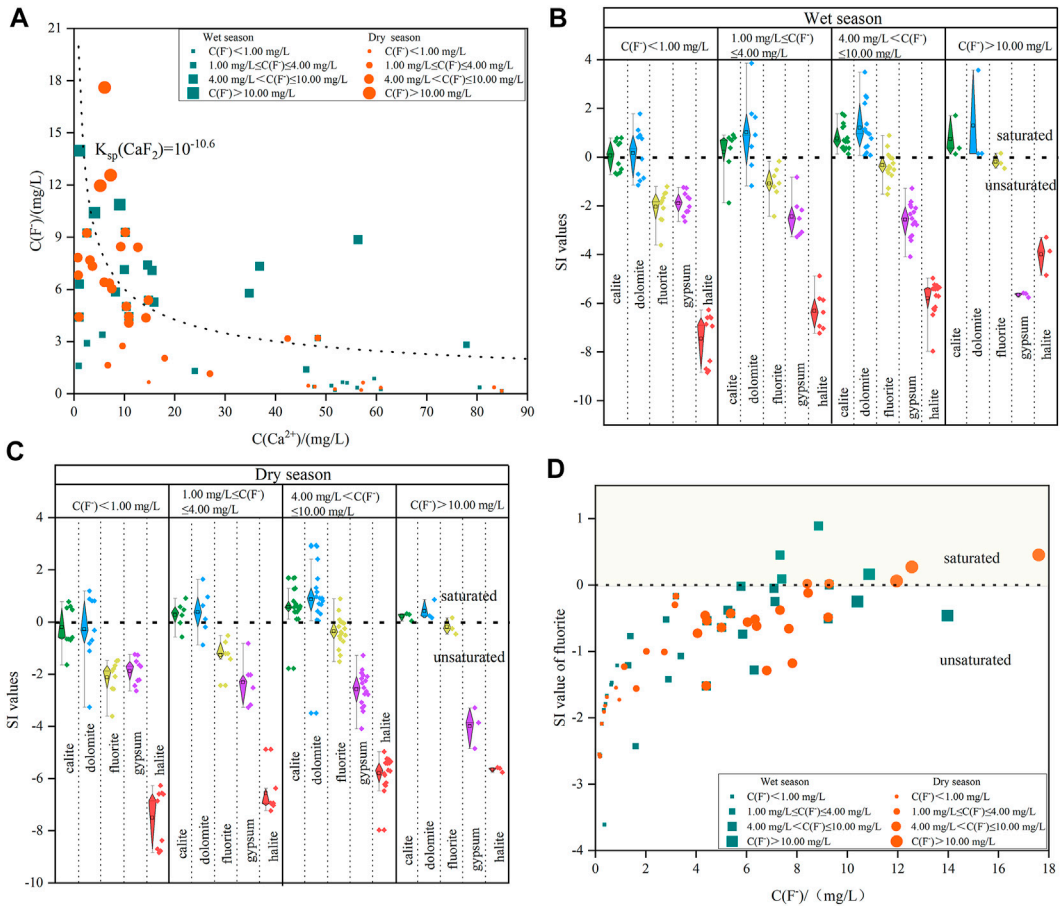

FIGURE 5
The plots of: **(A)** Ca^{2+} *versus* the F^- content; **(B)** the boxplots of SI values of minerals during the wet season; **(C)** the boxplots of SI value of minerals during the dry season; **(D)** the $SI_{fluorite}$ *versus* the F^- content in deep groundwater.

such as fluorite (CaF_2), muscovite ($KAl_3(AlSi_3O_{10})F_2$) and biotite ($KMg_3(AlSi_3O_{10})F_2$) in the J_{1-2y} stratum. Long-term water-rock interaction with F-bearing minerals inevitably increased enrichment of F^- in deep groundwater. Although the F^- concentration in deep groundwater was largely dependent on the rate and degree of fluorite dissolution, a precipitate state of calcium minerals such as calcite and dolomite could decrease Ca^{2+} concentrations and accelerate the promotion of F^- concentrations (Li et al., 2018; Noor et al., 2022). The SI values of calcium minerals could provide a thorough explanation of this process. The proportions of low-F^- deep groundwater samples showing negative SI values for calcite and dolomite were 55.56% and 55.56%, respectively, during both wet and dry seasons. However, the proportions of high-F^- deep groundwater samples showing negative SI values were 11.54% and 15.38%, respectively, during both dry and wet seasons (Figure 5B). Moreover, all deep groundwater samples with F^- concentrations above 10.00 mg/L were oversaturated with dolomite and calcite, demonstrating that the precipitation of dolomite and calcite can promote the dissolution of fluorite, resulting in an elevated F^- content in deep groundwater owing to a low Ca^{2+} content (Rafique et al., 2015; Rashid et al., 2018; Thapa et al., 2018).

Similarly, as depicted in Figures 5B,C, the SI values of fluorite during the dry season ranged between -2.59 and 1.54, with a mean of -0.83, whereas the SI values of fluorite during the wet season ranged between -3.61 and 0.89, with a mean of -0.65. The proportions of all deep groundwater samples showing positive $SI_{fluorite}$ values were 17.14% and 14.29% during the wet and dry seasons, respectively. This indicated that the majority of fluorite in the study area was in an unsaturated state and tended to continue dissolving. The positive correlation identified between F^- and $SI_{fluorite}$ (Figure 5D) were observed in both the wet and dry seasons for deep groundwater, further indicating that fluorite dissolution was the key driving agent for the elevation of F^- concentrations (Eang et al., 2018; Wu et al., 2018).

Higher HCO_3^- concentrations and alkaline pH values promoted the release of F^- into groundwater (Ali et al., 2018;

Ali et al., 2019; Wang et al., 2021). It is well known that the concentration of HCO_3^- increases as the pH increases, hence the F^-concentration in a constant pH (7.00–8.33) groundwater environment is often dominated by HCO_3^-. As shown in Table 2, 74.28% and 82.86% of deep groundwater samples had pH ranges of 7.00–8.33 during the wet and dry seasons, respectively. In this study, deep groundwater samples overall have a relatively lower average pH value during the dry season than that during the wet season, indicating higher F^- concentration may have other sources in deep groundwater during the dry season. Correspondingly, the mean SO_4^{2-} concentration (184.54 ± 178.56 mg/L) of deep groundwater during the wet season is less than that during the dry season in Table 2. A previous study (Hao et al., 2022) had showed that the oxidation of pyrite in a coal seam can generate SO_4^{2-} concentration enrichment, and then prevent the precipitation of CaF_2, promoting higher F^- content in deep groundwater.

Previous studies had revealed that pH values of 7.40–9.60 can make the surface charge of the clay minerals (e.g., muscovite and biotite) neutral or slightly negative and inhibit the adsorption of negatively charged F^- ions (Singh et al., 2011; Guo et al., 2012; Xiao et al., 2015). In addition, F^- and OH^- frequently replace each other on the mineral surfaces with similar ionic radii when the aqueous environment is favorable (Currell et al., 2011; Xiao et al., 2015). Compared to the wet season, the correlation between fluoride concentration and pH was positively stronger during the dry season (Figure 4), indicating pH played a significant role in F^- concentration elevations during the dry season. Therefore, the OH^- replaced the exchangeable F^- on the surfaces of clay minerals throughout the dry season, increasing the F^- concentrations in deep groundwater.

The process could be described by Eqs 4, 5:

$$KAl_3(AlSi_3O_{10})F_2 + 2OH^- \rightarrow KAl_2(AlSi_3O_{10})(OH)_2 + 2F^- \quad (4)$$

$$KMg_3(AlSi_3O_{10})F_2 + 2OH^- \rightarrow KMg_3(AlSi_3O_{10})(OH)_2 + 2F^- \quad (5)$$

During the dry season, the observed relationship between F^- and HCO_3^- has a poor correlation ($R^2 = 0.16$) in Figure 4, whereas competitive absorption was a contributing factor in F^- desorption in deep groundwater cannot be ignored. Ali et al. (2019) and Guo et al. (2012) confirmed that the presence of HCO_3^- would reduce the number of available absorbent sites and lead to the release of F^- from clay minerals, consequently increasing the F^- concentration in deep groundwater.

The poor correlation between F^- and HCO_3^- during the dry season.

There was a moderately positive correlation ($R^2 = 0.74$) between F^- and NO_3^- during the dry season (Figure 4). Previous studies showed that groundwater with high F^- concentrations typically had low NO_3^- concentrations (>5 mg/L) (Hao et al., 2021c; Li et al., 2021; Mwiathi et al., 2022). The presence of more than 5 mg/L NO_3^- in 36% of the high-F- deep groundwater indicated the impacts of anthropogenic activities such as fertilizer application and waste discharge from agricultural, domestic, and industrial sources (Ali et al., 2019; Su et al., 2021; Yadav et al., 2021). The highest observed deep groundwater NO_3^- concentration was 8.17 mg/L in the Buertai mining area. The entry of polluted mine water into the deep groundwater aquifer system promoted the enrichment of F^- concentrations *via* goaf fissures (Song et al., 2020; Zhang et al., 2021). The weak correlation ($R^2 = 0.19$) between F^- and NO_3^- during the wet season further suggested that anthropogenic activities were not the main contributor to high F^- levels in deep groundwater.

F^- positively correlated with Na^+ during both dry and wet season in deep groundwater (Figure 4). Cation exchange between Ca^{2+} and Na^+ was regarded as one of the primary sources of groundwater Na^+; therefore, the relationship between Cl^- - Na^+ - K^+ and HCO_3^- + SO_4^{2-} - Ca^{2+} - Mg^{2+} was extensively used to determine the cation exchange process in deep groundwater (Li et al., 2015; Ali et al., 2019; Liu et al., 2021). As shown in Figure 6, most deep groundwater samples were distributed along the 1:1 line during both the dry and wet seasons, indicating that the cation exchange process had an important influence on the F^- contents (Liu et al., 2021; Hao et al., 2022). Deep groundwater samples from both the wet and dry seasons were close to the 1:1 line and had high correlations with R^2 of 0.80 and 0.84, respectively. This suggested that the ion exchange reaction was more intense during the wet season than during the dry season. The results may explain why the concentration of F^- in deep groundwater was greater during the dry season than that during the wet season. The increase in Na^+ and decrease in Ca^{2+} concentrations in deep groundwater are typically caused by cation exchange reactions. Clay minerals (e.g., illite and kaolinite) are plentiful in the J_{1-2y} stratum, which contains abundant exchange sites for the displacement of Na^+ by Ca^{2+}. For convenience, the reaction process was represented by Eq. 6:

$$2NaX + Ca^{2+} \rightarrow 2Na^+ + CaX_2 \quad (6)$$

Therefore, as Ca-type water changed to Na-type water in the system, the Ca^{2+} concentration reduction accelerated the dissolution of fluorite and consequently released additional F^- into deep groundwater.

Two chloroalkaline ion exchange indices (CAI) are also evaluated whether ion exchanges occurring between Na^+ in the groundwater and Ca^{2+} in the stratum using the Eqs 7, 8. If both values of CAI 1 and CAI 2 are all positive, the Na^+ in groundwater have been exchanged for Ca^{2+} in the stratum. In contrast, if both values of CAI 1 and CAI 2 are negative, the Ca^{2+} in groundwater have been exchanged by Na^+ in the stratum. Moreover, the larger the absolute values of CAI, the stronger the ion exchange interaction (Li et al., 2015; Dehbandi et al., 2018; Hao et al., 2022).

$$CAI - 1 = [Cl^- - (Na^+ + K^+)]/Cl^- \quad (7)$$

$$CAI - 2 = [Cl^- - (Na^+ + K^+)]/(SO_4^{2-} + HCO_3^- + CO_3^{2-} + NO3_3^-) \quad (8)$$

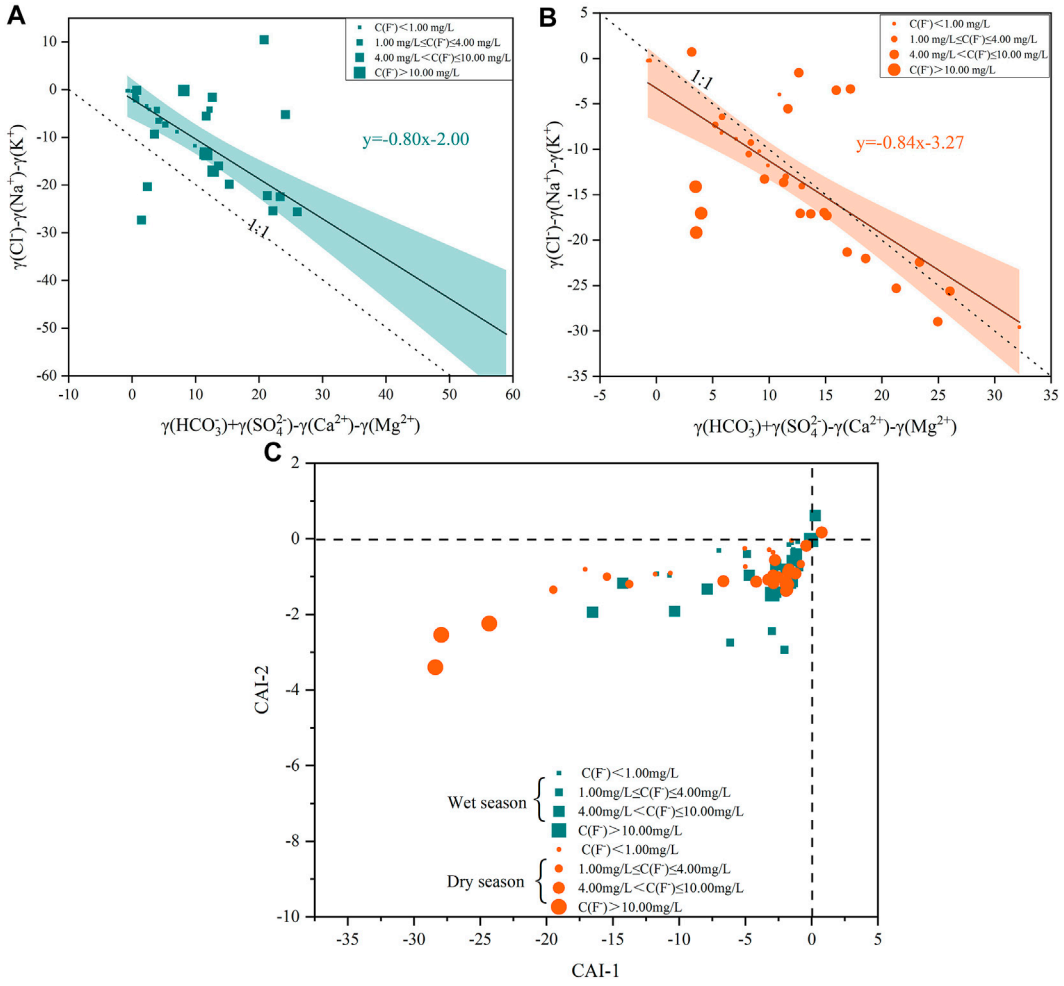

FIGURE 6
The plots of: **(A)** Cl^--Na^+-K^+ *versus* HCO_3^-+SO_4^{2-}-Ca^{2+}-Mg^{2+} during the wet season; **(B)** Cl^--Na^+-K^+ *versus* HCO_3^-+SO_4^{2-}-Ca^{2+}-Mg^{2+} during the dry season; **(C)** CAI-1 *versus* CAI-2 during the wet and dry season in deep groundwater.

As shown in Figure 6C, 94.28% and 97.14% of the deep groundwater samples show negative CAI 1 and CAI 2 values during the wet and dry season, respectively, indicating the Ca^{2+} and Mg^{2+} in the deep groundwater have been exchanged by K^+ and Na^+ in the stratum and explaining F^- enrichment in deep groundwater. In addition, the CAI 1 and CAI 2 absolute values of deep groundwater during the dry season was higher than that during the wet season, further implying that ion exchange interactions were more dominant. Thus, the cation exchange process primarily increases the F^- concentration in deep groundwater during the dry season (Li et al., 2015; Hao et al., 2022).

The TDS values exhibited a positive correlation with F^- in the study area during both dry and wet seasons (Figure 4D), indicating that an enhancement of ionic strength increased F^- concentrations in deep groundwater (Dehbandi et al., 2018; Wu et al., 2018; Laxmankumar et al., 2019). Atmospheric precipitation, evaporation, and rock weathering can reflect hydrogeochemical processes in Gibbs diagrams. All high-F^- deep groundwater samples from both the dry and wet seasons fell under rock weathering and evaporation dominance with medium to high TDS, high Na/(Na+Ca) and low Cl/(Cl+HCO_3) ratios (Supplementary Figure S2), indicating that the rock weathering and evaporation processes were dominant geochemical factors for increasing the F^- content in deep groundwater (Dehbandi et al., 2018; LaFayette et al., 2020; Hao et al., 2021d).

Irrigation water quality

The irrigation water quality was thoroughly assessed and the results are presented in Figure 7. The United States salinity hazard diagram (Figure 7A) illustrated that 25.71%, 14.29%,

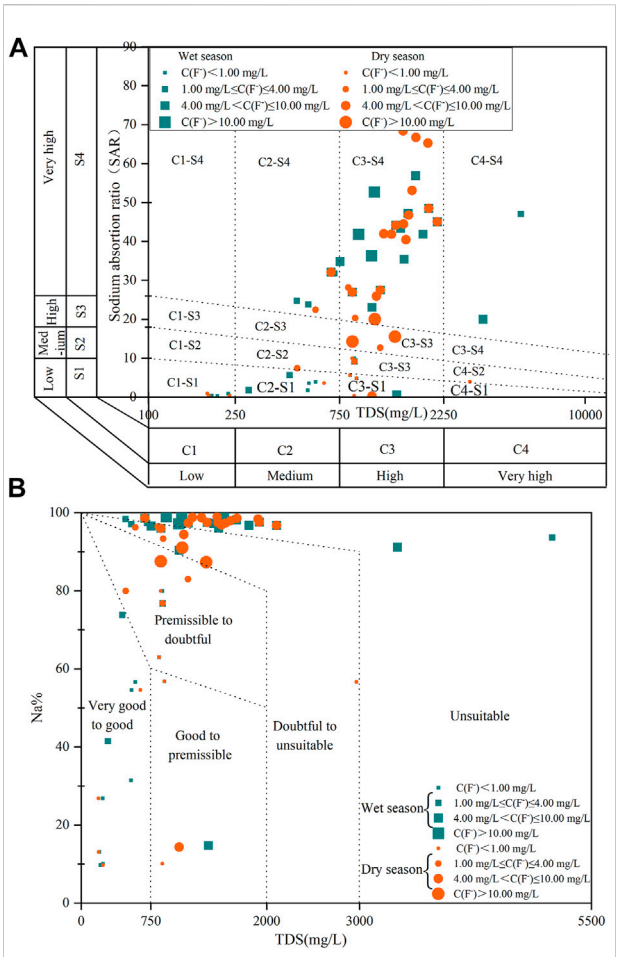

FIGURE 7
The plots of: **(A)** USSL classification of irrigation quality; **(B)** Wilcox of irrigation groundwater quality in the study area.

40.00%, and 5.71% of deep groundwater samples in the wet season fell in zones with low salinity and alkalinity, medium salinity and low and very high alkalinity, high salinity and very high alkalinity, and very high salinity and alkalinity, respectively. Similarly, 14.29%, 25.71%, 57.14%, and 2.86% of deep groundwater samples in the dry season were found in C1-S1, C2-S1-S2-S4, C3-S1-S2-S3-S4, and C4-S2 zones, indicating low salinity and alkalinity; medium salinity and low, medium, and very high alkalinity; high salinity and all alkalinity; and very high salinity and medium alkalinity, respectively.

Wilcox plots (Figure 7B) revealed that 100% and 88.89% of low-F^- deep groundwater samples fell in the very good to good field during the wet and dry seasons, respectively, indicating that most low-F^- deep groundwater samples had excellent irrigation water quality. However, 84.00% and 84.62% of high-F^- deep groundwater samples fell in the doubtful to unsuitable and unsuitable fields during the wet and dry seasons, respectively. With increasing F^- concentration, deep groundwater samples significantly diverged from suitable to unsuitable irrigation fields, indicating that F^- concentration in deep groundwater was a key variable in determining ecological risk in the study area.

Conclusion

In this study, we highlighted F^- contamination in deep groundwater in the vicinity of the Shendong mining area during the wet and dry seasons. A total of 65.71% (wet season) and 74.29% (dry season) of deep groundwater samples exhibited F^- concentrations exceeding the limit set by the drinking water guideline in China (1.00 mg/L). In addition, the mean F^- concentrations in deep groundwater were higher during the dry season than those during the wet season. The spatial distribution of F^- in deep groundwater was stable during both dry and wet seasons, with a noticeable increase from southeast to northwest.

Several geochemical processes, including the dissolution and precipitation of F^--bearing and calcium minerals, cation exchange, competitive adsorption, evaporation, and anthropogenic activities during both the wet and dry seasons, may have contributed to the F^- enrichment of deep groundwater. Importantly, the precipitation of dolomite, cation exchange, competitive adsorption, and mining activities may have been the primary causes of the seasonal differences in F^- content.

The risk of high-F^- deep groundwater to the ecological environment in the study area was assessed, and the results indicated that 100% and 88.89% of low-F^- deep groundwater samples had excellent irrigation water quality during the wet and dry seasons, respectively. However, at the same time, 84.00% and 84.62% of high-F^- deep groundwater samples were unsuitable for irrigation during the wet and dry seasons, respectively. The F^- concentration in deep groundwater was a key influential variable for ecological risk in the study area. Therefore, it is essential to devise effective pretreatment methods of minimizing the risk of the deep groundwater fluoride such as ion exchange, membrane separation, electrodialysis, precipitation, reverse osmosis, and adsorption before ecological irrigation.

Despite F^- enriched in deep groundwater during the wet and dry season, the influence of seasonal fluctuation of groundwater level on the formation of high fluoride water was not deeply discussed in the article. In addition, our findings are not assessed health risk for few rural residents and limited to promote the local govern management of deep groundwater resources within the study area. Hence, the studies will aid in the development of policies aimed at preventing high levels of F^- in deep groundwater in the study area, to protect the ecological environment and gain a better understanding of the seasonal distribution and

geochemical factors of F^- in deep groundwater in the vicinity of the Shendong mining area.

Data availability statement

The datasets presented in this study can be found in online repositories. The names of the repository/repositories and accession number(s) can be found in the article/ Supplementary Material.

Author contributions

Conceptualization, methodology, and writing- original draft preparation, CH; data curation, visualization, and investigation, YW; software and investigation, KH; supervision, writing-reviewing, and editing, HG. All authors contributed to manuscript revision, read, and approved the submitted version.

Funding

This work was supported by the Natural Science Foundation of Hebei Province (D2021508004), Open Fund of Key Laboratory of Mine Water Resource Utilization of Anhui Higher Education Institutes, Suzhou University (Grant No. KMWRU202101), and Open Fund of State Key Laboratory of Coal Resources and Safe Mining (Grant No. SKLCRSM22KFA03).

Acknowledgments

We would like to thank Editage (www.editage.cn) for English language editing.

Conflict of interest

The authors declare that the research was conducted in the absence of any commercial or financial relationships that could be construed as a potential conflict of interest.

Publisher's note

All claims expressed in this article are solely those of the authors and do not necessarily represent those of their affiliated organizations, or those of the publisher, the editors and the reviewers. Any product that may be evaluated in this article, or claim that may be made by its manufacturer, is not guaranteed or endorsed by the publisher.

Supplementary material

The Supplementary Material for this article can be found online at: https://www.frontiersin.org/articles/10.3389/fenvs.2022.1024797/full#supplementary-material

References

Adeyeye, O. A., Xiao, C., Zhang, Z., Yawe, A. S., and Liang, X. (2021). Groundwater fluoride chemistry and health risk assessment of multi-aquifers in Jilin Qianan, Northeastern China. *Ecotoxicol. Environ. Saf.* 211, 111926. doi:10.1016/j.ecoenv.2021.111926

Aghapour, S., Bina, B., Tarrahi, M. J., Amiri, F., and Ebrahimi, A. (2018). Distribution and health risk assessment of natural fluoride of drinking groundwater resources of Isfahan, Iran, using GIS. *Environ. Monit. Assess.* 190 (3), 137. doi:10.1007/s10661-018-6467-z

Ali, S., Shekhar, S., Bhattacharya, P., Verma, G., Chandrasekhar, T., and Chandrashekhar, A. K. (2018). Elevated fluoride in groundwater of Siwani Block, Western Haryana, India, A potential concern for sustainable water supplies for drinking and irrigation. *Groundw. Sustain. Dev.* 7, 410–420. doi:10.1016/j.gsd.2018.05.008

Ali, W., Aslam, M. W., Junaid, M., Ali, K., Guo, Y., Rasool, A., et al. (2019). Elucidating various geochemical mechanisms drive fluoride contamination in unconfined aquifers along the major rivers in Sindh and Punjab, Pakistan. *Environ. Pollut.* 249, 535–549. doi:10.1016/j.envpol.2019.03.043

Araya, D., Podgorski, J., Kumi, M., Mainoo, P. A., and Berg, M. (2022). Fluoride contamination of groundwater resources in Ghana, Country-wide hazard modeling and estimated population at risk. *Water Res.* 212, 118083. doi:10.1016/j.watres.2022.118083

Blasco, M., Auqué, L. F., and Gimeno, M. J. (2019). Geochemical evolution of thermal waters in carbonate – evaporitic systems, the triggering effect of halite dissolution in the dedolomitisation and albitisation processes. *J. Hydrol. X.* 570, 623–636. doi:10.1016/j.jhydrol.2019.01.013

Borzi, G. E., Garcia, L., and Carol, E. S. (2015). Geochemical processes regulating F^-, as and NO_3^- content in the groundwater of a sector of the Pampean Region. *Argent. Sci. Total Environ.* 530-531, 154–162. doi:10.1016/j.scitotenv.2015.05.072

Chen, J., Gao, Y., Qian, H., Ren, W., and Qu, W. (2021). Hydrogeochemical evidence for fluoride behavior in groundwater and the associated risk to human health for a large irrigation plain in the Yellow River Basin. *Sci. Total Environ.* 800, 149428. doi:10.1016/j.scitotenv.2021.149428

Chicas, S. D., Omine, K., Prabhakaran, M., Sunitha, T. G., and Sivasankar, V. (2022). High fluoride in groundwater and associated non-carcinogenic risks at Tiruvannamalai region in Tamil Nadu, India. *Ecotoxicol. Environ. Saf.* 233, 113335. doi:10.1016/j.ecoenv.2022.113335

Currell, M., Cartwright, I., Raveggi, M., and Han, D. (2011). Controls on elevated fluoride and arsenic concentrations in groundwater from the Yuncheng Basin, China. *Appl. Geochem.* 26 (4), 540–552. doi:10.1016/j.apgeochem.2011.01.012

Dehbandi, R., Moore, F., and Keshavarzi, B. (2018). Geochemical sources, hydrogeochemical behavior, and health risk assessment of fluoride in an endemic fluorosis area, central Iran. *Chemosphere* 193, 763–776. doi:10.1016/j.chemosphere.2017.11.021

Duan, L., Wang, X., and Sun, Y. (2021). Occurrence characteristics and ecological risk assessment of fluorine in coal gangue. *Coal Convers.* 44 (2), 1–10. doi:10.19726/j.cnki.ebcc.202102011

Duggal, V., and Sharma, S. (2022). Fluoride contamination in drinking water and associated health risk assessment in the Malwa Belt of Punjab, India. *Environ. Adv.* 8, 100242. doi:10.1016/j.envadv.2022.100242

Eang, K. E., Igarashi, T., Kondo, M., Nakatani, T., Tabelin, C. B., and Fujinaga, R. (2018). Groundwater monitoring of an open-pit limestone quarry, Water-rock interaction and mixing estimation within the rock layers by geochemical and statistical analyses. *Int. J. Min. Sci. Technol.* 28 (6), 849–857. doi:10.1016/j.ijmst.2018.04.002

Emenike, C. P., Tenebe, I. T., and Jarvis, P. (2018). Fluoride contamination in groundwater sources in Southwestern Nigeria, Assessment using multivariate statistical approach and human health risk. *Ecotoxicol. Environ. Saf.* 156, 391–402. doi:10.1016/j.ecoenv.2018.03.022

Gu, D., Li, J., and Cao, Z. (2021). Technology and engineering development strategy of water protection and utilization of coal mine in China. *J. China Coal Soc.* doi:10.13225/j.cnki.jccs.2021.0917

Gu, D. Z. (2014). Water resource protection and utilization engineering technology of coal mining in "energy golden triangle" region. *Coal Eng.* 46 (10), 33–37. doi:10.11799/ce201410008

Guo, H., and Wang, Y. (2005). Geochemical characteristics of shallow groundwater in Datong basin, northwestern China. *J. Geochem. Explor.* 87 (3), 109–120. doi:10.1016/j.gexplo.2005.08.002

Guo, H., Zhang, Y., Xing, L., and Jia, Y. (2012). Spatial variation in arsenic and fluoride concentrations of shallow groundwater from the town of Shahai in the Hetao basin, Inner Mongolia. *Appl. Geochem.* 27 (11), 2187–2196. doi:10.1016/j.apgeochem.2012.01.016

Guo, Y., Yang, J., Zhang, Z., Li, G., Ting, L., and Wang, L. (2021). Hydrogen and oxygen isotope characteristics of mine water in the Shendong mine area and water-rock reactions mechanism of the formation of high-fluoride mine water. *J. China Coal Soc.* 46 (S2), 948–959. doi:10.13225/j.cnki.jccs.2021.0388

Hao, C., Liu, M., Peng, Y., and Wei, Z. (2021d). Comparison of antimony sources and hydrogeochemical processes in shallow and deep groundwater near the xikuangshan mine, hunan province, China. *Mine Water Environ.* 41 (1), 194–209. doi:10.1007/s10230-021-00833-8

Hao, C., Liu, M., Zhang, W., He, P., Lin, D., and Gui, H. (2021a). Spatial distribution, source identification, and health risk assessment of fluoride in the drinking groundwater in the Sulin coal district, northern Anhui Province, China. *Water Supply* 21 (5), 2444–2462. doi:10.2166/ws.2021.048

Hao, C., Sun, X., Xie, B., and Hou, S. (2022). Increase in fluoride concentration in mine water in Shendong mining area, Northwest China, Insights from isotopic and geochemical signatures. *Ecotoxicol. Environ. Saf.* 236, 113496. doi:10.1016/j.ecoenv.2022.113496

Hao, C., Zhang, W., and Gui, H. (2021b). Geochemical behaviours and formation mechanisms for elevated fluoride in the drinking groundwater in sulin coal-mining district, northern Anhui province, China. *Pol. J. Environ. Stud.* 30 (4), 3565–3578. doi:10.15244/pjoes/131193

Hao, C., Zhang, W., and He, R. (2021c). Formation mechanisms for elevated fluoride in the mine water in Shendong coal-mining district. *J. China Coal Soc.* 46 (6), 1966–1977. doi:10.13225/j.cnki.jccs.ST21.0160

He, J., An, Y., and Zhang, F. (2013). Geochemical characteristics and fluoride distribution in the groundwater of the Zhangye Basin in Northwestern China. *J. Geochem. Explor.* 135, 22–30. doi:10.1016/j.gexplo.2012.12.012

He, X., Ma, T., Wang, Y., Shan, H., and Deng, Y. (2013). Hydrogeochemistry of high fluoride groundwater in shallow aquifers, Hangjinhouqi, Hetao Plain. *J. Geochem. Explor.* 135, 63–70. doi:10.1016/j.gexplo.2012.11.010

Huang, L., Sun, Z., Zhou, A., Bi, J., and Liu, Y. (2022). Source and enrichment mechanism of fluoride in groundwater of the hotan oasis within the tarim basin, northwestern China. *Environ. Pollut.* 300, 118962. doi:10.1016/j.envpol.2022.118962

Jakóbczyk-Karpierz, S., Sitek, S., Jakobsen, R., and Kowalczyk, A. (2017). Geochemical and isotopic study to determine sources and processes affecting nitrate and sulphate in groundwater influenced by intensive human activity - carbonate aquifer Gliwice (southern Poland). *Appl. Geochem.* 76, 168–181. doi:10.1016/j.apgeochem.2016.12.005

Jeong, S. W., Wu, Y. H., Cho, Y. C., and Ji, S. W. (2018). Flow behavior and mobility of contaminated waste rock materials in the abandoned Imgi mine in Korea. *Geomorphology* 301, 79–91. doi:10.1016/j.geomorph.2017.10.021

Kumar, P., Singh, C. K., Saraswat, C., Mishra, B., and Sharma, T. (2019). Evaluation of aqueous geochemistry of fluoride enriched groundwater, A case study of the Patan district, Gujarat, Western India. *Water Sci.* 31 (2), 215–229. doi:10.1016/j.wsj.2017.05.002

Kumar, S., Venkatesh, A. S., Singh, R., Udayabhanu, G., and Saha, D. (2018). Geochemical signatures and isotopic systematics constraining dynamics of fluoride contamination in groundwater across Jamui district, Indo-Gangetic alluvial plains, India. *Chemosphere* 205, 493–505. doi:10.1016/j.chemosphere.2018.04.116

LaFayette, G. N., Knappett, P. S. K., Li, Y., Loza-Aguirre, I., and Polizzotto, M. L. (2020). Geogenic sources and chemical controls on fluoride release to groundwater in the Independence Basin, Mexico. *Appl. Geochem.* 123, 104787. doi:10.1016/j.apgeochem.2020.104787

Laxmankumar, D., Satyanarayana, E., and Dhakate, R. (2019). Hydrogeochemical characteristics with respect to fluoride contamination in groundwater of Maheshwarm mandal, RR district, Telangana state, India. *Groundw. Sustain. Dev.* 8, 474–483. doi:10.1016/j.gsd.2019.01.008

Li, C., Gao, X., and Wang, Y. (2015). Hydrogeochemistry of high-fluoride groundwater at Yuncheng Basin, northern China. *Sci. Total Environ.* 508, 155–165. doi:10.1016/j.scitotenv.2014.11.045

Li, D., Gao, X., Wang, Y., and Luo, W. (2018). Diverse mechanisms drive fluoride enrichment in groundwater in two neighboring sites in northern China. *Environ. Pollut.* 237, 430–441. doi:10.1016/j.envpol.2018.02.072

Li, Y., Bi, Y., Mi, W., Xie, S., and Ji, L. (2021). Land-use change caused by anthropogenic activities increase fluoride and arsenic pollution in groundwater and human health risk. *J. Hazard. Mat.* 406, 124337. doi:10.1016/j.jhazmat.2020.124337

Liu, J., Peng, Y., Li, C., Gao, Z., and Chen, S. (2021). A characterization of groundwater fluoride, influencing factors and risk to human health in the southwest plain of Shandong Province, North China. *Ecotoxicol. Environ. Saf.* 207, 111512. doi:10.1016/j.ecoenv.2020.111512

Mamatchi, M., Rajendran, R., Lumo, A. K., Arumugam, G., Kpemissi, M., Sadikou, A., et al. (2019). Cardiovascular dysfunction and oxidative stress following human contamination by fluoride along with environmental xenobiotics (Cd & Pb) in the phosphate treatment area of Togo, West Africa. *J. Trace Elem. Med. Biol.* 56, 13–20. doi:10.1016/j.jtemb.2019.07.002

Mondal, D., Gupta, S., Reddy, D. V., and Nagabhushanam, P. (2014). Geochemical controls on fluoride concentrations in groundwater from alluvial aquifers of the Birbhum district, West Bengal, India. *J. Geochem. Explor.* 145, 190–206. doi:10.1016/j.gexplo.2014.06.005

Mwiathi, N. F., Gao, X., Li, C., and Rashid, A. (2022). The occurrence of geogenic fluoride in shallow aquifers of Kenya Rift Valley and its implications in groundwater management. *Ecotoxicol. Environ. Saf.* 229, 113046. doi:10.1016/j.ecoenv.2021.113046

Najamuddin, T. P., Sanusi, H. S., and Nurjaya, I. W. (2016). Seasonal distribution and geochemical fractionation of heavy metals from surface sediment in a tropical estuary of Jeneberang River, Indonesia. *Mar. Pollut. Bull.* 111 (1-2), 456–462. doi:10.1016/j.marpolbul.2016.06.106

Nizam, S., Virk, H. S., and Sen, I. S. (2022). High levels of fluoride in groundwater from Northern parts of Indo-Gangetic plains reveals detrimental fluorosis health risks. *Environ. Adv.* 8, 100200. doi:10.1016/j.envadv.2022.100200

Noor, S., Rashid, A., Javed, A., Khattak, J. A., and Farooqi, A. (2022). Hydrogeological properties, sources provenance, and health risk exposure of fluoride in the groundwater of Batkhela, Pakistan. *Environ. Technol. Innov.* 25, 102239. doi:10.1016/j.eti.2021.102239

Olaka, L. A., Wilke, F. D., Olago, D. O., Odada, E. O., Mulch, A., and Musolff, A. (2016). Groundwater fluoride enrichment in an active rift setting, Central Kenya Rift case study. *Sci. Total Environ.* 545-546, 641–653. doi:10.1016/j.scitotenv.2015.11.161

Orland, I. J., Burstyn, Y., Bar-Matthews, M., Kozdon, R., Ayalon, A., Matthews, A., et al. (2014). Seasonal climate signals (1990–2008) in a modern Soreq Cave stalagmite as revealed by high-resolution geochemical analysis. *Chem. Geol.* 363, 322–333. doi:10.1016/j.chemgeo.2013.11.011

Rafique, T., Naseem, S., Ozsvath, D., Hussain, R., Bhanger, M. I., and Usmani, T. H. (2015). Geochemical controls of high fluoride groundwater in umarkot sub-district, thar desert, Pakistan. *Sci. Total Environ.* 530-531, 271–278. doi:10.1016/j.scitotenv.2015.05.038

Rashid, A., Guan, D. X., Farooqi, A., Khan, S., Zahir, S., Jehan, S., et al. (2018). Fluoride prevalence in groundwater around a fluorite mining area in the flood plain of the River Swat, Pakistan. *Sci. Total Environ.* 635, 203–215. doi:10.1016/j.scitotenv.2018.04.064

Rehman, F., Siddique, J., Shahab, A., Azeem, T., Bangash, A. A., Naseem, A. A., et al. (2022). Hydrochemical appraisal of fluoride contamination in groundwater and human health risk assessment at Isa Khel, Punjab, Pakistan. *Environ. Technol. Innov.* 27, 102445. doi:10.1016/j.eti.2022.102445

Sahu, M., Sar, S. K., Baghel, T., and Dewangan, R. (2020). Seasonal and geochemical variation of uranium and major ions in groundwater at Kanker district of Chhattisgarh, central India. *Groundw. Sustain. Dev.* 10, 100330. doi:10.1016/j.gsd.2020.100330

Singh, A. K., Mahato, M. K., Neogi, B., Mondal, G. C., and Singh, T. B. (2011). Hydrogeochemistry, elemental flux, and quality assessment of mine water in the pootkee-balihari mining area, jharia coalfield, India. *Mine Water Environ.* 30 (3), 197. doi:10.1007/s10230-011-0143-7

Song, H., Xu, J., Fang, J., Cao, Z., Yang, L., and Li, T. (2020). Potential for mine water disposal in coal seam goaf, Investigation of storage coefficients in the Shendong mining area. *J. Clean. Prod.* 244, 118646. doi:10.1016/j.jclepro.2019.118646

Su, H., Kang, W., Li, Y., and Li, Z. (2021). Fluoride and nitrate contamination of groundwater in the Loess Plateau, China, Sources and related human health risks. *Environ. Pollut.* 286, 117287. doi:10.1016/j.envpol.2021.117287

Thapa, R., Gupta, S., Gupta, A., Reddy, D. V., and Kaur, H. (2018). Geochemical and geostatistical appraisal of fluoride contamination, an insight into the Quaternary aquifer. *Sci. Total Environ.* 640-641, 406–418. doi:10.1016/j.scitotenv.2018.05.360

Toolabi, A., Bonyadi, Z., Paydar, M., Najafpoor, A. A., and Ramavandi, B. (2021). Spatial distribution, occurrence, and health risk assessment of nitrate, fluoride, and arsenic in Bam groundwater resource, Iran. *Groundw. Sustain. Dev.* 12, 100543. doi:10.1016/j.gsd.2020.100543

Wang, B., Xu, H., Wang, D., and He, S. (2021). The influence mechanism of HCO_3^- on fluoride removal by different types of aluminum salts. *Colloids Surfaces A Physicochem. Eng. Aspects* 126124. doi:10.1016/j.colsurfa.2020.126124

Wu, C., Wu, X., Qian, C., and Zhu, G. (2018). Hydrogeochemistry and groundwater quality assessment of high fluoride levels in the Yanchi endorheic region, northwest China. *Appl. Geochem.* 98, 404–417. doi:10.1016/j.apgeochem.2018.10.016

Xiao, J., Jin, Z., and Zhang, F. (2015). Geochemical controls on fluoride concentrations in natural waters from the middle Loess Plateau, China. *J. Geochem. Explor.* 159, 252–261. doi:10.1016/j.gexplo.2015.09.018

Xiao, W., Lv, X., Zhao, Y., Sun, H., and Li, J. (2020). Ecological resilience assessment of an arid coal mining area using index of entropy and linear weighted analysis, A case study of Shendong Coalfield, China. *Ecol. Indic.* 109, 105843. doi:10.1016/j.ecolind.2019.105843

Xu, J., Zhu, W., Xu, J., Wu, J., and Li, Y. (2021). High-intensity longwall mining-induced ground subsidence in Shendong coalfield, China. *Int. J. Rock Mech. Min. Sci.* 141, 104730. doi:10.1016/j.ijrmms.2021.104730

Yadav, K., Raphi, M., and Jagadevan, S. (2021). Geochemical appraisal of fluoride contaminated groundwater in the vicinity of a coal mining region, Spatial variability and health risk assessment. *Geochemistry* 81 (1), 125684. doi:10.1016/j.chemer.2020.125684

Yang, Z., Li, W., Li, X., Wang, Q., and He, J. (2019). Assessment of eco-geo-environment quality using multivariate data, A case study in a coal mining area of Western China. *Ecol. Indic.* 107, 105651. doi:10.1016/j.ecolind.2019.105651

Yuan, S., Sui, W., Han, G., and Duan, W. (2022). *An optimized combination of mine water control, treatment, utilization, and reinjection for environmentally sustainable mining, A case study. Mine Water Environ.* 41 (3) 828–839. doi:10.1007/s10230-022-00886-3

Zango, M. S., Pelig-Ba, K. B., Anim-Gyampo, M., Gibrilla, A., and Sunkari, E. D. (2021). Hydrogeochemical and isotopic controls on the source of fluoride in groundwater within the Vea catchment, northeastern Ghana. *Groundw. Sustain. Dev.* 12, 100526. doi:10.1016/j.gsd.2020.100526

Zhang, J., Chen, L., Hou, X., Ren, X., Li, J., and Chen, Y. (2022). Hydrogeochemical processes of carboniferous limestone groundwater in the yangzhuang coal mine, huaibei coalfield, China. *Mine Water Environ.* 41 (2), 504–517. doi:10.1007/S10230-022-00861-Y

Zhang, Z., Li, G., Su, X., Zhuang, X., Wang, L., Fu, H., et al. (2021). Geochemical controls on the enrichment of fluoride in the mine water of the Shendong mining area, China. *Chemosphere* 284, 131388. doi:10.1016/j.chemosphere.2021.131388

Zhao, B., and Wei, N. (2020). Study on content distribution and occurrenceform of fluorine in Shaanxi coal. *Coal Qual. Technol.* 35 (6), 34–39.

frontiers | Frontiers in Environmental Science

TYPE Original Research
PUBLISHED 20 October 2022
DOI 10.3389/fenvs.2022.1010367

OPEN ACCESS

EDITED BY
Yong Xiao,
Southwest Jiaotong University, China

REVIEWED BY
Linxian Huang,
University of Jinan, China
Fatemeh Barzegari Banadkooki,
Payame Noor University, Iran

*CORRESPONDENCE
Yuan Liu,
2930648938@qq.com

SPECIALTY SECTION
This article was submitted to Freshwater Science,
a section of the journal
Frontiers in Environmental Science

RECEIVED 03 August 2022
ACCEPTED 12 October 2022
PUBLISHED 20 October 2022

CITATION
Su C, Liu Y, Cheng Z, Wang W and Zheng Z (2022), Hydrochemical process and controls on the hydrochemistry of river water in the Muling-Xingkai Plain, Northeast China.
Front. Environ. Sci. 10:1010367.
doi: 10.3389/fenvs.2022.1010367

Hydrochemical process and controls on the hydrochemistry of river water in the Muling-Xingkai Plain, Northeast China

Chen Su[1,2], Yuan Liu[3]*, Zhongshuang Cheng[1,2], Wenzhong Wang[1,2] and Zhaoxian Zheng[1,2]

[1]Institute of Hydrogeology and Environmental Geology, Chinese Academy of Geological Sciences, Shijiazhuang, China, [2]Key Laboratory of Groundwater Science and Engineering, Ministry of Natural Resource, Shijiazhuang, China, [3]Shanxi Geological Engineering Exploration Institute CO., Ltd. Shanxi, Taiyuan, China

Rivers are the main supply sources in inland areas for human activities, but they are also regarded as the most susceptible water bodies to pollutants. Understanding the key factors influencing the chemical characteristic is the basis for water supply and public health concern. And it is helpful for the protection of surface water under the influence of human activities. To reveal the hydrochemical process of river water and the key factors affecting the chemical compositions, a total of 33 samples from rivers in Muling-Xingkai Plain are collected for principal component analysis and hydrochemical analysis. Results indicate that river water is characterized by the type of HCO_3-Ca and mixed HCO_3-Ca·Na. But some samples with relative high nitrate content have Cl^- as the dominant anion. The natural sources of chemical ions in river water are silicate and carbonate minerals. The chemical fertilizers only slightly influence the chemical compositions of river water due to the retardation of black soil with weak permeability. The chemical compositions of river water in Muling river are significantly influenced by domestic sewage compared with that in Abuqin river and Qihulin river. The widespread thick black soils play a key roles in protecting the river quality and groundwater quality, and human activities only play a limited roles in determining the river quality in the Muling-Xingkai Plain. At present, the contents of major chemical ions in river water meet the irrigation standard. Although the irrigation with river water do not lead to the food safety issue, the government agencies should adopt adequate measures to control the indiscriminate discharge of domestic sewage and application of fertilizers for preventing the accumulation of pollutants in rivers. This study is beneficial to the efficient management of surface water resources in agricultural areas with similar geological conditions and hydrogeological conditions.

KEYWORDS

hydrochemistry, human activities, surface water, Muling-Xingkai Plain, groundwater

1 Introduction

Due to the widespread availability and accessibility, river water plays a vital roles in social and economic development. Rivers usually are the important water resources for domestic, industrial and agricultural purposes (Rehman Qaisar et al., 2018; Xiao et al., 2019). However, rivers also play a crucial role in accepting industrial, agricultural and domestic wastewater, and they are regarded as the most susceptible water bodies to pollutants (Marzieh et al., 2020; Liu et al., 2021). River water with high level of chemical components exceeding the relevant standard is indirectly or directly influencing the human health (Huang et al., 2018; Kaline et al., 2020). Understanding the chemical characteristic of river water is a prerequisite for effective and efficient water management (Tiyasha et al., 2020; He et al., 2022).

The chemical characteristic of river water has attracted great attention all over the world (Peter et al., 2020; Feng et al., 2022). Many studies were concentrated on the famous rivers, such as the Amazon river (Ríos-Villamizar et al., 2017), the Nile (Wael et al., 2021), the Yangtze river (Zhang et al., 2022) and the Yellow river (Lv et al., 2022), etc. Their results were contributed to the protection and conservation of water resources and other natural resources. Generally, the chemical compositions of river water depend on natural factors such as recharge water quality and soil-water-rock interaction. Moreover, human activities can also impact surface water chemistry and profoundly alter the chemical compositions of river water to such an extent that surface water suitability becomes limited (Tripathee et al., 2016; Singh et al., 2017; Daou et al., 2018; Soares et al., 2020). The influences of human activities on the chemical compositions of river water are not only by inputting pollutants, but also by influencing the quality of groundwater recharging rivers (Yemeli et al., 2021). So the chemistry of river water is regulated by complex interactions under various physical, chemical, and biological environments (Barzegar et al., 2019; Hakimi et al., 2021). Understanding the sources of chemical ions in river water is the basis of the prediction and prevention of river pollution (Pandey et al., 2018; Richard and Irfan, 2020). Thus, it is of great significance to distinguish the effects of geogenic and anthropogenic factors on chemical compositions of river water for the sustainable development of water resource and society.

Many useful approaches are used to distinguish the sources of chemical components in groundwater and river water (Xiao et al., 2021). Hydrochemical analyse is an effective method which is performed based on the correlation among different chemical variables (Qaisar et al., 2020; Xiao et al., 2022a). Principal component analysis (PCA) is an unbiased method which can indicate associations between variables. These methods have been widely used to investigate chemical patterns, to determine various factors controlling the chemical evolution processes, and to show the origin and mobility of both geogenic and anthropogenic pollutants (Liu and Han, 2020; Sunkari et al., 2021; Laouni et al., 2022). These studies have provided a solid foundation for the protection of natural resources.

Muling-Xingkai Plain (MXP), locating in the northeast part of China, is one of the largest and most important grain production bases in China. River water is the important supply source for agricultural production. Previous study showed the chemical compositions of river water were influenced by agricultural activities (Cao et al., 2012). But a hydrogeochemical investigation conducted by author found that, a certain amount of domestic sewage was directly discharged into river channels. This process could contribute pollutant to river water. At present, knowledge about natural factors and human influences on water quality of river water in the MXP is still unclear, which has important constrains on agricultural irrigation management and food security. Additionally, the hydrochemical process of river water with the influence of agricultural activities in northeast China are not identified. Thus, a typical agricultural zone of northeast China was selected to deal with the hydrogeochemical characteristics, governing mechanisms, and chemical evolution processes of river water. Specifically, the main objectives of this study are to 1) show the sources of chemical ions in river water, 2) identify the factors influencing the chemical compositions of river water, and 3) provide some implications for the management on water resource in the MXP. The results will be beneficial to the protection of water resources and the sustainable development of agricultural production in the MXP and the areas with similar geological conditions and hydrogeological conditions.

2 Study area

MXP locates between longitudes of 131°30′–133°40′ E and latitudes of 45°05′–46°17′ N, with an area of about 10,000 km^2. MXP is one of the most important grain production bases in China, and the farmlands are widely distributed. Rice is one of the important crops in the MXP, and the rice plant area is more than 85% in the whole crop areas. The climate is a temperate monsoon climate, characterized by hot summer and cold winter. The average annual precipitation is 570 mm, ranging from 360 mm to 850 mm. The precipitation is mainly concentrated in the summer (June to August), accounting for 53% of the total precipitation. The annual mean temperature is approximately 3.5°C.

Abuqin River (AR), Qihulin (QR) and Muling River (MR) are three major rivers in the MXP, and the flow direction of rivers is from west to east (Figure 1). AR and QR originate from northwestern mountains in the MXP, with the lengths of 145 km and 260 km, respectively. MR originates from the Laoye mountains far away from the MXP, and passes through several cities and towns along its course. The length of downstream part of MR in the MXP is only 200 km. The

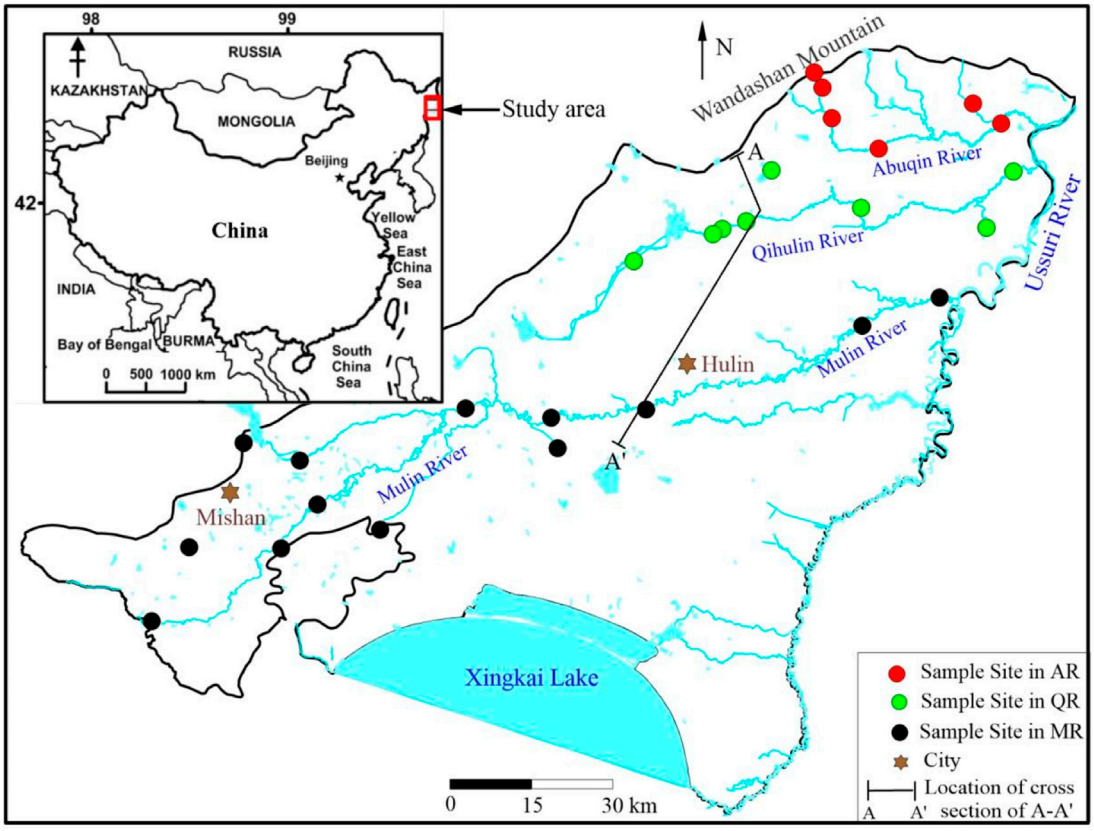

FIGURE 1
The location of the study area and sampling sites.

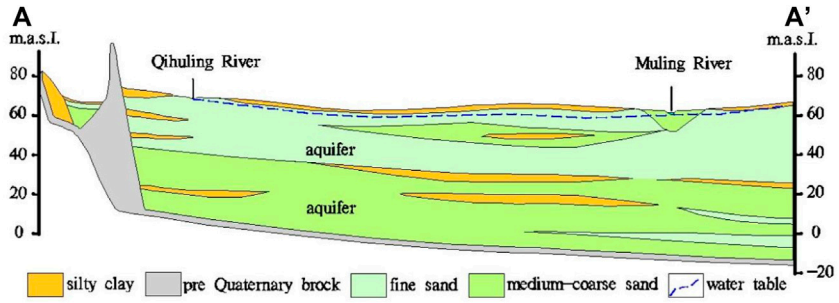

FIGURE 2
Hydrogeologic cross section A-A′ shown in Figure 1.

annual runoffs of AR, QR and MR are 20 $m^3 s^{-1}$, 30 $m^3 s^{-1}$ and 70 $m^3 s^{-1}$, respectively.

River water is mainly recharged by the meteoric water and the groundwater in the riverine areas. In addition, a certain mount of rural wastewater is directly discharged into river channels in the local zones. Thus, wastewater from human activities can be regarded as one of the recharge sources. River water is principally discharged by evaporation, artificial extraction, and flowing into the Wusuli River. River water is the important supply source for agricultural irrigation.

Aquifers principally consist of Quaternary alluvial deposits, and the depth to groundwater is about 2–20 m. Phreatic aquifer is

widely overlain by the black clay layer with small infiltration coefficient. Coarse-textured soils with high infiltration capacity only distribute in the riverine areas (Figure 2). Rock debris and soils are consisted of quartz (52%), plagioclase (21%), clay mineral (16%), potassium feldspar (10%) and carbonates (1%) (Su et al., 2022).

3 Materials and methods

3.1 Sampling and laboratory analysis

A total of 33 river water samples were collected in July 2018, and 7, 12, and 14 river water samples were collected from AR, QR and MR, respectively (Figure 1). Water samples were collected from each site at depth of 30 cm beneath the surface. Water temperature and pH were performed in site using a portable pH instrument. River water samples were collected in 1500-ml high density polyethylene sampling bottles. Prior to sample collection, sampling bottles were rinsed third times with the water to be sampled. Samples were stored under a temperature of 4°C, and were filtrated through 0.45-μm filter membranes once sent to the laboratory. Major cations (K^+, Na^+, Ca^{2+}, and Mg^{2+}) were determined by inductively coupled plasma-mass spectrometry. Anions (NO_3^-, Cl^-, and SO_4^{2-}) were measured by anion chromatography. The detection limits of ion analyses were 0.05ppm. HCO_3^- was measured by HCl titration on the spot. TDS values were obtained based on the above analysis data. The accuracy and precision of the analytical technique were evaluated by analyzing a certified standard reference material, certified waste water trace metals solution. Uncertainties were less than ± 5% for all analyzed elements. All the analyses were carried out at the Groundwater Mineral Water and Environmental Monitoring Center of the Institute of Hydrogeology and Environmental Geology, Chinese Academy of Geological Sciences.

3.2 Methodology

In this study, PCA and hydrochemical analysis were used to determine the hydrochemical process and controls on the hydrochemistry of river water in the MXP. PCA can be used to identify the principal components and their significance, and to further show various environmental issues (Khound and Bhattacharyya, 2018). The rotation of principal components (PCs) was carried out using varimax method. The terms "strong," "moderate," and "weak" classified by Liu et al. (2003) were applied to PC loading, corresponding to the absolute loading values of >0.75, 0.75–0.5, and 0.5–0.3, respectively.

Hydrochemical analysis was carried out based on the Gibbs diagram, piper trilinear diagram, correlation analysis of chemical

TABLE 1 Descriptive statistics of the chemical variables in river water.

Parameter	Unit	Mean of three rivers					AR				QR				MR			
		min	Max	Mean	SD	CV(%)	min	Max	Mean	SD	min	Max	Mean	SD	min	Max	Mean	SD	CV(%)
pH		6.37	7.18	6.76	0.21	3.12	6.37	6.66	6.54	0.10	6.38	7.03	6.72	0.17	6.47	7.18	6.88	0.18	2.65
K	mg/L	1.26	3.74	2.69	0.76	28.06	0.70	1.89	1.27	0.46	2.09	4.08	2.95	0.65	1.26	4.08	2.69	0.73	27.22
Na	mg/L	5.38	19.07	13.46	4.04	29.99	1.57	4.38	2.97	0.89	3.23	10.71	7.09	2.33	5.38	19.07	13.46	3.91	29.05
Ca	mg/L	10.89	30.29	20.44	5.19	25.40	5.46	7.47	6.43	0.64	6.56	13.96	10.98	2.09	10.89	30.29	20.44	5.01	24.49
Mg	mg/L	2.94	8.66	5.92	1.47	24.90	1.88	3.02	2.44	0.38	3.31	6.66	4.95	0.98	2.94	8.66	5.92	1.43	24.12
Cl	mg/L	6.64	16.07	13.70	3.28	23.92	1.42	5.33	2.84	1.65	8.77	15.79	12.34	2.31	6.64	19.21	13.70	3.19	23.25
SO_4	mg/L	12.40	24.57	19.38	3.82	19.73	5.82	7.21	6.60	0.47	5.93	13.09	9.01	2.04	12.40	24.57	19.38	3.85	19.84
HCO_3	mg/L	20.24	134.50	74.11	29.73	40.12	21.40	41.57	28.78	6.61	13.45	73.37	46.93	16.09	20.24	134.50	74.11	28.73	38.77
NH_4	mg/L	0.05	0.21	0.12	0.10	83.32	0.13	0.22	0.17	0.03	0.06	0.21	0.11	0.05	0.05	0.36	0.12	0.10	80.83
NO_3	mg/L	1.81	10.84	8.12	4.80	59.06	3.20	5.77	4.49	1.02	3.23	7.65	4.23	1.35	1.81	21.47	8.12	4.62	56.92
TDS	mg/L	79.51	183.80	134.63	26.37	19.59	32.80	68.16	49.65	11.40	61.40	101.90	79.00	14.46	79.51	183.80	134.63	25.42	18.88

Note: SD, standard deviation; CV, coefficient of variation.

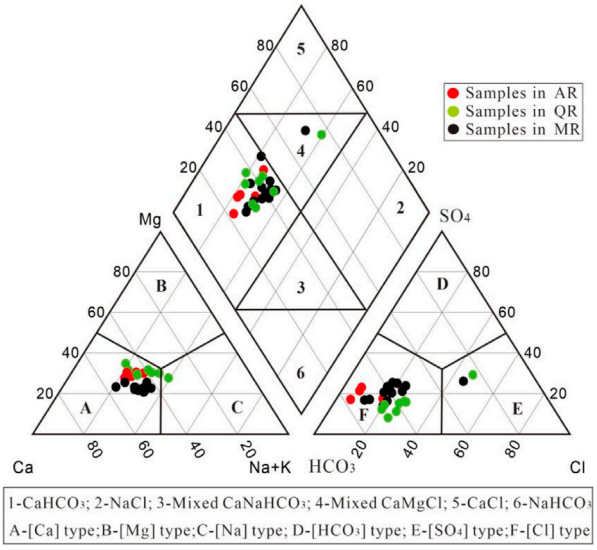

FIGURE 3
Piper ternary diagram of the surface water samples in the MXP.

variables. Gibbs diagram was mapped to identify the natural source of chemical ions in river water. Piper trilinear diagram was drawn to understand the dominant water types. Correlation analysis of chemical variables was mainly used to evaluate various hydrochemical evolution process in river water. These methods were jointly used to determine the chemical characteristics and dominate factors controlling the chemical compositions of river water.

4 Results and Discussion

4.1 General chemical characterization

The descriptive statistics of major chemical variables in river water are summarized in Table 1, including minimum, maximum, mean value, the standard deviation, and coefficient of variation (CV). Ca^{2+} (20.44 mg/L) is the most abundant major cation followed by Na^{+} (13.46 mg/L), Mg^{2+} (5.92 mg/L), K^{+} (2.69 mg/L), and NH_4^{+} (0.12 mg/L). Variable coefficient of NH_4^{+} and Na^{+} is highest. HCO_3^{-} (74.11 mg/L) is the most dominant major anion followed by SO_4^{2-} (19.38 mg/L), Cl^{-} (13.70 mg/L), and NO_3^{-} (8.12 mg/L). But NO_3^{-} has the most significant variation. The high variation of chemical variables in river water can be attributed to the multiple geogenic and anthropogenic sources.

Concentrations of the main chemical ions in MR are highest, while the values of chemical variables in AR are lowest. The mean concentration of chemical ions in QR is slightly higher than that in AR. Samples from MR are characterized by high NO_3^{-} content with low coefficient of variation (CV), which is related to the human activities. The CVs of Ca^{2+}, HCO_3^{-} and NO_3^{-} in AR are lowest compared with other two rivers. The chemical compositions of river water in AR are stable, reflecting the slight influence by external factors.

Piper diagram was introduced to identify the hydrochemical types and chemical characteristics of river water samples in the MXP (Figure 3). It can be seen that most samples have Ca^{2+} as the dominant cation, and only one sample collected from QR has Na^{+} as the dominant cation. Most samples have HCO_3^{-} as the dominant anion, and two samples collected from QR and MR have Cl^{-} as the dominant anion.

Two hydrochemical facies HCO_3-Ca and mixed HCO_3-Ca·Na were determined from the Piper plot, indicating river water undergone an evolution from HCO_3-Ca type to mixed type. Specifically, samples from AR are characterized by the water type of Ca·Mg-HCO_3. The water types of samples from QR are Ca·Mg-HCO_3 and Ca·Mg-HCO_3·Cl. The water types of samples from MR are predominantly Ca·Na-HCO_3, but some samples are characterized by the water type of Ca·Mg·Na-HCO_3 and Ca·Na·Mg-HCO_3·Cl. The difference of water types among rivers indicates that the chemical compositions of river water are affected by multiple factors. The samples with low nitrate content are dominated by HCO_3-Ca type, and those with relative high nitrate content are mainly mixed HCO_3-Ca·Na type and HCO_3·Cl type. The dominant anions show a significant gradual evolving trend from HCO_3^{-} to Cl^{-} with the increase of nitrate content. Thus, anthropogenic factor is influencing the chemical composition of river water in the MXP.

4.2 Geogenic source of chemical ion in river water

Chemical ions in river water have multiple sources from physical, chemical, and biological processes, including atmospheric precipitation, mineral weathering (e.g., carbonates, silicates, and evaporites), and human activities (Rehman Qaisar et al., 2018; Barzegar et al., 2019). Gibbs plot, mixing diagram and ion ratios of major constitutes in water can be used to identify the source of chemical ions.

Gibbs plot can detect three natural factors dominating the chemical compositions of river water: precipitation, rock dominance, and evaporation. As shown in Figure 4, the weight ratios of $Na^{+}/(Na^{+}+Ca^{2+})$ and $Cl^{-}/(Cl^{-} + HCO_3^{-})$ of most samples are less than 0.5, with mean TDS of 100 mg/L. The chemical compositions of river water are strongly influenced by the rock weathering in the MXP (Marandi and Shand, 2018). Rivers pass through various rocks and soils, which are the main contributors to the high levels of minerals in river water. The dissolution of various minerals leads to an abundance of

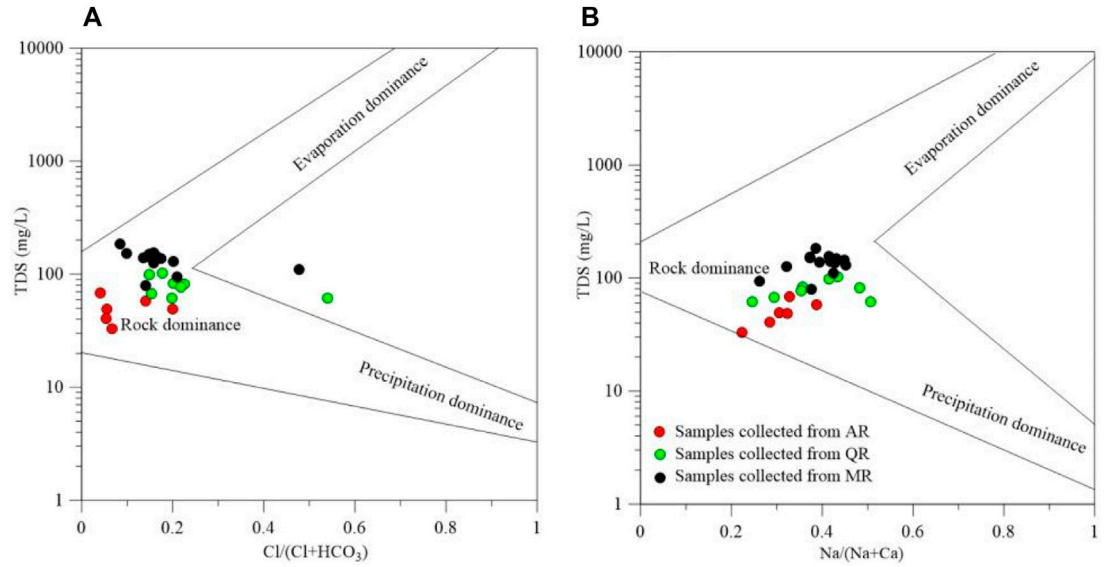

FIGURE 4
Ratios of **(A)** Cl/(Cl + HCO_3) vs. TDS and **(B)** Na/(Na + Ca) vs. TDS.

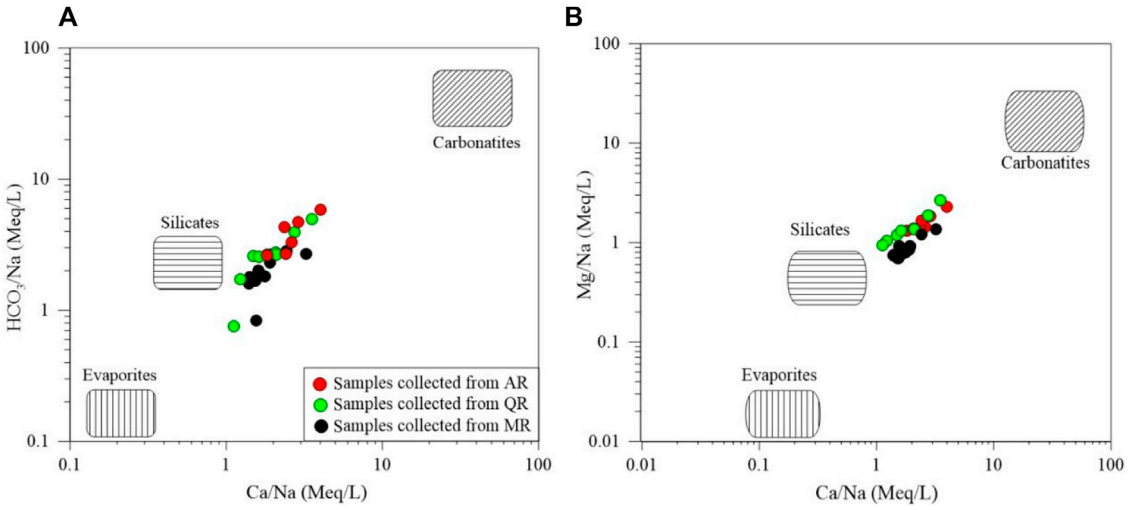

FIGURE 5
Bivariate diagrams of **(A)** (HCO_3/Na) vs. (Ca/Na), and **(B)** (Mg/Na) vs. (Ca/Na) for surface water samples in the study area.

chemical ions in river water. Precipitation is only the original source of chemical ions in river water. Evaporation is not the key factors dominating the concentration of chemical ions due to the humid climate and abundant rainfall in the study area.

Weathering of carbonate rocks may contribute Ca^{2+}, Mg^{2+}, and HCO_3^-, and weathering of silicate rocks can produces Na^+, K^+, Ca^{2+}, Mg^{2+}, and HCO_3^-. Dissolution of evaporites mainly produces SO_4^{2-}, Ca^{2+},Cl^-, and Na^+ (Paudyal et al., 2016). Dissolution of different minerals can lead to different combinations of major ions in water. The mixing diagram can be used to infer dissolution of minerals with respect to three representative lithology. The mixing diagram is depicted based on Na^+-normalized molar ratios (Figure 5). Most of samples lie close to the end-member of silicate, indicating that the chemical

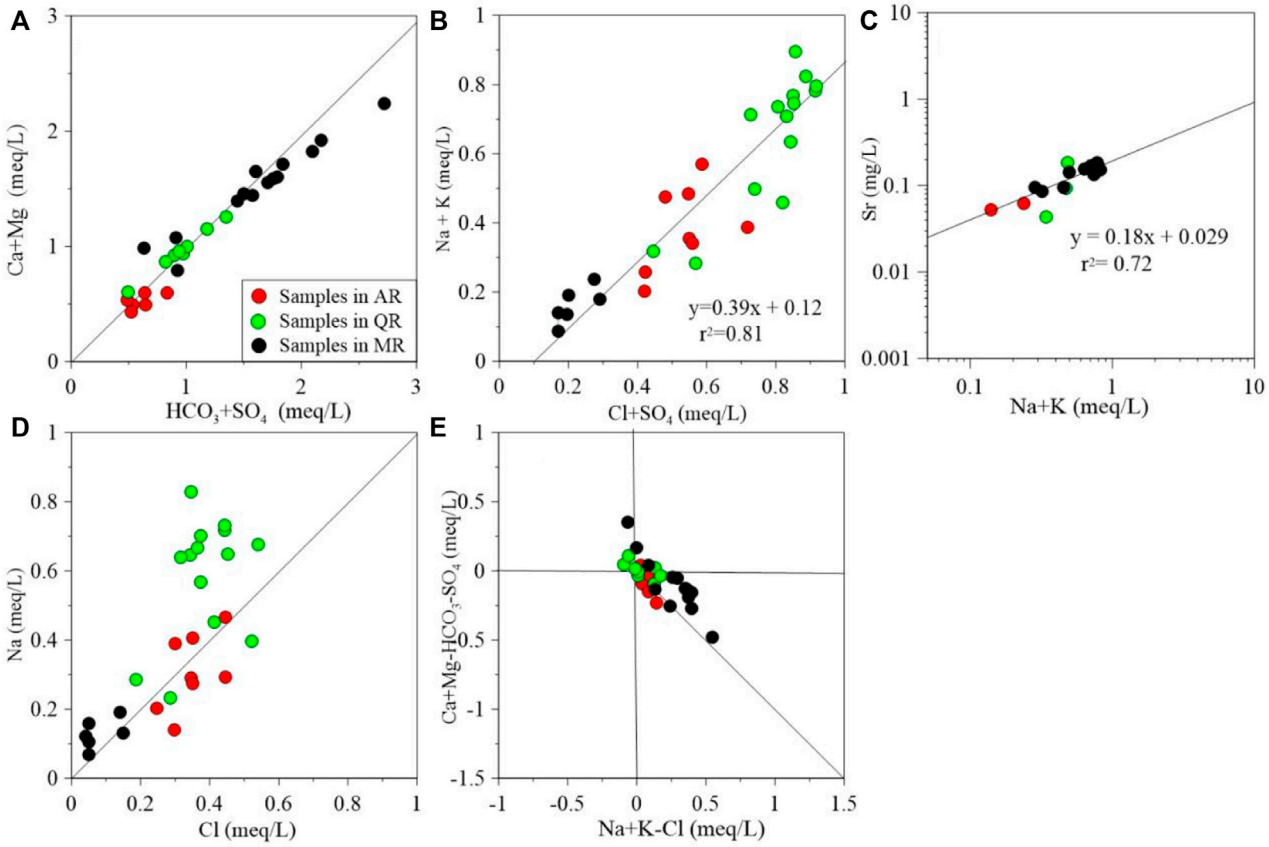

FIGURE 6
Bivariate diagrams of **(A)** (Ca + Mg) vs. (HCO_3 + SO_4), **(B)** (Na + K) vs. (Cl + SO_4), **(C)** Sr vs. (Na + K), **(D)** Na vs. Cl, **(E)** (Ca + Mg-HCO_3-SO_4) vs. (Na + K-Cl).

compositions of river water are dominated by the silicate dissolution.

The mineralogical analysis has shown the compositions of rocks and soils are silicate minerals. That is why the chemical weathering of silicate rocks is the main contributor to the chemistry of river water in the MXP.

The concentration ratios of chemical ions can indicate various hydrochemical processes. The sources of Ca^{2+}, Mg^{2+} and HCO_3^- can be deduced from the milliequivalent ratio of $c(Ca^{2+}+Mg^{2+})/cHCO_3^-$. As shown in Figure 6A, most of samples from these three rivers are close to the 1:1 equivalent line, showing that the Ca^{2+}, Mg^{2+} and HCO_3^- in river water are derived from dissolution of silicate and carbonate minerals. However, some samples from MR fall below the 1:1 equivalent line, suggesting the silicate dissolution is responsible for the relevant chemical compositions of river water. There is a significant relationship between the c (Cl^- + SO_4^{2-}) and c (Na^++K^+) (r^2 = 0.81) in the rives (Figure 6B), which suggests their similar source. When the halite is dominant in river water, cNa^+/cCl^- would be approximately 1.0. And if it is >1.0, the source of Na^+ is other Na-bearing salt. As shown in Figure 6D, averaged cNa^+/cCl^- of samples from AR and MR is much higher than 1.0 (AR = 1.79, and MR = 1.55). Then, dissolution of other Na-bearing salts or ion exchange are influencing the Na^+ contents of river water. Figure 6C shows that Sr^{2+} concentrations are linearly correlated with the concentration of (Na^++K^+) (r^2 = 0.81). This further identifies the chemical compositions of river water in the MXP are dominated by the silicate minerals dissolution.

4.3 Anthropogenic source of chemical ion in river water

As shown in Figure 6D, the averaged cNa^+/cCl^- of samples from QR is slightly less than 1.0 (QR = 0.89). The plot of (Ca + Mg)—(HCO_3 + SO_4) against (Na + K—Cl) could be employed to evaluate the role of water-rock interaction on hydrochemistry. If the relation between these two parameters is linear with a slope of −1.0, ion exchange is significant in controlling geochemical

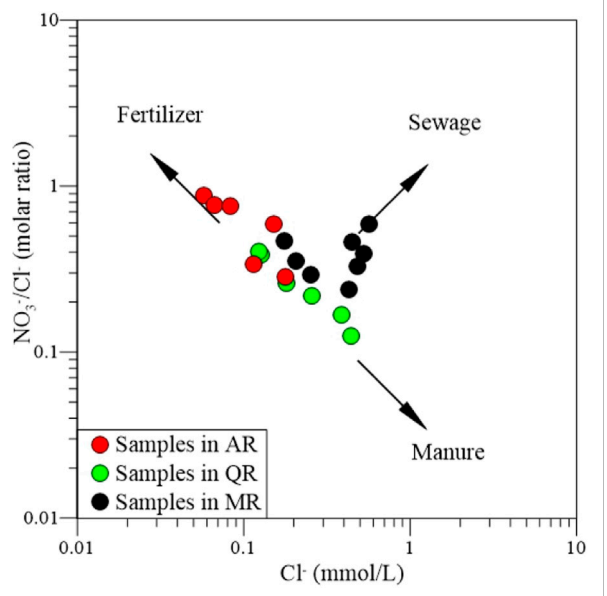

FIGURE 7
Bivariate diagrams of NO_3/Cl vs Cl.

compositions. Figure 6E shows that water samples do not fall along the line with a slope of −1.0. Therefore, chemical compositions of river water in the MXP are not significantly dominated by ion exchange.

The major anthropogenic components in the groundwater and surface water include Cl^- and NO_3^-, as well as SO_4^{2-}. Groundwater and surface water has a small ratio of NO_3^-/Cl^- under natural condition, otherwise it is assumed to have been influenced by anthropogenic activities (Xiao et al., 2022b). The relation between NO_3^-/Cl^- ratio and Cl^- content can provide important information to distinguish the input sources of NO_3^- and Cl^- in water.

As shown in Figure 7, some samples collected from MR and QR are mainly plotted in the dominance of sewage input. This suggests the source of nitrate is the domestic effluents. Most samples collected from AR and QR are mainly plotted in the dominance of fertilizer and manure inputs, but the ratio of NO_3^-/Cl^- is less than 0.22. Generally, natural water sampled outside of human influence usually has a ratio of NO_3^-/Cl^- ranging from 0.05 to 0.22. Thus, the nitrate contribution of agricultural practices would be considerable negligible. Although the nitrogenous fertilizers and ammonium chloride fertilizers are widely used in the MXP, agricultural activities only play a slight role in determining the chemical compositions.

A certain amount of rural wastewater is directly discharged into the river channels or the seepage pits as the lack of sewage treatment plant in the rural areas. Thus, discharge of domestic sewage can directly and indirectly influence the chemical compositions of river water, especially for the water from MR. Therefore, the hydrochemistry of nitrate enriched river water are governed by domestic sewage from the residential areas.

4.4 Factors in dominating the chemical compositions of river water

PCA can be used to discuss the key factors dominating the chemical compositions. 11 physico-chemical variables have been analyzed in water samples based on data integrity. The results are shown in Table 2. The chemical compositions of river water are controlled by a two-factor model, and the cumulative variance of two PCs is 79.15%. PC1, which comprises strong loading of TDS, HCO_3^-, Ca^{2+}, Mg^{2+}, Na^+, SO_4^{2-}, pH and Cl^-, accounts for 68.19% of the total variance. TDS values increase with the concentrations of HCO_3^-, Ca^{2+}, Mg^{2+} and Na^+. Water-rock interactions are mainly responsible for their existence in river water (Huang et al., 2018). PC2 with high positive loading of Cl^- and NO_3^-, accounts for 16.23% of the total variance. Domestic sewage and agricultural effluent contain abundant ammonia nitrogen and chloride in the MXP. Thus, the discharge of wastewater from human activities is responsible for the high level of Cl^- and NO_3^- in river water.

For AR, PC1 with high positive loading of TDS, HCO_3^-, K^+, Na^+ and Mg^{2+}, indicating the contribution of minerals to the chemical compositions. PC2 has high positive loading of Cl^- and NO_3^-, accounting the impact of human activities. For QR, PC1 has high positive loading of pH, Ca^{2+}, Na^+ and HCO_3^-, indicating the chemical compositions of river water are controlled by water-rock interaction. PC2 has high positive loading of K^+, Na^+, Cl^-, and NO_3^-, suggesting the human activities are influencing the chemical compositions of river water. For MR, PC1 with high positive loading of HCO_3^-, pH, Ca^{2+}, Mg^{2+}, and TDS, indicates the water-rock interaction is influencing the chemical compositions of river water. PC2 with high positive loading of NO_3^- and Cl^-, showing that the chemical compositions of river water have been influenced by human activities.

Based on the discussion above mentioned, it is can be concluded that the natural sources of chemical ions in river water are the silicate minerals and the carbonate minerals, and the anthropogenic sources are the agricultural fertilizers and domestic sewage. The contribution of each sources can be quantified based on PCA (Figure 8).

The chemical compositions of river water in the MXP are mainly dominated by the dissolution of the silicate and carbonate minerals. Fertilizer and sewage only play a limited role in determine the qualities of river water. However, the density of population in the riverine areas of MR is largest compared with other two rivers. A large quantity of wastewater is discharged into MR or the seepage pits in the riverine areas. So the influence of sewage on the chemical compositions of river water in MR is significant. Thus, the impact of external factors on chemical

TABLE 2 Principal component loading for water samples in three rivers.

Chemical parameter	AR		QR		MR		All three rivers	
	PC1	PC2	PC1	PC2	PC1	PC2	PC1	PC2
TDS	0.82	0.394	0.572	0.459	0.751	0.606	0.978	0.062
pH	−0.438	0.843	0.987	−0.002	0.868	−0.117	0.782	−0.313
K	0.974	0.069	0.074	0.951	0.181	0.866	0.687	0.138
Ca	0.39	0.863	0.812	-0.011	0.853	0.448	0.961	−0.081
Na	0.662	0.647	0.257	0.789	0.696	0.628	0.972	0.054
Mg	0.838	0.524	0.815	0.289	0.761	0.574	0.955	−0.099
HCO_3	0.952	0.033	0.904	0.052	0.924	0.318	0.904	-0.371
Cl	−0.224	0.964	−0.162	0.929	−0.198	0.912	0.37	0.77
SO_4	0.585	0.228	−0.91	0.298	0.63	0.464	0.865	0.202
NO_3	0.194	0.942	0.071	0.906	−0.876	0.869	0.16	0.849
NH_4	−0.093	−0.083	0.863	0.354	0.409	0.434	0.115	−0.717
Eigenvalue	4.47	4.17	5.12	2.91	5.37	3.42	7.02	1.69
Explained variance (%)	59.62	21.89	57.52	22.41	52.8	27.11	61.79	17.36
Cumulative of variance (%)	59.62	81.51	57.52	79.93	52.8	79.91	63.79	79.15

compositions is closely related to the density of population in the riverine areas.

The anthropogenic factors have influenced the chemical compositions of river water in the MXP. But the concentrations of major chemical ions in river water do not exceed the irrigation standard. Agricultural production and discharge of domestic sewage do not lead to the food safety issue.

The lateral discharge of groundwater into rivers is an important way of anthropogenic influence on the chemical compositions of river water. Most of crops grow in rich, black soil in the MXP. Black soils with weak permeability can deter or retard the downward infiltration of irrigation water with abundant chemical fertilizers. At present, most of groundwater samples in the MXP is characterized by low level of chemical ions (Su et al., 2020). Thus, agricultural activities do not influence the chemical composition of river water significantly due to the weak permeability of black soil. The saturation index of calcite, dolomite and gypsum is below zero, suggesting the river water is in an unsaturated state. The dissolution of silicate minerals and carbonate minerals still will be the main source of chemical ions in river water.

4.5 Suggestions for protection of river water

Due to the discharge of domestic sewage in the riverine zones with coarse sediments, some groundwater samples along the

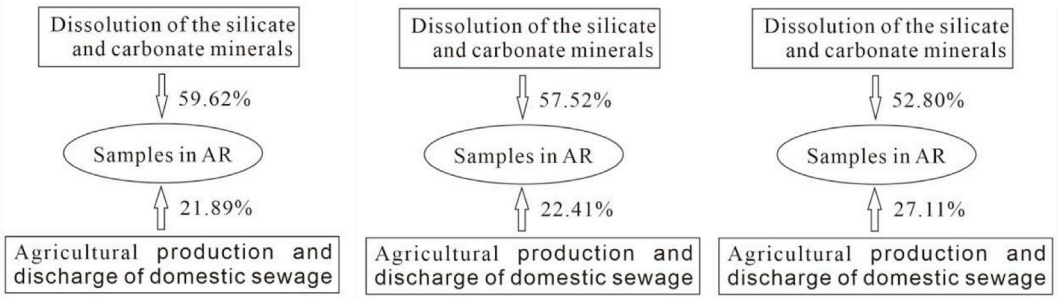

FIGURE 8
Factors dominating the chemical characteristics of river water in the MXP.

rivers are characterized by high level of NO_3^-, Cl^-, and SO_4^{2-} (Su et al., 2020). Although the chemical compositions of river water are slightly influenced by groundwater, the continuous inflow of contaminants by groundwater discharge is a potential threat to river quality. Therefore, some measures should be adopted to further protect the groundwater and surface water resources for maintaining the food security. It is helpful for the management of surface water resource in agricultural areas.

Anthropogenic factors can be effectively controlled (Huang et al., 2013). The specific strategies are: 1) to keeping the use of chemicals to an absolute minimum; 2) to monitor and control the discharge of the wastewater in the riverine areas; 3) to construct the sewage disposal system in the rural zone near rivers; 4) to set the key protection region in the riverine areas; and 5) to regularly monitor the quality of groundwater in the riverine zones and river water.

5 Conclusion

The present study was conducted to elucidate the hydrochemical process and controls on the hydrochemistry of river water in an agricultural region of northeast Chain. The main findings are as follows:

(1) Most samples in the MXP have Ca^{2+} and HCO_3^- as the dominant ions, and only few samples have Na^+ and Cl^- as the dominant ions. River water is characterized by the type of HCO_3-Ca and mixed HCO_3-Ca·Na. But few samples with relative high nitrate content have Cl^- as the dominant anion. Natural and anthropogenic factors are jointly influencing the chemical compositions of river water.
(2) The chemical compositions of river water in the MXP are mainly dominated by the natural dissolution of silicate minerals and carbonate minerals. Agricultural activities do not lead to the deterioration of river water quality. Domestic sewage only slightly influence the chemical compositions of river water in MR. The widespreadly thick black soils play a key roles in protecting the river quality and groundwater quality. So the human activities only play a limited roles in determine the river quality. At present, the surface-water irrigation do not lead to food security issues, and the concentrations of major chemical ions in river water meet the standard for irrigation.
(3) Water protection, that based on chemical characteristic of river water and human activities intensity, is recommended to guarantee food safe and residents' health in the study area. Due to the coarse sediments overlying the aquifers in the riverine zones, the government agencies should adopt some strategies to control the discharge of various wastewater for preventing the accumulation of pollutants in surface water and groundwater.

Data availability statement

The raw data supporting the conclusion of this article will be made available by the authors, without undue reservation.

Author contributions

This article is the combined effort of all the author. CS and YL formulated and wrote the article, with contributions from all coauthors ZC wrote a detailed the introduction CS and WW contributed to the analysis. ZZ collected the samples in study area.

Funding

This study was financially supported by the National Natural Science Foundation of China (No. 41602268) and China Geological Survey's project (No. DD20160311).

Conflict of interest

Author YL was employed by the Shanxi Geological Engineering Exploration Institute CO., Ltd. Shanxi

The remaining author declares that the research was conducted in the absence of any commercial or financial relationships that could be construed as a potential conflict of interest.

Publisher's note

References

Barzegar, R., Moghaddam, A. A., Soltani, S., Baomid, N., Tziritis, E., Adamowski, J., et al. (2019). Natural and anthropogenic origins of selected trace elements in the surface waters of Tabriz area, Iran. *Environ. Earth Sci.* 78 (8), 254. doi:10.1007/s12665-019-8250-z

Cao, Y. J., Tang, C. Y., Song, X. F., Liu, C. M., and Zhang, Y. H. (2012). Characteristics of nitrate in major rivers and aquifers of the Sanjiang Plain, China. *J. Environ. Monit.* 14 (10), 2624. doi:10.1039/C2EM30032J

Daou, C., Salloum, M., Legube, B., Kassouf, A., and Ouaini, N. (2018). Characterization of spatial and temporal patterns in surface water quality: A case study of four major Lebanese rivers. *Environ. Monit. Assess.* 190 (8), 485. doi:10.1007/s10661-018-6843-8

Feng, W., Lu, H. W., Yao, T. C., Guan, Y. L., Xue, Y. X., and Yu, Q. (2022). Water environmental pressure assessment in agricultural systems in central asia based on an integrated excess nitrogen load model. *Sci. Total Environ.* 803, 149912. doi:10.1016/j.scitotenv.2021.149912

Hakimi, Y., Orban, P., Deschamps, P., and Brouyere, S. (2021). Hydrochemical and isotopic characteristics of groundwater in the continental intercalaire aquifer system: Insights from mzab ridge and surrounding regions, north of the Algerian sahara. *J. Hydrology Regional Stud.* 34, 100791. doi:10.1016/j.ejrh.2021.100791

He, J., Tao, L., Peng, Y. E., Tong, L., Zhao, X. W., Shao, X., et al. (2022). Distribution and impacts on the geological environment of antiviral drugs in major waters of Wuhan, China. *zgdzyw.* 5 (3), 402–410. doi:10.31035/cg2022047

Huang, G. X., Liu, C. Y., Sun, J. C., Zhang, M., Jing, J. H., and Li, L. P. (2018). A regional scale investigation on factors controlling the groundwater chemistry of various aquifers in a rapidly urbanized area: A case study of the pearl river delta. *Sci. Total Environ.* 625, 510–518. doi:10.1016/j.scitotenv.2017.12.322

Huang, G. X., Sun, J. C., Zhang, Y., Chen, Z. Y., and Liu, F. (2013). Impact of anthropogenic and natural processes on the evolution of groundwater chemistry in a rapidly urbanized coastal area, South China. *Sci. Total Environ.* 463-464 (5), 209–221. doi:10.1016/j.scitotenv.2013.05.078

Kaline, M., Ricardo, H. T., Felipe, R. P., Roberta, A. V., Timothy, O. R., Diego, R. M., et al. (2020). Multiscale land use impacts on water quality: Assessment, planning, and future perspectives in Brazil. *J. Environ. Manag.* 270, 110879. doi:10.1016/j.jenvman.2020.110879

Khound, N. J., and Bhattacharyya, K. G. (2018). Assessment of water quality in and around Jia-Bharali river basin, North Brahmaputra Plain, India, using multivariate statistical technique. *Appl. Water Sci.* 8 (8), 221. doi:10.1007/s13201-018-0870-z

Laouni, B., Belkacem, B., and Laouni, G. (2022). Multivariate analysis and geochemical investigations of groundwater in a semi-arid region, case of Ghriss Basin superficial aquifer North-West Algeria. *J. Groundw. Sci. Eng.* 10 (3), 233–249. doi:10.19637/j.cnki.2305-7068.2022.03.003

Liu, C. W., Lin, K. H., and Kuo, Y. M. (2003). Application of factor analysis in the assessment of groundwater quality in a Blackfoot disease area in Taiwan. *Sci. Total Environ.* 313 (1-3), 77–89. doi:10.1016/S0048-9697(02)00683-6

Liu, J., and Han, G. (2020). Major ions and δ^{34}S-SO_4 in Jiulongjiang River water: Investigating the relationships between natural chemical weathering and human perturbations. *Sci. Total Environ.* 724, 138208. doi:10.1016/j.scitotenv.2020.138208

Liu, R. P., Li, Z. Z., Liu, F., Dong, Y., Jiao, J. P., Sun, P. P., et al. (2021). Microplastic pollution in Yellow River: Current status and research progress of biotoxicological effects. *China Geol.* 4, 1–8. doi:10.31035/cg2021081

Lv, D. Y., Yu, C., Zhuo, Z. J., Meng, S. R., and Liu, S. B. (2022). The distribution and ecological risks of antibiotics in surface water in key cities along the lower reaches of the Yellow River:A case study of Kaifeng City, China. *China Geol.* 5, 411–420. doi:10.31035/cg2022032

Marandi, A., and Shand, P. (2018). Groundwater chemistry and the Gibbs diagram. *Appl. Geochem.* 97, 209–212. doi:10.1016/j.apgeochem.2018.07.009

Marzieh, M., Ali, S., and Vahideh, S. (2020). Effects of heavy metal contamination on river water quality due to release of industrial effluents. *J. Clean. Prod.* 277, 123380. doi:10.1016/j.jclepro.2020.123380

Pandey, L. K., Lavoie, I., Morin, S., Park, J., Lyu, J., Choi, S., et al. (2018). River water quality assessment based on a multi-descriptor approach including chemistry, diatom assemblage structure, and non-taxonomical diatom metrics. *Ecol. Indic.* 84, 140–151. doi:10.1016/j.ecolind.2017.07.043

Paudyal, R., Kang, S., Sharma, C. M., Tripathee, L., Huang, J., Rupakheti, D., et al. (2016). Major ions and trace elements of two selected rivers near Everest region, southern Himalayas, Nepal. *Environ. Earth Sci.* 75, 46. doi:10.1007/s12665-015-4811-y

Peter, J. R., Ricardo, G. P., David, J. V., Justin, K. R., Justin, N., and Aashish, K. (2020). Water quality impacts of urban and non-urban arid-land runoff on the Rio Grande. *Sci. Total Environ.* 729, 138443. doi:10.1016/j.scitotenv.2020.138443

Qaisar, M., Muhammad, A., and Muhammad, R. (2020). Integration of geoelectric and hydrochemical approaches for delineation of groundwater potential zones in alluvial aquifer. *J. Groundw. Sci. Eng.* 8 (4), 366–380. doi:10.19637/j.cnki.2305-7068.2020.04.007

Rehman Qaisar, F. U., Zhang, F., Pant, R. R., Wang, G. X., Khan, S., and Zeng, C. (2018). Spatial variation, source identification, and quality assessment of surface water geochemical composition in the Indus River Basin, Pakistan. *Environ. Sci. Pollut. Res.* 25 (13), 12749–12763. doi:10.1007/s11356-018-1519-z

Richard, J. C., and Irfan, A. B. (2020). Impacts of irrigation water used allocations on water quality and crop productivity: The lee irrigation system in Pakistan. *Irrig. Drain.* 69, 38–51. doi:10.1002/ird.2402

Ríos-Villamizar, E. A., Piedade, M. T. F., Junk, W. J., and Waichman, A. V. (2017). Surface water quality and deforestation of the Purus river basin, Brazilian Amazon. *Int. Aquat. Res.* 9, 81–88. doi:10.1007/s40071-016-0150-1

Singh, H., Singh, D., Singh, S. K., and Shukla, D. N. (2017). Assessment of river water quality and ecological diversity through multivariate statistical techniques, and Earth observation dataset of rivers Ghaghara and Gandak. India. *Int. J. River Basin Manag.* 1-14, 347–360. doi:10.1080/15715124.2017.1300159

Soares, A. L. C., Pinto, C. C., and Oliveira, S. C. (2020). Impacts of anthropogenic activities and calculation of the relative risk of violating surface water quality standards established by environmental legislation: A case study from the piracicaba and paraopeba river basins, Brazil. *Environ. Sci. Pollut. Res.* 27, 14085–14099. doi:10.1007/s11356-020-07647-1

Su, C., Li, Z., Wang, W., Cheng, Z., Zheng, Z., and Chen, Z. (2022). Key factors dominating the groundwater chemical composition in a grain production base: A case study of muling–Xingkai Plain, northeast China. *Water* 14 (14), 2222. doi:10.3390/w14142222

Su, C., Zhang, F. E., Cui, X. S., Cheng, Z. Y., and Zheng, Z. X. (2020). Source characterization of nitrate in groundwater using hydrogeochemical and multivariate statistical analysis in the muling-xingkai plain, northeast China. *Environ. Monit. Assess.* 192, 456. doi:10.1007/s10661-020-08347-6

Sunkari, E. D., Abu, M., and Zango, M. S. (2021). Geochemical evolution and tracing of groundwater salinization using different ionic ratios, multivariate statistical and geochemical modeling approaches in a typical semi-arid basin. *J. Contam. Hydrology* 236, 103742. doi:10.1016/j.jconhyd.2020.103742

Tiyasha, T., Tung, T. M., and Yaseen, Z. M. (2020). A survey on river water quality modelling using artificial intelligence models: 2000–2020. *J. Hydrology* 585, 124670. doi:10.1016/j.jhydrol.2020.124670

Tripathee, L., Kang, S., Sharma, C. M., Rupakheti, D., Paudyal, R., Huang, J., et al. (2016). Preliminary health risk assessment of potentially toxic metals in surface water of the Himalayan rivers. Nepal. *Bull. Environ. Contam. Toxicol.* 97 (6), 855–862. doi:10.1007/s00128-016-1945-x

Wael, M. B., Octavian, G. D., Hussein, E. I. S., Atef, E., and Marina, V. F. (2021). A review of major and trace elements in Nile River and Western Red Sea sediments: An approach of geochemistry, pollution, and associated hazards. *Appl. Radiat. Isotopes* 170, 109595. doi:10.1016/j.apradiso.2021.109595

Xiao, J., Wang, L. Q., Deng, L., and Jin, Z. D. (2019). Characteristics, sources, water quality and health risk assessment of trace elements in river water and well water in the Chinese Loess Plateau. *Sci. Total Environ.* 650, 2004–2012. doi:10.1016/j.scitotenv.2018.09.322

Xiao, Y., Hao, Q. C., Zhang, Y., Zhu, Y. C., Yin, S. Y., Qin, L. M., et al. (2021). Investigating sources, driving forces and potential health risks of nitrate and fluoride in groundwater of a typical alluvial fan plain. *Sci. Total Environ.* 802, 149909. doi:10.1016/j.scitotenv.2021.149909

Xiao, Y., Liu, K., Hao, Q. C., Li, Y. S., Xiao, D., and Zhang, Y. J. (2022a). Occurrence, controlling factors and health hazards of fluoride-enriched groundwater in the lower flood plain of Yellow river, northern China. *Expo. Health* 14, 345–358. doi:10.1007/s12403-021-00452-2

Xiao, Y., Liu, K., Hao, Q. C., Xiao, D., Zhu, Y. C., Yin, S. Y., et al. (2022b). Hydrogeochemical insights into the signatures, Genesis and sustainable perspective of nitrate enriched groundwater in the piedmont of Hutuo watershed, China. *Catena* 212, 106020. doi:10.1016/j.catena.2022.106020

Yemeli, E. J., Temgoua, E., and Kengni, L. (2021). Hydro-geochemistry of groundwater and surface water in Dschang town (West Cameroon): Alkali and alkaline-Earth elements ascertain lithological and anthropogenic constraints. *J. Groundw. Sci. Eng.* 9 (3), 212–224. doi:10.19637/j.cnki.2305-7068.2021.03.004

Zhang, J., Guo, Q. G., Du, C. J., and Wei, R. F. (2022). Quantifying the effect of anthropogenic activities on water quality change in the Yangtze River from 1981 to 2019. *J. Clean. Prod.* 363, 132415. doi:10.1016/j.jclepro.2022.132415

frontiers | Frontiers in Environmental Science

TYPE Original Research
PUBLISHED 28 October 2022
DOI 10.3389/fenvs.2022.1058351

OPEN ACCESS

EDITED BY
Yong Xiao,
Southwest Jiaotong University, China

REVIEWED BY
Xiaolang Zhang,
The University of Hong Kong, Hong Kong SAR, China
Muhammad Imran,
COMSATS University, Pakistan
Hongchang Hu,
Tsinghua University, China

*CORRESPONDENCE
Qiulan Zhang,
qlzhang919@cugb.edu.cn

SPECIALTY SECTION
This article was submitted to Freshwater Science,
a section of the journal
Frontiers in Environmental Science

RECEIVED 30 September 2022
ACCEPTED 20 October 2022
PUBLISHED 28 October 2022

CITATION
Zhang L, Zhu J, Zhang Q, Shao J, Cui Y and Zhang A (2022), Transport of montmorillonite colloid in unsaturated packed column: The combined effects of sand grain size, flow rate and colloid concentration.
Front. Environ. Sci. 10:1058351.
doi: 10.3389/fenvs.2022.1058351

Transport of montmorillonite colloid in unsaturated packed column: The combined effects of sand grain size, flow rate and colloid concentration

Linlin Zhang[1], Jun Zhu[1,2], Qiulan Zhang[1]*, Jingli Shao[1], Yali Cui[1] and Aiming Zhang[2]

[1]Beijing Key Laboratory of Water Resources and Environmental Engineering, School of Water Resources and Environment, China University of Geosciences (Beijing), Beijing, China, [2]China Institute for Radiation Protection, Taiyuan, China

The transport of colloid in unsaturated porous media affects the migration of contaminants and thus is closely related to groundwater resources protection. To figure out the combined effects of grain size, colloid concentration and injection flow rate on montmorillonite colloid transport characteristics in unsaturated quartz sand, a total of 27 sets of column experiments were conducted with three kinds of quartz sand (20, 40, 60 mesh), three flow rates (1.98, 3.96, 5.94 cm^3/min) and three colloid concentrations (300, 600, 900 mg/L), using three packed columns with the inner diameter of 11 cm and the height of 40 cm. The experimental results showed that the transport of Na-montmorillonite colloid particles in the unsaturated quartz sand columnoccurred with significant retention. In the 20 mesh quartz sand column, the average peak values of the penetration curves for low and high concentration colloidal solutions of 300 and 900 mg/L increased by 44% and 27%, respectively, as the flow rate increased from 1.98 to 5.94 cm^3/min. The average peak value of the colloidal solution with concentration 300 mg/L increased 17% more than that of the colloidal solution with 900 mg/L for increasing flow rate. When the injection flow rate of the colloidal solution was increased from 1.98 to 5.94 cm^3/min, the effect of flow rate on colloidal transport was the most obvious, followed by the effect of media particle size, while the effect of colloidal solution concentration was the least. The calculation based on the total potential energy of Derjaguin-Landau-Verwey-Overbeek (DLVO) and collision efficiency further explained the retention of colloids in unsaturated porous media.

KEYWORDS

colloid transport, unsaturated sand column, flow rate, grain size, colloid concentration

1 Introduction

The clay colloids are widely distributed in subsurface aquifer and vadose zones, with the characteristics of small size, large specific surface area and high surface electrical potential (Vilks and Baik, 2001; Um and Papelis, 2002; Schoonheydt et al., 2018; Won et al., 2021; Xiao et al., 2022a). The transport of clay colloid in porous media is closely related to many processes in the field of environmental geoscience, including groundwater pollution and remediation, reinjection of geothermal water and gas filed produced water, oil and gas exploitation, as well as the radionuclides migration (Torok et al., 1990; Ohnuki et al., 2010; Yang et al., 2013; Syngouna et al., 2017; Won et al., 2021; Xiao et al., 2022b). Particularly, the clay colloids play a significant role intransporting contaminants in porous media. The high surface potential and large specific surface area of clay colloids favorably adsorb the heavy metals, organic pollutants, radionuclides, virus and bacteria, thus facilitating or hindering the migration of these contaminants, and ultimately determining the fate of the substances in the environmental systems (Um and Papelis, 2002; Kim et al., 2003; Syngouna and Chrysikopoulos, 2013; Syngouna and Chrysikopoulos, 2016; Won et al., 2019; Fountouli and Chrysikopoulos, 2020; Xiao et al., 2022c; Liu et al., 2022). Given that its high importance, it is necessary to understand the clay colloid migration for effective management of contaminants and other environmental resources.

The transport characteristics of clay colloids in saturated porous media are deeply influenced by many environmental parameters such as particle size (Wang et al., 2012; Zhang et al., 2020), matrix structure (Zhang et al., 2016), flow velocity (Saiers and Lenhart, 2003a; Syngouna et al., 2017), solution compositions and salinity (Grolimund et al., 1996; Saiers and Lenhart, 2003b), as well as the solution pH (Walshe et al., 2010; Ma et al., 2018). In order to clarify the migration and retention behaviors of clay colloids under different influencing factors, large research efforts have been carried out by many scholars on the basis of batch experiments, column experiments, mathematical model and numerical simulation (Lenhart and Saiers, 2002; Torkzaban et al., 2008; Zhang et al., 2014; Zhang and Hassanizadeh, 2017). Won et al. (2021) investigated the transport and retention behaviors of kaolinite and illite under different sand grain sizes and solution ionic strengths. The results show that 1) a decrease in the median sand grain size increases the amount of retained clay and 2) the presence of an ionic strength threshold allows for similar retention of clay colloids at 0.01 M and 0.1 M during an increase in ionic strength from 0 to 0.1 M strength. Bradford and Kim (2010) conducted the column experiments to investigate the efforts of the solution chemistry sequence on the clay release from sands with different grain sizes, which shows that clay release presents a relatively minor enhancement with increasing pH and decreasing ionic strength. However, when monovalent sodium ions on the clay and sand surfaces were exchanged for multivalent cations, clay release was significantly enhanced. Syngouna and Chrysikopoulos (2011) evaluated the combined effects of quartz sand particle size and pore water flow rate on the migration of three biocolloids in saturated quartz sand columns. The results showed that there is no obvious relationships between mass recovery of biocolloids and water flow rate or particle size, while better agreement between the Maxwell theoretical and experimental collision efficiencies was observed. The deposition and release of clay colloids in saturated porous media sand columns packed with biochar-modified sand was studied by Haque et al. (2017), the results showed that the deposition of clay colloids in biochar was more favorable than that in sand.

Furthermore, many researchers have put a lot of efforts into clay colloids migration and retention in partially saturated porous media. Zevi et al. (2005) conducted colloid migration in partially saturated quartz to directly observe and characterize colloid transport behaviors using pore scale visualization technologies. Torkzaban et al. (2008) used filled columns and mathematical models to study the effects of water saturation, pore water ionic strength and particle size on the transport of latex microspheres in porous media, which indicates that straining is the major mechanism of colloid retention for both fully and partially saturated conditions. Fountouli and Chrysikopoulos (2020) investigated the effects of kaolinite and montmorillonite on formaldehyde transport in unsaturated sandy media at different flow rates and saturation conditions. The results showed that the presence of clay particles would delay formaldehyde transport and significant clay colloid retention occurred at low flow rates. Additionally, calculation results on the basis of Derjaguin–Landau–Verwey–Overbeek (DLVO) theory demonstrated that permanent retention of clay colloids at solid-water interfaces and air-water interfaces was negligible.

In summary, the existing studies mainly focused on one or two factors affecting the migration and retention of colloids in fully or partially saturated porous media, column experiments in unsaturated porous media are mostly set to a certain degree of water saturation (Shang et al., 2008; Torkzaban et al., 2008; Fountouli and Chrysikopoulos, 2020). Nonetheless, media particle size, injection flow rate and initial colloid concentration all affect the migration and retention of colloids in porous media. The water content of the actual unsaturated zone increases with depth, rather than a fixed water content. Accordingly, the investigation on the combined effects of medium particle size, injection flow rate and initial concentration of colloidal solution on the migration of colloids in unsaturated porous media with variable water content is essential for a comprehensive understanding of the behaviors of colloids or colloid-borne contaminant transport. However, the corresponding studies in existing references remain

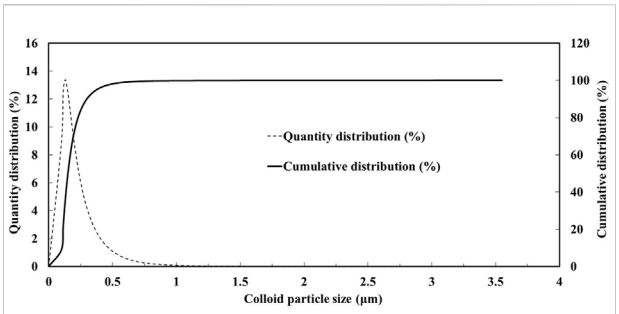

FIGURE 1
Montmorillonite colloid particle size distribution curve.

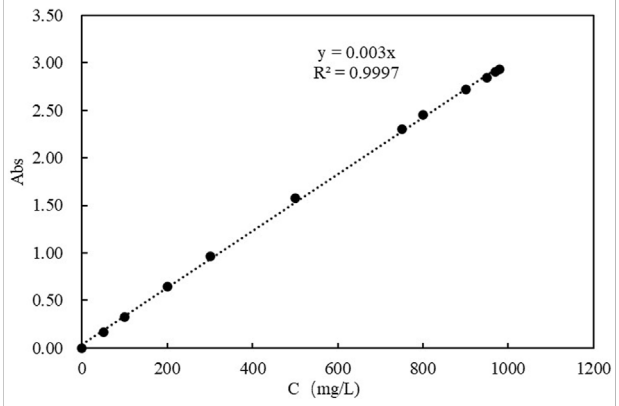

FIGURE 2
Standard curve of montmorillonite colloidal solution (Abs is the absorbance of the solution).

very limited. The objective of this study was to investigate the combined effects of media particle size, initial colloid concentrations and injection flow rates on Na-montmorillonite colloid migration behaviors in unsaturated quartz sand through prong the penetration time of colloid. The breakthrough curves were fitted by the cumulative Weibull model. The combined influences of three influencing factors on the key parameters of breakthrough curves were discussed. Furtherly, the relative importance of three influencing factors was ranked and discussed.

2 Materials and methods

2.1 Montmorillonite colloid preparation

SD1005 high purity (reagent grade) sodium montmorillonite colloid, made by Zhejiang Sanding Technology Co., Ltd., China, is used in the experiment. The sodium montmorillonite is a 2:1 layered aluminosilicate mineral composed of nanostructured micro crystals, and the particle size is less than 10 μm (Sposito et al., 1999; Schoonheydt et al., 2018). The particle size distribution of colloid was gauged by Malvin laser particle size analyzer (Mastersizer3000E, Malvern company, UK), which is roughly in the range of 0.1–1.5 μm (Figure 1).

The morphological characteristics of montmorillonite were obtained by scanning electron microscope (SU8240, Hitachi, Japan), as shown in Supplementary Figure S1. The representative transmission electron microscopy (TEM, FEI Tecnai G2 F20, FEI, US) image is shown in Supplementary Figure S1.

Montmorillonite colloids were prepared into colloid suspensions for sand column experiments with deionized water, and the concentrations were 300 mg/L, 600 mg/L and 900 mg/L respectively. A colloid concentration calibration curve was obtained by using sodium montmorillonite colloids, shown in Figure 2. As a result, the obtained relationship for estimating of the montmorillonite colloid concentration with high accuracy is as follow:

$$\textit{Montmorillonite colloid concentration}\ (mg/L) = Abs/0.003 \quad (1)$$

2.2 Quartz sand column preparation

Three sizes of quartz sand were used to pack the columns in this study: 1) coarse sand with a mean grain diameter of 0.9 mm (Sieve No 20), 2) medium sand with a mean grain diameter of 0.45 mm (Sieve No 40), and 3) fine sand with a mean grain diameter of 0.3 mm (Sieve No 60). According to the particle size of quartz sand, the sieve with corresponding mesh number was selected, and use swing sieve analyzer (AS200, Retsch Company, Germany) was used to screen the quartz sand to remove impurities and ensure that the particle size is consistent.

The pretreatment procedures for thoroughly washing sand are as follows. Firstly, washing the quartz sand with deionized water and ultrasonic for 5 times, then soaking it in 1 M NaOH and HCl solution for 24 h, respectively. Subsequently, the sand was washed it with deionized water and ultrasonic for 3 times to remove the residual alkali and acid solution. Finally, the sand was dried in muffle furnace (L15/11, Nabertherm GmbH, Germany) at 600°C for 8 h. The high temperature of 600°C can completely remove the organic matter in quartz sand. The treated quartz sand is placed in a cool and dry place and sealed for storage.

Supplementary Figure S2 displays the morphological characteristics of quartz sand particles obtained by scanning electron microscope. It can be seen from Supplementary Figure S2 that there are both smooth areas and rough areas on the surface of quartz sand particles.

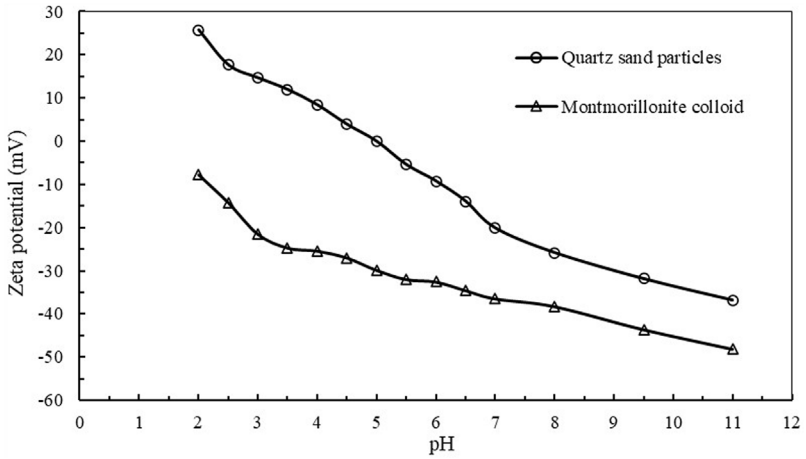

FIGURE 3
The average value of zeta potential value of montmorillonite colloid and quartz sand particles changing with pH in ionic water at 25°C.

2.3 Zeta potential

The zeta potential (ξ) represents a measure of the electrical potential of the mineral surfaces, determines the thickness of electrical double layer (EDL) at minerals surface, and controls the electrostatic interactions strength between mineral surface and polar species in aqueous solution (Shehata and Nasr-El-Din, 2015; Vinogradov and Jackson, 2015; Awan et al., 2022).

Given that its high importance, the zeta potentials of various colloid concentrations and sands used in this study were measured in deionized water by a ZetaPlus potential analyzer (ZetaPlus Nano, Malvern, UK). Note that the sand grains used in this work were too large for directly measurement of their zeta potential by the ZetaPlus potential analyzer. Consequently, a few sand grains were crushed into fine powder and then mixed with the deionized water to form suspension.

All zeta potential measurements were collected in triplicate. Figure 3 shows the average zeta potential values of montmorillonite colloid and quartz sand particles under different pH conditions. At 25°C deionized water, the zeta potential of quartz sand particles is determined to be -20.1 mV, and the zeta potential of montmorillonite colloid is determined to be -36.5 mV. In particular, the zeta potential of montmorillonite colloid is negative in the examined pH range.

2.4 Experiment procedure

All colloid transport experiments were conducted in three plexiglass columns, and each with a length of 40 cm and an inner diameter of 11 cm. Each column used in the experiments was filled with one size of quartz sand particles to obtain columns filled with 20 mesh, 40 mesh and 60 mesh quartz sand particles, respectively. The columns were evenly filled with dried sand in a layered manner. After each part of sand was filled, it needed to be compacted, and then roughened the sand with a thickness of 1 cm on the surface, so as to continue to fill quartz sand. As shown in Figure 4, the height of the filled sand was 33 cm. There were 2 cm and 5 cm spaces reserved at the top and bottom of the packed column without quartz sand filling, respectively. The 2 cm space was convenient for the uniform infiltration of the spray water at the top, and the 5 cm space was to prevent the deposition of the outflow liquid at the bottom. As the bottom boundary for the filling with 60 mesh quartz sand, we used a nylon membrane with mesh number of 120 supported by plexiglass porous sieve plate (80 mesh is used for the nylon membrane of the remaining two sand columns). The colloidal solutions were introduced into the column through a modified plexiglass cover (see Figure 4) with uniform hole distribution to ensure even distribution over the whole cross-section of the column. The bottom cover of the column was improved, and the internal surface was made into a conical appearance to ensure that the liquid flowing out of the porous sieve plate can smoothly converge to the outlet at the bottom of the column and then be collected.

The saturated permeability coefficients, pore volumes, bulk density and weight of filled quartz sand of packed columns are listed in Table 1. The saturated permeability coefficient was measured by the constant head method with the Markov bottle, the pore volume was measured by the saturation method, and the porosity was obtained by dividing the pore volume by the sand column volume. Bulk density is obtained by dividing the weight of the sand column by its volume. The saturated volumetric water content was solved by using the Van Genuchten (VG) (Genuchten, 1980) model. It should be noted that the saturated volumetric water content and porosity

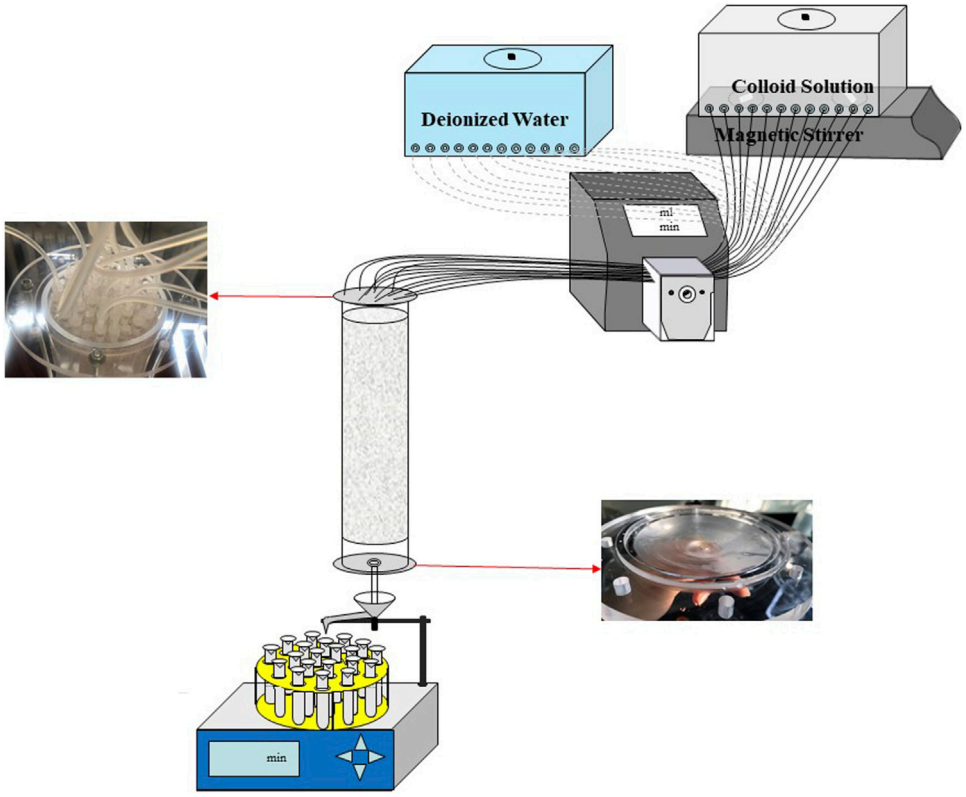

FIGURE 4
Schematic diagram of the experimental setup.

TABLE 1 The relevant parameters of packed columns.

	Coarse sand column	Medium sand column	Fine sand column
Quartz sand weight (g)	5246	5329	5185
Saturated permeability coefficient (cm/s)	0.25	0.09	0.04
Pore volume (L)	0.85	1.03	1.28
Porosity	0.27	0.33	0.41
Saturated volumetric water content	0.32	0.36	0.34
Bulk density (g/cm^3)	1.67	1.70	1.65

are not identical for each particle size of quartz sand. This is because the application of the VG model to solve for the saturated volume water content requires the use of the centrifuge method to calculate the water content for each centrifugal force condition, and the quartz sand has poor water holding capacity, which can lead to errors when using the centrifuge method.

Colloid transport experiments were conducted with the column vertically oriented. 12 flexible pipes were used to connect the water supply tank and the top cover of the column through the peristaltic pump, respectively. The colloid suspension was introduced into the column using the peristaltic pump at a fixed injection flow rate. Prior to each experiment, the pre-balance stage needs to be reached, that is, injecting deionized water at the same flow rate for 24 h before introducing colloidal suspension, so as to maintain a stable moisture content during the experiment. Initial leaching with deionized water was carried out for 24 h using downward flow from the top of the columns. At the end of the leaching process, the absorbance of the effluent was measured as the absorbance background value of each

TABLE 2 The experimental conditions and characteristic parameters.

No.	Sand mesh	Flow rate (cm^3/min)	Concentration (mg/L)	$\overline{C/C_{0\,max}}$	a (C/C_{0max}')	δ	R^2	α
1	20	1.98	300	0.595	0.536	1.15	0.990	0.064
2	20	1.98	600	0.655	0.658	1.63	0.986	0.053
3	20	1.98	900	0.664	0.647	1.02	0.992	0.051
4	20	3.96	300	0.840	0.736	1.42	0.987	0.046
5	20	3.96	600	0.780	0.779	2.02	0.992	0.054
6	20	3.96	900	0.804	0.785	1.77	0.992	0.047
7	20	5.94	300	0.855	0.792	2.17	0.986	0.046
8	20	5.94	600	0.860	0.821	2.27	0.991	0.045
9	20	5.94	900	0.842	0.816	2.23	0.991	0.051
10	40	1.98	300	0.527	0.585	2.69	0.990	0.035
11	40	1.98	600	0.626	0.606	2.60	0.996	0.026
12	40	1.98	900	0.702	0.680	2.78	0.995	0.020
13	40	3.96	300	0.763	0.693	2.89	0.991	0.026
14	40	3.96	600	0.659	0.768	3.95	0.993	0.039
15	40	3.96	900	0.740	0.736	2.89	0.993	0.028
16	40	5.94	300	0.791	0.746	3.72	0.993	0.030
17	40	5.94	600	0.812	0.794	3.28	0.995	0.027
18	40	5.94	900	0.829	0.816	3.71	0.996	0.024
19	60	1.98	300	0.604	0.568	4.00	0.990	0.013
20	60	1.98	600	0.613	0.613	4.69	0.996	0.012
21	60	1.98	900	0.671	0.663	3.38	0.993	0.010
22	60	3.96	300	0.765	0.703	4.39	0.991	0.011
23	60	3.96	600	0.641	0.732	6.00	0.997	0.019
24	60	3.96	900	0.695	0.732	6.70	0.996	0.015
25	60	5.94	300	0.783	0.748	5.38	0.995	0.014
26	60	5.94	600	0.779	0.775	5.51	0.995	0.014
27	60	5.94	900	0.787	0.776	5.40	0.994	0.014

experiment. Table 2 summarizes the experimental conditions of each column for a total of 27 sets of column experiments. Liquid samples were collected from the column effluent by using a partial automatic collector (BSZ-40, Jihui analytical instrument (Shanghai) Co., Ltd) with a fixed time interval.

After the pre balance stage, the 12 flexible pipes connecting the water tank filled with deionized water reconnected to the container filled with montmorillonite colloidal suspension. The colloidal solution was let through the quartz sand column at the set injection flow rate. The concentration of montmorillonite colloid in the collected effluent was measured until 300 effluent samples were collected, indicating that the penetration stage was completed. For 20 mesh and 40 mesh quartz sand columns, nearly 12 PV (Pore Volume) colloidal solution was applied to collect 300 outflow samples. While in the 60 mesh quartz sand column, about 9 PV was applied.

When the above operations were completed, the elution stage begins. The 12 flexible pipeswere reconnected to the water tank with deionized water. The deionized water was let pass through the column at the set flow rate to measure the absorbance in the effluent until its value is the same or similar to the background absorbance. According to the experimental results, about 39 effluent samples can be collected at this stage to meet the conditions and stop the experiment. The absorbances (Abs) of all effluent were measured by UV-VIS spectrophotometer (UV1800, Shanghai Meipuda Instrument Co., Ltd) at 243 nm wavelength. After subtracting the background absorbance, the colloid concentration in the solution was calculated according to the standard curve. The breakthrough curves were obtained by plotting relative colloid concentration *versus* pore volume.

In order to ensure the consistency of the quartz sand structure inside the column during each group of experiments, after each conditional column experiment, the quartz sand column was cleaned with 100 L deionized water using a large water head difference. Generally, the absorbance of the effluent after cleaning is less than 0.07.

It should be emphasized that the whole experimental processes were carried out under the condition of 25°C in the absence of sunlight, and the temperature was adjusted and controlled by air conditioning.

In this study, Hydrus-1D was applied to simulate the water content of each sand column at different flow rates, where the water content increased with depth in the column. The average volumetric water content obtained for the same mesh of quartz sand column at the three flow rate experimental conditions did not differ significantly, while the water content at the top of the column and the depth at which the saturated volumetric water content was initially reached differed in each case. For subsequent calculations, the average volumetric water contents of the 20-, 40-, and 60-mesh quartz sand columns were obtained as 0.300, 0.355, and 0.310, respectively, based on the model results.

2.5 Theoretical methods

2.5.1 Derjaguin-Landau-Verwey-Overbeek (DLVO) theory

Derjaguin-Landau-Verwey-Overbeek (DLVO) theory is the cornerstone of colloidal science, which is used to describe the force between colloid and solid surface. The force is also referred as DLVO force, mainly including van der Waals force, and electric double layer force generated by electrostatic interaction. According to the DLVO theory, the total potential energy between the colloid and quartz sand particles is calculated by Eq 2 (Loveland et al., 1996):

$$\phi_{DLVO}(h) = \phi_{vdw}(h) + \phi_{el}(h) \tag{2}$$

where $\phi_{vdw}(h)$ (J) is the van der Waals force potential energy, $\phi_{el}(h)$ (J) is the electrostatic potential energy of electric double layer, and h (nm) is the distance between the colloidal particles and the surface of the porous media particles.

For the sphere-plate particle geometry, the ϕ_{vdw} (J) is calculated by Eq 3 (Gregory, 1981; Chrysikopoulos and Syngouna, 2012):

$$\phi_{vdw}(h) = -\frac{A_{123}R}{6h}\left(1 + \frac{14h}{\lambda}\right)^{-1} \tag{3}$$

where R (nm) is the radius of colloid, λ (nm) is the characteristic wavelength (= 100 nm), A_{123} (J) is the combined Hamaker constant. The expression for the calculation of A_{123} is as follows (Israelachvili, 1992):

$$A_{123} = \left(\sqrt{A_{11}} - \sqrt{A_{22}}\right)\left(\sqrt{A_{33}} - \sqrt{A_{22}}\right) \tag{4}$$

where A_{11} (J) is the Hamaker constant for the colloid particle, A_{22} (J) is the Hamaker constant for the liquid, and A_{33} (J) is the Hamaker constant for the solid surface. The value of the Hamaker constant of montmorillonite colloid particles, deionized water, and the quartz sand particles are announced to be 1.23×10^{-19} J (Fountouli and Chrysikopoulos, 2020), 3.70×10^{-20} J, and 6.80×10^{-20} J (Tokunaga, 2011), respectively. According to the calculation, A_{123} is 1.08×10^{-20} J.

The potential energy of the bilayer electrostatic force can be calculated by Eq 5 (Hogg et al., 1966; Mitropoulou et al., 2013):

$$\phi_{el}(h) = \pi\varepsilon_0\varepsilon_r R\left\{\begin{array}{c} 2\psi_1\psi_2\, ln\left[\dfrac{1 + exp(-h/\kappa^{-1})}{1 - exp(-h/\kappa^{-1})}\right] + (\psi_1^2 + \psi_2^2) \\ * ln\left[1 - exp(-2h/\kappa^{-1})\right] \end{array}\right\} \tag{5}$$

where $\varepsilon_0 = 8.85 \times 10^{-12}$ ($C^2J^{-1}m^{-1}$) is the permittivity of free pace, ε_r = 76.58 (-) is the relative dielectric constant of water (Israelachvili, 2011), ψ_1 and ψ_2 are the surface potentials of colloid particles and collector surface, respectively, and κ (m^{-1}) is the reciprocal of the thickness of the diffusion electric double layer or the Debye-Huckel length. It is expressed as Eq 6 (Tokunaga, 2011; Chrysikopoulos and Syngouna, 2012; Mitropoulou et al., 2013; Zhang et al., 2020):

$$\kappa = \sqrt{\frac{2e^2 1000 I N_A}{\varepsilon_0\varepsilon_r k_B T}} \tag{6}$$

where $e = 1.6 \times 10^{-19}$ (C) is the electron charge, I (mol/L) is the ionic strength of the background electrolyte solution, N_A = 6.02×10^{23} (mol^{-1}) is the Avogadro's number, k_B = 1.38×10^{23} (J/K) is the Boltzmann constant, and T = 298 (K) is the Kelvin temperature of 25°C.

2.5.2 Collision efficiency

The collision efficiency α, is generally estimated from the results of column experiments by Eq 7 in unsaturated porous media (Tufenkji and Elimelech, 2004):

$$\alpha = -\frac{2}{3}\frac{d_c}{L(1-\theta_w)\eta_0} ln\left(\frac{C}{C_0}\right) \tag{7}$$

where d_c (m) is the diameter of collector, L (m) is the length of the filling medium in the column, θ_w is the volumetric water content, C (mg/L) is the concentration of effluent colloid, C_0 (mg/L) is the concentration of influent colloid, η_0 is the single collector efficiency, which is determined by Eq 8 (Tufenkji and Elimelech, 2004; Wang et al., 2012):

$$\eta_0 = 2.4A_S^{\frac{1}{3}}N_R^{-0.081}N_{Pe}^{-0.715}N_{vdw}^{0.052} + 0.55A_S N_R^{1.675}N_A^{0.125} + 0.22N_R^{-0.24}N_G^{1.11}N_{vdw}^{0.053} \tag{8}$$

where A_S is a porosity-related parameter, N_R is aspect ratio, N_{Pe} is Peclet number, N_{vdw} is van der Waals number, N_A is attraction number, N_G is gravity number. These parameters can be obtained from Eqs 9–15:

$$A_s = \frac{2(1-\gamma^5)}{2 - 3\gamma + 3\gamma^5 - 2\gamma^6} \tag{9}$$

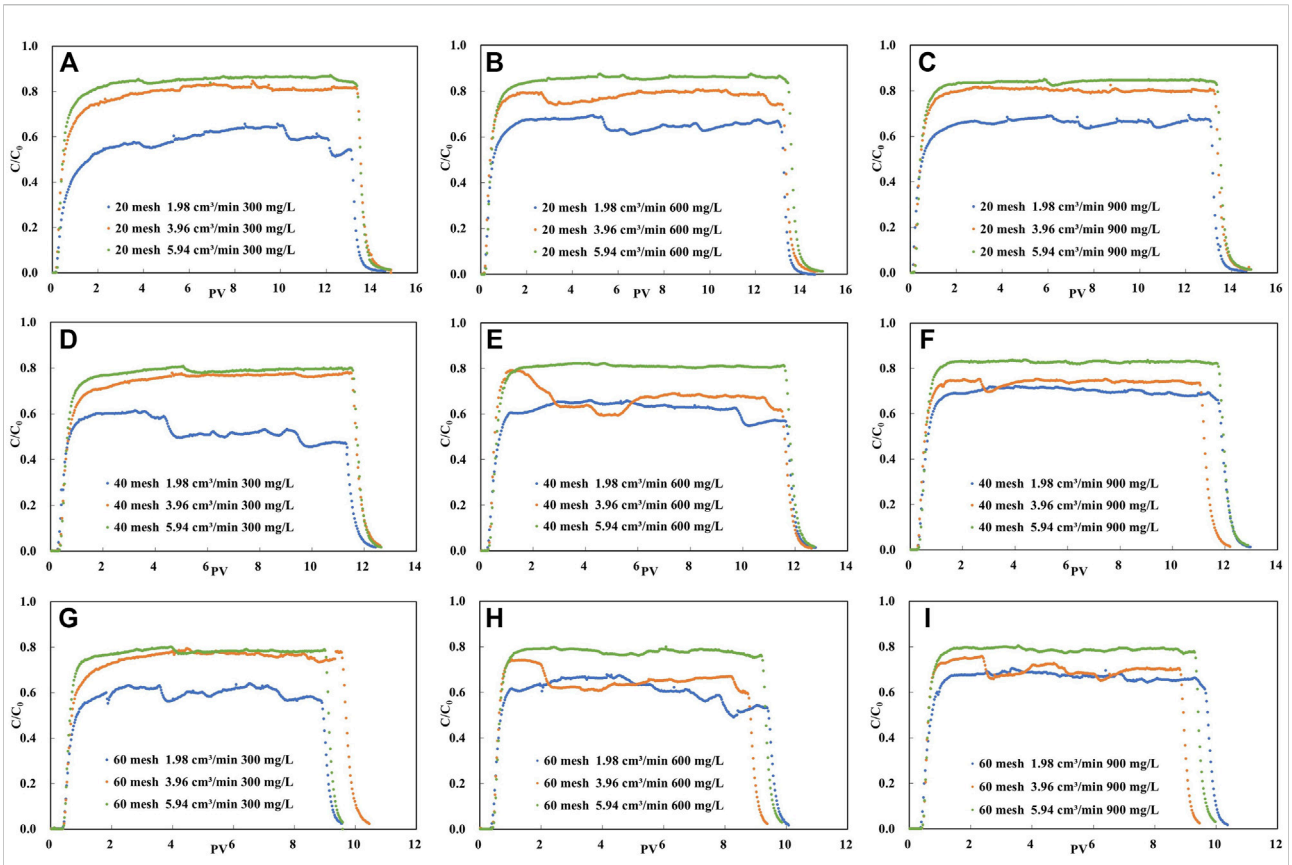

FIGURE 5
Experimental breakthrough data for the same concentration of colloid solution in the same mesh of quartz sand column under different flow rate conditions.

where $\gamma = (1-\theta_w)^{1/3}$

$$N_R = \frac{d_p}{d_c} \tag{10}$$

where d_p (m) is the diameter of (colloid) particle.

$$N_{Pe} = \frac{U d_c}{D'} \tag{11}$$

where U (m/s) is the approach (superficial) velocity of fluid, D' is the diffusion coefficient, it can be calculated by Eq 12:

$$D' = \frac{k_B T}{6\pi\mu r_p} \tag{12}$$

where $\mu = 8.91 \times 10^{-4}$ ($kgm^{-1}s^{-1}$) is viscosity of fluid (Fountouli and Chrysikopoulos, 2020), r_p (m) is the radius of (colloid) particle.

$$N_{vdw} = \frac{A_{123}}{k_B T} \tag{13}$$

$$N_A = \frac{A_{123}}{12\pi\mu r_p^2 U} \tag{14}$$

$$N_G = \frac{2r_p^2(\rho_p - \rho_f)g}{9\mu U} \tag{15}$$

where ρ_p = 2200 (kg/m^3) is the density of (colloid) particle (Olphen and Fripiar, 1979), ρ_f = 999.7 (kg/m^3) is the density of fluid (Fountouli and Chrysikopoulos, 2020), g = 9.81 (m/s^2) is the gravitational acceleration.

3 Results and discussion

3.1 The effect of flow rate on colloid transport

The experimental results of montmorillonite colloid transportation in unsaturated packed column are expressed as breakthrough curves (BTCs), shown as the variation of percentages of aqueous phase mass concentration (C/C_0) with PV. The breakthrough curves obtained for each experimental condition are shown in Figure 5. $\overline{C/C_{0\,max}}$ is the average value of

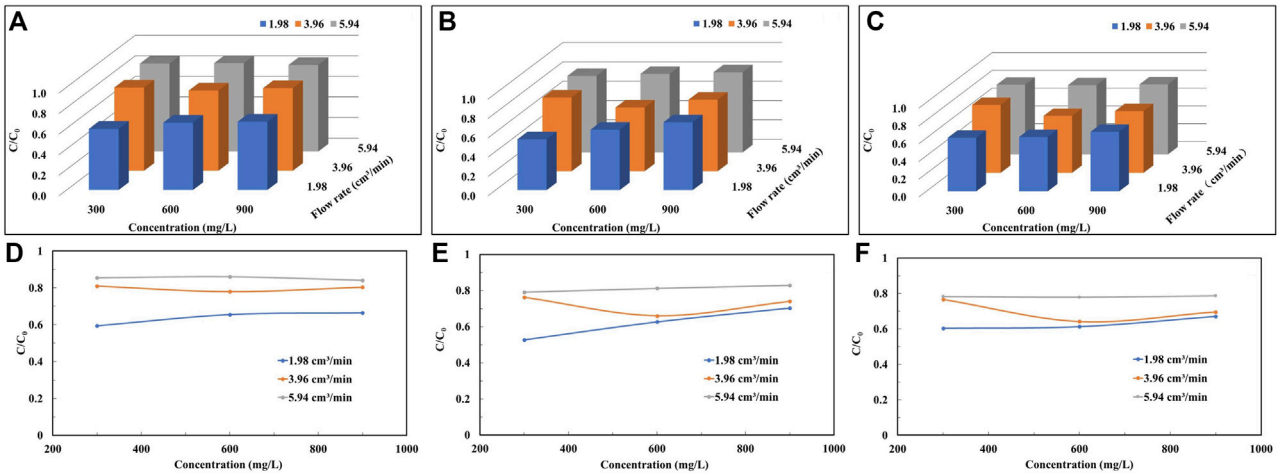

FIGURE 6
The peak plateau values of the penetration curves at different colloid concentrations and injection flow rates in unsaturated sand column: **(A,D)** 20 mesh, **(B,E)** 40 mesh, and **(C,F)** 60 mesh.

the plateau period value of the penetration curve of colloid is shown in Table 2.

As can be seen from Figure 5, on the whole, each penetration curve shows a steep front and a long peak plateau period. Moreover, none of the peak values of the penetration curves of the colloid solutions reached 1, which indicates that there is retention of montmorillonite colloids migrating in the sand column. When the quartz sand particles are of the same size, the higher the plateau that the C/C_0 of the penetration curve can reach as the flow rate increases from 1.98 cm^3/min to 5.94 cm^3/min. This was the case for all three colloidal concentration conditions.

In order to better compare the characteristics of the penetration curves of colloid solution obtained under various experimental conditions, the cumulative Weibull model is used to fit these penetration curves. The cumulative Weibull model is also known as the 'stretch index' function. It adds a parameter delta, which allows you to modify the inflection point. Moreover, the upper asymptote of the model is the maximum value of Y, and the lower asymptote can be non-zero. This model is usually used to simulate particle size during dissolution of solid dosage forms. The equation of this model is as follows:

$$Y = a - b \cdot e^{-m \cdot x^{\delta}} \tag{16}$$

where, a is the maximum value of Y in the curve (upper asymptote), b is the lower asymptote, m is the x value of the control inflection point, δ is the steepness of the curve.

The variance obtained from each set of experimental model fits is greater than 0.9. The closer the R^2 is to 1, the more accurate the model fit is proven.

As shown in Figure 5, the transport of colloids in unsaturated porous media is influenced by particle size, colloid concentration and injection flow rate. For analyze the effect of flow rate on colloid migration, we plot the peak variation of the penetration curve at different flow rates as demonstrated in Figure 6. The maximum of the peak mean values of the colloid breakthrough curves are 0.860 (Figure 6D), 0.829 (Figure 6E) and 0.787 (Figure 6F) for the three sand grain size cases, respectively. The maximum values are in the experimental condition with the highest flow rate and the minimum values are almost always in the experimental condition with the lowest flow rate (Figure 6).

As shown in Figure 6D; Table 2, the average value of the peak of the breakthrough curve is 0.595 at a flow rate of 1.98 cm^3/min under the coarse particle and low concentration condition, and nearly 40% of the colloids is deposited in the medium quartz sand during the transport in the sand column. Nevertheless, when the flow rate is increased to 5.94 cm^3/min, the mean value of the peak penetration curve obtained in the experiment increases by 44%. In coarse particles and high concentration conditions, the peak mean value increases by 27% with increasing flow rate. The mean values of the peaks obtained by increasing the flow rate increase by 50% and 29% for medium and fine particle conditions, respectively, when the colloid solution concentration is low. Under the same conditions, the peak mean values increase by 18% and 17%, respectively, when the concentration of colloid solution is higher. When the quartz sand particle size is determined, the effect of increasing the colloid injection flow rate on the peak of the permeation curve is more pronounced at lower concentrations of colloid solution compared to higher concentrations of montmorillonite colloid solution.

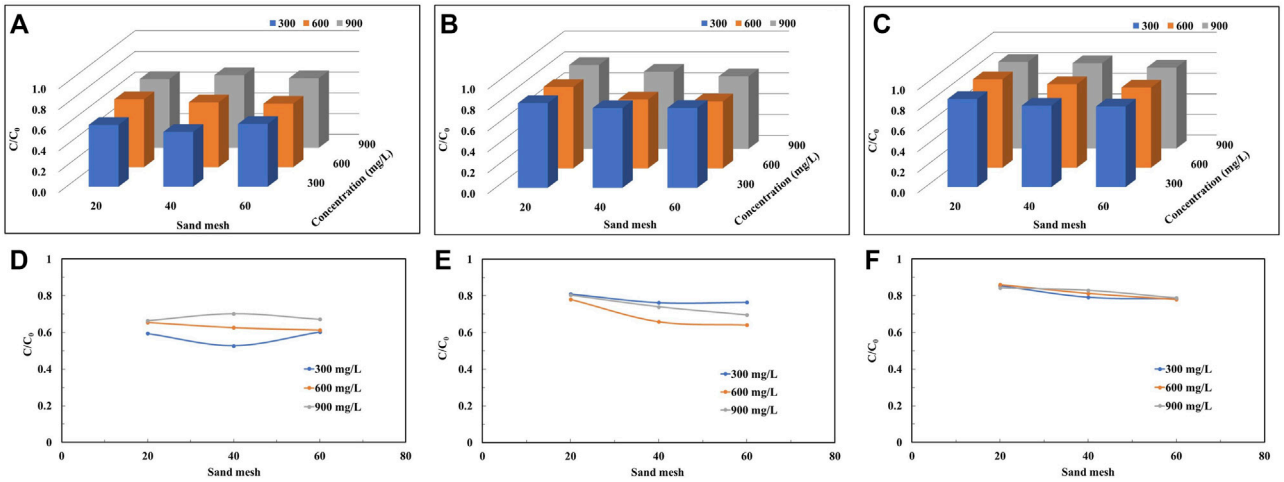

FIGURE 7
The peak plateau values of the penetration curves of quartz sand particles of different mesh sizes at different colloid concentrations under the conditions of injection flow rates: **(A,D)** 1.98 cm^3/min, **(B,E)** 3.96 cm^3/min, and **(C,F)** 5.94 cm^3/min.

As the flow rate increases, the migration of colloids in the sand column increases and the peak of the colloid penetration curve rises. This indicates that the increase in flow rate facilitates the migration of colloids in porous media. Similar findings have been reported by others (Shang et al., 2008; Fountouli and Chrysikopoulos, 2020). This is due to the fact that when the flow rate increases, the contact time between the colloid and the quartz sand particles decreases, reducing the possibility of colloid adsorption on the surface of the quartz sand particles, which is conducive to the migration of colloids. Another reason is that the increase of the flow velocity will generate a greater hydraulic shear force, which makes the colloids get more propulsion and migrate to the water, along the trajectory of the liquid phase (Chowdhury et al., 2011; Knappenberger et al., 2014), which will result in more colloids at the outflow end.

3.2 The effect of colloid concentration on colloid transport

It can be seen from Figure 5 that when the mesh number of quartz sand is the same as the injection flow rate of colloidal solution, the peak platform value of penetration curve changes little with the initial concentration of colloidal solution, and the peak platforms almost coincide under each group of conditions.

According to Table 2, when the solution injection flow rate is 1.98 cm^3/min and the colloid concentration remains unchanged, the difference of the peak platform value of the penetration curve obtained under the three types of quartz sand mesh is less than 0.1, and the same situation occurs when the flow rate is 5.94 cm^3/min. Nevertheless, under the last flow rate, the difference of the peak platform value of the penetration curve obtained under the three types of quartz sand mesh is greater than 0.1.

Figure 5 demonstrates the variation of peak mean values of the penetration curves of colloid solutions with colloid concentration for the same injection flow rate and quartz sand particle size conditions. Under low flow rate conditions (Figure 7D), the peak mean values increase with increasing colloidal solution concentration and increase by 12%, 33% and 11% with increasing concentration as the quartz sand particles change from coarse to fine, respectively. However, under high flow rate conditions (Figure 7F), the peak mean values of the colloid breakthrough curves obtained for each quartz sand size condition do not vary significantly with concentration.

The mean values of the peak penetration curves obtain for colloid solutions of high concentration are larger than the results for other concentrations, both at low and high flow rates and for almost every grain size condition. When the concentration of colloid solution increases, the number of colloids in the solution increases per unit volume, and at the same time, there is competition for spots in the settling process, leading to a decrease in the settling rate, which enhances the migration.

3.3 The effect of grain size on colloid transport

The mean value of the peak increases with increasing flow rate by 44% (Figure 8D), 31% (Figure 8E) and 27% (Figure 8F) for the three concentration conditions in the coarse-grained sand column, respectively. Similarly, in the fine-grained sand column,

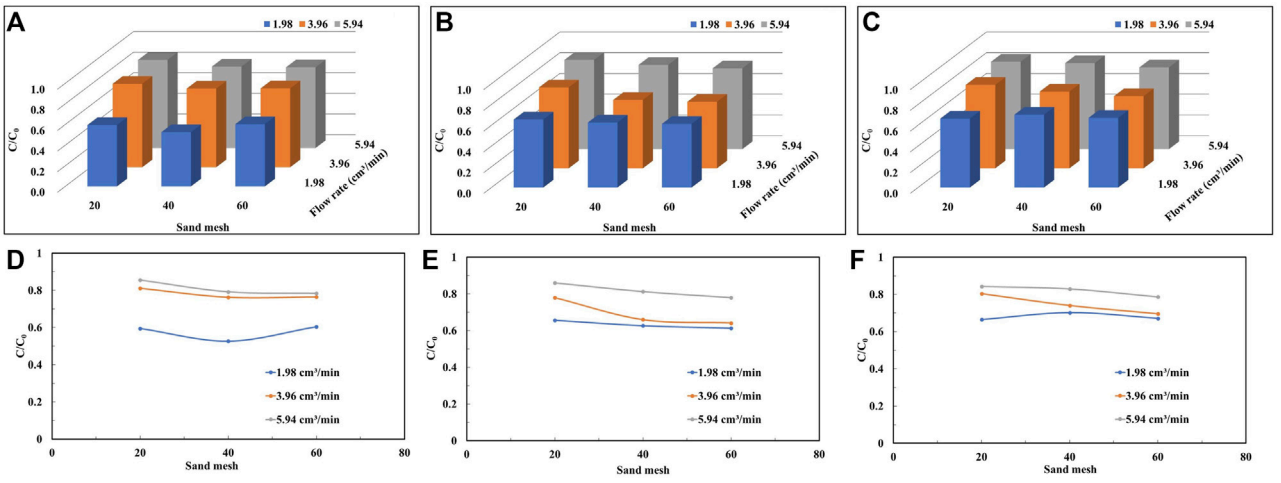

FIGURE 8
The peak plateau values of the penetration curves of quartz sand particles of different mesh sizes at different injection flow rates under the conditions of colloid concentration: **(A,D)** 300 mg/L, **(B,E)** 600 mg/L, and **(C,F)** 900 mg/L.

the peak mean values increase by 30%, 27% and 17% with increasing flow rate, respectively. Compared to the coarse particle-filled quartz sand column, the peak mean values obtain for each concentration of solution in the fine sand condition show less variation with increasing flow rate. As the particle size becomes smaller, the pore volume used to be able to detect colloids in the effluent increases (Figure 5).

Figure 8; Table 2 show that regardless the colloid concentration, the peak mean values tend to decrease with smaller particle size of the quartz sand particles when the flow rate are 3.96 cm^3/min and 5.94 cm^3/min. At high flow rates, the peak mean values decrease by 8%, 9%, and 7%, respectively, as the number of sand mesh becomes larger. While at moderate flow rates, the peak mean values decrease by 6%, 18%, and 14%, respectively. This indicates that when the quartz sand particles change from coarse to fine, the specific surface area of sand particles increases, so the contact area between colloid and particles increases, which is favorable for the deposition of colloid particles. It is worth noting that the variation of the peak mean values at low flow rates, when the colloid solution is at low and high concentrations, is not the same as the results for other conditions.

3.4 Calculation of DLVO interaction energy

In this study, although natural montmorillonite colloids are not spherical, it is assumed that the colloids are spherical and apply the equations mentioned previously to calculate the forces acting on the colloidal particles (Shang et al., 2008; Fountouli and Chrysikopoulos, 2020). According to the DLVO theory, Figure 9 shows the total DLVO potential energy of the interaction between the montmorillonite colloid and the solid-water interface (SWI) and the colloid and the air-water interface (AWI) under the experimental conditions in this study. According to the colloidal particle size distribution curve (Figure 1), the diameters of D10 (100 nm), D50 (150 nm), D60 (160 nm) and D90 (280 nm) were used to calculate DLVO potential energy, where D50 is used to indicate the average particle size of colloidal particle size (Figure 9).

In this experiment, the average particle size of montmorillonite colloid was 150 nm, and its potential barrier in the deionized water and quartz sand system was calculated as 116.10 k_BT (Table 3), while the absence of secondary energy minima (φ_{min2}) indicates that the colloidal particles are unlikely to be permanently retained on the surface of quartz sand particles. Correspondingly, the retention of colloid particles at the air-water interface (AWI) is not permanent. The interactions of colloids with the solid-water interface (SWI) as well as the colloids with the air-water interface (AWI) show repulsive energy potentials, which could prevent the attachment of colloids to the solid surface and the AWIs. However, the peak plateau value of the penetration curve of the colloid solution did not reach 1. It is obvious that there are stagnant colloids present in the quartz sand column, which contradicts the calculation of DLVO. Therefore, another non-DLVO force needs to be considered in this study of colloid migration in unsaturated quartz sand columns to explain the deviation from the DLVO calculation (Fountouli and Chrysikopoulos, 2020).

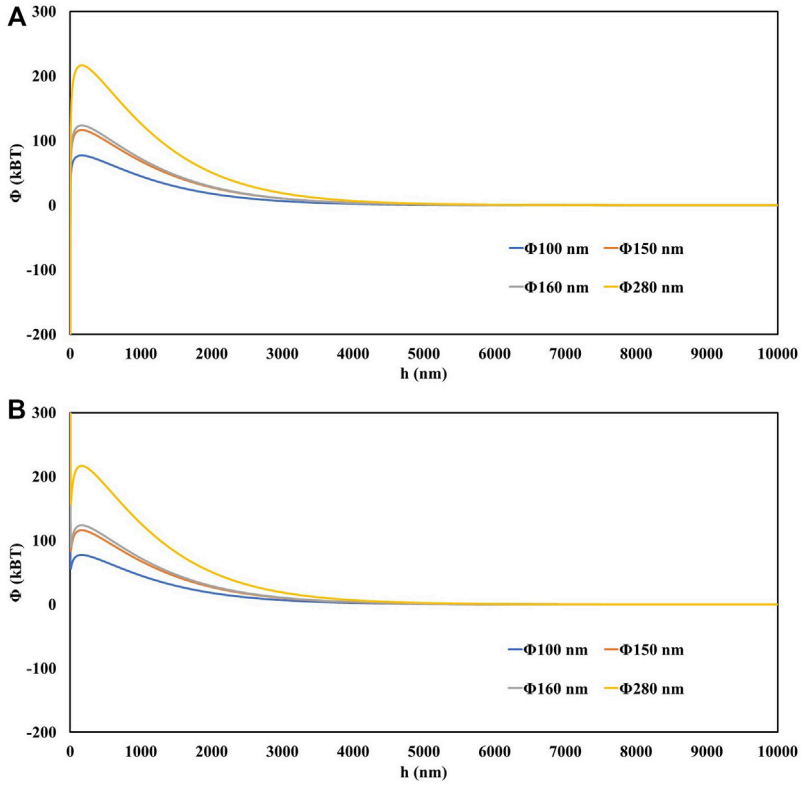

FIGURE 9
The total DLVO energy profile for: **(A)** montmorillonite colloid–SWI and **(B)** montmorillonite colloid–AWI, as a function of separation distance.

TABLE 3 Estimated φ_{max}, φ_{min1} and φ_{min2} using DLVO theory for the colloid particle size of 150 nm.

	ϕ_{max} (k_BT)	ϕ_{min1} (k_BT)	ϕ_{min2} (k_BT)
Colloid - SWI	116.10	-668.5	NA
Colloid - AWI	116.16	NA	NA

NA: not applicable.

This experiment considers unsaturated conditions, where AWIs exist during colloid migration and non-DLVO interactions such as hydrophobic, hydrodynamic and capillary forces may occur for colloids on AWIs (Bradford and Torkzaban, 2008). The capillary energy is calculated from the distance the colloid protrudes from the film or the air-water-solid interface, and the values obtained in the studies

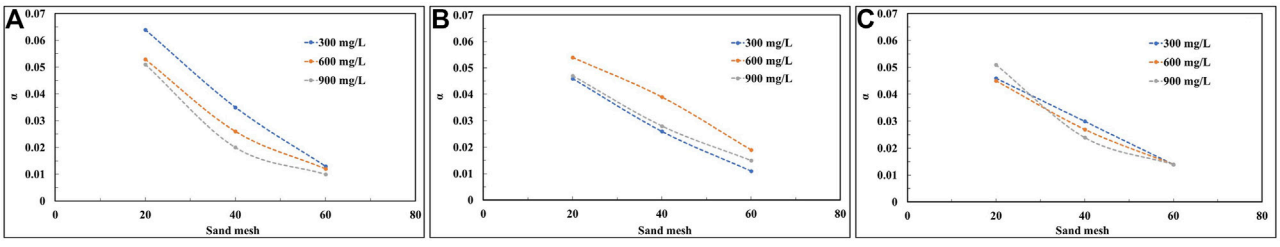

FIGURE 10
The collision efficiencies of: **(A)** 1.98 cm^3/min, **(B)** 3.96 cm^3/min, and **(C)** 5.94 cm^3/min.

are several orders of magnitude larger than the total DLVO potential obtained (Syngouna and Chrysikopoulos, 2015; Fountouli and Chrysikopoulos, 2020). Thus, the capillary energy is sufficient to push the colloid to the quartz sand surface, where it is attracted by van der Waals forces, leading to the retention of the colloid (Gao et al., 2008).

3.5 Calculation of collision efficiencies

The collision efficiency α, was calculated for all experiments according to Eqs 7-15 and the results are presented in Table 2. Combining Table 2; Figure 10, it can be seen that the α obtained in the sand column of the same quartz sand grain size under high flow rate experimental conditions does not differ much. According to the colloid filtration theory (CFT), an increase in the interstitial flow rate decreases the number of collisions occurring between the passive colloid particles and the collectors, which does not favor the retention of colloids and leads to an increase in the number of movable colloids (Walshe et al., 2010; Fountouli and Chrysikopoulos, 2020). This is consistent with the phenomenon that the peak of the breakthrough curve of colloids is the largest at high flow rate conditions as shown in Figure 8. Moreover, the peak of the breakthrough curve for the same particle size of quartz sand hardly varies with the colloid concentration at high flow rates, also because the fast flow rate reduces the number of effective collisions, and the flow rate affects the colloid migration to a greater extent than the effect of colloid concentration changes.

Under low flow rate conditions, increasing colloid solution concentrations lowers the α value (Figure 10A). Figure 7D demonstrates that an increase in colloid concentration reduces the collision between colloid particles and the collector, with a consequent increase in the peak of the penetration curve. However, in the experiment with a flow rate of 3.96 cm^3/min, the α value did not change similarly to the low flow rate condition (Figure 10B). The reason for this is presumed to be that when the flow rate increased from 1.98 to 3.96 cm^3/min, the flow rate dominated the degree of influence of flow rate and colloid concentration on colloid transport.

4 Conclusion

In this study, quartz sand column experiments were used to determine the impact of flow rate, grain size, and colloid concentration on the transport of sodium montmorillonite colloids through the porous media. The experimental results of the study indicated that colloid retention occurred under all experimental conditions.

(1) When the size of the quartz sand particles is determined, an increase in the flow rate reduces the retention of colloids, regardless of whether the concentration of the colloid solution is low or high. For the coarse particle and low concentration cases, an increase in flow rate from 1.98 cm^3/min to 5.94 cm^3/min increased the peak mean by 44%, while for the high concentration case, the peak mean increased by only 27%. Flow rate effects on the migration of colloids are more significant at lower concentration.

(2) At a flow rate of 5.94 cm^3/min, the peak mean values of the breakthrough curves decreased by 8%, 9% and 7% with increasing the number of quartz sand mesh, respectively. Under the same flow rate condition, the peak average value of the breakthrough curve almost does not change with the change of colloid concentration.

(3) In the case of montmorillonite colloid solution transport in a column of unsaturated quartz sand, the injection flow rate of the solution plays a major role in the migration of the colloid, the size of the porous medium grains plays a secondary role, and then followed by the initial concentration of the solution (that is, flow rates > grain size > concentration).

(4) By calculating the total DLVO potential energy between the colloid and the quartz sand, it is inferred that there is a non-DLVO force—capillary force effect on the colloid retention phenomenon appearing in this study.

The experimental results of this study would be useful for the environmental decision-makers to prevent water resource contamination migrate through the carrier band of colloid in the water flow.

Data availability statement

The raw data supporting the conclusion of this article will be made available by the authors, without undue reservation.

Author contributions

LZ: analyzing data, and drafting the manuscript. JZ: designing experiments. QZ: revising and editing the manuscript. JS and YC: development or design of methodology. AZ: analyzing conclusions.

Funding

This work was supported by Platform Open Fund of China Institute for Radiation Protection-Key Laboratory of Radiation Environment and Health: National of Environmental Protection

and the National Natural Science Foundation of China (Grant No. 42272295).

Acknowledgments

The authors are thankful to the China Institute for Radiation Protection for their help in providing the laboratory.

Conflict of interest

The authors declare that the research was conducted in the absence of any commercial or financial relationships that could be construed as a potential conflict of interest.

Publisher's note

Supplementary material

The Supplementary Material for this article can be found online at: https://www.frontiersin.org/articles/10.3389/fenvs.2022.1058351/full#supplementary-material

References

Awan, F. U. R., Al-Yaseri, A., Akhondzadeh, H., Iglauer, S., and Keshavarz, A. (2022). Influence of mineralogy and surfactant concentration on zeta potential in intact sandstone at high pressure. *J. Colloid Interface Sci.* 607, 401–411. doi:10.1016/j.jcis.2021.08.015

Bradford, S. A., and Kim, H. (2010). Implications of cation exchange on clay release and colloid-facilitated transport in porous media. *J. Environ. Qual.* 39 (6), 2040–2046. doi:10.2134/jeq2010.0156

Bradford, S. A., and Torkzaban, S. (2008). Colloid transport and retention in unsaturated porous media: a review of interface-, collector-, and pore-scale processes and models. *Vadose zone J.* 7, 667–681. doi:10.2136/vzj2007.0092

Chowdhury, I., Hong, Y., Honda, R. J., and Walker, S. L. (2011). Mechanisms of tio2 nanoparticle transport in porous media: role of solution chemistry, nanoparticle concentration, and flowrate. *J. Colloid Interface Sci.* 360 (2), 548–555. doi:10.1016/j.jcis.2011.04.111

Chrysikopoulos, C. V., and Syngouna, V. I. (2012). Attachment of bacteriophages MS2 and ΦX174 onto kaolinite and montmorillonite: Extended-DLVO interactions. *Colloids Surfaces B Biointerfaces* 92, 74–83. doi:10.1016/j.colsurfb.2011.11.028

Fountouli, T. V., and Chrysikopoulos, C. V. (2020). Effect of clay colloid particles on formaldehyde transport in unsaturated porous media. *Water* 12, 3541. doi:10.3390/w12123541

Gao, B., Steenhuis, T. S., Zevi, Y., Morales, V. L., Nieber, J. L., Richards, B. K., et al. (2008). Capillary retention of colloids in unsaturated porous media. *Water Resour. Res.* 44 (4), 135–157. doi:10.1029/2006WR005332

Genuchten, M. T. V. (1980). A closed-form equation for predicting the hydraulic conductivity of unsaturated soils. *Soil Sci. Soc. Am. J.* 44 (5), 892–898. doi:10.2136/sssaj1980.03615995004400050002x

Gregory, J. (1981). Approximate expressions for retarded van der waals interaction. *J. Colloid Interface Sci.* 83 (1), 138–145. doi:10.1016/0021-9797(81)90018-7

Grolimund, D., Borkovec, M., Barmettler, K., and Sticher, H. (1996). Colloid-facilitated transport of strongly sorbing contaminants in natural porous media: a laboratory column study. *Environ. Sci. Technol.* 30 (10), 3118–3123. doi:10.1021/es960246x

Haque, M. E., Shen, C., Li, T., Chu, H., Wang, H., Li, Z., et al. (2017). Influence of biochar on deposition and release of clay colloids in saturated porous media. *J. Environ. Qual.* 46 (6), 1480–1488. doi:10.2134/jeq2017.06.0223

Hogg, R., Cahn, D. S., Healy, T. W., and Fuerstenau, D. W. (1966). Diffusional mixing in an i-deal system. *Chem. Eng. Sci.* 21 (11), 1025–1038. doi:10.1016/0009-2509(66)85098-4

Israelachvili, J. N. (1992). *Intermolecular and surface forces*. 2nd ed. London, U. K: Academic.

Israelachvili, J. N. (2011). *Intermolecular and surface forces*. 3rd ed. London: Academic, 275.

Kim, S. B., Corapcioglu, M. Y., and Kim, D. J. (2003). Effect of dissolved organic matter and bacteria on contaminant transport in riverbank filtration. *J. Contam. Hydrol.* 66 (1/2), 1–23. doi:10.1016/S0169-7722(03)00025-1

Knappenberger, T., Flury, M., Mattson, E. D., and Harsh, J. B. (2014). Does water content or flow rate control colloid transport in unsaturated porous media? *Environ. Sci. Technol.* 48, 3791–3799. doi:10.1021/es404705d

Lenhart, J. J., and Saiers, J. E. (2002). Transport of silica colloids through unsaturated porous media: experimental results and model comparisons. *Environ. Sci. Technol.* 36 (4), 769–777. doi:10.1021/es0109949

Liu, R., Liu, F., Dong, Y., Jiao, J., Rm, E., and Zhu, L. (2022). Microplastic contamination in lacustrine sediments in the Qinghai-Tibet Plateau: Current status and transfer mechanisms. *China Geol.* 5, 421–428. doi:10.31035/cg2022030

Loveland, J. P., Ryan, J. N., Amy, G. L., and Harvey, R. W. (1996). The reversibility of virus attachment to mineral surfaces. *Colloids Surfaces A Physicochem. Eng. Aspects* 107, 205–221. doi:10.1016/0927-7757(95)03373-4

Ma, J., Guo, H., Weng, L., Li, Y., Lei, M., and Chen, Y. (2018). Distinct effect of humic acid on ferrihydrite colloid-facilitated transport of arsenic in saturated media at different pH. *Chemosphere* 212 (12), 794–801. doi:10.1016/j.chemosphere.2018.08.131

Mitropoulou, P. N., Syngouna, V. I., and Chrysikopoulos, C. V. (2013). Transport of colloids in unsaturated packed columns: role of ionic strength and sand grain size. *Chem. Eng. J.* 232, 237–248. doi:10.1016/j.cej.2013.07.093

Ohnuki, T., Kozai, N., Sakamoto, F., Ozaki, T., Francis, A. J., Suzuki, Y., et al. (2010). Associati-on of actinides with microorganisms and clay: implications for radionuclide migration fro-m waste-repository sites. *Geomicrobiol. J.* 27 (3), 225–230. doi:10.1080/01490450903456715

Olphen, V., and Fripiar, J. J. (1979). *Data handbook for clay materials and other non-metallic minerals*. Oxford: Pergamon Press. doi:10.1346/CCMN.1980.0280215

Saiers, J. E., and Lenhart, J. J. (2003a). Colloid mobilization and transport within unsaturated porous media under transient-flow conditions. *Water Resour. Res.* 39 (1), SBH 10–11. doi:10.1029/2002WR001370

Saiers, J. E., and Lenhart, J. J. (2003b). Correction to "Ionic-strength effects on colloid transport and interfacial reactions in partially saturated porous media". *Water Resour. Res.* 41 (9), 149–163. doi:10.1029/2004WR003917

Schoonheydt, R. A., Johnston, C. T., and Bergaya, F. (2018). Clay minerals and their surfaces. *Dev. Clay Sci.* 9, 1–21. doi:10.1016/B978-0-08-102432-4.00001-9

Shang, J., Flury, M., Chen, G., and Zhuang, J. (2008). Impact of flow rate, water content, and capillary forces on *in situ* colloid mobilization during infiltration in unsaturated sediments. *Water Resour. Res.* 44 (6), 376–380. doi:10.1029/2007WR006516

Shehata, A. M., and Nasr-El-Din, H. A. (2015). "Zeta potential measurements: impact of salinity on sandstone minerals," in SPE International Symposium on Oilfield Chemistry, Texas, USA, April 13-15, 1–17. doi:10.2118/173763-MS

Sposito, G., Skipper, N. T., Sutton, R., Park, S. h., Soper, A. K., and Greathouse, J. A. (1999). Surface geochemistry of the clay minerals. *Proc. Natl. Acad. Sci. U. S. A.* 96 (7), 3358–3364. doi:10.1073/pnas.96.7.3358

Syngouna, V. I., and Chrysikopoulos, C. V. (2013). Cotransport of clay colloids and viruses in water saturated porous media. *Colloids Surfaces A Physicochem. Eng. Aspects* 416, 56–65. doi:10.1016/j.colsurfa.2012.10.018

Syngouna, V. I., and Chrysikopoulos, C. V. (2016). Cotransport of clay colloids and viruses through water-saturated vertically oriented columns packed with glass beads: gravity effects. *Sci. Total Environ.* 545-546, 210–218. doi:10.1016/j.scitotenv.2015.12.091

Syngouna, V. I., and Chrysikopoulos, C. V. (2015). Experimental investigation of virus and clay particles cotransport in partially saturated columns packed with glass beads. *J. Colloid Interface Sci.* 440 (440), 140–150. doi:10.1016/j.jcis.2014.10.066

Syngouna, V. I., Chrysikopoulos, C. V., Kokkinos, P., Tselepi, M. A., and Vantarakis, A. (2017). Cotransport of human adenoviruses with clay colloids and TiO_2 nanoparticles in saturated porous media: effect of flow velocity. *Sci. Total Environ.* 598, 160–167. doi:10.1016/j.scitotenv.2017.04.082

Syngouna, V. I., and Chrysikopoulos, C. V. (2011). Transport of biocolloids in water saturated columns packed with sand: effect of grain size and pore water velocity. *J. Contam. Hydrol.* 126 (3-4), 301–314. doi:10.1016/j.jconhyd.2011.09.007

Tokunaga, T. K. (2011). Physicochemical controls on adsorbed water film thickness in unsatu-rated geological media. *Water Resour. Res.* 47, W08514. doi:10.1029/2011WR010676

Torkzaban, S., Bradford, S. A., Genuchten, M., and Walker, S. L. (2008). Colloid transport in unsaturated porous media: the role of water content and ionic strength on par-ticle straining. *J. Contam. Hydrol.* 96 (1-4), 113–127. doi:10.1016/j.jconhyd.2007.10.006

Torok, J., Buckley, L. P., and Woods, B. L. (1990). The separation of radionuclide migration by solution and particle transport in soil. *J. Contam. Hydrol.* 6 (2), 185–203. doi:10.1016/0169-7722(90)90045-I

Tufenkji, N., and Elimelech, M. (2004). Correlation equation for predicting single-collector efficiency in physicochemical filtration in saturated porous media. *Environ. Sci. Technol.* 38 (2), 529–536. doi:10.1021/es034049r

Um, W., and Papelis, C. (2002). Geochemical effects on colloid-facilitated metal transport through zeolitized tuffs from the Nevada Test Site. *Environ. Geol.* 43 (1-2), 209–218. doi:10.1007/s00254-002-0646-4

Vilks, P., and Baik, V. (2001). Laboratory migration experiments with radionuclides and natural colloids in a granite fracture. *J. Contam. Hydrol.* 47 (2-4), 197–210. doi:10.1016/S0169-7722(00)00149-2

Vinogradov, J., and Jackson, M. D. (2015). Zeta potential in intact natural sandstones at elevated t-emperatures. *Geophys. Res. Lett.* 42, 6287–6294. doi:10.1002/2015GL064795

Walshe, G. E., Pang, L., Flury, M., Close, M. E., and Flintoft, M. (2010). Effects of pH, ionic strength, dissolved organic matter, and flow rate on the co-transport of ms2 bacteriophages with kaolinite in gravel aquifer media. *Water Res.* 44 (4), 1255–1269. doi:10.1016/j.watres.2009.11.034

Wang, C., Bobba, A. D., Attinti, R., Shen, C., Lazouskaya, V., Wang, L. P., et al. (2012). Retention and transport of silica nanoparticles in saturated porous media: effect of concentration and particle size. *Environ. Sci. Technol.* 46 (13), 7151–7158. doi:10.1021/es300314n

Won, J., Wirth, X., and Burns, S. E. (2019). An experimental study of cotransport of heavy metals with kaolinite colloids. *J. Hazard. Mat.* 373, 476–482. doi:10.1016/j.jhazmat.2019.03.110

Won, J., Kim, T., Kang, M., Choe, Y., and Choi., H. (2021). Kaolinite and illite colloid transport in saturated porous media. *Colloids Surfaces A Physicochem. Eng. Aspects* 626 (80), 127052. doi:10.1016/j.colsurfa.2021.127052

Xiao, Y., Hao, Q., Zhang, Y., Zhu, Y., Yin, S., Qin, L., et al. (2022a). Investigating sources, driving forces and potential health risks of nitrate and fluoride in groundwater of a typical alluvial fan plain. *Sci. Total Environ.* 802, 149909. doi:10.1016/j.scitotenv.2021.149909

Xiao, Y., Liu, K., Hao, Q., Li, Y., Xiao, D., and Zhang, Y. (2022b). Occurrence, controlling factors and health hazards of fluoride-enriched groundwater in the lower flood plain of yellow river, northern China. *Expo. Health* 14, 345–358. doi:10.1007/s12403-021-00452-2

Xiao, Y., Liu, K., Hao, Q., Xiao, D., Zhu, Y., Yin, S., et al. (2022c). Hydrogeochemical insights into the signatures, Genesis and sustainable perspective of nitrate enriched groundwater in the piedmont of Hutuo watershed, China. *CATENA* 212, 106020. doi:10.1016/j.catena.2022.106020

Yang, Y., Saiers, J. E., and Barnett, M. O. (2013). Impact of interactions between natural organic matter and metal oxides on the desorption kinetics of uranium from heterogeneous colloidal s-uspensions. *Environ. Sci. Technol.* 47 (6), 2661–2669. doi:10.1021/es304013r

Zevi, Y., Dathe, A., McCarthy, J. F., Richards, B. K., and Steenhuis, T. S. (2005). Distribution of colloid particles onto interfaces in partially saturated sand. *Environ. Sci. Technol.* 39 (18), 7055–7064. doi:10.1021/es048595b

Zhang, P., Bai, B., Jiang, S., Wang, P., and Li, H. (2016). Transport and deposition of suspended particles in saturated porous media: effect of hydrodynamic forces and pore structure. *Water Supply* 16 (4), 951–960. doi:10.2166/ws.2016.011

Zhang, Q., Hassanizadeh, S. M., Liu, B., Schijven, J. F., and Karadimitriou, N. K. (2014). Effect of hydrophobicity on colloid transport during two-phase flow in a micromodel. *Water Resour. Res.* 50 (10), 7677–7691. doi:10.1002/2013WR015198

Zhang, Q., and Hassanizadeh, S. M. (2017). The role of interfacial tension in colloid retention and remobilization during two-phase flow in a polydimethylsiloxane micro-model. *Chem. Eng. Sci.* 168, 437–443. doi:10.1016/j.ces.2017.04.038

Zhang, Q., Yu, Y., and Cui, Y. (2020). The role of particle size and molar ratio of ca2+/na+ in the retention and remobilization of colloids in saturated porous media. *Arab. J. Geosci.* 13 (6), 273. doi:10.1007/s12517-020-5220-4

frontiers | Frontiers in Environmental Science

TYPE Original Research
PUBLISHED 31 October 2022
DOI 10.3389/fenvs.2022.1053362

OPEN ACCESS

EDITED BY
Lichun Wang,
Tianjin University, China

REVIEWED BY
Shujun Ye,
Nanjing University, China
Litang Hu,
Beijing Normal University, China

*CORRESPONDENCE
Haipeng Guo,
pengfei7971@sohu.com

SPECIALTY SECTION
This article was submitted to Freshwater Science,
a section of the journal
Frontiers in Environmental Science

RECEIVED 25 September 2022
ACCEPTED 18 October 2022
PUBLISHED 31 October 2022

CITATION
Guo H, Hao A, Li W, Zang X, Wang Y, Zhu J, Wang L and Chen Y (2022), Land subsidence and its affecting factors in Cangzhou, North China Plain.
Front. Environ. Sci. 10:1053362.
doi: 10.3389/fenvs.2022.1053362

Land subsidence and its affecting factors in Cangzhou, North China Plain

Haipeng Guo[1,2]*, Aibing Hao[1,2], Wenpeng Li[1,2], Xisheng Zang[1,2], Yunlong Wang[1,2], Juyan Zhu[1,2], Liya Wang[3] and Ye Chen[4]

[1]Hebei Cangzhou Groundwater and Land Subsidence National Observation and Research Station, Cangzhou, China, [2]China Institute of Geo-Environment Monitoring, Beijing, China, [3]Beijing Institute of Geo-Environment Monitoring, Beijing, China, [4]School of Water Resources and Environment, China University of Geosciences, Beijing, China

Land subsidence is a typical geo-hazard in Cangzhou, North China Plain, having caused severe damages to transportation networks, public utilities, and other civil infrastructures. The mechanism of land subsidence and its affecting factors were revealed by theoretical model analysis, and doing geotechnical tests and monitoring of soil deformation as well as groundwater level. Theoretical analysis shows that groundwater withdrawal from both unconfined and confined aquifers can lead to land subsidence. Land subsidence of the Cangzhou Plain is mainly caused by the exploitation of deep confined groundwater. Geotechnical tests show a general trend that the compressive modulus increases with the increase of soil depth. The strata of the Upper Pleistocene and Holocene are mostly normally consolidated and partially under-consolidated, which are prone to produce large compression after pumping. Land subsidence in the Cangzhou Plain has a strong hysteresis because of seepage consolidation and creep. The deformation characteristics of strata change at different depth. The shallow aquifers are mainly elastic deformation. The area of severe land subsidence in the Cangzhou Plain is closely related to rainfall, mainly because the large amount of water are used for agricultural irrigation. InSAR results show a sudden change in regional subsidence across the Cangdong fault, which is caused by the difference in the thickness of Quaternary sediments and the difference in the deep confined groundwater level.

KEYWORDS

Cangzhou, land subsidence, soil deformation, groundwater level, confined aquifer

1 Introduction

Land subsidence, leading to the decrease in ground elevation within a certain area, is a geological phenomenon that the underground loose rock layers are consolidated and compressed due to factors such as extraction of underground fluids. As a geological disaster, land subsidence has serious negative effects in many countries and regions in the world (Hu et al., 2004; Ovando-Shelley et al., 2007; Motagh et al., 2008; Pacheco-Martínez et al., 2013). The North China Plain (NCP) is the largest affected area with the fastest

subsiding rate in China. In recent decades, soil deformation mechanism with the influence of groundwater level change in aquifer systems has received great attention from scholars. Researches mainly focus on the rheological characteristics of soil layers, especially clay layers, and the quantitative research on soil stress-strain relationship. He et al. (2020) designed physical model tests to study the deformation characteristics of sand and clay layers and the change of pore water pressure caused by groundwater recharge and discharge, and proposed three groundwater development models that were conducive to alleviate the development of land subsidence. With the deepening of researches on land subsidence, more and more researchers gradually realized that the soil compression induced by water pumping contains a certain proportion of rheological deformation, and not only clayey soil may creep (Sivasithamparam et al., 2015; Sexton et al., 2016), but also sand or gravel aquifers may creep (Enomoto et al., 2015; Zhu et al., 2018). Test results showed that the creep deformation of sand could reach 10% of the total deformation under monotonic load (Augustesen et al., 2004). Terzaghi's consolidation theory is a simple elastic deformation model, which has been widely used in soil compression analysis due to the simple mechanism and the linear characteristics of the governing equations. If the field monitoring and laboratory test data of soil deformation can be obtained, a more realistic soil deformation constitutive model may be established and used for land subsidence simulation and prediction (Gambolati and Teatini, 2015). Tsai and Hsu (2018) proposed a visco-elasto-plastic (VEP) model, which consisted of a visco-elastic model and a visco-plastic model, and the use of the visco-plastic model was controlled by a single-pole double-throw (SPDT) switch. It has been verified that the calculation results of this model have a small relative error. Based on the Euler formula, Zhuang et al. (2020) obtained the analytical solution of the elastic deformation of an overconsolidated aquitard driven by the change of the groundwater level in the aquifer, and used it to evaluate the vertical hydraulic conductivity and elastic skeletal specific storage of a 35.54 m thick aquitard in Shanghai. Results showed that the analytical method could quantitatively explain the hysteresis characteristics of land subsidence and effectively evaluate the hydraulic parameters of overconsolidated aquitards. Land subsidence caused by pumping and drainage is actually a coupling problem of seepage field and stress field. In recent years, researchers have explored the numerical calculation methods of fully coupled models (Tsai, 2015; Asadi and Ataie-ashtiani, 2016), and have successfully applied them to the simulation and prediction of land subsidence in Venice, Las Vegas, Shanghai, *etc.* (Hernandez-marin and Burbey, 2012; Castelletto et al., 2015; Ye et al., 2016). Pham et al. (2019) developed the program module SUB$^+$ based on the elastic mechanics theory of porous media, which could realize fully coupled water-stress simulation.

Land subsidence is a typical geo-hazard in the Cangzhou Plain. The strata in the Cangzhou Plain are mainly composed of clay and silty clay with relatively high plasticity, it thus easy to form permanent subsidence (Guo et al., 2015). The occurrence and development of land subsidence in the Cangzhou Plain are closely related to the history of groundwater exploitation. Due to the complex affecting factors of land subsidence, the development rate and scope of land subsidence have great differences in different spaces and times. From the 1970s to the 1990s, the demand for water resources for industrial and agricultural development in the Cangzhou Plain increased with years. Due to serious over-exploitation and slow replenishment, the deep groundwater level dropped seriously, forming a large area of deep groundwater depression cones and induced land subsidence disasters. The substantial increase in groundwater extraction in small and medium-sized cities and rural areas caused land subsidence to expand from urban to rural areas and to consolidate regionally. In the 21st century, land subsidence in the urban area of Cangzhou had been gradually controled due to the closure of groundwater wells, but it was still developing in other areas.

With the advancement of science and technology, monitoring methods of land subsidence have been improved, which has continuously expanded the depth and breadth of land subsidence research. Since the 1990s, the synthetic aperture radar interferometry (InSAR) technology has become increasingly mature and has become an important technical means to monitor the temporal and spatial changes of regional land subsidence (Khan et al., 2013; Tomas et al., 2014; Amighpey and Arabi, 2016; Castellazzi et al., 2016; Chaussard et al., 2017). InSAR, GPS, leveling, borehole extensometers and other ground and underground monitoring technologies complement each other, and have become important components of the land subsidence monitoring system in the North China Plain as well as the Cangzhou Plain. The main objective of this paper is to put forward new understandings on the mechanism of land subsidence in Cangzhou Plain, and provide reference for the prevention and control of land subsidence in the future. At first, a five-layer conceptual model is established to investigate the characteristics and of soil deformation driven by groundwater level variations. Multiple correlation analysis is performed to explore the relationship among land subsidence, groundwater level and groundwater extraction. Based on geotechnical tests, the influence of soil mechanical parameters such as compression modulus and soil consolidation degree on land subsidence are estimated and discussed. Then, we rely on water well and extensometer data to analyze the deformation characteristics of strata with different buried depths in the subsidence center of the central urban area. Finally, we discuss the relationship between rainfall and land subsidence, and the control effect of faults on land subsidence.

2 Study area

The Cangzhou Plain, the plain area of Cangzhou City, Hebei Province, is located in the central and eastern part of the NCP

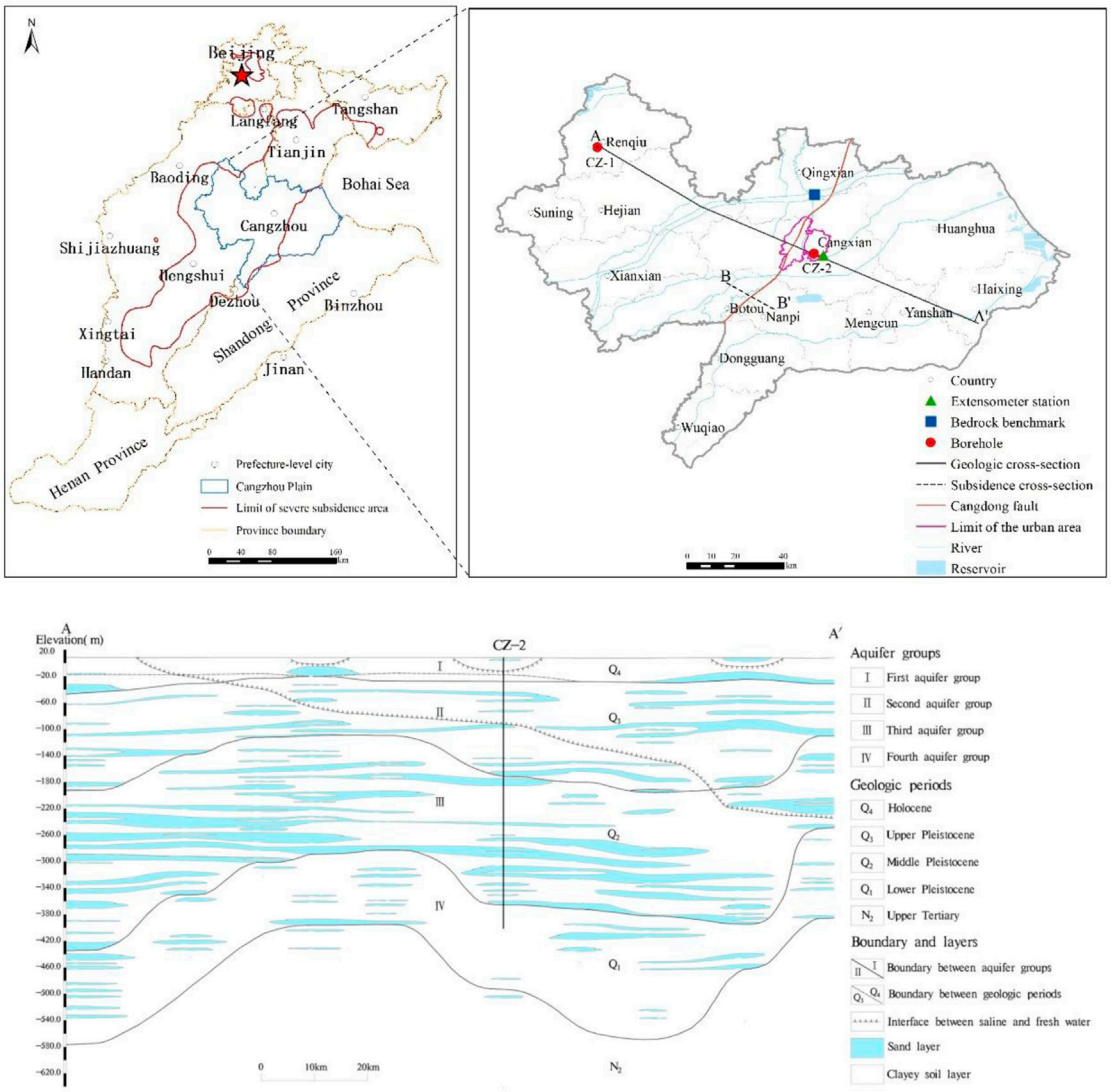

FIGURE 1
Sketch map of the North China Plain and the Cangzhou Plain showing distribution of the major land subsidence areas, and a hydrogeological cross section A-A′.

and adjacent to Bohai Sea (see Figure 1). Cangzhou Plain is about 181 km from east to west and 165 km from north to south, with a total area of 14,000 km^2 (the central urban area is 195 km^2), accounting for 10% of the total area of the NCP. The terrain in this region is low and flat, and inclines from southwest to northeast, with a slope of 0.07‰–0.13‰. The ground elevation is generally 2–15 m, and the ground elevation along the coastline in the east is 1–4 m. This region belongs to a warm temperate continental monsoon climate, with an average annual rainfall of about 600 mm. The rainfall is unevenly distributed throughout the year with great inter-annual variation. Generally, the flood season starts from June to September. The rainfall during the flood season accounts for about 75% of the annual rainfall. Due to limited precipitation and the construction of upstream reservoirs, most rivers in the Cangzhou Plain have been seasonally or even dried up. Therefore, groundwater has been the main source of water for agriculture, industry and domestic use.

The Cangzhou Plain contains two distinct hydrogeological settings in Quaternary sediments: an alluvial plain with many abandoned river channels and a coastal plain zone around the Bohai Sea (Foster et al., 2004). The main strata in this region are loose unconsolidated Quaternary sediments with the thickness ranging from 350 m to over 550 m, mainly composed of sand, silt and clay. The main type of groundwater is pore water in loose Quaternary sediments. Aquifer system is composed with multiple sand aquifers which separated by extensive and thick

aquitards of silt or clay (Figure 1). Freshwater aquifers of the aquifer system are overlaid by saline/brackish aquifers, increasing in thickness from tens of meters in the west to over 200 m in the coastal areas (Figure 1). The stratigraphy can be divided into four aquifer groups. The bottom depth of the first aquifer group is 20–30 m, which roughly correspond to the bottom boundary of the Holocene (Q_4) and the upper part of the Upper Pleistocene (Q_3). The first aquifer group has good conditions for precipitation infiltration, runoff and recharge. The bottom depth of the second aquifer group is 120–170 m, corresponding to the bottom boundary of Q_3. The vertical infiltration recharge condition is poor, and the underground runoff is stagnant. The lower boundary of the third aquifer is located between 250 and 350 m underground, corresponding to the bottom boundary of Middle Pleistocene (Q_2). The third aquifer group has poor recharge conditions, which is the main exploitation layer of deep confined groundwater in the Cangzhou Plain. The water abundance (represented by yield of single well) in the central and western regions of Cangzhou is generally between 1,000 m^3/d and 2000 m^3/d, the water abundance in the central and eastern regions is generally between 500 m^3/d and 1,000 m^3/d, and the water abundance in some regions of Huanghua is less than 500 m^3/d. The bottom boundary of the fourth aquifer group is buried at a depth of 350–550 m, with a local depth of 600 m, corresponding to the bottom boundary of Lower Pleistocene (Q_1). The permeability and water richness are poor, and the lateral runoff supply is weak. The first and second aquifer groups have unconfined or semi-confined hydraulic properties, and the third and fourth aquifer groups have confined hydraulic properties.

3 Materials and methods

3.1 Theoretical models

3.1.1 The influence of water level drop on land subsidence

The principle of effective stress by Terzaghi can be described as following (Craig, 2004):

$$\sigma = \sigma' + \mathrm{u}, \tag{1}$$

where σ is the total stress, σ' is effective stress, and u is the pore water pressure.

When no tectonic stresses are present, the total stress can be expressed as the sum of the loading on the soil surface and the geostatic stress (Poland and Davis 1969; Zeitoun and Wakshal 2013).

$$\sigma = \sigma_{load} + \gamma_m d_m + \gamma_s d_s, \tag{2}$$

$$\gamma_m = \gamma_g(1 - \mathrm{n}) + \gamma_w n_w, \tag{3}$$

$$\gamma_s = \gamma_g(1 - \mathrm{n}) + \gamma_w n, \tag{4}$$

and the hydrostatic stress can be expressed as following:

$$u = d_s \gamma_w, \tag{5}$$

where γ_m is the unit weight of moist sediments above the water table; γ_g is the unit weight of sediments grains; γ_s is the unit weight of saturated sediments below the water table; γ_w is the unit weight of water; n is the porosity; n_w is the moisture content of sediments in the unsaturated zone, as a fraction of total volume; d_m is the depth below land surface in the unsaturated-zone interval, land surface $z = 0$ to the water table $z = z_{wt}$; and d_s is the thickness of interest in the saturated zone.

Figures 2, 3 show a typical aquifer structure, one unconfined aquifer and two confined aquifers separated by two confining units, respectively. With Eqs 1–4, the variation of effective stresses in response to water level changes in the unconfined and confined aquifers can be summarized in Table 1 (Poland and Davis, 1969; Zhou, 2012; Guo et al., 2015).

When water-level drops in the unconfined aquifer, the land subsidence can be calculated as:

$$S = S_C - S_r, \tag{6}$$

$$S_C = (1 - n + n_w)\gamma_w \left(\frac{\Delta h_{wt}^2}{2E_1} + \frac{(H_1 - |\Delta h_{wt}|)|\Delta h_{wt}|}{E_1} + \frac{H_z|\Delta h_{wt}|}{2E_2} \right), \tag{7}$$

$$S_r = (n - n_w)\gamma_w \left(\frac{(H_2 - H_z)|\Delta h_{wt}|}{2E_{2r}} + \sum_{i=3}^{5} \frac{(H_i|\Delta h_{wt}|}{E_{ir}} \right), \tag{8}$$

where E_i is the modulus of compression, which is equal to the reciprocal of coefficient of volume compressibility, and E_{ir} is the modulus of resilience. Note that there exists a point Z (Figure 2) where the change of effective stress is zero, and the distance from point A to Z is calculated as following:

$$H_z = (1 - n + n_w)H_2 \tag{9}$$

Figure 2 indicates the relationships between geostatic, hydrostatic and effective stresses and the changes after a water table drop of 40 m in the unconfined aquifer when fluid-pressure equilibrium is reached. The effective stress in the unconfined aquifer increases 29.2 m and that in confined aquifers and confining unit 2 decreases by only 10.8 m. The point Z is calculated as 0.73 H_2 below the top of confining unit 1.

When water levels in the confined aquifers fall, the land subsidence can be calculated as following:

$$S_C = \gamma_w \left(\frac{H_2|\Delta h_{C1}|}{2E_2} + \frac{H_3|\Delta h_{C1}|}{E_3} + \frac{H_4(|\Delta h_{C1}| + |\Delta h_{C2}|)}{2E_4} + \frac{H_5|\Delta h_{C2}|}{E_5} \right). \tag{10}$$

Figure 3 indicates variation of geostatic, hydrostatic and effective stresses as water head drops 40 m in confined aquifer 1 and declines 80 m in confined aquifer 2. After the water head

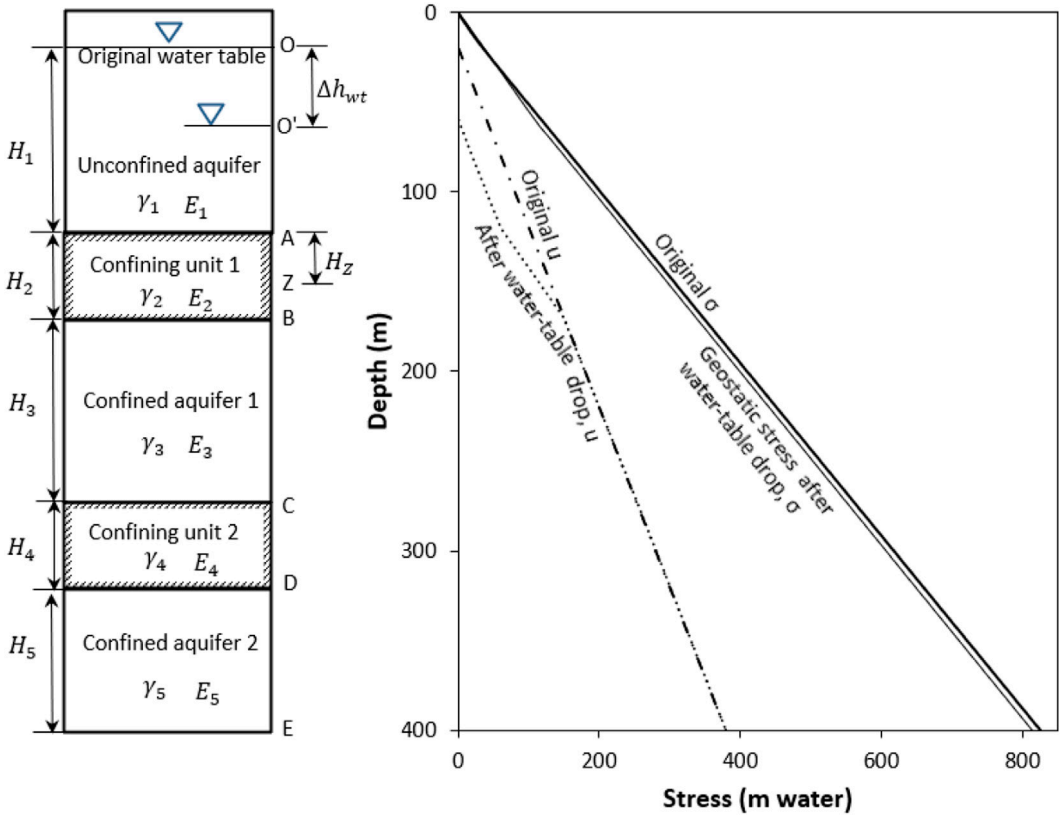

FIGURE 2
Stress diagrams for a water table drop of 40 m in an unconfined aquifer (γ_g = 2.6 × $10^4 N/m^3$; γ_w = 9.8 × $10^3 N/m^3$; n = 0.35; n_w = 0.08).

decreases, the effective stress of the unconfined aquifer remains unchanged, and the effective stress of the confined aquifer 1 and confined aquifer 2 increases by 40 m and 80 m, respectively. The effective stress of confining unit 1 and confining unit 2 increases by 20 m and 60 m on average, respectively.

3.1.2 Pumping induced soil deformation in a confined aquifer

When a well is pumped in a completely confined aquifer, the water is obtained from the elastic or specific storage of the aquifer. The elastic storage is water that is released from storage by the expansion of the water as pressure in the aquifer is reduced and by expulsion as the pore space is reduced as the aquifer compacts. The drawdown s can be calculated as following (Fetter, 2001):

$$s = \frac{Q}{4\pi T} W(u). \tag{11}$$

When $u \leq 0.05$, Eq. 11 can be simplified as:

$$s = \frac{Q}{4\pi T} ln \frac{2.25Tt}{r^2 S}, \tag{12}$$

where s is the drawdown (L), Q is the constant pumping rate (L^3/T), T is the aquifer transmissivity (L^2/T), t is the time since pumping began (T), r is the radial distance from the pumping well (L), S is the aquifer storativity (dimensionless), and $u = r^2 S/4Tt$.

Then the following equation can be obtained:

$$\frac{\Delta M}{M_0} = \alpha \bullet u \, ln \frac{0.563}{u}, \tag{13}$$

where $\alpha = \gamma_w Qt/\pi ESr^2$, ΔM is the compression amount of the aquifer, M_0 is the original aquifer thickness, and E is the modulus of compression.

One can easily see from Eq. 13 that the compression amount of the aquifer increases with t, and decreases with r, E and S. The calculated data for the dimensionless compression amount of the aquifer, $\Delta M/M_0$, as a function of 1/u, at an observation well are plotted in Figure 4, indicating that the aquifer compression decreases with the aquifer transmissivity.

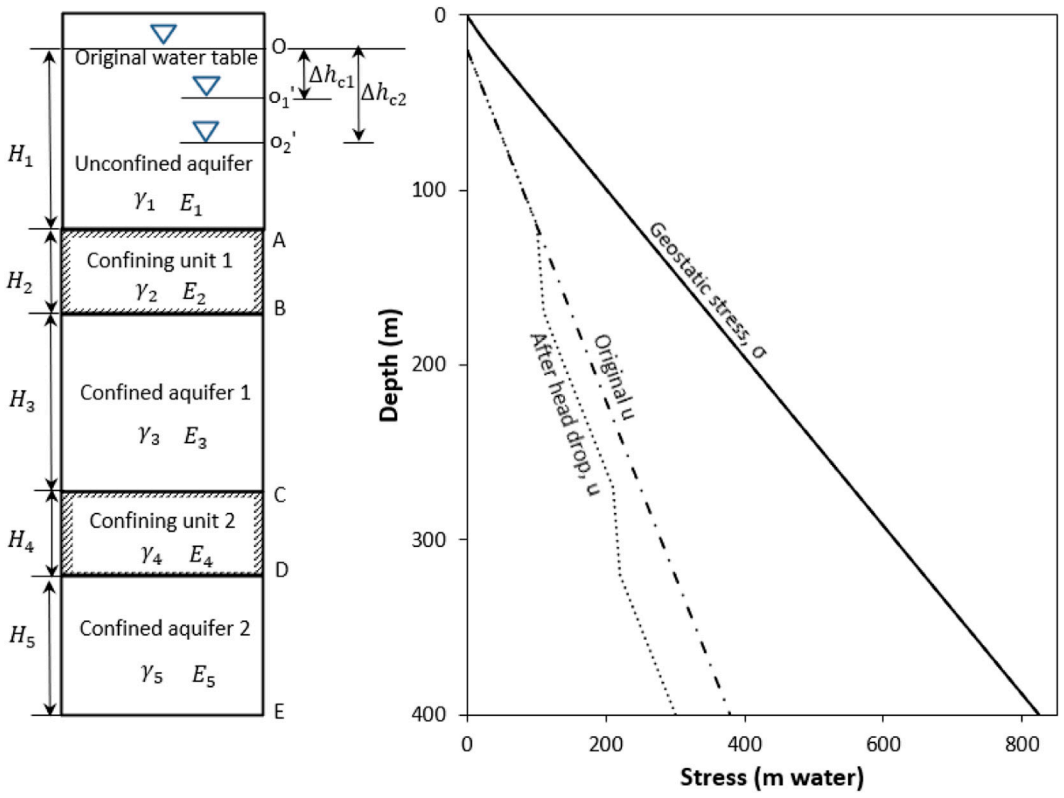

FIGURE 3
Stress diagrams for a water head drop of 40 m in confined aquifer 1, and 80 m in confined aquifer 2 ($\gamma_g = 2.6 \times 10^4 N/m^3$; $\gamma_w = 9.8 \times 10^3 N/m^3$; $n = 0.35$; $n_w = 0.08$).

TABLE 1 Variation of stresses due to water level changes in the aquifer.

Points	Variation of stresses when water levels decline		
	Geostatic pressure, $\Delta\sigma$	Pore pressure , Δu	Effective pressure, $\Delta\sigma'$
O	0	0	0
O′	$\gamma_w(n-n_w)\Delta h_{wt}$	$\gamma_w\Delta h_{wt}$	$-\gamma_w(1-n+n_w)\Delta h_{wt}$
A	$\gamma_w(n-n_w)\Delta h_{wt}$	$\gamma_w\Delta h_{wt}$	$-\gamma_w(1-n+n_w)\Delta h_{wt}$
B	$\gamma_w(n-n_w)\Delta h_{wt}$	$\gamma_w\Delta h_{c1}$	$\gamma_w(n-n_w)\Delta h_{wt}-\gamma_w\Delta h_{c1}$
C	$\gamma_w(n-n_w)\Delta h_{wt}$	$\gamma_w\Delta h_{c1}$	$\gamma_w(n-n_w)\Delta h_{wt}-\gamma_w\Delta h_{c1}$
D	$\gamma_w(n-n_w)\Delta h_{wt}$	$\gamma_w\Delta h_{c2}$	$\gamma_w(n-n_w)\Delta h_{wt}-\gamma_w\Delta h_{c2}$
E	$\gamma_w(n-n_w)\Delta h_{wt}$	$\gamma_w\Delta h_{c2}$	$\gamma_w(n-n_w)\Delta h_{wt}-\gamma_w\Delta h_{c2}$

Note: Δh_{wt}, Δh_{c1}, Δh_{c2} denote water level changes in the unconfined aquifer, confined aquifer1 and confined aquifer 2, respectively.

3.1.3 Delay in draining aquitards

Residual compaction in aquitards may continue long after the heads are initially lowered in adjacent aquifers. Riley (1969) pointed out that the time of delay in a doubly draining aquitard, representing the time required for 93% of the excess pore water within a confining unit to dissipate, could be expressed as following:

$$\tau = \frac{S_s'\left(b'/2\right)^2}{K_v'}, \tag{14}$$

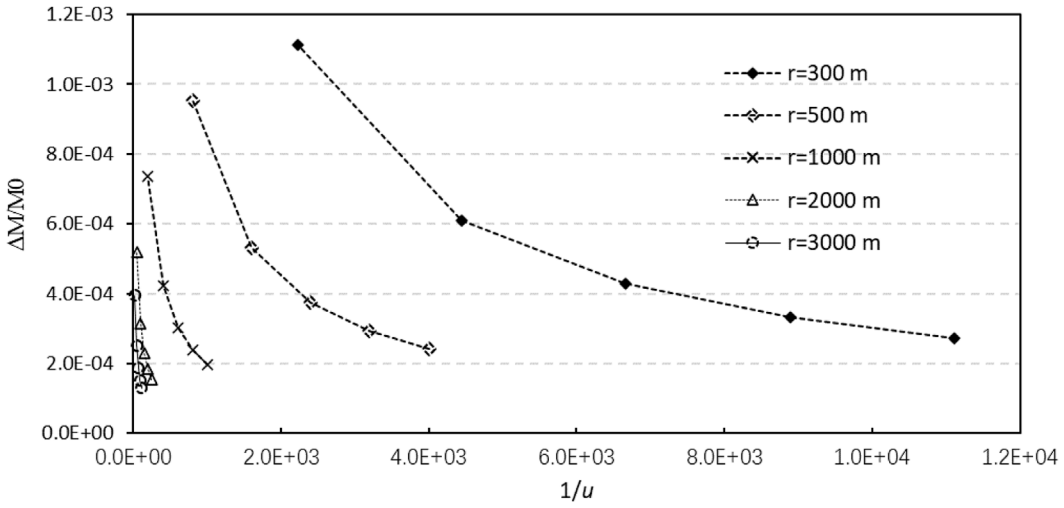

FIGURE 4
Plots of dimensionless compression $\Delta M/M_0$ as a function of $1/u$.

where b' is the thickness of the aquitard, K'_v is the vertical hydraulic conductivity, and S'_s is the specific storage of the aquitard, defined as following:

$$S'_s = S'_{sk} + S_{sw}, \tag{15}$$

$S'_{sk}$is the skeletal specific storage, and S_{sw} is the water specific storage, and $S'_s \cong S'_{skv}$ for the inelastic range of stress, where S'_{skv} is inelastic skeletal specific storage.

3.2 Multiple correlation analysis

Given variables x, y, and z, the multiple correlation coefficient can be defined as following (Schmuller, 2009):

$$R_{z,xy} = \sqrt{\frac{r_{xz}^2 + r_{yz}^2 - 2r_{xz}r_{yz}r_{xy}}{1 - r_{xy}^2}}, \tag{16}$$

where x and y are viewed as the independent variables and z is the dependent variable, and r is the correlation coefficient between every two samples. The multiple coefficient of determination (R^2 or R-square), defined as the square of the multiple correlation coefficient, is a statistical measure in a regression model that shows how well the data fits the model.

3.3 Soil sample collection and testing

Two boreholes with the drilling depth of 400 m are located in Renqiu and the central urban area, numbered CZ-1 and CZ-2, respectively (see Figure 1 for the borehole locations). Clay samples were cut 30 cm from borehole cores, placed in soil sample cylinders, sealed with wax and wrapped with tape before being sent to the laboratory. A specimen with a diameter of 61.8 mm and a height of 20 mm was prepared by a ring cutter for consolidation test, and the remaining soil was used for the determination of physical parameters. Consolidation tests were performed using an electronic compression rheometer to study the time-dependent behavior of the clayey soil during one-dimensional consolidation. The experimental data were used to estimate the preconsolidation pressure, compression modulus and consolidation coefficient of test specimens at different depths. During the consolidation tests, the lateral movement of the soil was prevented by containing the soil in a hard metal ring. A series of pressures were applied to the specimen, each held for 24 h, during which time deformation readings were taken at appropriate intervals. During the test, the room was kept at constant temperature and humidity.

4 Discussion

4.1 Variation of compressive modulus with pressure and depth

Physico-mechanical properties of ten soil specimens taken from boreholes CZ-1 and CZ-2 are shown in Table 2. The relation between compression module and applied pressures for the above ten specimen are shown in Figure 5. It can be seen from Figure 5 that with the increase of pressure, the variation of compression modulus can be divided into 4 stages. The following is an example of soil specimen CZ-2-25. In the first stage (0–160 kPa), the compression modulus under the first and second pressure increments is very small

TABLE 2 Physico-mechanical properties of ten soil specimens taken from borehole CZ-1 and CZ-2.

Specimen no.	Depth (m)	Moisture content (%)	Natural density (g/cm^3)	Void ratio	Liquid limit (%)	Plastic limit (%)	Plasticity index	Liquidity index
CZ-1-22	58.9	25.9	1.99	0.73	35.8	20.2	15.6	0.37
CZ-1-35	94.1	21.0	2.06	0.6	34.3	20.9	13.4	0.01
CZ-1-102	263.6	22.8	2.00	0.67	33.8	20.5	13.3	0.17
CZ-1-106	280.5	23.6	2.03	0.66	37.4	21.5	15.9	0.13
CZ-1-122	333.1	21.4	2.09	0.59	37.7	22.1	15.6	−0.04
CZ-2-25	68.8	20.3	2.05	0.59	26.6	16.2	10.4	0.39
CZ-2-40	98.7	19.3	2.07	0.58	36.7	19.7	17.0	−0.02
CZ-2-83	223.5	22.9	2.05	0.64	40.7	23.7	17.0	−0.05
CZ-2-113	349.4	21.1	2.02	0.64	37.4	22.2	15.2	−0.07
CZ-2-121	378.9	18.6	2.13	0.52	37.3	22.1	15.2	−0.23

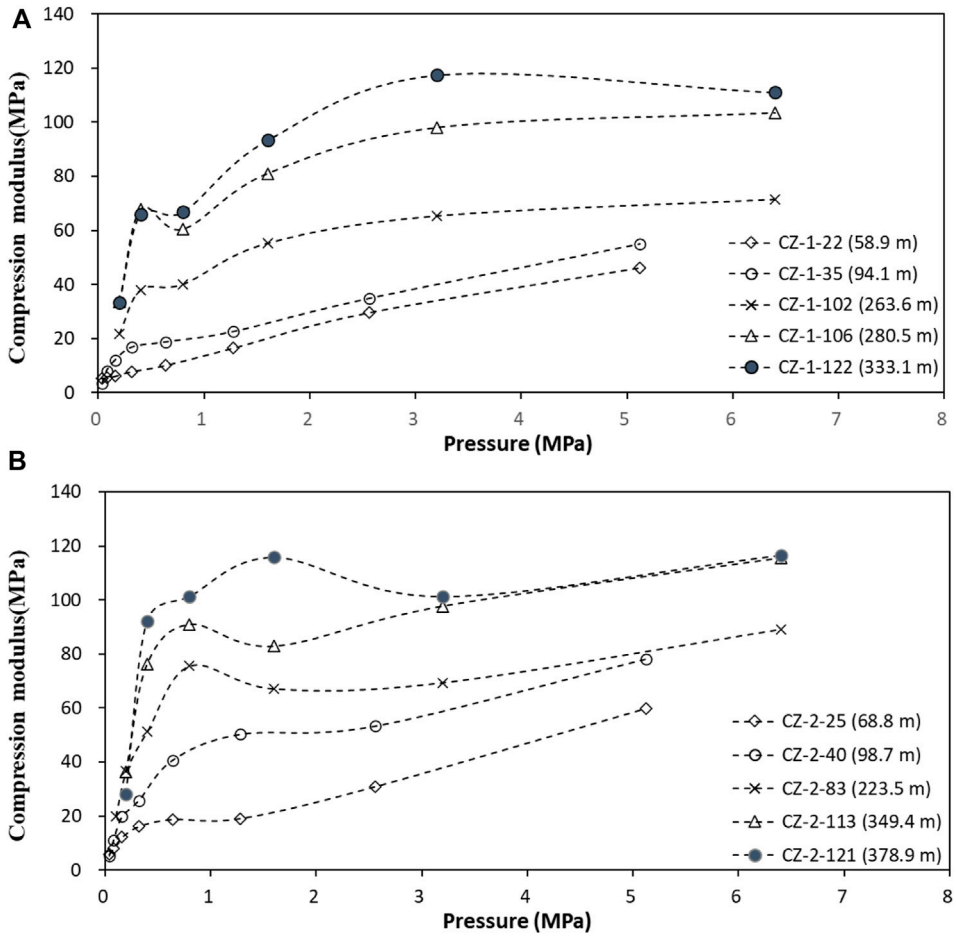

FIGURE 5
Compression modulus of soil samples at different depths in boreholes CZ-1 **(A)** and CZ-2 **(B)** as a function of pressure.

due to the stress relief generated by the sampling and sample preparation process, which is shown as a rapid increase of the compression modulus in the compression modulus-pressure curves. The second stage (about 160–640 kPa) is the compression stage before the soil structure yields, and the growth of the compression modulus in this stage is slower than that of the first stage. The third stage (about 640–1,280 kPa) is the yield stage of the soil structure, the compression modulus decreases with the increase of pressure, and the soil structure is destroyed; the pre-consolidation pressure obtained by the Casagrande method on the e-lgP curve is 767 kPa, which is within the pressure variation range at this stage. The fourth stage (after 1280 kPa) is the compression stage after the structure yields, and the compression modulus increases gradually with the increase of the load. It should be noted that sometimes no obvious structural yield stage exists due to excessive loading ratio, such as specimen CZ-1-22 in Figure 5A.

The above analysis shows that there is a stress release and compensation stage for the soil specimens in the first stage, and the compression modulus of this stage cannot represent the real situation of the soil. Therefore, the compression modulus of the second to third stages is selected to analyze the variation of the compressive modulus with depth. Figure 5 shows a general trend that in the same pressure range, the compressive modulus increases with the increase of soil depth as a whole. Due to the exploitation of groundwater, the pore pressure of the clayey soil decreases, and the soil layer is consolidated under the action of the effective stress due to its own weight. The deep soil has a higher effective stress, resulting in a higher degree of consolidation and a relatively large compression modulus.

According to Table 1, when the water table decreases, the increase of effective stress in the unconfined aquifer and the upper part of the confining 1 is much greater than the decrease of effective stress in the underlying aquifer or confining units. In general, the resilience modulus of the soil layer is much larger than the compression modulus, and the deformation modulus of the deep soil is larger than that of the shallow soil (Figure 5). Therefore, according to Eqs 6–8, the compression of the OZ section (Figure 2) caused by the drop of the phreatic level is greater than the rebound of the underlying strata, so groundwater extraction from unconfined aquifers may also lead to land subsidence.

4.2 Deep confined groundwater extraction is the major reason of land subsidence

The Cangzhou Plain is an extremely water-deficient area under the dual pressure from population and environment. Due to the lack of surface water and the large-scale distribution of saline/brackish water in shallow aquifers, the whole region mainly relies on overexploitation of deep groundwater to maintain the growing needs of national economic development. Surface water accounts for about 20% of the total utilization of water resources in Cangzhou, while groundwater accounts for the rest 80%. In the whole groundwater exploitation, deep water takes up to the ration of 70%. Deep groundwater is mainly pumped for the use of agriculture, which accounts for 66.1% in 2013 (Li, 2015). The development and utilization of deep groundwater in the Cangzhou Plain began in the mid-1960s when the groundwater could spew out of the ground surface due to the high groundwater heads. With the increase of the number of machine-operated wells and the increase of the mining volume, the groundwater level dropped, and the regional groundwater level depression cone was gradually formed. As a result, the pore water pressure of the aquifer decreased and the clayey soil layers lost water due to compaction, resulting in land subsidence. From 1976 to 1980, the average annual mining volume was 2.6×10^8 m^3, which did not require for a large amount of groundwater. From 1981 to 1995, the annual average mining volume was between 4.4×10^8 and 5.2×10^8 m^3. Rapid economic and agricultural development had greatly increased groundwater consumption. After 1996, the mining volume increased continuously. The average annual mining volume during this period was 6.5×10^8 m^3, and it reached as high as 9.2×10^8 m^3 during 2001–2003 (Li, 2015).

In recent 5 years, land subsidence in the Cangzhou Plain has gradually slowed down. The most serious land subsidence occurred in 2017, with the area of severe land subsidence (the area with subsidence rate greater than 50 mm/year) reaching 1,400 km^2. At present, the area of severe subsidence in Cangzhou covers an area of about 300 km^2, mainly distributed in the west and south of Cangzhou. The maximum cumulative subsidence of the central urban area is more than 2.5 m (Bai et al., 2022), and the urban areas of Qingxian, Renqiu, Hejian, Suning, Huanghua, Botou, and Nanpi also have great cumulative subsidence exceeding 1.0 m. Damages caused by land subsidence began to appear in the central urban area of Cangzhou City in 1972. By 2005, the accumulated subsidence in the subsidence center had exceeded 2 m. To mitigate land subsidence, local government had implemented policies since 2005 to limit the extraction of confined groundwater and to increase the supply of surface water from the Dalangdian Reservoir and the South-to-North Water Diversion Project. From 2005 to 2007, the self-provided wells were closed in the central urban area, the groundwater level recovered, and the subsidence rate was basically controlled within the range of 10–20 mm/year.

It can be seen from Table 1 that the effective stress increment of the unconfined aquifer caused by the drop of water table is smaller than that of the confined aquifer caused by equivalent drop of the confined water level. Furthermore, when the same amount of groundwater is pumped, the water level drop in the confined aquifer is greater than that in the unconfined aquifer. Also, the recharge condition of unconfined aquifers is better than

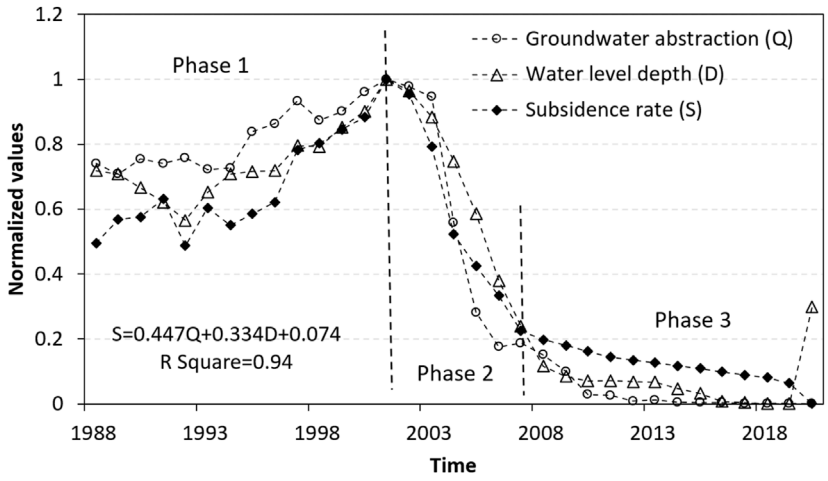

FIGURE 6
Temporal variation of groundwater abstraction and the water-level depth and subsidence rate of the subsidence center in the central urban area of Cangzhou City (All the values are normalized).

that of the confined aquifers, and the water table generally does not drop significantly. It should be noted that the Cangzhou Plain mainly relies on the extraction of deep groundwater to maintain the needs of national economic development due to the large amount of saline/brackish water distributed in the shallow aquifer. Therefore, the land subsidence in the Cangzhou Plain is mainly caused by abstraction of deep groundwater. In addition, fine clays and silts with organic matter in confined aquifers typically demonstrates high compressibility and storativity and low transmissivity, which is conductive to trigger the land subsidence (Figure 4). Hence serious land subsidence has occurred in the Cangzhou Plain.

The exploitation of confined groundwater in the central urban area of Cangzhou is mainly from the third aquifer group, which is also the main cause of land subsidence. During the rapid development of land subsidence (1991–2010), the annual groundwater extraction of the second, third and fourth aquifer groups was 30, 310, and 75 million m^3, respectively, of which the third aquifer group accounted for 75%. As shown in Figure 6, the development of the land subsidence of the subsidence center in the central urban area has gone through three main stages. Prior to 2001, the rate of land subsidence continued to increase as groundwater extraction and water level depth increased in the third aquifer group (i.e., the main groundwater abstraction layer). In 2001, the groundwater level was buried at a depth of about 90 m, and the subsidence rate exceeded 100 mm/year. From 2001 to 2007, the subsidence rate decreased significantly due to the closure of self-contained wells and the reduction of groundwater extraction. After 2007, the subsidence rate decreased slowly and stabilized. Multiple correlation analysis indicates that the land subsidence rate (S), groundwater withdrawal (Q) and groundwater level depth (D) of the Cangzhou subsidence center have a good correlation, which can be described as Eq. 17. The coefficient of determination (R^2 or R-square) is calculated as 0.94, indicating that the goodness of fit is high.

$$S = 0.447Q + 0.334D + 0.074. \quad (17)$$

4.3 The relation between the recorded soil compaction and the variation of groundwater levels

Highly sensitive borehole extensometers can provide data that define the compression characteristics of the compacting aquifer systems. In 2003, a bedrock benchmark was installed in the northern part of Cangzhou Plain (Figure 1). Since 2010, borehole extensometers were installed at several sites throughout the region. The monitoring data from the extensometer in the central urban area (Figure 1) are used to illustrate the variation characteristics of groundwater level and soil deformation.

A geophysical log interpretation from the borehole CZ-2 (see Figure 1 for borehole location), indicates alternating sand and clay layers scattered throughout the vertical aquifer sections (Figure 7). Extensometer site S1 is near borehole CZ-2, with 5 extensometers installed at depths of 5 m, 69 m, 196 m, 253 m, and 375 m to measure consolidation (vertical deformation) in each two depth intervals. The extensometers are numbered as F1, F2, F3, F4, and F5, respectively. In addition, four groundwater monitoring wells numbered as W_1, W_2, W_3, and W_4, respectively, were also installed to measure the groundwater level variations in the first aquifer group, the second aquifer group, the upper and lower parts of the third aquifer group. These four monitoring

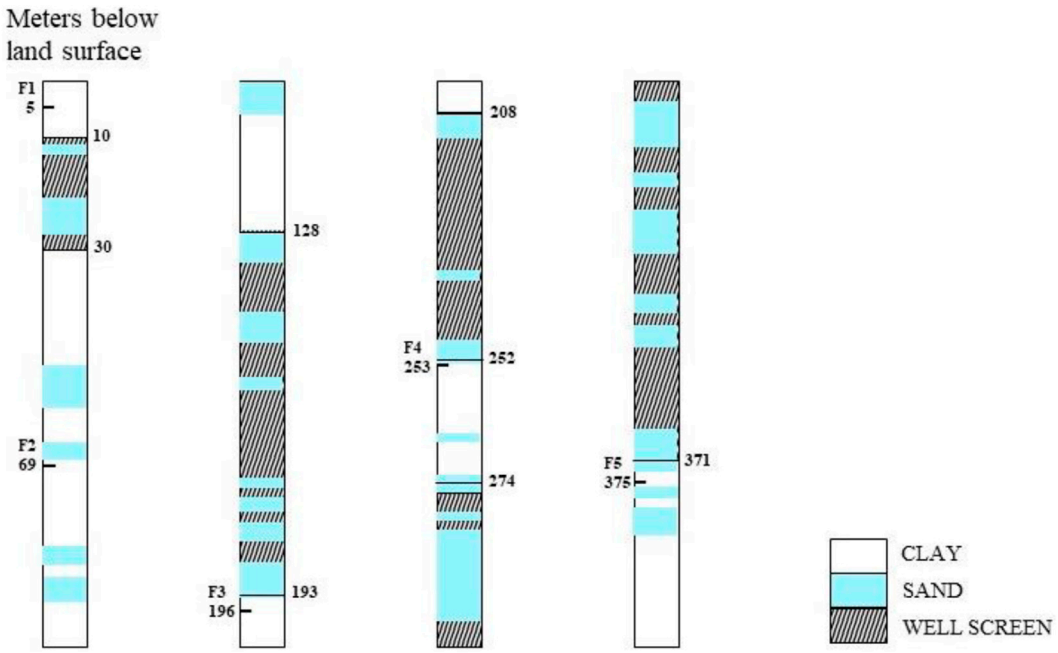

FIGURE 7
Soil profile: the central urban area of Cangzhou. Solid vertical lines indicate the interval of well perforation.

wells have the screen depths of 10–30 m, 128–193 m, 208–252 m, and 274–371 m, which are within the depth range of the soil compression layers $F_{1\text{-}2}$, $F_{2\text{-}3}$, $F_{3\text{-}4}$, and $F_{4\text{-}5}$, respectively. Figure 8A shows, in the uppermost plot, the history of groundwater depths in W_1, and that of compaction between 5 m and 69 m below land surface (the first compression layer $F_{1\text{-}2}$), an interval corresponds approximately to the first aquifer group and the upper part of the second aquifer group. Figure 8B shows, in the middle plot, the history of groundwater depths in W_3, and compaction between 196 m and 253 m below land surface (the third compression layer $F_{3\text{-}4}$), an interval corresponds approximately to the upper part of the third aquifer group. Figure 8C shows, in the lowermost plot, the history of groundwater depths in W_4, and compaction between 253 m and 375 m below land surface (the fourth compression layer $F_{4\text{-}5}$), an interval corresponds approximately to the lower part of the third aquifer group.

Due to the difference in stratum lithology and stress loading process (pattern of groundwater level change), the deformation characteristics of soil layers with different buried depths under groundwater level changes are quite different, showing elastic, visco-elastic, and visco-elastic-plastic characteristics. The first compression layer, $F_{1\text{-}2}$, exhibits obvious elastic deformation characteristics (Figure 8A). The water levels of the aquifer fluctuated seasonally, and the weakly permeable layer or the aquifer containing low-permeability lens was subjected to repeated loading and unloading. With the increase of the number of cycles, the soil layer presented a deformation characteristic dominated by elastic deformation. Despite the fact that the effective stress fluctuated with years, each major episode of stress was accompanied by additional permanent compaction in $F_{3\text{-}4}$ (Figure 8B). During fall and winter seasons of water level recovery, the effective stresses declined and compaction ceased, and a slight expansion of the aquifer system was recorded (Figure 8B). Apparently, the expansion of the aquifer is masked by the continued compaction of the interbedded aquitards, as water continues to be drained under the influence of the high pore pressure maintained in the middle region of the clay beds. As the water head of the aquifer rises, the thinnest and most permeable aquitards with the least excess pore pressure will rapidly respond elastically; however, the thickest and least permeable clay layers may continue to compact at a decreasing rate during most or even all the period of head recovery. Since November 2015, groundwater levels began to increase in a slow rate and the subsiding rate, the slope of the cumulative deformation, diminished gradually (Figure 8B). The groundwater level of W_4 shows similar variation characteristics to W_3; but soil compaction in $F_{4\text{-}5}$, which has different characteristics compared to $F_{3\text{-}4}$, stopped in December 2015 and then continued to rebound as the water level continued to rise (Figure 8C).

The degree of soil consolidation is an important indicator that affects soil compression. Under-consolidated strata have not yet been consolidated under the self-weight pressure. Even

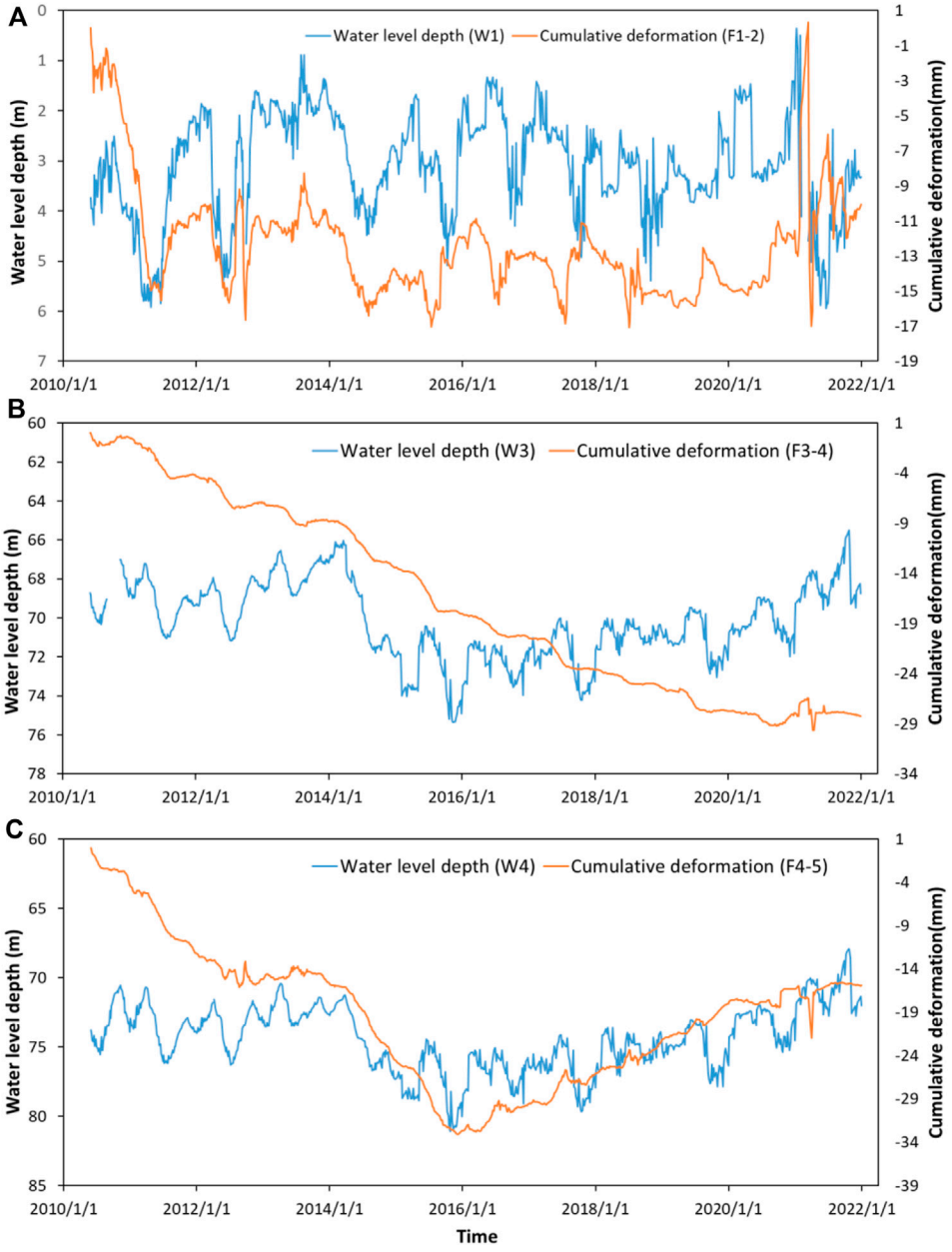

FIGURE 8
Hydrographs and cumulative deformation: **(A)** well W_1 and compression layer $F_{1\text{-}2}$; **(B)** well W_3 and compression layer $F_{3\text{-}4}$; **(C)** well W_4 and compression layer $F_{4\text{-}5}$. The negative sign in the cumulative deformation indicates compression.

if no external load exists, under the action of self-weight load, such strata will slowly consolidate and drain, causing the strata to slowly compress and cause land subsidence. For normally consolidated strata, as long as there is an external additional load or a drop in the groundwater level, the strata can be compressed, resulting in land subsidence. Only when the additional load is greater than the difference between the pre-consolidation pressure and the self-weight pressure, the over-consolidated strata will produce obvious compression and deformation and cause land subsidence. The Upper Pleistocene and Holocene strata in the Cangzhou Plain are mostly in a normal consolidation state, while in the deep strata, due to the significant drop in groundwater levels, the pore water in the corresponding aquitards or lens has been gradually discharged, and the effective stress increases. As a result, the deep strata are mostly over-consolidated after

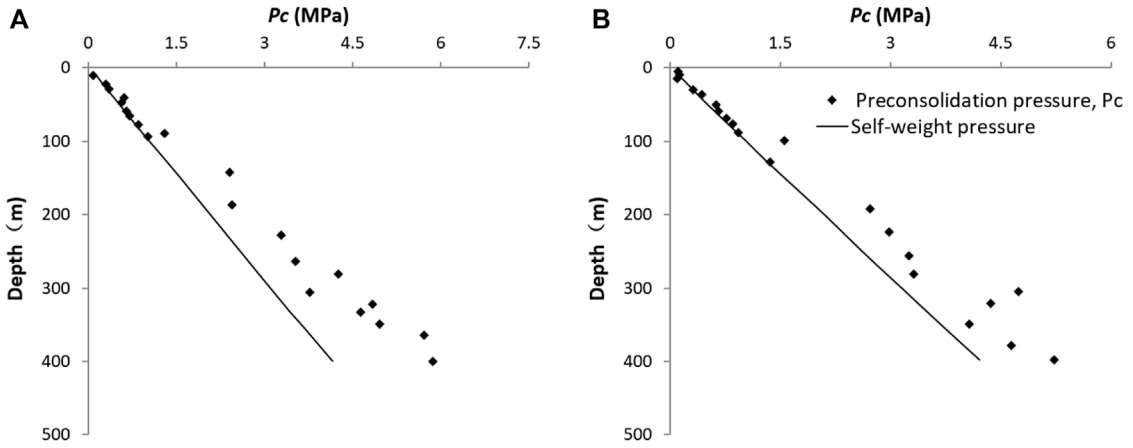

FIGURE 9
Change of *Pc* with depth in the borehole CZ-1 **(A)** and CZ-2 **(B)**.

continuous compression. The first compression layer $F_{1\text{-}2}$ mainly distributes saline/brackish water, and the amount of groundwater exploitation is small, but it still contributes 12% to the land subsidence. The main reason is the low degree of consolidation in this layer, which is mostly normally consolidated and partially under-consolidated (Figure 9).

The monitoring data of borehole extensometers show that the land subsidence has a strong hysteresis, which means that the land subsidence will continue even if the groundwater level stops falling or even rises. The delay of land subsidence in Cangzhou Plain is mainly due to the delayed drainage of low permeability aquitards (or aquifers sandwiched by low-permeability lens). As shown in Eq. 14, the time of delay increases with the thickness and the specific storage of the aquitards, and decreases with the increase of the vertical hydraulic conductivity. Thus, the length of the lag time depends on the stratum structure such as the thickness of the clayey soil layers and horizontal continuity, as well as the mineral composition and the degree of soil consolidation. Pumping tests show that the hydraulic conductivities of the confining layers are significantly lower compared with the aquifers in the study area; thus, land subsidence may lag behind the groundwater level after groundwater level changes. From the autumn of 2010 to the spring of 2014, although the water level in well W_3 rose slightly during this period, the compressive deformation of the strata in the third compression layer $F_{3\text{-}4}$ continued to increase (Figure 8B), indicating that the soil layer has not only residual plastic deformation, but also creep deformation that develops over time. The soil consolidation test results show that the soil in the middle and late Pleistocene strata in the Cangzhou Plain has obvious creep characteristics under different loading conditions. The strain-log(t) curve of the silty clay sample at a depth of 70 m in the central urban area of the Cangzhou City is shown in Figure 10, which proves the existence of creep. Studies have shown that not only clay soils may creep, but also sands. However, to well define creep exists in the sandy layers in the study area, further research should be done.

4.4 Other affecting factors of land subsidence in the Cangzhou Plain

Population growth and economic development have led to excessive exploitation of groundwater, especially deep confined groundwater, which is the main cause of inducing land subsidence in the Cangzhou Plain. However, people often ignore or underestimate the indirect impact of climate change on land subsidence. Drought climate has a dual impact on groundwater level change. On the one hand, it reduces groundwater recharge; on the other hand, in order to meet water supply needs during droughts, more groundwater is pumped to make up for the lack of surface water supply. Under the dual influence of drought, the groundwater level will fall significantly and the land subsidence will increase accordingly. The groundwater in the Cangzhou Plain is mainly used for agricultural irrigation, so the influence of climate is more significant. It can be seen from Figure 11 that the proportion of severe subsidence area to total area in Cangzhou Plain has a good correlation with rainfall, and the severe subsidence area here refers to the area with subsidence rate greater than 50 mm/year. In general, the area of severe land subsidence decreases when the rainfall increases, and *vice versa*. In 2020, the Cangzhou Plain is a wet year with the rainfall of 579 mm, increased by 125 mm compared with 2019. At the same time, due to the comprehensive control of groundwater over-exploitation, the South-to-North Water Diversion and

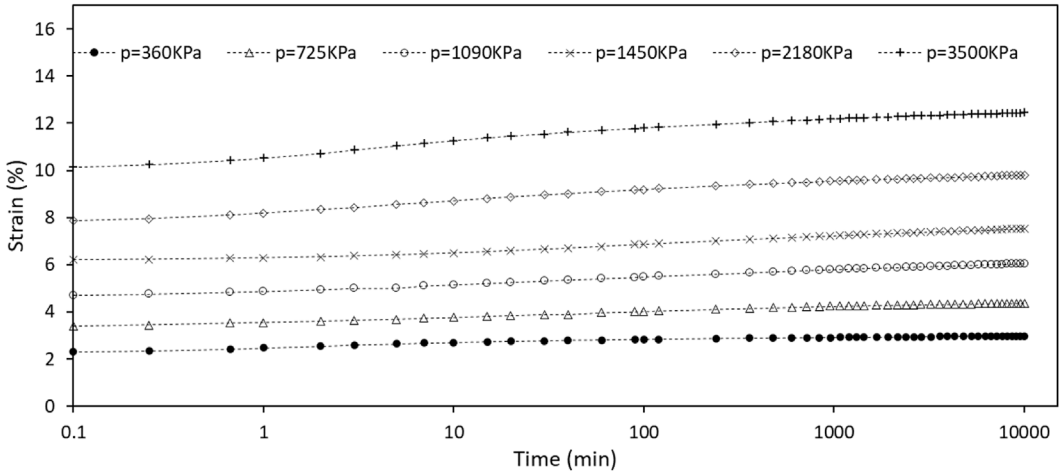

FIGURE 10
The creep curves for a silt clay sample at 70 m depth taken in the central urban area of the Cangzhou Plain.

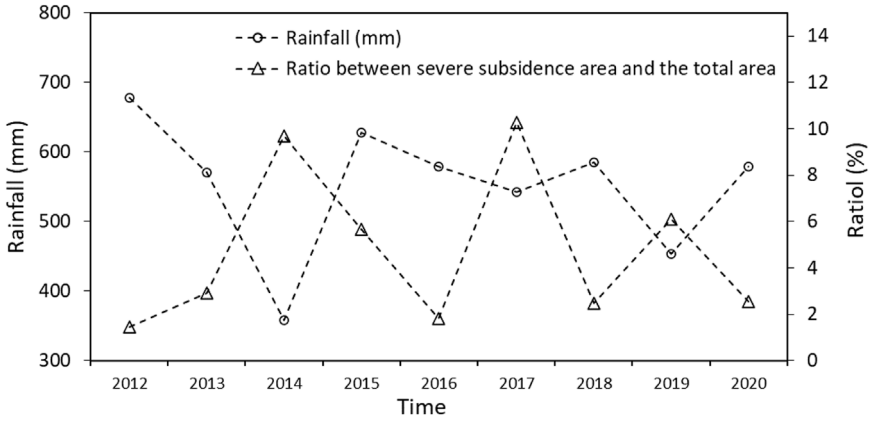

FIGURE 11
Temporal variation of rainfall and the ratio between severe subsidence area and the total area of the Cangzhou Plain.

other factors, the development trend of land subsidence has further slowed down, and the area of severe land subsidence has decreased by more than 50% year-on-year (Figure 11).

Engineering construction is a new factor affecting land subsidence of the Cangzhou Plain in recent years. With the continuous acceleration of the urbanization process, the renovation of old urban areas and the expansion of new urban areas have led to an increase in the number and height of buildings, resulting in an increase in ground loads. Under-consolidated soils or soft soils tend to consolidate under heavy loads, thereby inducing land subsidence. The development of underground resources such as oil and natural gas leads to the compaction of the Tertiary under-consolidated oil and gas layers, which is also an affecting factor for the development of land subsidence.

The spatial distribution of land subsidence is often controlled by faults. InSAR results show that the Cangdong fault in Botou (see Figure 1 for the fault location) has an obvious effect on the spatial distribution of ground subsidence, and the ground subsidence rate on both sides of the fault changes abruptly (Figure 12), which provides a good indication for the understanding of the development and characteristics of the fault. Abrupt areal changes in subsidence can be the result of faults separating compressible from less-compressible deposits or acting as barriers to groundwater flow, creating groundwater level differences across the faults (Galloway, et al., 1999).

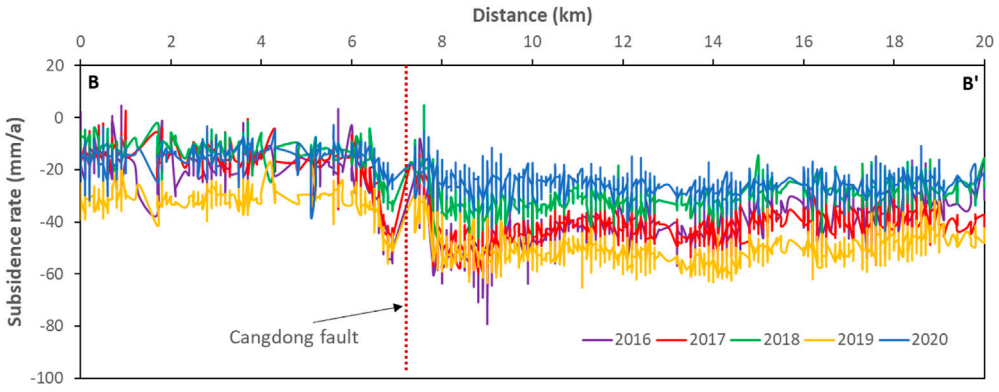

FIGURE 12
Variation of subsidence rate with distance from 2016 to 2020 for the BB′ section (see Figure 1 for the section location).

Analyses of lithological and geophysical logs of wells provide clues about the observed subsidence patterns that terminate or change features near the fault. We collected audiomagnetotellurics (AMT) data along a profile across the fault, using the Geometrics StrataGem EH4 system, a four-channel, natural and controlled-source tensor system recording in the range of 10–92,000 Hz (Geometrics, 2000). The AMT method is used to reveal subsurface structure and stratigraphy, results showing that the thickness difference of Quaternary sediments on both sides of the fault can reach about 80 m. According to monitoring data, the deep confined groundwater level in the southeast is several to 10 m lower than that in the northwest. The compressibility and thickness differences of sediments and the groundwater level difference may be the main reasons for the abrupt areal changes in subsidence across the fault.

5 Summary and conclusion

By collecting monitoring data of land subsidence, soil deformation, groundwater levels, *etc.*, the mechanism of land subsidence in the Cangzhou plain was studied using theoretical model analysis and multiple correlation analysis. The main conclusions are as follows:

1) A five-layer conceptual model was constructed, consisting of an unconfined aquifer, confining unit 1, confined aquifer 1, confining unit 2, and confined aquifer 2. Theoretical analysis shows that when the water level of the unconfined aquifer decreases, the effective stress of the unconfined aquifer increases, while the effective stress of the confined aquifers and the confining unit 2 decreases slightly. Note that there is a critical point in confining unit 1 where the effective stress remains unchanged. After the water head in confined aquifers declines, the effective stress of the unconfined aquifer remains unchanged, and the effective stress of both confined aquifers and confining units increases. Ground subsidence occurs whether groundwater is pumped from unconfined or confined aquifers.
2) The land subsidence of the Cangzhou Plain is mainly caused by the exploitation of deep confined groundwater. After taking measures to close the self-provided wells, the land subsidence in the central urban area of Cangzhou City has been gradually controlled. The monitoring data of the land subsidence center in the central urban area show that land subsidence has a very good correlation with groundwater extraction and groundwater level.
3) Geotechnical tests show that the change in compressive modulus with increasing pressure can be divided into 4 stages, and that the compressive modulus increases with the increase of soil depth as a whole. The degree of soil consolidation is an important index that affects soil compression, and soil layers with low degree of consolidation are easy to compress. Land subsidence in the Cangzhou Plain has a strong hysteresis because the excess pore water pressure dissipating in the low-permeability aquitards needs long time. At the same time, the creep characteristics of soil under different load conditions are obvious, which is also a reason for the delay of land subsidence. Therefore, the creep factor of clayey soil layers should be considered in the calculation model of land subsidence. The deformation characteristics of strata driven by groundwater level variations change greatly with buried depths, and those of the shallow aquifer are mainly elastic.
4) The area of severe land subsidence is closely related to rainfall. Reduced rainfall will lead to reduced groundwater recharge and increased groundwater abstraction, which will exacerbate the development of land subsidence. The thickness difference of Quaternary sediments and deep confined groundwater level

differences across the fault may be the main reasons for the abrupt areal changes in subsidence across the Cangdong fault. InSAR results can provide a good indication for understanding the development and characteristics of the fault.

Data availability statement

The original contributions presented in the study are included in the article/Supplementary Material, further inquiries can be directed to the corresponding author.

Author contributions

Conceptualization, HG, AH, and WL; data curation, HG; formal analysis, HG, AH, and WL; funding acquisition, HG; investigation, HG, XZ, YW, and YC; methodology, HG; supervision, XZ, JZ, LW, and YC; writing—original draft, HG; writing—review and editing, HG, AH, WL, XZ, and LW. All authors have read and agreed to the published version of the manuscript.

Funding

This work was supported by the National Natural Science Foundation of China (Grant No. 41877294) and the China Geological Survey (Grant Nos. DD20160235 and DD20190679).

Conflict of interest

The authors declare that the research was conducted in the absence of any commercial or financial relationships that could be construed as a potential conflict of interest.

Publisher's note

All claims expressed in this article are solely those of the authors and do not necessarily represent those of their affiliated organizations, or those of the publisher, the editors and the reviewers. Any product that may be evaluated in this article, or claim that may be made by its manufacturer, is not guaranteed or endorsed by the publisher.

References

Amighpey, M., and Arabi, S. (2016). Studying land subsidence in Yazd province, Iran, by integration of InSAR and levelling measurements. *Remote Sens. Appl. Soc. Environ.* 4, 1–8. doi:10.1016/j.rsase.2016.04.001

Asadi, R., and Ataie-Ashtiani, B. (2016). Numerical modeling of subsidence in saturated porous media: A mass conservative method. *J. Hydrol. X.* 542, 423–436. doi:10.1016/j.jhydrol.2016.09.024

Augustesen, A., Liingaard, M., and Lade, P. V. (2004). Evaluation of time-dependent behavior of soils. *Int. J. Geomech.* 4 (3), 137–156. doi:10.1061/(asce)1532-3641(2004)4:3(137)

Bai, L., Jiang, L., Zhao, Y., Li, Z., Cao, G., Zhao, C., et al. (2022). Quantifying the influence of long-term over exploitation on deep groundwater resources across Cangzhou in the North China Plain using InSAR measurements. *J. Hydrol. X.* 605, 127368. doi:10.1016/j.jhydrol.2021.127368

Castellazzi, P., Martel, R., Galloway, D. L., Longuevergne, L., and Rivera, A. (2016). Assessing groundwater depletion and dynamics using GRACE and InSAR: Potential and limitations. *Groundwater* 54 (6), 768–780. doi:10.1111/gwat.12453

Castelletto, N., Gambolati, G., and Teatini, P. (2015). A coupled MFE poromechanical model of a large-scale load experiment at the coastland of Venice. *Comput. Geosci.* 19 (1), 17–29. doi:10.1007/s10596-014-9450-y

Chaussard, E., Milillo, P., Bürgmann, R., Perissin, D., Fielding, E. J., and Baker, B. (2017). Remote sensing of ground deformation for monitoring groundwater management practices: Application to the Santa Clara Valley during the 2012–2015 California drought. *JGR. Solid Earth* 122 (10), 8566–8582. doi:10.1002/2017jb014676

Craig, R. F. (2004). *Craig's soil mechanics*. New York, NJ: Spon Press

Enomoto, T., Koseki, J., Tatsuoka, F., and Sato, T. (2015). Creep failure of sands exhibiting various viscosity types and its simulation. *Soils Found.* 55 (6), 1346–1363. doi:10.1016/j.sandf.2015.10.002

Fetter, C. W. (2001).*Applied hydrogeology*. Editor 4 th ed.(New Jersey, NJ, USA: Prentice-Hall) .

Foster, S., Garduno, H., Evans, R., Olson, D., Tian, Y., Zhang, W., et al. (2004). Quaternary aquifer of the north China plain—Assessing and achieving groundwater resource sustainability. *Hydrogeol. J.* 12 (1), 81–93. doi:10.1007/s10040-003-0300-6

Galloway, D. L., Jones, D. R., and Ingebritsen, S. E. (1999). Land subsidence in the United States: *US Geological Survey Circular 1182*, 177. Reston, VA, USA: US Geological Survey.

Gambolati, G., and Teatini, P. (2015). Geomechanics of subsurface water withdrawal and injection. *Water Resour. Res.* 51 (6), 3922–3955. doi:10.1002/2014wr016841

Geometrics, Inc. (2000). *Operation manual for stratagem systems running IMAGEM. Ver. 2. 16*. San Jose, U.S.A.Geometrics, Inc

Guo, H., Zhang, Z., Cheng, G., Li, W., Li, T., and Jiao, J. J. (2015). Groundwater-derived land subsidence in the north China plain. *Environ. Earth Sci.* 74 (2), 1415–1427. doi:10.1007/s12665-015-4131-2

He, G. F., Yan, X. X., Zhang, Y., Yang, T. L., Wu, J. C., Bai, Y., et al. (2020). Experimental study on the vertical deformation of soils due to groundwater withdrawal. *Int. J. Geomech.* 20 (7), 4020076. doi:10.1061/(asce)gm.1943-5622.0001709

Hernandez-Marin, M., and Burbey, T. J. (2012). Fault-controlled deformation and stress from pumping-induced groundwater flow. *J. Hydrol. X.* 428, 80–93. doi:10.1016/j.jhydrol.2012.01.025

Hu, R. L., Yue, Z. Q., Wang, L. C., and Wang, S. J. (2004). Review on current status and challenging issues of land subsidence in China. *Eng. Geol.* 76 (1-2), 65–77. doi:10.1016/j.enggeo.2004.06.006

Khan, A. S., Khan, S. D., and Kakar, D. M. (2013). Land subsidence and declining water resources in Quetta Valley, Pakistan. *Environ. Earth Sci.* 70 (6), 2719–2727. doi:10.1007/s12665-013-2328-9

Li, J. (2015). Analysis on the effect of groundwater mining restriction in Cangzhou City. *Water Conservancy Sci. Technol. Econ.* 21 (12), 4–6. (in Chinese).

Motagh, M., Walter, T. R., Sharifi, M. A., Fielding, E., Schenk, A., Anderssohn, J., et al. (2008). Land subsidence in Iran caused by widespread water reservoir overexploitation. *Geophys. Res. Lett.* 35, L16403. doi:10.1029/2008GL033814

Ovando-Shelley, E., Ossa, A., and Romo, M. P. (2007). The sinking of Mexico City: Its effects on soil properties and seismic response. Soil. *Dyn. Earthq. Eng.* 27 (4), 333–343.

Pacheco-Martínez, J., Hernandez-Marín, M., Burbey, T. J., González-Cervantes, N., Ortíz-Lozano, J. Á., Zermeño-De-Leon, M. E., et al. (2013). Land subsidence and ground failure associated to groundwater exploitation in the Aguascalientes Valley, México. *Eng. Geol.* 164, 172–186. doi:10.1016/j.enggeo.2013.06.015

Pham, H. T., Rühaak, W., Schuster, V., and Sass, I. (2019). Fully hydro-mechanical coupled Plug-in (SUB+) for FEFLOW for analysis of land subsidence due to groundwater extraction. *SoftwareX* 9, 15–19. doi:10.1016/j.softx.2018.11.004

Poland, J. F., and Davis, G. H. (1969). "Land subsidence due to withdrawal of fluids," in *Reviews in engineering geology, 2*. Editors D. J. Varnes and G. Kiersch (Boulder, CO: Geological Society of America) 187–269.

Riley, F. S. (1969). "Analysis of borehole extensometer data from central California," in *Land subsidence, 89, no.2*. Editor L. J. Tison (Washington, D. C, USA: International Association of Scientific Hydrology), 423–431.

Schmuller, J. (2009). *Statistical analysis with Excel for dummies*. 3th ed. Wiley.Hoboken, NJ, USA

Sexton, B. G., McCabe, B. A., Karstunen, M., and Sivasithamparam, N. (2016). Stone column settlement performance in structured anisotropic clays: The influence of creep. *J. Rock Mech. Geotechnical Eng.* 8 (5), 672–688. doi:10.1016/j.jrmge.2016.05.004

Sivasithamparam, N., Karstunen, M., and Bonnier, P. (2015). Modelling creep behaviour of anisotropic soft soils. *Comput. Geotech.* 69, 46–57. doi:10.1016/j.compgeo.2015.04.015

Tomás, R., Romero, R., Mulas, J., Marturià, J. J., Mallorquí, J. J., López-Sánchez, J. M., et al. (2014). Radar interferometry techniques for the study of ground subsidence phenomena: A review of practical issues through cases in Spain. *Environ. Earth Sci.* 71 (1), 163–181. doi:10.1007/s12665-013-2422-z

Tsai, M. S., and Hsu, K. C. (2018). Identifying poromechanism and spatially varying parameters of aquifer compaction in Choushui River alluvial fan, Taiwan. *Eng. Geol.* 245, 20–32. doi:10.1016/j.enggeo.2018.07.025

Tsai, T. L. (2015). A coupled one-dimensional viscoelastic–plastic model for aquitard consolidation caused by hydraulic head variations in aquifers. *Hydrol. Process.* 29 (22), 4779–4793. doi:10.1002/hyp.10524

Ye, S., Luo, Y., Wu, J., Yan, X., Wang, H., Jiao, X., et al. (2016). Three-dimensional numerical modeling of land subsidence in Shanghai, China. *Hydrogeol. J.* 24 (3), 695–709. doi:10.1007/s10040-016-1382-2

Zeitoun, D. G., and Wakshal, E. (2013). *Land subsidence analysis in urban areas: The bangkok metropolitan area case study*. Springer Science & Business Media.Singapore

Zhou, Z. (2012). Mechanism research of land subsidence caused by groundwater extraction. *Geotechnical Investigation Surv.* 3, 22–26. (in Chinese).

Zhu, C., Zhang, Y., He, G. F., and Sun, T. (2018). *In-situ* tests of land subsidence caused by pumping in the Tianjin Binhai New Area. *Hydrogeology Eng. Geol.* 45 (2), 159–164. (in Chinese).

Zhuang, C., Zhou, Z., Illman, W. A., Dou, Z., and Wang, J. (2020). Parameter estimation of an overconsolidated aquitard subjected to periodic hydraulic head variations within adjacent aquifers. *J. Hydrol. X.* 583, 124555. doi:10.1016/j.jhydrol.2020.124555

frontiers | Frontiers in Environmental Science

TYPE Original Research
PUBLISHED 23 November 2022
DOI 10.3389/fenvs.2022.1056607

OPEN ACCESS

EDITED BY
Yong Xiao,
Southwest Jiaotong University, China

REVIEWED BY
Xuan Yu,
Sun Yat-sen University, Zhuhai Campus, China
Linxian Huang,
University of Jinan, China
Narsimha Adimalla,
Chang'an University, China

*CORRESPONDENCE
Xiaojuan Qiao,
qiaoxj2010@163.com

SPECIALTY SECTION
This article was submitted to Freshwater Science, a section of the journal Frontiers in Environmental Science

RECEIVED 29 September 2022
ACCEPTED 07 November 2022
PUBLISHED 23 November 2022

CITATION
Liu K, Qiao X, Wang S and Sun Y (2022), Understanding of groundwater evolution through chemical and age dating information in the Yongding River alluvial fan in Beijing.
Front. Environ. Sci. 10:1056607.
doi: 10.3389/fenvs.2022.1056607

Understanding of groundwater evolution through chemical and age dating information in the Yongding River alluvial fan in Beijing

Kai Liu[1,2], Xiaojuan Qiao[3,4,5]*, Shanshan Wang[6] and Ying Sun[7]

[1]School of Water Resources and Environment, China University of Geosciences (Beijing), Beijing, China, [2]Chinese Academy of Geological Sciences, Beijing, China, [3]Key Laboratory of Computational Geodynamics, Chinese Academy of Sciences, Beijing, China, [4]College of Earth and Planetary Sciences, University of Chinese Academy of Sciences, Beijing, China, [5]Beijing Yanshan Earth Critical Zone National Research Station, University of Chinese Academy of Sciences, Beijing, China, [6]Beijing Institute of Geology, Beijing, China, [7]Beijing Institute of Hydrogeology and Engineering Geology, Beijing, China

Groundwater plays important roles in human community development and the urbanization process as the results of global environmental change and rapid population growth. A clear understanding of the vertical and horizontal spatial distribution characteristics of groundwater and sediment is the premise of efficient groundwater resource management and utilization in alluvial plains. To explore the evolution process of groundwater and the distribution of sediment in the Yongding River (YDR) alluvial fan, a typical profile from Mentougou to Fengheying was chosen to conduct an extensive hydrogeological investigation with multiple hydrochemical, isotopic, and age dating analyses, which represents one of the most typical hydrogeological units in the YDR alluvial fan. The analysis results show that (i) along the profile, the water's chemistry type gradually changes from HCO_3-Ca·Mg to HCO_3-Na. The contents of coarse grain gradually decrease while fine particles regularly increase. Also, a similar evolution trend is found in the vertical direction. (ii) The annual renewable rate of groundwater is > 10% in the upper fan, 2%–8% nearby Daxing, and < 2% in Fengheying. (iii) In the proximal fan area, the average flow velocity of the single and double layer is about 65 m yr^{-1} and of approximately 18.9 m yr^{-1}. From the mid fan to distal fan, the value of velocity and hydraulic conductivity decreases from 12.4 m yr^{-1} to 3.75 m yr^{-1} and from 8.54 m yr^{-1} to 0.64 m yr^{-1}, respectively. (iv) The ^{14}C analysis results indicate that the age of shallow and deep groundwater ranges from 5a to 60a and from 4000a to 12000a, respectively. The groundwater age increases with depth in the vertical direction and increases from northwest to southeast along in the alluvial fan in the horizontal direction. Understanding the evolution process of sediment and hydrochemistry in the YDR alluvial fan provides a valuable reference for groundwater resource development, utilization, and pollution prevention in the alluvial fan.

KEYWORDS

age dating, conceptual model, groundwater renewability, hydrogeochemistry, Yongding River alluvial fan

1 Introduction

Water shortage, extreme climate, and vulnerable eco-environment are the most pressing problems for the urbanization process. More than half of the global population relies upon groundwater for drinking purpose, and the dependency with rapid growth of urban population is expected to continuously increase (LiBianLiHuangQiLiu et al., 2021; Xiao et al., 2022a). These acute problems cause the intensive extraction and utilization of groundwater, groundwater level decline, and water quality problems (Edmunds, 2009; LiuZhouLuoWangMcClainWang et al., 2022). Groundwater in the alluvial–proluvial plain is the foremost water source. The Yongding River (YDR) is the mother river of Beijing, and several urban water supply sources and observation wells are located along the YDR. The YDR alluvial plain is one of the most important hydrogeological units in northern China. Due to the complexity of hydrogeological conditions, identifying the spatial variability of the sediment and aquifer in the alluvial fan is difficult.

Spatial variability and zonation are universal characteristics in nature, such as vegetation distribution, topography, climate, geotherm, and precipitation (Naito et al., 1995; Guillen and Palanques, 1997; Sarkar and Guha, 1997; Mallik et al., 2001). The geological phenomena also show zoning characteristics, including the geological structure, magmatic activity, weathering crust, and enrichment state of geochemical elements (Robion et al., 1997; Wogelius et al., 1997; Piao et al., 2010; Brooke et al., 2018). Several previous studies have revealed the temporal and spatial distribution characteristics of groundwater and sediment in alluvial fans (Yang, 1986; Zhou et al., 2009; Straub and Wang, 2013; Forzoni et al., 2014; Litty et al., 2017; Ezquerro et al., 2019), including the distribution characteristics of joint and fracture (Cao et al., 2018), groundwater hydrochemical characteristics (Arenas et al., 2001; Wang et al., 2011), and the interaction between tectonism, sedimentary formation, and groundwater (Benvenuti, 2003; Harvey et al., 2005; Li et al., 2008a; Mas-Pla et al., 2016). For instance, in the Chaobai River alluvial fan, a hydrochemistry analysis and an environmental isotope analysis were used to determine the hydrogeological structure, estimate groundwater renewal rates, and analyze hydrodynamical characteristics (Li et al., 2008b; Zhai et al., 2013; Guo et al., 2014; Li et al., 2014). Based on the geological conditions and hydrogeological structure of the North China Plain, the analysis of ^{18}O, ^{3}H, and ^{14}C was used to reveal the horizontal and vertical hydrodynamic conditions and the zoning characteristics (Lou et al., 2006; Xiao et al., 2022b). In the Songliao Basin, the hydrodynamic intensity can be classified into strong, weak, and stagnant water zones with depth increase by analyzing groundwater dynamic field factors and chemical characteristics (Li et al., 2009). Most of the previous studies focused on a single object, groundwater or sediment, or applied a single hydrochemistry method to analyze, while a few studies applied multiple test methods to analyze the distribution characteristics of groundwater and sediment in the alluvial plain.

Alluvial aquifers of the YDR alluvial plain are the ideal representatives for identifying the spatial distribution characteristics of sediment and hydrochemicals in terms of geo-conditions. Although the hydrochemistry characteristics of the YDR alluvial fan has been reported in a number of studies (Cheng et al., 2001; Yu et al., 2007; Chen et al., 2010a; Chen et al., 2010b; Zhai et al., 2011a; Zhai et al., 2011b; Zhai et al., 2011c; Zhai et al., 2011d; Xun et al., 2011; Yu et al., 2011; Liu et al., 2012a; Liu et al., 2013a; Xiao et al., 2022c), knowledge of the evolution process of groundwater identified by multiple hydrochemical tests still remains relatively limited, especially from the two perspectives of groundwater and sediment analysis. To improve understanding of the groundwater evolution process in the YDR alluvial fan, the typical profile along the direction of Mentougou to Fengheying was chosen and analyzed by the isotopic analysis, sedimentary analysis, and age dating to identify the vertical and horizontal spatial distribution characteristics and develop a conceptual model to understand the groundwater evolution process, which is helpful to provide a scientific foundation for rational groundwater development and protection. This study analyzed the distribution characteristics of sediment and groundwater by a sedimentary test, hydrochemistry test, and isotope analysis. The aims were to (i) reveal aquifer spatial distribution characteristics in the alluvial fan based on sedimentation analysis; (ii) estimate the groundwater hydrodynamic characteristics, such as flow-renewal rate, flow velocity, and permeability-parameter distribution through water table investigation and residence-time dating (^{14}C and ^{3}H); (iii) evaluate groundwater quality from the hydrochemical horizontal and vertical distributions for different aquifer-unit elements and layers; and (iv) identify the concept model of groundwater evolution process in the alluvial plain. The results of the present study can improve the understanding of the groundwater evolution process and provide a valuable reference for managing groundwater resources in the alluvial plains worldwide.

2 Materials and methods

2.1 Topography and hydrological setting

The YDR alluvial–proluvial plain is located in the middle-southern part of the Beijing plain. The study area (116°50′–116°53′ E, 39°26′–40°05′ N) is approximately 2453 km^2 (Figure 1). The Western Hills are situated in the western part of the study area, including Dongling Mountain (elevation 2302 m) and Baihua Mountains (elevation 1991 m). The southeast plain area is formed by the alluvial–proluvial deposition. The YDR alluvial–proluvial plain formed in the

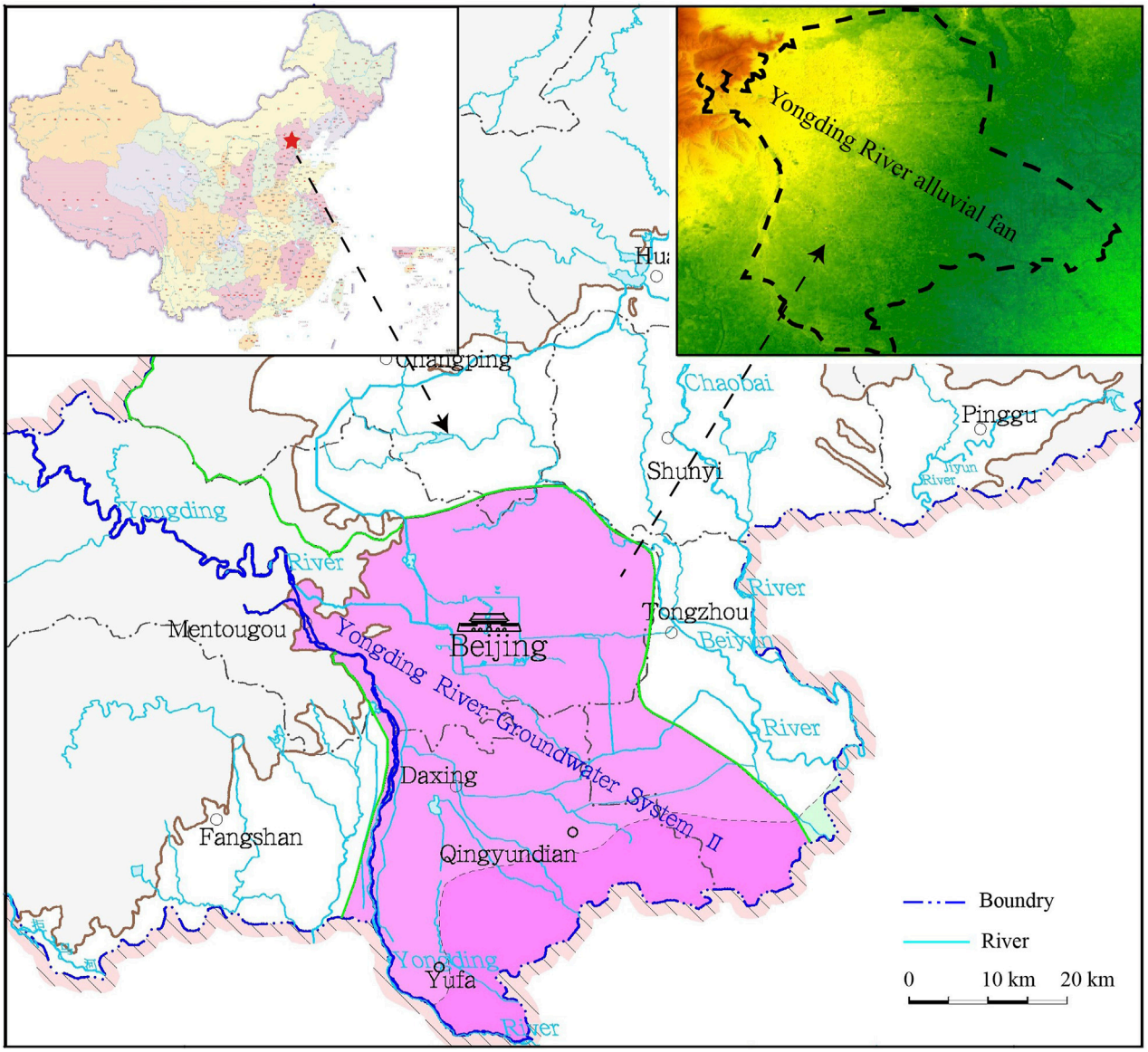

FIGURE 1
Schematic map of the YDR groundwater system in Beijing.

Late Pleistocene (12,000 year), and the river channels have changed several times, which cause a complex development of the alluvial fan throughout the evolution history. Shijingshan District, Beijing urban area, and Tongzhou District are the fan apex, the middle part of the fan, and marginal fan, respectively (Liu et al., 2012b; Lv, 2012; Liu et al., 2013b).

The climate characteristic of the study area is the semi-arid and semi-humid warm temperature continental monsoon climate. According to the monitoring data collected from Beijing Municipal Meteorological Station, the annual average value of air temperature is 11.54°C during the interval of 1959–2014, and the highest value of 28.2°C and the lowest value of −16.8°C occurred in July and January, respectively. The annual average values of rainfall and evaporation are 567.7 mm and 1816.49 mm, respectively. About 60–70% annual precipitation occurred between June and August.

2.2 Geological conditions

The study area is located in the upper-middle part of the sub-groundwater system of the YDR alluvial–proluvial fan (Liu et al., 2008; Liu et al., 2013b) (Figure 2A), which is in the fringe area terrain of the western uplift of Beijing. The

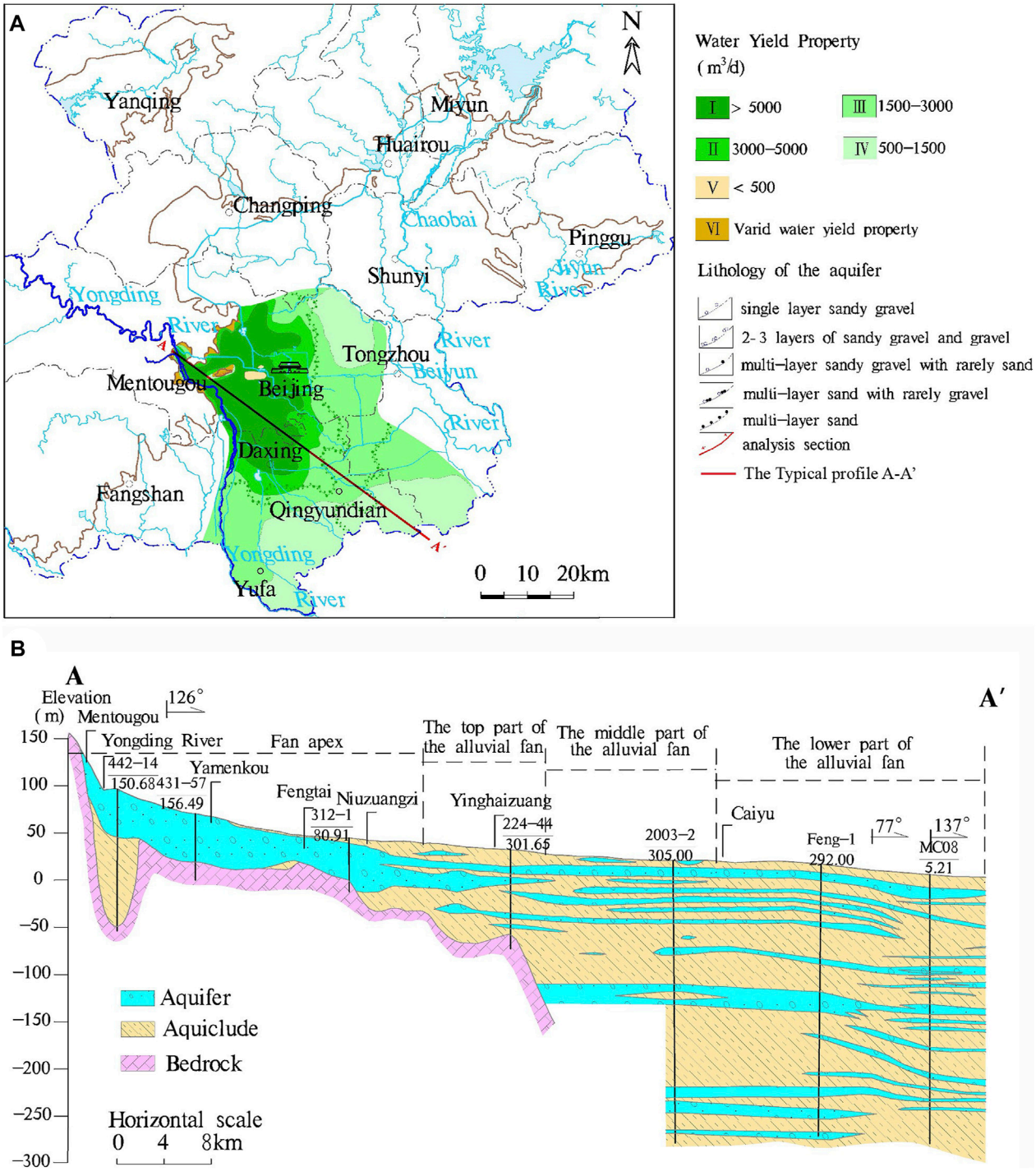

FIGURE 2
(A) Schematic map of groundwater yield property zoning and lithology of the Yongding River groundwater system in Beijing and **(B)** hydrogeological profile of the Yongding River alluvial fan.

stratigraphy of the study area includes from the Proterozoic to Cenozoic eras, except for the Upper–Middle Ordovician, Silurian, Devonian, Lower Carboniferous, and Triassic systems. The tectonics is well-developed with a series of complex folds. The direction of main faults, which are nearly perpendicular to second-order extension fractures, is

consistent with that of the fold axis. Pre-quaternary strata also elongate along the north east–east (NEE) direction in the western mountains. Figure 2A briefly describes the general geological setting of the study area including the lithology distribution and water yield property. The geologic cross-section (Figure 2B) shows that the tertiary strata are mostly underlain by Cenozoic sediments in the north of the third water plant of Beijing.

94% study area is covered by the quaternary stratum layer, which is characterized by notable spatial variations in lithofacies and lithology. Under the influence of several times change of river channels, the thickness of the Quaternary stratum gradually increases from northwest to southeast and extends to more than 300 m in Fengheying in the Daxing district. The lithology in the upstream part of the study area comprises gravel land and sand pebble sedimentation. In the southern part of the alluvial fan, alluvial facies sediments lie >100–200 m below the surface, which comprises a lithology of middle-coarse and-fine sand with thickness and high porosity interspersed with lens and interbedded with sandy gravel layers in certain locations.

In the YDR alluvial fan, the loose-rock pore water occurs in the Quaternary sediments, which is mainly distributed in the mountain valley and the eastern part of the plain. The plain is composed of the modern YDR channel, and the first terrace spans from Sanjiadian to Yongdingxincheng (Zhai et al., 2011d).

In the piedmont and mountain valley, the strata are predominated by eluvial facies, and a zonal distribution with heterogeneous water-yield property exists. In the upstream fan terrain, the aquifer lithology is gravel and coarse sand, and the aquifer is a single or double sand pebble structure with considerable thickness, which has the characteristic of high hydraulic conductivity. The single aquifer thickness ranges from 10 m to 20 m, and the aggregate thickness of the aquifer is about 30 m–70 m. The hydraulic conductivity ranges from 50 m d^{-1} to 300 m d^{-1} (Geological Mineral Authority of Beijing, 2008). In the downstream, the aquifer lithology comprises thick accumulations of fine-to-coarse sand with interbedded silt–clay layers of limited lateral extent within the aquifer system. Between the Dongrancun and the Baishiqiaoxi part of the alluvial fan, the aquifer is composed of two or three layers of sand and gravel aquifer with an intercalation (interlayer) of lenticular sand and clay (Figure 2A).

From the western part to the eastern part of the alluvial fan, lithology grain size changes from coarse to fine, the number of layers increases gradually, and the aquifer property changes from unconfined to confined. The results of the hydrostratigraphical analysis indicate that groundwater types can be classified into five groups based on the following background conditions (Figure 2B): ① the fan apex includes single-layer sandy gravel and two or three layers of sandy gravel and gravel; ② the top part of the alluvial fan includes multilayer sandy gravel with rarely sand; ③ the middle part of the alluvial fan is composed of multilayer sand with rarely gravel; and ④ the distal fan comprises multilayer sand.

Groundwater is mainly recharged by rainfall, undercurrent from the river valley, lateral subsurface inflow from surrounding hills, and irrigation return flow (Geological Mineral Authority of Beijing, 2008). Vegetation absorption, evaporation, and artificial exploitation are the main ways of groundwater discharge. Except for agricultural irrigation, urban water supply pumped from groundwater is the main way of groundwater discharge in the urban district of Beijing city. Over-pumping of groundwater over the past decades caused a continuous decline in groundwater table (Geological Mineral Authority of Beijing, 2008).

2.3 Investigation and sampling

Due to the several times change of the YDR channel, the hydrogeological characteristics of the aquifer in the YDR alluvial fan gradually change from a single-pebble aquifer with considerable thickness to a sandy aquifer with thin particles and multiple layers. The typical profile A–A′ in the YDR alluvial fan was chosen to investigate. Several hydrogeological boreholes were selected to analyze the characteristics of sediment and hydrogeology along this typical profile.

Based on the analysis and investigation results published by the Geological Mineral Authority of Beijing & Beijing Institute of Hydrogeology and Engineering Geology (Lv, 2012), a supplementary investigation was carried out, which collected 200 samples in 10 monitoring wells in the proximal fan, mid-fan, and distal fan of the YDR alluvial fan. The depth of monitoring wells ranges from 8.4 m to 128 m. In order to eliminate the external disturbance, all these wells were pumped before sampling for 30 min~4 h. We obtained 124 sets of hydrogeological test results, including physical properties and components, water level, water-quality testing, and isotopic-age data analysis.

The locations of the investigated points and testing samples were selected from three typical units of the groundwater flow system to reveal the zonality characteristics in the alluvial fan. The distribution of sampling sites along the hydrogeologic profile is shown in Figure 3.

2.4 Methods

2.4.1 Hydrochemistry and isotope testing

Geological and hydrogeological information, such as sedimentary features, vertical lithology log, and water-level distribution, was obtained by drilling and sampling. To reveal the structure of the alluvial fan, the sediment characteristics were initially analyzed by a soil-grading test along the A–A′ transect, which is representative of the YDR alluvial fan. A total of 124 samples were tested for grain-size analysis, and 10 datasets were used for calculation. In relation to major chemical compositions of groundwater for the water type

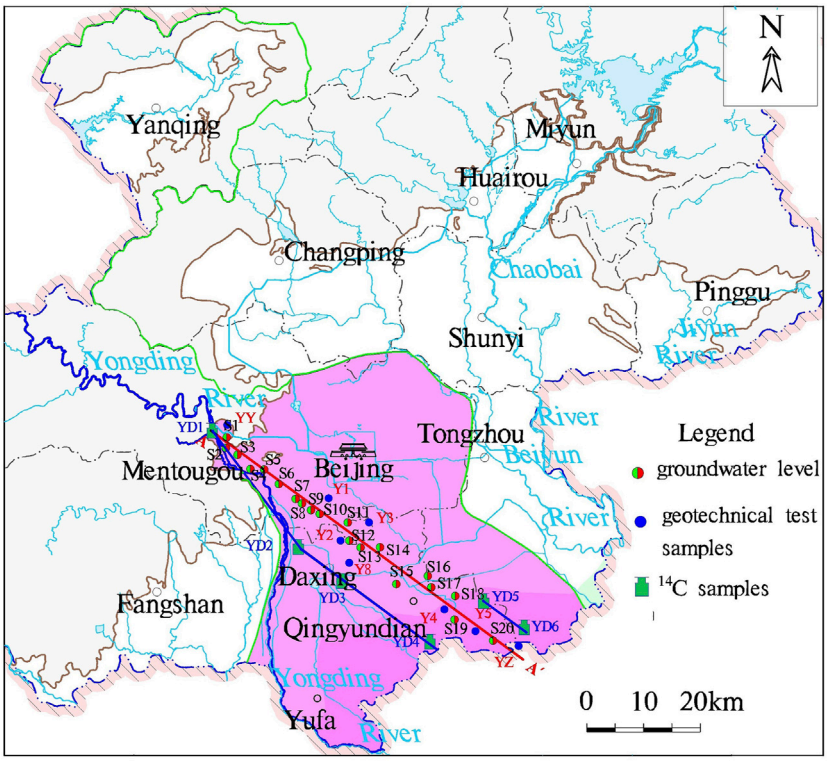

FIGURE 3
Location of the study area and the distribution of sampling sites.

analysis, ^{14}C and ^{3}H dating were used for groundwater dating and the flow-renewal rate, respectively. Flow velocity and permeability distribution were carried forward.

In 2006, nine samples from the shallow aquifers and five samples from the deep aquifer were collected to conduct the analysis of major ions and stable isotopes. The hydrogeochemical composition of all groundwater samples was analyzed in Beijing Institute of Hydrogeology and Engineering Geology. The filtered water samples were analyzed for cations (Na^+, K^+, Mg^{2+}, and Ca^{2+}). Cl and SO_4^{2-} were determined by high-performance liquid chromatography (SHIMADZU, LC-10ADvp). The error of oxygen isotope and ^{13}C analysis is less than ±0.1‰. The error of hydrogen isotope analysis is less than ±1‰. The ^{3}H test was conducted by electrolytic enrichment and measured by a Quantulus-1220 (LKB) low background liquid flash recorder with 21.17% detection efficiency (background: 0.81 cpm). ^{14}C was measured by the Quantulus-1220 (LKB) low background liquid flash meter. Chinese sugar carbon was used as the standard. The half-life was 5568 years, starting from 1950.

2.4.2 Groundwater-gradient calculation and groundwater renewal rate

According to water head and movement distance, we estimate the hydraulic gradient as follows:

$$I = H/L, \tag{1}$$

where I is the hydraulic gradient, H is the water head, and L is the movement distance.

According to the tritium isotope results (Zhai et al., 2011; Lv, 2012), groundwater-flow velocity can be estimated, and the renewal rate in shallow groundwater also can be calculated to investigate zonality characteristics.

The ^{3}H concentration in groundwater is influenced by the initial age and decay of radioactivity. The mixed model was introduced to calculate the renewal rate in shallow groundwater. Tritium's age is calculated by using the MATLAB program. Assuming that the system was stable before 1952, i.e., the input of water is equal to the output, the calculation formula is as follows:

$$A_{gwi} = (1 + R_{ri})A_{gwi-1}e^{-\lambda} + R_{Ri} + A_{0i}, \tag{2}$$

where R_{ri} is the annual renewal rate, A_{gwi} is the ^{3}H content of groundwater, A_{0i} is the ^{3}H content of input water, λ is the decay constant (^{3}H = 0.05626·yr^{-1}), and i is the time (year) from 0 to 53 (the difference between calculation year and initial year 1952).

The ^{3}H concentration in groundwater is calculated by the constant A_0. The results were calculated by the following formulae:

$$A_{gwi952} = \frac{A_0}{(\lambda/R_r + 1)}. \quad (3)$$

In view of the changes in annual precipitation and recharge, we assume that annual recharge is proportional to annual precipitation. The annual update rate R_{ri} can be obtained by weighted mean value Rr and annual precipitation, namely, $R_{ri} = R_r \times P_i/P_m$. However, the climate of the study area is semi-humid and semi-dry, and a correction factor is additionally required due to the hypothetical condition of no replenishment and minimum limit (P_t) of rainfall amount. Thus, the annual renewal rate is calculated as follows:

$$R_{ri} = \frac{R_r (P_i - P_t)}{(P_m - P_t)}. \quad (4)$$

2.4.3 Groundwater flow velocity and hydraulic conductivity estimation

The direction of the groundwater flow can be determined based on the contour map of the groundwater table. Along the groundwater flow direction, several groundwater samples with the difference in age were collected, and then the difference in age can be calculated. This difference refers to relative age, i.e., the time between two different sampled points. After measuring the distance between the two points, groundwater flow velocity can be estimated, as shown in Eq. 5:

$$u = L/t, \quad (5)$$

where L is the distance between (m), t is the age difference (a), and u is the groundwater-flow velocity (m yr^{-1}).

2.4.4 Piper diagrams

Piper diagrams, comprised by two separate trilinear plots and a central diamond, were drawn by AqQa, which were used to illustrate major cation and anion concentrations. The points in the central diamond are from the projection of two trilinear plots. The central diamond-shaped field is used to show the hydrochemical characteristics of groundwater samples.

3 Results

3.1 Sediment characteristics

In Table 1, 83 samples were collected along the A–A′ profile and analyzed for the geotechnical test, which were used to investigate the characteristics of sediment and lithology in the alluvial–proluvial plain. For each soil sample collected from different depths in hydrogeological drilling, the constituents of different particles and mineral composition in rock and clay were tested. The zonality characteristic of the particle size was identified. The analysis of mineral composition in rocks includes quartz, potassic feldspar, plagioclase feldspar, calcite, dolomite, pyrite, hornblende, and clay minerals. The clay mineral test includes illite mixed layer, illite, kaolinite, and chlorite. In Figure 4, the left and right panels of each borehole depict the clay mineral test results and mineral composition in rock, respectively. All results are expressed in the form of pie charts.

In Table 2 and Figure 5, the particle size shows significant zoning characteristics, which gradually becomes fine from piedmont to lowland. Sediment thickness is approximately 40 m–80 m in the proximal fan, 80 m–120 m in the mid-fan, and 300 m–500 m in the distal fan. The proximal fan mainly consists of gravel and sand, which gradually divide into two or three layers of the sand gravel stratum area in the mid-fan. The grain sizes of >2 mm and <0.075 mm in sample YY account for 67.9% and 0.7%, respectively. For sample Y1, the percent of 0.5–0.25, 0.25–0.075, and 0.075–0.005 mm is 20.50%, 55.80%, and 23.70%, respectively. The Caiyuan part of the distal fan is dominated by fine clay and interbedded sand and gravel. The 0.25–0.075 mm, 0.075–0.005 mm, and <0.005 mm of sample YZ are about 5.13%, 86.65%, and 8.22%, respectively.

The sedimentation characteristic and landform lithology of the YDR alluvial–proluvial fan show significant zonal characteristics. The sediment characteristic of the YDR profile is that the contents of coarse grain regularly decrease, whereas those of the fine particles increase. The closer to the proximal fan, the thicker the sediment is. The closer to the distal fan, the finer the particle size is. The characteristic of sedimentary dynamics is rapid torrent accumulation with drag-flow properties (Forzoni et al., 2014). In the Mentougou part of the proximal fan, the migration of the gravel pebble is dominated by bed load and supplemented by rare saltation and suspension. Transport relies mainly on saltation, whereas the bed-load subsidiary in mid-fan is predominated by sand. In the Caiyu and Fengheying part of the distal fan, the migration depends on the suspension and kinetic energy of water flow decline, which tends to stabilize static water deposition. The material migration also reveals the zonality characteristics of hydrodynamic condition from the proximal fan to distal fan in the YDR alluvial fan. Thus, the sedimentation of the YDR alluvial–proluvial fan is based on horizontal zonation characteristics.

3.2 Hydrodynamic characteristic

The monitored data of the groundwater level are collected from 20 observed wells. The detailed information of the groundwater level is summarized in Table 3. The depth of the groundwater level is about 35 m–40 m in the

TABLE 1 Percentage of constituents and mineral composition in rock and clay.

No.	Sample number	Sample location	Test content	Layer of drill core
YY	2	Fan apex	Percentage of constituents	
Y1	2	Front fan	Percentage of constituents	3
Y2	5	Mid fan		
Y3	5	Mid fan	Mineral composition in rock	29
Y8	5	Mid fan		18
Y4	5	Lower fan	Clay mineral test	13
Y5	5	Lower fan		16
YZ	8	Distal fan	Percentage of constituents	3

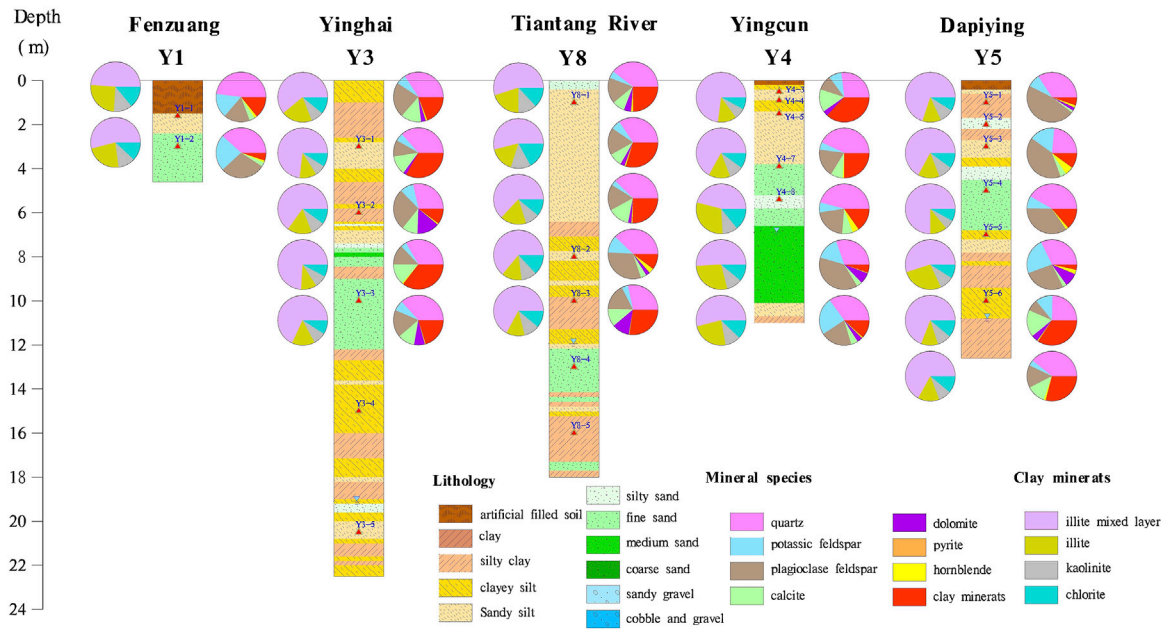

FIGURE 4
Lithology of borehole (Y1–Y5) along the A–A′ profile.

TABLE 2 Grain-size distribution in the Yongding River alluvial fan.

NO.	Units (mm)	Cobble	Gravel	Sand			Silt	Clay
		> 20	20–2	2–0.5	0.5–0.25	0.25–0.075	0.075–0.005	< 0.005
YY	Fan apex	29.20	38.70	8.80	12.90	9.70	0.70	
Y1	Front fan	—	—	—	20.50	55.80	23.70	
Y2	Mid fan	—	—	4.60	16.93	61.27	17.20	
Y3	Mid fan	—	—	—	16.45	62.00	21.55	
Y8	Mid fan	—	2.93	6.60	27.17	30.73	30.87	1.70
Y4	Lower fan	—	0.30	1.10	7.25	44.90	41.95	4.50
Y5	Lower fan	—	—	—	21.88	55.70	22.43	

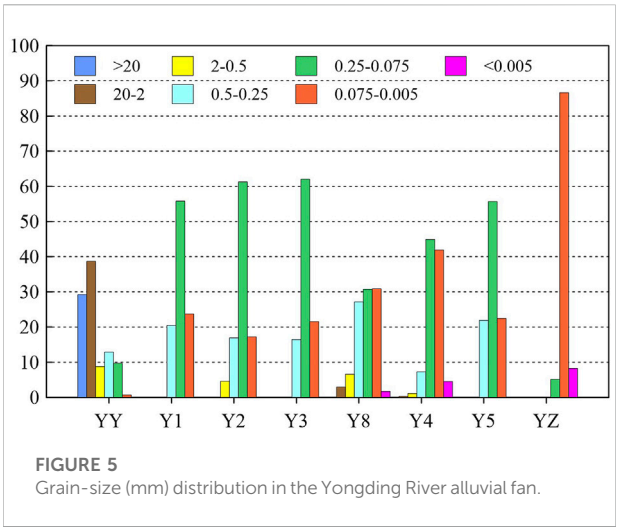

FIGURE 5
Grain-size (mm) distribution in the Yongding River alluvial fan.

Mentougou—Shijingshan part of the proximal fan area, and the groundwater level shows significant annual variation. From Lugou Bridge to Taixinggong, the depth of the groundwater level decreases to 20 m–25 m (Jiang et al., 2010; Liu et al., 2010). The depth gradually decreases from 20 m–25 m to 5 m–10 m in the Yinghai and Qingyundian part. In the Qingyundian part of the distal fan, the depth of groundwater is < 4 m, where the water table is stable. Thus, the depth of groundwater gradually decreases from the proximal fan and mid-fan to the distal fan. Figure 6 illustrates the isoline map of the water level.

The long-term monitored data of the groundwater level were used to calculate the hydraulic conductivity and hydraulic gradient and estimate the flow rate and the renewable rate in the YDR profile, which provide a good way to understand the zoning characteristic of the alluvial fan.

According to Eq. 1, the hydraulic gradient affected by topography is inversely proportional to the movement distance. Thus, the hydraulic gradient is about 0.55%–1.92% in the proximal fan, while it decreases to 0.22%–0.55% in the distal fan. If the groundwater-runoff condition is relatively bad, the hydraulic gradient ranges between 0.09% and 0.22% in the marginal fan area.

According to Eqs. 2–4, the results show that the renewable rate gradually decreases from the proximal fan to distal fan in the YDR (Table 4). In the proximal fan with a single layer of sand and gravel, the annual renewable rate is ≥ 10%. The annual renewal rate of groundwater in the two-to-three-layer area is about 8%–10%. The hydrodynamic renewal rate of multilayer sandy gravel with occasionally sandy composition ranges from 4% to 8% nearby Yinghaizhuang in Daxing. The value of the hydrodynamic renewable rate is < 2% in the multilayer sand of marginal zone from Caiyu to Fengheying in Tongzhou.

According to the ^{14}C analysis results, the age of shallow and deep groundwater ranges from 5a to 60a and from 4000a to 12000a, respectively. Vertically, the age of groundwater increases with depth. Horizontally, the age of the groundwater also increases from northwest to southeast along the direction of the groundwater flow in the alluvial–proluvial fan. The distribution characteristic of different age groundwater in the horizonal direction indicates that the condition of horizontal runoff is different. According to the hydrostratigraphical analysis, it can be divided into three different parts. The first part is single- or double-layer cobble and gravel with high permeability in the upper fan area. The average velocity from YD1–YD2 is approximately 64.9 m yr^{-1}. The second part is a multilayer with sand in the mid–lower fan. The average velocity from YD2 to YD4 is approximately 12.4 m yr^{-1}. The third part is fine sand with an intercalation (interlayer) of lenticular sand and clay in the proximal fan. The average velocity from YD5 to YD6 is approximately 3.75 m yr^{-1} (Table 5), which is consistent with the calculated results from Wang and Zhou (2006).

Based on Darcy's law, hydraulic conductivity can be estimated as follows:

$$v = u \bullet n, \tag{6}$$

$$K = V/I, \tag{7}$$

TABLE 3 Buried depth and the water level in the Yongding River profile.

No.	Buried depth (m)	Water level (m)	No.	Buried depth (m)	Water level (m)
S1	47.78	71.24	S11	16.86	13.52
S2	45.85	68.06	S12	13.45	12.44
S3	43.96	50.09	S13	10.50	10.88
S4	39.99	41.88	S14	8.08	10.08
S5	36.89	35.61	S15	6.43	11.46
S6	32.21	35.33	S16	5.59	18.41
S7	30.22	30.08	S17	4.94	18.34
S8	27.02	27.76	S18	4.77	16.74
S9	23.66	23.68	S19	4.74	14.47
S10	19.57	19.91	S20	4.70	9.71

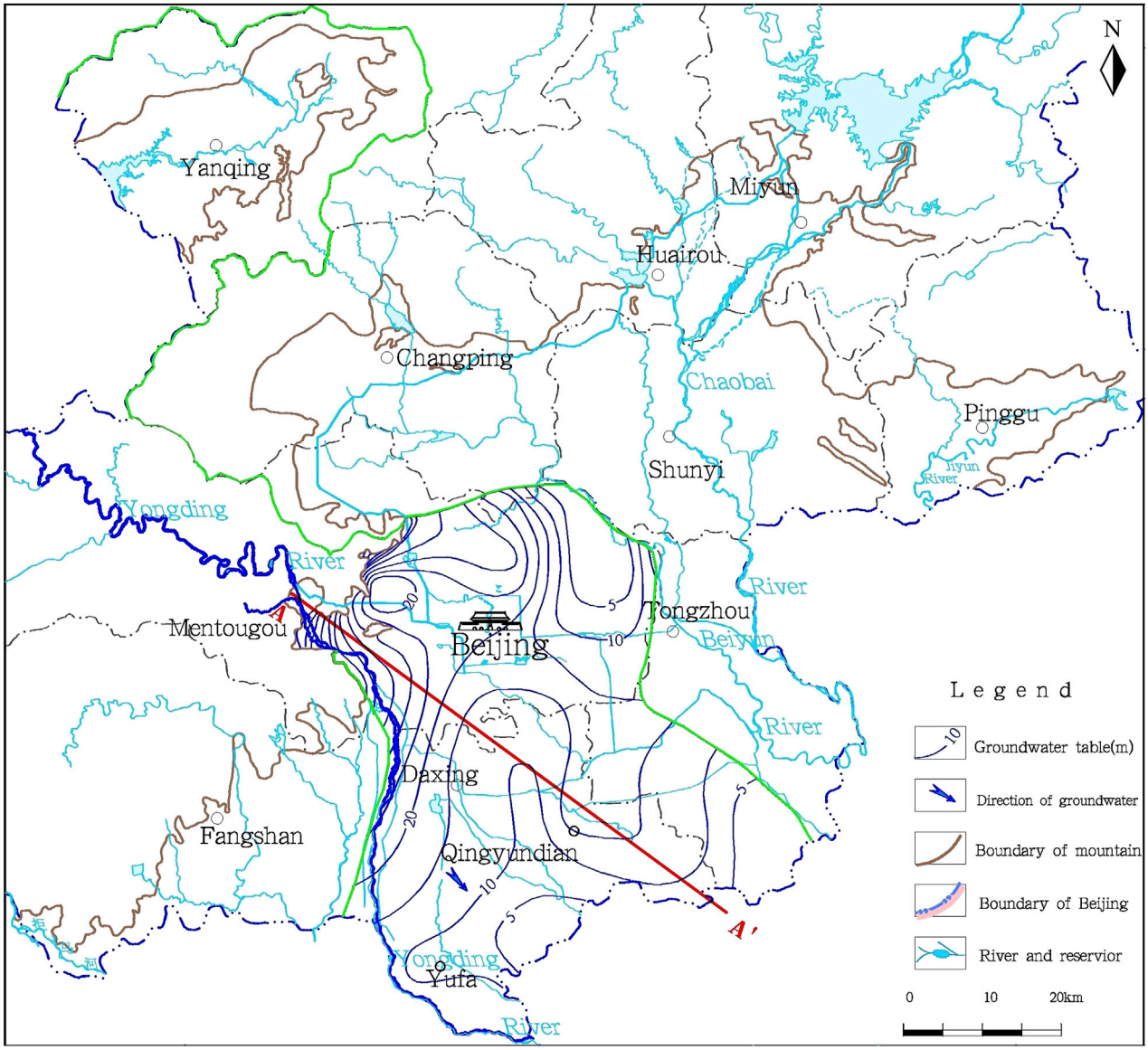

FIGURE 6
Contour map of the pore phreatic water level in Beijing.

where V is seepage velocity (m yr^{-1}), K is the hydraulic conductivity of the aquifer (m yr^{-1}), I is hydraulic gradient, n is effective porosity, and u is the actual velocity of groundwater (m yr^{-1}).

In the upper fan area (YD1 and YD2), the permeability of single-layer or double-layer cobble and gravel with is high. The average hydraulic conductivity is approximately 18.9 m yr^{-1}. In the mid–lower fan area (YD2, YD3, and YD4), the average hydraulic conductivity of multilayer sand is approximately 8.54 m yr^{-1}. In the distal fan (YD5 and YD6), the average permeability of fine sand with an intercalation (interlayer) of lenticular sand and clay is approximately 0.64 m yr^{-1}. The results of ^{14}C analysis reveals that the direction of groundwater flow is from YD6 to YD5, which is consistent with the distribution of groundwater level (Figure 7).

3.3 Hydrochemistry characteristics

The aquifer type of the YDR alluvial–proluvial fan can be classified into four different aquifers. The first aquifer is a phreatic aquifer. The depth of the phreatic aquifer is < 50 m. The second aquifer is an artesian aquifer, which is widely distributed in the YDR alluvial fan. The depth of this aquifer

TABLE 4 Renewal rate of shallow groundwater in the Beijing Plain.

No.	^{3}H (TU)	Sample location	Renewal rate (%)		Determine update rate (%)
H1	25.3	Mid-lower fan	2.6	6.4	2.6
H2	28.5	Fan apex	≥10	—	≥10
H3	22.9	Front fan	2	8	2
H4	30.6	Fan apex	≥10	—	≥10
H5	20.8	Lower fan	1.8	9	1.8
H6	15.6	Mid fan	1.1	20	1.1
H7	32.1	Upper fan	≥10	—	≥10
H8	23.20	Mid–upper fan	2.7	5.4	5.4
H9	9.81	Mid–lower fan	0.7	—	0.7

TABLE 5 ^{14}C dating results in groundwater age.

No.	^{14}C age	Distance (m)	Age difference	Velocity (m yr^{-1})	Average velocity	K-permeability (m yr^{-1})
YD1	843.4681					18.9
YD2	1235.272	25441.2	391.804	64.9		
YD2	1235.272				12.4	8.54
YD3	1862.233	5154.84	626.9612	8.22		
YD4	3097.457	20512.8	1235.224	16.6		
YD5	4497.366					0.64
YD6	2979.266	5687.64	1518.1	3.75		

ranges from 80 m to 100 m. It is consisted of multilayer sand gravel, sand, and clay. The aquifer lithology is the multilayer of sand gravel or sand in the west side of Beihai–Nanyuan, while the aquifer lithology changes from multilayer sand gravel with rarely sand to multilayer sand in the eastern side. For the third confined aquifer system, the depth varies from 150 m to 180 m, which exists in the mid-lower part of the alluvial fan. The aquifer lithology is multilayer sand. The depth of the fourth confined aquifer is approximately 300 m This aquifer is in the quaternary sediment, which is mainly distributed in Tongzhou Kuaizidian, Daxing, Caiyu, and Fengheying.

Groundwater was sampled along the typical profile for hydrochemical analysis, including K^+, Na^+, Ca^{2+}, Mg^{2+}, HCO_3^-, CO_3^{2-}, Cl^-, and SO_4^{2-} (Table 6). The groundwater age-dating data are summarized in Tables 7, 8. Due to the limitations of individual tracers, the combination of ^{14}C and ^{3}H tracer was applied to analyze by synthesis (Figure 8). In the YDR alluvial–proluvial fan, the groundwater hydrochemical type is different along the A–A' profile, which shows a significant change from a single type to a complex characteristic from the proximal fan to distal fan. The ion concentration of Ca^{2+}, Mg^{2+}, and HCO_3^- in groundwater gradually decreases with the increase of SO_4^{2-}, Cl^-, and Na + concentration from the piedmont to plain areas. However, in the central areas of the alluvial fan, the ion concentrations of SO_4^{2-}, Cl^-, and Na^+ are higher than those in other areas due to intense human activities (Figure 9).

3.3.1 Horizontal zonation of hydrochemical characteristics

The fan apex of the YDR alluvial fan is a single phreatic aquifer, and its hydrochemical component is predominated by the HCO_3-Ca-Mg type. Taking the first layer as an example to analysis, under the influence of industry, urban domestic sewage discharge, reclaimed water irrigation, and other human factors, the groundwater hydrochemical type has significant difference from the proximal part to distal part of the alluvial fan (Shijingshan District—the urban area of Beijing—Daxing District), which mainly includes HCO_3·Cl·SO_4-Ca·Mg, HCO_3·Cl-Ca·Mg, HCO_3-Mg·Na·Ca, and Cl·HCO_3-Ca·Mg. The groundwater hydrogeochemical type in other aquifers of the YDR alluvial fan also show significant horizontal zonation characteristics.

3.3.2 Vertical zonation of hydrochemical characteristics

In the Yongding River Basin, the distribution characteristics of sedimentation and lithology also show vertical zonality. Meanwhile,

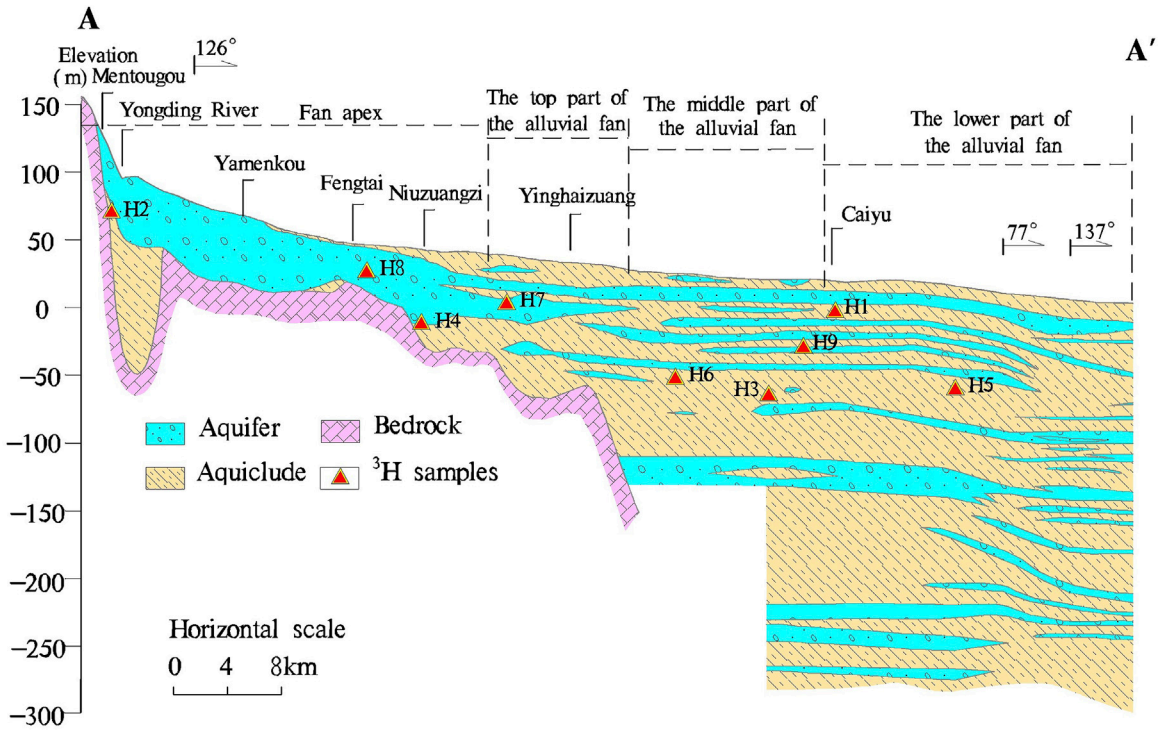

FIGURE 7
Distribution of ^{3}H sampling sites.

the groundwater hydrochemical type of shallow and deep aquifers is different in the vertical direction. In the marginal area of the alluvial–proluvial fan, HCO_3^- is the dominated anion in groundwater. For the groundwater from different depth aquifers, the ion concentration of Ca^{2+} and Mg^{2+} gradually decreases with the increase in depth, while the K+ and Na + concentration increases. The hydrochemical type shows obvious differences in different depth aquifers, changing from HCO_3-Ca·Mg·Na to HCO_3-Na·Ca and HCO_3-Na·Ca·Mg. In the middle part of the alluvial fan, the multilayer aquifer can be classified into four aquifers. The first aquifer is an unconfined aquifer, which is dominated by the HCO_3-Ca·Mg. The hydrochemical characteristic of the second aquifer is the same as that of the first aquifer. For the third or fourth aquifers near the apex fan, the hydrochemical type is predominated by HCO_3-Ca·Mg, which gradually changes from HCO_3-Ca·Mg·Na to HCO_3-Na·Ca·Mg and HCO_3-Na in the marginal area of the alluvial–proluvial fan (Figure 10).

4 Discussion

4.1 Hydrochemistry evolution

The hydrochemical characteristic is affected by several external influence factors, including dissolution filtration, cation exchange adsorption, mixing action, de-carbonic acid, de-sulfuric acid, concentration (inspissation), and human activities (Zhang et al., 1997; Wang et al., 1998; Shen and Wang, 2002; Song et al., 2007; Zhang et al., 2010; Zhao et al., 2012; Zheng et al., 2012).

In the upper parts of the alluvial–proluvial fan (the Mentougou and Haidian part), due to the thick sand gravel stratum, good runoff conditions, and deep buried depth, the function of evaporation, dissolution, and filtration in groundwater is extremely weak. The groundwater hydrochemical type is HCO_3-Ca·Mg, and the value of total dissolved solids (TDS) is < 0.5 g L^{-1} (e.g., SY15). In the middle part of the alluvial fan (the Daxing YinghaiZhuang part), the aquifer permeability decreases, and the phreatic level gradually increases with weakened runoff conditions. The function of cation exchange occurs in clays, and the hydrochemical type gradually changes to HCO_3-Na·Ca. TDS is approximately 1.0 g L^{-1} (e.g., SY17). In the marginal part of the alluvial fan (the Qingyundian–Fengyinghe part), the groundwater circulation rate is slow and the buried depth of phreatic level is < 5 m. Phreatic water is mainly affected by evaporation and gradually evolves into the function of inspissation. Due to the confluence of two rivers, Yongding River and Chaobai River, the mixing function also happens in groundwater. The hydrochemical type gradually changes to HCO_3·Cl-Na·CaMg and HCO_3·Cl-

TABLE 6 Ion concentration of water samples in the YRD profile (mg L^{-1}).

No.	K^+	Na^+	Ca^{2+}	Mg^{2+}	HCO_3^-	CO_3^{2-}	Cl^-	SO_4^{2-}
SY01	6.5	115.0	110.0	75.1	317	12	147	236
SY02	13.5	178.0	171.0	55.9	188	0	219	495
SY03	9.2	126.0	122.0	54.9	502	0	208	107
SY04	3.2	76.4	195.0	76.5	511	0	186	167
SY05	0.7	41.6	55.3	102.0	441	6	130	61
SY06	2.2	51.6	120.0	60.8	421	0	110	102
SY07	3.1	74.1	172.0	76.3	476	0	170	149
SY08	2.0	29.6	46.1	29.2	227	0	42	48
SY09	1.9	24.9	38.1	30.3	231	6	26	27
SY10	1.1	104.0	43.7	33.7	364	6	39	126
SY11	1.0	42.2	48.3	21.9	271	12	15	41
SY12	1.0	109.0	43.9	32.3	337	6	51	120
SY13	2.9	38.2	56.1	27.9	120	12	44	162
SY14	0.7	96.9	15.4	9.1	161	12	37	85
SY15	1.7	40.2	78.2	28.2	303.9	46.1	66.3	1.7
SY16	2.7	66.9	129.7	42.5	422.3	82.2	110.9	2.7
SY17	1.1	107.0	71.1	65.0	583.4	95.0	63.4	1.1
SY18	0.8	256.0	47.9	103.4	778.6	204.9	153.7	0.8
SY19	1.1	530.0	47.7	91.5	836.0	296.0	531.2	1.1
SY20	1.6	69.5	97.2	67.4	530.9	73.4	120.6	1.6
SY21	1.7	39.0	84.2	38.0	378.3	59.6	56.2	1.7
SY22	1.9	45.3	53.1	20.3	296.6	18.8	49.5	1.9

Na. The value of TDS ranges from 1.3 g L^{-1} to 2.6 g L^{-1} (e.g., SY18 and SY19). Thus, the evolution process of groundwater hydrochemical shows distinct zonality.

The groundwater buried depth nearby Daxing, Qingyundian (SY20, SY21, and SY22 in Table 2) is < 4 m. Due to the function of vadose soil capillarity and evapotranspiration, the shallow groundwater is intensely evaporated toward the atmosphere. In the vertical direction, TDS concentration slightly decreases with depth increase. Groundwater quality shows significant change from saline water in the upper part to the fresh water in the bottom part, which indicates that groundwater quality also shows vertical zonation.

4.2 Conceptual model for groundwater evolution

The distribution characteristic of sediment and lithology is zonality in the YDR alluvial–proluvial fan. From the proximal fan to the distal fan, the thickness of the sedimentary layer increases, the size of the sediment particle decreases, and the single layer gradually changes to multiple layers. The water-level data and the results of hydrochemical analysis and age-dating in groundwater were used to develop a conceptual model, which reveals the groundwater flow pattern and the evolution process of hydrochemical along the typical profile (Figure 11).

The groundwater level data reveal that the direction of groundwater flow is from west to east. (i) In the upper part of the alluvial fan (Mentougou), the annual renewable rate is > 10%. The renewable rate decreases to 4%–8% nearby the Daxing Yinghaizhuang part, where it is composed of multilayer sandy gravel with occasional sand. In the distal fan part, the values of the renewable rate are 2%–4% and <2% in Yinghaizhuang and Fengheying, respectively. (ii) Based on the result of ^{14}C dating,

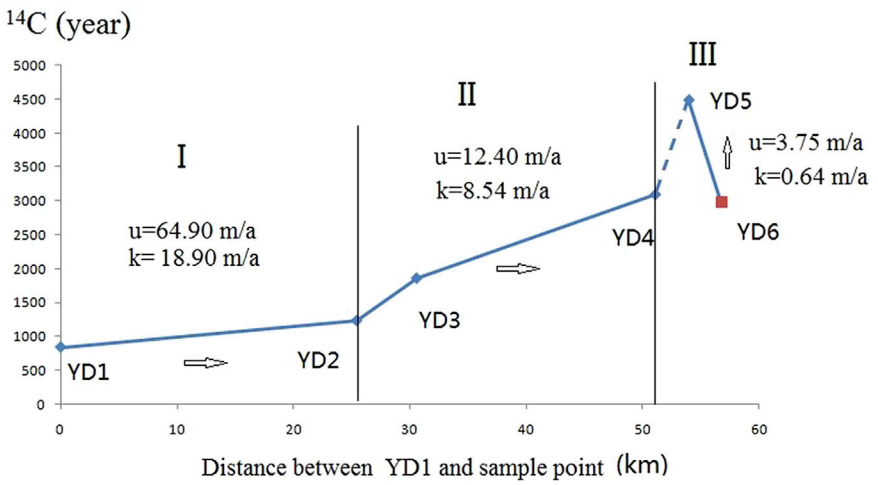

FIGURE 8
Zonality characteristics of groundwater flow velocity and aquifer permeability along the typical profile (I, II, and III indicates the upper part, middle part, and bottom part of the pluvial–alluvial fan, respectively; u is the water-flow velocity, and k is the permeability estimation).

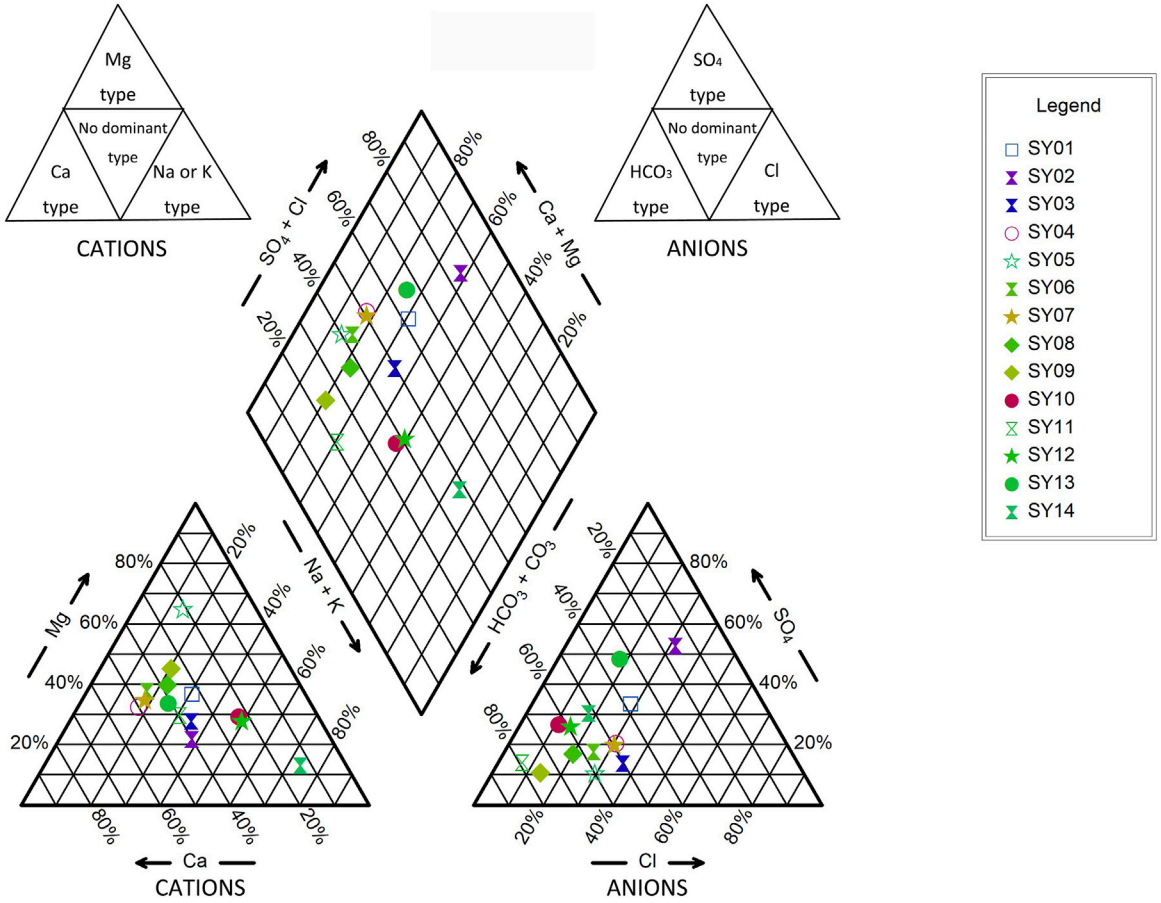

FIGURE 9
Piper diagrams of groundwater sampled from the Yongding River alluvial fan.

TABLE 7 Groundwater age-dating data (^{3}H).

No.	*^{3}H (TU)*	*^{3}H age* (year)	*Sample location*	*Aquifer structure*
H1	25.3	17	Mid-lower fan	Multilayer interbedded sandy gravel
H2	28.5	≤5	Fan apex	Single layer cobble and gravel upper fan
H3	22.9	19	Mid fan	Multilayer sand with rarely (occasional) sandy gravel
H4	30.6	≤5	Fan apex	Single layer to two–three layers of gravel transition
H5	20.8	21	Lower fan	Multilayer sand
H6	15.6	25	Mid fan	Multilayer sandy gravel with rarely (occasional) sand
H7	32.1	12	Upper fan	Single layer to two–three layers of gravel transition
H8	23.2	14	Fan apex	Multilayer sandy gravel with rarely (occasional) sand
H9	9.81	30	Mid-lower fan	Multilayer interbedded sand and gravel

the average value of groundwater flow velocity decreases from 65 m yr^{-1} to 3.75 m yr^{-1}~12.4 m yr^{-1} from the upper part to the margin part of the alluvial fan. The value of hydraulic conductivity also shows the same change tendency as groundwater flow velocity along the typical profile. The hydraulic conductivity is about 18.9 m yr^{-1} in the upper part of the alluvial fan, while it decreases to the 0.64 m yr^{-1} in the distal fan.

TABLE 8 Groundwater age-dating data (^{14}C).

No.	Sample location	^{14}C (PMC)	^{14}C age (year)	Depths	Sample location
YD1	Mayu in Shijingshan	90.3	843.4681	41.25–55	Fan apex
YD2	Lucheng in Daxing	86.12	1235.272	20.56–70	Mid–lower fan
YD3	Yihezhuang	79.83	1862.233	23.3–35.5	Front fan
YD4	Qingyundian in Daxing	75.24	2351.754	38.5–61.96	Lower fan
YD5	Fengheying in Daxing	69.74	2979.26	40–72	Distal fan
YD6	Anding in Daxing	68.75	3097.457	14.93–90	Lower fan
YD7	Caiyu in Daxing	58.04	497.366	25–57	Lower fan

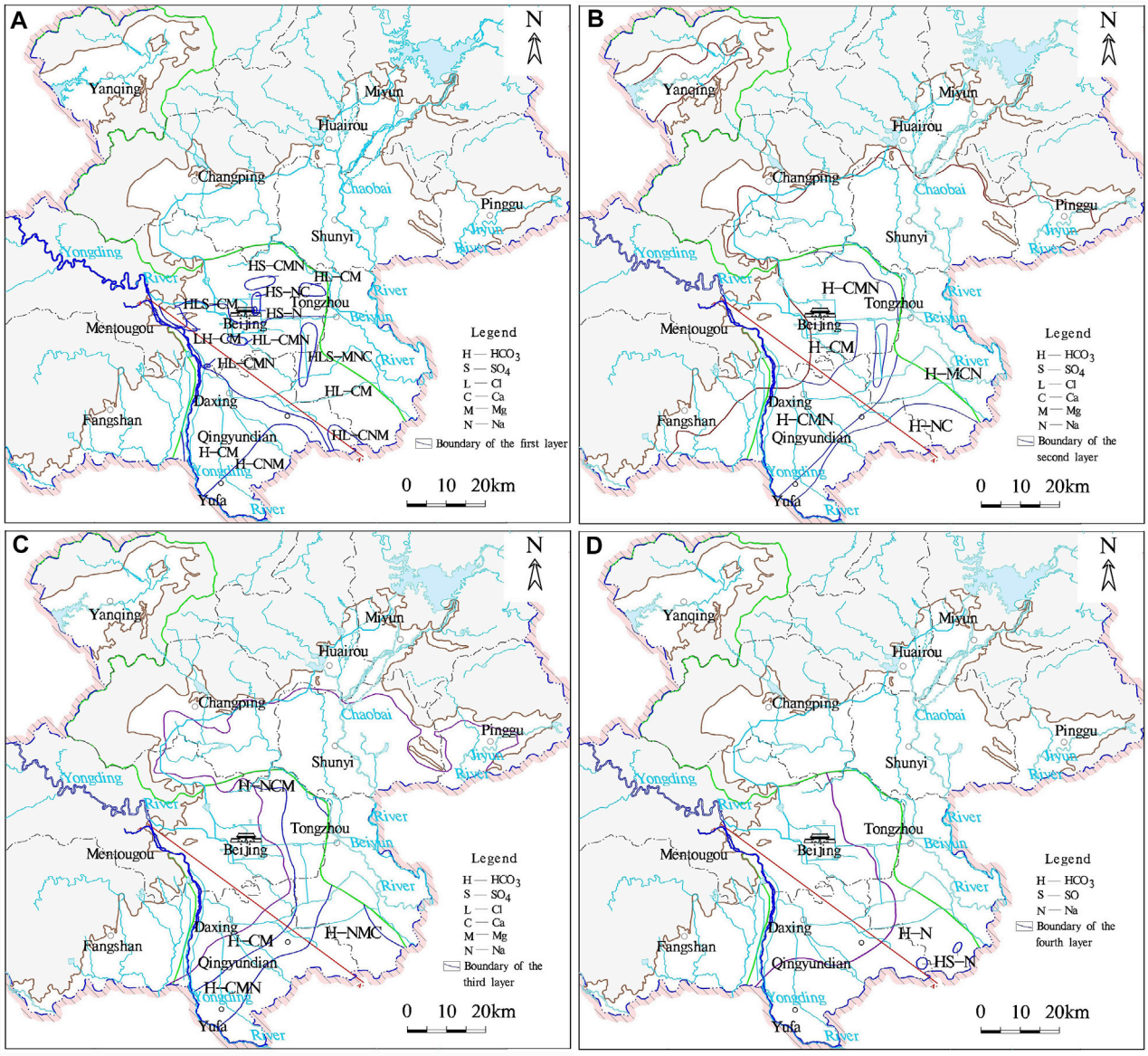

FIGURE 10
Distribution of hydrochemical types in the plain area in Beijing. **(A)** First aquifer, **(B)** second aquifer, **(C)** third aquifer, and **(D)** fourth aquifer.

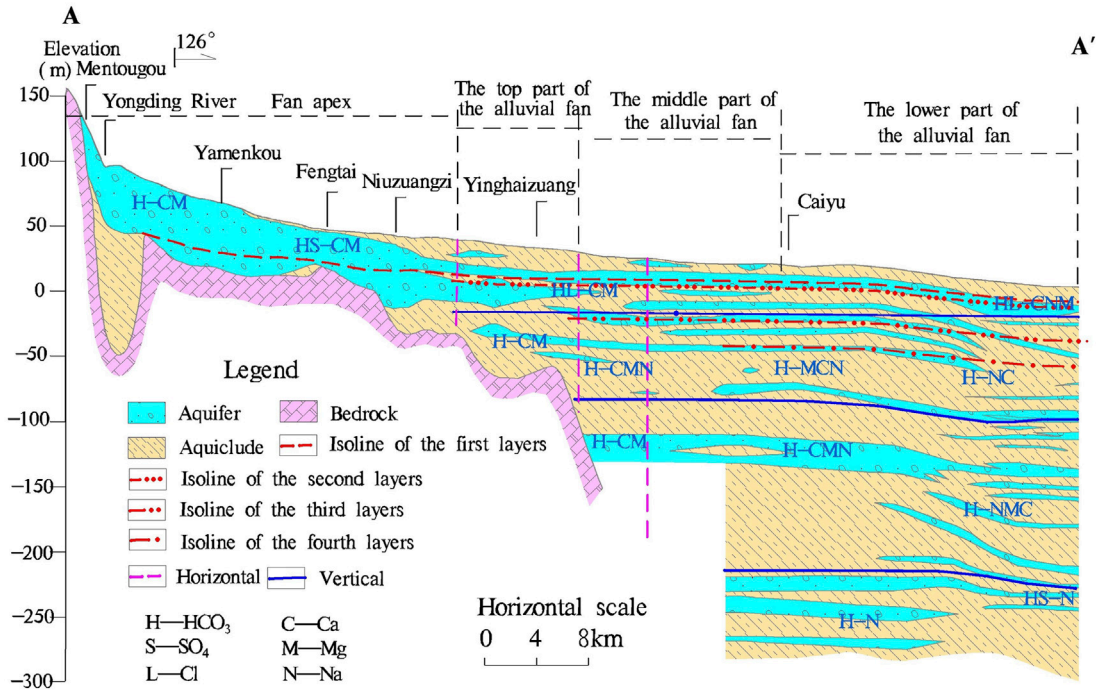

FIGURE 11
Hydrogeological profile of the Yongding River alluvial fan.

Combining the results of hydrochemical and isotopic analysis together with geology, topography, and hydrogeological conditions can improve the understanding of hydrogeologic processes and the reliability of groundwater-flow models. Typical zonality characteristics along the A–A′ profile (from Mentougou to Fengheying) reveal the conceptual model of the groundwater flow system in the YDR alluvial fan. The zoning characteristic of sediment and landform lithology is affected by the hydrodynamic conditions.

5 Conclusion

We provide a systematic analysis of groundwater evolution in the YDR alluvial fan. The analytic results are listed, as follows:

- The distribution characteristic of sediment and landform lithology is affected by the hydrodynamic conditions of the YRD alluvial fan. From the proximal fan to the distal fan in the typical profile, the sedimentary thickness increases from 40m–80 m in Mentougou to 300m–500 m in Caiyu and Fengheying. Coarse grains gradually decrease and fine particles gradually increase. The similar change trend is also found in the vertical direction.
- Zonality characteristics influence hydrodynamic behavior. The annual renewable rate of groundwater decreases from > 10% in the upper fan to 2%–8% nearby Daxing, which is < 2% in the distal fan. For the flow velocity and aquifer permeability, the average value of flow velocity in the single and double layer is 65 m yr^{-1} and 18.9 m yr^{-1} in the upper fan, respectively. From the mid fan to the distal fan, velocity decreases from 12.4 m yr^{-1} to 3.75 m yr^{-1} and permeability decreases from 8.54 m yr^{-1} to 0.64 m yr^{-1}.
- The hydrochemical characteristics of the second, third, and fourth aquifers show horizontal and vertical zonation. From the proximal fan to distal fan along the YDR, the hydrochemical type gradually changes from HCO_3-Ca·MgNa to HCO_3-Na. In the vertical direction, the ion concentration of Ca^{2+} and Mg^{2+} decreases, but K^+ and Na + increase with depth increase.
- The hydrochemical evolution process is obvious different in the different part of the alluvial fan. The function of dissolution and infiltration is the dominated hydrochemical process in the proximal fan area. From the mid fan to the distal fan, hydrochemical process changes to the function of cation-exchange absorption. In the area of the distal fan, the main hydrochemical process is the function of mixing and inspissation.

This study provides the essential and systematic analysis for identifying hydrochemical characteristics, hydrochemical evolution, and groundwater dynamics in the YDR alluvial fan, which is helpful to protect and manage the mother river of Beijing.

Data availability statement

The datasets presented in this study can be found in online repositories. The names of the repository/repositories and accession number(s) can be found in the article/ Supplementary Material.

Author contributions

Conceptualization: KL and XQ; methodology: KL; validation: KL, XQ, and SW; data curation: YS; writing—original draft preparation: KL; writing—review and editing: KL and XQ.

Funding

This study was funded by the China Geological Survey (No. DD20201165, DD20221677), CGS Research (No. JKY202004), National Key Research and Development Program of China (No. 2020YFC1807104) and Fundamental Research Funds for the Central Universities (E1E40411X2 and Y95401PXX2).

Acknowledgments

We would like to thank the professional reviewers and editors.

Conflict of interest

The authors declare that the research was conducted in the absence of any commercial or financial relationships that could be construed as a potential conflict of interest.

Publisher's note

All claims expressed in this article are solely those of the authors and do not necessarily represent those of their affiliated organizations, or those of the publisher, the editors, and the reviewers. Any product that may be evaluated in this article, or claim that may be made by its manufacturer, is not guaranteed or endorsed by the publisher.

References

Arenas, C., Millán, H., Pardo, G., and Pocoví, A. (2001). Ebro Basin continental sedimentation associated with late compressional pyrenean tectonics (north-eastern Iberia): Controls on basin margin fans and fluvial systems. *Basin Res.* 13, 65–89. doi:10.1046/j.1365-2117.2001.00141.x

Benvenuti, M. (2003). Facies analysis and tectonic significance of lacustrine fan-deltaic successions in the Pliocene-Pleistocene Mugello Basin, Central Italy. *Sediment. Geol.* 157, 197–234. doi:10.1016/s0037-0738(02)00234-8

Brooke, S. A. S., Whittaker, A. C., Armitage, J. J., D'Arcy, M., and Watkins, S. E. (2018). Quantifying sediment Transport dynamics on alluvial fans from spatial and temporal changes in grain size, Death Valley, California. *JGR. Earth Surf.* 123, 2039–2067. doi:10.1029/2018jf004622

Cao, W. G., Yang, H. F., Liu, C. L., Li, Y. J., and Bai, H. (2018). Hydrogeochemical characteristics and evolution of the aquifer systems of Gonghe Basin, Northern China. *Geosci. Front.* 9 (3), 907–916. doi:10.1016/j.gsf.2017.06.003

Chen, Z. Y., Liu, J., Yang, X. K., Chen, J., and Wang, Y. (2010). The environmental isotope markers of groundwater flow patterns of the Song-Nen Plain. *Earth Sci. Front.* 17 (6), 94–101. (in Chinese with English abstract).

Chen, Z. Y., Wang, Y., Liu, J., and Wei, W. (2010). Groundwater changes of selected groundwater systems in Northern China in recent fifty years. *Quat. Sci.* 30 (1), 115–126. (in Chinese with English abstract). doi:10.1016/j.proeps.2013.03.182

Cheng, D. Z., Chen, M., Shi, S. P., and Ma, Z. Z. (2001). Impact of anthropogenic modifications on the rainfall runoff in the upstream of Yongding River. *Des. Water Resour. Hydroelectr. Eng.* 20 (2), 19–21. (in Chinese with English abstract).

Edmunds, W. M. (2009). Geochemistry's vital contribution to solving water resource problems. *Appl. Geochem.* 24, 1058–1073. doi:10.1016/j.apgeochem.2009.02.021

Ezquerro, L., Luzón, A., Simón, J. L., and Liesa, C. L. (2019). Alluvial sedimentation and tectono-stratigraphic evolution in a narrow extensional zigzag basin margin (northern Teruel Basin, Spain). *J. Palaeogeogr.* 8, 29. doi:10.1186/s42501-019-0044-4

Forzoni, A., Storms, J., Whittaker, A., and de Jager, G. (2014). Delayed delivery from the sediment factory: Modeling the impact of catchment response time to tectonics on sediment flux and fluvio-deltaic stratigraphy. *Earth Surf. Process. Landf.* 39 (5), 689–704. doi:10.1002/esp.3538

Geological Mineral Authority of Beijing & Beijing Institute of Hydrogeology and Engineering Geology, (2008), *Groundwater of beijing*. China Land Press, Beijing.

Guillen, J., and Palanques, A. (1997). A shoreface zonation in the Ebro Delta based on grain size distribution. *J. Coast. Res.* 13, 867–878. doi:10.1016/S0924-2716(97)00008-7

Guo, G. X., Hou, Q. L., Xu, L., Liu, J. R., and Xin, B. D. (2014). Delamination and zoning characteristics of quaternary groundwater in Chaobai alluvial-proluvial fan, beijing, based on hydrochemical analysis. *Acta Geosci. Sin.* 35 (2), 204–210. (in Chinese with English abstract). doi:10.3975/cagsb.2014.02.12

Harvey, A. M., Mather, A. E., and Stokes, M. (2005). "Alluvial fans: Geomorphology, sedimentology, dinamics - introduction. A review of alluvial-fan research,". *Alluv. fans Geomorphol. Sedimentol. Din. Geological Society of London, special publication.*, 251, 1–7. doi:10.1144/GSL.SP.2005.251.01.01

Jiang, T. S., Yang, Z. S., Huang, Z. F., Shi, J. J., and Cai, L. (2010). Tendency and mechanism analysis of total hardness in shallow groundwater in the suburb of Beijing. *Hydrogeology Eng. Geol.* 37 (4), 33–37. doi:10.16030/j.cnki.issn.1000-3665.2010.04.007

Li, F. D., Pan, G. Y., Tang, C. Y., Zhang, Q. Y., and Yu, J. J. (2008). Recharge source and hydrogeochemical evolution of shallow groundwater in a complex alluvial fan system, southwest of North China Plain. *Environ. Geol.* 55, 1109–1122. doi:10.1007/s00254-007-1059-1

Li, Q., Zhou, J. L., Zhou, Y. Z., Bai, C. Y., Tao, H. F., Jia, R. L., et al. (2014). Variation of groundwater hydrochemical characteristics in the plain area of the Tarim Basin, Xinjiang Region, China. *Environ. Earth Sci.* 72, 4249–4263. doi:10.1007/s12665-014-3320-8

Li, X. Q., Zhang, L., and Hou, X. W. (2008). Use of hydrogeochemistry and environmental isotopes for evaluation of groundwater in Qingshuihe Basin, northwestern China. *Hydrogeol. J.* 16, 335–348. doi:10.1007/s10040-007-0269-7

Li, Y. H., Deng, Y. E., and Jia, S. Y. (2009). Hydrochemistry characteristics and hydrodynamic zone of groundwater of Tunnel in Wuzhi mountain. *Res. Soil & Water Conservation* 16 (1), 172–174. (in Chinese with English abstract). doi:10.1042/BSR20080061

LiBianLiHuangQiLiu, S. R. B. J. W. H., Li, B., and Qi, W. (2021). Hyporheic zone geochemistry of a multi-aquifer system used for managed aquifer recharge in Beijing, China. *Appl. Geochem.* 131, 105032. doi:10.1016/j.apgeochem.2021.105032

Litty, C., Schlunegger, F., and Viveen, W. (2017). Possible threshold controls on sediment grain properties of Peruvian coastal river basins. *Earth Surf. Dynam.* 5 (3), 571–583. doi:10.5194/esurf-5-571-2017

Liu, F., Li, Y. H., and Lin, J. (2008). A hydrogen and oxygen isotope study of groundwater in the Yongding River drainage of beijing and its environmental significance. *Acta Geosci. Sin.* 29 (2), 161–166. (in Chinese with English abstract). doi:10.3321/j.issn:1006-3021.2008.02.005

Liu, J. L., Pang, Z. H., Wang, S. F., Kong, Y. L., and Zhou, J. (2010). Impact of precipitation change and human activities on groundwter regime in the Chaobaihe alluvial and diluvial fan in Beijing in the last 30 years. *Quat. Sci.* 30 (1), 138–144. (in Chinese with English abstract). doi:10.3969/j.issn.1001-7410.2010.01.13

Liu, J. R., Lin, P., and Sun, Y. (2012). *Study on groundwater infiltration influence of the Yongding River*. Beijing: Beijing Institute of Hydrogeology and Engineering Geology. (in Chinese with English abstract).

Liu, K., Liu, J. R., Sun, Y., Liu, Y. C., Zhang, Y., and Wang, L. Y. (2013). River discharge by using regressive model in gorge of the Yongding River in Beijing. *Earth Sci. - J. China Univ. Geosciences* 38, 58–64. (in Chinesee with English abstract). doi:10.3799/dqkx.2013.S2.010

Liu, Y. Z., Wu, Q., Gao, Z. H., Lin, P., and Han, Z. (2013). Re-understanding of the variation laws of Quaternary groundwater in Beijing Plain. *Geotechnical Investigation Surv.* (5), 43–47. (in Chinese with English abstract).

Liu, Y. Z., Wu, Q., Lin, P., Liu, J. R., Xing, L. T., and Gao, Z. H. (2012). Restudy of the storage and migration model of the Quaternary groundwater in Beijing Plain area. *Sci. China Earth Sci.* 55 (7), 1147–1158. (in Chinese with English abstract). doi:10.1007/s11430-012-4417-0

LiuZhouLuoWangMcClainWang, S. Y. W. F. M. X., Luo, W., and McClain, M. E. (2022). A numerical assessment on the managed aquifer recharge to achieve sustainable groundwater development in Chaobai River area, Beijing, China. *J. Hydrology* 613, 128392. doi:10.1016/j.jhydrol.2022.128392

Lou, Z. H., Cheng, J. R., and Jin, A. M. (2006). Origin and evolution of the hydrodynamics in sedimentary basins-A case study of the Songliao basin. *Acta Sedimentol. Sin.* 24 (2), 193–201. (in Chinese with English abstract).

Lv, J. B. (2012). Geological background along the Banks of theYongding river. *Urban Geol.* 7 (1), 4–7. (in Chinese with English abstract).

Mallik, A. U., Lamb, E. G., and Rasid, H. (2001). Vegetation zonation among the microhabitats in a lacustrine environment: Analysis and application of belowground species trait patterns. *Ecol. Eng.* 18, 135–146. doi:10.1016/S0925-8574(01)00069-6

Mas-Pla, J., Menció, A., Bach, J., Soler, D., Zamorano, M., and Brusi, D. (2016). Trace element groundwater pollution hazard in regional hydrogeological systems (Empordà basin, NE Spain). *Water Air Soil Pollut.* 227, 218–240. doi:10.1007/s11270-016-2891-2

Naito, K., Fukahori, Y., He, P. M., Sakurai, W., Shimazaki, H., and Matsuhisa, Y. (1995). Oxygen and carbon isotope zonations of wall rocks around the Kamioka Pb-Zn skarn deposits, central Japan: Application to prospecting. *J. Geochem. Explor.* 54, 199–211. doi:10.1016/0375-6742(95)00044-5

Piao, S. L., Ciais, P., Huang, Y., Shen, Z. H., Peng, S. S., Li, J. S., et al. (2010). The impacts of climate change on water resources and agriculture in China. *Nature* 467, 43–51. doi:10.1038/nature09364

Robion, P., Kissel, C., de Lamotte, D. F., Lorand, J. P., and Guezou, J. C. (1997). Magnetic mineralogy and metamorphic zonation in the Ardennes Massif (France-Belgium). *Tectonophysics* 271, 231–248. doi:10.1016/S0040-1951(96)00268-5

Sarkar, A., and Guha, A. K. (1997). Pleistocene paleoclimatic zonation in northern Indian ocean as revealed from Globorotalia menardii abundance. *Indian J. Geo-Marine Sci.* 26, 84–87. doi:10.1007/s12594-012-0207-8

Shen, Z. L., and Wang, Y. X. (2002). Review and Outlook of water-rock interaction studies. *Earth Science-Journal China Univ. Geosciences* 27 (2), 127–133. (in Chinese with English abstract).

Song, X. F., Li, F. D., Yu, J. J., Tang, C. Y., Yang, C., Yang, X. C., et al. (2007). Characteristics of groundwater cycle using deuterium, oxygen-18 and hydrochemistry in Chaobai RIver Basin. *Geogr. Res.* 26 (1), 11–21. (in Chinese with English abstract). doi:10.3321/j.issn:1000-0585.2007.01.002

Straub, K. M., and Wang, Y. N. (2013). Influence of water and sediment supply on the long term evolution of alluvial fans and deltas: Statistical characterization of basin filling sedimentation patterns. *J. Geophys. Res. Earth Surf.* 118, 1602–1616. doi:10.1002/jgrf.20095

Wang, S. W., Kuo, Y. M., Kao, Y. H., Jang, C. S., Maji, S. K., Chang, F. J., et al. (2011). Influence of hydrological and hydrogeochemical parameters on arsenic variation in shallow groundwater of southwestern Taiwan. *J. Hydrology* 408, 286–295. doi:10.1016/j.jhydrol.2011.08.017

Wang, X. J., and Zhou, X. (2006). A preliminary analysis of the ^{14}C age of groundwater in the Yongdinghe River Plain in beijing. *Geol. Rev.* 52 (2), 283–288. (in Chinese with English abstract). doi:10.3321/j.issn:0371-5736.2006.02.019

Wang, Y. X., Ma, T., and Li, Y. M. (1998). Geochemical modeling of water-rock interaction in the Liulin karst system, Shanxi province. *Earth science-Journal China Univ. Geosciences* 23 (5), 519–522. doi:10.1016/S0022-1694(01)00376-6(in Chinese with English abstract)

Wogelius, R. A., Fraser, D. G., Wall, G. R. T., and Grime, G. W. (1997). Trace element and isotopic zonation in vein calcite from the Mendip Hills, UK, with spatial-process correlation analysis. *Geochimica Cosmochimica Acta* 61, 2037–2051. doi:10.1016/S0016-7037(97)00065-3

Xiao, Y., Hao, Q. C., Zhang, Y. H., Zhu, Y. C., Yin, S. Y., Qin, L. M., et al. (2022). Investigating sources, driving forces and potential health risks of nitrate and fluoride in groundwater of a typical alluvial fan plain. *Sci. Total Environ.* 802, , 149909. doi:10.1016/j.scitotenv.2021.149909

Xiao, Y., Liu, K., Hao, Q. C., Li, Y. S., Xiao, D., and Zhang, Y. J. (2022). Occurrence, controlling factors and health hazards of fluoride-enriched groundwater in the lower Flood Plain of Yellow River, northern China. *Expo. Health* 14, 345–358. doi:10.1007/s12403-021-00452-2

Xiao, Y., Liu, K., Hao, Q. C., Xiao, D., Zhang, Y. C., Yin, S. Y., et al. (2022). Hydrogeochemical insights into the signatures, Genesis and sustainable perspective of nitrate enriched groundwater in the piedmont of Hutuo watershed, China. *Catena* 212, 106020. doi:10.1016/j.catena.2022.106020

Xun, H., Wang, J. S., Zhai, Y. Z., and Zheng, J. Q. (2011). Chemical characteristics and evolution of groundwater in the Yongding River alluvial fan of Beijing plain. *Acta Geosci. Sin.* 32 (3), 357–366. (in Chinese with English abstract). doi:10.1007/s12182-011-0118-0

Yang, W. C. (1986). The sedimentary characteristics and the environmental changes of the Taizhi River alluvial fan. *Land & Resour.* (2), 117–128. (in Chinese with English abstract).

Yu, J. J., Song, X. F., Liu, X. C., Yang, C., Tang, C. Y., Li, F. D., et al. (2007). A study of groundwater cycle in Yongding River Basin by using δD, $\delta^{18}O$ and hydrochemical data. *J. Nat. Resour.* 22 (3), 415–423. (in Chinese with English abstract).

Yu, M., Wei, Y. S., Liu, J. G., Liu, P. F., Zhang, Z. M., Wei, W., et al. (2011). Impact of socioeconomic development on water resource and water enviroment of Yongding River in Beijing. *Acta Sci. Circumstantiae* 31 (9), 1817–1825. (in Chinese with English abstract). doi:10.13671/j.hjkxxb.2011.09.007

Zhai, Y. Z., Wang, J. S., Teng, Y. G., and Rui, Z. (2011). Variations of δD and $\delta^{18}O$ in water in beijing and their Implications for the local water cycle. *Resour. Sci.* 31 (1), 92–97. doi:10.1007/s40333-015-0048-6(in Chinese with English abstract)

Zhai, Y. Z., Wang, J. S., Teng, Y. G., and Zuo, R. (2011). Chemical and isotopic characteristics of groundwater in the Yongding River groundwater system of Beijing, Plain. *Acta Geosci. Sin.* 32 (1), 101–106. doi:10.1007/s40333-015-0048-6(in Chinese with English abstract)

Zhai, Y. Z., Wang, J. S., Zheng, J. Q., and Huan, H. (2011). Evolution and driving forces of water consumed structure in beijing during the past 30 years. *J. Nat. Resour.* 26 (4), 635–643. doi:10.3390/su14159596(in Chinese with English abstract)

Zhai, Y. Z., Wang, J. S., and Zhou (2013). J. Hydrochemical and isotopic markers of flow patterns and renewal Mode of groundwater in Chaobai RIver alluvial fan in beijing. *J. Basic Sci. Eng.* 21 (1), 32–44. (in Chinese with English abstract). doi:10.3969/j.issn.1005-0930.2013.01.004

Zhai, Y. Z., Wang, J. S., Zheng, J. Q., and Huan, H. (2011). Evolution and driving forces of water consumed structure in beijing during the past 30 years. *J. Nat. Res.* 26 (4), 635–643.

Zhai, Y. Z., Wang, J. S., Zuo, R., and Teng, Y. G. (2011). Progress in applications of groundwater ages in groundwater research. *Earth Environ.* 39 (1), 113–120. (in Chinese with English abstract).

Zhang, G. H., Liu, Z. P., Fei, Y. H., Lian, Y. L., Yan, M. J., and Wang, J. Z. (2010). The relationship between the distribution of irrigated Crops and the supply capability of regional water resources in north China plain. *Acta Geosci. Sin.* 31 (1), 17–22. (in Chinese with English abstract). doi:10.3724/SP.J.1231.2010.06586

Zhang, Z. H., Shi, D. H., Shen, Z. L., Zhong, Z. S., and Xue, Y. Q. (1997). Evolution and development of groundwater environment in north China Plain under human activities. *Acta Geosci. Sin.* 18 (4), 337–344. (in Chinese with English abstract).

Zhao, W., Lin, J., Guo, G. X., and Liu, Z. M. (2012). Development of layered monitoring and specialized inspection system of groundwater environment in beijing. *South-to-North Water Divers. Water Sci. Technol.* 10 (2), 83–87. (in Chinese with English abstract). doi:10.1186/gb-2010-11-s1-o10

Zheng, Y. J., Li, W. P., Wang, R. J., Liu, J. R., and Li, Y. M. (2012). Groundwater circulation and evolution characteristics in alluvial fan area of Chaobai River. *Yangtze River* 43 (15), 43–46. (in Chinese with English abstract). doi:10.1186/1744-859X-5-S1-S193

Zhou, X., Hu, F. S., and He, J. T. (2009). *Introduction to groundwater science*. BeijingChina: Geological Publishing House.

frontiers | Frontiers in Environmental Science

TYPE Original Research
PUBLISHED 07 December 2022
DOI 10.3389/fenvs.2022.1084286

OPEN ACCESS

EDITED BY
Lichun Wang,
Tianjin University, China

REVIEWED BY
Youquann Zhang,
Capital Normal University, China
Jahanzaib Israr,
University of Engineering and Technology, Lahore, Pakistan

*CORRESPONDENCE
Jianfeng Qi,
jianfengluck@163.com
Haipeng Guo,
pengfei7971@sohu.com

SPECIALTY SECTION
This article was submitted to Freshwater Science, a section of the journal Frontiers in Environmental Science

RECEIVED 30 October 2022
ACCEPTED 22 November 2022
PUBLISHED 07 December 2022

CITATION
Liu F, Qi J, Guo H, Wang Y, Guo K and Zang X (2022), Experimental study on consolidation characteristics of deep clayey soil in a typical subsidence area of the North China Plain.
Front. Environ. Sci. 10:1084286.
doi: 10.3389/fenvs.2022.1084286

Experimental study on consolidation characteristics of deep clayey soil in a typical subsidence area of the North China Plain

Fengjunnan Liu[1,2], Jianfeng Qi[2,3]*, Haipeng Guo[1,4]*, Yunlong Wang[1,4], Kaijie Guo[1,2] and Xisheng Zang[1,4]

[1]Hebei Cangzhou Groundwater and Land subsidence National Observation and Research Station, Cangzhou, China, [2]Laboratory of Water Resources Sustained Utilization and Development in Hebei Province, Shijiazhuang, China, [3]Key Laboratory of Intelligent Detection and Equipment for Underground Space of Beijing-Tianjin-Hebei Urban Agglomeration, Ministry of Natural Resources, Shijiazhuang, China, [4]China Institute of Geo-Environment Monitoring, Beijing, China

Land subsidence is an important environmental problem in the North China Plain (NCP). A typical subsidence area mainly located on adjoining areas of Beijing and Hebei provinces was selected to study the consolidation characteristics of deep clayey soil. Clay samples were collected from 14 boreholes at different depths, and the compression and consolidation behavior of the soil was analyzed by high-pressure oedometer tests. Results show that the deformation amount and deformation stabilization time in the primary consolidation stage increase with the load but decrease with the sampling depth. The nonlinear compression model of *e*-log(p) does not fit well for deep normally-consolidated clayey soil, the log(e+e_c)−logp model fit the shallow clayey soil better than the deep clayey soil, and the hyperbolic model fits almost all soil samples well. Based on statistical theory, the soil consolidation equation CE_NCP was established for calculating the relationship between the degree of consolidation and the time factor in subsidence areas. The equations were fitted with the data obtained from high-pressure consolidation tests to obtain three parameters *a, b* and *c*, which are applied to the consolidation calculations for soil samples at depths of 0–100 m, 100–200 m, 200–300 m and 300–400 m, respectively. The applicability of CE_NCP equation was evaluated by comparing it to the analytical solution of Terzaghi's consolidation equation, results showing that CE_NCP equation is more suitable for the calculation of the consolidation in the study area than the Terzaghi's analytical solution. Eventually, the CE_NCP equation was successfully used to estimate the degree of consolidation in a subsidence area of Lang Fang City in the NCP.

KEYWORDS

the North China Plain, land subsidence, clayey soil, consolidation, oedometer test

1 Introduction

Land subsidence is a potentially destructive hazard caused by various natural or man-made factors. Natural factors include, for example, tectonic motion, consolidation of soft soil and seismic activity. Man-made factors include withdrawal of groundwater, oil, and gas, engineering construction and so on. Studies have shown that excessive exploitation of groundwater is the main cause of land subsidence. The process of land subsidence is also the process of rock and soil compression and consolidation caused by pumping. The settlement mainly comes from the compression deformation of aquitards (clayey soil layers) and water-bearing sand layers. When the pore water pressure is restored, the compaction of sand layers can basically return to the original state. The compression of clay is permanent, which determines the irreversibility of land subsidence. With the continuous advancement of urbanization, the land subsidence caused by underground space development, foundation pit drainage, and large-scale landfilling has become increasingly prominent. The trend of high-rise and densification of urban

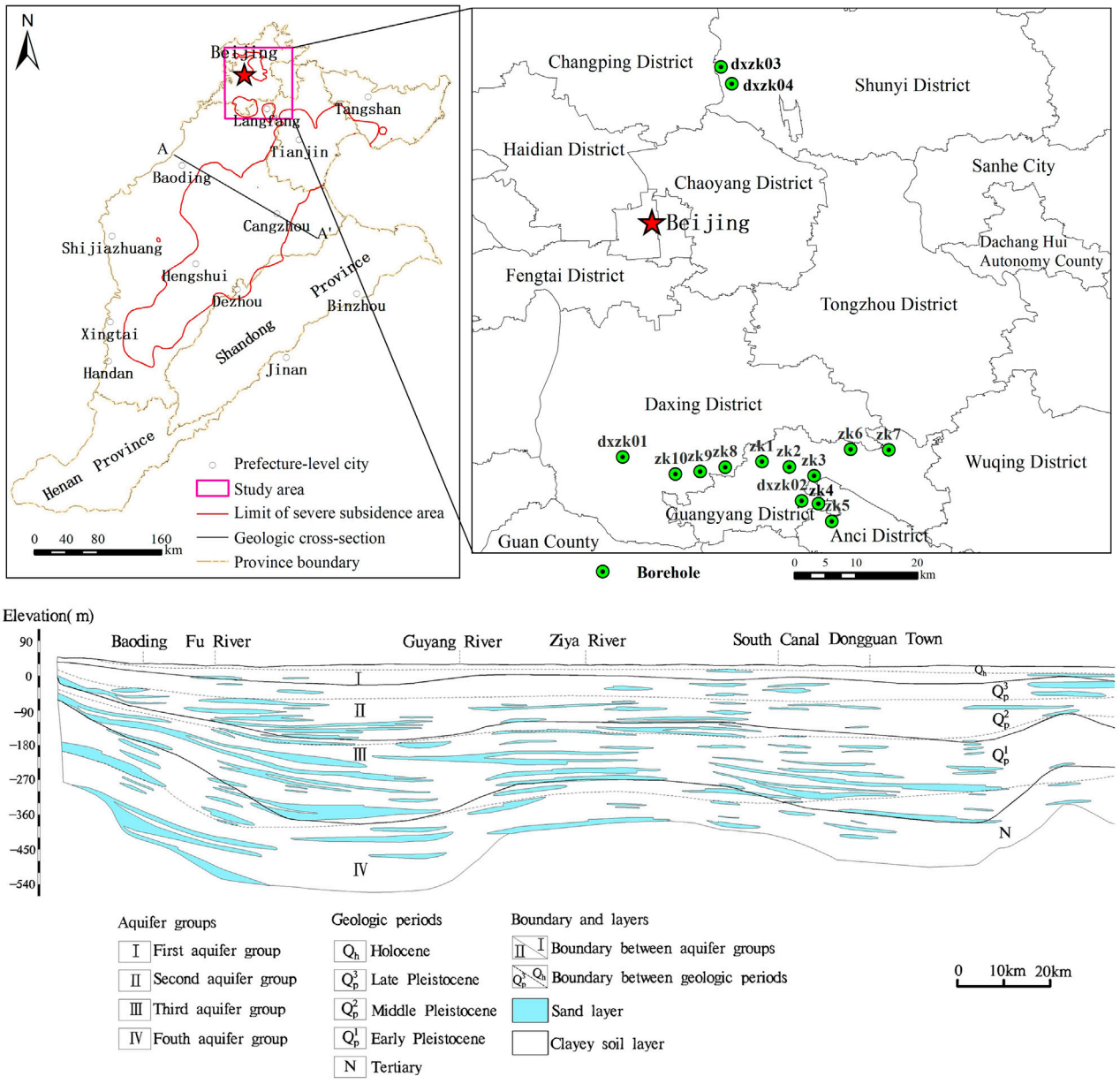

FIGURE 1
The study area and the distribution of sampling boreholes in a typical subsidence area of the NCP, and a typical hydrogeological cross section A-A'.

buildings is obvious, which gradually become a new important impacting factor of urban land subsidence.

Land subsidence is now a major environmental problem hindering regional sustainable development, occurring at more than 50 countries around the world, including United States, Japan, Mexico, Italy, Indonesia, India, Iran and China (Xiong et al., 2017; Figueroa-Mirandaet et al., 2018; Corbau et al., 2019; Bagheri et al., 2021; Gerardo et al., 2021; Guo et al., 2021; Kadiyan et al., 2021; Rafiee et al., 2022). The impact of land subsidence is expanding, and it is expected that by 2040, the global threat of land subsidence will involve nearly 20% of the population (Gerardo et al., 2021). In China, widespread subsidence is affecting rapidly developing cities, which are located in the major sedimentary basins such as the North China Plain (NCP). The NCP has the most serious and fastest developing land subsidence in China, with severe subsidence accounting for more than 80% of the country. More than 10 major cities, including Beijing, Tianjin, Cangzhou, Langfang, Hengshui and Dezhou, have experienced land subsidence (Figure 1). The development of land subsidence has caused severe condition in the NCP, with the maximum cumulative subsidence in Beijing, Tianjin and Hebei exceeding 1.7 m, 3.4 m and 2.6 m respectively (Cui and Lei, 2018). To promote the development of society and economy, regional aquifers of NCP have been over-exploited, resulting in the extrusion of clay layers, which is a major factor leading to land subsidence in this region. The deep groundwater depression cones are mainly distributed in the central and eastern plains of the NCP, consisting with the location of severe land subsidence areas. Land subsidence mainly occurred in the Quaternary loose sediments. Due to the low degree of soil consolidation, under the exploitation of underground fluids such as groundwater, geothermal fluid, oil and gas, the original pressure balance in the formation was broken, resulting in soil compression and land subsidence. In addition, the strata composed of a large amount of clayey soil with high plasticity (Figure 1), have possibility to form permanent settlement (Guo et al., 2017). Zhang et al. (2014) analyzed the deformation characteristics of soils in subsidence areas of the Beijing Plain using soil deformation and groundwater level data obtained by borehole extensometers, revealing the creep behavior and the elastic-plastic and viscoelastic-plastic mechanical behavior of the aquitards at different depths. They also concluded that the compressibility of the aquitards in the inelastic range is about one order of magnitude greater than in the elastic range.

In general, it is easier to estimate the total settlement of a soil than to estimate the time-dependent behavior of consolidation settlement. Terzaghi developed the theory of one-dimensional consolidation of saturated clays that has served as the basis for solving most practical soil mechanics and settlement problems. The aquitards (fine-grained interbeds) and confining beds mainly composed of clayey soil, have low permeability and high specific storage under virgin stressing. Thus, the escape of water and the adjustment of pore pressures is slow and time-dependent, and the stress increase by the hydraulic head decline in adjacent aquifers can induce nonlinear soil compaction in these fine-grained soil layers. Duncan. (1993) analyzed the limitations of conventional theory of clay consolidation settlement, concluding that factors such as the variation of the coefficient of consolidation (C_v) and nonlinear stress-strain relation can improve the accuracy of settlement estimation. For most clays, strains increase in proportion (or approximately in proportion) to the log of effective stress with a flat slope when the effective stress is low, and then increase rapidly as effective stresses exceed the preconsolidation pressure (Das and Sobhan, 2016). Laboratory tests and field observations have shown that the C_v value depends on the permeability and compressibility of the soil and varies with the consolidation process. Mesri et al. (1999) developed an inflection point method that is simpler than the most widely used graphical methods of Casagrande and Taylor for calculating C_v. Chan (2003) used the least square method to determine the C_v value, and calculated results were more accurate than traditional methods because the entire range of primary consolidation data was used. The finite difference and circular arc endpoint methods were used to determine C_v, taking into account changes in permeability and compressibility during the consolidation to reduce the error of graphical method (Abbaspout et al., 2015). Akbarimehr et al. (2020) found that the soil compression index has good correlations with the physical properties of undisturbed and remolded Tehran clay by performing 125 consolidation tests and through determining the physical properties. Freire et al. (2022) studied vertical (C_v) and horizontal (C_h) consolidation coefficients of Guaratiba's soft soil by comparing CPTu and laboratory test data. They concluded that high values of the variability of C_v and C_h were probably due to the wide range of organic matter, sand lenses and the sand content. Zabłocka et al. (2020) found that the main factors affecting correlation between C_v and consolidation pressure trends were mechanisms controlling changes in soil volume (mechanical or physicochemical), which is different for expansive and non-expansive soils. An efficient methodology was proposed to predict C_v using machine learning models such as Multiple Linear Regression (MLR), Artificial Neural Network (ANN), Support Vector Regression (SVR), and Adaptive Network based Fuzzy Inference System (ANFIS) (Mittal et al., 2021). To better characterize the compressive behavior of soils, several non-linear compression models have been developed, such as the e-log(p) model (Davis and Raymond, 1965; Li et al., 2013), the log(e+e_c)-log(p) model (Chai et al., 2004), and the hyperbolic model (Wei, 1993).

Given the limitations of Terzaghi's theory, various attempts have been made to improve the accuracy of consolidation calculation, generating abundant achievements on one-dimensional consolidation theory and consolidation process of soft clay. Analytical solutions for one-dimensional nonlinear consolidation of single-layer and double-layered soft soil under constant loading were derived by introducing an

improved continuous drainage boundary condition (Zong and Wu, 2020; Zong, 2021), and the effects of different interface parameters and nonlinear parameters on soil consolidation characteristics were analyzed. The consolidation process of high organic peat soil was studied with one-dimensional consolidation tests in Dali, China, and the results showed that the consolidation process of the peat soil was divided into three stages (Feng et al., 2021). To improve the applicability of the consolidation theory in the actual soil consolidation calculation, the theory and methods for the settlement calculation of double-layer and multi-layer soils considering creep and rheological properties were developed (Chen et al., 2021; Cui et al., 2021). The microstructure evolution of soft soil during consolidation was explored through oedometer tests and field emission scanning electron microscopy tests, and the relationship between microstructure and macroscopic characteristics was analyzed (Zheng et al., 2021). The consolidation process and characteristics of saturated and unsaturated soils under different boundary and seepage conditions have also been widely studied. Governing equations for the one-dimensional large strain consolidation of a fully saturated clay layer were derived (Gibson et al., 1981; Xie and Leo, 2004), where the variation of soil compressibility and permeability during consolidation was taken into account. Compared with the small-strain theory, the large-strain theory predicts a smaller subsidence magnitude, while the subsidence develops and the excess pore water pressure dissipates faster (Xie and Leo, 2004). The discrepancy between large and small strain theories became smaller when the compressibility of soil was decreased and the magnitude of applied load was reduced. Hu et al. (2018) proposed a semi-analytical solution for the one-dimensional nonlinear consolidation problem of structured soil under single-stage loading. The one-dimensional consolidation problem of clay in land reclamation was obtained by considering the effects of self-weight and continuous drainage boundary conditions, and the calculation results were successfully applied to the settlement analysis of land reclamation (Feng et al., 2019). An approximate analytical solution for one-dimensional nonlinear consolidation of single-layer and multi-layer foundation under fixed load and cyclic load was derived by considering the change of compressibility and permeability of saturated soil layer (Kim et al., 2020a; 2020b). To reveal stress- and suction-dependency of primary and secondary consolidation responses of the soil, Rezania et al. (2020) carried out one-dimensional consolidation tests on natural and reconstituted London clay samples under saturated and unsaturated conditions by using a newly designed unsaturated soil consolidation instrument. Based on the piecewise linear consolidation model, Liu et al. (2021) proposed a consolidation model for cohesive soils considering drainage conditions and non-Darcy flow. The calculation results showed that both continuous drainage boundary and Hansbo's flow could significantly slow down the consolidation process. Kim et al. (2021) studied the radial consolidation characteristics of unsaturated soil under cyclic loading based on the Fredlund and Hasan's consolidation theory. The effects of different parameters on the radial consolidation of unsaturated soil subjected to various cyclic loadings were examined. Yin et al. (2022) proposed a simplified calculation method for consolidation settlement, which can be conveniently applied to the settlement calculation of layered cohesive soil foundation. According to Selvadurai (2021), the irreversibility of the skeletal deformations should be considered when quasistatic loading cycles are encountered.

The above studies mainly improve several defects in Terzaghi's theory, such as nonlinearity of C_v, large deformation, finite deformation and rheological problems. Due to the complexity of clay, researchers do not have a unified understanding of the properties of soil, which will inevitably affect the accuracy of analytical solutions, making it difficult to apply these methods to engineering practice. Furthermore, the above experiments and theoretical analysis are mainly aimed at shallow clayey soil, while the deep clayey soil buried more than 50–100 m is rarely involved. The land subsidence of the NCP is serious due to human activities, especially the excessive exploitation of deep groundwater. Due to the limitation of the complex influencing factors and large variation in space of aquifer systems, the research on consolidation characteristics of deep clayey soils is weak so far, which restricts the scientific evaluation of the development trend for land subsidence and its forecast and early warning. In this paper, clayey samples at various depths were collected from 14 boreholes in a typical subsidence area located at the junction of Beijing and Hebei provinces. Then high-pressure oedometer tests were carried out to study the consolidation characteristics of clayey soil and to evaluate the applicability of the existing nonlinear compression deformation models. In addition, a model CE_NCP for calculating the consolidation degree of clayey soil was established to provide theoretical support for the study of land subsidence. The derived CE_NCP equation was used to investigate the degree of consolidation in a typical land subsidence area in Langfang, Hebei Province, China, where subsidence was mainly caused by deep groundwater abstraction.

2 Materials and methods

2.1 Soil used in the study

The study area is located in a typical subsidence area in the NCP, mainly in the north of Langfang City, Hebei Province, and the south of Daxing District and Shunyi District in Beijing (Figure 1). In order to meet the demand of water resources, the deep groundwater was developed on a large scale, which has induced the formation of groundwater depression cones and severe subsidence areas. The strata composed of multi-layer aquifer systems with deep confined aquifers and thick

compressible clay layers, have geological and hydrogeological conditions favorable for the development of land subsidence. The mechanism of land subsidence in the study area is typical and representative in the NCP. Figure 1 also shows the distribution of sampling boreholes. There are eight drilling holes in Langfang City, of which the drilling depth of zk1-zk7 is 80m, and the drilling depth of dxzk02 is 402 m. There are four boreholes in Daxing District, of which zk8-zk10 boreholes have a depth of 80m, and dxzk01 borehole has a depth of 407 m. The other two boreholes marked with dxzk03 and dxzk04 are located in Shunyi District, having the drilling depth of 400 m and 300m, respectively. Basic physical parameter tests and high-pressure consolidation tests were carried out on 156 groups of clay samples at different depths, including 60 clay samples and 96 silty clay samples. The sampling intervals for each borehole was approximately 10 m. A total of 60 samples were collected from 0 to 50 m below the ground surface, and 96 samples were collected from 50 m or more below the surface.

2.2 Experimental set-up

Each clay sample was cut 30 cm from the borehole core, placed in a soil sample cylinder, sealed with wax and wrapped with tape, and sent to the laboratory. During preparation, the experimenters place the soil sample tube in the direction of natural deposition, remove the wax seal and tape, open the soil sample tube to take unearthed samples, and check whether the soil sample has been disturbed. A sample with the diameter of 61.8 mm and the height of 20 mm was prepared by a ring cutter for consolidation test, and the remaining soil was used for the determination of physical parameters. Consolidation tests were carried out with an electronic compression rheometer to investigate the time-dependent behavior of the clayey soil during one-dimensional consolidation. The test data were used to estimate the preconsolidation pressure, compression modulus and consolidation coefficient of test specimens at different depths. In the compression rheometer lateral movement of the soil was prevented by containing the soil in a stiff metal ring so that only vertical soil movements were possible. In practice the condition of zero lateral strain is satisfied approximately in the case where the area of the aquifer is much larger than the thickness. The stress measurement system is BK-2 precision sensor, and the maximum consolidation stress can reach 70 MPa. A series of pressures were applied to the specimen, ranging from 0.04 MPa to 40.96MPa, each being double the previous value. Each pressure was maintained for 24 h, during which compression readings were observed at appropriate intervals. During the test, the room was kept at a constant temperature and humidity.

2.3 Determination of soil parameters

The value of coefficient of consolidation (C_v) for a particular pressure increment in the test can be obtained by comparing the characteristics of the experimental and theoretical consolidation curves, which is referred as curve-fitting. Once the value of C_v has been determined, the permeability can be calculated. In this paper, the root time method (Craig, 2004) was used to determine the value of C_v, where C_v is given by

$$C_v = 0.848\bar{h}^2 / t_{90} \quad (1)$$

where $\bar{h}$ is the longest drainage distance of the specimen (L), t_{90} is the time corresponding to 90% degree of consolidation (T).

The degree of consolidation U_t of a soil is the ratio of the average dissipation value of the pore water pressure to the initial pore water pressure at a certain time during the consolidation process under a certain level of load, or the ratio of the compression amount at a certain time to the final compression amount. The value of t_{90} can be obtained when calculating C_v, and the deformation corresponding to U_t = 100% on the test curve can be determined in proportion. Then, the degree of consolidation can be calculated by comparing the deformation of test specimen at each time with that at 100% consolidation. According to Terzaghi's one-dimensional consolidation theory, the degree of consolidation degree U_t is clearly related to the dimensionless time factor T_v. The formula for calculating the time factor is as follows:

$$T_v = C_v t / \bar{h}^2 \quad (2)$$

where C_v is the coefficient of consolidation (L^2/T), t is the time of consolidation (T), and $\bar{h}$ is the longest drainage distance (L). During the test, both the upper and lower boundaries of the specimen are free-draining, so $\bar{h}$ is taken as half the thickness of the specimen.

3 Results

3.1 Time-dependent compression behavior of the clayey soils

The results of four specimens in borehole dxzk02 (Table 1), located in the subsidence area of Langfang, were selected to analyze the time-dependent consolidation characteristics. These specimens were all clayey soil and were taken from depths of 52.3 m, 145.5 m, 292.3 m and 395.1 m, respectively. The time-dependent compression process under various loads is shown by plotting deformation versus time (Figure 2). Time is plotted on a logarithmic scale.

It can be seen from Figure 2 that under different loads, the deformation of clayey soil increases with time, and the growth rate increases first and then decreases gradually. From the

TABLE 1 Physico-mechanical properties of four soil samples taken from borehole dxzk02.

NO.	Soil type	Depth (m)	Density (g/cm^3)	Moisture content (%)	Void ratio	Plasticity index	Liquidity index	Specific gravity	Self-weight stress (kPa)
1	clay	52.3	1.96	28.06	0.790	17.24	0.45	2.74	595.65
2	clay	145.5	1.97	27.64	0.782	19.97	0.23	2.75	1498.64
3	clay	292.3	2.05	20.49	0.610	17.20	−0.02	2.74	3194.08
4	clay	395.1	2.06	22.57	0.636	20.07	−0.05	2.75	4243.16

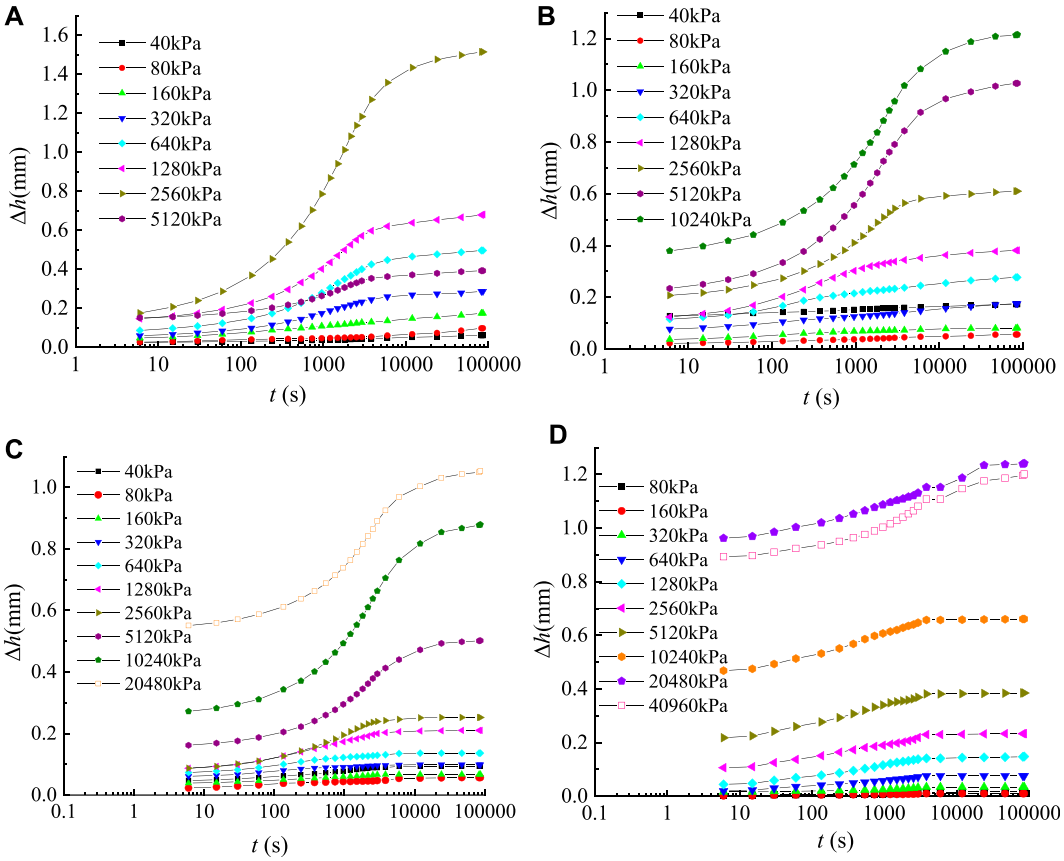

FIGURE 2
Time-varying deformation curves of soil samples under different loads with sampling depths of 52.3 m **(A)**, 145.5 m **(B)**, 292.3 m **(C)** and 395.1 m **(D)**, respectively.

plot, we can observe three distinct stages, i.e., the initial compression, the primary consolidation and the secondary consolidation. Mainly due to the compression of a small amount of air in the soil, the initial compression occurs within 0–6 s, and in general, the deformation during this period increases with the increase of the load. For the undisturbed soil samples, due to the non-uniform compaction degree and composition of the soil, the phenomenon of large load leading to small deformation occurred in the experiment. Under the same load, the deformation of different depths within 0–6 s does not change significantly, and no obvious decreasing trend with the increase of depth occurs. The primary consolidation phase begins after the instantaneous deformation is completed. In

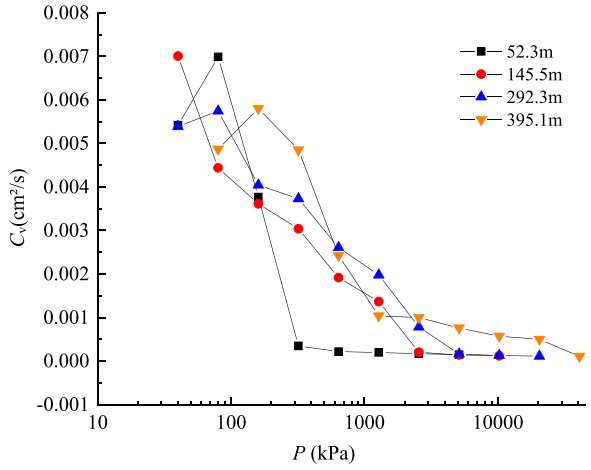

FIGURE 3
The relationship between the evaluation value of C_v and the pressure.

this stage, the deformation amount increases rapidly, but the growth rate gradually decreases, and finally the deformation reaches a stable state.

Figure 2 also indicates that the deformation law of the primary consolidation stage has a certain relationship with the load and soil sampling depth. At the same sampling depth, the deformation of the primary consolidation stage, the proportion of deformation to total deformation and the consolidation stabilization time increase with the increase of the load. For soil samples with a depth of 292.3 m, the primary consolidation deformation at 1280kPa and 2560 kPa is 0.140 mm and 0.164 mm, respectively, the deformation ratio is 53.8% and 65.0%, and the consolidation stabilization time is 49 min and 200 min, respectively. Under the same load, the primary consolidation deformation and the stabilization time decrease with the increase of depth. The main reason for this phenomenon is that the sampling depth is positively correlated to the pressure of overlying soil, and also positively correlated to the pre-consolidation pressure after the soil sample was taken out. Due to different stress history, soil samples with greater depths have less deformation and less consolidation time when the same load is applied. For example, when the load is 2560kPa, the primary consolidation deformations of the four specimens at depth of 52.3 m, 145.5 m, 292.3 m and 395.1 m are 1.322 mm, 0.399 mm, 0.164 mm and 0.124 mm respectively. The corresponding deformation ratios are 87.3%, 65.4%, 65.0% and 53.2%, and the stabilization times are 784 min, 784 min, 200 min and 100 min respectively. The above indicators all decrease with the increase of depth. When the primary consolidation is completed, the deformation increases slowly over time. Eventually the compression of the soil continues at a slow rate for an indefinite period of time and is called secondary consolidation. The amount of secondary consolidation is minor within 24 h, accounting for about 0.4%–1.3% of the total deformation. The relevance of secondary consolidation with respect to time or duration of the applied load need be studied in the future.

3.2 Analysis of coefficient of consolidation

The coefficient of consolidation C_v reflects the speed of soil consolidation, which is proportional to the rate of the dissipation of pore water pressure. The larger the C_v is, the greater the dissipation rate of the pore water pressure. According to the root time method, the C_v value of each load was determined. Figure 3 exhibits the C_v values for four clayey soil samples at depths of 52.3 m, 145.5 m, 292.3 m and 395.1 m, taken from the borehole dxzk02 (Table1). The estimated results show that the value of C_v varies with the pressure and depth, and the estimated values are in the range of 1.0×10^{-4}cm^2/s—7.0×10^{-3} cm^2/s, as shown in Figure 3. In general, at the same pressure, the C_v increases with the depth of soil sampling. For example, at a pressure of 2560kPa, the determined values of C_v are 1.69×10^{-4}cm^2/s, 2.02×10^{-4}cm^2/s, 7.82×10^{-4}cm^2/s and 9.99×10^{-4}cm^2/s, corresponding to the sampling depths of 52.3 m, 145.5 m, 292.3 m and 395.1 m. As the depth increases, the consolidation state gradually changes to overconsolidation, and the time t_{90} required to reach 90% consolidation degree is shorter, so the value of C_v obtained by graphic method becomes larger. When the pressure is less than 80–160 kPa, the C_v increases with the pressure, and when the pressure increases further, the C_v decreases with the pressure. Eventually, the rate of change of C_v with pressure becomes slow.

3.3 Analysis of degree of consolidation

Figure 4 compares the calculated U_t versus T_v curves at different pressures for four specimens of clayey soil collected at different depths (Table 1). The degree of consolidation increases rapidly when the time factor is in the range of 0–1.0. As T_v is greater than 1, the growth rate of U_t slows down gradually until the deformation stabilizes (U_t = 1). Under the same time factor, the degree of consolidation generally increases with the pressure. For example, when T_v of the sample at 395.1 m is equal to 2, the U_t increases from 70% to 76.7%, to 85.1% as the pressure increases from 2560kPa to 5120kPa, to 10240 kPa. When T_v is the same, the difference of U_t under high pressure and low pressure conditions increases with the increase of sampling depth, indicating that the consolidation process of deep clayey soil under low pressure is slower than that under high pressure. Deep clayey soil usually has large initial self-weight stress, high degree of consolidation, and is

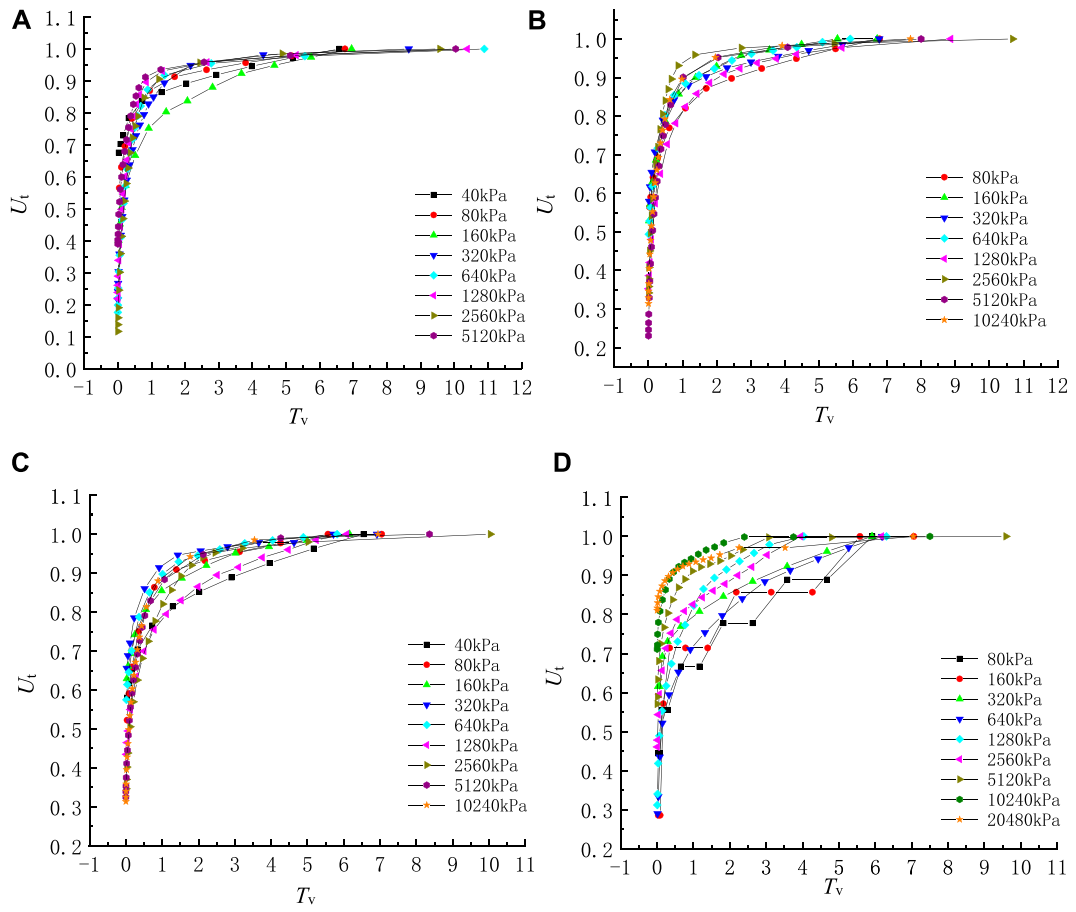

FIGURE 4
Relationship between U_t and T_v under different loads at sampling depths of 52.3 m **(A)**, 145.5 m **(B)**, 292.3 m **(C)** and 395.1 m **(D)**.

in a dense and hard state. When the load is low, especially less than the self-weight stress of the soil, the compaction response of the specimen is relatively low. In this case, as shown in Figures 4C,D, U_t increases relatively slowly with T_v.

4 Discussion

4.1 Verification of typical one-dimensional compression and consolidation models

4.1.1 Verification of one-dimensional nonlinear compression models

The compression response of clayey soil is usually defined by the relation between the settlement (after consolidation is complete) and the effective stress, which is usually nonlinear. It is conventional to investigate the compression response using a plot of void ratio against the vertical effective stress. The widely used nonlinear models describing the relation between the settlement and the effective stress are as follows.

4.1.1.1 *e*-log(*p*) model

The void ratio is an important indicator of soil consolidation characteristics. The test data show that the void ratio has a certain linear relationship with log(*p*), as shown in Eqs 3–5 (Davis and Raymond, 1965; Li et al., 2013).

$$e_0 - e = C_c log\left(\frac{P}{P_0}\right) \tag{3}$$

For over-consolidated soil, the *e*-log(p) model is modified as follows

$$e_0 - e = C_r log\left(\frac{P}{P_0}\right) \quad (\mathrm{P} \le \mathrm{Pc}) \tag{4}$$

$$e_0 - e = C_r log\left(\frac{P_c}{P_0}\right) + C_c log\left(\frac{P}{P_c}\right) \quad (\mathrm{P} > \mathrm{Pc}) \tag{5}$$

where e_0 is the initial void ratio, P_0 is the initial effective stress, e and P are respectively the void ratio and effective pressure of soil at a certain time, C_c is the compression index, P_c is the preconsolidation pressure and C_r is the recompression index.

TABLE 2 The estimated parameters of the compression models for ten soil samples.

NO.	Sampling depth (m)	*e*-log(*p*)			log(*e*)-log(*p*)		log(*e*+1)-log(*p*)		Hyperbolic model		
		C_c	C_r	R^2	C_0	R^2	C_1	R^2	n	E_0	R^2
1	29.6	0.132	—	0.900	0.11	0.87	0.038	0.887	5.89	4687	0.962
2	35.35	0.121	—	0.905	0.085	0.877	0.033	0.895	5.18	3803	0.967
3	41.55	0.089	—	0.888	0.077	0.846	0.026	0.866	6.08	5100	0.937
4	52.3	0.284	0.116	0.922	0.114	0.855	0.044	0.875	3.18	10010	0.914
5	61.55	0.477	0.135	0.940	0.152	0.795	0.062	0.82	1.96	8852	0.770
6	292.3	0.085	—	0.795	0.076	0.741	0.025	0.778	4.40	38226	0.927
7	313.6	0.099	—	0.758	0.098	0.687	0.03	0.738	3.13	41840	0.910
8	324.3	0.245	0.049	0.972	0.067	0.751	0.023	0.783	5.70	28082	0.885
9	343.55	0.254	0.046	0.975	0.061	0.751	0.024	0.772	3.49	76022	0.981
10	369.5	0.226	0.043	0.966	0.078	0.771	0.027	0.798	3.68	90860	0.997

The *e*-log(*p*) model is commonly used to describe the compression deformation of soil. However, the *e*-log(*p*) curve may not be linear due to differences in soil structure. Therefore, sometimes it is unreasonable to use only the compression (or recompression) index C_c (or C_r) to represent the characteristics of soil compression deformation.

4.1.1.2 log(*e*+e_c)-log(*p*) model

Chai et al. (2004) developed the log(*e*+e_c)- log(*p*) model as described below.

$$log\,(e + e_c) = log\,(e_0 + e_c) - C_{cr} log\left(\frac{P}{P_0}\right) \tag{6}$$

where C_{cr} is the modified compression index, that is, the slope of the log(*e*+e_c)-log(*p*) line; e_c is a test parameter, ranging from -1 to 1. when e_c is 0, the model is simplified to the log(*e*)-log(*p*) model, and when e_c is 1, the model is simplified to the log(1 + *e*)-log(*p*) model. The slopes of the straight lines corresponding to these two models are C_0 and C_1, respectively.

4.1.1.3 Hyperbolic compression model

Wei. (1993) found that the shape of a general *ε*-*p* curve is similar to a hyperbola, and the expression is

$$\frac{P}{\varepsilon} = E_0 + nP \tag{7}$$

where E_0 and n are model parameters, *ε* is vertical strain of soil.

10 groups of soil samples from borehole dxzk02 in Langfang City were selected to verify the suitability of the above three compression models. The experimental data of the above 10 sets of typical clayey soil samples were analyzed, and different compression models were used to fit them, and the model parameters and coefficient of determination R^2 were obtained (Table 2).

Table 2 shows that the *e*-log(*p*) model parameter C_c ranges from 0.085 to 0.477, parameter C_r ranges from 0.043 to 0.135, the log(*e*)-log(*p*) model parameter C_0 ranges from 0.061 to 0.152, the log(1 + *e*)- log(*p*) model parameter C_1 ranges from 0.023 to 0.062, the hyperbolic model parameter *n* ranges from 1.96 to 6.08, and the parameter E_0 ranges from 3803 to 90860 kPa for 10 sets of clayey samples. From the fitting results of each model and the test data of each soil sample, it can be seen that the hyperbolic model and *e*-log(p) models have the best fitting effect, the R^2 values of multiple samples are all above 0.92, and the mean R^2 value are 0.93 and 0.9, respectively. The R^2 of the log(e)-log(p) and log(1 + e)-log(p) models is generally in the range of 0.69–0.89, and the fitting effect is not as good as the hyperbolic model and *e*-log(p) models. It can also be seen that the *e*-log(p) model does not fit well for deep normally-consolidated soils, the R^2 is only 0.79 and 0.76 for the normally-consolidated soil samples at depths of 292.3 m and 313.6 m, respectively. The log(e)-log(p) and log(1 + e)-log(p) models fit the shallow clayey samples better than the deep clayey samples, while the hyperbolic model fits almost all soil samples well. The strain-stress curves are presented for the clay samples at depths of 29.6 m and 292.3 m, respectively, which are compared to the *e*-log(p), log(e)-log(p), log(1 + e)-log(p) and hyperbolic models (Figure 5). As shown in Figure 5, the above conclusion is also proved to be correct by comparing the strain-stress curves with the compression models.

4.1.2 Verification of Terzaghi's one-dimensional consolidation equation

The average degree of consolidation U_t can be expressed as (Craig, 2004):

$$U_t = 1 - \sum_{m=0}^{\infty} \frac{2}{M^2} \cdot e^{-M^2 T_v} \tag{8}$$

where M = (2m + 1)*π*/2. Eq. 8 can be expanded to:

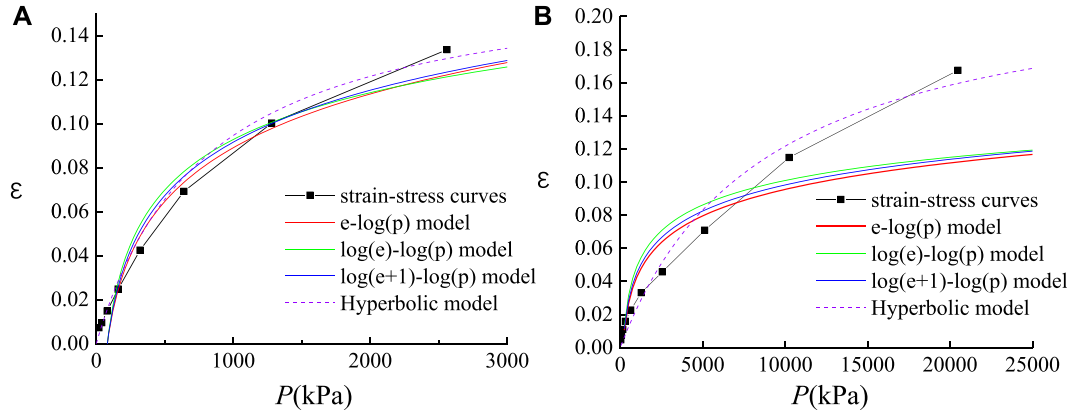

FIGURE 5
The strain-stress curves with comparisons to the compression models at sampling depths of 29.6 m **(A)** and 292.3 m **(B)**.

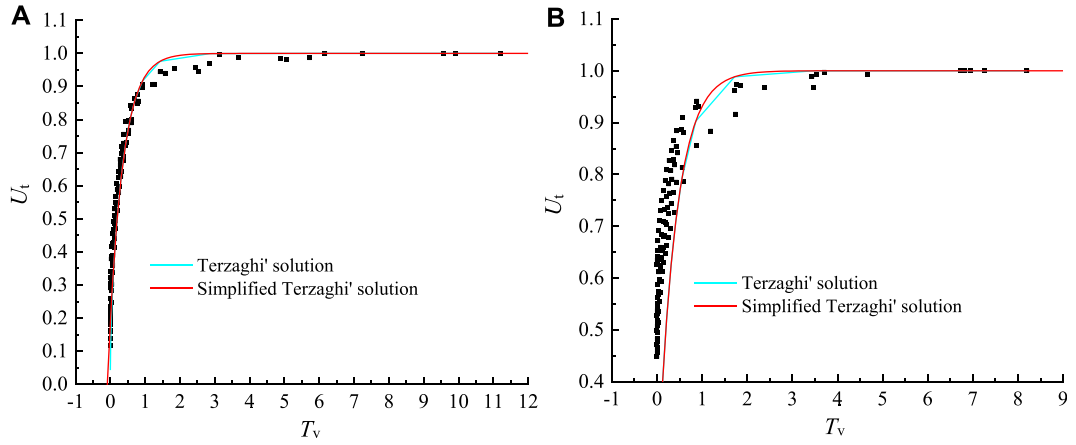

FIGURE 6
Data fitting of the solution of Terzaghi's 1D consolidation equation to experimental data for shallow clay at p = 2560 kPa **(A)** and deep clay at p = 20480 kPa **(B)**.

$$U_t = 1 - \frac{8}{\pi^2}\left(e^{-\frac{\pi^2}{4}T_v} + \frac{1}{9}e^{-\frac{9\pi^2}{4}T_v} + \ldots\right) \quad (9)$$

Since the series in the brackets of Eq. 9 converges quickly, the first term can be used in practice, see Eq. 10:

$$U_t = 1 - \frac{8}{\pi^2}e^{-\frac{\pi^2}{4}T_v} \quad (10)$$

Eqs 9, 10 are analytical solution for Terzaghi's one-dimensional consolidation equation and simplified forms, respectively. The accuracy of these solutions was tested by plotting the degree of consolidation and time factor data for five sets of shallow and deep clayey soil samples under loads of 2560 kPa and 20480 kPa, respectively (Figure 6). As shown in Figure 6A, the analytical solution of the Terzaghi's equation is similar to the simplified solution, which is in good agreement with the test data of the shallow clayey soil samples. For deep clayey soil, the solution appears to underestimate the value of U_t when the time factor T_v is in the range 0–1, and overestimate the value of U_t when T_v is greater than 1 (Figure 6B).

4.2 A new solution for one-dimensional consolidation of deep clayey soil

4.2.1 Equation derivation

Since the analytical solution of Terzaghi's consolidation equation has a certain error in calculating the consolidation degree of deep clayey soil, it is necessary to establish a new

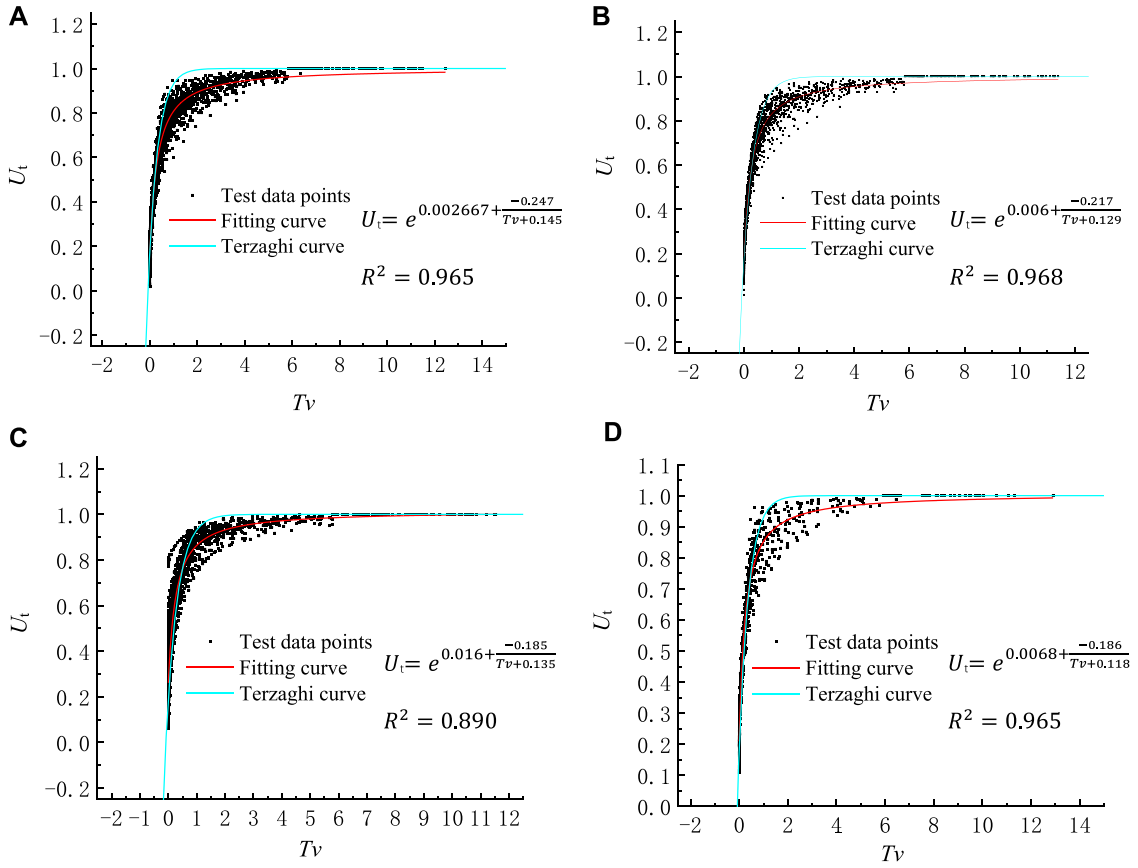

FIGURE 7
Data fitting of U_t -T_v curves for the clayey soil samples at depth of 0–100 m under loads of 0.64 MPa **(A)**, 1.28 MPa **(B)**, 2.56 MPa **(C)** and 5.12Mpa **(D)**.

relationship between U_t and T_v. Accordingly, 156 groups of clayey soil samples with depths of 0–400 m were collected from 14 boreholes in Langfang, Shunyi and Daxing areas, and the relationship between U_t and T_v under various loads was analyzed. For soil layers with a buried depth of less than 400 m, the sum of self-weight stress and additional stress caused by pumping and building loads is less than 10MPa, thus, the load applied to the soil specimens in the laboratory is selected as 640kPa-10.24 MPa. The data analysis software ORIGIN was used to fit the U_t - T_v data. According to the change trend of the data points, the fitting function was judged to conform to the exponential function. After repeated fitting of the data, an exponential equation (Eq. 11, abbreviated as CE_NCP) was established for the relationship between U_t and T_v.

$$U_t = e^{\left(a+\frac{b}{T_v+c}\right)} \tag{11}$$

The results of test data and fitting curves are shown in Figures 7, 8, indicating that CE_NCP fits the test data better than the analytical solution of Terzaghi' consolidation equation, which overestimates the degree of consolidation as a whole. The mean value of R^2 for the CE_NCP equation is 0.946, indicating that the overall fit of the test data is good. The mean R^2 values of the specimens at depths of 0–100 m, 100–200 m, 200–300 m and 300–400 m are 0.947, 0.949, 0.937 and 0.950, respectively, implying that CE_NCP is suitable for the consolidation calculation of both shallow and deep clayey soils.

To more accurately reflect the consolidation process, CE_NCP was applied to all soil sample data from 0 to 400 m depth. The parameters *a*, *b* and *c* were averaged under various loads, and Equations 12-15 were obtained as follows.

$$U_t = e^{\left(0.008+\frac{-0.209}{T_v+0.132}\right)} \quad \text{(soil depth of 0 – 100m)} \tag{12}$$

$$U_t = e^{\left(0.0131+\frac{-0.256}{T_v+0.162}\right)} \quad \text{(soil depth of 100 – 200m)} \tag{13}$$

$$U_t = e^{\left(0.011+\frac{-0.23}{T_v+0.168}\right)} \quad \text{(soil depth of 200 – 300m)} \tag{14}$$

$$U_t = e^{\left(-0.0066+\frac{-0.26}{T_v+0.175}\right)} \quad \text{(soil depth of 300 – 400m)} \tag{15}$$

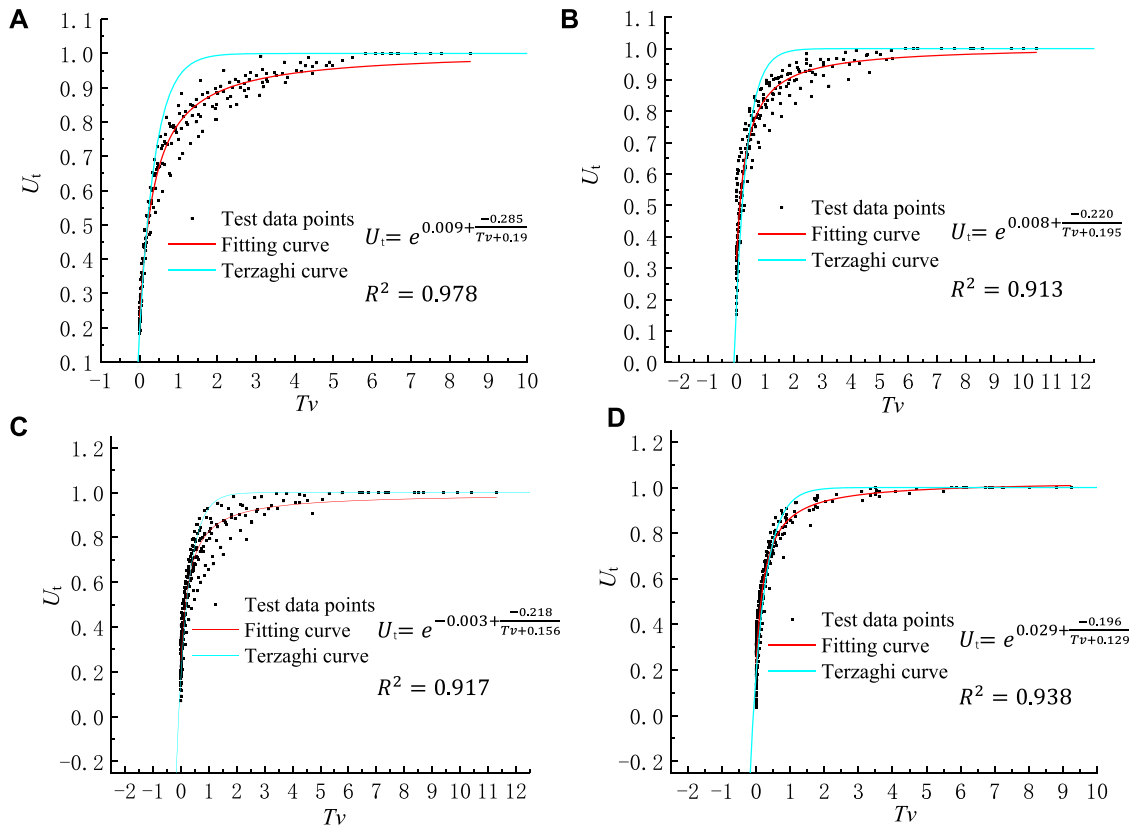

FIGURE 8
Data fitting of U_t -T_v curves for the clayey soil samples at depth of 200–300 m under loads of 1.28 MPa **(A)**, 2.56 MPa **(B)**, 5.12 MPa **(C)** and 10.24 MPa **(D)**.

TABLE 3 The estimated parameters *a*, *b* and *c* for the CE_NCP consolidation equation.

NO.	Depth (m)	Parameter	Data range	Mean value	Equation
1	0–100 m	*a*	0.0027 to 0.016	0.008	$U_t = e^{(0.008+\frac{-0.209}{T_v+0.132})}$
		b	−0.247 to −0.185	−0.209	
		c	0.118 to 0.145	0.132	
2	100–200 m	*a*	−0.001 to 0.035	0.0131	$U_t = e^{(0.0131+\frac{-0.256}{T_v+0.162})}$
		b	−0.301 to −0.208	−0.256	
		c	0.124 to 0.195	0.162	
3	200–300 m	*a*	0.003 to 0.029	0.0108	$U_t = e^{(0.011+\frac{-0.23}{T_v+0.168})}$
		b	−0.285 to −0.196	−0.23	
		c	0.129 to 0.195	0.168	
4	300–400 m	*a*	−0.039 to 0.026	−0.0066	$U_t = e^{(-0.0066+\frac{-0.26}{T_v+0.175})}$
		b	−0.327 to −0.217	−0.26	
		c	0.146 to 0.213	0.175	

4.2.2 Parametric analysis

Analysis of the parameters *a*, *b* and *c* is important to understand the variation range and physical meaning. The data ranges and mean values of the parameters are presented in Table 3. Analysis results show that the parameter *b* increases with the increase of the load. For example, when the loads are 0.64MPa, 1.28MPa, 2.56 MPa and 5.12MPa, the values of parameter *b* for 100–200 m samples

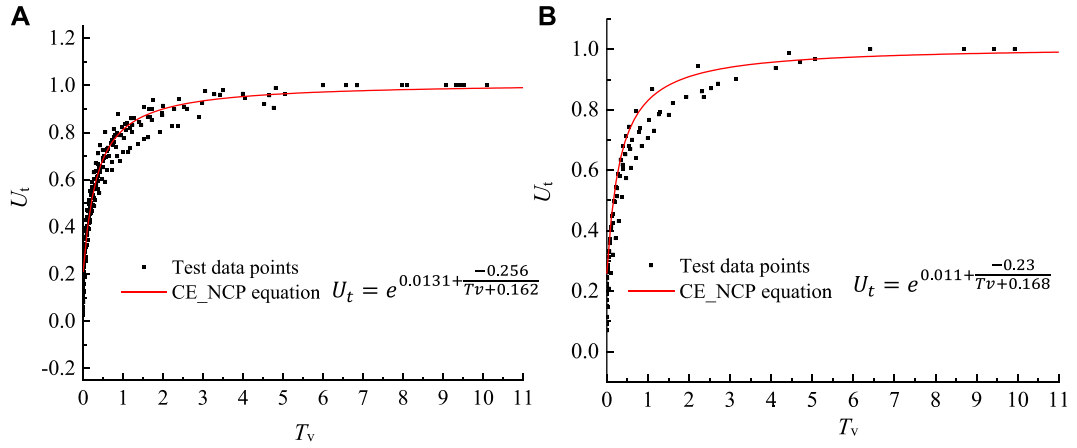

FIGURE 9
Applicability verification of CE_NCP equation, when the load is 5.12 MPa with depth of 100–200 m **(A)** and the load is 5.12 MPa with depth of 200–300 m **(B)**.

are −0.301, −0.281, −0.234 and −0.208, respectively. As the depth increases to 200–300 m, the *b* value increases from −0.285 to −0.22, to −0.218, to −0.196, corresponding to loads of 1.28 MPa, 2.56 MPa, 5.12 MPa and 10.24 MPa, respectively. In general, for soil samples with different depths, the mean values of parameters *b* and *c* in the proposed equations do not change much.

Sensitivity of the U_t-T_v relationship to the model parameters was analyzed by expanding or reducing the size of one parameter by 10 times while the other two parameters remained unchanged. Results show that the U_t-T_v curve is more sensitive to parameters *a* and *b* than c. That is, the variation of parameters *a* and *b* has a greater influence on the fitting results than the parameter c. Analysis also shows that the parameter *a* mainly affects the part of the *Ut-Tv* curves after the inflection point where the slope of the curve changes from large to small. Table 3 shows that the variation range of parameter *b* is small, from −0.26 to −0.209, so the change of parameter *b* has little effect on the calculation results because it is limited to a small range, even though the U_t-T_v curve is sensitive to parameter *b*. Therefore, parameter *a* is the most important control parameter in CE_NCP.

4.2.3 Verification and application of CE_NCP

To verify the suitability of the developed consolidation equation CE_NCP, the test data of the soil samples taken from the boreholes located in Shunyi, i.e., dxzk03 and dxzk04, were selected for the fitting (Figure 9). The results show that the equatioin CE_NCP fits well with the test data.

To put the proposed equation into practice, the degree of consolidation of clay near borehole dxzk02 in Langfang was estimated, and the calculated degree of consolidation was compared with the consolidation state of the strata. Langfang City is located at the junction of the Hebei Plain and the Beijing Plain, and the Quaternary loose soil layer is thick. Due to the influence of human activities, especially over-exploitation of deep groundwater, the subsidence rate gradually increased, and by 2015, the maximum subsidence rate had exceeded 80mm/annum. The strata of Langfang City can be divided into four aquifer groups. Groundwater in the first and second aquifer groups is defined as shallow groundwater with unconfined or semi-confined hydraulic properties. Groundwater in the third and fourth aquifer groups is confined and is defined as deep groundwater. There are extensive and thick aquifers in all four aquifer groups. Due to poor quality of shallow groundwater, deep groundwater was mainly exploited locally. The relationship between the variation of groundwater depression cones and land subsidence shows that most serious subsidence areas coincide well with the distribution of depression cones of deep groundwater. The increase of groundwater extraction resulted in the decrease of deep groundwater levels, which led to the increasing of land subsidence rate and the influence area. The decline of groundwater levels is the main influencing factor of land subsidence in this area. There are regional differences in the intensity of groundwater exploitation, and the decline in water levels varies from place to place. In 2019, the depth of shallow groundwater in the area was measured to be 7m–13m, and the depth of deep groundwater reached 80 m.

To study the deformation law of the clayey soil driven by groundwater abstraction, in 2019, a borehole dxzk-02 with a drilling depth of 402.3 m was constructed near the groundwater depression cone in Langfang City, and undisturbed clayey soil samples were collected every 2 m. According to the drilling histogram, the total thickness of the clay in the borehole was is 214.3 m, accounting for 52.9% of the total thickness. The proportion of clayey soil for the third and fourth aquifers was 56.8% and 52.8%,

TABLE 4 Aquifer group division and stratigraphic thickness of lithologies.

Aquifer group	Depth of top and bottom (m)	Thickness of clayey soil (m)	Thickness of silt and sand (m)	Proportion of clayey soil (%)
1	0.0–21.4	8.3	13.1	38.8
2	21.4–110.0	44.05	44.55	49.7
3	110.0–265.6	88.35	67.25	56.8
4	265.6–402.3	73.61	65.79	52.8

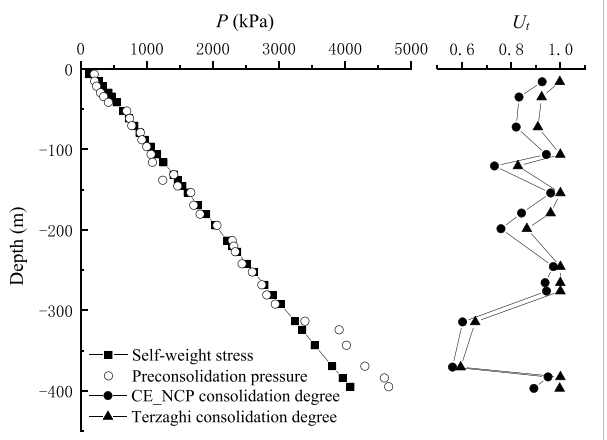

FIGURE 10
Change of self-weight stress, preconsolidation pressure, and degree of consolidation with depth.

respectively (Table 4). Clayey soil and coarse-grained soil were mutually distributed, and the thickest layer of clayey soil was located in the fourth aquifer group, reaching to 21.1 m.

Through geotechnical tests and high-pressure consolidation tests, the time-varying compression curves of soil samples at different depths and mechanical indicators such as pre-consolidation pressure, consolidation coefficient, compression index, and rebound index were obtained. By comparing the self-weight stress and pre-consolidation pressure, the soil layer with a depth of less than 300 m is basically normally consolidated, and the soil layer with a depth of more than 300 m is slightly over-consolidated (Figure 10).

Assuming that the clay layer only bears the additional load caused by groundwater extraction, the additional load is calculated as a 13 m drop in the shallow groundwater table and an 80 m drop in the deep groundwater level. The Langfang groundwater depression cone was formed in 1978. With the development of the city, the depression cone has been deepened and expanded. By the end of the drilling construction in 2019, it has been 41 years. Therefore, the action time of additional load caused by pumping is calculated as 41 years. Since the thickness of the clay layers at different depths is known, the degree of consolidation of the clay layers can be calculated by the Terzaghi's equation and the CE_NCP equation proposed in this paper, as shown in Figure 10. The degree of consolidation calculated by CE_NCP equation at the depth of 0–400 m was in the range of 0.56–0.97, and the degree of consolidation obtained by Terzaghi's equation was from 0.59 to 1.0. With the increase of depth, the variation law of consolidation degree calculated by Terzaghi's equation and CE_NCP equation is consistent, but the values calculated by CE_NCP equation are all smaller than those calculated by Terzaghi's equation. These phenomena are consistent with the conclusion in Section 4.2.1. The results of these two solutions indicate that the clayey soil in the study area is still not fully consolidated, and may still be compressed and result in continued land subsidence. In fact, the groundwater levels in Langfang City have stopped dropping due to the measures to control groundwater exploitation in recent years, but the land subsidence in this region is still developing, which implies that the consolidation of the clay layers have not been fully completed. The thick and low-permeability clay layers may continue to compact at a decreasing rate during the hydraulic head stabilization or recovery.

5 Conclusion

Based on the test data of undisturbed soil samples from 14 boreholes in typical land subsidence areas of Langfang, Daxing and Shunyi, the deformation and consolidation laws of deep clayey soils were analyzed in this paper, and the model CE_NCP was developed to estimate the degree of consolidation. This study has great scientific value and practical implications to improve the accuracy of land subsidence calculation, forecast and early warning, and will provide technical support to effectively relieve the disasters of land subsidence caused by groundwater exploitation in the NCP. The main conclusions are as follows:

1) The time-dependent compression process of clayey soil is roughly divided into three stages, namely the initial compression stage, the primary consolidation stage and the secondary consolidation stage. Overall, the instantaneous deformation caused by the initial compression is positively related to the load. The deformation amount and

deformation stabilization time in the primary consolidation stage increase with the increase of the load and decrease with the increase of depth. Geotechnical tests show a general trend that the coefficient of consolidation decreases with the load. With the same soil depth and time factors, the degree of consolidation increases with increasing load. With the same time factor, the difference in the degree of consolidation obtained under high load and low load conditions increases with the increase of sampling depth, indicating that the consolidation process of deep clayey soils becomes slower under low load. Under the same time factor T_v, the degree of consolidation U_t generally increases with the pressure, and the difference of U_t under high pressure and low pressure conditions increases with the increase of sampling depth.

2) Existing compression models were evaluated for their applicability in the study area. Compared with the log(e)-log(p) and log(1 + e)-log(p) models, the hyperbolic and *e*-log(p) models have better fitting effects. However, the *e*-log(p) model does not fit well for deep normally-consolidated soils. The log(e)-log(p) and log(1 + e)-log(p) compression models fit the shallow clayey soil samples better than the deep clayey samples. The hyperbolic model fits almost all soil samples well.
3) For deep clayey soils, the Terzaghi's consolidation equation deviates considerably from the experimental data. Through statistical analysis of a large number of test data, we proposed the CE_NCP consolidation equation, which is more suitable for calculation of the consolidation process of deep clayey soil in the study area than the Terzaghi's equation. Among the three model parameters *a, b* and *c* involved in CE_NCP, parameter *a* has the greatest influence on the calculation results. The CE_NCP consolidation equation was applied successfully in calculating the degree of consolidation in the subsidence area of Lang Fang City.

Data availability statement

The original contributions presented in the study are included in the article/supplementary material, further inquiries can be directed to the corresponding authors.

Author contributions

Conceptualization, JQ, HG, and FL; data curation, FL, YW, and KG; formal analysis, FL, JQ, and HG; funding acquisition, HG; investigation, YW, FL, XZ, and KG; methodology, JQ, HG, and FL; supervision, FL and YW; writing—original draft, FL, JQ, and HG; writing—review and editing, FL, JQ, HG, and XZ. All authors have read and agreed to the published version of the manuscript.

Funding

This work was supported by the National Natural Science Foundation of China (Grant No. 41877294) and the China Geological Survey (Grant Nos. DD20160235 and DD20190679).

Acknowledgments

Thanks for the support of the above funding and the Science and Technology Innovation Team Project of Hebei GEO University.

Conflict of interest

The authors declare that the research was conducted in the absence of any commercial or financial relationships that could be construed as a potential conflict of interest.

Publisher's note

References

Abbaspout, M., Porhoseini, R., Barkhordari, K., and Ghorbani, A. (2015). Coefficient of consolidation by end of arc method. *J. Cent. South Univ.* 22, 332–337. doi:10.1007/s11771-015-2526-6

Akbarimehr, D., Eslami, A., Aflaki, E., and Imam, R. (2020). Using empirical correlations and artificial neural network to estimate compressibility of low plasticity clays. *Arab. J. Geosci.* 13, 1225. doi:10.1007/s12517-020-06228-3

Bagheri-Gavkosh, M., Hosseini, S. M., Ataie-Ashtiani, B., Sohani, Y., Ebrahimian, H., Morovat, F., et al. (2021). Land subsidence: A global challenge. *Sci. Total Environ.* 778, 146193. doi:10.1016/j.scitotenv.2021.146193

Chai, J. C., Miura, N., Zhu, H. H., and Yudhbir (2004). Compression and consolidation characteristics of structured natural clay. *Can. Geotech. J.* 41 (6), 1250–1258. doi:10.1139/t04-056

Chan, A. H. C. (2003). Determination of the coefficient of consolidation using a least squares method. *Géotechnique* 53 (7), 673–678. doi:10.1680/geot.2003.53.7.673

Chen, Z. J., Feng, W., and Yin, J. H. (2021). A new simplified method for calculating short-term and long-term consolidation settlements of multi-layered soils considering creep limit. *Comput. Geotechnics* 138, 104324. doi:10.1016/J.COMPGEO.2021.104324

Corbau, C., Simeoni, U., Zoccarato, C., Mantovani, G., and Teatini, P. (2019). Coupling land use evolution and subsidence in the Po delta, Italy: Revising the past

occurrence and prospecting the future management challenges. *Sci. Total Environ.* 654, 1196–1208. doi:10.1016/j.scitotenv.2018.11.104

Craig, R. F. (2004). *Craig's soil mechanics*. New York, USA: Spon Press.

Cui, P. L., Liu, Z. Y., Zhang, J. C., and Fan, Z. C. (2021). Analysis of one-dimensional rheological consolidation of double-layered soil with fractional derivative Merchant model and non-Darcian flow described by non-Newtonian index. *J. Cent. South Univ.* 28 (1), 284–296. doi:10.1007/S11771-021-4602-4

Cui, W., and Lei, K. (2018). Some ideas on land subsidence working from the view of coordinated development in Beijing-Tianjin-Hebei Regions. *Urban Geol.* 13 (2), 25–30. (in Chinese).

Das, B. M., and Sobhan, K. (2016). *Principles of geotechnical engineering*. 9th edn. Boston: Cengage Learning.

Davis, E. H., and Raymond, G. P. (1965). A non-linear theory of consolidation. *Géotechnique* 15 (2), 161–173. doi:10.1680/geot.1965.15.2.161

Duncan, J. M. (1993). Limitations of conventional analysis of consolidation settlement. *J. Geotech. Engrg.* 119, 1333–1359. doi:10.1061/(asce)0733-9410(1993)119:9(1333)

Feng, J. X., Ni, P. P., and Mei, G. X. (2019). One-dimensional self-weight consolidation with continuous drainage boundary conditions: Solution and application to clay-drain reclamation. *Int. J. Numer. Anal. Methods Geomech.* 43, 1634–1652. doi:10.1002/nag.2928

Feng, R. L., Peng, B., Wu, L. J., Cai, X. P., and Sheng, Y. P. (2021). Three-stage consolidation characteristics of highly organic peaty soil. *Eng. Geol.* 294, 106349. doi:10.1016/j.enggeo.2021.106349

Figueroa-Miranda, S., Tuxpan-Vargas, J., Ramos-Leal, J. A., Hernández-Madrigal, V. M., and Villaseñor-Reyes, C. I. (2018). Land subsidence by groundwater over-exploitation from aquifers in tectonic valleys of central Mexico: A review. *Eng. Geol.* 246, 91–106. doi:10.1016/j.enggeo.2018.09.023

Freire, M. M., Marques, M. E. S., Tassi, M. C., and Berbert, L. A. (2022). Comparison between coefficients of consolidation from CPTu and laboratory tests for Guaratiba's soft soil, Rio de Janeiro, Brazil. *Cone Penetration Test.*, 427–431. doi:10.1201/9781003308829-59

Gerardo, H. G., Pablo, E., Roberto, T., Béjar-Pizarro, M., López-Vinielles, J., Rossi, N., et al. (2021). Mapping the global threat of land subsidence. *Science* 371 (6524), 34–36. doi:10.1126/SCIENCE.ABB8549

Gibson, R. E., Schiffman, R. L., and Cargill, K. W. (1981). The theory of one dimensional consolidation of saturated clays: II. Finite nonlinear consolidation of thick homogeneous layers. *Can. Geotech. J.* 18 (2), 280–293. doi:10.1139/t81-030

Guo, H. P., Bai, J. B., and Zhang, Y. Q. (2017). The evolution characteristics and mechanism of the land subsidence in typical areas of the North China Plain. *Geol. China* 44 (06), 1115–1127. (in Chinese).

Guo, H. P., Li, W. P., Wang, L. Y., Chen, Y., Zang, X. S., Wang, Y. L., et al. (2021). Present situation and research prospects of the land subsidence driven by groundwater levels in the North China Plain. *Hydrogeol. Eng. Geol.* 48 (3), 162–171. (in Chinese).

Hu, A. F., Xia, C. Q., Cui, J., Li, C. X., and Xie, K. H. (2018). Nonlinear consolidation analysis of natural structured clays under time-dependent loading. *Int. J. Geomech.* 18 (2), 04017140. doi:10.1061/(ASCE)GM.1943-5622.0001059

Kadiyan, N., Chatterjee, R. S., Pranjal, P., Agrawal, P., Jain, S. K., Angurala, M. L., et al. (2021). Assessment of groundwater depletion–induced land subsidence and characterisation of damaging cracks on houses: A case study in mohali-chandigarh area, India. *Bull. Eng. Geol. Environ.* 80, 3217–3231. doi:10.1007/S10064-021-02111-X

Kim, P., Kim, H. S., Pak, C. U., Paek, C. H., Ri, G. H., and Myong, H. B. (2020a). Analytical solution for one-dimensional nonlinear consolidation of saturated multi-layered soil under time-dependent loading. *J. Ocean Eng. Sci.* 6 (1), 21–29. doi:10.1016/j.joes.2020.04.004

Kim, P., Ri, K. S., Kim, Y. G., Sin, K. N., Myong, H. B., and Paek, C. H. (2020b). Nonlinear consolidation analysis of a saturated clay layer with variable compressibility and permeability under various cyclic loadings. *Int. J. Geomech.* 20 (8), 04020111. doi:10.1061/(ASCE)GM.1943-5622.0001730

Kim, P., Ri, M. C., Ri, K. S., Rim, M. C., and Jong, S. G. (2021). Radial consolidation analysis of unsaturated soil with vertical drains under various cyclic loadings. *Int. J. Numer. Anal. Methods Geomech.* 2021, 1549–1568. doi:10.1002/NAG.3213

Li, G. X., Zhang, B. Y., and Yu, Y. Z. (2013). *Soil mechanics*. 2th edn. Beijing: Tsinghua University Press.

Liu, Z. Y., Zhang, J. C., Yang, C. Y., and Xu, C. Y. (2021). Piecewise-linear model for one-dimensional consolidation considering non-Darcian flow under continuous drainage boundary. *Int. J. Geomech.* 21 (5), 06021011. doi:10.1061/(ASCE)GM.1943-5622.0002017

Mesri, G., Feng, T. W., and Shahien, M. (1999). Coefficient of consolidation by inflection point method. *J. Geotech. Geoenviron. Eng.* 125125 (8), 7168–7718. doi:10.1061/(asce)1090-0241(1999)125:8(716)

Mittal, M., Satapathy, S. C., Pal, V., Agarwal, B., Goyal, L. M., and Parwekar, P. (2021). Prediction of coefficient of consolidation in soil using machine learning techniques. *Microprocess. Microsystems* 82, 103830. doi:10.1016/j.micpro.2021.103830

Rafiee, M., Ajalloeian, R., Dehghani, M., and Mahmoudpour, M. (2022). Artificial neural network modeling of the subsidence induced by overexploitation of groundwater in Isfahan-Borkhar Plain, Iran. *Bull. Eng. Geol. Environ.* 81, 170. doi:10.1007/s10064-022-02646-7

Rezania, M., Bagheri, M., and Nezhad, M. M. (2020). Creep and consolidation of a stiff clay under saturated and unsaturated conditions. *Can. Geotech. J.* 57 (5), 728–741. doi:10.1139/cgj-2018-0398

Selvadurai, A. P. S. (2021). Irreversibility of soil skeletal deformations: The Pedagogical Limitations of Terzaghi's celebrated model for soil consolidation. *Comput. Geotechnics* 135, 104137. doi:10.1016/j.compgeo.2021.104137

Wei, R. L. (1993). Derivation for coefficient of consolidation from settlement observation. Chinese. *J. Geotech. Eng.* 15 (2), 12–19. (in Chinese).

Xie, K. H., and Leo, C. J. (2004). Analytical solutions of one-dimensional large strain consolidation of saturated and homogeneous clays. *Comput. Geotechnics* 31, 301–314. doi:10.1016/j.compgeo.2004.02.006

Xiong, X. F., Shi, X. Q., and Wu, J. F. (2017). 3D numerical simulation of elasto-plastic land subsidence induced by groundwater pumping. *Hydrogeol. Eng. Geol.* 44 (2), 151–159. (in Chinese).

Yin, J. H., Chen, Z. J., and Wei, Q. (2022). A general simple method for calculating consolidation settlements of layered clayey soils with vertical drains under staged loadings. *Acta Geotech.* 17 (8), 3647–3674. doi:10.1007/s11440-021-01318-2

Zabłocka, K., Lendo-Siwicka, M., and Wrzesiński, G. (2020). The influence of mineralogical composition of soil on the consolidation coefficient value. *Acta Sci. Pol. Archit.* 19 (3), 83–90. doi:10.22630/ASPA.2020.19.3.30

Zhang, Y. Q., Gong, H. L., Gu, Z. Q., Wang, R., and Zhao, W. (2014). Characterization of land subsidence induced by groundwater withdrawals in the plain of Beijing city, China. *Hydrogeol. J.* 22, 397–409. doi:10.1007/s10040-013-1069-x

Zheng, Y. M., Sun, H., Hou, M. X., and Ge, X. R. (2021). Microstructure evolution of soft clay under consolidation loading. *Eng. Geol.* 293, 106284. doi:10.1016/j.enggeo.2021.106284

Zong, M. F. (2021). *Theoretical and experimental study on one-dimensional nonlinear consolidation of soft soil based on continuous drainage boundary. PhD thesis*. Wuhan P.R. China: China University of Geosciences. (in Chinese).

Zong, M. F., Wu, W. B., El Naggar, M. H., Mei, G., Ni, P., and Xu, M. (2020). Analytical solution for one-dimensional nonlinear consolidation of double-layered soil with improved continuous drainage boundary. *Eur. J. Environ. Civ. Eng.*, 1–22. doi:10.1080/19648189.2020.1813207

frontiers | Frontiers in Environmental Science

TYPE Original Research
PUBLISHED 20 January 2023
DOI 10.3389/fenvs.2022.1084151

OPEN ACCESS

EDITED BY
Yong Xiao,
Southwest Jiaotong University, China

REVIEWED BY
Hongzhuo Fan,
Université de Lille, France
Shuo Ma,
Zhejiang University of Technology, China
Zhanfeng Fan,
Chengdu University, China

*CORRESPONDENCE
Yan Zhang,
zhangyan2020@cdut.edu.cn
Chunchi Ma,
machunchi17@cdut.edu.cn

SPECIALTY SECTION
This article was submitted to Freshwater Science,
a section of the journal
Frontiers in Environmental Science

RECEIVED 30 October 2022
ACCEPTED 29 November 2022
PUBLISHED 20 January 2023

CITATION
Gao Y, Zhang Y, Ma C, Zheng X, Li T, Zeng P and Jin J (2023), Failure process and stability analysis of landslides in Southwest China while considering rainfall and supporting conditions. *Front. Environ. Sci.* 10:1084151. doi: 10.3389/fenvs.2022.1084151

Failure process and stability analysis of landslides in Southwest China while considering rainfall and supporting conditions

Yaohui Gao[1], Yan Zhang[2]*, Chunchi Ma[2]*, Xiangsheng Zheng[2], Tianbin Li[2], Peng Zeng[2] and Juncheng Jin[3]

[1]PowerChina Huadong Engineering Corporation Limited, Hangzhou, China, [2]State Key Laboratory of Geohazard Prevention and Environment Protection, Chengdu University of Technology, Chengdu, China, [3]Chongqing 208 Geological Environment Research Institute Co., Ltd, Chongqing, China

Landslides frequently occur in several mountainous areas because of their unique engineering–geological conditions and other external factors (earthquakes, rainfall, etc.). In this paper, the landslide in Southwest China is used as the research objective to examine the landslide's stability under different working conditions. The influencing factors and the formation mechanism of the landslide are analyzed based on the geological environment and essential characteristics of the landslide. In addition, the transfer coefficient method and the GeoStudio software were used to assess the landslide stability. The analysis results demonstrate that the joint action of landforms, geological structures, rainfall, and other factors caused the landslide. Furthermore, the slipped tension fracture induced the failure mode. The transfer coefficient method results showed that the landslide was stable under natural conditions and unstable under rainstorm conditions, which is consistent with the numerical simulation result. The shear strength sensitivity analysis results depicted an apparent linear relationship among cohesion c, internal friction angle φ, and stability coefficient. Moreover, the stability of the unstable slope is more sensitive to φ than to c.

KEYWORDS

landslide, failure process, stability analysis, numerical simulation, transfer coefficient method

1 Introduction

Landslide refers to the sliding phenomenon of slope rock mass along the penetrating shear failure surface. China is one of the countries that face the world's most pervasive and severe landslide hazards (Fan et al., 2019; Tang et al., 2019; Gong et al., 2021; Luo et al., 2021). The landslides cause imbalance and destruction of the ecological environment and a variety of property losses and casualties, substantially impairing the local socio-

economic development. Therefore, it is crucial to investigate the formation mechanism and stability of landslides.

The principle of primary prevention and timely treatment is followed in the prevention and management of landslides. The most critical issue in landslide warning and treatment is assessing landslide stability. Numerous methods, such as the limit equilibrium method and numerical analysis method, can be used to study landslide's stability.

The limit equilibrium method is mainly based on theoretical calculation. Duncan (1996) reviewed the limit equilibrium method. Zhou et al. (2010) theoretically analyzed the limit equilibrium method by solving high-order equations. Based on the slice method, many scholars have assessed the stability of landslides with other knowledge (Chen et al., 2016; Guo et al., 2019). Xu et al. (2009) applied the shear strength reduction finite element method to examine the stability and potential failure mechanism of three landslides in the Huangla rock group upstream of the Three Gorges Dam. Zhou et al. (2019) investigated the stability of the circular slope at the foot of the slope using random field theory from the probability perspective and analyzed the relationship between the failure probability and the related length of the circular slope at the uniform foot of the slope. Sarkar et al. (2021) conducted a quantitative stability assessment *via* rock mass classification and finite element analysis. The cutting slope was divided into different risk grades according to the obtained stability grade and safety factor values. Although applying the limit equilibrium method provides more flexibility, there are still some limitations. Firstly, the deformation of the geological body was not considered, and the material is considered rigid. Second, the stress-strain relationship between rock and soil in the slope was also not considered. Third, the safety factor was only assumed to be the average safety factor on the slip surface.

Compared with the limit equilibrium method, the numerical analysis method is based on theoretical calculation and depends on the computer to calculate the landslide's stability. The stress-strain relationship of the rock and soil is obtained *via* computer processing while dealing with heterogeneous, non-linear, and complex boundary slopes. The excavation, support, and groundwater seepage of the slope can be simulated to analyze the interaction between the rock and soil and the supporting structure. With the advancements in computer technologies, some software, such as GEOSLOPE, FLAC^{3D}, ANSYS, among others, are used to calculate of landslides' stability. The finite element method, finite difference method, boundary element method, and discrete element method are some frequently used numerical calculation methods (Cheng et al., 2008; Zhao et al., 2020; Luo et al., 2021; Li et al., 2022). Some researchers have evaluated the stability of landslides based on these four methods. Zhao et al. (2020) applied a three-dimensional distance potential discrete element model to simulate the whole process of the Tangjiashan landslide movement. Tao et al. (2019) used the GEOSLOPE software to evaluate the effects of rock and soil parameters on the sensitivity of the Shimen landslide through a single characteristic factor analysis. Zhang et al. (2019) implemented GeoStudio software to select three factors, internal friction angle, cohesion, and rainfall, for an orthogonal test and used the range analysis method to assess the sensitivity of landslide's stability. Ma et al. (2021) examined the slope's stability using FLAC while considering the complex stress state, change in groundwater level, and seepage conditions.

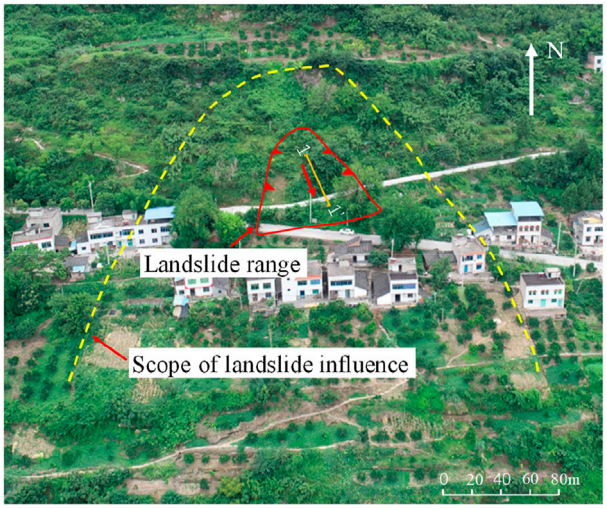

FIGURE 1
Overview of Xinjin Township landslide.

This research uses the landslide in Xinjin Township, Yunyang County, as an example. It combines the collected regional data and the field survey results to analyze the deformation characteristics and formation mechanism of the landslide in Xinjin Township. The landslide's stability under different working conditions was calculated by the transfer coefficient method. Three limit equilibrium methods, Morgenstern-Price, Bishop, and Janbu, were further compared with the transfer coefficient method to investigate the landslide's stability through the GeoStudio software. The research results are valuable for the stability analysis of landslides under various working conditions.

2 Overview and cause analysis of landslide

2.1 Overview of a landslide

The landslide was situated in Xinjin Village, Xinjin Township, Yunyang County. It was about 40 m long in the longitudinal direction and 20–40-m wide in the transverse direction. The sliding body's thickness was 6.8–20.9 m, with an average thickness of about 14 m. The entire landslide's

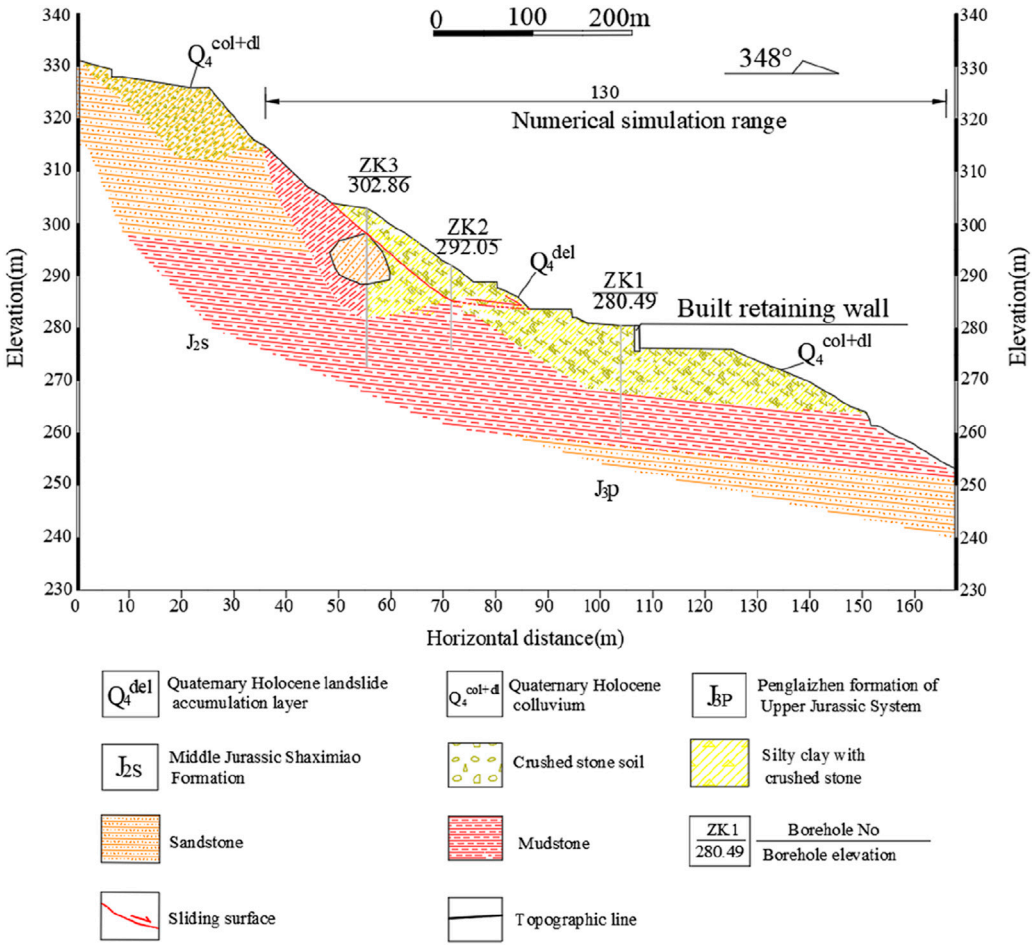

FIGURE 2
Engineering–geological profile of the Xinjin Township landslide. (1–1′ profile in Figure 1).

volume was approximately 1.7 $m^3 \times 10^4$ m^3, making it a small, medium-sized soil landslide. The landslide primarily threatens the safety of lives and properties of 22 households, more than 101 individuals, 240 m of county road, 140 m of the village road, pedestrians and vehicles, and the safety of rural road traffic, which may result in direct economic losses of around 14.313 million yuan. Figures 1, 2 illustrate the complete picture and the profile of the landslide, respectively.

2.1.1 Topography

The landslide area consists of tectonic denudation and the erosion of the low mountain slope landscape. It is situated on the right bank of the Yangtze river, encompassing the overall terrain of high south and low north. The landslide zone descends slowly, with a trailing edge and central slope angle of 30°–40°. The leading edge of the terrain slope angle has a ladder-like appearance, and the slope generally lies between 10° and 15°. The terrain slope in the landslide area is typically slow-steep-slow. Surface vegetation, which is dominated mainly by shrubs, is present in this area.

2.1.2 Geological structure

The landslide area is located on the near axis of the southeast wing of the Wanzhou syncline. It has a monoclinic rock stratum, and the dominant rock stratum is at 350°∠6°. Bedrock fissures are also present in this area. The leading characteristics of the two groups of dominant fissures are as follows. LX1: 0°–20°∠81°–84°, relatively straight, opening width = 2–40 cm, extension = 3–13 m, spacing = 1–6 m, local mud filling, poor combination, belonging to the weak structural plane. LX2: 273°–335°∠83°–88°, opening width = 2–25 cm, extension = 2–6 m, spacing = 1–8 m, local mud filling, combined with general. It has a hard structural plane (LX1 and LX2 represent the two groups of primary fractures developed in bedrock).

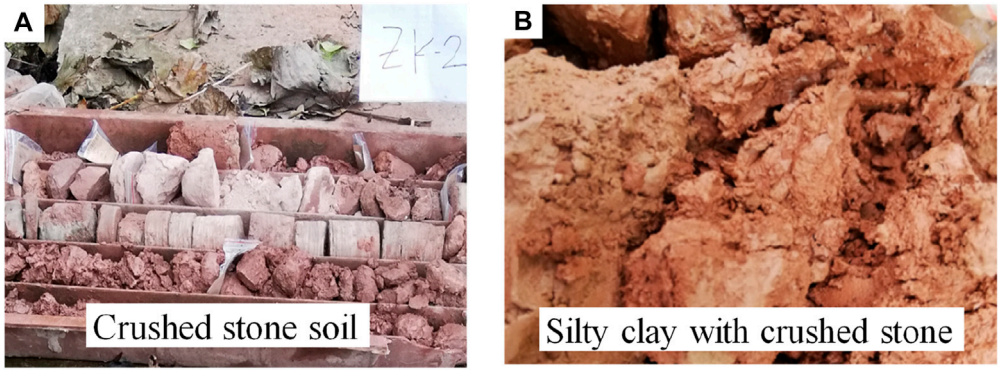

FIGURE 3
(A) Crushed stone soil in ZK2. **(B)** Sliding zone soil in ZK3.

2.1.3 Hydrogeological conditions

The landslide region has a subtropical warm and humid monsoon climate zone with complex topography. Atmospheric rainfall is the primary source of groundwater. The excellent surface water discharge conditions are attributable to the significant terrain height difference in the area and the steep terrain slope. The rain is mostly released directly to the slope toe along the slope surface and cracks, and less water infiltrates into the soil layer. Simultaneously, the soil layer mainly comprises broken stone soil. The uneven distribution of stone, good permeability, and interbedded mudstone and sandstone are some features of the bedrock. The mudstone exhibits a water-blocking effect; therefore, a poor amount of groundwater is found in the landslide area.

2.2 Landslide characteristics

2.2.1 Material composition of landslide

1) Slider. The primary material composition of the sliding mass is the quaternary colluvial layer (Q_4^{col+dl}) broken stone soil (Figure 3A). The crushed rock soil comprises crushed rock and silty clay. The structure is slightly dense and wet. The content of crushed rock is 55%–75%, the particle size is 2–10 cm, and the maximum size is 1.1 m. It is subangular and consists of sandstone and mudstone. Silty clay is brown yellow, purple-brown, and plastic. Its thickness is 6.8–12.9 m.
2) Sliding belt. The drilling process revealed that the sliding zone's thickness was 0.2–0.3 m, mostly comprising brownish-yellow silty clay with gravel (Figure 3B). Its gravel content is 25%–30%, with the particle size of 0.2–4 cm and subangular to subcircular shapes. The gravel composition is sandstone and mudstone and is strongly weathered. The silty clay is in a plastic state.
3) Sliding bed. The sliding bed comprises a broken line along the main sliding direction. With steep upper and slow lower parts, its average inclination angle is about 28°. The trailing edge sliding bed is broken stone soil. The content of the broken stone is 60%–75%, the particle size is generally 2–8 cm, the maximum is about 9.7 m, and the layer thickness is generally 1.5–16.2 m. The front sliding bed is sandstone and mudstone of the Upper Jurassic Penglaizhen Formation (J_3P). The rock stratum is at 350°∠6°, strongly weathered, and has a thickness of 0.7–2.1 m.

2.2.2 Landslide boundary

The plane shape of the landslide has an appearance of a "tongue." The rock and soil steep slopes are present over the trailing edge boundary. The other boundary is the landslide accumulation of block stone soil (Figure 4A). The terrain slope of the leading edge boundary is steep, with primarily exposed lower outer slope body. No evident sign of deformation was present (Figure 4B). The bedrock surface binds the left and right sides of the landslide. There is locally exposed bedrock, thin soil, and no evidence of deformation on the slope on the west side of the left boundary (the east side of the right boundary) (Figure 4C). The slope's soil thickness on the east side of the left boundary (the west side of the right boundary) is relatively large, with the apparent deformation of the slope (Figure 4D).

2.2.3 Landslide deformation characteristics

The deformation trend slowed down in 1982 following substantial deformation, such as tensile cracks in the trailing edge of the landslide. However, a trend of active deformation has been observed in recent years. A local slip occurred at the trailing edge of the landslide in August 2008. From 2015 to 2018, the cracks at the trailing edge of the landslide became large, with an extension length of around 12 m and an opening width of about 5–10 cm. It was filled with silty clay mixed with gravel (Figure 5A). In June 2018, the local collapse occurred in the middle of the landslide. Consequently, the sliding soil interrupted the highway traffic (Figure 5B).

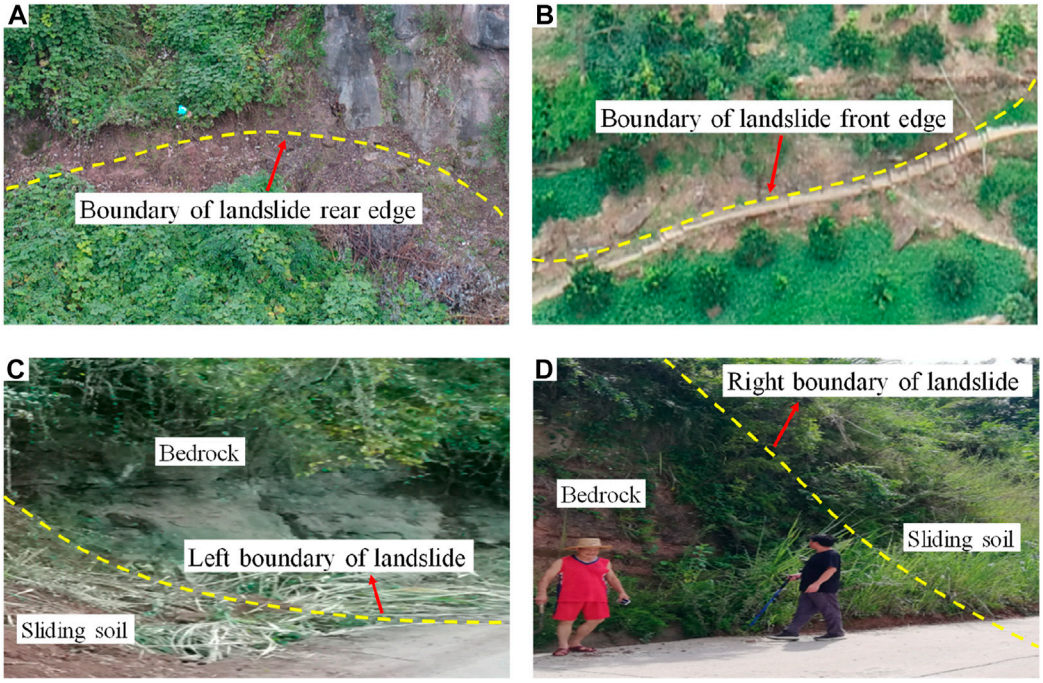

FIGURE 4
Landslide boundary. **(A)** The rear edge of the landslide. **(B)** The front edge of the landslide. **(C)** The left boundary of the landslide. **(D)** The right boundary of the landslide.

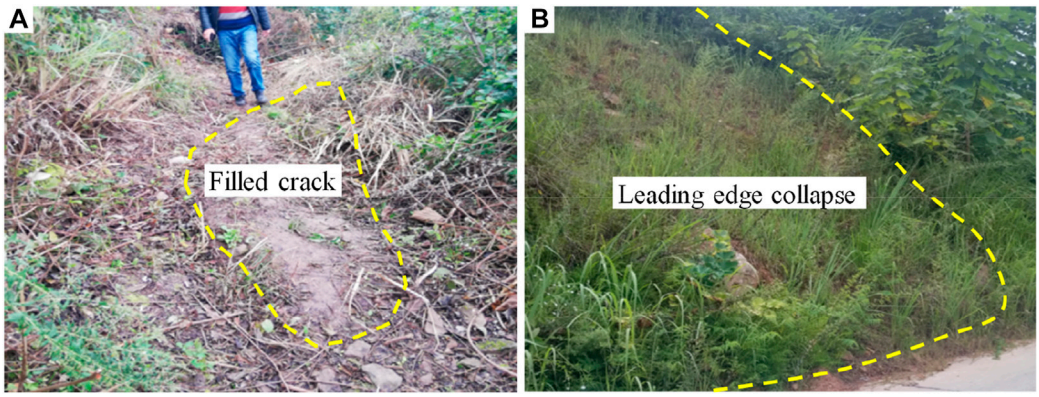

FIGURE 5
Deformation characteristics of landslide. **(A)** Trailing edge crack. **(B)** The local collapse in the middle.

2.3 Influencing factors and formation mechanism of landslides

2.3.1 Influencing factors

The following factors are mainly responsible for the formation of the landslide.

1) Rainfall: The continuous and concentrated rainfall is the main trigger factor for landslides. Heavy rainfall increases the soil weight of the sliding body and reduces the shear strength of the sliding surface, resulting in the deformation and failure of the sliding body.
2) Topography: The landslide area is a low mountain slope landform with structural denudation and erosion. The deeply cut valley, the large terrain height difference, and the steep slope of the front edge of the landslide are the free conditions that cause shear in the landslide.
3) Geological structure and stratum lithology: the landslide region is located in the adaxial part of the southeast wing of the Wanzhou

10.3389/fenvs.2022.1084151

TABLE 1 Physical and mechanical parameters of rock and soil of Xinjin landslide.

Type	Natural weight (kN/m^3)	Saturated weight (kN/m^3)	Natural c (kPa)	Naturalφ(°)	Saturated c (kPa)	Saturatedφ(°)
Gravel soil	20.22	21.21	20	19	18	17
Silty clay with crushed stone	20.00	20.50	18.60	15.50	16.50	13
mudstone	25.10	25.30	265	29.06	150	25
Bedrock	25.20	25.30	980	35.08	650	33

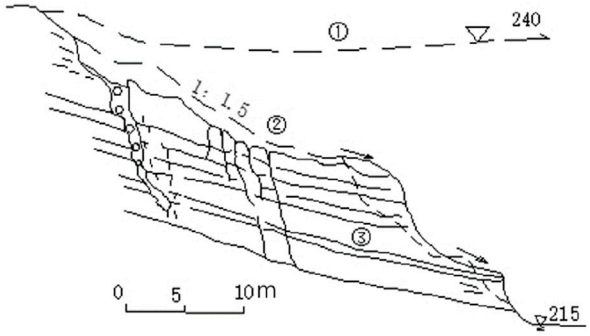

①-Original ground line; 2-Excavate the slope before deformation;
③-A deformed fracture body sliding along the shale interbedded plane.

FIGURE 6
Sliding-cracking landslide failure mode (Zhang et al., 2016).

syncline. Some of its characteristics are the monoclinic rock stratum and the prevalent bedrock fissures. The rock stratum tendency is consistent with the slope direction, and the stratum lithology comprises interbedded mudstone and sandstone. Due to differential weathering, it is easy for the rock mass to create a mudstone cavity, leading to the further formation of dangerous rock mass and a large number of accumulation bodies at the foot of the slope. This feature provides structural conditions and material sources for the formation of landslides.

4) Material composition: the landslide mainly consists of broken stone soil with a loose to medium-density structure and good permeability. The infiltration of atmospheric rainfall surface water increases the sliding body's weight. As a result, the mechanical properties of the sliding zone are reduced, thereby decreasing the landslide's stability.
5) Human engineering activities: Figure 1 shows a path in the middle and front of the landslide. The unloading effect of excavation during construction somewhat diminishes the anti-sliding force of the landslide. Simultaneously, agricultural activities of farmers at the rear edge of the landslide also increased the sliding force of the landslide to a certain extent. Together, they both act to lower the landslide's stability.

2.3.2 Formation mechanism

The slope of the terrain in the landslide area ranges from 15° to 40°. The steeper slope of the trailing edge has slower middle and front parts. The overlying soil layer is loose, broken stone soil. The large soil block stone content in the area has a relatively permeable layer. Rainfall infiltration changes the physical and mechanical properties of the shallow soil. The slope is deformed because of gravity. The stress is further concentrated under the accumulation of long-term deformation, leading to sliding.

The steep and gentle changes in the slope's shape create suitable terrain conditions for its slip (Hou et al., 2013). Moreover, the stratum tendency is the same as that of the rock stratum tendency.

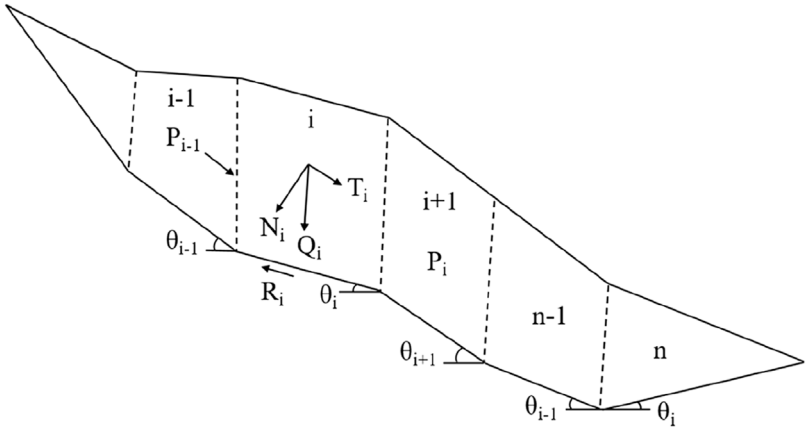

FIGURE 7
Schematic diagram of the implicit solution calculation model of the transfer coefficient method for slope with broken line sliding surface (In this paper, the landslide 1–1′ section is divided into nine blocks for overall stability calculation, and the stability of two possible secondary shear outlets is also calculated) (Baker et al., 1980; Hutchinson et al., 1982).

TABLE 2 Stability calculation results of transfer coefficient method.

Working condition	Stability factor	Safety factor	Residual sliding force (kN/m)	Stability determination
Natural working condition	1.212	1.15	0	Stable
Rainstorm condition	1.040	1.15	139.19	Unstable

TABLE 3 Classification of landslide stability.

Stability factor fs	Fs < 1.00	1.00 ≤ Fs < 1.05	1.05 ≤ Fs < Fst	Fs ≥ Fst
stability	instable	Unstable	Basically stable	stable

The landslide section depicts the thin upper rock stratum of the sliding body and the delicate lower part. Moreover, tensile cracks are present at the trailing edge of the landslide. The landslide has a medium dip angle. When it rains heavily, the surface water penetrates downward. The water flow is concentrated in the weak rock at the bottom of the landslide, thus accelerating the softening of the soft rock, reducing the bearing capacity of the rock, and then causing sliding. Therefore, the landslide conforms to the sliding-cracking failure mode (Figure 6).

3 Landslide stability analysis

3.1 Calculation model and calculation method

Because the leading edge of the landslide body does not enter into the water, and there is no steady groundwater level during the exploration period, the effects of pore water static pressure and hydrodynamic pressure are not considered in the calculation (Liu and Yin, 2003; Troncone et al., 2020). The potential sliding surface of the landslide is undulating and uneven. The implicit solution (broken line sliding surface) of the transfer coefficient method is applied to calculate the landslide's stability. The calculation model (Figure 7) and formula are presented as follows.

Calculation method:

$$P_n = 0 \tag{1}$$

$$P_i = P_{i-1}\psi_{i-1} + T_i - R_i/F_s \tag{2}$$

$$\psi_{i-1} = \cos(\theta_{i-1} - \theta_i) - \sin(\theta_{i-1} - \theta_i)\tan\varphi_i/F_s \tag{3}$$

$$T_i = (G_i + G_{bi})\sin\theta_i + Q_i\cos\theta_i \tag{4}$$

$$R_i = c_i l_i + [(G_i + G_{bi})\cos\theta_i - Q_i\sin\theta_i - U_i]\tan\varphi_i \tag{5}$$

where P_n is the residual slide force per unit width of the nth block; P_i is the residual sliding force per unit width of the i calculation block and the $i+1$ calculation block. When $P_i < 0$ ($i < n$), $P_i = 0$. T_i is the unit width gravity of the ith slice and the sliding force caused by other external forces; R_i first calculates the anti-sliding force caused by the unit width

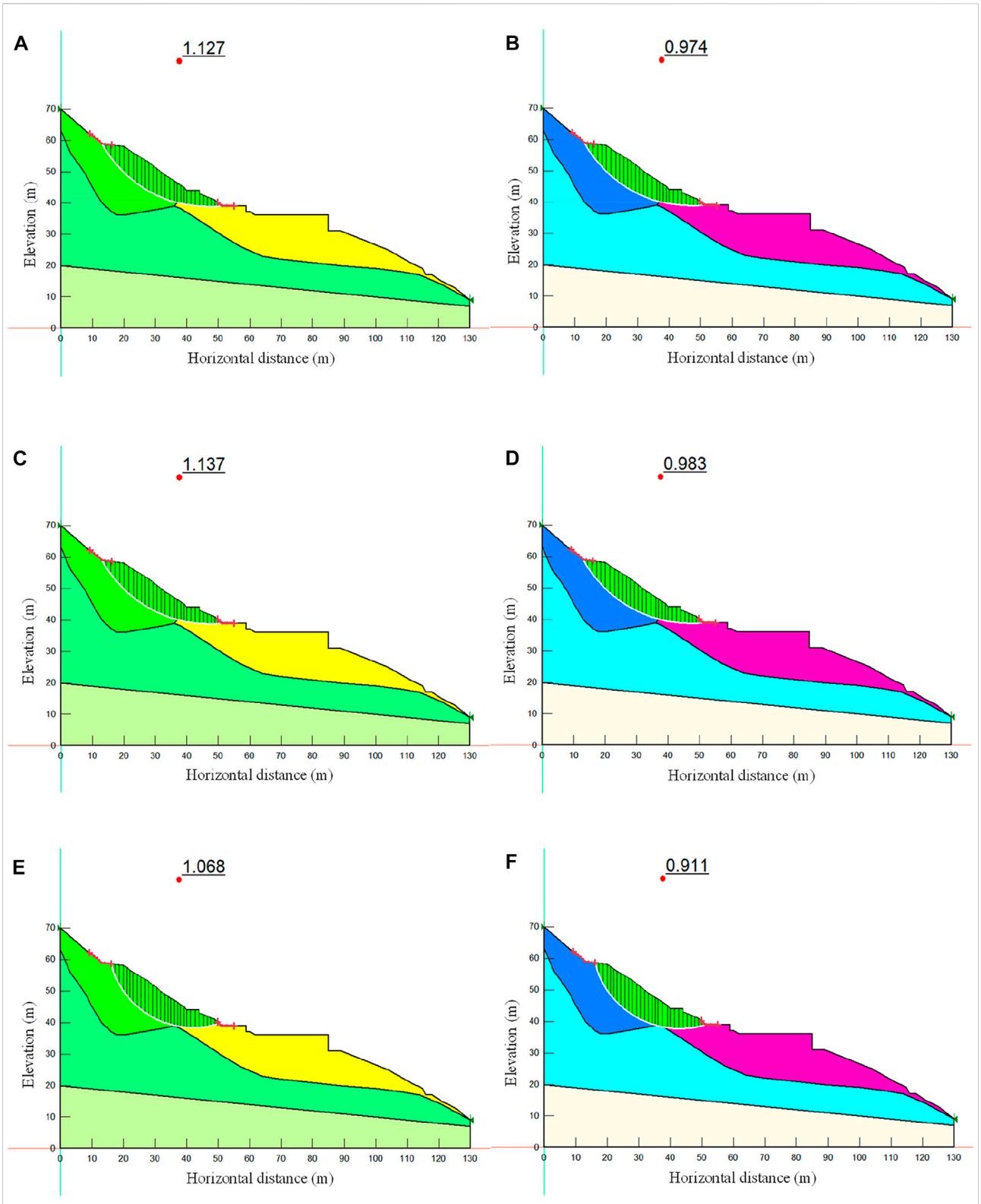

FIGURE 8
Simulation results of stability. **(A)** Morgenstern-Price natural state. **(B)** Morgenstern-Price rainstorm status. **(C)** Bishop natural state. **(D)** Bishop rainstorm status. **(E)** Janbu natural state. **(F)** Janbu rainstorm status.

TABLE 4 Numerical simulation results of the safety coefficient.

Method	Morgenstern-price	Bishop	Janbu	Stability discrimination
Natural working condition	1.128	1.137	1.061	Basically stable
Rainstorm working condition	0.974	0.984	0.916	Instable

gravity and other external forces; Ψ_{i-1} calculates the transfer coefficient of the block for the i–1 to the i; φ_i calculates the internal friction angle of the slice soil for the ith; c_i is the cohesion of the ith calculated slice soil; l_i is the length of sliding surface of the ith calculated slice; G_i is the weight per unit width of the slipping mass calculated for the first i; G_{bi} is the unit width additional load of the ith slice slider; θ_i is the first i to calculate the dip angle of the slip surface of the strip; Q_i is the horizontal load per unit width of the ith calculated slider; U_i is the unit total water pressure of the ith calculated sliding block; and Fs is the safety factor.

3.2 Calculation conditions and parameter selection

The earthquake's effects are not considered because of the location of the landslide area (Du et al., 2015; Mi and Wang, 2021). Rainfall is one of the fundamental reasons for the instability of unsaturated soil (Feng et al., 2013; Liu et al., 2018). A large amount of rainwater penetrates the slope soil, thus altering the mechanical properties of the slope soil and causing instability in the slope. Therefore, the following two conditions are used to calculate the landslide's stability. The safety factor is 1.15 according to the interpolation method. A safety factor is the ratio of anti-sliding force and sliding force on the sliding surface, which is the crucial index to evaluate the landslide's stability. The safety factor is greater than 1, indicating that the landslide is stable. The larger the value, the smaller the possibility of sliding. A safety factor of less than 1 suggests that the landslide is unstable. The smaller the value, the greater the possibility of sliding.

Natural conditions: self-weight + surface load; it is regarded as the full saturation state below the groundwater level, and the other is the natural state.

Rainstorm conditions: weight + surface load + rainstorm; the landslide body is the state of full saturation.

Table 1 shows the parameters selected according to the geotechnical test results and engineering experience.

3.3 Calculation results

Table 2 presents the calculation results of landslide stability.

According to the calculation results and the landslide stability classification table (Table 3), the landslide is stable under natural conditions and unstable under rainstorm conditions.

4 Numerical simulation analysis

4.1 Simulation software

The GeoStudio software developed by the GeoSlope Company of Canada is used in this simulation. This software includes the following eight modules: SLOPE/W, SEEP/W, SIGMA/W, QUAKE/W, TEMP/W, CTRAN/W, AIR/W, and VADOSE/W. The analysis results of each module are interchangeable. The SLOPE/W module built in the GeoStudio software applies the limit equilibrium theory to analyze the stability of slopes with different soil types, complex strata, and slip surface shapes, which can directly obtain the safety factor of slopes. Alternative limit equilibrium methods include Morgenstern-Price, Bishop, Janbu, Sarma, GLE, Spencer, among others. Morgenstern-Price, Bishop, and Janbu are used for simulation in this paper.

4.2 Model establishment

The simulation does not consider groundwater's effects on the landslide's stability. The section having a length of 130 m and a height of 70 m is selected as the calculation model. According to the different lithologies, the slope is divided into four areas: broken stone soil, silty clay with gravel, mudstone, and bedrock. It is assumed that the constitutive relationship between the stress and strain of slope rock mass is elastic-plastic. The failure of rock mass follows the Mohr-Coulomb criterion. The horizontal and vertical axes are selected as the stress and deformation boundaries of the model.

The simulation steps are as follows. Firstly, according to the landslide profile, the software automatically creates a closed graph *via* the input plane coordinates, namely the landslide model outline, to determine the plane coordinates of the feature points. Second, the landslide contour map is divided into four different material areas by coordinate inputs, namely broken stone soil, silty clay with gravel, mudstone, and bedrock, according to the plane characteristics of the landslide body, the sliding zone and the sliding bed of the landslide, and the lithology of the stratum. Next, the parameters of the four material areas, gravity, cohesion, and internal friction angle, are input. Finally, the landslide model can be calculated by selecting the entry and exit parts of the landslide to obtain the most dangerous sliding surface position of the landslide and its corresponding safety factors.

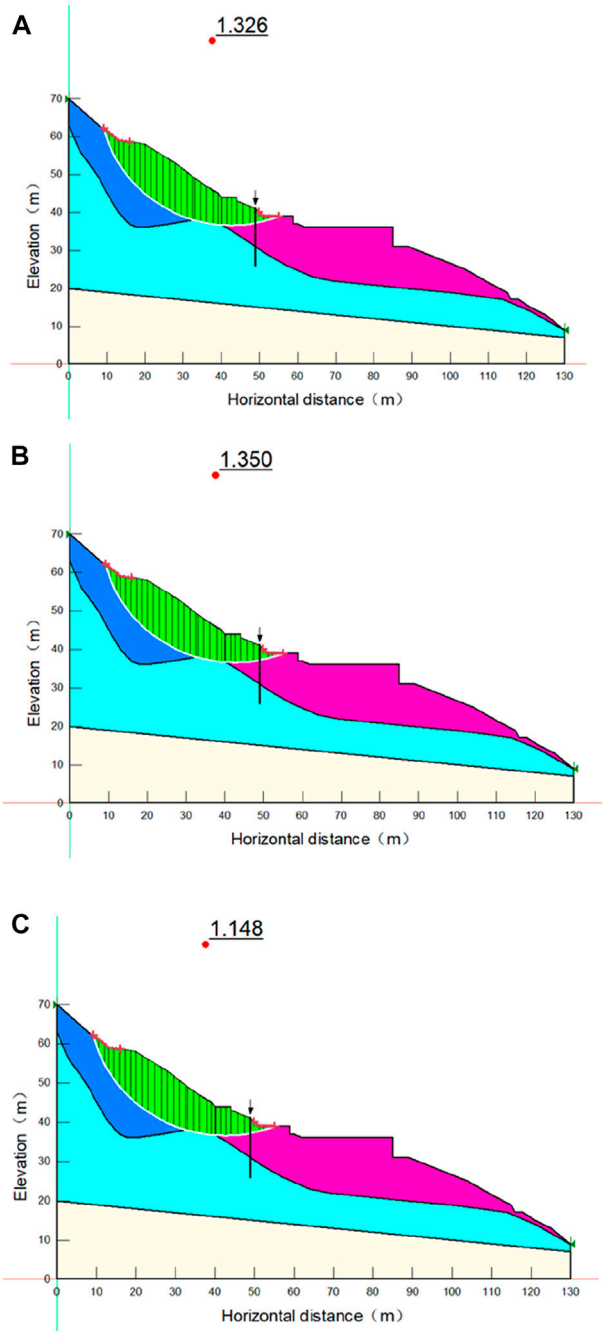

FIGURE 9
Numerical simulation results after treatment (The black line crossing the stratum in the figure represents the anti-slide pile set). **(A)** Morgenstern-Price. **(B)** Bishop. **(C)** Janbu.

4.3 Calculation conditions and parameter selection

The simulation is conducted under two working conditions (the natural state and the rainstorm state). The stability safety factor is 1.15. The selection of calculation parameters is determined by indoor soil test results and engineering experience (Table 1).

4.4 Simulation results

Figure 8 depicts the simulation results of the three methods, and Table 4 presents the verification results.

The numerical simulation results demonstrate that the stability coefficients obtained under rainstorm conditions are smaller than those obtained under natural conditions. Under the same conditions, the stability coefficient obtained by the Bishop method is the largest, followed by the Morgenstern-Price method and the Janbu method. According to the simulation results and Table 3, the landslide is basically stable under natural conditions and unstable under rainstorm conditions.

4.5 Comprehensive evaluation of stability

The calculation results of the transfer coefficient method illustrate that the landslide is in a stable state under natural conditions and in an unstable state under rainstorm conditions. The numerical simulation results depict that the landslide is basically stable under natural conditions and unstable under heavy rain conditions. The limit equilibrium method in the numerical simulation adopts the slice method in the analysis and calculation; this reason accounts for the difference between these two outcomes. The slice method does not consider the force between the slices, which may cause some errors and generate fewer results. Based on the findings of the above two approaches, the landslide is in a stable state under natural conditions and in an unstable state under rainstorm conditions.

The investigation of the landslide reveals that the landslide has no apparent deformation during the dry season. Moreover, evident signs of deformation are visible in the middle and rear parts of the landslide during the rainstorm. The current situation is in a stable state. Under adverse conditions, such as heavy rainfall, the landslide is in an unstable state as a whole, with a possibility of overall shear slip (Han et al., 2019; Ogbonnaya and Chidinma, 2019). In summary, the landslide stability calculation results are basically consistent with the actual stable state.

4.6 Preventive measures

4.6.1 Drainage works

According to the above analysis, the landslide is unstable under rainstorm conditions. A perfect surface and underground drainage system must be installed on the landslide's location to address the stability problem of the landslide, ensure the smooth

TABLE 5 Comparison of simulation results before and after treatment.

Governance states	Morgenstern-price	Bishop	Janbu	Stability discrimination
Before governance	0.974	0.983	0.911	unstable
After governance	1.326	1.350	1.148	stable

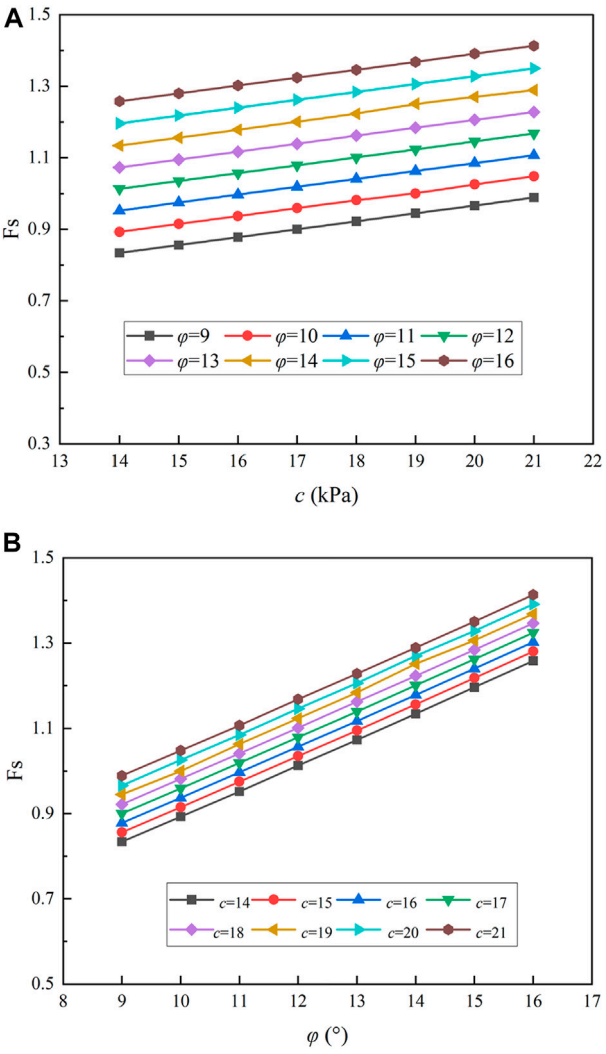

FIGURE 10
Influence of parameters on stability coefficient. **(A)** *C* value. **(B)** φ value.

release of water, and reduce the adverse rainfall effects on the landslide's stability. In the preliminary design, a 100-m long longitudinal drainage ditch is arranged based on the existing gullies on the landslide, which is connected with the village's drainage system to expedite the surface water drainage.

4.6.2 Retaining works

A gravity-retaining wall with a length of about 43 m, a height of about 7 m, and an area of about 300 m^2 is constructed on the landslide; this wall enhances the landslide's stability to a certain extent. Anti-slide piles are installed at the front edge of the landslide according to the terrain, vegetation, and construction conditions of the landslide. Cast-in-situ retaining plates are used between the piles to stabilize the landslide under rainstorm conditions. The length of the anti-slide bank is about 15 m, the pile section size is 1.5 m × 2.0 m, the pile spacing is 3 m, and the pile shaft concrete is C30.

4.6.3 Simulation after treatment

The 1–1' section of the landslide is taken as the research objective, and the reinforcement load is selected as the anti-slide pile. Sections 3.1 and 3.2 provide details on the selection of simulation steps and parameters. Three different methods are used to conduct numerical simulations under rainstorm conditions. Figure 9 shows the simulation results.

The comparison between Figures 8, 9 shows that the safety factor of the landslide has altered before and after the treatment (Table 5).

Table 5 shows that under the rainstorm condition, the safety factors of the landslide before treatment are less than 1, and the landslide is in an unstable state. Following treatment, the safety factor of the landslide is increased. In addition, the average safety factor obtained by the three methods is more than 1.15, indicating that the landslide is in a stable state and that the prevention and control measures have effectively increased the landslide's stability.

5 Discussions

The shear strength of soil can be divided into two parts. One is related to the normal stress between particles, whose essence is friction. The other part that does not depend on normal stress is called cohesion. When the shear stress generated by the external load reaches the shear strength of the soil, the soil is destroyed. In severe cases, a landslide will occur. The soil lithology of the Xinjinxiang landslide sliding zone is silty clay mixed with gravel, and the gravel with limited content plays a vital role in stability. This paper selected the 1–1' section of the landslide to slide as a whole and conducted the sensitivity analysis of shear strength

under a rainstorm to investigate the effects of landslide stability on the sensitivity of shear strength parameters (Figure 10).

The results show an apparent linear relationship among c, φ, and the stability coefficient. The stability of an unstable slope is more sensitive to the φ value than the c value. The reason for this outcome is that the sliding mass of the landslide mainly comprises silty clay with crushed stone, wherein the crushed stone accounts for a large proportion, resulting in a low binding force between particles. Hence, the landslide's stability is not significantly affected by the value of c. Analyzing the sensitivity of shear strength parameters to slope safety factors can guide the selection of soil slope rock mass parameters and provide a foundation for selecting landslide prevention measures.

6 Conclusion

1) The plane shape of the landslide has a tongue-shaped appearance. The bedrock surface bounds the left and right sides, and obvious deformation signs can be seen at the boundary. The trailing edge is bounded by the rock steep slope and the soil steep slope, and the rock steep slope binds the leading edge. The volume is about 1.7 $m^3 \times 10^4$ m^3, which signifies a small middle-level soil landslide. The landslide formation results from the interaction of topography, geological structure, lithology, and rainfall. According to the field investigation and analysis, the failure mode of the landslide is determined to be a slip crack.
2) The calculation results of the transfer coefficient method demonstrate that the landslide is in a stable state under natural conditions. In contrast, the landslide is in an unstable state under rainstorm conditions.
3) The numerical simulation results illustrate that the landslide is stable under natural and unstable under rainstorm conditions. Under the same conditions, the Bishop method has the largest value of the stability coefficient, followed by the Morgenstern-Price method, with the second highest value, and the Janbu method, with the smallest value of the stability coefficient.
4) Compared with the transfer coefficient method, the stability coefficient obtained by numerical simulation is smaller. Combining the results of the two methods revealed that the landslide is in a stable state under natural conditions and in an unstable state under rainstorm conditions.
5) The stability coefficient of the landslide is improved following the installation of the anti-slide pile and retaining wall. Notably, the unstable state becomes stable under rainstorm conditions, indicating that the control measures have improved the landslide's stability. Such prevention and control measures can also be implemented for similar small rock slopes.
6) The shear strength sensitivity analysis of the landslide profile under rainstorm conditions shows a clear linear relationship among c, φ, and stability coefficient, and the stability of unstable slope is more sensitive to φ than to c.

Data availability statement

The raw data supporting the conclusions of this article will be made available by the authors, without undue reservation.

Author contributions

All authors listed have made a substantial, direct, and intellectual contribution to the work and approved it for publication.

Funding

This study is supported by the National Natural Science Foundation of China (Nos. 42107211 and 51808458), Sichuan Science and Technology Program (No. 2021YFS0317) and Natural Science Foundation of Sichuan Province (No. 2022NSFSC1063). This study is also supported by the China Postdoctoral Science Foundation (No. 2021M691000).

Conflict of interest

Author YG was employed by PowerChina Huadong Engineering Corporation Limited. Author JJ was employed by Chongqing 208 Geological Environment Research Institute Co., Ltd.

The remaining authors declare that the research was conducted in the absence of any commercial or financial relationships that could be construed as a potential conflict of interest.

Publisher's note

References

Baker, R. (1980). Determination of the critical slip surface in slope stability computations. *Int. J. Numer. Anal. Methods Geomech.* 4 (4), 333–359. doi:10.1002/nag.1610040405

Chen, X. P., Zhu, H. H., Huang, J. W., and Liu, D. (2016). Stability analysis of an ancient landslide considering shear strength reduction behavior of slip zone soil. *Landslides* 13 (1), 173–181. doi:10.1007/s10346-015-0629-7

Cheng, X. Z., Tang, H. M., Yang, Y. C., Hu, B., and Ni, J. (2008). 3D analysis of landslide stability based on strength reduction FLAC~3D: Taking baigunshu paleo-landslide group in the three Gorges reservoir area as an example. *Hydrogeology Eng. Geol.* 2008(2), 24–28. doi:10.1016/S1876-3804(08)60015-4

Du, F., Ren, G. M., Xia, M., Gao, B., Yu, T. B., and Wu, L. K. (2015). Numerical simulation of recurrence mechanism of old landslide under earthquake loading. *Mt. Res.* 33 (2), 233–239. doi:10.16089/j.cnki.1008-2786.000030

Duncan, J. M. (1996). State of the art: Limit equilibrium and finite-element analysis of slopes. *J. Geotech. Engrg.* 122 (7), 577–596. doi:10.1061/(asce)0733-9410(1996)122:7(577)

Fan, R. L., Zhang, L. M., and Shen, P. (2019). Evaluating volume of coseismic landslide clusters by flow direction-based partitioning. *Eng. Geol.* 260, 105238. doi:10.1016/j.enggeo.2019.105238

Feng, W., Wang, J. Y., Zhang, C. H., and Gaq, B. (2013). Analysis on the influence of the rainfall infiltration on the stability of qiujialiang landslide. *Northwest. Geol.* 46 (2), 195–200. doi:10.3969/j.issn.1009-6248.2013.02.024

Gong, W. P., Juang, C. H., and Wasowski, J. (2021). Geohazards and human settlements: Lessons learned from multiple relocation events in Badong, China–Engineering geologist's perspective. *Eng. Geol.* 285, 106051. doi:10.1016/j.enggeo.2021.106051

Guo, M. W., Liu, S. J., Yin, S. D., and Wang, S. L. (2019). Stability analysis of the Zhangmu multi-layer landslide using the vector sum method in Tibet, China. *Bull. Eng. Geol. Environ.* 78 (6), 4187–4200. doi:10.1007/s10064-018-1386-3

Han, Z., Su, B., Li, Y. E., Ma, Y. F., Wang, W. D., and Chen, G. Q. (2019). Comprehensive analysis of landslide stability and related countermeasures: A case study of the lanmuxi landslide in China. *Sci. Rep.* 9 (1), 12407–12412. doi:10.1038/s41598-019-48934-3

Hou, T. S., Xu, G. L., Shen, Y. J., Wu, Z. Z., Zhang, N. N., and Wang, R. (2013). Formation mechanism and stability analysis of the Houba expansive soil landslide. *Eng. Geol.* 161, 34–43. doi:10.1016/j.enggeo.2013.04.010

Hutchinson, J. N. (1982). *Methods of locating slip surface in landslides*. London, UK: British Geomorphological Research Group.

Li, A., Dai, F., Liu, Y., Liu, K., and Wang, K. (2022). Deformation characteristics of sidewall and anchorage mechanisms of prestressed cables in layered rock strata dipping steeply into the inner space of underground powerhouse cavern. *Int. J. Rock Mech. Min. Sci.* 159, 105234. doi:10.1016/j.ijrmms.2022.105234

Liu, G., Tong, F. G., Zhao, Y. T., and Tian, B. (2018). A force transfer mechanism for triggering landslides during rainfall infiltration. *J. Mt. Sci.* 15 (11), 2480–2491. doi:10.1007/s11629-018-5043-x

Liu, L. L., and Yin, K. L. (2003). Discrete element method applied to stability analysis of landslides along reservoir shoreline. *Hydrogeology Eng. Geol.* 30 (4), 63. doi:10.1007/s11769-003-0044-1

Luo, Y. H., Zhang, Y., Wang, Y. S., He, Y., Zhang, Y. Y., and Cao, H. (2021). A unique failure model for a landslide induced by the Wenchuan earthquake in the Liujiawan area, Qingchuan County, China. *Eng. Geol.* 295, 106412. doi:10.1016/j.enggeo.2021.106412

Ma, Z. Y., Zhu, C. H., Yao, X. L., and Dang, F. N. (2021). Slope stability analysis under complex stress state with saturated and unsaturated seepage flow. *Geofluids* 2021, 1–11. doi:10.1155/2021/6637098

Mi, Y., and Wang, J. H. (2021). Finite-element modeling of submarine landslide triggered by seismic loading in saturated cohesive soil deposits. *Bull. Eng. Geol. Environ.* 80 (2), 951–965. doi:10.1007/s10064-020-02005-4

Ogbonnaya, I., and Chidinma, C. (2019). Slope stability analysis of mine waste dumps at a mine site in Southeastern Nigeria. *Bull. Eng. Geol. Environ.* 78 (4), 2503–2517. doi:10.1007/s10064-018-1304-8

Sarkar, S., Pandit, K., Dahiya, N., and Chandna, P. (2021). Quantified landslide hazard assessment based on finite element slope stability analysis for Uttarkashi–Gangnani Highway in Indian Himalayas. *Nat. Hazards (Dordr).* 106 (3), 1895–1914. doi:10.1007/s11069-021-04518-x

Tang, H. M., Wasowski, J., and Juang, C. H. (2019). Geohazards in the three Gorges reservoir area, China–lessons learned from decades of research. *Eng. Geol.* 261, 105267. doi:10.1016/j.enggeo.2019.105267

Tao, Y. F., Xue, Y. G., Li, S. C., Qiu, D. H., Li, Z. Q., and Zhang, K. (2019). Parameter susceptibility analysis of the shimen landslide (liaoning Province, China). *Soil Mech. Found. Eng.* 56 (1), 7–11. doi:10.1007/s11204-019-09562-1

Troncone, A., Pugliese, L., and Conte, E. (2020). Run-out simulation of a landslide triggered by an increase in the groundwater level using the material point method. *Water* 12 (10), 2817. doi:10.3390/w12102817

Xu, W. J., Hu, R. L., Yue, Z. Q., and Tan, R. J. (2009). Genesis and stability of the zhoujiawan landslide, three Gorges, China. *Bull. Eng. Geol. Environ.* 68 (1), 47–54. doi:10.1007/s10064-008-0154-1

Zhang, Y., Yin, K. L., Guo, Z. Z., Liang, X., Tan, M. J., and Yang, Y. G. (2019). Evaluation of the Stability of Maliulin Landslide under the Reservoir Water Level Fluctuation Combined with Rainfall. *Geol. Sci. Tech. Inf.* 38 (6), 198–205. doi:10.19509/j.cnki.dzkq.2019.0623

Zhang, Z. Y., Wang, L. S., and Wang, S. T. (2016). *Principles of Engineering Geological Analysis*. 4th Edn. Beijing: Geological Publishing House.

Zhao, L. H., Liu, X. N., Mao, J., Shao, L. Y., and Li, T. C. (2020). Three-dimensional distance potential discrete element method for the numerical simulation of landslides. *Landslides* 17 (2), 361–377. doi:10.1007/s10346-019-01282-9

Zhou, J. W., Xu, W. Y., Yang, X. G., Shi, C., and Yang, Z. H. (2010). The 28 october 1996 landslide and analysis of the stability of the current huashiban slope at the liangjiaren hydropower station, southwest China. *Eng. Geol.* 114 (1-2), 45–56. doi:10.1016/j.enggeo.2010.04.001

Zhou, X. P., Zhu, B. Z., and Wong, L. N. Y. (2019). A stability analysis of landslides based on random fields-Part I: Toe circle slope. *Bull. Eng. Geol. Environ.* 78 (1), 103–115.

frontiers | Frontiers in Environmental Science

TYPE Original Research
PUBLISHED 15 March 2023
DOI 10.3389/fenvs.2023.1116220

OPEN ACCESS

EDITED BY
Yong Xiao,
Southwest Jiaotong University, China

REVIEWED BY
Vahab Amiri,
Yazd University, Iran
Vasant Madhav Wagh,
Swami Ramanand Teerth Marathwada University, India
Yinzhu Zhou,
Center for Hydrogeology and Environmental Geology Survey, China

*CORRESPONDENCE
Michael E. Omeka,
omeka.ekuru@unical.edu.ng
michaelekuru@gmail.com
Antonio Scopa,
antonio.scopa@unibas.it

SPECIALTY SECTION
This article was submitted to Freshwater Science, a section of the journal Frontiers in Environmental Science

RECEIVED 05 December 2022
ACCEPTED 22 February 2023
PUBLISHED 15 March 2023

CITATION
Saraswat A, Nath T, Omeka ME, Unigwe CO, Anyanwu IE, Ugar SI, Latare A, Raza MB, Behera B, Adhikary PP, Scopa A and AbdelRahman MAE (2023), Irrigation suitability and health risk assessment of groundwater resources in the Firozabad industrial area of north-central India: An integrated indexical, statistical, and geospatial approach. *Front. Environ. Sci.* 11:1116220. doi: 10.3389/fenvs.2023.1116220

Irrigation suitability and health risk assessment of groundwater resources in the Firozabad industrial area of north-central India: An integrated indexical, statistical, and geospatial approach

Anuj Saraswat [1,2], Triyugi Nath[2], Michael E. Omeka [3]*, Chinanu O. Unigwe [4], Ifeanyi E. Anyanwu [5], Samuel I. Ugar[3], Ashish Latare[2], Md Basit Raza [6], Biswaranjan Behera [7], Partha P. Adhikary [7], Antonio Scopa [8]* and Mohamed A. E. AbdelRahman [9]

[1]Department of Soil Science, G.B. Pant, University of Agriculture and Technology, Pantnagar, Uttarakhand, India, [2]Department of Soil Science and Agricultural Chemistry, Institute of Agricultural Sciences, Banaras Hindu University, Varanasi, Uttar Pradesh, India, [3]Department of Geology, University of Calabar, Calabar, Nigeria, [4]Boone Pickens School of Geology, Oklahoma State University, Stillwater, OK, United States, [5]Department of Geology, University of Nigeria, Nsukka, Nigeria, [6]ICAR-Indian Institute of Soil and Water Conservation, Dehradun, India, [7]ICAR-Indian Institute of Water Management, Bhubaneswar, India, [8]Scuola di Scienze Agrarie, Forestali, Alimentari ed Ambientali (SAFE), University of Basilicata, Potenza, Italy, [9]Division of Environmental Studies and Land Use, National Authority for Remote Sensing and Space Sciences (NARSS), Cairo, Egypt

The recent global upsurge in anthropogenic activities has resulted in a decline in the quality of water. This by extension has resulted in increased ubiquity of water pollution in terms of sources. The application of traditional water quality assessment methods usually involves the use of conventional water quality parameters and guideline values. This may be associated with bias and errors during the computation of various sub-indices. Hence, to overcome this limitation, it is critical to have a visual appraisal of the water quality in terms of source and human health risks exposure for sustainable water resource management and informed decision-making. Therefore, the present study has integrated multiple water quality assessment indices, spatio-temporal, and statistical models to assess the suitability of fifty groundwater samples (n = 50) within the Firozabad industrial area for irrigation and drinking; as well as the likely health risks from oral intake and dermal contact by inhabitants. Electrical conductivity (mean = 1,576.6 µs/cm), total hardness (mean = 230.9 mg/L), dissolved sodium (mean = 305.1 mg/L) chloride (mean = 306.1 mg/L) and fluoride (mean = 1.52 mg/L) occurred in the water at concentrations above the recommended standards; attributed influxes from agricultural and industrial wastewater. The pollution index of groundwater and water quality index revealed that 100% of the groundwater samples are extremely polluted; this was also supported by the joint multivariate statistical analyses. The majority of the irrigational water quality indices (sodium adsorption ratio, Kelly's Ratio,

permeability index, percent sodium) revealed that the long-term use of the groundwater for irrigation in the area will result in reduced crop yield unless remedial measures are put in place. Higher Hazard index (HI > 1) for nitrate and fluoride ingestion was recorded in water for the children population compared to adult; an indication that the children population is more predisposed to health risks from the oral intake of water. Generally, risk levels from ingestion appear to increase in the western and north-eastern parts of the study area. From the findings of this study, it is highly recommended that adequate agricultural practices, land use, and water treatment regulatory strategies be put in place for water quality sustainability for enhanced agricultural production and human health protection.

KEYWORDS

fluoride health risk, firozabad, irrigation water quality, agricultural productivity, water quality

Introduction

The importance of groundwater for drinking, domestic, irrigated agriculture, and industrial uses cannot be overemphasized. In the recent past, higher preference and demand have been put on groundwater due to its perceived low vulnerability to pollution compared to surface water (Egbueri et al., 2021; Liu, 2021). This assumption has been based on the fact that groundwater is located within the subsurface and "protected" by a confined subsurface aquifer layer, which tends to shield it from contamination. However, recent studies have found that due to the varying subsurface aquifer characteristics peculiar to different geologic formations (such as porosity, permeability, depth to the water table, topography, *etc.*), over-exploitation (over-abstraction of groundwater), groundwater is also found to be highly vulnerable to pollution (Omeka et al., 2022b; Omeka and Egbueri, 2022). Given the increasing demand and the need for sustainable agriculture to meet the increasing population, quality water for irrigation becomes crucial for sustainable agriculture, especially in arid and semi-arid areas of the world (FAO, 2003; Qadir and Oster, 2004; Abrahao et al., 2011; Wang et al., 2021). According to global projections on agricultural productivity, higher agricultural yield has been experienced from irrigational agriculture compared to non-irrigated agriculture. The implication of this is that the demand for agricultural land and quality water for irrigation is expected to increase in years to come (Qadir and Oster, 2004), thereby, putting more pressure on the available water resources and agricultural lands (Abrahao et al., 2011). Hence, ensuring quality water for irrigation will enhance agricultural productivity and sustainable management of agricultural soil (Brady, 2002; Omeka, 2023). Given these challenges, ensuring quality irrigation water will involve designing state-of-the-art models and cutting-edge, non-conventional multi-criteria approach towards quality water resource prediction, management, and sustainability.

The Firozabad city, where the present study is carried out is located in Firozabad district of Uttar Pradesh, one of India's basins where there is intense demand of water for irrigation purpose. The major source of irrigation water in the area is groundwater and canals. The long-term annual average rainfall in the area is 715.2 mm. The climate of the area is sub-humid with a dry climate occurring throughout the year except during the monsoon season where high rainfall occurs from June to September, resulting in high percolation of water into the aquifer. In recent years, increased evapotranspiration, low precipitation, and overexploitation have been observed in the area resulting in a decrease in the level of groundwater in the area (Prasad, 2008). According to the long-term groundwater level fluctuation for 1 decade (1998–2007) for three groundwater monitoring wells, there has been a decline in groundwater level from 0.0171 to 0.0264 my^{-1} (Prasad, 2008). Overexploitation of the groundwater resources in the area is known to deplete the water table, thereby increasing the vulnerability of aquifers to contamination from irrigational water run-off, percolation, and leaching from return irrigational water flow enriched in toxic chemical substances such as nitrate (NO_3^-) and fluoride (F^-) (Shah and Deb Roy 2002). These pollutants in water can portend high health risks to consumers and may impede crop yield when used for irrigation.

In the past decades, several efforts have been put in for regular monitoring and assessment of water quality for several purposes, locally and internationally through legislative guidelines (BIS, 2012; WHO, 2017; Rahman et al., 2021). This has been done through the estimation of an element background level and setting up the standard value of each element in water to a particular benchmark for different purposes. The background levels are either estimated temporally or spatially. Temporal estimation is done by taking into consideration the concentration of the elements in the natural environment over anthropogenic controls, while spatial estimation considers only the areas not influenced by anthropogenic activities (Omeka and Igwe, 2021; Rahman et al., 2021). However, for pollutants like NO_3^- and F^- which occur from both anthropogenic and natural sources, with varying pollution sources (such as point and non-point sources), the use of only the conventional approach in assessment may not be adequate for a holistic and unbiased water quality assessment. NO_3^- and F^- are essential elements for humans, however, their excessive intake through drinking water may be harmful to human health (WHO, 2017; Liu, 2021; Aghamelu et al., 2022; Unigwe C. O. et al., 2022; Xiao et al., 2022a; Unigwe C. O. et al., 2022; Xiao et al., 2022b). Human health issues from F^- contamination have been highly documented in recent times globally (Shahzad et al., 2017; Mirzabeygi et al., 2017; Yousefi et al., 2018; Amiri et al., 2020). According to global health projections, about two hundred million people worldwide are exposed to risks from F^- ingestion in drinking water (Daw, 2004; Ayoob et al., 2008). Among these, regions like China, India, and Africa seem to be more affected (Mumtaz et al., 2015). In a study carried out on the seasonal variation of F^-

concentration in groundwater samples in the Urmia coastal aquifer (northwest Iran), high concentration of F^- was observed in the shallow aquifers; attributed mainly to influx from anthropogenic activities such as intensive use of inorganic fertilizers and untreated waste water (Amiri et al., 2020). According to the 2017 report by World Health Organization, out of 80% of diseases amounting to poor drinking water quality globally, 65% are attributed to endemic fluorosis (WHO, 2017). Long-term ingestion of F^- in drinking water, at a concentration greater than 1.5 mg L^{-1}, is known to be responsible for dental fluorosis (Dehghani et al., 2019; Xiao et al., 2022c). According to the National Research Council (NRC, 2001), harmless daily consumption level of F^- content in water for different age groups have been given as follows: 0.1–0.5 mg d^{-1} (infants of <6 months), 0.2–1.0 mg d^{-1} (infants 6–12 months), 0.5–1.0 mg d^{-1} (children, 1–3 years), 1,0–2.5 mg/d^{-1} (children 4–6 years), 1.5–2.5 mg/day (children 7 years above) and 1.5–4.0 mg d^{-1} (adults). Nitrates on the other hand make up the most essential part of most inorganic fertilizers. They can be released into groundwater bodies through percolation and infiltration from agricultural fields, release from industrial and domestic wastes and burning of fossil fuels (WHO, 2017; Egueri et al., 2021; Omeka and Egbueri, 2022). High nitrate ingestion in drinking water has been associated with life-threatening illnesses like methemoglobinemia (blue baby syndrome) and stomach cancer (Dehghani et al., 2019; Okamkpa et al., 2022). The maximum permissible limit of nitrate in drinking water has been set at 50 mg L^{-1} according to WHO (2017). Elevated concentration of nitrate in drinking water have been found to result in carcinogenic and non-carcinogenic human health risks (Amiri et al., 2022).

Several multiple numerical models have been developed by several researchers for environmental quality monitoring, appraisal, and prediction for irrigation, drinking, and industrial purposes (Edet and Offiong, 2002; Amiri et al., 2021; Igwe and Omeka, 2021; Omeka et al., 2022a; Shukla et al., 2022; Egbueri et al., 2023). These models are based on water quality assessment for heavy metal concentration and overall chemical constituents of chemical elements in the water. Based on heavy metal concentration, numerical models such as heavy metal pollution index (HPI), heavy metal evaluation index (HEI), degree of contamination (C_{deg}) and geo-accumulation index (I-geo) have been mostly used. Based on overall chemical constituents, indices such as the pollution index of groundwater (PIG), pollution load index (PLI), the overall index of pollution (OIP), and water quality index (WQI), have been widely used for drinking water quality analysis. Conversely, numerical indices for irrigation water quality assessment include sodium adsorption ratio (SAR), magnesium hazard (MH), permeability index (PI), residual sodium carbonate (RSC), and salinity hazard. However, a common drawback among these models is their inability to carry out a composite unbiased assessment of water quality. This can be attributed to differences in input variables and sub-index computation methods. As such, one model can certify particular water as suitable while the other may disagree, resulting in a bias in judgment and decision. Hence, for a holistic and unbiased water quality assessment, the use of the integrated approach is recommended for better decision-making (Egbueri et al., 2021; Omeka et al., 2023). Other health risk assessment indices have been based on only the children and adult population sizes and taking into account only the ingestion pathway (Adamu et al., 2015). It is thought that the assessment of the health risk implications of the toxic elements in ingestion water should include more age groups (male, female and children), which will enhance a robust and more reputable health risk assessment for a particular region (Sohrabi et al., 2021; Kadam et al., 2022). Additionally, evaluating the possible health risks from ingestion and dermal contact will afford a more enhanced and flexible approach to health risk assessment. Hence, in the present study, the health risk assessment for the male, female, and children population size has been evaluated, with consideration of two exposure pathways-ingestion and dermal contact with an emphasis on NO_3^- and F^- contamination.

Groundwater sources in the Firozabad city have been exposed to contamination from chemicals (especially NO_3^- and F^-). No known study has been carried out in the area concerning the irrigation suitability assessment of groundwater within the area. Moreover, no literature has reported health risk assessment of groundwater in the area based on NO_3^- and F^-. Although several studies have been carried out in nearby areas such as Agra, on the health risk implications of only fluoride using different stochastic and simulation models (Ali et al., 2017). No literature has carried out an integrated and composite assessment of the drinking water and irrigation water quality assessment of groundwater in the area using numerical indexical approaches. Hence, in this study, multiple numerical indices, multivariate statistical models, and multipath health risk models have been integrated for a holistic assessment of the drinking water quality, irrigation suitability status, and health risk level of groundwater from the industrial region of Firozabad city, Uttar Pradesh, India. The objectives of the present study are 1) to appraise the quality of drinking water in the area using WQI-PIG multi-criteria study approach, 2) to carry out a composite human health risk assessment of the exposure of contaminated water to inhabitants by considering two exposure routes (ingestion and dermal contact) and three age groups (female, male and children) with emphasis on NO_3^- and F^-, 3) to attempt a generic identification and classification of the possible source of contaminants as well as the association between numerical models using multivariate statistics, 4) to evaluate the suitability of the groundwater in the area for irrigation purposes using multiple irrigation water quality indices and 5) to propose a state-of-the-art futuristic water treatment/waste management approach for the study area for water quality sustainability. It is hoped that the findings from this research would be helpful to decision-makers for equitable and robust decision-making regarding water quality management and sustainability for enhanced agricultural production globally. The findings and suggested remediation measures can serve as a template for other parts of the world for enhanced water quality and resource availability.

2 Material and method

2.1 Study area description

Firozabad, famed for its numerous small-scale glass industries, is located in the western part of Uttar Pradesh (latitude: 27°12′ to 27°18′ N; longitude: 78°35′ to 78°42′ E), north-central India (Figure 1). The city is covered by the Etah district in the north, Mainpuri and Etawah districts in the east, while the Yamuna River covers its southern boundary. The region has a sub-humid climate

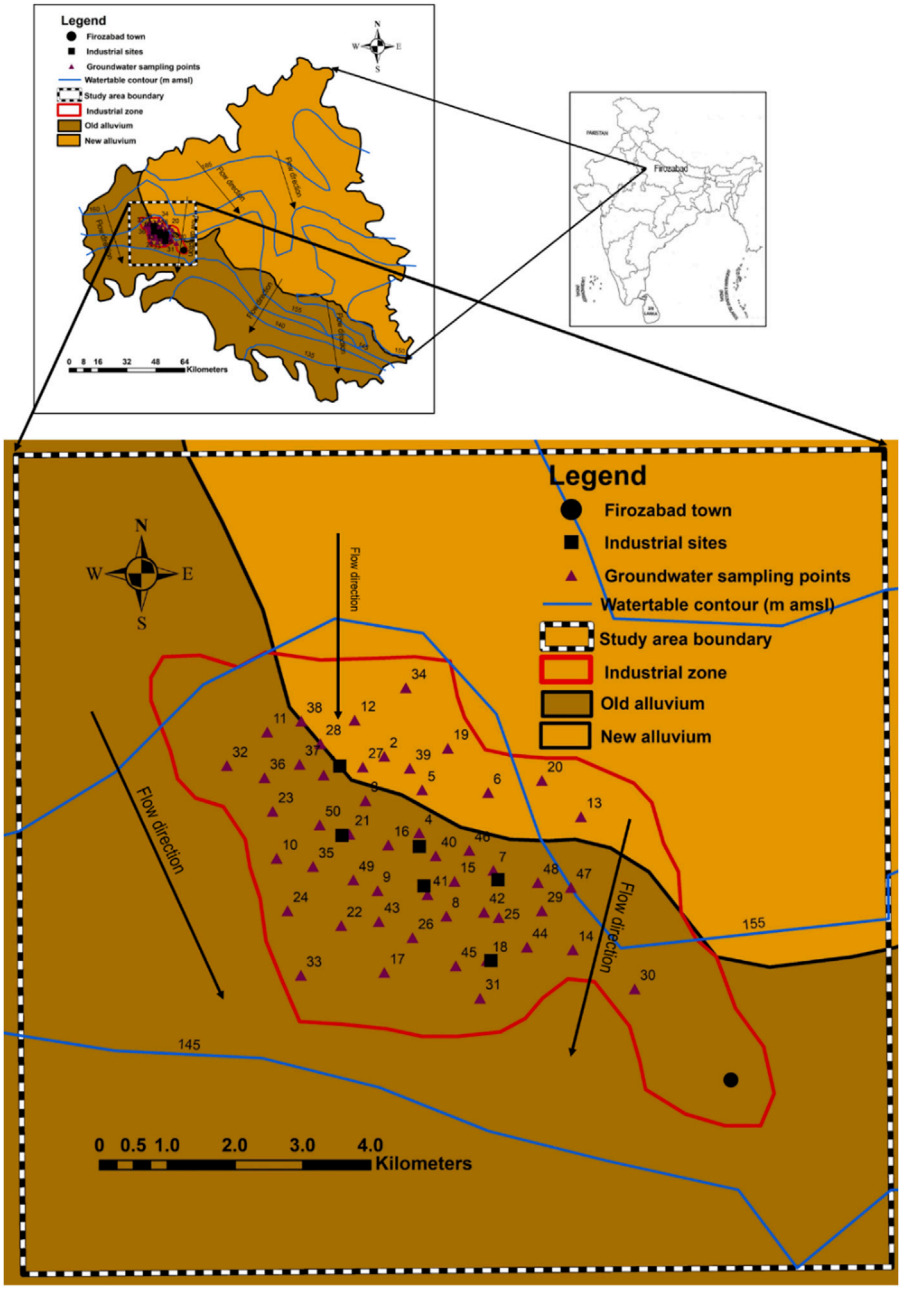

FIGURE 1
Map showing the sampling location, geology, hydrogeology and groundwater flow direction in the study area.

with an average annual rainfall of 715.2 mm, the major portion being received during the summer monsoon period (June to September). The city employs a sizeable proportion of its population in centuries-old glass manufacturing units. Over five crore bangles are sold every day in the country, the supply of which is entirely credited to Firozabad city, earning it the name of 'suhag nagri'. The multi-level bangle-making industry lacks improved technologies for glass processing and waste disposal. Glass is recycled and reused, however, the process requires a huge quantity of water for molding, cooling, washing, and glazing, which is drained away without treatment, contaminating land and subterranean water. Not only land and water but the air is also polluted by the pollutants spewed from the glass industries contributing to the deteriorating health condition of local peoples and making the ecosystem more fragile.

Since, the average annual precipitation in the region is inadequate to meet the demands of agricultural operations year-round, the water from canals and bore well helps the farmers to take up multiple crops in a year. The untreated effluents from the glass industries being drained directly into the nearby water channel, pollute the main stream water which flows down to the Yamuna *via* its tributaries' *viz.* Sirsa, Senger and Arind Nadi.

TABLE 1 Relative weights of parameters used in PIG and WQI evaluation.

Parameters	wi	Relative weight (wi)
F^-	4	0.0655
TDS	2	0.0327
pH	2	0.0328
EC	2	0.0328
K	2	0.0327
Mg	3	0.0492
Ca	2	0.0328
NO_3^-	4	0.0656
Na	2	0.0328
SO4	3	0.0492
Cl	4	0.0656
HCO_3	1	0.0164
Cu	4	0.0655
Fe	3	0.0492
Mn	3	0.0492
Zn	3	0.0493
Cr	4	0.0656
Ni	4	0.0656
Pb	5	0.0812
Cd	4	0.0655
	∑wi = 61	∑Wi = 1

2.2 Geology and hydrogeology

The geology of the Firozabad district is underlain by sands of various grades, gravels, silt, and clay. The result of exploratory drilling indicates that in the central and south-western parts of the district where the Firozabad city (where study area lies), encounters the Vindhyan sandstone as basement (with varying depths) and the alluvial sediment thickness increases from south-western part to northern parts (Ali et al., 2017). Additionally, there is also a shift from older alluvium (Bhangar) to newer alluvium (Khadar) in the same direction (Figure 1). Based on borehole data, a three-tier system of aquifers exists in the Firozabad district. Groundwater occurs under unconfined to semi-confined conditions, although this may depend on the nature and occurrence of the number of local/semi-regional clay beds.

Based on the depth to water level data of groundwater monitoring stations, the pre-monsoon water level varies from 2.42 to 25.1 m, while in the post-monsoon period, depth to water varies from 1.55 to 25.3 m (Prasad, 2008) Water level fluctuation varies from 0.23 to 1.38 m. Water level is deeper along the bank of Yamuna which takes it source from the southern part of the study area. The long-term water level trend is a falling one and varies from 0.0171 to 0.0264 m/year. The yield of deep tube-well varies from 1900 to 2,600 L per meter (lpm) for normal drawdowns, whereas the yield of shallow tube-well varies from 1,000 to 2000 lpm (Prasad, 2008). The transmissivity varies from 17.0 to 42.8 m/day. At the western part of the study area, there is presence of a small clay lens that can create a perched aquifer; serving as a major sink for anthropogenic contaminants. The groundwater flow direction is towards south (Figure 1), thus facilitating the possible migration of contaminants towards southern direction within the study area. It can therefore be deduced that due to the high porosity of the geologic units, coupled with the low depth to water table, the aquifer within this area is highly susceptible to contaminant influx from nearby industries and agricultural fields (Aghamelu et al., 2022; Okamkpa et al., 2022).

2.3 Groundwater sampling and analysis

To conduct a water quality assessment, a total of fifty (n = 50) groundwater samples were collected randomly from the nearby glass industrial area in the Firozabad city, which consists of shallow hand pumps and tube wells, from January–February 2021. The samples were collected in polypropylene bottles with 1 L capacity. In the laboratory, all analytical procedures were conducted based on American Public Health Association (APHA 1995, 2012, 2017) standard procedures. The water samples were filtered using Whatman-42 filter paper and a few drops of toluene were added to each of the samples and were stored at 4°C until further analysis. The samples were analyzed for sodium (Na^+), potassium (K^+), calcium (Ca^{2+}), magnesium (Mg^{2+}), chloride (Cl^-), sulphate (SO_4^{2-}), fluoride (F^-), nitrate (NO_3^-), bicarbonate (HCO_3^-), and total hardness (TH) by using standard procedures (APHA 1995, 2012). The pH and electrical conductivity (EC) were measured in water samples employing a combined digital pH and conductivity meter (Eutech PC 700, Thermo Fisher Scientific Inc.). The total dissolved solids (TDS) (mg L^{-1}) of the water samples was measured by multiplying EC (dS m^{-1}) by a factor of 640 (Eaton et al., 1995; Corwin and Yemoto, 2017). The Na and K were determined using a flame photometer (Systronics Type-130). The SO_4^{2-} in groundwater sample was analyzed by $BaCl_2$ turbidimetric method, while NO_3^- was analyzed following the Cd-reduction method and measuring the absorbance at 543 nm using the UV spectrophotometric method (Labtronics Model LT-291). The F^- in groundwater sample was estimated by using the F^- ion selective electrode as per Corwin and Yemoto (2017). The heavy metals such as iron (Fe), copper (Cu), manganese (Mn), and zinc (Zn) were determined using flame atomic absorption spectroscopy (FAAS) (Agilent Technologies 200 series AA), while chromium (Cr), nickel (Ni), cadmium (Cd), and lead (Pb) were analyzed using graphite furnace atomic absorption spectroscopy (GFAAS) (Agilent Technologies 200 series AA) (Igwe and Omeka, 2021). For preparing standard solutions, 100 mg L^{-1} inductively coupled plasma (ICP) multi-element standard stock solution was purchased from Certipur® Merck KGaA (Germany). All concentrations are expressed in mg L^{-1}, except pH and EC (dS m^{-1}).

To ensure quality assurance and control of analytical data, it was necessary to calculate the ionic balance error (IBE) to ensure the accuracy of the hydrochemical data. The IBE is based on the principle of electro-neutrality as proposed by Freeze and Cherry

(1979). The principle follows that the sum of all the anions in a particular water sample must equal that of cations (expressed in meq/L) (Eq. 1). Based on the computed IBE, all water samples showed IBE within the acceptable standard value of ≥5%

$$\text{IBE} = \frac{\sum\text{Anions} - \sum\text{Cations}}{\sum\text{Anions} + \sum\text{Cations}} \text{ x } 100 \quad (1)$$

2.4 GIS-based geospatial analysis

The use of use spatiotemporal maps in the present study was to give a visual assessment of the human health risks to different population sizes through different exposure routes. The spatiotemporal maps were generated using Surfer (ver. 21.1). The location of the sample points (as collected during field studies using longitudes and latitudes values from GPS) were interpolated into the map by integrating the inverse distance weighting (IDW) technique and simple kriging (SK) in the Surfer (ver. 2.1.1) environment. Additionally, to determine the groundwater flow direction of the area, hydraulic head values were used as the input parameters, using the relation shown in Eq. 2 as per Okamkpa et al. (2022).

$$\text{H} = \text{GSE} - \text{SWL} \quad (2)$$

where H represents the hydraulic head layer, GSE represents the ground surface elevation (in meters), and SWL represents the static water level (in meters).

IDW is a geostatistical analytical method that fits a surface to three dimensions (XYZ). It involves the use of known Z values weights determined as a function of distances between the known and known points (Philips & Watson 1982). As such, in IDW, distant points have less influence than those that are close. In other words, only known Z values and distant weights are used to derive the unknown areas. In the present study the Z-values were represented by the health risk assessment values for different population sizes for different exposure pathways, with X and Y dimensions representing latitude and longitude values respectively.

2.5 Drinking water quality assessment

2.5.1 Water quality index

The WQI provides a complete summary assessment of the drinking water quality level of water samples (Igwe and Omeka, 2021; Xiao et al., 2021). To do so, distinct weights (wi) ranging from one to five are assigned to various water quality variables depending on their relative concentration and importance in terms of drinking water quality; the relative weights (Wi) of each parameter are then calculated. (Eq. (3); Table 1).

$$\text{Wi} = \frac{wi}{\sum_{i=1}^{n}(wi)} \quad (3)$$

where n represents the total number of parameters.

The quality rating scale for each parameter (qi) was then calculated following Eq. (4)

$$qi = \left(\frac{Ci}{Si}\right)x\,100 \quad (4)$$

Where C_i indicates the concentration of individual water parameters; S_i is the WHO (2017) standard limit.

The sub-index of the *i*th parameter (SI), was thereafter computed using Eq. 5. Finally, the WQI was estimated as shown in Eq. 6

$$SI = Wi\,x\,qi \quad (5)$$

$$WQI = \sum_{i=1}^{n}(SI) \quad (6)$$

2.5.2 Pollution index of groundwater

The level of pollution from the individual chemical elements on the groundwater quality can be evaluated using the PIG. This index was proposed by Subba Rao (2012) and takes into consideration the values of both physicochemical and heavy metals. To do this, the relative weights (Rw) (varying between 1 and 5) are apportioned to each chemical parameter according to their relative effect on human health (Table 1). Thereafter, the weight parameter (Wp) is derived for each analyzed chemical parameter to calculate the relative importance of each parameter on the general drinking water quality (Eq. (7)). Furthermore, the individual parameter in each water sample is divided by the standard drinking water quality limit to determine the concentration status (Sc) for each sample point (Eq. (8)). The overall drinking water quality (Ow) is then derived following the relation in Eq. 9. Finally, the obtained Ow values were then summed up to determine the PIG of the individual groundwater sample locations (Eq. (10))

$$\text{Wp} = \text{R}_\text{w} \Big/ \sum \text{R}_\text{w} \quad (7)$$

$$\text{Sc} = \frac{\text{c}}{\text{D}_\text{S}} \quad (8)$$

$$\text{Ow} = \text{w}_\text{p}{}^{*}\text{S}_\text{C} \quad (9)$$

$$\text{PIG} = \sum \text{O}_\text{W} \quad (10)$$

Based on the PIG classification scheme as proposed by Subba Rao (2012), PIG <1 denotes negligible pollution level, 1 ≥ PIG ≤1.5 depicts low pollution, 1.5 ≥ PIG ≤2 indicates moderate or mild pollution level, 2 ≥ PIG ≤2.5 indicates high pollution, and PIG >2.5 depicts very high pollution level.

2.6 Irrigation water quality assessment

A comprehensive assessment of the irrigation water quality was carried out by computing various irrigation parameters including magnesium hazard (MH), sodium adsorption ratio (SAR), residual sodium carbonate (RSC), Kelly's Ratio, (KR), electrical conductivity (EC), potential salinity (PS), and permeability index (PI). The parameters were then combined to evaluate the joint influences from various chemical parameters on crop productivity. Crop yield and soil quality can be influenced by the quality of irrigation water; hence it becomes necessary to carry out a comprehensive assessment of irrigation water quality using various irrigation water quality indices (Wang et al., 2022) Thus, this necessitates the need for the appraisal of our water quality for irrigational purposes. The equations for the calculation of the various irrigation water quality indices and their respective references are presented in Table 2.

TABLE 2 Equations and references for irrigation water quality assessment.

Irrigation parameter	Equation	References
Sodium adsorption ratio (SAR)	$\frac{Na^{+}}{\sqrt{Ca^{2+}+Mg^{2+}/2}}$	Richards (1954)
Kelly's Ratio (KR)	$Na^{2+}/(Ca^{2+}\ Mg^{2+})$	Kelly (1940)
Permeability index (PI)	$\frac{Na^{+}\sqrt{(HCO_3^{-}\times 100)}}{Ca^{2+}+Mg^{2+}+Na^{+}}$	Todd (1980)
Potential salinity (PS)	$Cl^{-}+\sqrt{SO_4^{2-}}$	Doneen (1964)
Percentage sodium (%Na)	$\frac{(Na^{+}+K^{+})}{(Ca^{2+}+Mg^{2+})}\ x\ 100$	Wilcox (1955)
Magnesium Hazard (MH)	$\frac{Mg^{2+}}{(Ca^{2+}+Mg^{2+})}\ x\ 100$	Nagaraju et al. (2014)
Residual sodium carbonate (RSC)	$((HCO_3^{-})-(Ca^{2+}+Mg^{2+}))$	Ragunath (1987); Singh et al. (2019)
Chloro-alkaline index I (CAI-I)	$(Cl^{-}-(Na^{+}+K^{+}))/Cl^{-}$	Schoeller (1967)
Chloro-alkaline index II (CAI-II)	$(Cl^{-}-(Na^{+}+K^{+}))/(SO_4^{2-}+HCO_3^{-}+NO_3^{-})$	Schoeller (1967)

2.7 Health risk assessment

Two main exposure pathways are taken into account while evaluating human health risks from drinking water, according to the US Environmental Protection Agency (US-EPA, 1989). The two significant mechanisms are exposure *via* dermal contact and exposure *via* ingestion or oral route (Rahman et al., 2021; Amiri et al., 2022). In this study, three groups of exposed individuals—men, women, and children—were taken into account when assessing the health risks of three selected elements (nitrate, chloride and fluoride). Both oral and dermal contact exposure pathways are used in the process of calculating the non-carcinogenic health risk, as given in the following equations:

a) Oral intake:

$$CDM = \frac{C\ x\ EF\ x\ ED\ IR}{ABW\ x\ AET} \tag{11}$$

$$HQ_{oral} = \frac{CDI}{RfD} \tag{12}$$

b) Dermal contact:

$$DAD = \frac{C\ x\ TC\ KI\ x\ CF\ x\ EV\ x\ SSA}{ABW\ x\ AET} \tag{13}$$

$$HQ_{dermal} = \frac{DAD}{RfD} \tag{14}$$

$$HI_{dermal} = \sum_{i=1}^{n} (HQ_{oral} + HQ_{dermal} \tag{15}$$

Chronic daily intake is denoted in Eq. 11 by "CDI" (in mg/kg/day); the concentration of individual elements is denoted by "C" (in mg L^{-1}); and daily groundwater ingestion rate is denoted by "IR" (in L d^{-1}), with 2.5 L d^{-1} for males and females and 1 L d^{-1} for children. EF denotes the exposure (in days/year). The exposure frequency is 365 days per year for males, females, and children. ED denotes the exposure duration (in a year); 12 years for children, 67 years for females, and 64 years for males. ABW indicates the average body weight, which is 65 kg for men, 55 kg for women, and 15 kg for children. The average exposure times (AET) for males, females, and children are given as 23,360 days, 24,455 days, and 4,380 days, respectively. The hazard quotient is denoted as HQ in Eq. 12

RfD represents the reference dosage of nitrate, chloride, and fluoride contamination (in mg/kg/day), which is 1.6 mg/kg/day, 0.1 mg/kg/day, and 0.06 mg/kg/day respectively. In Eq. 13, DAD denotes the dermal absorbed dose (mg/kg day); TC is the contact time (in h/day) taken as 0.4 h/day; Ki is the dermal adsorption parameters (in cm/h) taken as 0.001 cm h^{-1}, and CF is the conversion factor taken as 0.001. EV denotes bathing frequency (in times/day) and is considered one time per day, whereas SSA denotes skin surface area (in cm^2). SSA values are taken as 16,600 square centimeters for both males and females and 12,000 square centimeters for children. HI is the hazard index in Eqs. 14, 15, and its value denotes non-carcinogenic human health risks. A HI value larger than one indicates a potential human health danger from nitrate contamination, while HI value less than one indicates a tolerable level of human health risk (Amiri et al., 2020; Rahman et al., 2021; Amiri et al., 2022).

2.8 Multivariate statistical analysis

In the present study, two multivariate statistical models (Q-mode hierarchical cluster analysis and principal component analyses) were used to identify possible sources of contamination as well as the interrelationships between the water quality parameters and water quality indices. All analyses were performed using the IBM SPSS (v. 25) statistical model. Details of the methodology of the models have been described in section 3.

3 Results and discussion

3.1 Overall groundwater quality description

Overall physicochemical results of groundwater samples are presented in Supplementary Table S1 (Supplementary Material), while a descriptive statistical summary of physicochemical results is shown in Table 3. The results were also compared with standard limits of the World Health Organization (WHO, 2017) and Bureau of Indian standards (BIS, 2012). A classification criterion as per

TABLE 3 Descriptive statistical summary of the physicochemical parameters compared to quality standard.

Chemical parameter	Unit	Min	Max	Mean	WHO (2017)	BIS (2012)
pH	-	7.52	8.55	7.87	7	7
EC	µs/cm	1,161.0	2,541.0	1,576.6	1,000	1,000
Ca	mg/L	48.5	92.1	65.31	200	200
Mg	mg/L	12.2	23.1	16.4	200	200
Na	mg/L	210.9	421.6	305.1	200	200
K	mg/L	6.0	31.0	13.4	30	30
SO4	mg/L	15.0	92.0	33.4	100	100
Cl	mg/L	211.9	422.6	306.1	250	250
F^-	mg/L	0.39	2.63	1.52	1.5	1.5
NO_3^-	mg/L	2.0	9.00	4.96	45	45
HCO3	mg/L	116.3	159.9	133.1	250	250
TDS	mg/L	708.6	1,591.8	974.5	1,000	1,000
TH	mg/L	171.34	325.2	230.9	100	100
Cu	mg/L	0.309	1.75	0.791	0.01	0.01
Mn	mg/L	0.00	0.09	0.01	0.2	0.2
Fe	mg/L	0.00	0.62	0.09	0.3	0.3
Zn	mg/L	0.00	1.012	0.08	3	3
Cr	mg/L	0.00	0.12	0.02	0.02	0.02
Ni	mg/L	0.00	0.07	0.03	0.07	0.07
Cd	mg/L	0.02	0.04	0.03	0.003	0.003
Pb	mg/L	0.30	0.48	0.40	0.01	0.01

Langenegger (1990) for all the physicochemical parameters has also been provided (Table 4). The study area is an agrarian region saddled with intensive anthropogenic influxes from agricultural activities and poor management of its effluents from industries. Additionally, other human-mediated influx from poor solid waste management also poses as a major source of pollution to both the drinking and irrigation water quality, thereby putting more stress on the available groundwater sources. Hence, it was necessary to carry out a composite physicochemical analysis of all the groundwater quality parameters for both drinking and irrigation purposes.

Generally, based on their values, EC, TH, Na^+, Cl^-, and F^- , recorded their respective values above the WHO (2017) recommended standards for drinking water quality, while other parameters were within the required standard. The water conductivity (EC) ranged between 1,161 µS cm^{-1} and 2,541 µS cm^{-1} with a mean value of 1,576.6 µS cm^{-1}. High electrical conductivity in groundwater has a direct bearing on the total dissolved solids in water (Igwe and Omeka, 2021). The high TDS values observed in this seem to correspond with the conductivity values observed. Moreover, the high EC values appear to be in tandem with the corresponding high concentration of dissolved ions such as Cl and Na in the water. The elevated concentration of EC in the results could be sourced from infiltration and dissolution of chemical constituents from agricultural return water. High water conductivity harms soil fertility and can affect crop roots, thereby reducing plant yield. (Singh et al., 2019). Based on the Langenegger (1990) classification scheme, 56% of the total water samples are brackish while 44% are saline (Table 4). Based on the Davis and De Wiest (1966) classification criterion for TDS for drinking and irrigation, 60% of the total groundwater samples fall under the "permissible" category for drinking, while 40% are useful for irrigation. TDS is an important indicator of dissolved chemical constituents in water. TDS ranged from 708.6 mg/L to 1,591.8 mg L^{-1} with an average value of 974.5 mg L^{-1} (Table 4). Results from Table 3 shows that the groundwater pH is alkaline with values varying between 7.5 and 8.5 (mean = 7.8). The high alkalinity observed in the water can be attributed to dilution and increased buffering from precipitation and rock water interaction (Aghamelu et al., 2022; Omeka et al., 2022b).

The total hardness (TH) ranged from 171.3 mg L^{-1}–325.2 mg L^{-1} with a mean value of 230.98 mg L^{-1}. Water hardness is controlled by geogenic processes such as the dissolution of calcium and magnesium-bearing minerals from rocks enriched in alkali Earth metals (Ca, Mg) and alkaline metals (Na and K). The study area is underlain by sands of various grades, gravels, silt, clay, and alluvium deposits. The sands and alluvium are highly enriched in silicate and feldspar minerals (Barzegar et al., 2018); thereby giving rise to the high concentration of these minerals and the corresponding elevated hardness. Based on the McGowan (2000)

TABLE 4 Classification of all groundwater samples based on physicochemical characteristics (Modified after Langenegger, 1990; Davis and De Wiest, 1966; McGowan, 2000).

Parameter	Range	Water quality class	% Of sample in category
TDS (mg/L)	<500	Desirable for drinking	-
	500–1,000	Permissible for drinking	60
	≤3,000	Useful for irrigation	40
	>3,000	Unfit for drinking and irrigation	-
EC (μs/cm)	0–333	Excellent	-
	333–500	Good	-
	500–1,100	Permissible	-
	1,110–1,500	Brackish	56
	1,500–10,000	Saline	44
TH (mg/L)	<60	Soft	-
	60–120	Moderate	-
	120–180	Hard	4
	>180	Very hard	96
Nitrate hazard	<5	Excellent	42
	5–10	Good	58
	10–50	Permissible	-
	>50	Poor	-
Calcium hazard	≤100	Excellent	100
	≤250	Good	
	≤400	Permissible	
	>400	Poor	
Chloride hazard	≤50	Excellent	
	≤150	Good	
	≤250	Permissible	18
Sodium Hazard	>250	Poor	82
	<10	Good	100
	10–18	Poor	
	18–26	Moderate	
	>26	Very poor	

classification scheme, 4% and 96% of the total water samples were classified as hard and very hard, respectively. The implication of this is that the high TH values are a result of highly dissolved divalent metallic ions (such as Ca^{2+}, Mg^{2+}) from the underlying aquifer material (Unigwe et al., 2022).

Sodium (Na) concentration varied from 210.9 mg L^{-1}–421.6 mg L^{-1}, averaging 305.1 mg L^{-1} (Table 3). Based on their mean values, Na concentration in the analyzed groundwater samples is above the WHO (2017) prescribed standard for drinking water. The elevated concentration of Na in the groundwater could be attributed to geogenic controls, such as the dissolution of calcic-bearing mineral rocks that underlie the area. Chloride (Cl^-) ranged from 210.9 mg L^{-1}–421.6 mg L^{-1} having a mean value of 305.1 mg L^{-1}, with values occurring above the WHO (2017) permissible limit. According to the chloride hazard classification criteria (Table 4), 82% of the water are of poor quality, while 18% occurs within the "permissible" class. According to Yıldız and Karakas (2019), if Cl^- in irrigation water occurs at values above 100 mg L^{-1}, it can result in the reduction of soil permeability, thereby leading to plant toxicity and a reduction in crop yield. Fluoride concentration varied from 0.39 mg L^{-1}–2.63 mg L^{-1}, recording an average concentration value of 1.52 mg L^{-1}. Based on the mean values, the groundwater samples in

the Firozabad city have F^- concentration above the WHO required values for drinking water quality. Long-term ingestion of fluoride in drinking water, with concentration greater than 1.5 mg L^{-1}, is known to be responsible for dental fluorosis (Kotecha et al., 2012; Dehghani et al., 2019). Similar results have been found in some studies in the Agra district, a nearby area (Ali et al., 2017). Based on the findings of Ali et al. (2017), fluoride concentration varied between 0.14 and 4.88 mg L^{-1} in 45 villages in the Agra district, with concentrations occurring above the WHO standards. A similar study by Amouei et al. (2012) also showed an elevated concentration of F^- in drinking water wells at a concentration ranging between 0.11 and 3.59 mg L^{-1}. There is a similarity in both areas in terms of anthropogenic influxes, this may account for the similar values in F^- content observed for the present study.

Based on their mean values, the concentration of heavy metals among the analyzed groundwater samples decreased in the order of Cu > Pb > Fe > Zn > Ni > Cd > Cr > Mn. Among the heavy metals, Cd, Pb, Cu, and Cr occurred in a concentration above the WHO and BIS recommended standards for drinking water quality. Cd has been ranked among the first ten carcinogenic elements according to the Toxic Substances Disease and Registry (ASTDR, 2018). The concentration of Cd ranged from 0.02 to 0.04 mg L^{-1} with a mean value of 0.033 mg L^{-1}. High Cd concentration in groundwater is usually associated with the weathering and dissolution of sulfide minerals such as chalcopyrite and pyrites in subsurface aquifers enriched in Pb and Zn (Obasi and Akudinobi, 2020; Omeka and Igwe, 2021). The subsurface geology of the present study area is devoid of such rock minerals. Hence, the high concentration of Cd among the water samples can be attributed to anthropogenic influxes emanating from poor waste management and agricultural activities. Long-term ingestion of Cd in drinking water has been reported to be responsible for human renal dysfunction and kidney disease (Obasi and Akudinobi, 2020; Devi et al., 2021). The concentration of Pb varied between 0.30 mg L^{-1} and 0.48 mg L^{-1} recording an average value of 0.40 mg L^{-1}. Leaching from solid waste materials and agricultural effluents may have given rise to the high Pb concentration among the groundwater samples. The long-term consumption of Pb in drinking water has been reported to result in abnormities in human fetal development in pregnant (Tüzen, 2013; Kumar et al., 2022). The concentration of Cr ranged from 0.00 mg/L (below detection limit) to 0.12 mg/L, having a mean concentration of ≈0.03 mg/L; with concentration slightly occurring below the drinking water quality. The occurrence of Cr among the water samples can be attributed to geogenic sources from source rocks that make up the subsurface geology. Sands, silts, and alluvium have been reported to make up the major litho-stratigraphic constituent of the underlying geology. The dissolution of these rocks can serve as a natural source of Cr in the groundwater (Obasi and Akudinobi, 2020).

The results of physicochemical analysis have so far revealed that the groundwater from the Firozabad city is largely influenced by anthropogenic influxes from agricultural activities and to a lesser extent by geogenic processes such as rock water interaction, weathering, and dissolution of chemical species within the underlying aquifer system.

3.2 Dynamics of groundwater flow and contaminant transport

The geology of the area is underlain by sands, gravels, silt, and clay, with high primary porosity and permeability. Their high porosity and permeability properties can influence the movement of contaminant species into the aquifer through infiltration and percolation. Additionally, the groundwater depth-to water table has been found to vary between 2.42 and 25.1 m (during pre-monsoon) and 1.55–25.3 m during post-monsoon (Prasad, 2008). The low depth to water table together with the high permeability and porosity of the underlying geology could serve as sources for contaminant influx into the groundwater nearby industries and agricultural fields (Aghamelu et al., 2022; Okamkpa et al., 2022). An observation of Figure 1 shows that the groundwater flows dominantly towards the south-western direction of the area. The major water source in the area is made up of majorly hand-dug wells. However, these wells are not well cased, and are drilled very proximate to industries and agricultural fields. Additionally, the few boreholes within the area are drilled without consideration of environmental safety standards, hence making them vulnerable to contamination influx. Contaminants within a porous media tend to follow the trend of groundwater flow (Fetter, 2018).

Hence, it can be deduced that contaminants flow within the aquifer will tend to flow along the path of groundwater flow, towards adjacent aquifers through recharge and infiltration. In the study area, most of the streams serve as sinks for disposal of untreated industrial and agricultural waste water and effluents. These streams can serve as recharge to the aquifer, therefore exposing them to pollution. As observed in Figure 1, the vector lines tend to move dominantly from the northwestern direction towards the southwestern parts of the study area. The implication is that water wells around the south and southwestern parts will be highly susceptible to contaminant influxes. Unfortunately, most of the industrial activities within the Firozabad city are confined within the south-western region. It is therefore recommended that drinking water wells should be prohibited from being drilled within the southern and south-western regions until remedial measures are put in place to ameliorate the spread of contaminants. However, the north-western and south-eastern regions may be suitable sites for drilling boreholes and hand-dug wells for drinking purposes.

3.2 Drinking water quality assessment

3.2.1 Pollution index of groundwater

A descriptive statistical summary, as well as the rating scale of final PIG results (∑Ow), are presented in Table 5; Supplementary Table S2 (Supplementary Material) shows the detailed PIG results. From the detailed results of PIG (S2), the Ow for all individual analyzed parameters, except for Cu, recorded values less than 1.0 indicating that Cu had a greater impact on the groundwater quality. The overall PIG (∑Ow) ranged from 3.69 to 12.7 with a mean value of 6.79 (Table 5). According to the PIG classification criteria (Subba Rao, 2012), all the groundwater samples showed very high pollution (PIG >2.5). Results from PIG have so far shown that the groundwater quality of the study area is in a very deplorable state due to toxic element influxes from anthropogenic activities (such as

TABLE 5 Summary statistical results of WQI and PIG and their rating scale.

Sample ID	WQI	PIG	Index parameter	Range	Water category	% Sample
S1	375.8	3.762	**WQI**	<50	Excellent	-
S2	539.4	5.394		50–100	Good	-
S3	634.1	6.341		100–200	poor	-
S4	369.2	3.692		200–300	very poor	-
S5	608.3	6.084		>300	unsuitable	100
S6	683.1	6.832				
S7	748.1	7.483	**PIG**	PIG (<1.0)	Insignificant pollution	-
S8	488.1	4.881		PIG (<1.0–1.5)	Low pollution	-
S9	1,156.9	11.569		PIG (1.5–2.0)	Moderate pollution	-
S10	658.1	6.581		PIG (2.0–2.5)	High pollution	-
S11	790.5	7.905		PIG (>2.5)	Very high pollution	100
S12	552.7	5.527				
S13	511.2	5.112				
S14	387.1	3.871				
S15	568.0	5.680				
S16	653.4	6.534				
S17	479.8	4.798				
S18	507.7	5.077				
S19	671.9	6.719				
S20	1,277.6	12.776				
S21	895.9	8.959				
S22	731.3	7.313				
S23	591.4	5.914				
S24	448.0	4.480				
S25	540.9	5.409				
S26	545.5	5.455				
S27	414.1	4.141				
S28	948.3	9.483				
S29	749.3	7.493				
S30	694.3	6.943				
S31	649.7	6.497				
S32	699.5	6.993				
S33	563.3	5.633				
S34	784.3	7.889				
S35	534.9	5.349				
S36	1,271.8	12.718				
S37	613.5	6.176				
S38	560.8	5.608				

(Continued on following page)

TABLE 5 (*Continued*) Summary statistical results of WQI and PIG and their rating scale.

Sample ID	WQI	PIG	Index parameter	Range	Water category	% Sample
S39	648.1	6.481				
S40	740.1	7.402				
S41	883.2	8.832				
S42	787.4	7.874				
S43	806.2	8.062				
S44	897.9	8.979				
S45	1,208.8	12.088				
S46	751.6	7.516				
S47	633.3	6.333				
S48	537.3	5.373				
S49	603.0	6.030				
S50	552.6	5.526				
MIN	**369.2**	**3.692**				
MAX	**1,277.6**	**12.77**				
MEAN	**678.9**	**6.791**				

the indiscriminate use of agrochemicals in agricultural fields). This calls for an urgent need for the implementation of remedial measures to protect the available groundwater resources.

3.2.2 Water quality index

Table 5 shows the summary statistical results of WQI as well as their rating scale. The WQI results ranged between 369.2 and 1,277.6 with an average value of 678.9. The WQI classification criteria have been given as WQI <50 (excellent drinking water quality), WQI = 50–100 (good drinking water quality), WQI 100–200 (mild pollution or poor drinking water quality), WQI 200–300 (very poor drinking water quality); WQI >300 (unsuitable or critical drinking water condition) (Ukah et al., 2019). Following this classification index, all the groundwater samples appear to fall under unsuitable or critical drinking water conditions. The results of the WQI seem to be commensurate perfectly with those of PIG. Hence, the integration of the two models in this study validates each other in water quality analysis, and as such are considered good tools for water quality prediction.

3.3 Irrigation water quality assessment

A comprehensive assessment of the irrigation water quality was carried out by computing various irrigation parameters (MH, SAR, Na, RSC, KR, EC, PS, PI). The parameters were then combined to evaluate the joint influences from various chemical parameters on crop productivity. Previous studies have focused only on the evaluation of individual irrigation water quality parameters (Unigwe et al., 2022), it is thought that integrating the various irrigation water quality parameters will provide adequate information that will aid in the proper management of soil and irrigation water for enhanced agricultural productivity (Subba Rao, 2018).

3.3.1 Sodium adsorption ratio and salinity

The SAR is used to evaluate the amount of monovalent sodium (Na^+) that is replaced by divalent ions, such as such Ca^{2+} and Mg^{2+}. It is derived from the ratio of sodium hazard in irrigated water and its effect on soil. The soil structure can be affected by variations in ionic strength which is a function of dissolved ions in irrigation water. This variation can be depicted by the electrical conductivity values of the irrigation water (Aravinthasamy et al., 2019). Hence, the U.S Salinity Laboratory diagram (USSL, 1954) which combines the composite effects of SAR (S) and EC (C) on crop yield can be used for a comprehensive assessment of the effect of ionic strength on crop yield (Figure 2). According to the USSL (1954) classification criteria, the salinity hazard (C), can be grouped into four sub-zones: C1: <250 μS cm^{-1} (low salinity hazard), C2: 250–750 μS cm^{-1} (medium salinity hazard), C3: 750–2,250 μS cm^{-1} (high salinity hazard), and C4: >2250 μS cm^{-1} (very high-salinity hazard), with each group depicting good, poor moderate, and very poor water quality types respectively. On the other hand, sodium hazard (S), can be grouped into four sub-zones: S1: <10 (low sodium hazard), S2: 10–18 (medium sodium hazard), S3: 18–26 (high sodium hazard), and S4: >26 (very high sodium hazard), represented as good, poor, moderate, and very poor water quality types, respectively. Based on this classification chart, a total of 48 groundwater samples (96%) recorded a high salinity hazard (C3), while a very high salinity

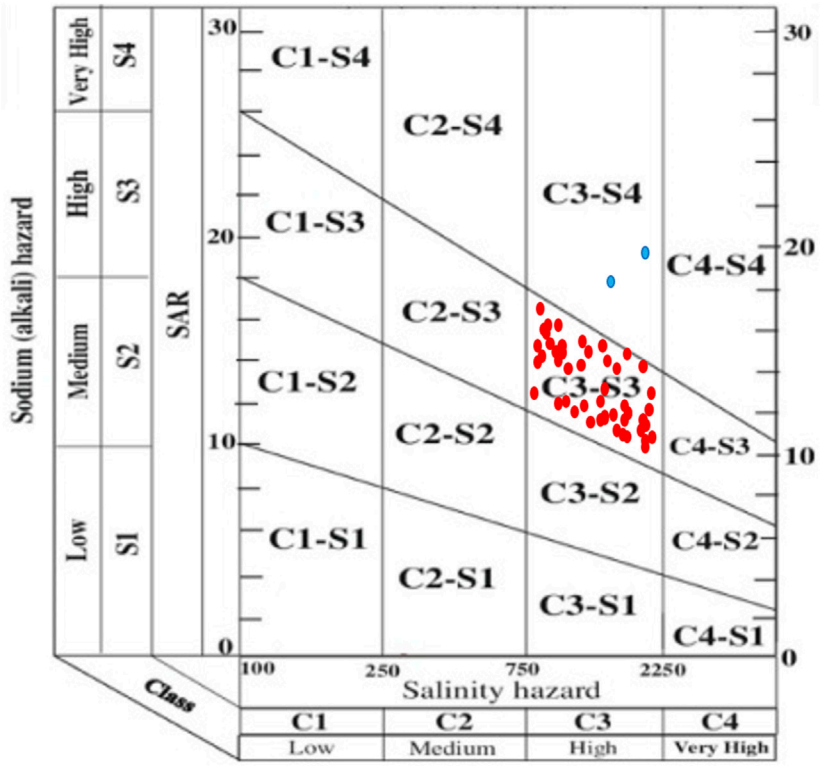

FIGURE 2
Irrigation water classification based on United States Salinity Laboratory diagram (USSL 1954).

hazard (C4) was recorded in two samples (4%) (Table 6). It can therefore be depicted from Figure 2 that 96% of the water samples occurred within the C3-S3 zone (high salinity and high sodium hazard zone), while 4% occurred within the C3-S4 zone (high salinity and very high sodium hazard zone). According to Subba Rao (2017); Subba Rao (2018), the use of this water for irrigation will be unsuitable, especially when being used in soils with poor drainage. Even if the soil has good drainage capacity, special management approaches will need to be put in place to reduce the salinity (Aravinthasamy et al., 2019).

3.3.2 Sodium percent and salinity

Percent Na is evaluated as the increase in monovalent sodium ion (Na^+) in irrigation water resulting from the ionic exchange occurring between divalent cations (Mg^{2+} and Ca^{2+}) (Mohammed et al., 2017). The resultant increase in sodium ions in irrigation water can result in the formation of bicarbonates (HCO_3^-) and other precipitates in the soil. Through combination reaction, sodium ions can react with precipitates ($CaCO_3$) to produce $NaCO_3$ in the soil phase (Kumar et al., 2009). The occurrence of $NaCO_3$ in the soil can lead to reduced permeability in soil, which can lead to stunted growth in plants (Ayers and Westcot, 1985; Todd and Mays, 2005). According to the classification scheme in Table 6, irrigation water quality based on sodium percent is grouped into five categories: excellent (Na% < 20), good (Na% 20–40) permissible (Na% 40–60), doubtful (Na% 60–80) and unsuitable (Na% > 80) as per Ayers and Westcot (1985). Accordingly, 100% of the water samples fall under the "doubtful" category. The Wilcox plot is used to show the relationship between the percent sodium and the electrical conductivity of water. According to the Wilcox plot (Figure 3), all the groundwater samples occur within the doubtful to unsuitable zone. The implication of this regarding the irrigation suitability assessment of Firozabad is that the increased sodium hazards from the exposure of the groundwater sources to contaminant influx will result in reduced crop yield in the area over time unless remedial measures are put in place.

3.3.3 Magnesium hazard

MH depicts the level of elevated dissolved Mg^{2+} in irrigation water that may cause a reduction in crop yield. Based on the Ayers and Westcot (1985) classification scheme (Table 6), 100% of the water samples are suitable for irrigation based on magnesium hazard.

3.3.4 Permeability index

The PI evaluates the irrigation water quality based on the percentage of dissolved cations and anions in water (Ca^{2+}, Mg^{2+}, Na^+) and anions (Cl^-, HCO_3^-) in water (Donean, 1964). These dissolved chemical species are known to influence the permeability of soil (Unigwe C. O. et al., 2022). According to the Doneen (1964) classification criteria, proposed three water quality categories can be obtained based on the PI: Class I (100%), class II (75%–100%), class III (25%–75%), and class IV (<25%), with each class depicting excellent, good, doubtable, and unsuitable water quality classes

TABLE 6 Classification criteria of irrigation water quality parameters (in meq/L).

Parameter	Range	Class category	Number of samples in category	% Of samples per category
MH	<50	Suitable	50	100
	>50	Unsuitable	-	-
SAR	0–10	Low	50	100
	10–18	Medium		
	18–26	High		
	>26	Very high		
Na%	20–40	Good		
	40–60	Permissible		
	60–80	Doubtful	50	100
	>80	Unsuitable		
RSC	<1.25	Good	50	100
	1.25–2.50	Doubtful		
	>2.50	Unsuitable		
KR	<1	Good		
	1–2	Doubtful		
	>2	Unsuitable	50	100
EC	<250	Low		
	250–750	Medium		
	750–2,250	High	48	
	>2,250	Very high	2	96
				4
PS	<5	Excellent to good		
	5–10	Good to injurious	39	78
	>10	Injurious to unsatisfactory	11	22
PI	>75	Suitable		
	25–75	Acceptable		
	<25	Unsuitable	50	100

respectively. Accordingly, in the present study, the PI varied from 2.97 to 4.05 with a mean value of 3.48 (Table 7). Based on the PI classification scheme (Table 6), 100% of the water samples are unsuitable for irrigation (class 1V).

3.3.5 Kelly's ratio

Kelly's ratio is a measure of monovalent Na^+ ions against divalent Ca^{2+} and Mg^{2+} ions concentration irrigation water (Kelly 1940). According to the index, if the KR is greater than 2, it indicates an excess concentration of Na^+; depicting unsuitable water for irrigation. On the other hand, KR less than two is indicative of low Na^+ concentration in irrigation water. In the present study, KR ranged between 2.57 and 3.14 with an average value of 2.87 (Table 7). Following KR classification criteria (Table 6), all the water samples are unsuitable for irrigation.

3.3.6 Residual sodium carbonate

The RSC is used to evaluate the alkalinity hazard in the soil as a result of poor irrigation water quality. The index determines the elevated amount of dissolved Ca^{2+} and Mg^{2+} ionic species in water and their effect on irrigation water quality (Raghunath, 1987; Singh et al., 2019). According to this index, when the sum of bicarbonates and carbonates in water occurs in a concentration below that of Calcium and Magnesium, there is a likelihood of the excess precipitation of Ca^{2+} and Mg^{2+} in water which may impede crop yield when used for irrigation. Based on the RSC classification scheme, RSC <1.25 indicates suitable water; RSC = 1.25–2.5 indicates doubtful water and RSC> 2.5 signifies unsuitable water for irrigation (Raghunath, 1987). RSC for the present study varied between −3.93 and −1.55 with an average value of −2.46 (Table 7). Based on RSC classification criteria, all

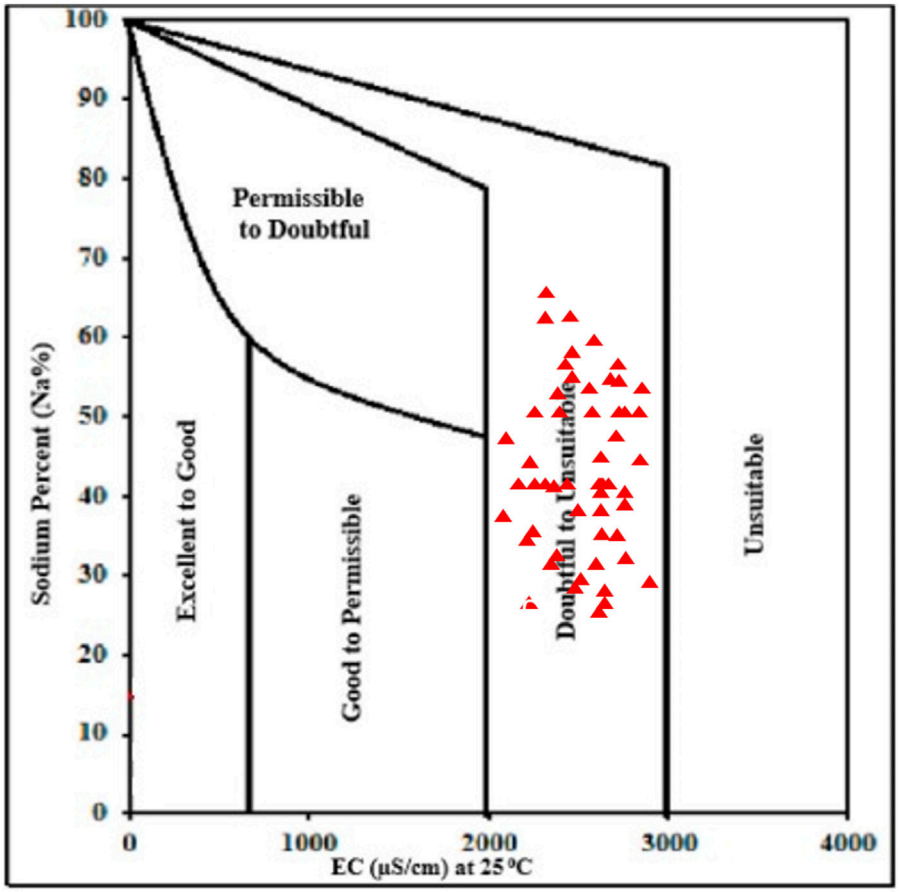

FIGURE 3
Irrigation water classification based on Wilcox diagram.

the water samples occur within the "good" category for irrigation water quality. The recorded negative RSC values observed in the present study are indicative of incomplete precipitation of divalent Mg^{2+} and Ca^{2+} in water. The incomplete precipitation of these ions in water occurred as a result of opposing the concentration of the ions which posed little or no threat to Na^{+} concentration in the water (Unigwe C. O. et al., 2022).

3.3.7 Chloro-alkaline index

The ionic exchanges occurring in water can be determined using the Chloro-alkaline indices (CAI-1 and CAI-2). The occurrence of chemical elements in water can be influenced by the ionic exchanges occurring between dissolved ions in water; and this may influence their interaction in the soil phase (Egbueri et al., 2021; Omeka et al., 2022b). Ion exchange occur in two phases-forward ion exchange (negative exchange) and reversed ion exchange (positive exchange). According to Schoeller (1967), the forward ion exchange involves the replacement of the monovalent ions (K^{+}, Na^{+}) with divalent ions (Ca^{2+}, Mg^{2+}). The reverse ion exchange process on the other hand is the displacement of alkaline-earth metals (Mg^{2+}, Ca^{2+}) by alkali metals (K^{+} and Na^{+}) within the aquifer system. In the present study, the CAI-1 ranged from −0.61 to −0.55, with a mean value of −0.57, while CAI-2 ranged between −2.24 and −1.25 with an average value of −1.69 (Table 7). The results from the present study indicate that the reversed ion exchange appears to be the prevalent ion exchange process occurring within the groundwater aquifer system.

3.3.8 Potential salinity

The PS was developed by Doneen (1961) and explains the number of salts in irrigation water that are likely to accumulate in soil from irrigation. Over time, these salts tend to accumulate in concentration that may enhance their concentration in the soil phase (Singh et al., 2019). The index is represented as the concentration of Cl^{-} plus half of SO_4^{2-}. According to the PS index, PS < 5 is indicative of excellent to good water for irrigation; PS 5–10 indicates good to injurious irrigation water quality; PS > depicts injurious to unsatisfactory (Doneen 1961). Accordingly, the calculated PS for the present study varied between 6.13 and 12.87 averaging at 8.98 (Table 7). Based on the PS classification chart, 39 of the groundwater samples (78%) occur within the "Good to injurious" category while 11 of the analyzed groundwater samples (22%) are within the "Injurious to unsatisfactory" category (Table 6).

3.4 Health risk assessment

A comprehensive health risk assessment was carried out for all the analyzed groundwater samples used for drinking purposes.

TABLE 7 Overall results of all irrigation water quality parameters (measured in meq/L).

Sample ID	SAR	MH	%Na	PI	PS	KR	RSC	CAI-1	CAI-2
S1	5.257	29.523	72.836	3.131	7.047	2.636	−1.945	−0.563	−1.514
S2	5.458	29.514	72.785	3.235	7.723	2.621	−2.221	−0.568	−1.452
S3	5.771	29.503	72.629	3.396	8.705	2.601	−2.671	−0.569	−1.519
S4	5.337	29.518	72.961	3.171	7.481	2.629	−2.054	−0.577	−1.347
S5	5.174	29.526	72.995	3.085	6.922	2.643	−1.834	−0.571	−1.357
S6	5.026	29.534	73.176	3.013	6.577	2.656	−1.642	−0.577	−1.267
S7	5.664	29.505	72.530	3.341	8.174	2.607	−2.515	−0.557	−1.690
S8	5.354	29.518	72.811	3.181	7.377	2.628	−2.079	−0.566	−1.507
S9	6.208	29.487	72.403	3.625	9.886	2.579	−3.342	−0.565	−1.934
S10	5.537	29.510	72.689	3.277	7.900	2.615	−2.332	−0.564	−1.5074
S11	6.086	29.492	72.497	3.560	9.517	2.585	−3.148	−0.569	−1.803
S12	6.121	29.491	72.444	3.579	9.611	2.583	−3.204	−0.566	−1.821
S13	6.557	29.479	72.257	3.804	11.147	2.565	−3.911	−0.563	−1.892
S14	5.696	29.505	72.950	3.358	8.847	2.605	−2.563	−0.591	−1.278
S15	5.257	29.523	73.024	3.131	7.060	2.636	−1.946	−0.578	−1.532
S16	5.092	29.532	73.413	3.046	6.553	2.650	−1.726	−0.601	−1.602
S17	4.943	29.539	73.14	2.9709	6.125	2.664	−1.535	−0.570	−1.501
S18	5.588	29.508	72.740	3.302	8.024	2.612	−2.407	−0.570	−1.586
S19	5.276	29.522	73.102	3.141	7.414	2.634	−1.971	−0.585	−1.257
S20	6.141	29.488	72.742	3.589	10.340	2.582	−3.234	−0.590	−1.346
S21	5.459	29.514	73.123	3.236	7.677	2.621	−2.229	−0.596	−1.628
S22	6.016	29.494	72.496	3.524	9.377	2.588	−3.048	−0.566	−1.7033
S23	5.617	29.508	72.556	3.317	8.097	2.610	−2.447	−0.557	−1.607
S24	6.186	29.488	72.649	3.613	9.916	2.580	−3.306	−0.584	−1.845
S25	5.266	29.522	73.432	3.135	7.093	2.635	−1.957	−0.612	−1.622
S26	7.268	29.493	76.074	3.910	11.429	3.109	−3.088	−0.574	−1.961
S27	6.345	29.518	76.381	3.474	8.899	3.122	−2.066	−0.593	−1.563
S28	6.311	29.519	76.392	3.457	8.717	3.122	−2.0289	−0.593	−1.611
S29	6.573	29.511	76.3882	3.580	9.627	3.118	−2.303	−0.595	−1.517
S30	6.979	29.499	76.331	3.773	10.365	3.112	−2.754	−0.594	−2.198
S31	6.416	29.516	76.361	3.506	8.7489	3.121	−2.137	−0.592	−2.012
S32	6.202	29.523	76.498	3.406	8.242	3.124	−1.917	−0.602	−1.890
S33	6.011	29.535	76.375	3.316	7.694	3.128	−1.725	−0.588	−1.803
S34	6.845	29.503	76.006	3.707	10.044	3.114	−2.597	−0.565	−1.923
S35	6.439	29.515	76.012	3.517	8.876	3.120	−2.162	−0.562	−1.795
S36	7.545	29.486	76.176	4.043	12.862	3.106	−3.425	−0.585	−1.551
S37	6.675	29.507	76.538	3.629	9.551	3.117	−2.415	−0.610	−1.999
S38	7.386	29.489	76.463	3.967	11.694	3.107	−3.231	−0.609	−2.243

(Continued on following page)

TABLE 7 (*Continued*) Overall results of all irrigation water quality parameters (measured in meq/L).

Sample ID	SAR	MH	%Na	PI	PS	KR	RSC	CAI-1	CAI-2
S39	7.436	29.488	76.308	3.989	12.442	3.107	−3.286	−0.595	−1.607
S40	6.472	29.514	76.311	3.532	9.473	3.126	−2.196	−0.588	−1.411
Sample ID	SAR	MH	%Na	PI	PS	KR	RSC	CAI-1	CAI-2
S41	6.653	34.147	74.67	3.699	10.1667	2.908	−2.991	−0.559	−1.908
S42	6.311	29.519	76.10	3.457	8.501	3.122	−2.029	−0.569	−1.872
S43	6.094	29.527	76.159	3.356	7.911	3.126	−1.809	−0.571	−1.840
S44	5.898	29.536	76.08	3.265	7.457	3.131	−1.617	−0.562	−1.678
S45	6.743	29.505	76.14	3.661	9.807	3.116	−2.489	−0.5767	−1.872
S46	6.335	29.518	76.35	3.469	8.753	3.122	−2.054	−0.590	−1.690
S47	7.457	29.488	75.88	4.001	11.885	3.107	−3.317	−0.559	−2.171
S48	6.575	29.510	76.12	3.582	9.304	3.118	−2.307	−0.572	−1.820
S49	7.296	29.491	75.93	3.924	11.488	3.108	−3.123	−0.562	−1.92
S50	6.780	29.504	75.95	3.678	10.026	3.115	−2.530	−0.560	−1.729
Min	4.942	29.479	72.257	2.9709	6.125	2.565	−3.911	−0.612	−2.243
Max	7.545	34.147	76.53	4.043	12.862	3.131	−1.535	−0.557	−1.257
Mean	6.142	29.606	74.48	3.473	8.971	2.862	−2.457	−0.578	−1.694

Health risk assessment was carried out for nitrate and fluoride. These elements were selected based on their elevated concentration among the analyzed groundwater samples, their release into the environment through intensive agricultural activities from the use of agrochemicals, their high anthropogenic variance (they occur from both point and non-point sources), and their high human health toxicity hazard. According to The National Research Council (NRC, 2001), long-term ingestion of fluoride in drinking water, at a concentration greater than 1.5 mg L^{-1} is known to be responsible for dental fluorosis. High nitrate ingestion in drinking water has been associated with life-threatening illnesses like methemoglobinemia (blue baby syndrome) and stomach cancer (Dehghani et al., 2019; Okamkpa et al., 2022).

The health risk assessment was carried out bearing in mind the population likely to be vulnerable to toxic element ingestion and dermal contact. To this end, three population sizes (male, female, and children) were considered in the risk assessment. Accordingly, two exposure pathways-ingestion (oral) and dermal contact were considered. This was done following the United States Environmental Protection Agency risk assessment criteria (US-EPA, 1989; 2017). Results of the hazard index for the three population sizes and exposure pathways are presented in Tables 8–10. To have a visual appraisal of the risk levels of these elements in the groundwater within the Firozabad city, a spatial distribution risk map was generated for Nitrate and fluoride for the three population sizes (Figures 4–7). Having a visual appraisal of the risk and hazard exposure levels in the area will aid decision-makers and water managers alike in futuristic water quality monitoring and assessment.

3.4.1 Nitrate health risk assessment

Results of the health risk assessment for the three population sizes are shown in Tables 8–10. Additionally, spatial maps were also generated based on the results of the Hazard index ($HI_{(Total)}$) and presented in Figures 4–6. For the children population, the $HI_{(Oral)}$ ranged from 0.20 to 0.93 with a mean value of 0.51; the $HI_{(dermal)}$ all occurred at a negligible value (±0.00 E+00). For the female population, the $HI_{(oral)}$ ranged from 0.05 to 0.25 with a mean of 0.14; the $HI_{(dermal)}$ were all negligible (±0.00 E+00). However, for the male population, the $HI_{(oral)}$ ranged from 0.04 to 0.21 averaging at 0.11. Similarly, the HI (dermal) were all negligible values (±0.00 E+00). The results of the hazard index for all the population sizes have shown that the health hazards from dermal contact are at a very negligible level. The implication of this is that nitrate health risk from the consumption of groundwater in this study area is more associated with oral intake (ingestion) than dermal contact. As such, they are low nitrate risks from the use of water for bathing than drinking across all population sizes in the study area, although all the water samples appear to be within the safe water category based on nitrate concentration (US-EPA, 2017). According to the US-EPA (1989), HI < 1 signifies safe water while HI > signifies an adverse health risk to human health.

The $HI_{(Total)}$ values for the children population ranged from 0.20 to 0.93 with a mean of 0.51; for the Female population, it ranged from 0.05 to 0.25 with a recorded mean of 0.14. However, for the male, it varied between 0.048 and 0.216 with a mean of 0.19. Based on the overall HI results for nitrate, the risk level for three population sizes decreased in the order of children > female > male. This implies that over time the children population will be

TABLE 8 Results of Chloride, fluoride and Nitrate health risk assessment for children population.

	Cl^- (children)			F^- (children)			NO_3^-(Children)		
Sample ID	HI (oral)	HI (dermal)	HI (total)	HI (oral)	HI (dermal)	HI (total)	HI (oral)	HI (dermal)	HI (total)
S1	80.687	0.001	80.688	0.458	0.00 E+00	0.458	0.313	0.00 E+00	0.313
S2	87.433	0.001	87.434	0.596	0.00 E+00	0.596	0.729	0.00 E+00	0.729
S3	98.460	0.001	98.461	0.725	0.00 E+00	0.725	0.625	0.00 E+00	0.625
S4	83.353	0.001	83.354	0.679	0.00 E+00	0.679	0.521	0.00 E+00	0.521
S5	77.967	0.001	77.968	0.813	0.00 E+00	0.813	0.729	0.00 E+00	0.729
S6	73.273	0.001	73.274	0.663	0.00 E+00	0.663	0.729	0.00 E+00	0.729
S7	94.633	0.001	94.635	0.400	0.00 E+00	0.400	0.521	0.00 E+00	0.521
S8	83.967	0.001	83.968	0.575	0.00 E+00	0.575	0.208	0.00 E+00	0.208
S9	114.900	0.002	114.902	0.783	0.00 E+00	0.783	0.208	0.00 E+00	0.208
S10	90.167	0.001	90.168	0.888	0.00 E+00	0.888	0.938	0.00 E+00	0.938
S11	110.153	0.001	110.155	0.929	0.00 E+00	0.929	0.833	0.00 E+00	0.833
S12	111.513	0.001	111.515	0.896	0.00 E+00	0.896	0.938	0.00 E+00	0.938
S13	128.833	0.002	128.835	0.792	0.00 E+00	0.792	0.625	0.00 E+00	0.625
S14	95.820	0.001	95.821	0.708	0.00 E+00	0.708	0.208	0.00 E+00	0.208
S15	80.713	0.001	80.714	0.958	0.00 E+00	0.958	0.417	0.00 E+00	0.417
S16	75.327	0.001	75.328	0.658	0.00 E+00	0.658	0.313	0.00 E+00	0.313
S17	70.633	0.001	70.634	0.450	0.00 E+00	0.450	0.313	0.00 E+00	0.313
S18	91.993	0.001	91.995	0.721	0.00 E+00	0.721	0.833	0.00 E+00	0.833
S19	81.327	0.001	81.328	0.667	0.00 E+00	0.667	0.521	0.00 E+00	0.521
S20	112.260	0.001	112.261	0.792	0.00 E+00	0.792	0.208	0.00 E+00	0.208
S21	87.527	0.001	87.528	0.729	0.00 E+00	0.729	0.208	0.00 E+00	0.208
S22	107.513	0.001	107.515	0.904	0.00 E+00	0.904	0.521	0.00 E+00	0.521
S23	92.980	0.001	92.981	0.400	0.00 E+00	0.400	0.417	0.00 E+00	0.417
S24	114.020	0.001	114.021	0.713	0.00 E+00	0.713	0.313	0.00 E+00	0.313
S25	80.980	0.001	80.981	0.883	0.00 E+00	0.883	0.313	0.00 E+00	0.313
S26	130.567	0.002	130.568	0.958	0.00 E+00	0.958	0.417	0.00 E+00	0.417
S27	99.267	0.001	99.268	0.888	0.00 E+00	0.888	0.625	0.00 E+00	0.625
S28	98.100	0.001	98.101	0.492	0.00 E+00	0.492	0.938	0.00 E+00	0.938
S29	106.533	0.001	106.535	0.371	0.00 E+00	0.371	0.938	0.00 E+00	0.938
S30	120.317	0.002	120.318	0.746	0.00 E+00	0.746	0.521	0.00 E+00	0.521

(Continued on following page)

10.3389/fenvs.2023.1116220

TABLE 8 (*Continued*) Results of Chloride, fluoride and Nitrate health risk assessment for children population.

	Cl^- (children)			F^- (children)			NO_3^-(Children)		
Sample ID	HI (oral)	HI (dermal)	HI (total)	HI (oral)	HI (dermal)	HI (total)	HI (oral)	HI (dermal)	HI (total)
S31	101.433	0.001	101.435	0.225	0.00 E+00	0.225	0.521	0.00 E+00	0.521
S32	94.700	0.001	94.701	0.383	0.00 E+00	0.383	0.313	0.00 E+00	0.313
S33	88.833	0.001	88.835	0.179	0.00 E+00	0.179	0.729	0.00 E+00	0.729
S34	115.533	0.002	115.535	0.683	0.00 E+00	0.683	0.521	0.00 E+00	0.521
S35	102.200	0.001	102.201	0.433	0.00 E+00	0.433	0.833	0.00 E+00	0.833
S36	140.867	0.002	140.869	0.542	0.00 E+00	0.542	0.625	0.00 E+00	0.625
S37	109.950	0.001	109.951	0.783	0.00 E+00	0.783	0.938	0.00 E+00	0.938
S38	134.933	0.002	134.935	0.908	0.00 E+00	0.908	0.625	0.00 E+00	0.625
S39	136.633	0.002	136.635	0.413	0.00 E+00	0.413	0.313	0.00 E+00	0.313
	Cl^- (children)			F^- (children)			NO_3^-(Children)		
Sample ID	HI (oral)	HI (dermal)	HI (total)	HI (oral)	HI (dermal)	HI (total)	HI (oral)	HI (dermal)	HI (total)
S40	103.233	0.001	103.235	0.592	0.00 E+00	0.592	0.208	0.00 E+00	0.208
S41	117.017	0.002	117.018	1.096	0.00 E+00	1.096	0.625	0.00 E+00	0.625
S42	98.133	0.001	98.135	0.217	0.00 E+00	0.217	0.313	0.00 E+00	0.313
S43	91.400	0.001	91.401	0.163	0.00 E+00	0.163	0.208	0.00 E+00	0.208
S44	85.533	0.001	85.534	0.621	0.00 E+00	0.621	0.208	0.00 E+00	0.208
S45	112.233	0.001	112.235	0.367	0.00 E+00	0.367	0.521	0.00 E+00	0.521
S46	98.900	0.001	98.901	0.738	0.00 E+00	0.738	0.417	0.00 E+00	0.417
S47	137.567	0.002	137.568	0.250	0.00 E+00	0.250	0.208	0.00 E+00	0.208
S48	106.650	0.001	106.651	0.300	0.00 E+00	0.300	0.729	0.00 E+00	0.729
S49	131.633	0.002	131.635	0.733	0.00 E+00	0.733	0.833	0.00 E+00	0.833
S50	113.467	0.001	113.468	0.917	0.00 E+00	0.917	0.208	0.00 E+00	0.208
MIN	70.633	0.001	70.634	0.163	0.00 E+00	0.163	0.208	0.00 E+00	0.208
MAX	140.867	0.002	140.869	1.096	0.00 E+00	1.096	0.938	0.00 E+00	0.938
MEAN	102.041	0.001	102.043	0.636	0.00 E+00	0.636	0.517	0.00 E+00	0.517

10.3389/fenvs.2023.1116220

TABLE 9 Results of Chloride, fluoride and Nitrate health risk assessment for Female population.

	Cl^-(Female)			F^- (female)			NO_3^-(Female)		
Sample ID	HI (oral)	HI (dermal)	HI (total)	HI (oral)	HI (dermal)	HI (total)	HI (oral)	HI (dermal)	HI (total)
S1	22.005	0.000	22.006	0.125	0.00 E+00	0.125	0.085	0.00 E+00	0.085
S2	23.845	0.000	23.846	0.163	0.00 E+00	0.163	0.199	0.00 E+00	0.199
S3	26.853	0.000	26.853	0.198	0.00 E+00	0.198	0.170	0.00 E+00	0.170
S4	22.733	0.000	22.733	0.185	0.00 E+00	0.185	0.142	0.00 E+00	0.142
S5	21.264	0.000	21.264	0.222	0.00 E+00	0.222	0.199	0.00 E+00	0.199
S6	19.984	0.000	19.984	0.181	0.00 E+00	0.181	0.199	0.00 E+00	0.199
S7	25.809	0.000	25.810	0.109	0.00 E+00	0.109	0.142	0.00 E+00	0.142
S8	22.900	0.000	22.900	0.157	0.00 E+00	0.157	0.057	0.00 E+00	0.057
S9	31.336	0.001	31.337	0.214	0.00 E+00	0.214	0.057	0.00 E+00	0.057
S10	24.591	0.000	24.591	0.242	0.00 E+00	0.242	0.256	0.00 E+00	0.256
S11	30.042	0.001	30.042	0.253	0.00 E+00	0.253	0.227	0.00 E+00	0.227
S12	30.413	0.001	30.413	0.244	0.00 E+00	0.244	0.256	0.00 E+00	0.256
S13	35.136	0.001	35.137	0.216	0.00 E+00	0.216	0.170	0.00 E+00	0.170
S14	26.133	0.000	26.133	0.193	0.00 E+00	0.193	0.057	0.00 E+00	0.057
S15	22.013	0.000	22.013	0.261	0.00 E+00	0.261	0.114	0.00 E+00	0.114
S16	20.544	0.000	20.544	0.180	0.00 E+00	0.180	0.085	0.00 E+00	0.085
S17	19.264	0.000	19.264	0.123	0.00 E+00	0.123	0.085	0.00 E+00	0.085
S18	25.089	0.000	25.090	0.197	0.00 E+00	0.197	0.227	0.00 E+00	0.227
S19	22.180	0.000	22.180	0.182	0.00 E+00	0.182	0.142	0.00 E+00	0.142
S20	30.616	0.001	30.617	0.216	0.00 E+00	0.216	0.057	0.00 E+00	0.057
S21	23.871	0.000	23.871	0.199	0.00 E+00	0.199	0.057	0.00 E+00	0.057
S22	29.322	0.001	29.322	0.247	0.00 E+00	0.247	0.142	0.00 E+00	0.142
S23	25.358	0.000	25.359	0.109	0.00 E+00	0.109	0.114	0.00 E+00	0.114
S24	31.096	0.001	31.097	0.194	0.00 E+00	0.194	0.085	0.00 E+00	0.085
S25	22.085	0.000	22.086	0.241	0.00 E+00	0.241	0.085	0.00 E+00	0.085
S26	35.609	0.001	35.610	0.261	0.00 E+00	0.261	0.114	0.00 E+00	0.114
S27	27.073	0.000	27.073	0.242	0.00 E+00	0.242	0.170	0.00 E+00	0.170
S28	26.755	0.000	26.755	0.134	0.00 E+00	0.134	0.256	0.00 E+00	0.256
S29	29.055	0.001	29.055	0.101	0.00 E+00	0.101	0.256	0.00 E+00	0.256
S30	32.814	0.001	32.814	0.203	0.00 E+00	0.203	0.142	0.00 E+00	0.142
S31	27.664	0.001	27.664	0.061	0.00 E+00	0.061	0.142	0.00 E+00	0.142
S32	25.827	0.000	25.828	0.105	0.00 E+00	0.105	0.085	0.00 E+00	0.085
S33	24.227	0.000	24.228	0.049	0.00 E+00	0.049	0.199	0.00 E+00	0.199
S34	31.509	0.001	31.510	0.186	0.00 E+00	0.186	0.142	0.00 E+00	0.142
S35	27.873	0.001	27.873	0.118	0.00 E+00	0.118	0.227	0.00 E+00	0.227
S36	38.418	0.001	38.419	0.148	0.00 E+00	0.148	0.170	0.00 E+00	0.170
S37	29.986	0.001	29.987	0.214	0.00 E+00	0.214	0.256	0.00 E+00	0.256

(Continued on following page)

TABLE 9 (*Continued*) Results of Chloride, fluoride and Nitrate health risk assessment for Female population.

	Cl^-(Female)			F^- (female)			NO_3^-(Female)		
Sample ID	HI (oral)	HI (dermal)	HI (total)	HI (oral)	HI (dermal)	HI (total)	HI (oral)	HI (dermal)	HI (total)
S38	36.800	0.001	36.801	0.248	0.00 E+00	0.248	0.170	0.00 E+00	0.170
S39	37.264	0.001	37.264	0.113	0.00 E+00	0.113	0.085	0.00 E+00	0.085
S40	28.155	0.001	28.155	0.161	0.00 E+00	0.161	0.057	0.00 E+00	0.057
S41	31.914	0.001	31.914	0.299	0.00 E+00	0.299	0.170	0.00 E+00	0.170
S42	26.764	0.000	26.764	0.059	0.00 E+00	0.059	0.085	0.00 E+00	0.085
S43	24.927	0.000	24.928	0.044	0.00 E+00	0.044	0.057	0.00 E+00	0.057
S44	23.327	0.000	23.328	0.169	0.00 E+00	0.169	0.057	0.00 E+00	0.057
S45	30.609	0.001	30.610	0.100	0.00 E+00	0.100	0.142	0.00 E+00	0.142
S46	26.973	0.000	26.973	0.201	0.00 E+00	0.201	0.114	0.00 E+00	0.114
S47	37.518	0.001	37.519	0.068	0.00 E+00	0.068	0.057	0.00 E+00	0.057
S48	29.086	0.001	29.087	0.082	0.00 E+00	0.082	0.199	0.00 E+00	0.199
S49	35.900	0.001	35.901	0.200	0.00 E+00	0.200	0.227	0.00 E+00	0.227
S50	30.945	0.001	30.946	0.250	0.00 E+00	0.250	0.057	0.00 E+00	0.057
MIN	19.264	0.000	19.264	0.044	0.00 E+00	0.044	0.057	0.00 E+00	0.057
MAX	38.418	0.001	38.419	0.299	0.00 E+00	0.299	0.256	0.00 E+00	0.256
MEAN	27.829	0.001	27.830	0.173	0.00 E+00	0.173	0.141	0.00 E+00	0.141

more susceptible to nitrate health risks (from drinking and bathing) than the adult population. This has been attributed to the lower body weight of children compared to adults (Rahman et al., 2021).

Spatial maps of nitrate health risks based on the HI (total) values for children, females, and males are shown in Figures 4B–6B. From the spatial maps, nitrate health risk appears to increase in the south-western parts of the study area, with some parts of the north-eastern parts showing increased risk levels. The increased risk levels towards the south-western parts can be attributed to the dominant flow trend within the study area. It must be noted that the groundwater flow map showed the groundwater to increase towards the south-western direction of the area. Hence, it is expected that contamination risks from nitrate pollution will also follow the same trend. The implication of this is that if remedial measures are not put in place to curb anthropogenic inputs of nitrate through the regulation of agricultural activities (such as the indiscriminate use of agrochemicals), water sources within the south-western parts of the area will continue to be at a deplorable state due to nitrate contamination, hence making water sources within this region unsuitable for both drinking and bathing.

3.4.2 Fluoride health risk assessment

The HI (oral) for the children population ranged from 0.16 to 1.09 with a mean value of 0.63; Fluoride health risk assessment: the HI (dental) range for the female population, were all negligible (±0.00 E+00). For the Female population, the $HI_{(oral)}$ varied from 0.04 to 0.29 with a mean of 0.17; the $HI_{(dermal)}$ were all negligible (±0.00 E+00). For the male population, however, the $HI_{(oral)}$ varied from 0.03 to 0.25 with a mean value of 0.14; the $HI_{(dermal)}$ were all negligible (±0.00 E+00). The results of fluoride health risks appear to be similar to those obtained for nitrate, with nitrate health risks from the consumption of groundwater appearing to be more associated with oral intake (ingestion) than dermal contact. A slight contrast was observed for the $HI_{(oral)}$ values for the children population. One sample (S41) showed HI values >1 (adverse human health risk). Higher risk values of fluoride were also observed for the children compared to the adult population. Implying that children around the Firozabad city will be more prone to dental fluorosis from the intake of water. From the spatial distribution maps for fluoride health risk for the children, female and male populations, fluoride risk appears to increase towards the north-western parts of the study area with considerable high-risk levels also found in patches around the southern and east-central parts of the study area (Figures 4A–6A). The variability of fluoride risks within the area can be highly attributed to the groundwater flow movement. This agrees with information obtained from the groundwater flow map. Hence, it can be agreed the use of the groundwater flow map in the visual assessment of groundwater is highly efficient.

TABLE 10 Results of Chloride, fluoride and Nitrate health risk assessment for Male population.

	Cl^- (male)			F^- (male)			NO_3^- (male)		
Sample ID	HI (oral)	HI (dermal)	HI (total)	HI (oral)	HI (dermal)	HI (total)	HI (oral)	HI (dermal)	HI (total)
S1	18.620	0.000	18.620	0.106	0.00 E+00	0.106	0.072	0.00 E+00	0.072
S2	20.177	0.000	20.177	0.138	0.00 E+00	0.138	0.168	0.00 E+00	0.168
S3	22.722	0.000	22.722	0.167	0.00 E+00	0.167	0.144	0.00 E+00	0.144
S4	19.235	0.000	19.236	0.157	0.00 E+00	0.157	0.120	0.00 E+00	0.120
S5	17.992	0.000	17.993	0.188	0.00 E+00	0.188	0.168	0.00 E+00	0.168
S6	16.909	0.000	16.910	0.153	0.00 E+00	0.153	0.168	0.00 E+00	0.168
S7	21.838	0.000	21.839	0.092	0.00 E+00	0.092	0.120	0.00 E+00	0.120
S8	19.377	0.000	19.377	0.133	0.00 E+00	0.133	0.048	0.00 E+00	0.048
S9	26.515	0.000	26.516	0.181	0.00 E+00	0.181	0.048	0.00 E+00	0.048
S10	20.808	0.000	20.808	0.205	0.00 E+00	0.205	0.216	0.00 E+00	0.216
S11	25.420	0.000	25.420	0.214	0.00 E+00	0.214	0.192	0.00 E+00	0.192
S12	25.734	0.000	25.734	0.207	0.00 E+00	0.207	0.216	0.00 E+00	0.216
S13	29.731	0.001	29.731	0.183	0.00 E+00	0.183	0.144	0.00 E+00	0.144
S14	22.112	0.000	22.113	0.163	0.00 E+00	0.163	0.048	0.00 E+00	0.048
S15	18.626	0.000	18.626	0.221	0.00 E+00	0.221	0.096	0.00 E+00	0.096
S16	17.383	0.000	17.383	0.152	0.00 E+00	0.152	0.072	0.00 E+00	0.072
S17	16.300	0.000	16.300	0.104	0.00 E+00	0.104	0.072	0.00 E+00	0.072
S18	21.229	0.000	21.230	0.166	0.00 E+00	0.166	0.192	0.00 E+00	0.192
S19	18.768	0.000	18.768	0.154	0.00 E+00	0.154	0.120	0.00 E+00	0.120
S20	25.906	0.000	25.907	0.183	0.00 E+00	0.183	0.048	0.00 E+00	0.048
S21	20.198	0.000	20.199	0.168	0.00 E+00	0.168	0.048	0.00 E+00	0.048
S22	24.811	0.000	24.811	0.209	0.00 E+00	0.209	0.120	0.00 E+00	0.120
S23	21.457	0.000	21.457	0.092	0.00 E+00	0.092	0.096	0.00 E+00	0.096
S24	26.312	0.000	26.313	0.164	0.00 E+00	0.164	0.072	0.00 E+00	0.072
S25	18.688	0.000	18.688	0.204	0.00 E+00	0.204	0.072	0.00 E+00	0.072
S26	30.131	0.001	30.131	0.221	0.00 E+00	0.221	0.096	0.00 E+00	0.096
S27	22.908	0.000	22.908	0.205	0.00 E+00	0.205	0.144	0.00 E+00	0.144
S28	22.638	0.000	22.639	0.113	0.00 E+00	0.113	0.216	0.00 E+00	0.216
S29	24.585	0.000	24.585	0.086	0.00 E+00	0.086	0.216	0.00 E+00	0.216
S30	27.765	0.001	27.766	0.172	0.00 E+00	0.172	0.120	0.00 E+00	0.120
S31	23.408	0.000	23.408	0.052	0.00 E+00	0.052	0.120	0.00 E+00	0.120
S32	21.854	0.000	21.854	0.088	0.00 E+00	0.088	0.072	0.00 E+00	0.072
S33	20.500	0.000	20.500	0.041	0.00 E+00	0.041	0.168	0.00 E+00	0.168
S34	26.662	0.000	26.662	0.158	0.00 E+00	0.158	0.120	0.00 E+00	0.120
S35	23.585	0.000	23.585	0.100	0.00 E+00	0.100	0.192	0.00 E+00	0.192
S36	32.508	0.001	32.508	0.125	0.00 E+00	0.125	0.144	0.00 E+00	0.144
S37	25.373	0.000	25.374	0.181	0.00 E+00	0.181	0.216	0.00 E+00	0.216

(Continued on following page)

TABLE 10 (*Continued*) Results of Chloride, fluoride and Nitrate health risk assessment for Male population.

	Cl^- (male)			F^- (male)			NO_3^- (male)		
Sample ID	HI (oral)	HI (dermal)	HI (total)	HI (oral)	HI (dermal)	HI (total)	HI (oral)	HI (dermal)	HI (total)
S38	31.138	0.001	31.139	0.210	0.00 E+00	0.210	0.144	0.00 E+00	0.144
S39	31.531	0.001	31.531	0.095	0.000	0.095	0.072	0.000	0.072
	Cl^- (male)			F^- (male)			NO_3^- (male)		
Sample ID	HI (oral)	HI (dermal)	HI (total)	HI (oral)	HI (dermal)	HI (total)	HI (oral)	HI (dermal)	HI (total)
S40	23.823	0.00 E+00	23.824	0.137	0.00 E+00	0.137	0.048	0.00 E+00	0.048
S41	27.004	0.00 E+00	27.004	0.253	0.00 E+00	0.253	0.144	0.00 E+00	0.144
S42	22.646	0.00 E+00	22.647	0.050	0.00 E+00	0.050	0.072	0.00 E+00	0.072
S43	21.092	0.00 E+00	21.093	0.038	0.00 E+00	0.038	0.048	0.00 E+00	0.048
S44	19.738	0.00 E+00	19.739	0.143	0.00 E+00	0.143	0.048	0.00 E+00	0.048
S45	25.900	0.00 E+00	25.900	0.085	0.00 E+00	0.085	0.120	0.00 E+00	0.120
S46	22.823	0.00 E+00	22.823	0.170	0.00 E+00	0.170	0.096	0.00 E+00	0.096
S47	31.746	1.00E-03	31.747	0.058	0.00 E+00	0.058	0.048	0.00 E+00	0.048
S48	24.612	0.00 E+00	24.612	0.069	0.00 E+00	0.069	0.168	0.00 E+00	0.168
S49	30.377	1.00E-03	30.377	0.169	0.00 E+00	0.169	0.192	0.00 E+00	0.192
S50	26.185	0.00 E+00	26.185	0.212	0.00 E+00	0.212	0.048	0.00 E+00	0.048
MIN	16.300	0.00 E+00	16.300	0.038	0.00 E+00	0.038	0.048	0.00 E+00	0.048
MAX	32.508	1.00E-03	32.508	0.253	0.00 E+00	0.253	0.216	0.00 E+00	0.216
MEAN	23.548	0.00 E+00	23.548	0.147	0.00 E+00	0.147	0.119	0.00 E+00	0.119

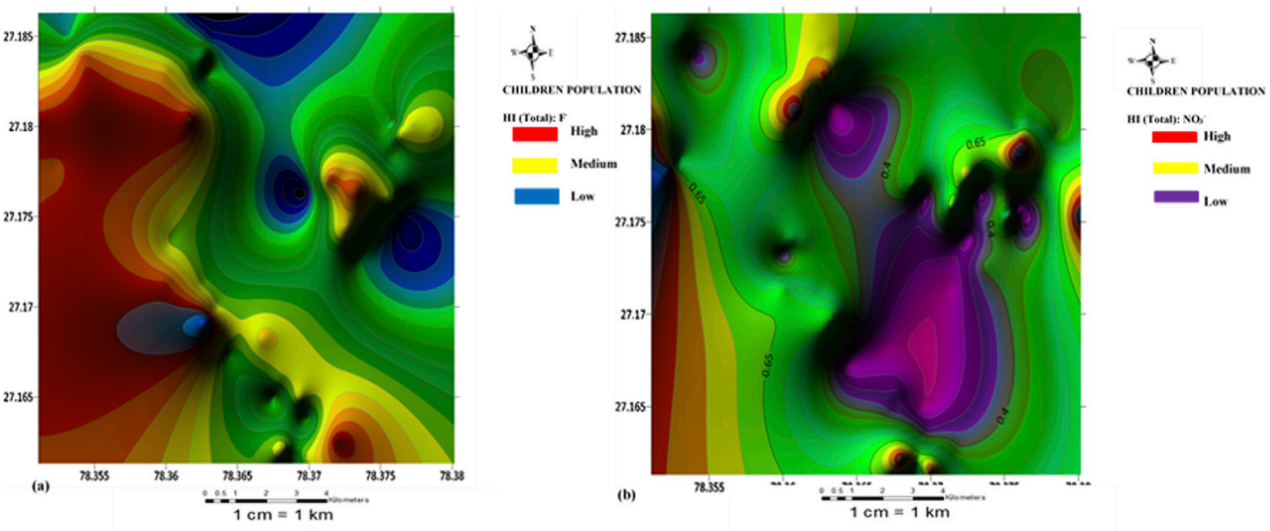

FIGURE 4
Spatial distribution health risk map of **(A)** fluoride and **(B)** nitrate risk for children population.

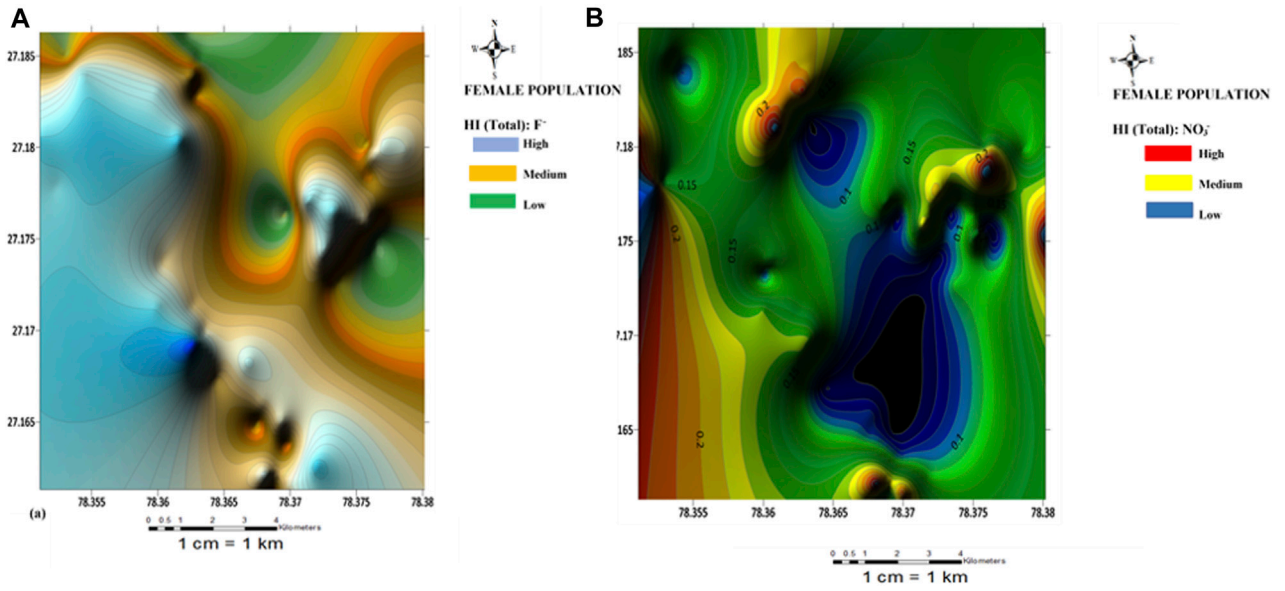

FIGURE 5
Spatial distribution health risk map of **(A)** fluoride and **(B)** nitrate risk for female population.

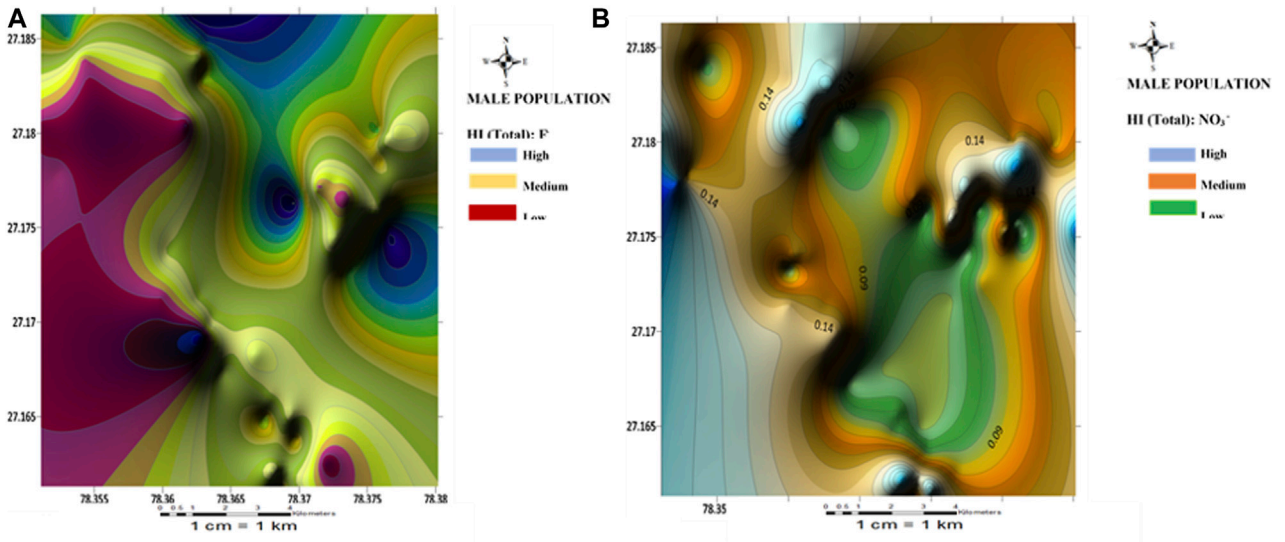

FIGURE 6
Spatial distribution health risk map of **(A)** fluoride and **(B)** nitrate risk for male population.

3.4.3 Chloride health risk assessment

Results of the chloride health risk assessment are presented in Tables 8–10. As observed, very high hazard index (HI_{oral}) values (HI > 1) are observed for all the water samples for all the population sizes. The high chloride content in the water can be attributed to inputs from untreated wastewater from the glass industry within the area. For the children population, the $HI_{(oral)}$ varied between 70.6 and 140.8 with a mean of 102.4; $HI_{(dermal)}$ ranged from 0.001 to 0.002 with a mean of 0.001. For the female population, the $HI_{(oral)}$ ranged from 19.264 to 38.418 averaging at 27.8; $HI_{(dermal)}$ ranged from 0.00 to 0.01 with a mean of 0.01.

3.5 Multivariate statistical analysis

3.5.1 Principal component analysis

Table 11 shows the unrotated principal component scores for both physicochemical and heavy metals of the analyzed

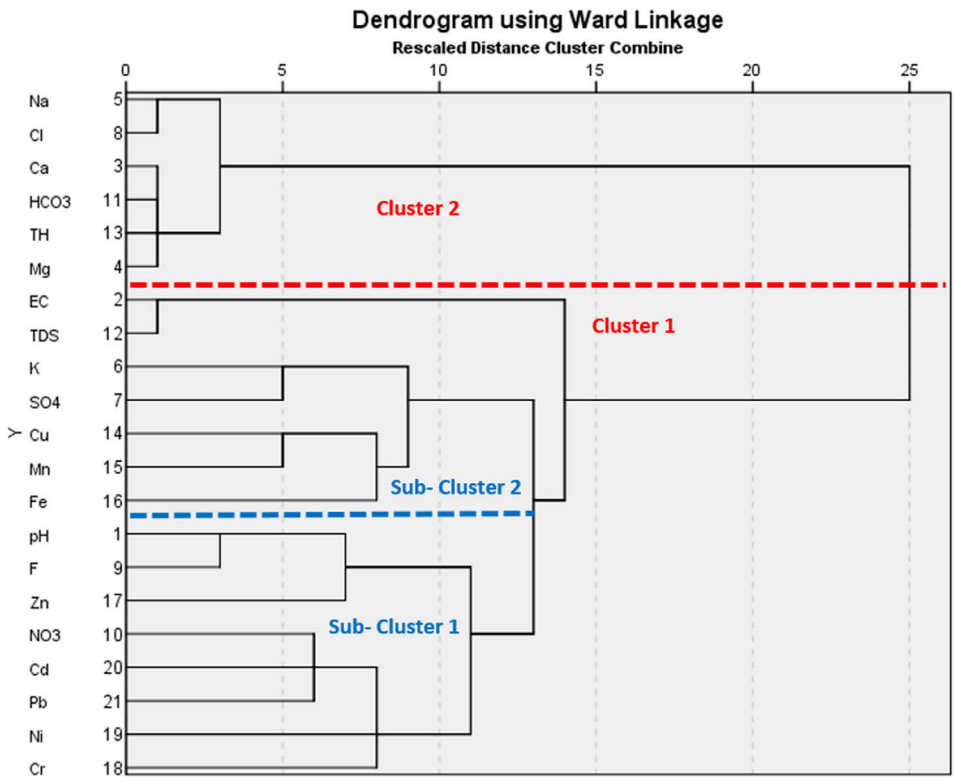

FIGURE 7
A dendrogram representing the cluster groupings of the groundwater samples based on WQI and PIG.

groundwater samples. The principal component analysis was carried out to evaluate the relationship existing between the analyzed groundwater parameters, as well as validate the results of the physicochemical and heavy metals (Wagh et al., 2020). Data standardization was done based on the Kaiser (1960) normalization criterion where only component classes with eigenvalues ≥1 is considered significant. Accordingly, component loadings of <0.50 were considered low, those between 0.50 and 0.75 were considered medium while loadings >0.75 signified high loadings (Cui et al., 2011; Omeka et al., 2022a). A total of eight principal components (PCs) were extracted accounting for 79.78% of the overall data variance. The high number of extracted components observed from the results is an indication of high variability in the geochemical composition of the groundwater (Krishna-Kumar et al., 2014; Okamkpa et al., 2022). PC1 (with 29.271% variance) showed high positive significant loadings for Ca^{2+}, Mg^{2+}, Na^{+}, Cl^{2-} , HCO_3^{-}, and TH. This component class indicates that the chemical weathering and dissolution of major cations (Ca^{2+}, Mg^{2+}, Na^{+}) and anions (HCO_3^{-}) within the groundwater aquifer system were major contributors to the groundwater hardness. The high significant loading observed for Cl^{-} in this component class signifies that the source of contamination in the groundwater was from both geogenic and anthropogenic influxes. The occurrence of Cl^{-} can be attributed to leaching from fertilizer application. PC2 which accounted for 11.17% of the total variance, showed positive significant loadings for EC and TDS and a significant negative loading (*-0.552*) for Cu. The implication of the loadings expressed in this component class is that the observed high conductivity of the water was influenced by the total dissolved species in the groundwater. The significant negative loading observed for Cu implies that the occurrence of Cu in the groundwater was from a different source from other elements. Cu may have been sourced from the leaching of solid waste materials and agricultural effluents.

PC3 explained 8.835% of the variance, having positive significant loadings for EC and TDS and a negative significant loading for pH and F^{-}. The significant negative loading observed for pH in this component class implies that the groundwater pH had little or no influence on the dissolution of chemical species in water and *vice versa*. Similarly, the negative significant loading (*-0.609*) observed for F^{-} indicates that its concentration in the groundwater occurred from anthropogenic influxes from the use of agrochemicals. The highly significant loading observed for NO_3^{-}in PC4 affirms that the groundwater is being polluted by the leaching of fertilizer components probably from the N-P-K species. Negative significant loading was observed for Mn. This implies that the occurrence of Manganese in the groundwater was from a different source other than nitrate, possibly from the weathering and dissolution of underlying rock materials. Mn tends to form strong organic metal complexes with soil organic matter. Moreover, Mn usually occurs in association with other elements in water such as Fe, oxygen, sulphur, and chlorine (ATSDR 2012).

PC5 showed high significant loading for Cd. The high significant positive loading observed for Cd in this component class validates the results from the physicochemical analysis. High Cd

TABLE 11 Unrotated principal component scores for both physicochemical and heavy metals of the analyzed groundwater samples.

Parameters	Communalities	Component classes							
		1	2	3	4	5	6	7	8
pH	0.824	0.242	0.402	***−0.557***	−0.239	0.084	0.392	0.275	−0.026
EC	0.97	0.155	**0.794**	**0.506**	−0.129	0.024	0.182	−0.046	0.086
Ca	0.968	**0.974**	0.045	−0.051	0.033	−0.042	−0.046	−0.088	0.051
Mg	0.966	**0.972**	0.051	−0.109	0.019	−0.059	−0.022	−0.048	0.029
Na	0.94	**0.929**	−0.105	0.161	0.074	−0.054	−0.128	0.126	−0.006
K	0.724	0.286	−0.343	0.354	0.27	0.380	0.341	0.056	−0.248
SO_4^{2-}	0.61	0.329	−0.369	0.265	0.127	0.449	0.276	−0.032	0.019
Cl	0.94	**0.929**	−0.105	0.161	0.074	−0.054	−0.128	0.126	−0.006
F^-	0.812	0.321	0.231	***−0.609***	0.026	0.361	0.333	0.182	−0.098
NO_3^-	0.687	0.051	0.152	−0.159	**0.724**	0.072	−0.262	0.182	0.069
HCO_3	0.968	**0.974**	0.045	−0.051	0.033	−0.042	−0.046	−0.088	0.051
TDS	0.97	0.155	**0.794**	**0.506**	−0.129	0.024	0.182	−0.046	0.086
TH	0.975	**0.978**	0.047	−0.069	0.029	−0.047	−0.039	−0.077	0.044
Cu	0.666	0.279	***−0.552***	−0.034	−0.205	−0.146	0.129	−0.125	0.432
Mn	0.859	0.135	−0.191	0.001	***−0.701***	0.142	−0.159	0.337	0.377
Fe	0.699	0.065	−0.049	0.333	−0.254	0.169	−0.395	**0.505**	−0.278
Zn	0.568	0.082	0.256	−0.47	−0.153	0.168	−0.273	−0.384	−0.04
Cr	0.667	−0.146	−0.168	−0.023	0.185	−0.326	0.492	0.442	0.199
Ni	0.471	0.049	0.253	−0.17	0.142	−0.277	−0.271	0.436	−0.124
Cd	0.839	−0.232	0.099	−0.039	0.124	**0.748**	−0.248	0.101	0.357
Pb	0.632	−0.202	0.228	0.054	0.416	−0.087	−0.077	0.055	**0.589**
Total		6.147	2.346	1.855	1.596	1.353	1.286	1.136	1.036
% of Variance		29.271	11.171	8.835	7.598	6.442	6.124	5.41	4.935
Cumulative %		29.271	40.442	49.276	56.874	63.316	69.44	74.85	79.785

Significant loadings at: ±0.5 = poor loadings; > ± 0.5 = high loadings.
The bold-italic values represent negative significant component loadings at: ≥0.5.

concentration in groundwater is usually associated with the weathering and dissolution of sulfide minerals such as chalcopyrite and pyrites in subsurface aquifers enriched in Pb and Zn (Obasi and Akudinobi, 2020; Omeka and Igwe, 2021). These rock types are absent in the geology of the present study. Hence, its concentration may only have come from anthropogenic inputs from poor waste management and agricultural activities. PC7 and PC8 showed significant loadings for Fe and Pb respectively. Fe and Pb are chalcophile elements (they have the affinity to form complexes with sulphide mineral species). However, the present study area is devoid of sulphide mineral species within the subsurface. Hence, the occurrence of these elements could only be traced to anthropogenic influences from the leaching of agrochemicals into the groundwater aquifer system.

So far, results from PCA have shown that the groundwater quality of the Firozabad city is jointly influenced by geogenic (weathering and dissolution of rock mineral species) and anthropogenic influxes (leaching and infiltration of land-derived effluents from the use of agrochemicals).

3.5.2 Q-mode hierarchical cluster analysis

The Q-mode HCA was used in this study to have a comprehensive comparative assessment of the groundwater quality within the Firozabad city for drinking purposes (Figure 7). Sources of water pollution is known to be highly ubiquitous as a result, certain water sources may tend to be more vulnerable to pollution than others. Hence, it important to identify the groundwater sources with the highest exposure to contamination for proper remediation (Gaikwad et al., 2020; Aghamelu et al., 2022). The two numerical water quality indices (PIG and WQI) were validated using the HCA. The model standardization was done using the zero-score standardization

criteria to minimize any bias that may arise from variation in outputs between the two numerical models (Gaikwad et al., 2020). To achieve this, a dendrogram was generated, with two major clusters and two sub-clusters produced as output (Figure 7). The first major cluster (Cluster 1) comprised fifteen groundwater samples (S1, S2, S6, S7, S9, S10, S12, S14, S15, S16, S17, S18, S19, S20, S21), accounting for fifteen water quality parameters (Cr, Ni, Pb, Cd, NO_3, Zn, F, pH, Fe, Mn, Cu, SO_4, TDS, and EC). The implication of this is that these groundwater samples are majorly exposed to the influx of the listed contaminant parameters. An observation of Table 6 shows that these listed water samples were among those with very high contamination levels from the results of PIG and WQI. The second cluster group accounted for six sample points (S3, S4, S5, S8, S11, S13), enlisted with Mg, TH, HCO_3, Cl, Ca, and Na. These water samples had lower values compared to those obtained for Cluster 1. Although from the results of physicochemical analysis, Cl showed very high values, however, their overall input in groundwater quality seems to fall under the second cluster group.

Two sub-clusters were also generated from the Q-mode HCA. Among the sub-clusters, sub-cluster one accounted for eight water samples (S1, S9, S10, S17, S18, S19, S20, S21) enlisted with pH, Fe, Zn, NO_3, Cd, Pb, Ni, and Cr. Sub-cluster two accounted for six water samples (S2, S6, S7, S12, S14, S15, S16) consisting of six water quality parameters (EC, TDS, K, SO_4, Mn, Fe). Generally, the sub-clusters were more enlisted with heavy metals compared to the major cluster groups. This correlates well with the results of the physic-chemical analysis; the heavy metals showed very low concentration among the groundwater samples compared to other chemical parameters. Hence, the use of HCA in this analysis has been integral in validating the results of WQI, PIG, and physic-chemical analysis.

The Q-mode HCA has been successful in applying water quality assessment in other parts of the world. In Nigeria for instance, Unigwe C. O. et al. (2022) have used this model for the assessment of the pollution sources, and drinking water quality as well as the validation of two drinking water quality indices-water quality index (WQI) and overall index of pollution (OIP). Results from their study revealed that the majority of the water samples which showed high WQI and OIP values were grouped in the same cluster group, thereby validating the model in water quality assessment. In a similar study conducted in two metropolises in southeastern Nigeria, Omeka and Egbueri (2022) used the Q-mode HCA for the drinking water quality assessment of the Nnewi and Awka metropolises in southeastern Nigeria. In their study, the Q-mode HCA was used to validate two drinking water quality indices-WQI and the pollution index of groundwater (PIG). Their study showed that the results from HCA clustering were in perfect commensuration with those obtained from physicochemical analysis and health risk models. The study went further to show that based on the pollution level and agreement between the two models from the different water samples, the Awka area appear to be more prone to contaminant inputs compared to the Nnewi area. This variation was attributed to the lower depth of water table of the Awka area compared to Nnewi. The application of the Q-mode HCA in this study has shown that there is a relationship between the dissolved chemical species from both geogenic and anthropogenic influxes (mostly from poor industrial waste management and agriculture). These same species had a greater influence on the general water quality, as evidenced by their parity in the cluster groupings. Hence, the use of this model in this study is valid.

4 Conclusion and recommendations

This study carried out an integrated assessment of irrigation water quality, drinking water quality, and health risk assessment of groundwater resources from the industrial area located in the Firozabad city, Uttar Pradesh, India. The study integrated two multiple numerical water quality (PIG and WQI) and health risk assessment (HI and HQ) indices to assess the suitability of the groundwater for drinking purposes, as well as the associated health risks from their consumption by several age groups. Several irrigational suitability indices were also integrated to ascertain the suitability of the water for irrigation purposes. Finding from the physicochemical analysis revealed that some chemical and chemical elements (e.g., EC, TH, Na, Cl^-, and F^-) occurred in concentrations above the World Health Organization and Bureau of Indian Standards recommended standards for drinking water quality; attributed to the high influx from agricultural and industrial wastewater. PIG and WQI classified 100% of the groundwater as highly polluted and unsuitable for drinking, while the multivariate statistical models (Q-mode HCA and PCA) showed that the groundwater quality is jointly influenced by geogenic (weathering and dissolution of rock mineral species) and anthropogenic influxes (leaching and infiltration of land-derived effluents from the use of agrochemicals).

The majority of the irrigational water quality indices (sodium adsorption ratio, Kelly's Ratio, permeability index, percent sodium) showed that the long-term use of the groundwater for irrigation in the area will result in reduced crop yield unless remedial measures are put in place. These results were strongly supported by the Wilcox and USSL plots; as the majority of the water samples plotted within the high salinity, high sodium hazard, and unsuitable zone for irrigation use. The non-carcinogenic health risk associated with chloride, nitrate, and fluoride ingestion and dermal contact was evaluated for three population sizes (children, females, and males). Results showed that the children population is more predisposed to Nitrate, Chloride, and fluoride health risks from oral intake and dermal contact. Geospatial maps revealed that risk levels from ingestion appear to increase in the western and northeastern parts of the study area.

From the findings of this study, it is highly recommended that special attention be given to the children population to avoid future health problems associated with contaminant ingestion. This can be done through adequate water treatment strategies and remedial measures such as pump-and-treat, and the construction of barrier walls around the drinking boreholes to avoid the further spread of contaminants. Additionally, special environmental management measures such as the use of biodegradable fertilizers, pre-treatment of industrial effluents before disposal, and reduction of soil salinity (through leaching with low salt-content water) will need to be put in place to improve soil quality and crop yield.

Data availability statement

The raw data supporting the conclusions of this article will be made available by the authors, without undue reservation.

Author contributions

AS contributed to conceptualization, manuscript-writing, review and editing, sampling, laboratory analysis, data analysis, TN contributed to resource funding, supervision, manuscript-review and editing; MO contributed to Manuscript design, Manuscript writing, map digitization, and data analysis; CU, IA, and SU contributed to the computation of numerical indices, manuscript-review and editing; AL contributed to resource funding, supervision, manuscript-review and editing, MR and BB contributed to manuscript review and editing, computation of numerical indices, PA contributed to mapping, manuscript-review and editing, AS, MA, Contributed to manuscript-writing, review and editing.

Conflict of interest

The authors declare that the research was conducted in the absence of any commercial or financial relationships that could be construed as a potential conflict of interest.

Publisher's note

Supplementary material

The Supplementary Material for this article can be found online at: https://www.frontiersin.org/articles/10.3389/fenvs.2023.1116220/full#supplementary-material

References

Abrahao, R., Causape, J., Garcıa-Garizabal, I., and Merchan, D. (2011). Implementing irrigation: Water balances and irrigation quality in the Lerma basin (Spain). *Agric. Water Manag.* 102, 97–104. doi:10.1016/j.agwat.2011.10.010

Adamu, C. I., Nganje, T. N., and Edet, A. (2015). Heavy metal contamination and health risk assessment associated with abandoned barite mines in Cross River State, southeastern Nigeria. *Environ. Nanotechnol. Monit. Manag.* 3, 10–21. doi:10.1016/j.enmm.2014.11.001

Agency for toxic substances & Disease Registry (ASTDR) (2018). *Toxicological Profile for hazardous substances*. US Department of Health and Human Service.

Aghamelu, O. P., Omeka, M. E., and Unigwe, C. O. (2022). Modeling the vulnerability of groundwater to pollution in a fractured shale aquifer in SE Nigeria using information entropy theory, geospatial, and statistical modeling approaches. *Model. Earth Syst. Environ.* 2022, 1–22. doi:10.1007/s40808-022-01640-y

Ali, S., Kumari, M., Gupta, S. K., Sinha, A., and Mishra, B. K. (2017). Investigation and mapping of fluoride-endemic areas and associated health risk—a case study of Agra, Uttar Pradesh, India. *Hum. Ecol. Risk Assess. Int. J.* 23 (3), 590–604. doi:10.1080/10807039.2016.1255139

Amiri, V., and Berndtsson, R. (2020). Fluoride occurrence and human health risk from groundwater use at the west coast of Urmia Lake, Iran. *Arab. J. Geosci.* 13, 921. doi:10.1007/s12517-020-05905-7

Amiri, V., Bhattacharya, P., and Nakhaei, M. (2021). The hydrogeochemical evaluation of groundwater resources and their suitability for agricultural and industrial uses in an arid area of Iran. *Groundw. Sustain. Dev.* 12, 100527. doi:10.1016/j.gsd.2020.100527

Amiri, V., Sohrabi, N., Li, P., and Amiri, F. (2022). Groundwater quality for drinking and non-carcinogenic risk of nitrate in urban and rural areas of Fereidan, Iran. *Expo. Health*. doi:10.1007/s12403-022-00525-w

Amouei, A., Mahvi, A., Mohammadi, A., Asgharnia, H., Fallah, S., and Khafajeh, A. (2012). Fluoride concentration in potable groundwater in rural areas of Khaf city, Razavi Khorasan province, Northeastern Iran. *Int. J. Occup. Environ. Med.* 3, 201–203.

Aravinthasamy, P., Karunanidhi, D., Subramani, T., Anand, B., Roy, P. D., and Srinivasamoorthy, K. (2019). Fluoride contamination in groundwater of the Shanmuganadhi River Basin (south India) and its association with other chemical constituents using geographical information system and multivariate statistics. *Geochemistry* 12, 55–87.

Ayers, R., and Westcot, D. (1985). *Water quality for agriculture*. Rome: FAO Irrigation and drainage paper 29 Rev. 1. Food and Agricultural Organization, 74.

Ayoob, S., Gupta, A. K., and Bhat, V. T. (2008). A conceptual Overview on sustainable technologies for the Defluoridation of drinking water. *Crit Rev Environ. Sci. Technol.* 38 (6), 401–470. doi:10.1080/10643380701413310

Barzegar, R., Moghaddam, A. A., Adamowski, J., and Nazemi, A. M. (2018). Assessing the potential origins and human health risks of trace elements in groundwater: A case study in the Khoy plain Iran. *Environ. Geochem. Health* 87, 981–1002. doi:10.1007/s10653-018-0194-9

BIS (2012). *IS, specification for drinking water ISI: 10500*. New Delhi: Bureau of Indian Standards.

Brady, N. C. (2002). *The nature and properties of soil*. 10th edn. New Delhi: Prentice-Hall.

Corwin, D. L., and Yemoto, K. (2017). Salinity: Electrical conductivity and total dissolved solids. *Methods soil analysis*. doi:10.2136/sssabookser5.3.c14

Cui, Z., Qiao, B. Z., and Wu, N. (2011). Contamination and distribution of heavy metals in urban and suburban soils in Zhangzhou City, Fujian, China. *Environ. Earth Sci.* 64 (6), 1607–1615. doi:10.1007/s12665-011-1179-5

Davis, S. N., and de Wiest, R. J. M. (1966). *Hydrogeology*. New York: Wiley.

Daw, R. K. (2004). "Experiences with domestic fluoridation in India," in Proceedings of the 30th WEDC International Conference on People-Centred Approaches to Water and Environmental Sanitation, Vientiane, Lao PDR, 25, 467–473.

Dehghani, M. H., Zarei, A., Yousef, M., Asghari, F. B., and Haghighat, G. A. (2019). Fluoride contamination in groundwater resources in the southern Iran and its related human health risks. *Desalin Water Treat.* 153, 95–104. doi:10.5004/dwt.2019.23993

Devi, R., Behera, B., Raza, M. B., Mangal, V., Altaf, M. A., Kumar, R., et al. (2021). An insight into microbes mediated heavy metal detoxification in plants: A review. *J. Soil Sci. Plant Nutr.* 22, 914–936. doi:10.1007/s42729-021-00702-x

Doneen, L. D. (1964). *Notes on water quality in agriculture published as a water science and engineering paper 4001*. Oakland, CA, USA: Department of Water Science and Engineering, University of California.

Eaton, A. D., Clesceri, L. S., Greenberg, A. E., and Franson, M. A. H. (1995). *APHA. AWWA, WEF, Standard methods for the examination of water and wastewater*. 19th edn. Washington, DC, USA: APHA.

Edet, A. E., and Offiong, O. E. (2002). Evaluation of water quality pollution indices for heavy metal contamination monitoring: A study case from akpabuyo-odukpani area, lower cross river basin (southeastern Nigeria). *Geol. J.* 57, 295–304. doi:10.1023/b:gejo.0000007250.92458.de

Egbueri, J. C., Igwe, O., Omeka, M. E., and Agbasi, J. C. (2023). Development of MLR and variedly optimized ANN models for forecasting the detachability and liquefaction potential index of erodible soils. *Geosystems Geoenvironment* 2 (1), 100104. doi:10.1016/j.geogeo.2022.100104

Egbueri, J. C., Unigwe, C. O., Omeka, M. E., and Ayejoto, D. A. (2021). Urban groundwater quality assessment using pollution indicators and multivariate statistical tools: A case study in southeast Nigeria. *Int. J. Environ. Anal. Chem.* doi:10.1080/03067319.2021.1907359

FAO (2003). *Unlocking the water potential of agriculture. Food and agriculture organization of the united nations*. Rome: FAO.

Fetter, C. W. (2018). *Applied hydrogeology*. Long Grove, IL, USA: Waveland Press.

Gaikwad, S. K., Kadam, A. K., Ramgir, R. R., Kashikar, A. S., Wagh, V. M., Kandekar, A. M., et al. (2020). Assessment of the groundwater geochemistry from a part of west coast of India using statistical methods and water quality index. *HydroResearch* 3, 48–60. doi:10.1016/j.hydres.2020.04.001

Igwe, O., and Omeka, M. E. (2021). Hydrogeochemical and pollution assessment of water resources within a mining area, SE Nigeria, using an integrated approach. *Int. J. Energy Water Resour.* 2021, 1–22. doi:10.1007/s42108-021-00128-2

Kadam, A., Wagh, V., Jacobs, J., Patil, S., Pawar, N., Umrikar, B., et al. (2022). Integrated approach for the evaluation of groundwater quality through hydro geochemistry and human health risk from Shivganga river basin, Pune, Maharashtra, India. *Environ. Sci. Pollut. Res.* 29 (3), 4311–4333. doi:10.1007/s11356-021-15554-2

Kaiser, H. F. (1960). The application of electronic computers to factor analysis. *Educ. Psychol. Meas.* 20, 141–151. doi:10.1177/001316446002000116

Kotecha, P. V., Patel, S. V., Bhalani, K. D., Shah, D., Shah, V. S., and Mehta, K. G. (2012). Prevalence of dental fluorosis & dental caries in association with high levels of drinking water fluoride content in a district of Gujarat, India. *Indian J. Med. Res.* 135, 873–877.

Krishna-Kumar, S., Bharani, R., Magesh, N. S., Godson, P. S., and Chandrasekar, N. (2014). Hydrogeochemistry and groundwater quality appraisal of part of south Chennai coastal aquifers, Tamil Nadu, India using WQI and fuzzy logic method. *Appl. Water Sci.* 4, 341–350. doi:10.1007/s13201-013-0148-4

Kumar, R., Qureshi, M., Vishwakarma, D. K., Al-Ansari, N., Kuriqi, A., Elbeltagi, A., et al. (2022). A review on emerging water contaminants and the application of sustainable removal technologies. *Case Stud. Chem. Environ. Eng.* 6, 100219. doi:10.1016/j.cscee.2022.100219

Kumar, S. K., Rammohan, V., Sahayam, J. D., and Jeevanandam, J. (2009). Assessment of groundwater quality and hydrogeochemistry of Manimuktha River basin, Tamil Nadu, India. *Environ. Monit. Assess.* 159, 341–351. doi:10.1007/s10661-008-0633-7

Langenegger, O. (1990). *Groundwater quality in rural areas of western Africa, UNDP project INT/81/026*, 10.

Liu, R., Zhu, H., Liu, F., Dong, Y., and El-Wardany, R. M. (2021). Current situation and human health risk assessment of fluoride enrichment in groundwater in the loess plateau: A case study of dali county, shaanxi province, China. *China Geol.* 4, 492–502. doi:10.31035/cg2021051

McGowan, W. (2000). *Water processing: Residential, commercial, light-industrial*. third ed. Lisle: Water Quality Association.

Mirzabeygi, M., Yousef, N., Abbasnia, A., Youzi, H., Alikhani, M., and Mahvi, A. H. (2017). Evaluation of groundwater quality and assessment of scaling potential and corrosiveness of water supply networks, Iran. *J. Water Supply Resour. Technol.* 66 (6), 416–425. doi:10.2166/aqua.2017.128

Mohammed, M. M., Murad, A., and Chowdhury, R. (2017). Evaluation of groundwater quality in the eastern district of abu Dhabi Emirate, UAE. *Bull. Environ. Contam. Toxicol.* 98, 1–7. doi:10.1007/s00128-016-2017-y

Mumtaz, N., Pandey, G., and Labhasetwar, P. K. (2015). Global fluoride occurrence, available technologies for fluoride removal and electrolytic deflluoridation: A review. *Crit. Rev. Environ. Sci. Technol.* 2015, 1046768. doi:10.1080/10643389.2015.1046768

National Research Council (NRC) (2001). *National research Council*. Washington, DC: National Academics Press.

Obasi, P. N., and Akudinobi, B. B. (2020). Potential health risk and levels of heavy metals in water resources of lead–zinc mining communities of Abakaliki, southeast Nigeria. *Appl. Water Sci.* 10, 184. doi:10.1007/s13201-020-01233-z

Okamkpa, J. R., Omeka, M. E., Igwe, O., and Iyiokwu, M. U. (2022). An integrated geochemical and spatiotemporal assessment of groundwater resources within an industrial suburb, Southeastern Nigeria. *Int. J. Energy Water Resour.* 2022, 1–20. doi:10.1007/s42108-022-00183-3

Omeka, M. E. (2023). Evaluation and prediction of irrigation water quality of an agricultural district, SE Nigeria: An integrated heuristic GIS-based and machine learning approach. *Environ. Sci. Pollut. Res.* doi:10.1007/s11356-022-25119-6

Omeka, M. E., and Egbueri, J. C. (2022). Hydrogeochemical assessment and health-related risks due to toxic element ingestion and dermal contact within the Nnewi-Awka urban areas, Nigeria. *Environ. Geochem. health* 2022, 1–29. doi:10.1007/s10653-022-01332-7

Omeka, M. E., Egbueri, J. C., and Unigwe, C. O. (2022b). Investigating the hydrogeochemistry, corrosivity, and scaling tendencies of groundwater in an agrarian area (Nigeria) using graphical, indexical, and statistical modeling. *Arabian J. Geosciences* 15 (13), 1–24. doi:10.1007/s12517-022-10514-7

Omeka, M. E., and Igwe, O. (2021). Heavy metals concentration in soils and crop plants within the vicinity of abandoned mine sites in Nigeria: An integrated indexical and chemometric approach. *Int. J. Environ. Anal. Chem.* 2021, 1–19. doi:10.1080/03067319.2021.1922683

Omeka, M. E., Igwe, O., Onwuka, O. S., Nwodo, O. M., Ugar, S. I., Undiandeye, P. A., et al. (2023). Efficacy of GIS-based AHP and data-driven intelligent machine learning algorithms for irrigation water quality prediction in an agricultural-mine district within the Lower Benue Trough, Nigeria. *Environ. Sci. Pollut. Res.* doi:10.1007/s11356-023-25291-3

Omeka, M. E., Igwe, O., and Unigwe, C. O. (2022a). An integrated approach to the bioavailability, ecological, and health risk assessment of potentially toxic elements in soils within a barite mining area, SE Nigeria. *Environ. Monit. Assess.* 194 (3), 212–230. doi:10.1007/s10661-022-09856-2

Prasad, J. (2008). *Groundwater brochure of Firozabad district, Utter Pradesh. A.A.P '2007-2008'. 19*.

Qadir, M., and Oster, J. D. (2004). Crop and irrigation management strategies for saline-sodic soils and waters aimed at environmentally sustainable agriculture. *Sci. Total Environ.* 323, 1–19. doi:10.1016/j.scitotenv.2003.10.012

Raghunath, H. M. (1987). *Groundwater*. New Delhi: Wiley Eastern Ltd., 344–369.

Rahman, A., Mondal, N. C., and Tiwari, K. K. (2021). Anthropogenic nitrate in groundwater and its health risks in the View of background concentration in a semi-arid area of Rajasthan, India. *Sci. Rep.* 11, 9279. doi:10.1038/s41598-021-88600-1

Shahzad, A., Kumari, M., Kumar Gupta, S., Sinha, A., and Mishra, B. K. (2017). Investigation and mapping of fluoride-endemic areas and associated health risk—a case study of Agra, Uttar Pradesh, India. *Hum. Ecol. Risk Assess. An Int. J.* 23 (3), 590–604. doi:10.1080/10807039.2016.1255139

Shukla, S., Khan, R., Varshney, S. K., Ganguly, R., Amiri, V., Hussain, C. M., et al. (2022). Appraisal of groundwater chemistry, its suitability for crop productivity in Sonipat district and human health risk evaluation. *Hum. Ecol. Risk Assess. An Int. J.* 2022, 1–22. doi:10.1080/10807039.2022.2137779

Singh, G., Madhuri, S. R., and Arora, N. K. (2019). Integrated GIS-based modelling approach for irrigation water quality suitability zonation in parts of Satluj River Basin, Bist Doab region, North India. *Appl. Sci.* 1, 1438. doi:10.1007/s42452-019-1405-4

Sohrabi, N., Kalantari, N., Amiri, V., Saha, N., Berndtsson, R., Bhattacharya, P., et al. (2021). A probabilistic-deterministic analysis of human health risk related to the exposure to potentially toxic elements in groundwater of Urmia coastal aquifer (NW of Iran) with a special focus on arsenic speciation and temporal variation. *Stoch. Environ. Res. risk Assess.* 35 (7), 1509–1528.

Subba Rao, N. (2018). Groundwater quality from a part of Prakasam district, Andhra Pradesh, India. *Appl. Water Sci.* 80, 30. doi:10.1007/s13201-018-0665-2

Subba Rao, N. (2017). *Hydrogeology: Problems with solutions*. New Delhi: Prentice Hall of India.

Subba Rao, N. (2012). Pig: A numerical index for dissemination of groundwater contamination zones. *Hydrol. Process.* 26 (22), 3344–3350. doi:10.1002/hyp.8456

Todd, D. K., and Mays, L. W. (2005). *Groundwater hydrology*. Hoboken: Wiley, 636.

Tüzen, M. (2003). Determination of heavy metals in soil, mushroom, and plant samples by atomic absorption spectrometry. *Microchem. J.* 74 (3), 289–297. doi:10.1016/s0026-265x(03)00035-3

Ukah, B. U., Egbueri, J. C., Unigwe, C. O., and Ubido, O. E. (2019). The extent of heavy metals pollution and health risk assessment of groundwater in a densely populated industrial area, Lagos, Nigeria. *Int. J. Energy Water Resour.* 3, 291. doi:10.1007/s42108-019-00039-3

Unigwe, C. O., Egbueri, J. C., and Omeka, M. E. (2022a). Geospatial and statistical approaches to nitrate health risk and groundwater quality assessment of an alluvial aquifer in SE Nigeria for drinking and irrigation purposes. *J. Indian Chem. Soc.* 2022, 100479. doi:10.1016/j.jics.2022.100479

Unigwe, C. O., Igwe, O., Onwuka, O. S., Egbueri, J. C., and Omeka, M. E. (2022b). Roles of hydro-geotechnical and slope stability characteristics in the erosion of Ajali and Nanka geologic formations in southeastern Nigeria. *Arab. J. Geosci.* 15, 1492. doi:10.1007/s12517-022-10771-6

US-EPA (US Environmental Protection Agency) (2017). National recommended water quality criteria-aquatic life criteria table and human health criteria table. Available at: https://www.epa.gov.wqc/nationalrecommended-water-quality-criteria-aquatic-life-criteria-table.

USEPA (1989). *Risk assessment guidance for Superfund, human health evaluation manual (Part A)*. Office of Emergency and Remedial Response, I. Washington, DC, USA: USEPA.

USSL (1954). *Diagnosis and improvement of saline and alkaline soils*. Agriculture Handbook No. 60 USDA. Guangzhou: USSL, 160.

Wagh, V., Mukate, S., Muley, A., Kadam, A., Panaskar, D., and Varade, A. (2020). Study of groundwater contamination and drinking suitability in basaltic terrain of Maharashtra, India through PIG and multivariate statistical techniques. *J. Water Supply Res. Technology-Aqua* 69 (4), 398–414. doi:10.2166/aqua.2020.108

Wang, F., Yang, H., Zhang, Y., Wang, S., Liu, K., Qi, Z., et al. (2022). Solute geochemistry and water quality assessment of groundwater in an arid endorheic watershed on Tibetan plateau. *Sustain. Switz.* 14. doi:10.3390/su142315593

Wang, Z., Wang, L. J., Shen, J. S., Nie, Z. L., Meng, L. Q., Cao, L., et al. (2021). Groundwater characteristics and climate and ecological evolution in the Badain Jaran Desert in the southwest Mongolian Plateau. *China Geol.* 4, 422–433. doi:10.31035/cg2021056

World Health Organization (WHO) (2017). *Guidelines for drinking water quality*. 3rd ed. Geneva: World Health Organization.

Xiao, Y., Hao, Q., Zhang, Y., Zhu, Y., Yin, S., Qin, L., et al. (2022b). Investigating sources, driving forces and potential health risks of nitrate and fluoride in groundwater of a typical alluvial fan plain. *Sci. Total Environ.* 802, 149909. doi:10.1016/j.scitotenv.2021.149909

Xiao, Y., Liu, K., Hao, Q., Li, Y., Xiao, D., and Zhang, Y. (2022c). Occurrence, controlling factors and health hazards of fluoride-enriched groundwater in the lower flood plain of Yellow River, Northern China. *Expo. Health* 14, 345–358. doi:10.1007/s12403-021-00452-2

Xiao, Y., Liu, K., Hao, Q., Xiao, D., Zhu, Y., Yin, S., et al. (2022a). Hydrogeochemical insights into the signatures, Genesis and sustainable perspective of nitrate enriched groundwater in the piedmont of Hutuo watershed, China. *Catena (Amst)* 212, 106020. doi:10.1016/j.catena.2022.106020

Xiao, Y., Liu, K., Yan, H., Zhou, B., Huang, X., Hao, Q., et al. (2021). Hydrogeochemical constraints on groundwater resource sustainable development in the arid Golmud alluvial fan plain on Tibetan plateau. *Environ. Earth Sci.* 80. doi:10.1007/s12665-021-10076-z

Yildiz, S., and Karakuş, C. B. (2019). Estimation of irrigation water quality index with development of an optimum model: A case study. *Environ. Dev. Sustain.* 22 (5), 4771–4786. doi:10.1007/s10668-019-00405-5

Yousef, M., Ghoochani, M., and Mahvi, A. H. (2018). Health risk assessment to fluoride in drinking water of rural residents living in the Poldasht city, Northwest of Iran. *Ecotoxicol. Environ. Saf.* 148, 426–430. doi:10.1016/j.ecoenv.2017.10.057

Frontiers in
Environmental Science

Explores the anthropogenic impact on our natural world

An innovative journal that advances knowledge of the natural world and its intersections with human society. It supports the formulation of policies that lead to a more inhabitable and sustainable world.

Discover the latest Research Topics

See more →

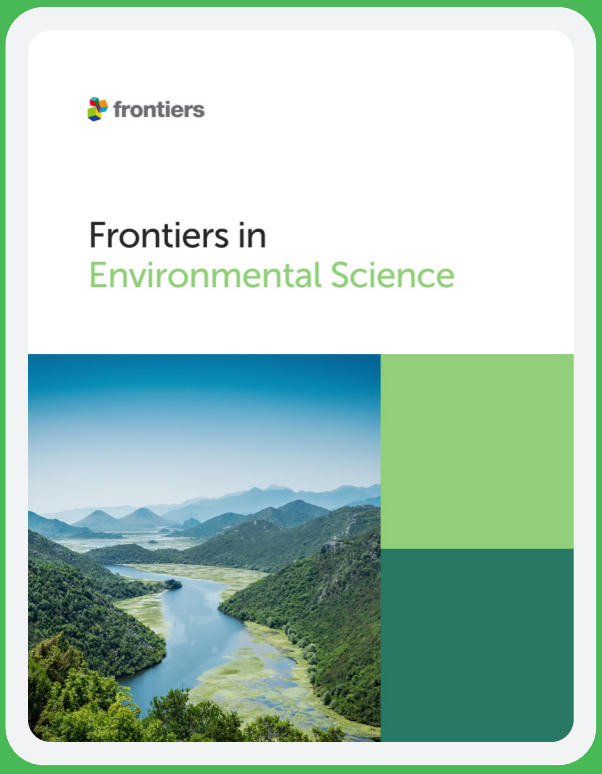

Frontiers

Avenue du Tribunal-Fédéral 34
1005 Lausanne, Switzerland
frontiersin.org

Contact us

+41 (0)21 510 17 00
frontiersin.org/about/contact